University of Oxford

Department of Chemistry



Unsymmetrical Group 4 Permethylindenyl *Ansa*-Metallocenes as Polymerisation Catalysts

Jessica Victoria Lamb

Balliol College

Hilary 2019

This thesis is submitted in partial fulfilment of the requirement for the degree of Doctor of Philosophy at the University of Oxford

Preface

The work described in this thesis was carried out in the Chemistry Research Laboratory at the University of Oxford between October 2015 and April 2019 under the supervision of Professor Dermot O'Hare. All the work was performed by the author unless otherwise stated, and no part has been previously submitted for any other degree.

Jessica Victoria Lamb

Balliol College

April 2019

The work contained in this thesis has been published in the following journal papers:

1. J. V. Lamb, J.-C. Buffet, Z. R. Turner and D. O'Hare, *Polym. Chem.*, 2019, **10**, 1386-1398.
2. J. V. Lamb, J.-C. Buffet, J. E. Matley, C. M. R. Wright, Z. R. Turner and D. O'Hare, *Dalton Trans.*, 2019, **48**, 2510-2520.

The work is also covered under the following patent:

1. D. O'Hare, J.-C. Buffet, J. Lamb, T. Khamnaen, M. Charernsuk, T. Parawan and S. Charoenchaidet, "*Unsymmetrical Metallocene Catalysts and Uses Thereof*", WO 2017194943 A1.

Abstract

Unsymmetrical Group 4 Permethylindenyl *Ansa*-Metallocenes as Polymerisation Catalysts

Jessica V. Lamb **D.Phil. Thesis**

Balliol College **Hilary Term 2019**

The primary aims of the thesis were to: (i) discover catalyst systems that maintained high α-olefin polymerisation activities in the presence of hydrogen while producing polymers with low molecular weights (M_w <10 kg mol^{-1}) and (ii) find new single-site initiators for the ring-opening polymerisation (ROP) of lactide monomers.

The thesis begins by offering a brief introduction to α-olefin and lactide polymerisation, including discussions on known polymerisation catalysts. The synthesis and characterisation of a series of well-defined group 4 *ansa*-bridged permethylindenyl complexes based on the ^{Me_2}SB(Cp^R,I*)ZrX(Y) ({(η^5-C$_9$Me$_6$)Me$_2$Si(η^5-C$_5$H$_3$R)}ZrX(Y) where R = H, Me and ^{n}Bu) motif is then discussed. The application of these complexes as α-olefin polymerisation catalysts, both in solution-phase and when immobilised on a range of inorganic solid supports (MAO modified silica, MAO modified layered double hydroxide and solid MAO) is then detailed. It was found that solid MAO supported catalytic systems exhibited some of the highest slurry-phase polymerisation activities reported in the literature. The systems produced HDPE with minimal branching, uniform polymer morphology and low polymer molecular weights (M_w <100 kg mol^{-1} at 80 °C). A variety of polymerisation conditions were studied, including the effects of temperature, scale, pressure, scavenger, catalyst loading and time.

The slurry-phase ethylene/1-hexene copolymerisation ability of the catalysts is then demonstrated. The effects of hydrogen on ethylene polymerisation activity and polymer properties are also discussed. The overall effect of 1-hexene was found to depend on the identity of the catalyst and the amount of co-monomer in the system. All catalysts demonstrated remarkable stability in the presence of hydrogen, which was accompanied by a significant decrease in polymer molecular weights to produce commercially viable polyethylene waxes.

Finally, four unsymmetrical permethylindenyl zirconocenes are presented as initiators for the ROP of *L*-, *D*- and *rac*-lactide. The kinetics of polymerisation, overall rate equations and the effects of temperature, initiator concentration, scale and co-initiator concentration are discussed. A variety of techniques were used to characterise the polymers in order to deduce tacticity, molecular weights and chain end groups.

Acknowledgements

Firstly, I would like to thank my supervisor Professor Dermot O'Hare for giving me the opportunity to study within his research group, and for all his help and advice throughout my D.Phil. Secondly, I am grateful to SCG Chemicals Co., Ltd. (Thailand) for their financial support, which has not only permitted me to undertake this project but has also facilitated travel to present my work at national and international conferences and to visit SCG Chemicals Co., Ltd. in Thailand.

A huge thank you goes to JC and Zoë; I would not have progressed as far in my research without your guidance and advice. Your help has been enormously appreciated and I have learnt a great amount over the past few years due to your patient support and tuition. I am also very grateful to the rest of the O'Hare group, both past and present, who have made the past few years so enjoyable. Whether it was watching the office area turn into a sports recovery zone, Katarina's amazing baking, visiting Thailand with Duncan and Tom, the well-deserved trips to the pub, actually helping each other every once in a while, and all laughs and jokes in between.

Thanks also goes to the people who have helped with some of the chemistry; Nick for SSNMR, Zoë for single-crystal X-ray diffraction, Duncan and Chris for PLA GPC, Norner AS (Norway) for PE and PP GPC and large scale testing, HTExplore (University of Naples) for high-throughput studies and SCG Chemicals Co., Ltd. (Thailand) for large-scale catalyst testing. I am also grateful to everyone who found the time to proof-read this thesis; your suggestions have been invaluable.

Outside of the lab, I want to thank all the people at Balliol who have contributed to some amazing memories, both at fancy dinners and while relaxing around the manor.

An extra special thank you also goes to Rach; the hours on Skype and multiple weekend visits over the past four years have provided a welcome break from the Oxford bubble. I also want to thank Matthew for always being by my side and for the many great experiences and adventures we have shared together. Finally, I am forever grateful to my family for their continuous help, support and encouragement throughout the years. I would not be where I am today without them.

Nomenclature

Below is a summary of some of the commonly used terms throughout the thesis.

Term	Definition
$\{^1H\}$	Proton decoupled
Å	Ångström, 10^{-10} m
acac	Acetylacetonate, $CH_3COCHCOCH_3$
α	Ring tilt angle
AMO-LDH	Aqueous miscible organic layered double hydroxide
AMOST	Aqueous miscible organic solvent treatment
b	Broad
BDI	β-diketiminato
$BnNH_2$	Benzylamine, $C_6H_5CH_2NH_2$
BnOH	Benzyl alcohol, $C_6H_5CH_2OH$
CEF	Crystallisation elution fractionation
cent	Centroid
CGC	Constrained geometry catalyst
COSY	2D correlation spectroscopy
Cp	Cyclopentadienyl, C_5H_5
Cp*	Pentamethylcyclopentadienyl, C_5Me_5
CP/MAS	Cross-polarisation magic-angle spinning
d	Doublet
DBP-H	Di-tert-butylphenol, 2,4-^{t}Bu-C_6H_3OH
DCTB	*Trans*-2-[3-(4-*tert*-Butylphenyl)-2-methyl-2-propenylidene]malononitrile, $C_{17}H_{18}N_2$
DEPT	Distortionless enhancement by polarisation transfer

DHB	2,5-Dihydroxybenzoic acid, $(HO)_2C_6H_3CO_2H$
DME	Dimethoxyethane, $CH_3OCH_2CH_2OCH_3$
DP/MAS	Direct polarisation magic angle spinning
DSC	Differential scanning calorimetry
δ	Chemical shift
δ	Angle about the metal centre
$\Delta H^{\ddagger}$	Enthalpy of activation
ΔH_c	Enthalpy of crystallisation
ΔH_m	Enthalpy of melting
$\Delta S\ddagger$	Entropy of activation
EBI	Ethylenebis(1-indenyl), $C_9H_6(CH_2CH_2)C_9H_6$
EBI*	Ethylenebis(permethylindenyl), $C_9Me_6(CH_2CH_2)C_9Me_6$
η	Hapticity
Flu	Fluorenyl, $C_{13}H_9$
FTIR	Fourier transform infrared
GPC	Gel permeation chromatography
HDPE	High-density polyethylene
HMBC	Heteronuclear multiple bond correlation
I	Indenyl, C_9H_7
I*	Permethylindenyl, C_9Me_7
Ind	Indenyl, C_9H_7
$Ind^{\#}$	Hexamethyl indenyl ligand, C_9Me_6H
Ind*	Permethylindenyl, C_9Me_7
^{i}Pr	Isopropyl, $CHMe_2$
IR	Infrared
k_{obs}	Observed rate constant

k_p	Propagation rate constant
KTFA	Potassium trifluoroacetate, $KO_2C_2F_3$
LA	Lactide
LDH	Layered double hydroxide
LDHMAO	Methyaluminoxane modified layered double hydroxide
LDPE	Low-density polyethylene
m	Multiplet
MALDI-TOF	Matrix-assisted laser desorption/ionisation time of flight
MAO	Methylaluminoxane
Me	Methyl, CH_3
^{Me_2}CB	Dimethyl carbon bridge (isopropylidene bridge), CMe_2
^{Me_2}SB	Dimethylsilyl bridge, $SiMe_2$
^{Me_2}SBI	Dimethylsilylbis(1-indenyl), $C_9H_6(SiMe_2)C_9H_6$
^{Me_2}SBI*	dimethylsilylbis(hexamethyl-1-indenyl), $C_9Me_6(SiMe_2)C_9Me_6$
^{Me_4}DSB	Tetramethyldisilyl bridge, Si_2Me_4
M_n	Number average molecular weight
MS	Mass spectrometry
M_w	Weight average molecular weight
MWD	Molecular weight distribution, M_w/M_n
μ	Bridging
^{n}Bu	*n*-butyl, $CH_2CH_2CH_2CH_3$
NMR	Nuclear magnetic resonance
PDLA	Poly-*D*-lactide
PE	Polyethylene
PFP	Pentafluorophenol, C_6F_5OH
Ph	Phenyl, C_6H_5

PLA	Polylactide
PLLA	Poly-*L*-lactide
P_m	Probability of forming a *meso* linkage
Pn*	Permethylpentalene, C_8Me_6
PP	Polypropylene
P_r	Probability of forming a *racemic* linkage
q	Quartet
ROESY	Rotating-frame nuclear Overhauser effect spectroscopy
ROP	Ring-opening polymerisation
RT	Room temperature
s	Singlet
SEM	Scanning electron microscopy
SHC	Supported homogeneous catalysis
sMAO	Solid polymethylaluminoxane
sMAO(1G)	First-generation solid polymethylaluminoxane
sMAO(3G)	Third-generation solid polymethylaluminoxane
sMAO(GAS)	Gas phase solid polymethylaluminoxane
sMAO(PFP)	Third-generation solid polymethylaluminoxane modified with pentafluorophenol at 40 wt%
SOMC	Surface organometallic chemistry
SSMAO	Methylaluminoxane modified silica
SSNMR	Solid-state nuclear magnetic resonance
t	Triplet
^tBu	*Tert*-butyl, CMe_3
T_c	Crystallisation temperature
TEA	Triethylaluminium, $Al(CH_2Me)_3$
$T_{el,max.}$	Temperature at maximum elution

T_g	Glass transition temperature
THF	Tetrahydrofuran, C_4H_8O
TiBA	Triisobutylaluminium, Al^iBu_3
T_m	Melting temperature
TMA	Trimethylaluminium, $AlMe_3$
ULMWPE	Ultra-low molecular weight polyethylene
XRD	X-ray diffraction

Complex Identification

Number	Name	Symbol
1	^{Me_2}SB(Cp,I*)ZrCl$_2$	Square
2	^{Me_2}SB(Cp,I*)ZrBr$_2$	Sphere
3	^{Me_2}SB(Cp^{Me},I*)ZrCl$_2$	Triangle
4	^{Me_2}SB(Cp^{Me},I*)ZrBr$_2$	Hexagon
***E*-5**	*E*-^{Me_2}SB(Cp$^{n\text{Bu}}$,I*)ZrCl$_2$	Pentagon
***Z*-5**	*Z*-^{Me_2}SB(Cp$^{n\text{Bu}}$,I*)ZrCl$_2$	Star
6	^{Me_2}SB(Cp,I*)Zr(CH$_2$Ph)$_2$	Diamond
7	^{Me_2}SB(Cp^{Me},I*)Zr(CH$_2$Ph)$_2$	Down Triangle
8	^{Me_2}SB(Cp,I*)ZrMe$_2$	Left Triangle
9	^{Me_2}SB(Cp^{Me},I*)ZrMe$_2$	Ring
***Z*-10**	*Z*-^{Me_2}SB(Cp,I*)ZrCl(O-2,6-Me-C$_6$H$_3$)	Circle
***E*-11**	*E*-^{Me_2}SB(Cp,I*)ZrCl(O-2,6-^{i}Pr-C$_6$H$_3$)	Right Triangle

Table of Contents

Chapter 1 - Introduction **1**

1.1 Overview **1**

1.2 Homogeneous α-Olefin Polymerisation **2**

1.2.1 Group 4 metallocene catalysts for α-olefin polymerisation 2

1.2.2 Polymer tacticity 4

1.2.3 The co-catalyst role 6

1.2.4 Hydrogen effects on ethylene polymerisation 9

1.2.5 Ethylene and α-olefin copolymerisation 11

1.3 Heterogeneous α-Olefin Polymerisation **13**

1.3.1 Heterogeneous catalysts 13

1.3.2 Silica 15

1.3.3 Clays and layered double hydroxides 16

1.3.4 Solid polymethylaluminoxane 18

1.3.5 Templating effect of the solid support 20

1.3.6 Role of the scavenger 21

1.4 Ring-Opening Polymerisation of Lactide **23**

1.4.1 Biodegradable polymers 23

1.4.2 Structure of PLA 23

1.4.3 Mechanism of lactide polymerisation 25

1.4.4 Initiators for the ROP of lactide 27

1.4.5 Stereochemical control 32

1.4.6 Polymer tacticity 34

1.5 Scope of the Thesis **36**

1.6 References **37**

Chapter 2 - Synthesis and Characterisation of $^{Me_2}SB(Cp^R,I^*)ZrX(Y)$ **46**

2.1 Introduction **46**

2.1.1 Overview 46

2.1.2 Definitions of geometric parameters 47

2.2 Synthesis of $^{Me_2}SB(Cp^R,I^*)ZrX_2$ (R = H, Me, ^{n}Bu; X = Cl , Br) **48**

2.2.1 NMR spectroscopy 49

2.2.2 X-ray crystallography 54
2.3 Synthesis of ^{Me_2}SB(Cp^{R},I*)ZrX$_2$ (R = H, Me; X = Me, CH$_2$Ph) 61
2.3.1 NMR spectroscopy 62
2.3.2 X-ray crystallography 67
2.3.3 Synthesis of [^{Me_2}SB(Cp,I*)ZrMe]$^+$ [X-MAO]$^-$ 69
2.4 Synthesis of ^{Me_2}SB(Cp,I*)ZrCl(O-2,6-R-C$_6$H$_3$) (R = Me, ^{i}Pr) 71
2.4.1 NMR spectroscopy 71
2.4.2 X-ray crystallography 76
2.5 Conclusions 79
2.6 References 80
Chapter 3 - Olefin Polymerisation 82
3.1 Introduction 82
3.1.1 Overview 82
3.1.2 Gel permeation chromatography (GPC) 83
3.2 Homogeneous Polymerisation 84
3.2.1 Propylene polymerisation 84
3.2.2 Ethylene polymerisation 86
3.3 Slurry-Phase Ethylene Polymerisation 88
3.3.1 Support morphology 89
3.3.2 Complex immobilisation 90
3.3.3 Catalyst characterisation 90
3.3.4 Slurry-phase ethylene polymerisation 92
3.3.5 Polymer characterisation 96
3.4 Solid MAO Support Variation 101
3.4.1 Support morphology 102
3.4.2 Complex immobilisation 103
3.4.3 Catalyst characterisation 104
3.4.4 Slurry-phase ethylene polymerisation 105
3.4.5 Polymer characterisation 108
3.4.6 Scale increase 111
3.5 sMAO(1G) Polymerisation 115
3.5.1 Slurry-phase ethylene polymerisation 116
3.5.2 Polymer characterisation 124
3.5.3 Conditions variation 130

3.6 Conclusions **138**
3.7 References **140**
Chapter 4 - Ethylene/1 Hexene Copolymerisation and Hydrogen Response **144**
4.1 Introduction **144**
4.1.1 Overview 144
4.1.2 High-throughput screening 145
4.2 Ethylene/1-Hexene Copolymerisation **146**
4.2.1 Slurry-phase ethylene/1-hexene copolymerisation 146
4.2.2 High-throughput ethylene/1-hexene copolymerisation 150
4.2.3 Large scale copolymerisation studies 154
4.3 Ethylene/Hydrogen Homopolymerisation **157**
4.3.1 Slurry-phase ethylene/hydrogen homopolymerisation 157
4.3.2 High-throughput ethylene/hydrogen polymerisation 159
4.3.3 Large scale ethylene/hydrogen homopolymerisation 162
4.3.4 Solution-phase ethylene/hydrogen homopolymerisation 165
4.4 Ethylene/1-Hexene/Hydrogen Copolymerisation **168**
4.4.1 Slurry-phase ethylene/1-hexene/hydrogen copolymerisation 168
4.4.2 High-throughput ethylene/1-hexene/hydrogen copolymerisation 169
4.4.3 Large scale ethylene/1-hexene/hydrogen copolymerisation 171
4.5 Conclusions **173**
4.6 References **175**
Chapter 5 - Ring-Opening Polymerisation of *L*- , *D*- and *rac*-Lactide **177**
5.1 Introduction **177**
5.1.1 Overview 177
5.2 ROP of Lactide **178**
5.2.1 Monomer variation 178
5.2.1.1 ROP of *L*-lactide 179
5.2.1.2 ROP of *D*-lactide 187
5.2.1.3 ROP of *rac*-lactide 191
5.2.2 Scale dependency 196
5.2.3 Co-initiator concentration dependency 199
5.2.4 Initiator concentration dependency 202
5.2.5 Temperature variation 205
5.2.6 Solvent variation 207

5.3 Conclusions **208**
5.4 References **210**
Chapter 6 - Experimental **212**
6.1 General Details **212**
6.1.1 Air- and moisture-sensitive compounds 212
6.1.2 Commercially supplied reagents 212
6.1.3 Synthesis of literature compounds 213
6.1.4 Solvent preparation 213
6.1.5 Solution nuclear magnetic resonance (NMR) spectroscopy 214
6.1.6 Solid-state nuclear magnetic resonance (NMR) spectroscopy 214
6.1.7 Elemental analysis (EA) 215
6.1.8 Fourier transform infrared (FTIR) spectroscopy 215
6.1.9 Mass spectrometry (MS) 215
6.1.10 Single crystal X-ray diffraction (XRD) 215
6.1.11 Scanning electron microscopy (SEM) 216
6.1.12 Differential scanning calorimetry (DSC) 216
6.2 Experimental Details for Chapter 2 ..... **217**
6.2.1 Synthesis of Ind*$SiMe_2Cl$ 217
6.2.2 Synthesis of $^{Me_2}SB(Cp,I^*)Li_2$ 217
6.2.3 Synthesis of $^{Me_2}SB(Cp,I^*)ZrCl_2$ (1) 218
6.2.4 Synthesis of $^{Me_2}SB(Cp,I^*)ZrBr_2$ (2) 219
6.2.5 Synthesis of $^{Me_2}SB(Cp^{Me},I^*)Li_2$ 220
6.2.6 Synthesis of $^{Me_2}SB(Cp^{Me},I^*)ZrCl_2$ (3) 220
6.2.7 Synthesis of $^{Me_2}SB(Cp^{Me},I^*)ZrBr_2$ (4) 221
6.2.8 Synthesis of $^{Me_2}SB(Cp^{nBu},I^*)Li_2$ 223
6.2.9 Synthesis of $^{Me_2}SB(Cp^{nBu},I^*)ZrCl_2$ (5) 223
6.2.10 Synthesis of $^{Me_2}SB(Cp,I^*)Zr(CH_2Ph)_2$ (6) 225
6.2.11 Synthesis of $^{Me_2}SB(Cp^{Me},I^*)Zr(CH_2Ph)_2$ (7) 226
6.2.12 Synthesis of $^{Me_2}SB(Cp,I^*)ZrMe_2$ (8) 227
6.2.13 Synthesis of $^{Me_2}SB(Cp^{Me},I^*)ZrMe_2$ (9) 228
6.2.14 Synthesis of $[^{Me_2}SB(Cp,I^*)ZrMe]^+$ $[X\text{-}MAO]^-$ 229
6.2.15 Synthesis of *Z*-$^{Me_2}SB(Cp,I^*)ZrCl(O\text{-}2,6\text{-}Me\text{-}C_6H_3)$ (*Z*-10) 229
6.2.16 Synthesis of *E*-$^{Me_2}SB(Cp,I^*)ZrCl(O\text{-}2,6\text{-}^{i}Pr\text{-}C_6H_3)$ (*E*-11) 230

6.3 Experimental Details for Chapter 3 232
6.3.1 Solution-phase propylene polymerisation 232
6.3.2 Solution-phase ethylene polymerisation 232
6.3.3 Synthesis of activated supports (SSMAO and LDHMAO) 232
6.3.4 Synthesis of supported catalysts 233
6.3.5 Slurry-phase ethylene polymerisation 235
6.3.6 Larger scale slurry-phase ethylene polymerisation 235
6.3.7 Gel-permeation chromatography (GPC) 236
6.4 Experimental Details for Chapter 4 237
6.4.1 Ethylene/1-hexene and ethylene/1-hexene/hydrogen copolymerisation 237
6.4.2 Ethylene/hydrogen polymerisation 237
6.4.3 High throughput screening (HTExplore, University of Naples) 237
6.4.4 Large scale polymerisation (SCG Chemicals Co., Ltd. (Thailand)) 239
6.5 Experimental Details for Chapter 5 240
6.5.1 Lactide polymerisation 240
6.5.2 Larger scale lactide polymerisation 240
6.5.3 Gel-permeation chromatography (GPC) 241
6.5.4 MALDI-TOF mass spectrometry 241
6.6 References 242
Concluding Remarks 243
Appendix A-1
Chapter 2 ..... A-2
Chapter 3 ..... A-9
Chapter 4 ..... A-16
Chapter 5 ..... A-33
References A-48

Chapter 1

Introduction

1.1 Overview

Polyolefins dominate the polymer market and make up over 60% of all polymers produced; annual global production of polyethylene (PE) and polypropylene (PP) in excess of 100 and 80 million tonnes respectively.[1] Therefore, there is still a significant demand for the discovery of highly active olefin polymerisation catalysts which can selectively control polymer properties such as molecular weights, co-monomer incorporation and stereochemistry.[2] However, due to the high durability of polyolefins, their decomposition takes hundreds of years and the microplastics produced remain in the environment indefinitely.[3] Routes to alternative, biodegradable polymers, which can be broken down into smaller molecules (such as CO_2, CH_4 and H_2O) by microorganisms are therefore highly sought after.[4]

This chapter discusses some of the properties of group 4 homogeneous and heterogeneous α-olefin polymerisation catalysts; including how their structure and characteristics can affect polymerisation activity and polymer properties. It also gives a brief introduction to ring-opening polymerisation (ROP) routes to biodegradable polymers, such as polylactic acid (PLA), and how polymer properties can be controlled and determined.

1.2 Homogeneous α-Olefin Polymerisation

1.2.1 Group 4 metallocene catalysts for α-olefin polymerisation

Group 4 metallocenes (Cp_2MX_2) are d^0 organometallic compounds containing two η^5-cyclopentadienyl (C_5H_5, Cp) ligands and two σ-type ligands. Some of the earliest reported metallocene catalysts for homogeneous α-olefin polymerisation were titanocenes, such as Cp_2TiCl_2, in combination with alkyl aluminium co-catalysts such as diethylaluminium chloride and dimethylaluminium chloride.[5, 6] However, these species were found to be relatively poor catalysts for ethylene polymerisation. Utilising zirconium rather than titanium was found to produce very active α-olefin polymerisation catalysts in the presence of methylaluminoxane (MAO) co-catalyst.[7, 8] Kaminsky reported ethylene polymerisation activities up to 24360 $kg_{PE}\ mol_M^{-1}\ h^{-1}\ bar^{-1}$ using Cp_2ZrCl_2/MAO at 30 °C with 2.5 bar ethylene.[9] It is noted that catalyst activity is largely dependent on reaction conditions and the lack of standard methodology therefore makes direct comparisons challenging. Despite this, Gibson and co-workers collated data from a variety of sources in order to devise a scale of relative activity; according to their work, ethylene polymerisation catalysts with activities above 1000 $kg_{PE}\ mol_M^{-1}\ h^{-1}\ bar^{-1}$ are classed as having a very high activity.[10]

In comparison to traditional Ziegler-Natta catalysts,[11] metallocene catalysts provide a multitude of possibilities for synthesising and controlling the structure and properties of polymers.[12-14] The single-site nature of metallocene catalysts leads to the formation of a single type of active site, which results in polymers with unimodal molecular weight distributions.[15] Variation of the ancillary cyclopentadienyl ligands of Cp_2MX_2 species can influence polymerisation activity and polymer properties. The indenyl ligand (C_9H_7, Ind, I) is a common alternative to Cp. The enhanced ability of

indenyl to undergo an η^5-η^3 ring slip allows the metal to lose electrons in its valence shell without changing oxidation state,[16] which often results in increased substitution rates at the metal centre. *Ansa*-bridges between the two cyclopentadienyl substituents can be employed to prevent ligand rotation, which can then enforce complex rigidity and introduce chirality to the system.[17] This adaptability results in highly tuneable stereo-rigid metallocenes with a wide range of catalytic reactivity.[18-20] For example, bridged systems such as *rac*-EBIZrCl_2/MAO (where EBI is ethylenebis(1-indenyl)) and *rac*-^{Me_2}SBIZrCl_2/MAO (where ^{Me_2}SBI is dimethylsilylbis(1-indenyl)) demonstrate ethylene polymerisation activities of 20550 and 18450 $kg_{PE}\ mol_M^{-1}\ h^{-1}\ bar^{-1}$ respectively at 30 °C with 2 bar ethylene (Chart 1.1a and b).[16] The strain supplied by the *ansa*-bridge is determined by its geometric parameters, with a higher catalytic activity usually accompanying a wider dihedral angle between the planes of the two cyclopentadienyl rings and reduced steric bulk of the ligand.[17, 21] The bridges come in many forms including one atom silyl,[22-25] carbon[26-28] and tin,[29] two atom carbon,[30, 31] and longer bridges such as Si-O-Si.[32]

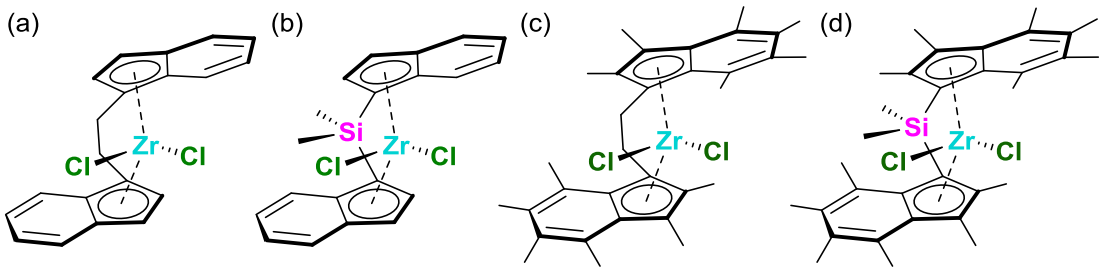


Chart 1.1 Structures of (a) *rac*-EBIZrCl_2,[17] (b) *rac*-^{Me_2}SBIZrCl_2,[17] (c) *rac*-EBI*ZrCl_2[33] and (d) *rac*-^{Me_2}SBI*ZrCl_2.[33, 34]

Permethylation of the indenyl ring affords the permethylindenyl ligand (C_9Me_7, Ind*, I*), which can lead to enhanced complex stability attributed to increased inductive donation and steric bulk around the metal centre.[35] Both ethyl- and silyl-bridged permethylindenyl zirconocene systems display promise as ethylene polymerisation

catalysts; *rac*-EBI*$ZrCl_2$/MAO (where EBI* is ethylenebis(hexamethylindenyl)) showed an activity of 61800 kg_{PE} mol_M^{-1} h^{-1} bar^{-1} at 70 °C with 10 bar ethylene and *rac*-^{Me_2}SBI*$ZrCl_2$/MAO (where ^{Me_2}SBI* is dimethylsilylbis(hexamethylindenyl)) showed an activity of 22622 kg_{PE} mol_M^{-1} h^{-1} bar^{-1} at 60 °C (Chart 1.1c and d).[33, 34]

An Ind*H derivative, the hexamethylindenyl ligand (C_9Me_6H, Ind$^{\#}$, I$^{\#}$),[36] is of particular interest as a synthetic precursor to *ansa*-bridged ligand frameworks, such as the silyl-bridged pro-ligand ^{Me_2}SBI*H_2 (Chart 1.2).[36] Recently, O'Hare and co-workers devised an optimised synthesis for the preparation of a permethylindenyl chlorosilane synthon, Ind*$SiMe_2Cl$,[37] opening up a pathway to unsymmetrical bridged systems.[38] Unsymmetrical systems offer further opportunities for control of polymer tacticity; symmetrical *rac*-EBI$ZrCl_2$MAO forms isotactic polypropylene,[39] while unsymmetrical ^{Me_2}CB(Cp,Flu)$HfCl_2$/MAO produces syndiotactic polypropylene (where ^{Me_2}CB is a dimethyl carbon bridge, and Flu is the fluorenyl ligand, $C_{13}H_9$).[40]

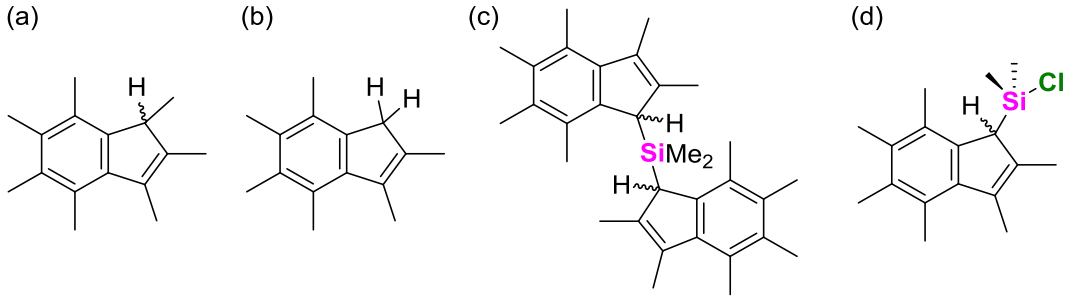


Chart 1.2 Pro-ligand structures of (a) Ind*H, (b) Ind$^{\#}$H,[36] (c) ^{Me_2}SBI*H_2[36] and (d) Ind*$SiMe_2Cl$.[37]

1.2.2 Polymer tacticity

The identity of the metallocene ligands, in addition to the symmetry of the catalyst, can alter the α-olefin polymerisation activity of metallocene catalysts and determine the resultant polymer stereochemistry.[12] Unlike ethylene, the monomers of higher α-olefins, such as propylene, can coordinate and insert into transition metal-carbon bonds in

different orientations and therefore produce polymers with different tacticities. There are two main pathways for controlling polymer tacticity; enantiomorphic and chain-end site control (i.e. whether the stereochemistry and ligand environment of the active metal site, or whether the orientation of the previously inserted monomer determines the configuration of the next inserted monomer).[12]

In the majority of cases, 'Ewen's Symmetry Rules' can predict polymer tacticity by considering the symmetry of the metal centre.[8, 12, 41-45] The rules predict that C_{2v}-symmetric catalysts such as $^{Me_2}SB(Flu)_2ZrCl_2$ will produce atactic polymers,[46] C_2-symmetric catalysts such as *rac*-$^{Me_2}SB(^{2\text{-}Me}Ind)_2ZrCl_2$ will form isotactic polymers,[47] achiral C_s-symmetric catalysts such as *meso*-$^{Me_2}SBIZrCl_2$ will produce atactic polymers,[48] prochiral C_s-symmetric catalysts such as $^{Me_2}CB(Cp,Flu)ZrCl_2$ will give syndiotactic polymers[40] and C_1-symmetric catalysts such as $^{Me_2}CB(Cp^{Me},Flu)ZrCl_2$ will produce hemi-isotactic polymers (Chart 1.3).[49] However, additional factors, such as the sterics of the catalyst system, can change the nature of the polymer produced. For example, C_1-symmetric $^{Me_2}CB(Cp^{Me},Flu)ZrCl_2$/MAO and $^{Me_2}CB(Cp^{tBu},Flu)ZrCl_2$/MAO produce hemi-isotactic and isotactic polypropylene respectively.[49, 50]

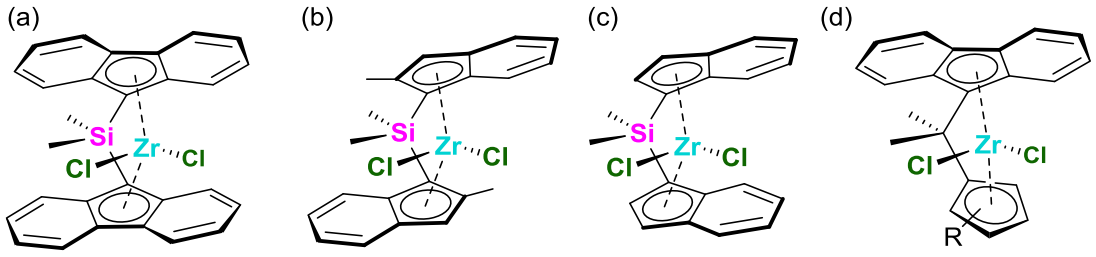


Chart 1.3 Structures of (a) $^{Me_2}SB(Flu)_2ZrCl_2$,[46] (b) *rac*-$^{Me_2}SB(^{2\text{-}Me}Ind)_2ZrCl_2$,[47] (c) *meso*-$^{Me_2}SBIZrCl_2$[48] and (d) $^{Me_2}CB(Cp^{R},Flu)ZrCl_2$ (R = Me and ^{t}Bu).[40, 49, 50]

1.2.3 The co-catalyst role

Kaminsky and co-workers were the first to discover that the addition of water to metallocene systems, such as Cp_2ZrMe_2 with trimethylaluminium (TMA) activator, caused ethylene polymerisation activities to increase due to the formation of a MAO-type species.[7] Since then, MAO has been found to be a highly efficient co-catalyst for homogeneous α-olefin polymerisation in a wide range of metallocene systems.[51-58]

MAO is the product of the partial hydrolysis of TMA and is composed of oligomeric $(Me_{\sim 1.5}AlO_{\sim 0.75})_n$ with significant amounts of TMA present as an inherent part of its composition.[59] Many possible MAO structures have been determined and studied computationally: linear,[60] cyclic,[59-61] cage,[59, 62, 63] and nanotube (Chart 1.4).[64, 65] It has been reported that cage-like structures of $(AlOMe)_n$ (n = 6–20) with accompanying free TMA,[62] and TMA capped AlOMe nanotubes with formula $(AlOMe)_n{\cdot}(AlMe_3)_m$ (n = 6–20 and m = 1–4) are the most stable.[64, 66] However, MAO is likely composed of a mixture of different structures, with the exact composition depending on the synthesis method, concentration and age.[20]

It has been observed that the abundance of $(AlOMe)_n{\cdot}(AlMe_3)_m$ nanotubes relative to $(AlOMe)_n$ cages (and free TMA) within the MAO composition decreases with an increase in temperature.[66] The shift in equilibrium between nanotubes and cages at higher temperatures may explain why the co-catalytic activity of MAO decreases as polymerisation temperature increases; $(AlOMe)_n{\cdot}(AlMe_3)_m$ nanotubes are expected to be the precursors for the active species in polymerisation, and the release of TMA into the MAO solution is predicted to poison polymerisation. For ethylene polymerisation using Cp_2ZrCl_2/MAO activity decreased from 778 to 33 $kg_{PE}\ mol_M^{-1}\ h^{-1}\ bar^{-1}$ at 50 °C

with 6 bar ethylene when MAO was heated at 20 and 250 °C respectively prior to polymerisation.[67]

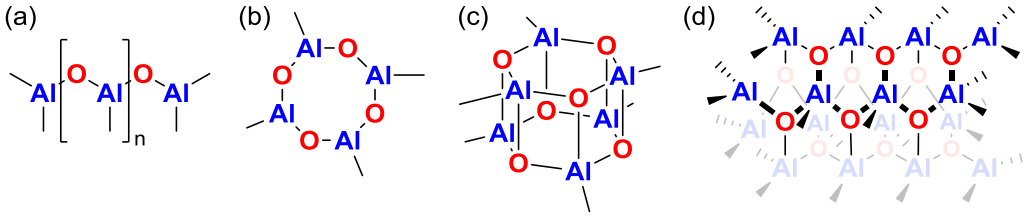
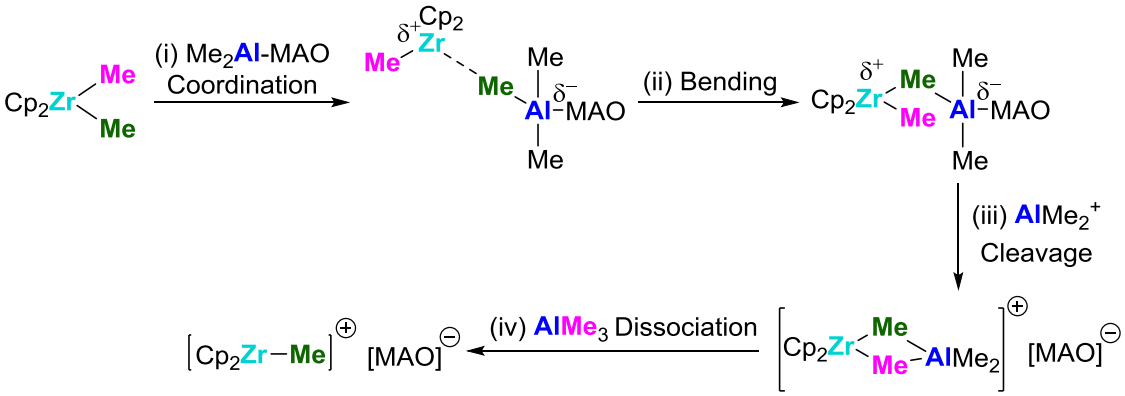


Chart 1.4 Proposed structures of MAO: (a) linear $(AlMeO)_n$,[60] (b) cyclic $(AlMeO)_4$,[59] (c) cage $(AlMeO)_6$[62] and (d) TMA capped nanotube $(AlOMe)_{12}\cdot(AlMe_3)_4$.[20, 65]

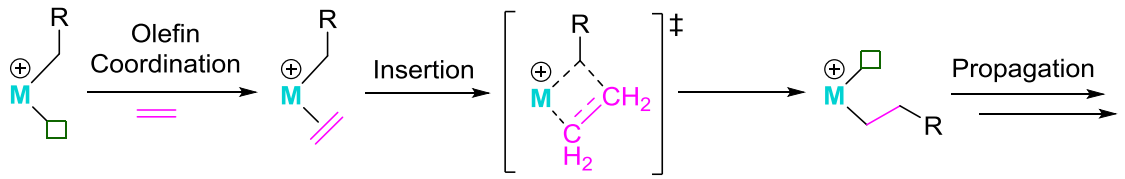
MAO is the most common activator used in homogeneous α-olefin polymerisation.[51-58] However, one of the main industrial disadvantages of homogeneous α-olefin polymerisation is the large excess of MAO required in order to achieve sufficiently high polymerisation activities (MAO content can be higher than $[Al_{MAO}]_0/[M]_0$ of 10000).[20] It is proposed that such a large excess is required due to the multiple roles of MAO during polymerisation: it methylates the metallocene, stabilises the active species and acts as a scavenger by removing traces of water, oxygen and other catalyst deactivating impurities.[20]

During polymerisation, MAO first methylates the complex, and then abstracts a methyl group from the pre-catalyst to generate the catalytically active electron-deficient ion-paired species $[Cp_2ZrMe]^+[X\text{-}MAO]^-$.[40, 53, 68, 69] This has been computationally confirmed *via* a MAO model; $(AlMeO)_8(AlMe_3)_2$ was shown to abstract a methyl group from a Cp_2ZrMe_2 pre-catalyst in order to form the cationic species $[Cp_2ZrMe]^+[MAO]^-$ (Scheme 1.1).[70] An olefin monomer can then coordinate to the free site on the active cationic metal centre, and polymerisation can occur following the Cossee-Arlman mechanism.[71-73]



Scheme 1.1 Formation of $[Cp_2ZrMe]^+$: (i) coordination of Cp_2ZrMe_2 to the MAO mimic, (ii) bending of the Zr-Me-Al moiety, (iii) $AlMe_2^+$ cleavage and (iv) dissociation of $AlMe_3$.[70]

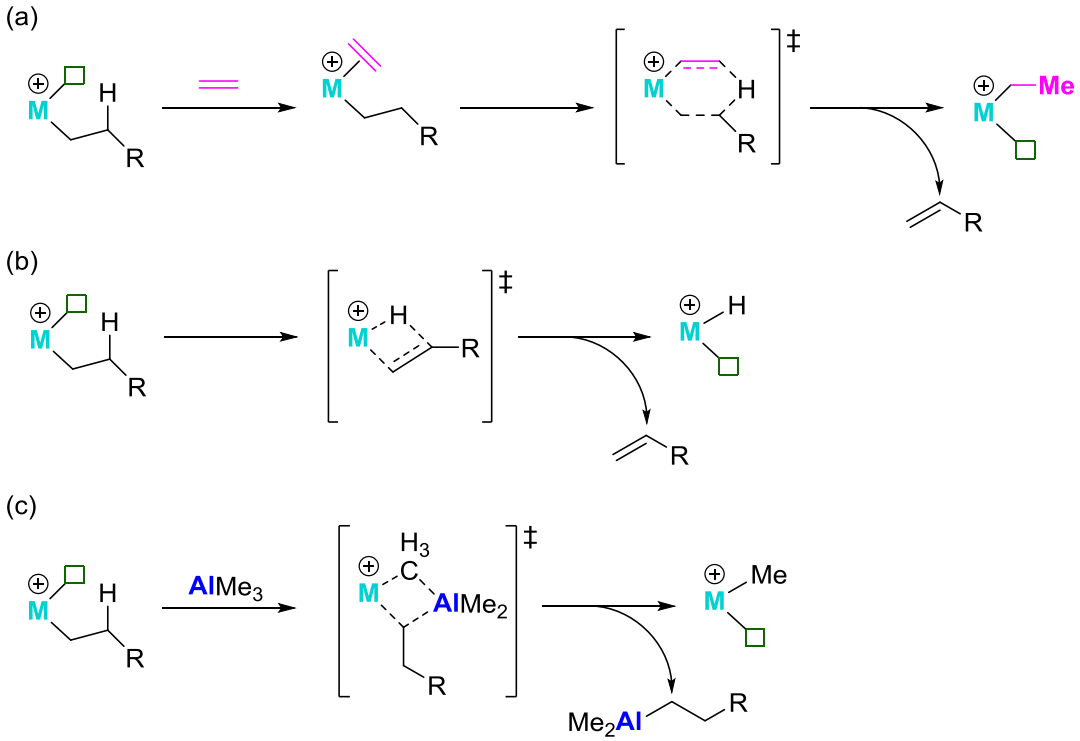
During the Cossee-Arlman α-olefin polymerisation mechanism, a metallocene catalyst with a free coordination site binds an olefin monomer through π-bonding interactions (Scheme 1.2).[71] The monomer then inserts into the growing polymer chain *via* a strained four-membered ring transition state. The rearrangement and insertion of the alkyl group is proposed to be the rate-determining step in the mechanism, with many olefin molecules coordinating and dissociating from the active metal centre before one of them reacts and is incorporated into the polymer chain.[71] The cationic metal alkyl species then either continues to coordinate and insert monomers to grow the polymer chain or undergoes a termination process.



Scheme 1.2 Cossee-Arlman mechanism of ethylene polymerisation.[12, 71-73] Free coordination sites are represented by □.

There are many possible termination pathways (Scheme 1.3).[74] These include transfer to another ethylene monomer and release of the polymer chain, β-hydride elimination where a stabilising α-agostic interaction facilitates the release of the

polymer chain and formation of a metal hydride species, and chain transfer to the aluminium co-catalyst.[74-76]



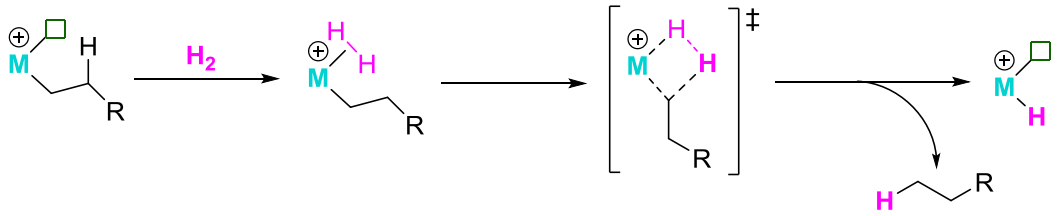
Scheme 1.3 Chain termination by (a) transfer to an α-olefin monomer,[74, 75] (b) β-hydride elimination[74, 75] and (c) transfer to an aluminium alkyl species.[76] Free coordination sites are represented by □.

1.2.4 Hydrogen effects on ethylene polymerisation

Polymer properties such as molecular weights, molecular weight distribution (MWD), degree of branching, comonomer incorporation and stereochemistry determine the potential applications of the polymer.[77] Hydrogen is a highly efficient chain transfer agent for the polymerisation of α-olefins by metallocene catalysts and is often employed to decrease and control polymer molecular weights.[78, 79] Contrary to conventional Ziegler-Natta catalysts, only a small quantity of hydrogen is required to reduce polymer molecular weights drastically.[78, 80, 81] Low molecular weight polyolefins find applications in plastic processing and end formulations to improve the physical appearance and thermal properties of the product.[82] Unfortunately, the introduction of

hydrogen also commonly lowers the ethylene polymerisation activity of the catalyst; Cp_2ZrCl_2/MAO experiences a decrease in activity from 45000 to 21400 $kg_{PE}\ mol_M^{-1}\ h^{-1}\ bar^{-1}$ in the presence of 0.04 bar hydrogen at 70 °C with 8 bar ethylene, which is accompanied by a reduction in polymer molecular weights from 135 to 56 kg mol^{-1}.[81]

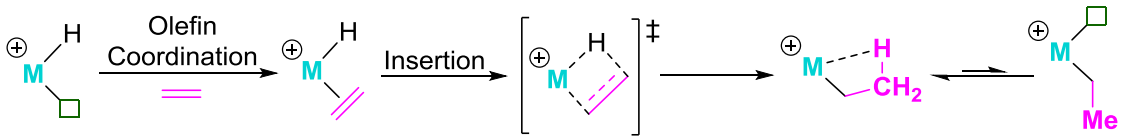
As discussed, α-olefin polymerisation usually occurs *via* the Cossee-Arlman mechanism, during which a metallocene catalyst binds and inserts olefin monomers until a termination process occurs (Scheme 1.3).[71] The presence of hydrogen offers an additional termination pathway to those previously discussed. Hydrogen can act as a chain transfer agent, which binds to the free coordination site of the metallocene catalyst and undergoes a similar transition state to that of β-hydride elimination, leading to release of the polymer chain and formation of a metal hydride species (Scheme 1.4).[75] When hydrogen is present, the increased probability of undergoing a termination process leads to a decrease in polymer molecular weights.



Scheme 1.4 Chain termination by hydrogen. Free coordination sites are represented by □.[75]

A reduction in polymerisation rate often accompanies the addition of hydrogen to metallocene ethylene polymerisation systems.[81, 83] This rate reduction can be justified due to an increase in the formation of the metal hydride termination product, which requires reactivation for propagation by insertion of a monomer unit,[75, 84] or by increased formation of a dormant resting state, such as $[(Cp_2MMe)_2(\mu\text{-}H)]^+$, which can be reactivated for polymerisation by the loss of Cp_2MMeH.[85, 86] The presence of

hydrogen can also lead to a reduction in ethylene concentration around the active sites and therefore decrease the rate of propagation.[29] For Ziegler-Natta type catalysts, it has been proposed that the deactivating effect of hydrogen in ethylene polymerisation may also be due to β-agostic interactions formed in the product of the first monomer insertion into the metal hydride species (Scheme 1.5).[87, 88] It is proposed that the ethyl group is in equilibrium between an open formation and a β-agostic coordinated state, with only 10% in the open formation. No further polymerisation can take place in the β-agostic coordinated complexes as the free coordination site on the metal centre is blocked.[87, 88] The same effects could also occur in metallocene systems.[89]



Scheme 1.5 Ethylene polymerisation using a metal hydride species. Free coordination sites are represented by □.

1.2.5 Ethylene and α-olefin copolymerisation

The incorporation of longer chain α-olefin monomers into polyethylene chains can increase the degree of polymer branching, and therefore lower the melting point, crystallinity and density.[90] This increases the flexibility of the polymer and allows applications in packaging, foams, elastic fibres and adhesives.[9]

Metallocene catalysts have a similar reactivity with both ethylene and longer chain α-olefins,[14] allowing them to incorporate much larger percentages of higher α-olefins than traditional Ziegler-Natta catalysts; $Cp^*TiCl_2(O\text{-}2,6\text{-}^iPr\text{-}C_6H_3)$ shows a 38 mol% comonomer incorporation for ethylene/1-hexene polymerisation at 40 °C with 7 bar ethylene and 1.45 M 1-hexene (where Cp* is pentamethylcyclopentadienyl, C_5Me_5).[91] Unlike Ziegler-Natta catalysts, copolymerisation using metallocene catalysts

often results in polymers with regular comonomer distributions, high strength and high clarity.[68, 92] Under the same conditions C_s-symmetric metallocenes are usually observed to be more active copolymerisation catalysts than C_2-symmetric metallocenes;[9] for the copolymerisation of ethylene and norbornene ^{Me_2}SB(Flu,Cp)$ZrCl_2$/MAO experienced an increase in activity from 470 to 2120 $kg_{PE}\ mol_M^{-1}\ h^{-1}\ bar^{-1}$, while ^{Me_2}SBI$ZrCl_2$/MAO experienced a decrease in activity from 9700 to 110 $kg_{PE}\ mol_M^{-1}\ h^{-1}\ bar^{-1}$ at 30 °C with 2 bar ethylene and norbornene/ethylene = 9.5.[93] Furthermore, bridged metallocene complexes have been shown to have much better comonomer incorporation than their unbridged analogues due to the opening up of the coordination space, which allows for easier accessibility of the bulky comonomers.[68, 94, 95] Imanishi and co-workers found that for the copolymerisation of ethylene and 1,7-octadiene, unbridged Ind_2ZrCl_2 showed 0.4 mol% comonomer incorporation, while bridged *rac*-EBI$ZrCl_2$ and *rac*-^{Me_2}SBI$ZrCl_2$ showed 13 and 15 mol% comonomer incorporation (40 °C, 1 bar ethylene, 10 mmol 1,7-octadiene and methylisobutylaluminoxane co-catalyst).[96]

Linked half-metallocenes containing amide ligands, such as the Dow Chemical Co. complexes ^{Me_2}SB($^{t\mathrm{Bu}}$N,Cp^{R})$TiMe_2$ and ^{Me_2}SB($^{t\mathrm{Bu}}$N,^{R}I)$TiMe_2$, are a class of metallocene that exhibit very efficient comonomer incorporation (Chart 1.5).[68, 97, 98] These constrained geometry catalysts (CGCs) are of industrial interest due to their enhanced ability to copolymerise ethylene and longer chain α-olefins.[77, 99, 100]

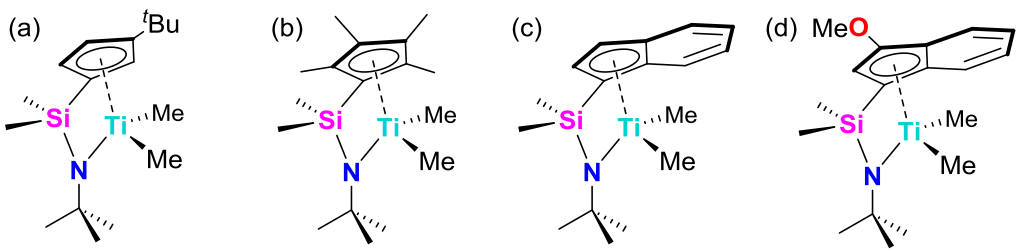


Chart 1.5 Structures of (a) ^{Me_2}SB($^{t\mathrm{Bu}}$N,Cp$^{3\text{-}t\mathrm{Bu}}$)$TiMe_2$, (b) ^{Me_2}SB($^{t\mathrm{Bu}}$N,Cp*)$TiMe_2$, (c) ^{Me_2}SB($^{t\mathrm{Bu}}$N,I)$TiMe_2$ and (d) ^{Me_2}SB($^{t\mathrm{Bu}}$N,$^{3\text{-OMe}}$I)$TiMe_2$.[77]

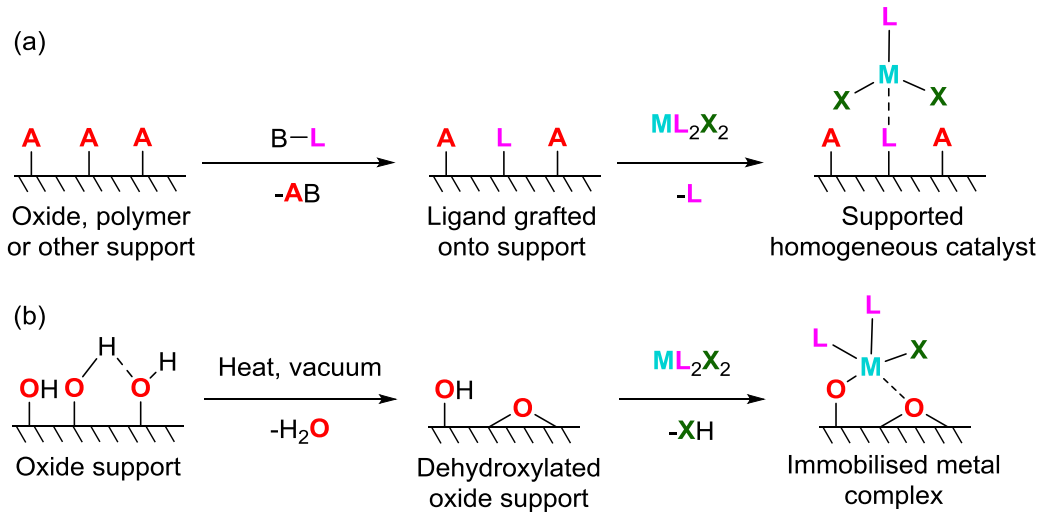
1.3 Heterogeneous α-Olefin Polymerisation

1.3.1 Heterogeneous catalysts

The goal of immobilising α-olefin polymerisation catalysts is to preserve the advantages of homogeneous polymerisation, such as high activity and selectivity while improving polymer morphology *via* the templating effect of the solid support and reducing reactor fouling.[101, 102] The chemical industry largely relies on heterogeneous catalysts as they are usually reasonably robust, can be integrated into continuous processes,[103] are often easier to inject, and the solid product is usually easier to remove from the reactor.[104, 105] Common inorganic supports for metallocene complexes include clays,[106] silicas,[33, 107] zirconium oxide,[108] magnesium chloride,[13, 109] alumina,[110] and zeolites.[111]

The two main methods to produce well-defined heterogeneous catalysts are either by supported homogeneous catalysis (SHC),[112-116] or by utilising the principles of surface organometallic chemistry (SOMC).[105, 112, 113, 117-121] During SHC methods, metal sites are bound to organic ligands which have been grafted onto a support material; this produces species with structures similar to those of the homogeneous catalysts (Scheme 1.6a).[113] The SHC approach often gives species with much lower polymerisation activities than the corresponding homogeneous catalysts due to the inhomogeneous distribution of the catalytically active sites.[113] In SOMC methods, the oxygen surface sites of the support (usually a high surface area oxide) act as anionic X-type ligands that covalently bond to the metal centre (Scheme 1.6b). This allows the organometallic species to be immobilised directly on the support surface by displacement of a labile ligand on the metal centre.[105, 113, 117, 122] SOMC allows for a higher degree of control than SHC as the density of the metal sites can be varied by changing the density of the oxygen surface sites on the support surface (e.g. by

calcination). The stoichiometric nature of SOMC also leads to catalytic systems with very high percentages of well-defined active catalytic sites.



Scheme 1.6 Preparation of supported catalysts by (a) supported homogeneous catalysis (SHC) and (b) surface organometallic chemistry (SOMC). Adapted from Copéret *et al.*.[113]

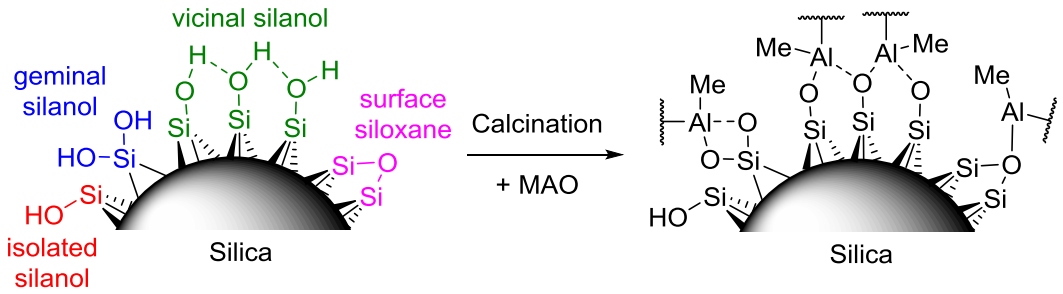
It is not only the nature of the immobilised complex that influences polymerisation performance and polymer properties, but also the identity of the support itself. Many different types of solid support can be used for the immobilisation of metallocene catalysts, including highly Lewis acidic species such as $MgCl_2$, SiO_2-Al_2O_3 and Al_2O_3, and neutral or moderately acidic species such as SiO_2 and MgO.[113, 123, 124] Immobilisation of metallocene complexes usually generates species that display low catalytic activities, unless they are activated post-immobilisation by an external Lewis acidic or an alkyl aluminium reagent.[113, 123-125] Alternatively, the surface of the support can be modified with an activator prior to immobilisation of the organometallic complex.[20, 51, 113, 123]

MAO is the most common activator for heterogeneous metallocene catalysts as its reaction with the metallocene complexes generates active species that behave similarly to the same complexes activated by MAO in solution.[104, 123, 126-129] Supports

which can activate complexes *in situ via* immobilisation reduce the number of synthetic steps and the amount of co-catalyst required, both of which are industrially desirable.

1.3.2 Silica

Silica (SiO_2) is the most common solid support for the immobilisation of single-site α-olefin polymerisation catalysts.[110, 130] Although silica exists in many phases,[110] the amorphous phase is generally used for the preparation of supported catalysts. Commercial silicas are typically provided in their fully hydroxylated form, with three distinct types of silanol groups present on the surface; isolated, germinal and vicinal (Equation 1.1).[118, 131] Silicas require thermal treatment *via* calcination before complex immobilisation in order to remove water molecules and reduce the number of surface silanol groups. The final silanol and water content depend on the calcination temperature; physically adsorbed water molecules desorb at 25–105 °C, hydrogen-bonded water molecules at 105–180 °C, and adjacent vicinal silanol groups condense to form surface siloxanes above 180 °C (Equation 1.1).[110]



Equation 1.1 Proposed structure of MAO activated silica (SSMAO).[110]

In order to activate the support, silica requires pre-treatment with an alkyl aluminium compound, such as MAO, prior to anchoring of the metallocene component (Equation 1.1). MAO-modified silica (SSMAO) has been well characterised and documented as a solid support for the immobilisation of single-site olefin polymerisation pre-catalysts.[33, 51, 110, 126, 132, 133] For example, Pn*ZrCpCl (where Pn* is

permethylpentalene, C_8Me_6) supported on MAO activated silica demonstrates an ethylene polymerisation activity of 943 $kg_{PE}\,mol_M^{-1}\,h^{-1}\,bar^{-1}$ at 80 °C with 2 bar ethylene.[51]

When treated with MAO, the surface silanol groups interact uniquely with both the $(AlMeO)_n$ and TMA components of MAO. Zakharov and co-workers demonstrated by infrared (IR) spectroscopy that isolated surface silanol groups rapidly react with TMA *via* protonolysis to yield methane, whereas MAO predominantly chemisorbs onto all variants of the surface hydroxyl groups without protolytic reaction.[134] The active species of metallocene-based catalysts are cationic $[Cp^R_2MR]^+$ complexes, formed from the interaction of the metallocene and Lewis acidic sites of the support, with $[MAO\text{-}X]^-$ acting as the charge balancing anion.[135, 136] It has been proposed that the metallocene species primarily interact with the strong Lewis acidic sites provided by adsorbed MAO, and not with the weak Lewis acidic sites resulting from the interaction of surface silanol groups with TMA.[134]

1.3.3 Clays and layered double hydroxides

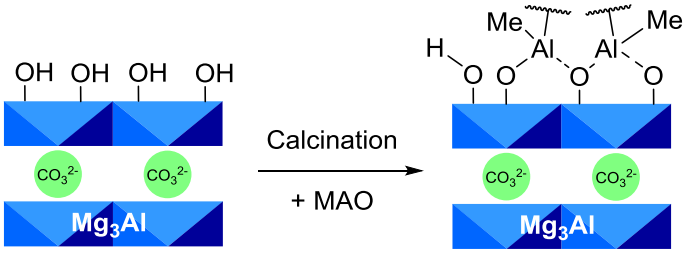
Phyllosilicate mineral clays are alternative solid supports for single-site polymerisation catalysts.[110] They are layered materials composed of aluminosilicate sheets, with octahedral Al and tetrahedral Si coordination.[137] In order to retain the activity of the metallocene catalyst the clays are either ion exchanged with a Brønsted acid, such as an ammonium salt, or they are impregnated with an alkylaluminium reagent prior to complex immobilisation.[138] This often affects the interlayer distances between the aluminosilicate sheets and allows the properties of the resulting polymer to be controlled by tailoring the properties of the support.[139, 140]

Layered double hydroxides (LDHs) are a class of anionic clays represented by the general formula $[M^{2+}_{1-x}M^{3+}_{x}(OH)_2]^{y+}(A^{n-})_{y/n}\cdot bH_2O$, where M^{2+} and M^{3+} form positively charged brucite-like layers, OH are surface-bound hydroxyl groups and A^{n-} represents weakly bound intercalated anions which provide a charge balance as divalent metal ions are substituted for trivalent ones.[141] LDHs synthesised by conventional methods are highly aggregated due to their high charge density and as a result, exhibit low surface areas and an inability to disperse in nonpolar liquids. However, a new family of dispersible, hydrophobic aqueous miscible organic layered double hydroxides (AMO-LDHs) of general formula $[M^{2+}_{1-x}M^{3+}_{x}(OH)_2]^{y+}(A^{n-})_{y/n}\cdot bH_2O\cdot c$(AMO-solvent) overcome some of these limitations.[142, 143] AMO-LDHs are the product of an aqueous miscible organic solvent treatment (AMOST) method, where the AMO solvent is typically acetone or ethanol. The resulting crystalline AMO-LDHs display uniform particle sizes (smaller than 0.5 μm) and possess surface areas and pore volumes significantly higher than conventional and commercial LDHs.[142, 143]

AMO-LDHs are highly tuneable as their surface contains both acidic and basic sites, which can be manipulated by calcination; thermal treatment at lower temperatures (below 200 °C) leads to the removal of surface and interlayer water, with further heating leading to dehydroxylation and loss of the intercalated anions to form layered double oxides.[144] Inorganic oxide supports are commonly impregnated with aluminium co-catalysts prior to immobilisation of the metallocene.[13, 110] For LDH supports, it is proposed that MAO binds to the surface hydroxyl groups of the support in an analogous fashion to MAO modified silica (Equation 1.2).

Recently, the use of MAO-activated thermally treated AMO-LDHs (LDHMAO) as well-defined supports for slurry-phase ethylene polymerisation has emerged.[145, 146] It

was found that calcination temperature had a large influence on the polymerisation activity of *rac*-EBIZrCl$_2$ immobilised on MAO treated AMO-LDH Mg$_3$Al-CO$_3$ (where the AMO solvent was acetone); a peak activity was observed at a calcination temperature of 150 °C (1276 kg_{PE} mol_M^{-1} h^{-1} bar^{-1}).[146] It was proposed that this was due to the removal of surface hydroxyl groups above 150 °C leading to more deactivating Lewis acidic sites,[144, 147] and the retention of surface water molecules below 150 °C hydrolysing MAO and reducing its performance as an activator. *rac*-EBIZrCl$_2$ supported on MAO modified AMO-LDH calcined at 150 °C demonstrated catalytic activities ten times higher than systems using conventionally synthesised and commercially available LDH supports.[146] AMO-LDH supports are industrially desirable as they are simple to synthesise on a large scale, more cost-effective than silica and show no evidence of reactor fouling or catalyst leaching.[142]

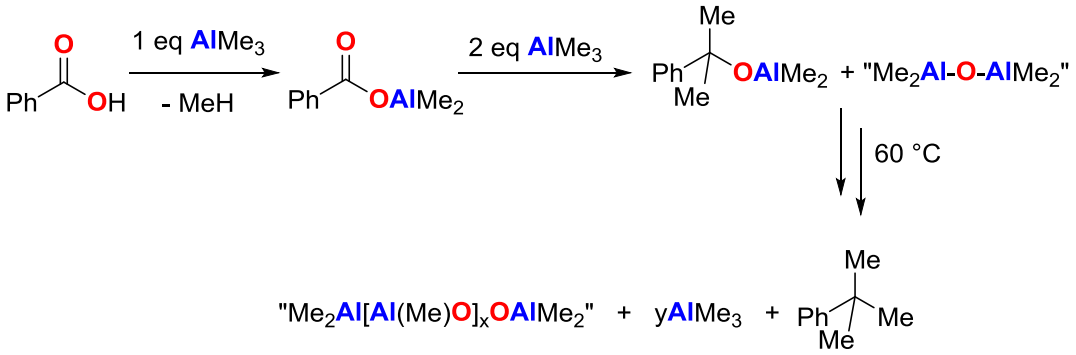


Equation 1.2 The proposed structure of MAO activated LDH (LDHMAO), based on the structure of MAO modified silica.[110]

1.3.4 Solid polymethylaluminoxane

Solid polymethylaluminoxane (sMAO) is an insoluble form of oligomeric MAO that has recently been exploited as a solid support for metallocene pre-catalysts in slurry-phase olefin polymerisation.[51, 148-150] It is an oligomeric product of the incomplete hydrolysis of TMA and consists of $(AlMeO)_n$, where n = 6–30 monomer units.[59]

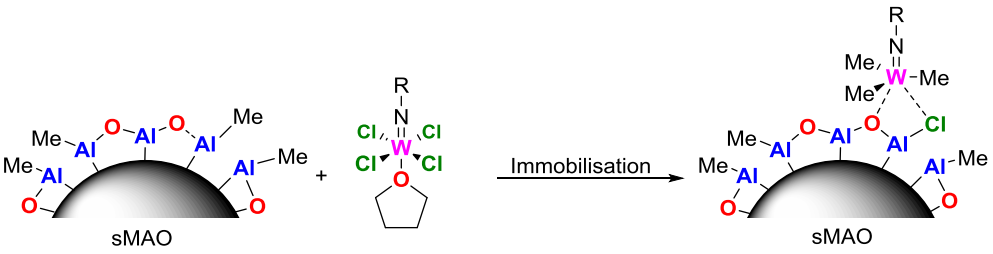
A commonly reported synthetic route to sMAO involves precipitation of solid cross-linked MAO from a commercial toluene solution of MAO.[151-153] However, sMAO can also be synthesised by the reaction of benzoic acid with TMA.[154] The product of the reaction was found to depend on the TMA:benzoic acid ratio, with a ratio of 3:1 at 60 °C leading to precipitation of insoluble MAO-like aluminoxane oligomers and free TMA *via* the self-condensation of "Me_2Al-O-$AlMe_2$" species (Scheme 1.7).[154-156] O'Hare and co-workers recently reported an extension of this work involving the controlled hydrolysis of TMA with benzoic acid to form an aluminoxane precursor, followed by a thermolysis step at 80 °C to form MAO and a further thermolysis step at 100 °C to form sMAO.[157]



Scheme 1.7 Synthesis of sMAO *via* the reaction of benzoic acid and TMA, followed by the self-condensation of "Me_2Al-O-$AlMe_2$".[155]

Similarly to MAO, the exact structure of sMAO is relatively undefined, although recent NMR spectroscopy studies imply a structure featuring long-chain aluminoxane oligomers, with the incorporation of free TMA and benzoate groups.[157] Theoretical structures that best match experimental data are MAO nanotubes $((AlOMe)_9 \cdot (AlMe_3)_3)$[64] and spherical MAO cages $((AlOMe)_{20} \cdot (AlMe_3)_m$ with m = 1 or 2 as they include the presence of free TMA.[66] It has been found that smaller cage structures where n <10 do not possess the long-range intra-atomic distances seen in experimental data.[157]

The key advantage of sMAO as a metallocene support is that it can act as a bifunctional support and activator without further modification. Rather than the dissociation of $AlMe_3$ suggested in Scheme 1.1 for the addition of a metallocene to $(AlMeO)_8(AlMe_3)_2$, for sMAO systems it is suggested the labile ligands of the metallocene become bound to the solid support (Equation 1.3).[158] In this way, ligands may act as 'non-innocent' initiation groups and may have some influence over polymerisation activity. sMAO has been found to be a very efficient support for metallocene complexes, with an activity of 6533 $kg_{PE}\ mol_M^{-1}\ h^{-1}\ bar^{-1}$ recorded for sMAO supported *rac*-EBIZrCl$_2$ at 70 °C with 2 bar ethylene.[157]



Equation 1.3 SOMC grafting procedure for a tungsten imido complex on sMAO. Adapted from Wright *et al.*.[158]

1.3.5 Templating effect of the solid support

In a typical slurry-phase α-olefin polymerisation using heterogeneous catalysts, it is generally accepted that polymerisation begins in the pores of the solid catalyst, and as it proceeds the initial catalyst support becomes fragmented and dispersed within the growing polymer matrix (Figure 1.1).[110, 159] Polymerisation initially occurs radially at the surface of the catalyst fragments by a coordination-insertion mechanism, leading to the formation of a polymer shell around the catalyst particle (a polymer 'microparticle'). This imposes a diffusion limitation and prevents uninhibited access of the monomer to the active catalyst sites,[110] causing polymerisation to continue in a layered fashion as the monomer diffuses through the polymer towards the catalyst

fragment.[160] As the polymer grows, the microparticles from a single catalyst fragment continue to adhere loosely to each other, resulting in a single large polymer particle (a polymer 'macroparticle'), or polymer bead, at the end of polymerisation.[159] The morphology of the starting support is replicated in the final polymer with uniform particle size dependent on a high surface area, homogeneous distribution of catalytically active centres and ready availability of the innermost parts of the catalyst fragment to the incoming monomer.[3]

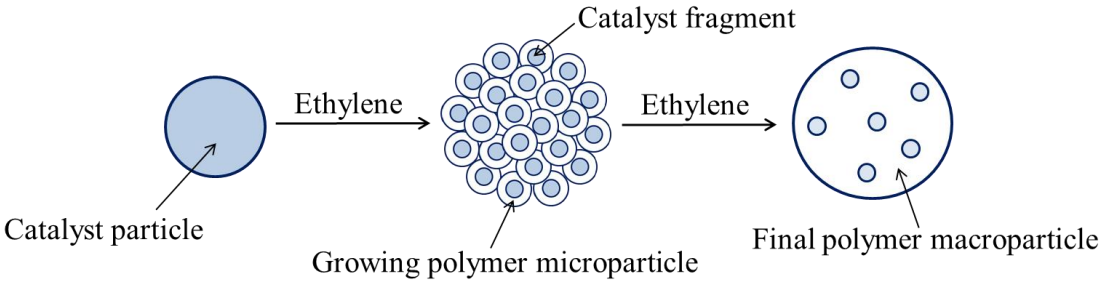


Figure 1.1 Polymer particle growth. Adapted from Severn *et al*..[110]

1.3.6 Role of the scavenger

Alkyl aluminium species are often added during slurry-phase polymerisation with metallocene catalysts immobilised on activated supports to scavenge impurities such as trace water and oxygen. However, they can also be used to control catalyst activity and influence polymer properties.[161-163] Trialkyl aluminium compounds are usually preferred as they typically give higher polymerisation activities than their halogen-containing analogues. Such compounds include trimethylaluminium (TMA), triethylaluminium (TEA), tri-*n*-hexylaluminium (T*n*HA), triisobutylaluminium (TiBA) and trioctylaluminium (ToA).[161, 164-166] It has been found that increasing the size of the alkyl group generally increases catalytic activity (up to $C_{11}H_{23}$)[163, 165] and polymer molecular weights,[163, 165] while also producing polymers with narrow molecular weight distributions.[163, 165, 167] It has also been observed that the amount of the alkyl aluminium

scavenger inside the reactor can affect polymerisation activity; if the concentration of the alkyl aluminium species is too high then the metallocene catalyst can be rendered inactive.[162] Additionally, a high concentration of scavenger in slurry-phase ethylene polymerisation with MAO activated supports can cause the alkyl aluminium species to interact with the MAO, leading to desorption of the metallocene from the support and subsequent reactor fouling from homogeneous polymerisation processes.[128, 168, 169]

1.4 Ring-Opening Polymerisation of Lactide

1.4.1 Biodegradable polymers

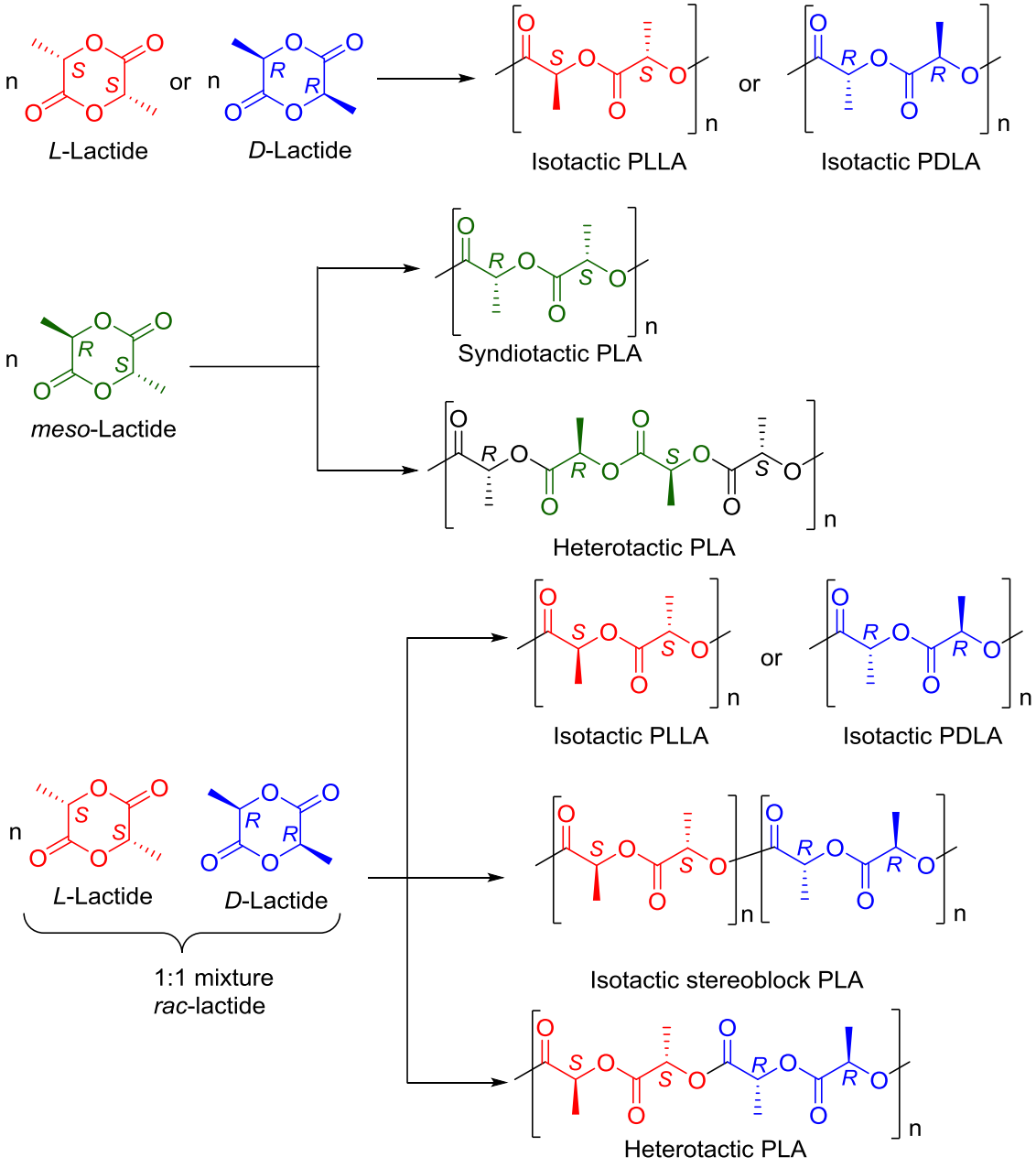
Polyolefins have a diverse range of uses, including packaging, agriculture and medical applications.[4] However, the resistance of these polymers to chemical, physical and biological degradation has become a serious environmental concern.[3] Therefore, there is a necessity for biodegradable and biocompatible polymers which can be broken down by microorganisms into smaller molecules (such as CO_2, CH_4 and H_2O).[4]

Polylactides (PLAs) are one the most versatile materials among biodegradable polymers due to their inherent biodegradability, biocompatibility, high mechanical strength, low toxicity and easy availability from renewable sources.[170-172] Lactic acid and lactide (LA) are produced on an industrial scale from the fermentation and processing of corn.[173] The versatile properties of PLAs enable use in a diverse range of applications, from biomedical and pharmaceutical materials for tissue engineering and wound dressings to biodegradable materials for bags and cutlery.[170, 174-176]

1.4.2 Structure of PLA

Lactide is a cyclic dimer of lactic acid produced by the thermal degradation of poly(lactic acid) oligomers.[171] Lactic acid possesses one asymmetric carbon and exists in two configurations (*S* and *R*), with the *S*- and *R*-configurations referred to as *L*- and *D*-lactic acid respectively. This leads to two stereogenic centres in the lactide monomer,[177] which results in three distinct isomers: (*S*,*S*)-lactide (*L*-lactide), (*R*,*R*)-lactide (*D*-lactide) and (*R*,*S*)-lactide (*meso*-lactide), with a 1:1 mixture of (*S*,*S*)-lactide and (*R*,*R*)-lactide formally referred to as *rac*-lactide. Consequently, different polymer tacticities can be produced, resulting in a variety of bulk physical

properties (Scheme 1.8).[171, 175] The stereochemistry of the monomer units leads to polymer chains with different stereochemical arrangements (atactic, isotactic, syndiotactic, heterotactic, isotactic stereoblock and isotactic stereocomplex),[171, 177] which play a crucial role in determining the mechanical, physical and thermal degradation properties of the resulting PLA. Stereospecific catalysts to prepare different PLA architectures are therefore of increasing interest.[171]



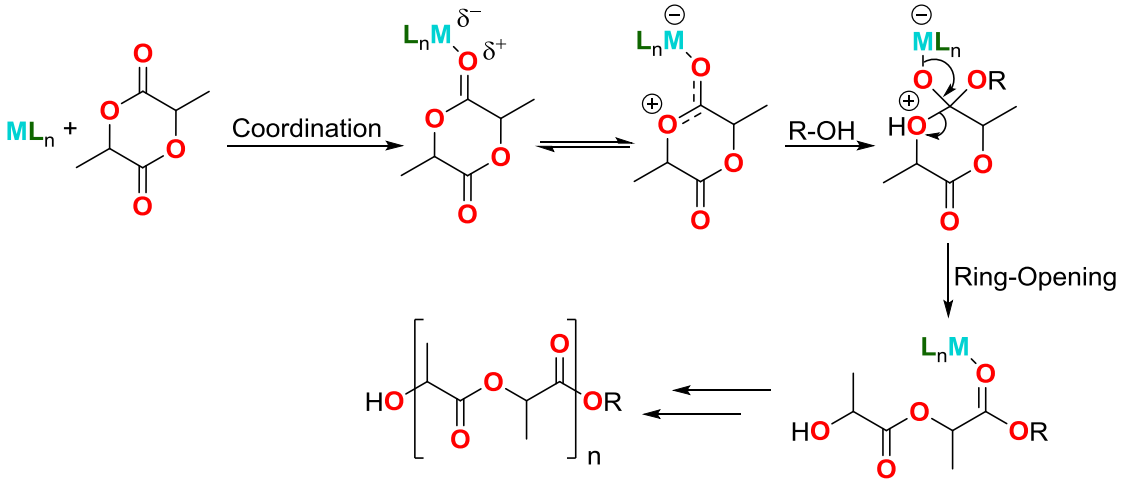
Scheme 1.8 PLA tacticity as a result of the polymerisation of different lactide monomer units.

1.4.3 Mechanism of lactide polymerisation

The most efficient and predictable synthesis of PLA is *via* the ring-opening polymerisation (ROP) of lactide using a metal-based single-site catalyst, and a variety of catalysts have been employed to this effect.[178-183] The ROP of lactide allows for greater control of polymer molecular weights, end group functionality and polydispersity than PLA synthesised from the polycondensation of lactic acid.[171, 172] Polycondensation is also disadvantaged by the limitations of step polymerisation, such as difficulties obtaining high molecular weight polymers and the need to remove water from the equilibrium mixture in order to drive the reaction to high conversions.[171]

Depending on the catalyst used for the ROP of lactide, there are many different possible polymerisation mechanisms such as cationic,[184-186] anionic,[187, 188] and coordination-insertion mechanisms.[178] Cationic and anionic mechanisms experience some key limitations; catalysts which act *via* a cationic mechanism have difficulty achieving high molecular weight PLAs, while the side reactions (epimerisation and transesterification) of catalysts which operate *via* an anionic mechanism leads to a lack of control of polymer molecular weights and molecular weight distributions.[171]

The cationic polymerisation of lactide typically proceeds *via* an active chain end mechanism, whereby the propagating species are located at the chain end. However, if the polymerisation is conducted in the presence of a nucleophilic/protic co-initiator, such as an alcohol, then polymerisation may proceed *via* an activated monomer mechanism (Scheme 1.9).[189] In this instance, the Lewis acidic metal centre of the catalyst activates the lactide monomer by coordination to the carbonyl oxygen. The nucleophilic co-initiator then initiates polymerisation *via* attack of the electrophilic carbon atom of the carbonyl group, resulting in ring-opening of the heterocycle.[190]



Scheme 1.9 Activated monomer mechanism of lactide polymerisation. Adapted from Ajellal *et al.*.[190]

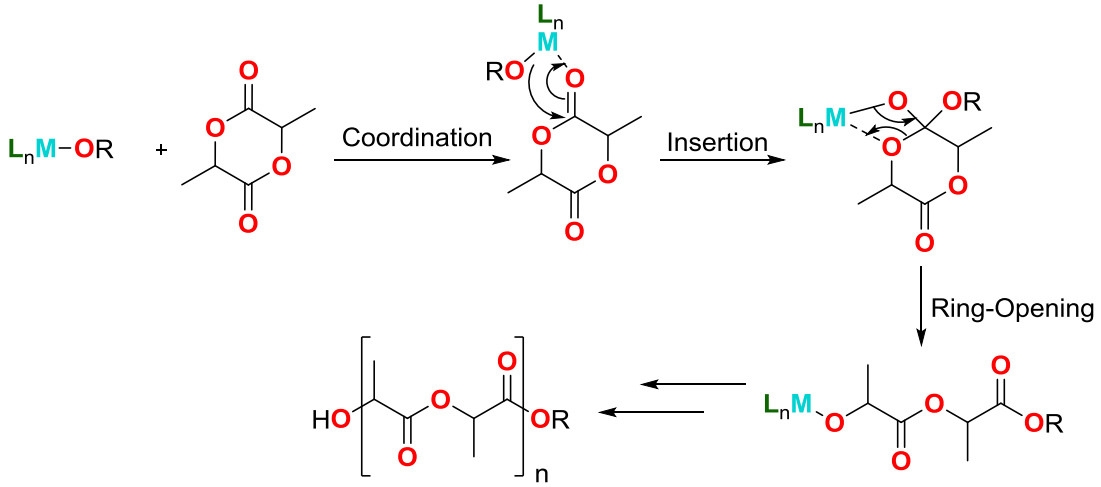
Formally, an activated monomer mechanism proceeds as if monomer molecules were incorporated into the R-OH bond of the initiating nucleophile.[184] The rate law for this polymerisation process is defined in Equations 1.1 and 1.2, where $-d[\mathrm{LA}]/d\mathrm{t}$ is the rate of monomer consumption, k_p is the propagation rate constant for the catalyst and k_obs is the observed rate constant.

$$-\frac{d[\mathrm{LA}]}{d\mathrm{T}} = k_\mathrm{p}\left[\mathrm{LA}\right]^\mathrm{a}\left[\mathrm{cat}\right]_0^\mathrm{b}\left[\mathrm{ROH}\right]_0^\mathrm{c} \qquad \textbf{Equation 1.1}$$

$$k_\mathrm{obs} = k_\mathrm{p}\left[\mathrm{cat}\right]_0^\mathrm{b}\left[\mathrm{ROH}\right]_0^\mathrm{c} \qquad \textbf{Equation 1.2}$$

Alternatively, the coordination-insertion mechanism of lactide polymerisation avoids most of the key disadvantages of cationic and anionic mechanisms. During coordination-insertion, a lactide monomer initially coordinates to the Lewis acidic metal centre of the aryloxide or alkoxide active species, which then inserts into the metal-alkoxide bond *via* nucleophilic addition (Scheme 1.10). Cleavage of the acyl-oxygen bond *via* a highly strained four-membered ring transition state results in ring-opening of the lactide monomer and releases a free coordination site on the metal

centre. This is followed by a continuous cycle of lactide monomer coordination and insertion, which is terminated by hydrolysis of the active polymer chain.[171]



Scheme 1.10 Coordination-insertion mechanism of lactide polymerisation. Adapted from Dijkstra *et al.*.[171]

The coordination-insertion mechanism differs from the activated monomer mechanism in that the nucleophile is an inherent part of the active catalyst, while in an activated monomer mechanism the nucleophile is an external molecule, independent from the catalyst.[190] The rate law for polymerisation *via* a coordination-insertion mechanism is defined in Equations 1.3 and 1.4.

$$-\frac{d[\mathrm{LA}]}{d\mathrm{T}} = k_{\mathrm{p}}\left[\mathrm{LA}\right]^{\mathrm{a}}\left[\mathrm{cat}\right]_0^{\mathrm{b}} \qquad \textbf{Equation 1.3}$$

$$k_{\mathrm{obs}} = k_{\mathrm{p}}\left[\mathrm{cat}\right]_0^{\mathrm{b}} \qquad \textbf{Equation 1.4}$$

1.4.4 Initiators for the ROP of lactide

Metal alkoxides are the most common initiators for the ROP of lactide.[191-194] Protic reagents are frequently employed as co-initiators when polymerising with metal complexes in order to generate active alkoxide initiators *in situ* by ligand substitution. An example of this is $Sn(Oct)_2$, which is used for the ROP of lactide on an industrial

scale.[171, 195] The true initiators of polymerisation are tin(II) alkoxides, formed from the reaction of $Sn(Oct)_2$ with protic reagents such as water, alcohols, lactic acid and acetic acid.[196] A major disadvantage of these highly active alkoxide initiators is the difficulty in controlling the molecular weights of the polylactides produced; the clustered form of the active species results in multiple polymer chains growing from one metal centre.[171]

Well-defined, single-site catalysts with the ability to control polymer properties and molecular weight distributions are therefore of particular interest. By carefully selecting combinations of ancillary ligands (L), initiating groups (X) and metal (M), catalysts of the type L_nMX_m can precisely control polymerisation rate, polymer molecular weights, polymer molecular weight distributions, co-monomer incorporation and polymer stereochemistry.[171] Protic reagents may also act as co-initiators for these complexes;[171] they can exchange with the labile ligands of L_nMX_m-type catalysts to form catalytically active metal alkoxide initiators *in situ*.[190]

Spassky *et al.* were among the first to discover the high stereocontrol that can be achieved using single-site initiators for the ROP of lactide. During the ROP of *rac*-lactide the authors observed that the chiral nature of the Schiff base salen-type aluminium methoxide complex (*R*-SalBinap)AlOMe led to the selective ring-opening of *D*-lactide to produce isotactic poly-*D*-lactide (PDLA) nineteen times faster than isotactic poly-*L*-lactide (PLLA) (Chart 1.6a). This was found to be due to an enantiomorphic site-control mechanism, whereby the stereochemistry and ligand environment of the active metal site determines the configuration of the next inserted monomer.[197] Since then many other single-site Schiff base aluminium aryloxide and alkoxide initiators have been employed for the controlled polymerisation of lactide monomers,[198-202] in addition to their zinc and calcium analogues.[203, 204]

More recently, salen-type ligand frameworks have been employed with metals such as indium,[205-208] yttrium,[209-214] lutetium,[215] lanthanum[215, 216] samarium,[216] and iron.[217] Of these species, phosphasalen yttrium and indium catalysts show very high activities for the ROP of *rac*-lactide with near-quantitative conversion to PLA achieved in a few seconds for some yttrium initiators (Chart 1.6b).[207, 210] The phosphasalen initiators showed significantly higher activities than analogous salen initiators; phosphasalen ligands are more electron-donating than salen ligands and the subsequent reduction in the Lewis acidity of the metal centre can labilise the metal-alkoxide bond and increase the rate of lactide insertion.[218] Polymerisation was found to proceed in a controlled manner *via* a chain-end control mechanism with high levels of isotactic stereocontrol achieved for indium initiators (P_m up to 0.87) and highly heterotactic PLA obtained for yttrium initiators (P_r >0.87).[207, 210] For the indium species, it was found that isoselectivity decreased with a decrease in steric bulk of the ligand due to a decrease in steric protection and direction at the metal centre.[207]

A multitude of other metal complexes and ligand frameworks have also been studied as single-site initiators for the stereoselective ROP of lactide. For example, aluminium complexes bearing tetradentate N,N'-disubstituted bis(amino-phenoxide) salen-type ligands show high activities for the ROP of *rac*-lactide in the presence of benzyl alcohol (Chart 1.6c).[219] These complexes show high degrees of stereocontrol, with polymer tacticity largely dependent on the ligand substituents; isotactic PLAs are produced with unsubstituted phenoxide groups (P_m up to 0.79), while highly heterotactic PLAs are obtained with 3,5-substituted phenoxide groups (P_r up to 0.96). For these ligand frameworks tacticity is also influenced by the size of the nitrogen substituents, with an increase in ligand size leading to an increase in isotacticity.

Zinc, tin and magnesium alkoxides with β-diiminate (BDI) ligand frameworks are another class of highly active initiators for the ROP lactide.[220-222] β-diiminate zinc complexes also show high selectivities during lactide polymerisation, affording highly heterotactic PLA from the ROP of *rac*-lactide (P_r up to 0.94) (Chart 1.6d).[220] The authors propose that the bulky β-diiminate ligand remains bound to the zinc centre during polymerisation and influences polymer stereochemistry by a chain-end control mechanism, while the isopropoxide group initiates polymerisation.[221] To validate this hypothesis, the substituents on the ligand framework were found to influence the degree of stereoselectivity; changing the ligand substituents from isopropyl to *n*-propyl was found to cause a decrease in heterotacticity (P_r = 0.90 and 0.76 respectively).

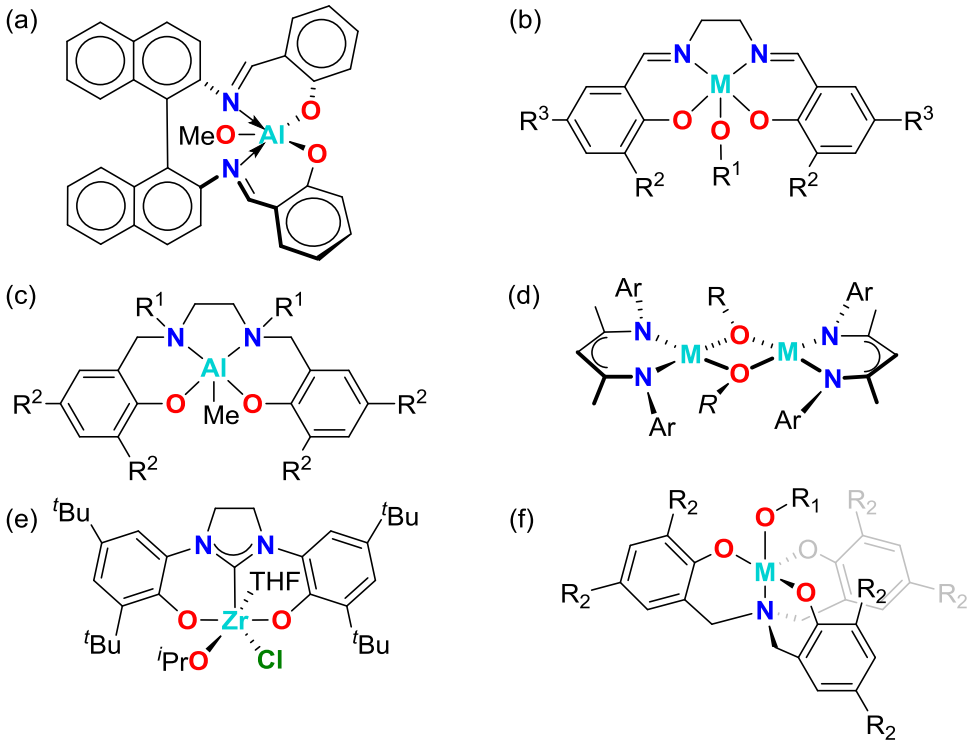


Chart 1.6 Structures of (a) (*R*-SalBinap)AlOMe,[197] (b) phosphasalen yttrium and indium complexes (R^1 = Et and ^{t}Bu; R^2 = $C(CH_3)_2Ph$ and ^{t}Bu; R^3 = $C(CH_3)Ph$, ^{t}Bu and OMe),[207, 210] (c) N,N'-disubstituted bis(amino-phenoxide) aluminium complexes (R^1 = Me and CH_2Ph; R^2 = H, Cl and Me),[219] (d) $[(BDI)M(\mu\text{-}O^iPr)]_2$ (M = Zn and Mg; Ar = 2,6-Et-C_6H_3, 2,6-^{i}Pr-C_6H_3 and 2,6-^{n}Pr-C_6H_3; R = ^{i}Pr, ^{n}Pr and Et),[220, 221] (e) $[N_2C_3H_4(3,5\text{-}^t\text{Bu-}C_6H_2O)_2]Zr(O^iPr)(Cl)(THF)$[223] and (f) $(R_1O)M[N(CH_2\text{-}2\text{-}O\text{-}3,5\text{-}R_2\text{-}C_6H_2)_3]$ (M = Zr and Hf).[224]

Group 4 zirconium and hafnium complexes also demonstrate stereocontrolled ROP of lactide.[225] For example, zirconium alkoxide compounds bearing a tridentate N-heterocyclic carbene-linked bis(phenolate) ligand have been reported to show controlled and highly stereoselective ROP of *rac*-lactide to yield heterotactic PLA under mild conditions (P_r >0.95 and M_w/M_n <1.11 with 91% conversion after 15 hours) (Chart 1.6e). In addition, these Zr–NHC alkoxide initiators are tolerant to protic impurities; in the presence of an external alcohol, polymerisation was shown to proceed in a controlled and immortal manner with high stereoselectivity (Pr >0.95 and M_w/M_n <1.11).[223] Zirconium and hafnium amine tris(phenolate) alkoxides also show high activity and stereocontrol for the ROP of *rac*-lactide; heterotactic PLA is produced under solvent-free conditions at 130 °C (P_r >0.90 and M_w/M_n <1.22 with 95% conversion after 30 minutes) (Chart 1.6f).[224]

Very few group 4 metallocene initiators for the ROP of lactide are found in the literature. Ning *et al.* showed that C_s-symmetric ^{Ph_2}CB(Cp,Flu)Zr(OC(O^{i}Pr)CMe$_2$)$_2$ was active for the ROP of *L*-lactide with 92% conversion to PLA recorded after 105 minutes at 80 °C (Chart 1.7a). However, they also observed that C_{2v}-symmetric Cp$_2$Zr(OC(O^{i}Pr)CMe$_2$)$_2$ and C_2-symmetric *rac*-EBIZr(OC(O^{i}Pr)CMe$_2$)$_2$ were poor initiators for ROP of *L*-lactide with only 7% conversion recorded after 26 and 18 hours respectively at 80 °C (Chart 1.7b and c).[226] The half-sandwich complex CpTiCl$_2$(OEt) has also been found to be a poor initiator for the ROP of *L*-lactide with full conversion reached after 48 hours at 130 °C (Chart 1.7d).[227]

Zirconium and titanium alkoxide and aryloxide complexes with a chiral cyclopentadienyl-derived (hydro)-permethylpentalenyl ligand have been found to be good initiators for the ROP of *L*- and *rac*-lactide with over 90% conversion recorded

after 1 hour at 100 °C (Chart 1.7e).[228] Recently, well-defined biscyclopentadienyl and bisindenyl zirconium alkoxide and aryloxide complexes were shown to be active for the ROP of *L*- and *rac*-lactide with the ROP of *L*-lactide by $(Ind)_2ZrMe(O^tBu)$ demonstrating 84% conversion after 8 hours at 80 °C (Chart 1.7f).[229]

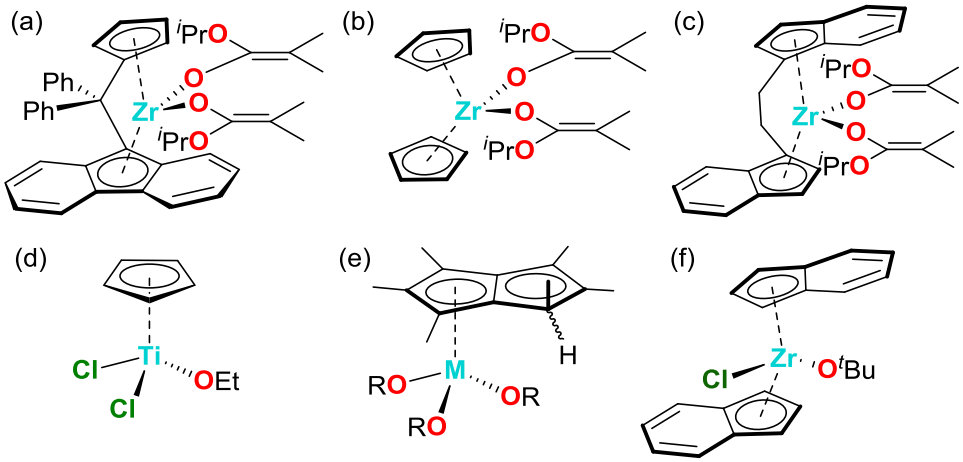


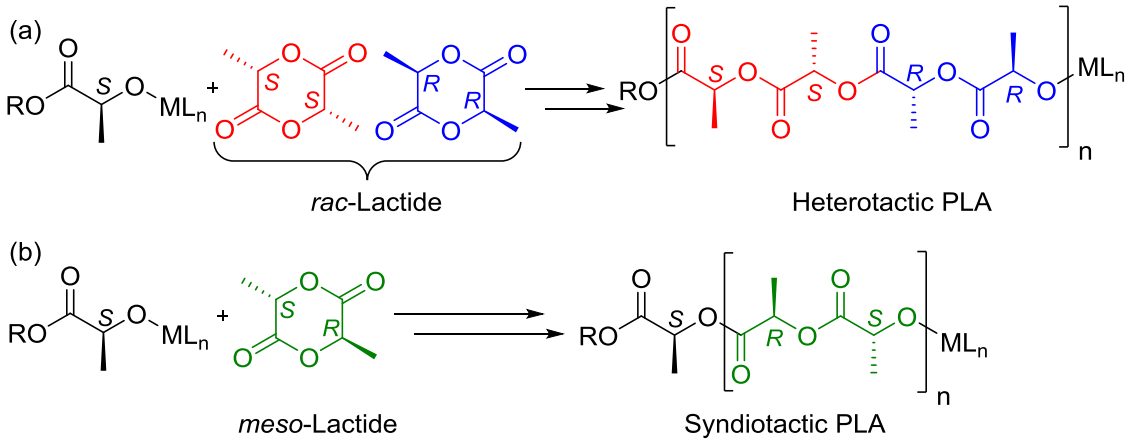
Chart 1.7 Structures of (a) $^{Ph_2}CB(Cp,Flu)Zr(OC(O^iPr)CMe_2)_2$,[226] (b) $Cp_2Zr(OC(O^iPr)CMe_2)_2$,[226] (c) *rac*-$EBIZr(OC(O^iPr)CMe_2)_2$,[226] (d) $CpTiCl_2(OEt)$,[227] (e) $Pn^*(H)M(OR)_3$[228] and (f) $(Ind)_2ZrMe(O^tBu)$.[229]

1.4.5 Stereochemical control

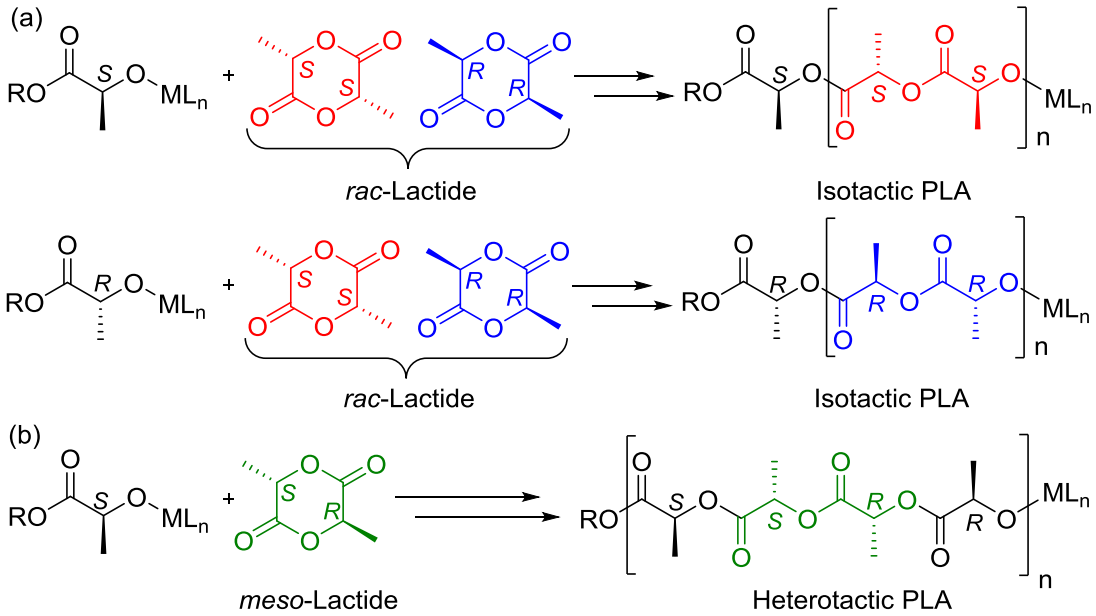
When there is a choice of stereogenic centre to insert into the growing polymer chain (i.e. during the polymerisation of *rac*- or *meso*-lactide) single-site catalysts function by two different control mechanisms in order to establish which stereocentre is favoured; chain-end-control and enantiomorphic site-control. For the polymerisation of *L*- and *D*-lactide, in the absence of epimerisation, the type of control mechanism is irrelevant; both stereogenic centres of *L*- and *D*-lactide monomers have the same stereochemistry and result in the formation of isotactic PLA.[172]

In chain-end-control, the configuration of the next inserted monomer in *rac*-lactide polymerisation, or the cleavage site of the next inserted monomer in *meso*-lactide polymerisation, is determined by the stereogenic centre of the propagating

chain-end.[171] If the stereogenic centre favours *racemic*-enchainment then heterotactic PLA is obtained from *rac*-lactide (i.e. alternation insertion of *L*- and *D*-lactide monomers) and syndiotactic PLA from *meso*-lactide (Scheme 1.11). However, if the stereogenic centre favours *meso*-enchainment then isotactic PLA is obtained from *rac*-lactide and heterotactic PLA from *meso*-lactide (Scheme 1.12).



Scheme 1.11 Chain-end-control for the ROP of (a) *rac*-lactide and (b) *meso*-lactide favouring *racemic*-enchainment.



Scheme 1.12 Chain-end-control for the ROP of (a) *rac*-lactide and (b) *meso*-lactide favouring *meso*-enchainment.

In enantiomorphic site-control, the configuration of the next inserted monomer for *rac*-lactide, or the cleavage site of next inserted monomer for *meso*-lactide, is determined by the configuration of the surrounding ligands or by the chirality of the catalyst.[171] If the ligand environment strongly favours one stereogenic centre over the other then the polymerisation of *rac*-lactide results in isotactic PLA, while the polymerisation of *meso*-lactide forms syndiotactic PLA.

1.4.6 Polymer tacticity

Lactide monomer composition, polymerisation kinetics, conversion and side reactions, such as epimerisation or transesterification during polymerisation or racemisation during polymer processing, can influence polymer tacticity.[177, 230] ^{1}H and ^{13}C{^{1}H} NMR spectroscopy can be used to determine PLA tacticity at the tetrad level; the chemical shifts of the ^{1}H and ^{13}C nuclei present in PLA are affected by the stereoconfiguration of 1–3 adjacent stereogenic centres on either side. In the ^{1}H NMR spectra, the splitting of the methine resonance due to coupling to the methyl protons in the polymer can be removed by homonuclear decoupling. The resonances can then be assigned based on the various *meso* (–*RR*– and –*SS*–) and *racemic* (–*RS*– and –*SR*–) linkages present in the polymer chain. The –*RR*– and –*SS*–, and –*RS*– and –*SR*– diads are indistinguishable in the NMR spectra and are referred to as '*m*' and '*r*' diads respectively.[177] The *meso* and *racemic* linkages can also be referred to as isotactic or syndiotactic relationships between adjacent stereocentres ('*i*' and '*s*' diads).[172] At the tetrad level the relationships between stereocentres can be described by three-letter sequences; isotactic PLLA and PDLA have repeating tetrads described by '*mmm*' (–*RRRR*– or –*SSSS*– linkages), while pure heterotactic PLA contains '*mrm*' and '*rmr*' tetrads (–*RRSS*– or –*RSSR*– linkages) (Figure 1.2).[172]

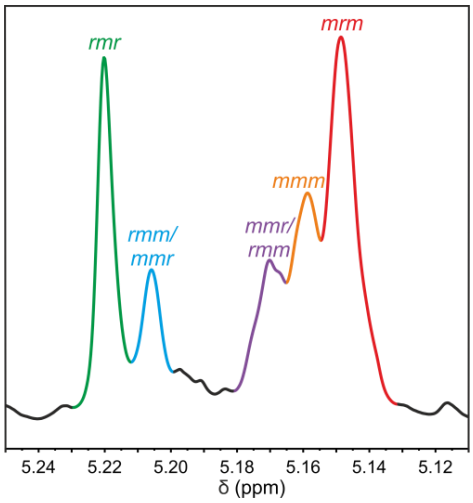


Figure 1.2 Example of a homonuclear decoupled $^{1}H\{^{1}H\}$ NMR spectrum of heterotactic enriched PLA (P_r = 0.84).

The degree of stereoregularity is expressed as the probability of forming a *racemic* or *meso* linkage (i.e. the probability of forming a new *racemic* (syndiotactic) or *meso* (isotactic) diad); referred to as P_r and P_m respectively. For the ROP of *rac*- and *meso*-lactide when P_r or P_m = 0.50 the polymer is atactic, and when P_r or P_m = 1.00 the polymers are heterotactic and syndiotactic respectively.[172] P_r and P_m can be calculated from the deconvoluted homonuclear decoupled $^{1}H\{^{1}H\}$ NMR spectra by taking into account the intensities of the resonances corresponding to each tetrad, and the probability of forming each tetrad (Table 1.1).[172]

Table 1.1 The probability of forming each tetrad for the ROP of *rac*-lactide ($P_r + P_m = 1$).[231]

Tetrad	Probability
rmr	$\frac{P_r^2}{2}$
rmm	$\frac{P_r P_m}{2}$
mmr	$\frac{P_r P_m}{2}$
mmm	$P_m^2 + \frac{P_r P_m}{2}$
mrm	$\frac{P_r^2 + P_r P_m}{2}$

1.5 Scope of the Thesis

The primary aims of the thesis are to (i) discover supported metallocene systems with sufficiently high α-olefin polymerisation activities and hydrogen response to produce ultra-low molecular weight polymers on an industrial scale, and (ii) find new single-site initiators for the ROP of lactide monomers.

The thesis primarily focuses on the slurry-phase polymerisation of ethylene using unsymmetrical permethylindenyl *ansa*-metallocenes based on the $^{Me_2}SB(Cp^R,I^*)ZrX(Y)$ motif. Chapter 2 discusses the synthesis and characterisation of the metallocene complexes. Chapter 3 then presents the ability of these complexes to function as homogeneous and slurry-phase α-olefin (propylene and ethylene) polymerisation catalysts, utilising a range of inorganic solid supports and polymerisation conditions. Chapter 4 showcases the ability of the heterogeneous catalysts for ethylene/1-hexene copolymerisation and discusses the effects of hydrogen on both polymerisation activity and polymer properties. Finally, Chapter 5 focuses on utilising the group 4 unsymmetrical permethylindenyl *ansa*-metallocene complexes as initiators for the ROP of lactide monomers. The kinetics of polymerisation are discussed and rate equations are determined based on polymerisation trends under a variety of conditions.

1.6 References

1. T. J. Hutley and M. Ouederni, in *Polyolefin Compounds and Materials: Fundamentals and Industrial Applications*, eds. M. Al-Ali AlMa'adeed and I. Krupa, Springer International Publishing, Cham, 2016, pp. 13-50.
2. G. W. Coates, *Chem. Rev.*, 2000, **100**, 1223-1252.
3. C. Romera-Castillo, M. Pinto, T. M. Langer, X. A. Alvarez-Salgado and G. J. Herndl, *Nat. Commun.*, 2018, **9**, 7.
4. G. E. Luckachan and C. K. S. Pillai, *J. Polym. Environ.*, 2011, **19**, 637-676.
5. J. C. W. Chien, *J. Am. Chem. Soc.*, 1959, **81**, 86-92.
6. D. S. Breslow and N. R. Newburg, *J. Am. Chem. Soc.*, 1959, **81**, 81-86.
7. H. Sinn, W. Kaminsky, H. J. Vollmer and R. Woldt, *Angew. Chem., Int. Ed. Engl.*, 1980, **19**, 390-392.
8. W. Kaminsky, K. Kulper, H. H. Brintzinger and F. Wild, *Angew. Chem.*, 1985, **24**, 507-508.
9. W. Kaminsky, *Macromol. Chem. Phys.*, 1996, **197**, 3907-3945.
10. G. J. P. Britovsek, V. C. Gibson and D. F. Wass, *Angew. Chem., Int. Ed.*, 1999, **38**, 428-447.
11. L. L. Bohm, *Angew. Chem., Int. Ed.*, 2003, **42**, 5010-5030.
12. L. Resconi, L. Cavallo, A. Fait and F. Piemontesi, *Chem. Rev.*, 2000, **100**, 1253-1346.
13. G. G. Hlatky, *Chem. Rev.*, 2000, **100**, 1347-1376.
14. W. Kaminsky, A. Funck and H. Haehnsen, *Dalton Trans.*, 2009, 8803-8810.
15. I. Sedov, V. Makhaev and P. E. Matkovskii, *Catal. Ind.*, 2012, **4**, 129-140.
16. M. J. Calhorda and L. F. Veiros, *Coord. Chem. Rev*, 1999, **185-6**, 37-51.
17. P. J. Shapiro, *Coord. Chem. Rev.*, 2002, **231**, 67-81.
18. B. Wang, *Coord. Chem. Rev.*, 2006, **250**, 242-258.
19. T. J. Peckham, P. Nguyen, S. C. Bourke, Q. Wang, D. G. Harrison, P. Zoricak, C. Russell, L. M. Liable-Sands, A. L. Rheingold, A. J. Lough and I. Manners, *Organometallics*, 2001, **20**, 3035-3043.
20. H. S. Zijlstra and S. Harder, *Eur. J. Inorg. Chem.*, 2015, 19-43.
21. A. Koppl, A. I. Babel and H. G. Alt, *J. Mol. Catal. A: Chem.*, 2000, **153**, 109-119.
22. C. S. Bajgur, W. R. Tikkanen and J. L. Petersen, *Inorg. Chem.*, 1985, **24**, 2539-2546.
23. N. Schneider, M. E. Huttenloch, U. Stehling, R. Kirsten, F. Schaper and H. H. Brintzinger, *Organometallics*, 1997, **16**, 3413-3420.
24. D. Stern, M. Sabat and T. J. Marks, *J. Am. Chem. Soc.*, 1990, **112**, 9558-9575.
25. H. G. Alt and M. Jung, *J. Organomet. Chem.*, 1998, **562**, 229-253.
26. M. L. H. Green and N. Ishihara, *J. Chem. Soc., Dalton Trans.*, 1994, 657-665.
27. T. J. Katz and N. Acton, *Tetrahedron Lett.*, 1970, **11**, 2497-2499.

28. G. Erker, C. Psiorz, R. Fröhlich, M. Grehl, C. Krüger, R. Noe and M. Nolte, *Tetrahedron*, 1995, **51**, 4347-4358.

29. W. A. Herrmann, M. J. A. Morawietz, H.-F. Herrmann and F. Küber, *J. Organomet. Chem.*, 1996, **509**, 115-117.

30. H. L. Lentzner and W. E. Watts, *Tetrahedron*, 1971, **27**, 4343-4351.

31. R. B. Grossman, R. A. Doyle and S. L. Buchwald, *Organometallics*, 1991, **10**, 1501-1505.

32. O. W. Lofthus, C. Slebodnick and P. A. Deck, *Organometallics*, 1999, **18**, 3702-3708.

33. J.-C. Buffet, T. A. Q. Arnold, Z. R. Turner, P. Angpanitcharoen and D. O'Hare, *RSC Adv.*, 2015, **5**, 87456-87464.

34. P. Ransom, A. E. Ashley, N. D. Brown, A. L. Thompson and D. O'Hare, *Organometallics*, 2011, **30**, 800-814.

35. T. K. Miyamoto, M. Tsutsui and L. B. Chen, *Chem. Lett.*, 1981, 729-730.

36. F. M. Alías, S. Barlow, J. S. Tudor, D. O'Hare, R. T. Perry, J. M. Nelson and I. Manners, *J. Organomet. Chem.*, 1997, **528**, 47-58.

37. T. A. Q. Arnold, D. Phil Thesis, University of Oxford, 2015.

38. J. E. Matley, Part II Thesis, University of Oxford, 2015.

39. L. Resconi, A. Fait, F. Piemontesi, M. Colonnesi, H. Rychlicki and R. Zeigler, *Macromolecules*, 1995, **28**, 6667-6676.

40. A. Razavi and J. Ferrara, *J. Organomet. Chem.*, 1992, **435**, 299-310.

41. J. A. Ewen, *J. Mol. Catal. A: Chem.*, 1998, **128**, 103-109.

42. J. A. Ewen, *J. Am. Chem. Soc.*, 1984, **106**, 6355-6364.

43. J. A. Ewen, M. J. Elder, R. L. Jones, L. Haspeslagh, J. L. Atwood, S. G. Bott and K. Robinson, *Makromol. Chem., Macromol. Symp.*, 1991, **48-9**, 253-295.

44. J. A. Ewen, R. L. Jones, A. Razavi and J. D. Ferrara, *J. Am. Chem. Soc.*, 1988, **110**, 6255-6256.

45. J. A. Ewen, M. J. Elder, R. L. Jones, S. Curtis and H. N. Cheng, in *Studies in Surface Science and Catalysis*, eds. T. Keii and K. Soga, Elsevier, 1990, vol. 56, pp. 439-482.

46. L. Resconi, R. L. Jones, A. L. Rheingold and G. P. A. Yap, *Organometallics*, 1996, **15**, 998-1005.

47. L. Resconi, F. Piemontesi, I. Camurati, O. Sudmeijer, I. E. Nifant'ev, P. V. Ivchenko and L. G. Kuz'mina, *J. Am. Chem. Soc.*, 1998, **120**, 2308-2321.

48. G. Odian, *Principles of Polymerization*, Wiley, 2004.

49. A. Razavi and J. L. Atwood, *J. Organomet. Chem.*, 1995, **497**, 105-111.

50. A. Razavi and J. L. Atwood, *J. Organomet. Chem.*, 1996, **520**, 115-120.

51. D. A. X. Fraser, Z. R. Turner, J.-C. Buffet and D. O'Hare, *Organometallics*, 2016, **35**, 2664-2674.

52. J. N. Pedeutour, K. Radhakrishnan, H. Cramail and A. Deffieux, *Macromol. Rapid Commun.*, 2001, **22**, 1095-1123.

53. W. Kaminsky and R. Steiger, *Polyhedron*, 1988, **7**, 2375-2381.

54. Y. Jian-ding, F. Zhi-qiang and W. Wei, *J. Zhejiang Univ., Sci., B*, 2005, **6**, 1009-1014.

55. W. J. Gauthier, J. F. Corrigan, N. J. Taylor and S. Collins, *Macromolecules*, 1995, **28**, 3771-3778.

56. C. Janiak, U. Versteeg, K. C. H. Lange, R. Weimann and E. Hahn, *J. Organomet. Chem.*, 1995, **501**, 219-234.

57. F. Benetollo, G. Cavinato, L. Crosara, F. Milani, G. Rossetto, C. Scelza and P. Zanella, *J. Organomet. Chem.*, 1998, **555**, 177-185.

58. T. A. Q. Arnold, J.-C. Buffet, Z. R. Turner and D. O'Hare, *J. Organomet. Chem.*, 2015, **792**, 55-65.

59. I. I. Zakharov, V. A. Zakharov, A. G. Potapov and G. M. Zhidomirov, *Macromol. Theory Simul.*, 1999, **8**, 272-278.

60. T. N. P. Luhtanen, M. Linnolahti and T. A. Pakkanen, *J. Organomet. Chem.*, 2002, **648**, 49-54.

61. S. Pasynkiewicz, *Polyhedron*, 1990, **9**, 429-453.

62. E. Zurek, T. K. Woo, T. K. Firman and T. Ziegler, *Inorg. Chem.*, 2001, **40**, 361-370.

63. I. I. Zakharov and V. A. Zakharov, *Macromol. Theory Simul.*, 2001, **10**, 108-116.

64. M. Linnolahti, J. R. Severn and T. A. Pakkanen, *Angew. Chem., Int. Ed.*, 2008, **47**, 9279-9283.

65. M. Linnolahti, J. R. Severn and T. A. Pakkanen, *Angew. Chem., Int. Ed.*, 2006, **45**, 3331-3334.

66. Z. Falls, N. Tyminska and E. Zurek, *Macromolecules*, 2014, **47**, 8556-8569.

67. V. N. Panchenko, V. A. Zakharov, I. G. Danilova, E. A. Paukshtis, I. I. Zakharov, V. G. Goncharov and A. P. Suknev, *J. Mol. Catal. A: Chem.*, 2001, **174**, 107-117.

68. A. Shamiri, M. H. Chakrabarti, S. Jahan, M. A. Hussain, W. Kaminsky, P. V. Aravind and W. A. Yehye, *Materials*, 2014, **7**, 5069-5108.

69. L. S. Santos, *J. Braz. Chem. Soc.*, 2011, **22**, 1827-1840.

70. J. T. Hirvi, M. Bochmann, J. R. Severn and M. Linnolahti, *ChemPhysChem*, 2014, **15**, 2732-2742.

71. P. Cossee, *J. Catal.*, 1964, **3**, 80-88.

72. E. J. Arlman and P. Cossee, *J. Catal.*, 1964, **3**, 99-104.

73. E. J. Arlman, *J. Catal.*, 1964, **3**, 89-98.

74. K. Thorshaug, J. A. Stovneng, E. Rytter and M. Ystenes, *Macromolecules*, 1998, **31**, 7149-7165.

75. A. T. Rappe, W. M. Skiff and C. J. Casewit, *Chem. Rev.*, 2000, **100**, 1435-1456.

76. E. Quintanilla, F. di Lena and P. Chen, *Chem. Commun.*, 2006, 4309-4311.

77. J. Klosin, P. P. Fontaine and R. Figueroa, *Acc. Chem. Res.*, 2015, **48**, 2004-2016.

78. A. E. Hamielec and J. B. P. Soares, *Prog. Polym. Sci.*, 1996, **21**, 651-706.

79. W. Kaminsky, *Catal. Today*, 1994, **20**, 257-271.

80. J. B. P. Soares and A. E. Hamielec, *Polymer*, 1996, **37**, 4599-4605.

81. W. Kaminsky and H. Lüker, *Makromol. Chem. Rapid. Comm.*, 1984, **5**, 225-228.

82. SCG Chemicals Company Limited, www.scgchemicals.com/en/.

83. K. J. Chu, J. B. P. Soares and A. Penlidis, *Macromol. Chem. Phys.*, 2000, **201**, 552-557.

84. W. Posch, in *Applied Plastics Engineering Handbook*, ed. M. Kutz, William Andrew Publishing, Oxford, 2011, pp. 23-48.

85. F. Q. Song, R. D. Cannon and M. Bochmann, *J. Am. Chem. Soc.*, 2003, **125**, 7641-7653.

86. M. Bochmann, *Organometallics*, 2010, **29**, 4711-4740.

87. T. Garoff, S. Johansson, K. Pesonen, P. Waldvogel and D. Lindgren, *Eur. Polym. J.*, 2002, **38**, 121-132.

88. Y. V. Kissin, R. I. Mink, T. E. Nowlin and A. J. Brandolini, *Top. Catal.*, 1999, **7**, 69-88.

89. R. F. Jordan, P. K. Bradley, N. C. Baenziger and R. E. Lapointe, *J. Am. Chem. Soc.*, 1990, **112**, 1289-1291.

90. B. Paredes, R. van Grieken, A. Carrero, I. Suarez and J. B. P. Soares, *Macromol. Chem. Phys.*, 2011, **212**, 1590-1599.

91. K. Osakada, in *Organometallic Reactions and Polymerization*, ed. K. Osakada, Springer-Verlag Berlin, Berlin, 2014, vol. 85, pp. 51-88.

92. J. Imuta, A. Todo, T. Tsutsui, T. Hachimori and N. Kashiwa, *Bull. Chem. Soc. Jpn.*, 2004, **77**, 607-615.

93. W. Kaminsky and A. Noll, *Polym. Bull.*, 1993, **31**, 175-182.

94. M. L. Britto, G. B. Galland, J. H. Z. dos Santos and M. C. Forte, *Polymer*, 2001, **42**, 6355-6361.

95. T. M. Ushakova, E. E. Starchak, V. G. Krasheninnikov, A. A. Samoilenko, P. V. Ivchenko, I. E. Nifant'ev and L. A. Novokshonova, *Kinet. Catal.*, 2012, **53**, 75-83.

96. N. Naga and Y. Imanishi, *Macromol. Chem. Phys.*, 2002, **203**, 2155-2162.

97. Y. Nakayama, Y. Sogo, Z. G. Cai and T. Shiono, *J. Polym. Sci., Part A: Polym. Chem.*, 2013, **51**, 1223-1229.

98. K. Unverhau, G. Kehr, R. Frohlich and G. Erker, *Dalton Trans.*, 2011, **40**, 3724-3736.

99. J. C. Stevens, F. J. Timmers, D. R. Wilson, G. F. Schmidt, P. N. Nickias, R. K. Rosen, G. W. Knight and S. Y. Lai, EP416815A2, 1991.

100. J. A. M. Canich, EP420436A1, 1991.

101. V. F. Tisse, F. Prades, R. Briquel, C. Boisson and T. F. L. McKenna, *Macromol. Chem. Phys.*, 2010, **211**, 91-102.

102. A. Entezami and P. N. Moghadam, *Polym. Int.*, 2005, **54**, 1326-1329.

103. G. Ertl, H. Knözinger, F. Schüth and J. Weitkamp, *Handbook of Heterogeneous Catalysis*, Wiley-VCH, Weinheim, 2nd edn., 2008.

104. M. A. Bashir, T. Vancompernolle, R. M. Gauvin, L. Delevoye, N. Merle, V. Monteil, M. Taoufik, T. F. L. McKenna and C. Boisson, *Catal. Sci. Technol.*, 2016, **6**, 2962-2974.

105. J. D. A. Pelletier and J.-M. Basset, *Acc. Chem. Res.*, 2016, **49**, 664-677.

106. P. A. Zapata, C. Belver, R. Quijada, P. Aranda and E. Ruiz-Hitzky, *App. Catal. A Gen.*, 2013, **453**, 142-150.

107. P. Wongwaiwattanakul and B. Jongsomjit, *Catal. Comm.*, 2008, **10**, 118-122.

108. E. V. Ramos-Fernandez, A. Sepulveda-Escribano and F. Rodriguez-Reinoso, *Catal. Comm.*, 2008, **9**, 1243-1246.

109. M. Sacchetti, S. Pasquali and G. Govoni, US5698487, 1997.

110. J. R. Severn, J. C. Chadwick, R. Duchateau and N. Friederichs, *Chem. Rev.*, 2005, **105**, 4073-4147.

111. S. I. Woo and Y. S. Ko, US5869417, 1999.

112. C. Copéret and J.-M. Basset, *Adv. Synth. Catal.*, 2007, **349**, 78-92.

113. C. Copéret, F. Allouche, K. W. Chan, M. P. Conley, M. F. Delley, A. Fedorov, I. B. Moroz, V. Mougel, M. Pucino, K. Searles, K. Yamamoto and P. A. Zhizhko, *Angew. Chem., Int. Ed.*, 2018, **57**, 6398-6440.

114. U. Diaz, D. Brunel and A. Corma, *Chem. Soc. Rev.*, 2013, **42**, 4083-4097.

115. S. Shylesh, M. J. Jia and W. R. Thiel, *Eur. J. Inorg. Chem.*, 2010, 4395-4410.

116. D. E. De Vos, M. Dams, B. F. Sels and P. A. Jacobs, *Chem. Rev.*, 2002, **102**, 3615-3640.

117. C. Copéret, A. Fedorov and P. A. Zhizhko, *Catal. Lett.*, 2017, **147**, 2247-2259.

118. C. Copéret, A. Comas-Vives, M. P. Conley, D. P. Estes, A. Fedorov, V. Mougel, H. Nagae, F. Nunez-Zarur and P. A. Zhizhko, *Chem. Rev.*, 2016, **116**, 323-421.

119. C. Copéret, M. Chabanas, R. P. Saint-Arroman and J.-M. Basset, *Angew. Chem., Int. Ed.*, 2003, **42**, 156-181.

120. R. Anwander, *Chem. Mater.*, 2001, **13**, 4419-4438.

121. P. Serna and B. C. Gates, *Acc. Chem. Res.*, 2014, **47**, 2612-2620.

122. M. K. Samantaray, E. Pump, A. Bendjeriou-Sedjerari, V. D'Elia, J. D. A. Pelletier, M. Guidotti, R. Psaro and J.-M. Basset, *Chem. Soc. Rev.*, 2018, **47**, 8403-8437.

123. K. Soga and M. Kaminaka, *Macromol. Chem. Phys.*, 1993, **194**, 1745-1755.

124. S. Collins, W. M. Kelly and D. A. Holden, *Macromolecules*, 1992, **25**, 1780-1785.

125. R. Guimaraes, F. C. Stedile and J. H. Z. dos Santos, *J. Mol. Catal. A: Chem.*, 2003, **206**, 353-362.

126. P. Angpanitcharoen, G. Hay, J.-C. Buffet, Z. R. Turner, T. A. Q. Arnold and D. O'Hare, *Polyhedron*, 2016, **116**, 216–222.

127. P. G. Belelli, M. L. Ferreira and D. E. Damiani, *Appl. Catal., A*, 2002, **228**, 189-202.

128. V. F. Tisse, C. Boisson and T. F. L. McKenna, *Macromol. Chem. Phys.*, 2014, **215**, 1358-1369.

129. W. Kaminsky and F. Renner, *Makromol. Chem., Rapid Commun.*,, 1993, **14**, 239-243.

130. G. Fink, B. Steinmetz, J. Zechlin, C. Przybyla and B. Tesche, *Chem. Rev.*, 2000, **100**, 1377-1390.

131. L. T. Zhuravlev, *Colloid Surf., A*, 2000, **173**, 1-38.

132. M. M. Mortazavi, S. Ahmadjo, J. H. Z. Dos Santos, H. Arabi, M. Nekoomanesh, G. H. Zohuri, R. Brambilla and G. B. Galland, *J. Appl. Polym. Sci.*, 2013, **130**, 4568-4575.

133. D. Bianchini, J. H. Z. dos Santos, T. Uozumi and T. Sano, *J. Mol. Catal. A: Chem.*, 2002, **185**, 223-235.

134. V. N. Panchenko, N. V. Semikolenova, I. G. Danilova, E. A. Paukshtis and V. A. Zakharov, *J. Mol. Catal. A Chem.*, 1999, **142**, 27-37.

135. E. Y.-X. Chen and T. J. Marks, *Chem. Rev.*, 2000, **100**, 1391-1434.

136. M. Bochmann, *J. Chem. Soc.*, 1996, **3**, 255-270.

137. D. L. Geatches, S. J. Clark and H. C. Greenwell, *J. Phys. Chem. A*, 2010, **114**, 3569-3575.

138. S. Hamura, H. Yasuda and M. Sato, US5906955, 1998.

139. A. Yano and M. Sato, US5830820, 1998.

140. C. Liu, T. Tang and B. Huang, *J. Catal.*, 2004, **221**, 162-169.

141. H. Zhang, F. Z. Zhang, L. L. Ren, D. G. Evans and X. Duan, *Mater. Chem. Phys.*, 2004, **85**, 207-214.

142. C. Chen, M. Yang, Q. Wang, J.-C. Buffet and D. O'Hare, *J. Mater. Chem. A.*, 2014, **2**, 15102-15110.

143. Q. Wang and D. O'Hare, *Chem. Commun.*, 2013, **49**, 6301-6303.

144. C. M. R. Wright, K. Ruengkajorn, A. F. R. Kilpatrick, J.-C. Buffet and D. O'Hare, *Inorg. Chem.*, 2017, **56**, 7842-7850.

145. J.-C. Buffet, N. Wanna, T. A. Q. Arnold, E. K. Gibson, P. P. Wells, Q. Wang, J. Tantirungrotechai and D. O'Hare, *Chem. Mater.*, 2015, **27**, 1495-1501.

146. J.-C. Buffet, Z. R. Turner, R. T. Cooper and D. O'Hare, *Polym. Chem.*, 2015, **6**, 2493-2503.

147. R. Van Grieken, A. Carrero, I. Suarez and B. Paredes, *Eur. Polym. J.*, 2007, **43**, 1267-1277.

148. T. A. Q. Arnold, Z. R. Turner, J.-C. Buffet and D. O'Hare, *J. Organomet. Chem.*, 2016, **822**, 85-90.

149. T. J. Williams, J.-C. Buffet, Z. R. Turner and D. O'Hare, *Catal. Sci. Technol.*, 2018, **8**, 5454-5461.

150. J.-C. Buffet, Z. R. Turner and D. O'Hare, *Chem. Commun.*, 2018, **54**, 10970-10973.

151. R. L. Geerts, US5436212, 1995.

152. R. L. Geerts, T. G. Hill and S. E. Kufeld, US5411925, 1995.

153. R. L. Geerts, S. E. Kufeld and T. G. Hill, US5354721, 1994.

154. H. Cramail, K. Radhakrishnan and A. Deffieux, *Compt. Rend.*, 2002, **5**, 49-52.

155. T. Dalet, H. Cramail and A. Deffieux, *Macromol. Chem. and Phys.*, 2004, **205**, 1394-1401.

156. E. Kaji and E. Yoshioka, US8404880, 2013.

157. A. F. R. Kilpatrick, J.-C. Buffet, P. Nørby, N. H. Rees, N. P. Funnell, S. Sripothongnak and D. O'Hare, *Chem. Mater.*, 2016, **28**, 7444-7450.

158. C. M. R. Wright, Z. R. Turner, J.-C. Buffet and D. O'Hare, *Chem. Commun.*, 2016, **52**, 2850-2853.

159. M. S. Bhagwat, S. S. Bhagwat and M. M. Sharma, *Ind. Eng. Chem. Res.*, 1994, **33**, 2322-2330.

160. P. Galli and J. C. Haylock, *Prog. Polym. Sci.*, 1991, **16**, 443-462.

161. N. Senso, S. Khaubunsongserm, B. Jongsomjit and P. Praserthdam, *Molecules*, 2010, **15**, 9323-9339.

162. H. Hammawa, T. M. Mannan, D. T. Lynch and S. E. Wanke, *J. Appl. Polym. Sci.*, 2004, **92**, 3549-3560.

163. D. T. Lynch, M. O. Jejelowo and S. E. Wanke, *Can. J. Chem. Eng.*, 1991, **69**, 657-664.

164. D. G. Boucher, I. W. Parsons and R. N. Haward, *Macromol. Chem. Phys.*, 1974, **175**, 3461-3473.

165. M. A. Bashir, V. Monteil, C. Boisson and T. F. L. McKenna, *J. Appl. Polym. Sci.*, 2018, **135**, 45670-45677.

166. A. Munozescalona, H. Garcia and A. Albornoz, *J. Appl. Polym. Sci.*, 1987, **34**, 977-988.

167. K. Fukuda, B. Liu, H. Nakatani, I. Nishiyama, M. Yamahiro and M. Terano, *Catal. Comm.*, 2003, **4**, 657-662.

168. V. N. Panchenko, L. G. Echevkaya, V. A. Zakharov and M. A. Matsko, *Appl. Catal., A*, 2011, **404**, 47-53.

169. J. P. J. Turunen and T. T. Pakkanen, *J. Appl. Polym. Sci.*, 2006, **100**, 4632-4635.

170. P. A. Gunatillake and R. Adhikari, *Eur. Cells Mater.*, 2003, **5**, 1-16.

171. P. J. Dijkstra, H. Z. Du and J. Feijen, *Polym. Chem.*, 2011, **2**, 520-527.

172. M. J. Stanford and A. P. Dove, *Chem. Soc. Rev.*, 2010, **39**, 486-494.

173. J. Lunt, *Polym. Degrad. Stabil.*, 1998, **59**, 145-152.

174. H. R. Kricheldorf, *Chemosphere*, 2001, **43**, 49-54.

175. R. E. Drumright, P. R. Gruber and D. E. Henton, *Adv. Mater.*, 2000, **12**, 1841-1846.

176. R. Dattatray Karande, V. K. Abitha, A. Vasudeo Rane and R. K. Mishra, *J. Mater. Sci. Eng. Adv. Tech.*, 2015, **12**, 1-37.

177. K. A. M. Thakur, R. T. Kean, E. S. Hall, J. J. Kolstad and E. J. Munson, *Int. J. Polym. Anal. Charact.*, 1998, **4**, 379-391.

178. O. Dechy-Cabaret, B. Martin-Vaca and D. Bourissou, *Chem. Rev.*, 2004, **104**, 6147-6176.

179. R. H. Platel, L. M. Hodgson and C. K. Williams, *Polym. Rev.*, 2008, **48**, 11-63.

180. J.-C. Buffet and J. Okuda, *Polym. Chem.*, 2011, **2**, 2758-2763.

181. B. J. O'Keefe, M. A. Hillmyer and W. B. Tolman, *J. Chem. Soc., Dalton Trans.*, 2001, 2215-2224.

182. C. M. Thomas, *Chem. Soc. Rev.*, 2010, **39**, 165-173.

183. H. Y. Ma, T. P. Spaniol and J. Okuda, *Angew. Chem. Int. Ed.*, 2006, **45**, 7818-7821.

184. M. Basko and P. Kubisa, *J. Polym. Sci. Polym. Chem.*, 2006, **44**, 7071-7081.

185. D. Bourissou, B. Martin-Vaca, A. Dumitrescu, M. Graullier and F. Lacombe, *Macromolecules*, 2005, **38**, 9993-9998.

186. L. Clark, G. B. Deacon, C. M. Forsyth, P. C. Junk, P. Mountford, J. P. Townley and J. Wang, *Dalton Trans.*, 2013, **42**, 9294-9312.

187. A. Bhaw-Luximon, D. Jhurry, N. Spassky, S. Pensec and J. Belleney, *Polymer*, 2001, **42**, 9651-9656.

188. D. S. McGuinness, E. L. Marshall, V. C. Gibson and J. W. Steed, *J. Polym. Sci. Polym. Chem.*, 2003, **41**, 3798-3803.

189. M. Basko and P. Kubisa, *J. Polym. Sci. Polym. Chem.*, 2008, **46**, 7919-7923.

190. N. Ajellal, J.-F. Carpentier, C. Guillaume, S. M. Guillaume, M. Helou, V. Poirier, Y. Sarazin and A. Trifonov, *Dalton Trans.*, 2010, **39**, 8363-8376.

191. P. Dubois, C. Jacobs, R. Jerome and P. Teyssie, *Macromolecules*, 1991, **24**, 2266-2270.

192. P. Degee, P. Dubois and R. Jerome, *Macromol. Symp.*, 1997, **123**, 67-84.

193. B. J. O'Keefe, S. M. Monnier, M. A. Hillmyer and W. B. Tolman, *J. Am. Chem. Soc.*, 2001, **123**, 339-340.

194. W. M. Stevels, M. J. K. Ankone, P. J. Dijkstra and J. Feijen, *Macromolecules*, 1996, **29**, 6132-6138.

195. P. Degee, P. Dubois, S. Jacobsen, H. G. Fritz and R. Jerome, *J. Polym. Sci. Polym. Chem.*, 1999, **37**, 2413-2420.

196. A. Kowalski, A. Duda and S. Penczek, *Macromolecules*, 2000, **33**, 7359-7370.

197. N. Spassky, M. Wisniewski, C. Pluta and A. LeBorgne, *Macromol. Chem. Phys.*, 1996, **197**, 2627-2637.

198. T. M. Ovitt and G. W. Coates, *J. Am. Chem. Soc.*, 2002, **124**, 1316-1326.

199. Z. Y. Zhong, P. J. Dijkstra and J. Feijen, *Angew. Chem., Int. Ed.*, 2002, **41**, 4510-4513.

200. Z. Y. Zhong, P. J. Dijkstra and J. Feijen, *J. Am. Chem. Soc.*, 2003, **125**, 11291-11298.

201. N. Nomura, R. Ishii, M. Akakura and K. Aoi, *J. Am. Chem. Soc.*, 2002, **124**, 5938-5939.

202. T. M. Ovitt and G. W. Coates, *J. Am. Chem. Soc.*, 1999, **121**, 4072-4073.

203. H. Y. Chen, H. Y. Tang and C. C. Lin, *Macromolecules*, 2006, **39**, 3745-3752.

204. D. J. Darensbourg, W. Choi, O. Karroonnirun and N. Bhuvanesh, *Macromolecules*, 2008, **41**, 3493-3502.

205. D. C. Aluthge, B. O. Patrick and P. Mehrkhodavandi, *Chem. Commun.*, 2013, **49**, 4295-4297.

206. M. Normand, E. Kirillov, T. Roisnel and J. F. Carpentier, *Organometallics*, 2012, **31**, 1448-1457.

207. D. Myers, A. J. P. White, C. M. Forsyth, M. Bown and C. K. Williams, *Angew. Chem., Int. Ed.*, 2017, **56**, 5277-5282.

208. S. Praban, P. Piromjitpong, V. Balasanthiran, S. Jayaraj, M. H. Chisholm, J. Tantirungrotechai and K. Phomphrai, *Dalton Trans.*, 2019, **48**, 3223-3230.

209. C. Bakewell, A. J. P. White, N. J. Long and C. K. Williams, *Inorg. Chem.*, 2015, **54**, 2204-2212.

210. C. Bakewell, T. P. A. Cao, N. Long, X. F. Le Goff, A. Auffrant and C. K. Williams, *J. Am. Chem. Soc.*, 2012, **134**, 20577-20580.

211. C. Bakewell, T. P. A. Cao, X. F. Le Goff, N. J. Long, A. Auffrant and C. K. Williams, *Organometallics*, 2013, **32**, 1475-1483.

212. E. Grunova, E. Kirillov, T. Roisnel and J. F. Carpentier, *Organometallics*, 2008, **27**, 5691-5698.

213. A. Alaaeddine, C. M. Thomas, T. Roisnel and J. F. Carpentier, *Organometallics*, 2009, **28**, 1469-1475.

214. W. K. Gu, P. F. Xu, Y. R. Wang, Y. M. Yao, D. Yuan and Q. Shen, *Organometallics*, 2015, **34**, 2907-2916.

215. C. Bakewell, A. J. P. White, N. J. Long and C. K. Williams, *Angew. Chem., Int. Ed.*, 2014, **53**, 9226-9230.

216. Y. F. Yu, D. Yuan, Y. R. Wang and Y. M. Yao, *J. Organomet. Chem.*, 2016, **819**, 37-45.

217. Y. Liang, R. L. Duan, C. Y. Hu, L. L. Li, X. Pang, W. X. Zhang and X. S. Chen, *Chin. J. Polym. Sci.*, 2018, **36**, 185-189.

218. T. P. A. Cao, A. Buchard, X. F. Le Goff, A. Auffrant and C. K. Williams, *Inorg. Chem.*, 2012, **51**, 2157-2169.

219. P. Hormnirun, E. L. Marshall, V. C. Gibson, A. J. P. White and D. J. Williams, *J. Am. Chem. Soc.*, 2004, **126**, 2688-2689.

220. B. M. Chamberlain, M. Cheng, D. R. Moore, T. M. Ovitt, E. B. Lobkovsky and G. W. Coates, *J. Am. Chem. Soc.*, 2001, **123**, 3229-3238.

221. M. Cheng, A. B. Attygalle, E. B. Lobkovsky and G. W. Coates, *J. Am. Chem. Soc.*, 1999, **121**, 11583-11584.

222. A. P. Dove, V. C. Gibson, E. L. Marshall, A. J. P. White and D. J. Williams, *Chem. Commun.*, 2001, 283-284.

223. C. Romain, B. Heinrich, S. Bellemin-Laponnaz and S. Dagorne, *Chem. Commun.*, 2012, **48**, 2213-2215.

224. A. J. Chmura, M. G. Davidson, C. J. Frankis, M. D. Jones and M. D. Lunn, *Chem. Commun.*, 2008, 1293-1295.

225. A. Sauer, A. Kapelski, C. Fliedel, S. Dagorne, M. Kol and J. Okuda, *Dalton Trans.*, 2013, **42**, 9007-9023.

226. Y. Ning, Y. Zhang, A. Rodriguez-Delgado and E. Y. X. Chen, *Organometallics*, 2008, **27**, 5632-5640.

227. N. Petzetakis, M. Pitsikalis and N. Hadjichristidis, *J. Polym. Sci., Part A: Polym. Chem.*, 2010, **48**, 1092-1103.

228. Z. R. Turner, J.-C. Buffet and D. O'Hare, *Organometallics*, 2014, **33**, 3891-3903.

229. J.-C. Buffet, G. R. Harris, J. J. Coward, T. A. Q. Arnold, Z. R. Turner and D. O'Hare, *J. Organomet. Chem.*, 2016, **801**, 87-95.

230. G. L. Baker, E. B. Vogel and M. R. Smith, *Polym. Rev.*, 2008, **48**, 64-84.

231. J. Coudane, C. UstarizPeyret, G. Schwach and M. Vert, *J. Polym. Sci. Polym. Chem.*, 1997, **35**, 1651-1658.

Chapter 2

Synthesis and Characterisation of

$^{Me_2}SB(Cp^R,I^*)ZrX(Y)$

2.1 Introduction

2.1.1 Overview

The ancillary cyclopentadienyl (C_5H_5, Cp) ligands of traditional Cp_2MX_2 group 4 metallocene catalysts can be varied in order to influence α-olefin polymerisation activity and polymer properties.[1, 2] Substitution of one cyclopentadienyl ligand results in the formation of unsymmetrical metallocene compounds, which show remarkable efficiency as α-olefin polymerisation catalysts with good control of polymer tacticity.[2, 3] In addition, slight variations of the cyclopentadienyl ring substituents and metal initiation groups have been shown to greatly influence catalytic activity,[4, 5] with electronic structure and spatial organisation of the active site having profound effects on polymer microstructure.[6]

This chapter discusses the synthesis and characterisation of twelve unsymmetrical group 4 metallocenes based on the $^{Me_2}SB(Cp^R,I^*)ZrX(Y)$ motif, with an aim to explore the effects of ligand variation on polymerisation activity and polymer properties.

2.1.2 Definitions of geometric parameters

In this work, Ind_{cent} refers to the centroid of the cyclopentadienyl ring of the permethylindenyl ligand, while Cp_{cent} refers to the centroid of the cyclopentadienyl ligand (Figure 2.1). δ is measured as the angle subtended at the metal centre by the two metal centroids and is expected to be 109.47° for a perfect tetrahedral structure. α is a measure of the tilt between the two cyclopentadienyl rings; it is measured as the dihedral angle between two planes (calculated as the least squares mean of the atoms that make up the cyclopentadienyl rings) and is expected to be complementary to δ (i.e. 70.53° for a perfect tetrahedral structure).[7]

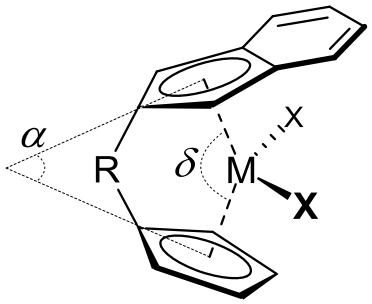


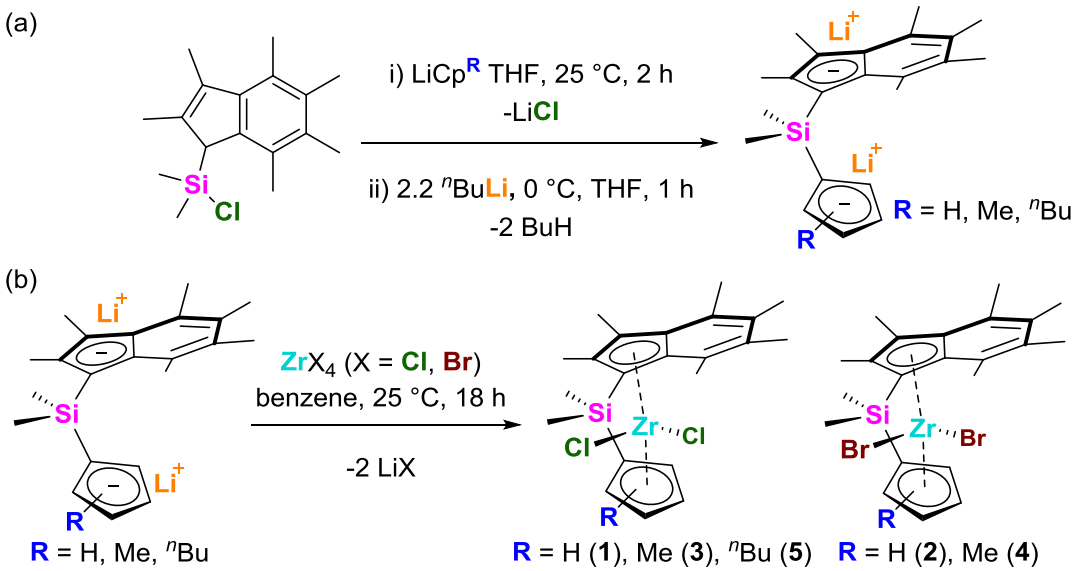
Figure 2.1 Geometric parameters of *ansa*-bridged metallocenes.

2.2 Synthesis of $^{Me_2}SB(Cp^R,I^*)ZrX_2$ (R = H, Me, ^{n}Bu; X = Cl, Br)

The dimethylchlorosilane synthon Ind*$SiMe_2Cl$ was prepared on a large scale *via* modification of a literature procedure;[8] Ind$^{\#}$H was deprotonated with 1.2 equivalents of ^{n}BuLi, followed by addition to 3.0 equivalents of $SiMe_2Cl_2$. The reaction of Ind*$SiMe_2Cl$ with $LiCp^R$ (R = H, Me and ^{n}Bu) followed by deprotonation with a slight excess of ^{n}BuLi afforded dilithium salts $^{Me_2}SB(Cp^R,I^*)Li_2$ (R = H, Me and ^{n}Bu) as pale orange powders in 78, 64 and 30% crude yield respectively (Scheme 2.1a). The ^{1}H NMR spectra of $^{Me_2}SB(Cp^R,I^*)Li_2$ (R = H, Me and ^{n}Bu) show multiplets corresponding to the cyclopentadienyl protons at 6.43–6.92 ppm, six singlets at 2.30–3.09 ppm corresponding to the permethylindenyl methyl groups, and one singlet at approximately 1.0 ppm attributed to the silyl bridge methyl groups (Figures A2.1–A2.3). The ^{1}H NMR spectrum of $^{Me_2}SB(Cp^{Me},I^*)Li_2$ shows an additional resonance at 3.02 ppm corresponding to the methyl group present on the cyclopentadienyl ring, while the ^{1}H NMR spectrum of $^{Me_2}SB(Cp^{n Bu},I^*)Li_2$ shows four multiplets at 0.78 (CH_3), 1.26 (CH_2), 1.64 (CH_2) and 3.08 ppm (CH_2) corresponding to the protons on the *n*-butyl chain. It is noted that the ^{1}H NMR spectra of $^{Me_2}SB(Cp^R,I^*)Li_2$ (R = H, Me and ^{n}Bu) show the presence of unreacted starting materials, however, increased stirring time and heating was unsuccessful in promoting the reactions and driving them to completion.

Equimolar quantities of the dilithium salts $^{Me_2}SB(Cp^R,I^*)Li_2$ (R = H, Me and ^{n}Bu) and either $ZrCl_4$ or $ZrBr_4$ were stirred in benzene at 25 °C for 16 hours. Following work-up, $^{Me_2}SB(Cp,I^*)ZrCl_2$ (**1**), $^{Me_2}SB(Cp,I^*)ZrBr_2$ (**2**), $^{Me_2}SB(Cp^{Me},I^*)ZrCl_2$ (**3**), $^{Me_2}SB(Cp^{Me},I^*)ZrBr_2$ (**4**), *E*-$^{Me_2}SB(Cp^{n Bu},I^*)ZrCl_2$ (***E*-5**) and *Z*-$^{Me_2}SB(Cp^{n Bu},I^*)ZrCl_2$ (***Z*-5**) were isolated as orange solids in 28, 15, 20, 5, 1 and 2% yield respectively

(Scheme 2.1b). For compounds **3** and **5**, the R substituent of the cyclopentadienyl ring was positioned at the least sterically hindered gamma positions; referred to as *E*- when the R group is directed away the I* ligand, and *Z*- when the R group is positioned underneath the I* ligand (Figure 2.2).



Scheme 2.1 Synthesis of (a) ^{Me_2}SB(Cp^R,I*)Li$_2$ and (b) ^{Me_2}SB(Cp^R,I*)ZrX$_2$ (R = H, Me and ^{n}Bu; X = Cl and Br).

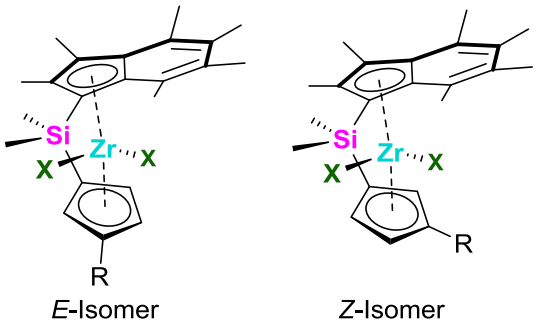


Figure 2.2 Structures of the two regioisomers of ^{Me_2}SB(Cp^R,I)ZrX$_2$.

2.2.1 NMR spectroscopy

The ^{1}H NMR spectra of **1-5** show multiplets of equal intensity with chemical shifts (δ) between 5.08 and 6.81 ppm corresponding to the cyclopentadienyl protons, singlets of equal intensity between 1.86 and 2.65 ppm corresponding to the permethylindenyl

methyl groups and resonances between 0.53 and 0.71 ppm corresponding to the silyl bridge methyl groups (Figures 2.3, 2.5, 2.7, A2.4 and A2.5).

The 2D heteronuclear multiple bond correlation (2D $^{1}H,^{13}C$ HMBC) NMR spectrum for **1** shows that the resonance corresponding to the carbon of the permethylindenyl ligand bound to the silicon atom of the bridge (δ = 84.0 ppm) couples to the most low frequency permethylindenyl methyl resonance at 1.97 ppm (Figure 2.4, navy); consistent with the shielding effect of electropositive silicon. It also shows that the resonance corresponding to the carbon of the cyclopentadienyl ligand bound to the silicon atom of the bridge (δ = 106.0 ppm) couples to the two lower frequency cyclopentadienyl resonances at 5.62 and 5.49 ppm (Figure 2.4, red).

The ^{1}H NMR spectrum of **1** shows four pseudo quartets corresponding to the four cyclopentadienyl protons; their magnetic inequivalence leads to both $^{3}J_{H\text{-}H}$ and $^{4}J_{H\text{-}H}$ coupling between each of the protons. The splitting patterns observed for the cyclopentadienyl protons of **1** are not unique for cyclopentadienyl protons in unsymmetrical metallocene systems, with similar multiplets also observed for $^{Me_2}SB(Cp,I)ZrCl_2$, $^{Me_2}SB(Cp,I)HfCl_2$ and $^{Me_2}CB(Cp,I)ZrCl_2$.[9, 10] Similar splitting patterns were also observed for the cyclopentadienyl protons in unsymmetrical $^{Me_2}SB(Cp,Flu)ZrCl_2$ and $^{R_2}CB(Cp,Flu)ZrCl_2$ (R = Me and Ph), where the authors reported multiplets and triplets respectively.[11-13] Razavi *et al*. suggested that the reason for the splitting pattern observed in $^{R_2}CB(Cp,Flu)ZrCl_2$ (R = Me and Ph) was due to virtual coupling,[13] whereby a proton which is well isolated from other protons in chemical shift can couple to a group of strongly coupled protons, which leads to unexpectedly complex and misleading multiplet splitting patterns.[14] In contrast, for symmetrical systems such as *rac*- and *meso*-$EBIZrCl_2$, the cyclopentadienyl protons on the indenyl ring appear as doublets; consistent with the molecular symmetry.[15]

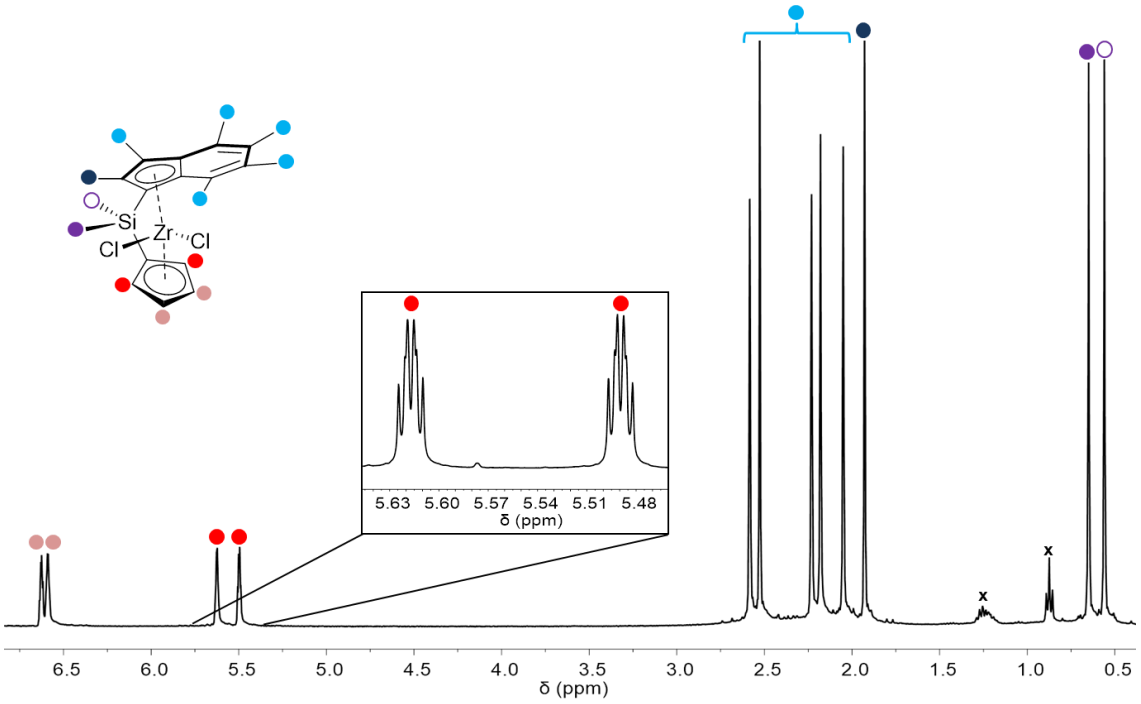


Figure 2.3 ^{1}H NMR spectrum (benzene-d_6, 500 MHz, 298 K) of ^{Me_2}SB(Cp,I*)ZrCl$_2$ (**1**). x is residual pentane.

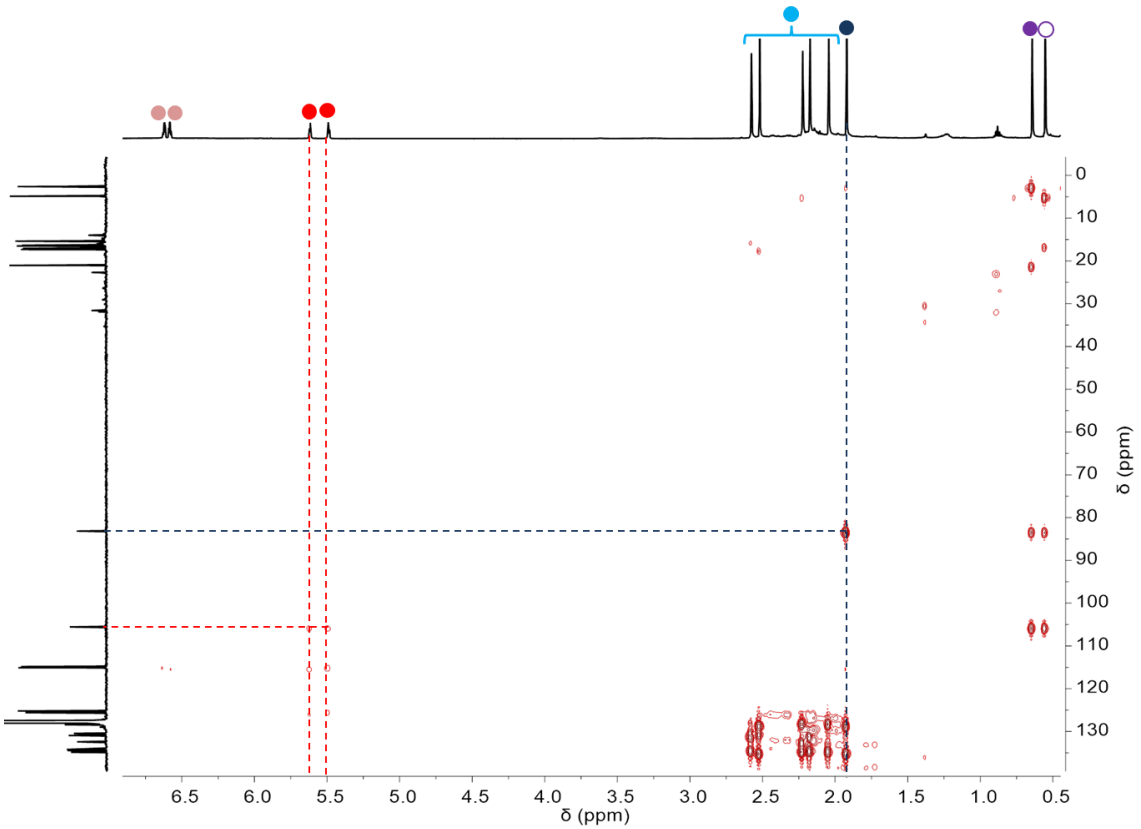


Figure 2.4 2D ^{1}H,^{13}C HMBC NMR spectrum (benzene-d_6, 500 and 125 MHz, 298 K) of ^{Me_2}SB(Cp,I*)ZrCl$_2$ (**1**).

The ^{1}H NMR spectra of **3** and **4** show a 60:40 mixture of two regioisomers with the methyl group positioned at the least sterically hindered gamma positions of the cyclopentadienyl ring (as demonstrated in Figure 2.2). When compared to **1** and **2**, the ^{1}H NMR spectra of **3** and **4** show additional resonances corresponding to the methyl group on the cyclopentadienyl ring (δ = 2.19 and 2.06 ppm for ***E*-3** and ***Z*-3** respectively; δ = 2.13 and 2.19 ppm for ***E*-4** and ***Z*-4** respectively) (Figures 2.5 and A2.5). In comparison to **1**, the cyclopentadienyl proton resonances are observed as pseudo triplets rather than pseudo quartets.

The correlated spectroscopy (^{1}H,^{1}H COSY) NMR spectrum of **3** confirms the presence of two individual regioisomers and demonstrates the coupling between each of the three cyclopentadienyl protons of the two separate isomers (Figure 2.6). The coupling observed in the ^{1}H,^{1}H COSY NMR spectrum for the cyclopentadienyl protons helps explain the observed splitting patterns; the pseudo triplets likely correspond to two overlapping roofed doublets. Each of the three cyclopentadienyl protons can be assigned based on the appearance of the resonances and the respective chemical shifts; the resonances at 5.65 and 5.53 ppm appear the most defined as they only experience long-range $^4J_{H\text{-}H}$ coupling, compared to the resonances at 6.34, 6.29, 5.32 and 5.13 ppm which are less defined as they experience both $^3J_{H\text{-}H}$ and $^4J_{H\text{-}H}$ coupling to the other cyclopentadienyl protons.

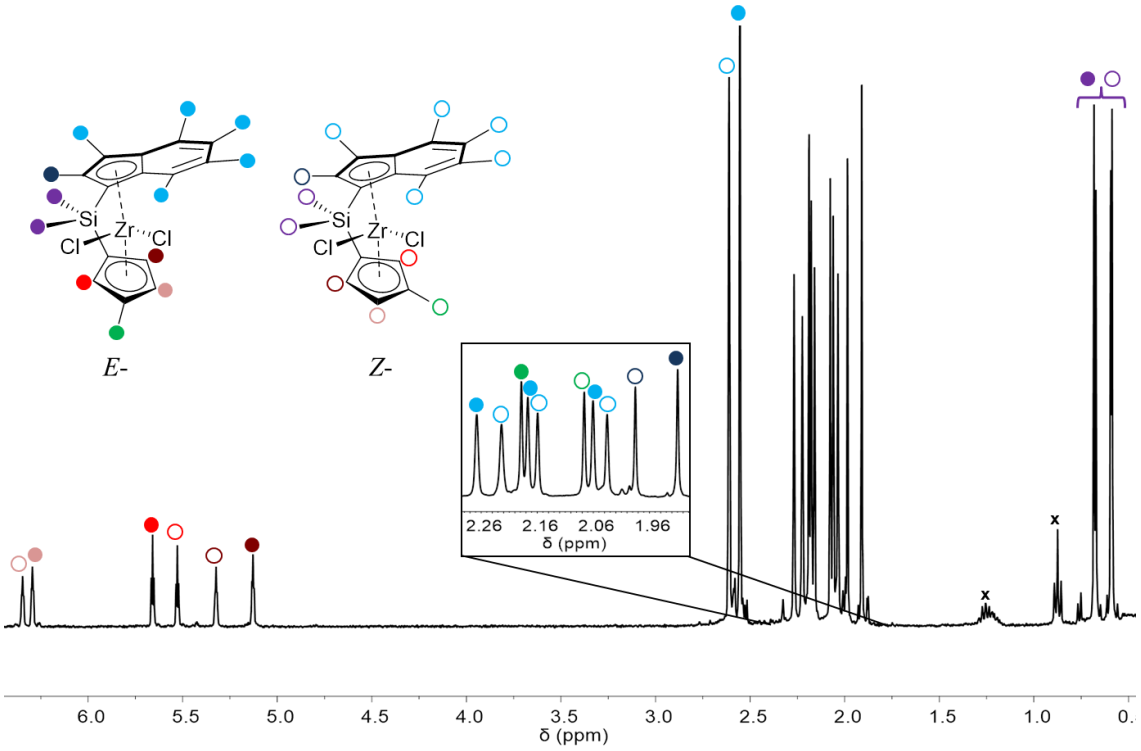


Figure 2.5 ^{1}H NMR spectrum (benzene-d_6, 400 MHz, 298 K) of *E*-^{Me_2}SB(Cp^{Me},I*)ZrCl$_2$ (***E*-3**, ●) and *Z*-^{Me_2}SB(Cp^{Me},I*)ZrCl$_2$ (***Z*-3**, ○). x is residual pentane.

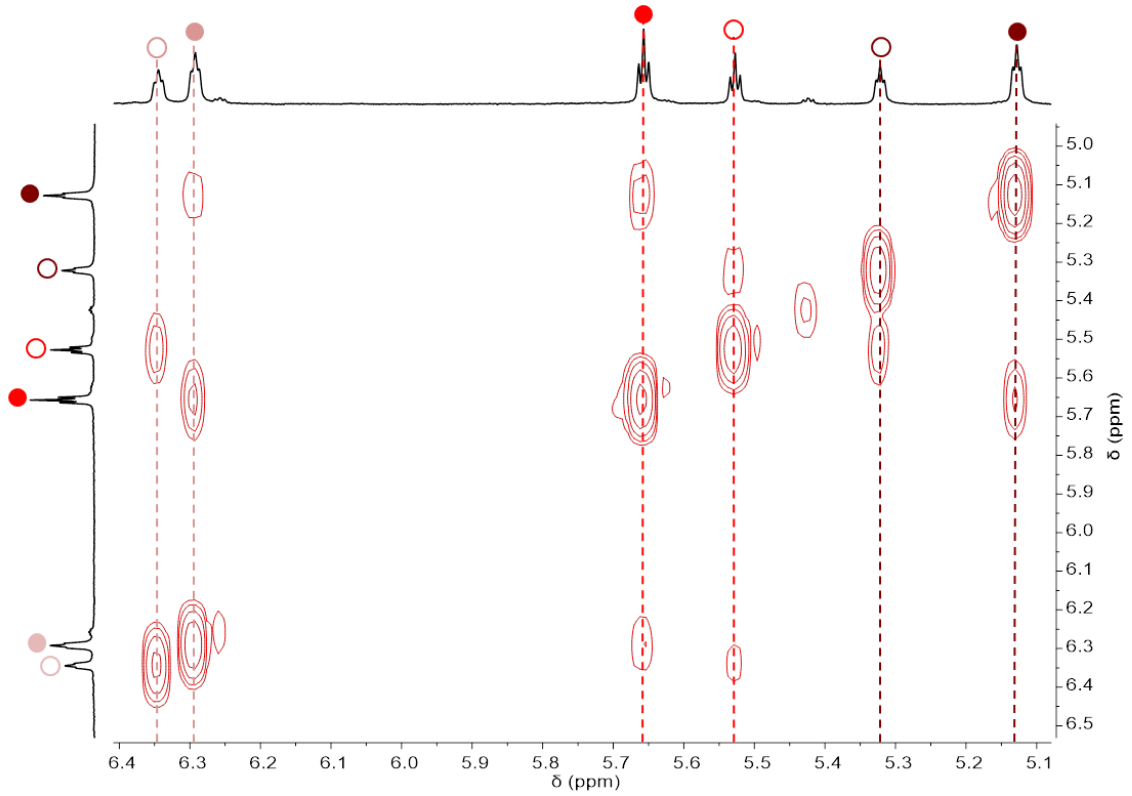


Figure 2.6 ^{1}H,^{1}H COSY NMR spectrum (benzene-d_6, 500 MHz, 298 K) of *E*-^{Me_2}SB(Cp^{Me},I*)ZrCl$_2$ (***E*-3**, ●) and *Z*-^{Me_2}SB(Cp^{Me},I*)ZrCl$_2$ (***Z*-3**, ○).

Unlike **3**, the *E*- and *Z*-isomers of ^{Me_2}SB(Cp^{nBu},I*)ZrCl$_2$ (**5**) were isolated through a series of pentane washes. The ^{1}H NMR spectra show the expected diagnostic resonances for the silyl bridge methyl (δ = 0.60–0.71 ppm), permethylindenyl (δ = 1.96–2.62 ppm) and cyclopentadienyl protons (δ = 5.32–6.44 ppm), in addition to four multiplets corresponding to the protons on the *n*-butyl chain (δ = 0.81, 1.25, 1.48, and 2.72 ppm for ***E*-5**; δ = 0.78, 1.18, 1.41 and 2.58 ppm for ***Z*-5**) (Figure 2.7).

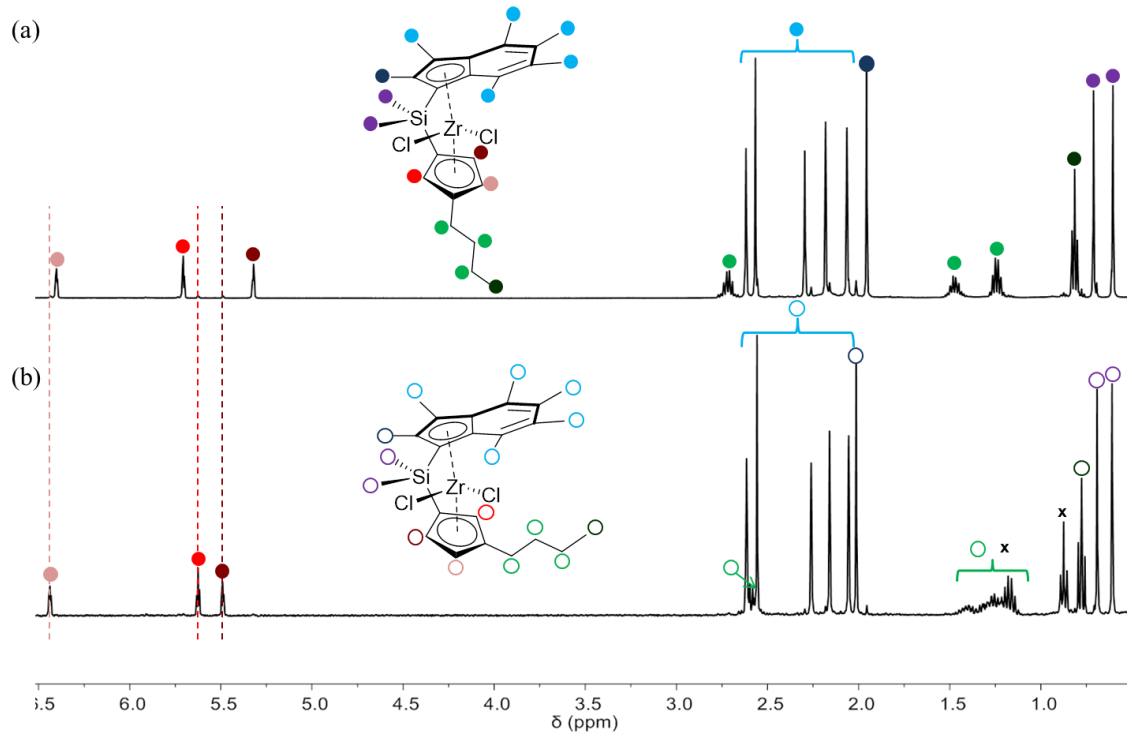


Figure 2.7 ^{1}H NMR spectrum (benzene-d_6, 400 MHz, 298 K) of (a) *E*-^{Me_2}SB(Cp^{nBu},I*)ZrCl$_2$ (***E*-5**) and (b) *Z*-^{Me_2}SB(Cp^{nBu},I*)ZrCl$_2$ (***Z*-5**). x is residual pentane.

Increasing the temperature of the ^{1}H NMR experiment up to 363 K in 10 K intervals did not affect the solution structures of ^{Me_2}SB(Cp,I*)ZrCl$_2$ (**1**) and ^{Me_2}SB(Cp^{Me},I*)ZrCl$_2$ (**3**) (Figures A2.8 and A2.9).

2.2.2 X-ray crystallography

Crystals of **1** suitable for a single-crystal X-ray diffraction study were obtained from a hexane solution at −34 °C in the monoclinic space group *I*2/*a* by Mr Joshua E. Matley.

Crystals of **2**, **3**, ***E*-5** and ***Z*-5** suitable for single-crystal X-ray diffraction study were isolated from saturated pentane solutions at −34 °C in the orthorhombic space group *Fdd*2, monoclinic space group $P2_1/n$, monoclinic space group $P2_1/n$ and triclinic space group $P\bar{1}$ respectively. The nature of the space groups shows that the structures do not possess mirror planes and that all except **2** have an inversion centre. This indicates that **1**, **3**, ***E*-5** and ***Z*-5** are chiral molecules and are present as racemates (Figure 2.8a); as is also observed for unsymmetrical ^{Me_2}SB(Cp,I)ZrCl$_2$, ^{Me_2}CB(Cp,Flu)ZrCl$_2$, ^{Me_2}CB(Cp,Flu)HfCl$_2$ and ^{Me_2}SB(^{tBu_2}Flu,I*)MCl$_2$ (M = Zr and Hf).[9, 11, 16] The solid-state molecular structures of **1**, **2**, ***E*-3**, ***Z*-3**, ***E*-5** and ***Z*-5** are depicted in Figure 2.8, with selected bond lengths and angles presented in Table 2.1. ^{Me_2}SB(Cp,I*)HfCl$_2$, crystallised by Mr Joshua E. Matley from a saturated pentane solution at −34 °C, is shown for comparison (Figure 2.8c). The complexes in this series show no rotational symmetry and are assigned the C_1 point group. In all cases, the arrangement of the ligands around the metal atom can be described as a distorted tetrahedral molecular geometry.

As expected for metals of similar size, the steric parameters of ^{Me_2}SB(Cp,I*)MCl$_2$ (M = Zr and Hf) are very similar. The M-Centroid distances of **1** (M-Ind$_{cent}$ = 2.2244 Å and M-Cp$^R_{cent}$ = 2.2076 Å) are shorter than those reported for unbridged bisindenyl bispermethylindenyl systems,[17, 18] and similar to or shorter than those reported for *ansa*-bridged bisindenyl bispermethylindenyl systems.[1, 6, 15] This indicates that the presence of the less sterically demanding cyclopentadienyl ring compared to indenyl and permethylindenyl allows the zirconium atom to position closer to the two cyclopentadienyl-type ligands. For example, (Ind*)$_2$ZrCl$_2$, *rac*-EBIZrCl$_2$ and *rac*-EBI*ZrCl$_2$ show average M-Ind$_{cent}$ distances of 2.257, 2.219 and 2.240 Å respectively.[1, 15, 17, 18]

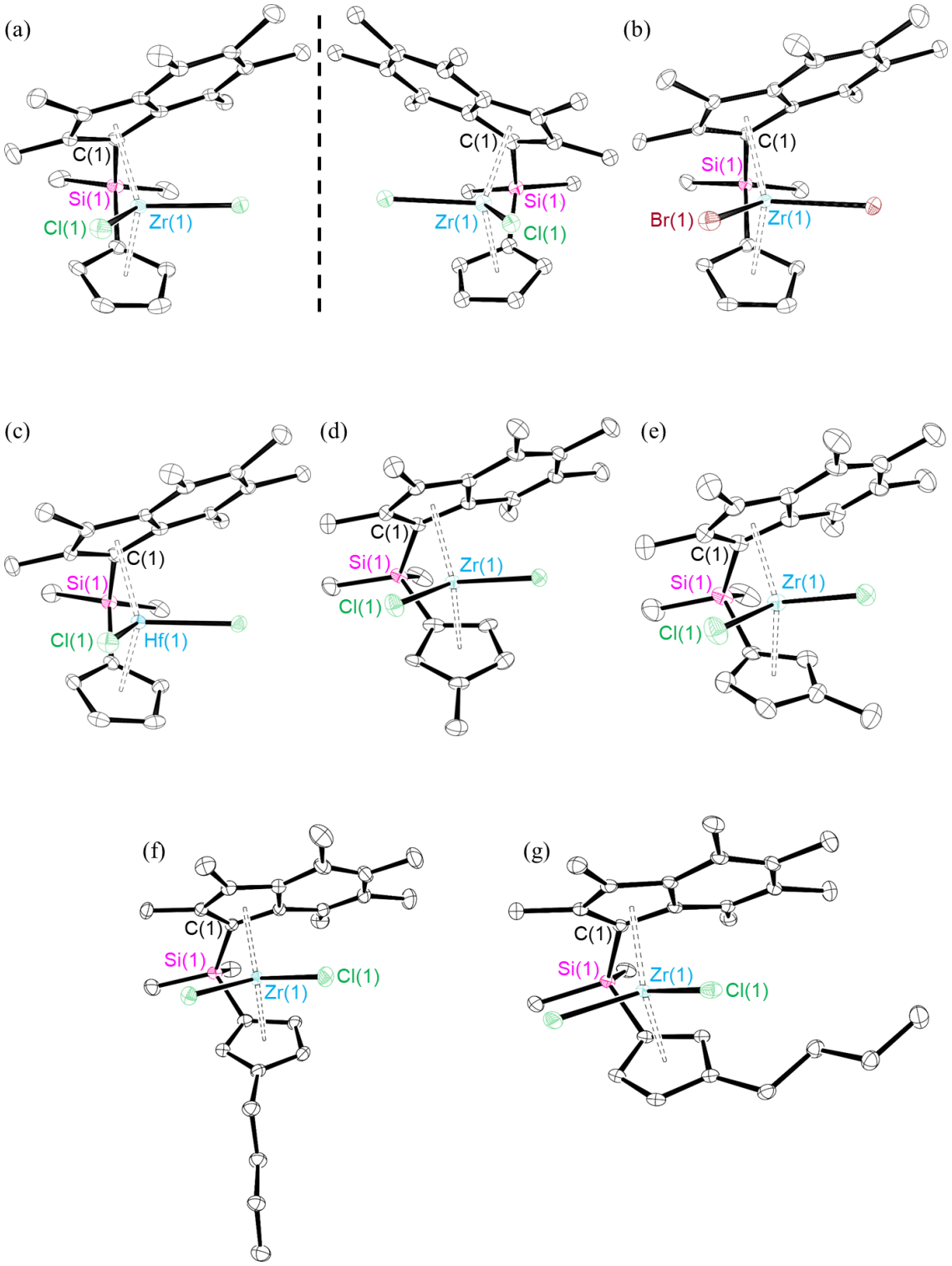


Figure 2.8 Solid-state molecular structures of (a) ^{Me_2}SB(Cp,I*)ZrCl$_2$ (**1**), (b) ^{Me_2}SB(Cp,I*)ZrBr$_2$ (**2**), (c) ^{Me_2}SB(Cp,I*)HfCl$_2$, (d) *E*-^{Me_2}SB(Cp^{Me},I*)ZrCl$_2$ (***E*-3**), (e) *Z*-^{Me_2}SB(Cp^{Me},I*)ZrCl$_2$ (***Z*-3**), (f) *E*-^{Me_2}SB(Cp^{nBu},I*)ZrCl$_2$ (***E*-5**) and (g) *Z*-^{Me_2}SB(Cp^{nBu},I*)ZrCl$_2$ (***Z*-5**). H atoms omitted for clarity; ellipsoids given at 30% probability.

Table 2.1 Selected bond lengths (Å) and angles (°) for $^{Me_2}SB(Cp,I^*)ZrCl_2$ (**1**), $^{Me_2}SB(Cp,I^*)ZrBr_2$ (**2**), $^{Me_2}SB(Cp,I^*)HfCl_2$, *E*-$^{Me_2}SB(Cp^{Me},I^*)ZrCl_2$ (***E*-3**), *Z*-$^{Me_2}SB(Cp^{Me},I^*)ZrCl_2$ (***Z*-3**), *E*-$^{Me_2}SB(Cp^{nBu},I^*)ZrCl_2$ (***E*-5**), *Z*-$^{Me_2}SB(Cp^{nBu},I^*)ZrCl_2$ (***Z*-5**) and other related zirconocenes.

Complex	**M-Ind$_{cent}$**	**M-Cp$^R_{cent}$**	***α***	***δ***
$^{Me_2}SB(Cp,I^*)ZrCl_2$	2.2244(1)	2.2076(1)	60.19	126.37(1)
$^{Me_2}SB(Cp,I^*)ZrBr_2$	2.2300(1)	2.2012(1)	60.14	126.32(1)
$^{Me_2}SB(Cp,I^*)HfCl_2$	2.2078(1)	2.1861(1)	59.47	126.87(1)
E-$^{Me_2}SB(Cp^{Me},I^*)ZrCl_2$	2.2202(1)	2.2194(1)	62.38	126.12(1)
Z-$^{Me_2}SB(Cp^{Me},I^*)ZrCl_2$	2.2202(1)	2.1935(1)	56.85	130.60(1)
E-$^{Me_2}SB(Cp^{nBu},I^*)ZrCl_2$	2.2308(1)	2.2011(1)	60.20	127.49(1)
Z-$^{Me_2}SB(Cp^{nBu},I^*)ZrCl_2$	2.2200(1)	2.2143(1)	60.25	126.98(1)
Ind_2ZrCl_2 [18]	2.231 [a]	-	59.3	128.3
$(Ind^*)_2ZrCl_2$ [17]	2.257 [a]	-	41.0	130.9
rac-EBIZrCl$_2$ [15]	2.219 [a]	-	60.8	124.5
meso-EBIZrCl$_2$ [15]	2.227 [a]	-	59.7	109.9
rac-EBI*ZrCl$_2$ [1]	2.240 [a]	-	57.2	129.4
meso-EBI*ZrCl$_2$ [1]	2.246 [a]	-	56.9	128.7
rac-$^{Me_2}SBI^*ZrCl_2$ [6]	2.251 [a]	-	58.5	130.4
$^{Me_2}SB(Cp,I)ZrCl_2$ [9]	2.227	2.198	60.4	126.9
$^{Me_2}CB(Cp,I)ZrCl_2$ [10]	2.209	2.118	71.6	117.1
$^{Me_2}CB(Cp,Flu)ZrCl_2$ [5]	2.238 [b]	2.168	71.9	118.6
$^{Me_2}SB(^{tBu_2}Flu,I^*)ZrCl_2$ [16]	2.227	2.300 [b]	62.0	131.0
$^{Me_4}DSB(^{tBu_2}Flu,I^*)ZrCl_2$ [19]	2.254	2.314 [b]	54.9	139.7

(a) Average M-Ind$_{cent}$ distance; (b) M-Flu$_{cent}$ distance.

Similarly to other unsymmetrical bridged systems such as ^{Me_2}SB(Cp,I)ZrCl$_2$, ^{Me_2}CB(Cp,I)ZrCl$_2$ and ^{Me_2}CB(Cp,Flu)ZrCl$_2$, the M-Ind$_{cent}$ distance of **1** is longer than the M-Cp$^R_{cent}$ distance;[9-11] for ^{Me_2}SB(Cp,I)ZrCl$_2$ M-Ind$_{cent}$ = 2.227 Å and M-Cp$^R_{cent}$ = 2.198 Å. This suggests that the increased steric bulk of the permethylindenyl ligand forces the zirconium atom closer to the smaller cyclopentadienyl ligand. The M-Ind$_{cent}$ and M-Cp$^R_{cent}$ distances of ^{Me_2}SB(Cp,I*)HfCl$_2$ are slightly shorter than **1**, most likely due to the differences in electronic structures of hafnium and zirconium; the f-electrons present in hafnium allow it to participate more strongly in metal-ligand σ-bonds than zirconium.[20]

1 has a ring tilt angle (α) and angle about the metal centre (δ) comparable to ^{Me_2}SB(Cp,I)ZrCl$_2$ (α = 60.2° and 60.4° respectively; δ = 126.4° and 126.9° respectively).[9] The slightly larger α of **1** compared to ^{Me_2}SB(Cp,I*)HfCl$_2$ and *rac*-^{Me_2}SBI*ZrCl$_2$ signifies that **1** has a more open and less sterically hindered metal centre (α = 60.2°, 59.5° and 58.5° respectively).[6] The decrease in δ of **1** compared to ^{Me_2}SB(Cp,I*)HfCl$_2$ and *rac*-^{Me_2}SBI*ZrCl$_2$ indicates that **1** experiences slightly less strain due to the *ansa*-bridge (δ = 126.4°, 126.9° and 130.4° respectively).[6] These effects are further enhanced when comparing dimethyl silyl and dimethyl carbon bridges; **1** experiences a much larger α and much smaller δ than ^{Me_2}CB(Cp,I)ZrCl$_2$ and ^{Me_2}CB(Cp,Flu)ZrCl$_2$ due to the additional strain provided by the dimethyl carbon bridge (α = 71.6° and 71.9° respectively; δ = 117.1° and 118.6° respectively).[9-11] The increase in α and accompanying decrease in δ that **1** experiences when compared to *rac*-EBI*ZrCl$_2$ (α = 57.2° and δ = 129.4°)[1], *meso*-EBI*ZrCl$_2$ (α = 56.9° and δ = 128.7°)[1] and tetramethyldisilyl bridged (^{Me_4}DSB) ^{Me_4}DSB(^{tBu_2}Flu,I*)ZrCl$_2$ (α = 54.9° and δ = 139.7°)[19] is expected due to the smaller length of the one atom bridge, which enforces a more pronounced bent sandwich geometry. It is noted that the angle about

the bridging atom is smaller for the silicon atom in **1** than for the carbon atom in ^{Me_2}CB(Cp,I)ZrCl$_2$ and ^{Me_2}CB(Cp,Flu)ZrCl$_2$ (94.6°, 99.5° and 99.4° respectively),[10, 11] indicating that the silicon atom is further away from the zirconium centre in **1**; as is expected due to the larger size of silicon compared to carbon.

The dibromide complex **2** displays steric parameters in good agreement with the dichloride complex **1**, however **2** shows a longer Zr-X distance (average Zr-X of 2.626 and 2.441 Å respectively), which is a reflection of the increase in size of the ionic radius on moving from chloride to bromide; 181 and 196 ppm respectively.[21] The X-Zr-X angle of **1** and **2** are very similar (97.73° and 96.66° respectively), which is complementary to the trend seen for the Cp$_2$ZrX$_2$ analogues (X-Zr-X = 96.2°, 97.0°, 96.7° and 96.2° when X = F, Cl, Br and I respectively).[18, 22, 23]

3 was found to crystallise as an inherent isomeric mixture in a 60:40 ratio of *E*- and *Z*-isomers, with the cyclopentadienyl methyl group directed away from the I* ring in the major isomer (***E*-3**). The crystallographic parameters of **3** differ only in the Cp^R ring substituent of the two isomers. The steric parameters of ***E*-3** and ***Z*-3** are very similar to **1**; for example, M-Cp$^R_{cent}$ = 2.2194, 2.1935 and 2.2076 Å respectively. Remarkable is the large difference in the size of α and δ for ***E*-3** (α = 62.38° and δ = 126.12°) and ***Z*-3** (α = 56.85° and δ = 130.60°), indicating that methyl group placement directly below the I* ring causes a lesser degree of ring tilt in addition to a less open and less available metal centre.

The steric parameters of ***E*-5** and ***Z*-5** are in good agreement with **1** and **3**. The M-Cp$^R_{cent}$ distance in ***Z*-5** is slightly longer than in ***Z*-3**, likely caused by the increased steric bulk of the *n*-butyl chain (M-Cp$^R_{cent}$ = 2.2143 and 2.1935 Å respectively). This is complementary to the metal-centroid distance recorded for ^{Me_2}SB(^{tBu_2}Flu,I*)ZrCl$_2$,

where the very bulky *t*-butylfluorenyl substituent forces the ligand further away from the zirconium centre than in the cyclopentadienyl analogue **1** (M-Flu$_{cent}$ = 2.300 Å and M-Cp$^{R}_{cent}$ 2.2076 Å respectively).[16] ***Z*-5** experiences a larger α and smaller δ than ***Z*-3**, indicative of a more open metal centre and implying that ***Z*-5** experiences less strain due to the *ansa*-bridge (α = 60.25° and 56.85° respectively; δ = 126.98° and 130.60° respectively).

The plane of the *n*-butyl group (defined by the atoms that make up the *n*-butyl chain) of ***E*-5** lies near-perpendicular to the plane of the cyclopentadienyl ring (defined by the atoms that make up the cyclopentadienyl ring) with an angle between planes of 87.89° (Figure 2.9). However, for ***Z*-5** the *n*-butyl chain is almost in the plane of the cyclopentadienyl ring with an angle between planes of 14.51°. This means that the steric parameters of ***E*-5** are very similar to the unsubstituted cyclopentadienyl complex **1**; for example, α = 60.20° and 60.19° respectively.

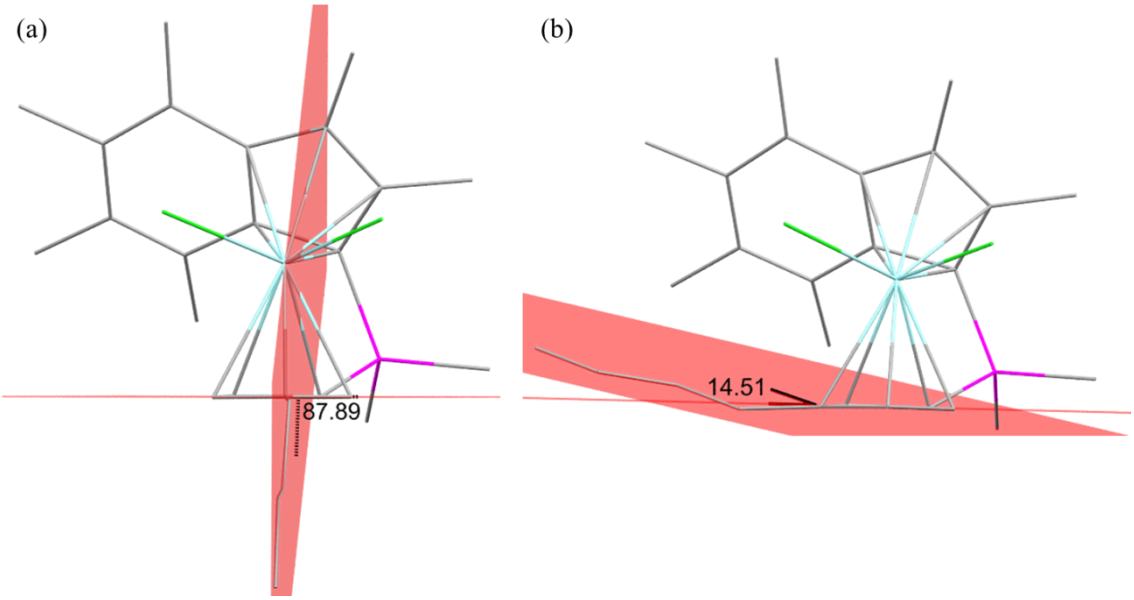
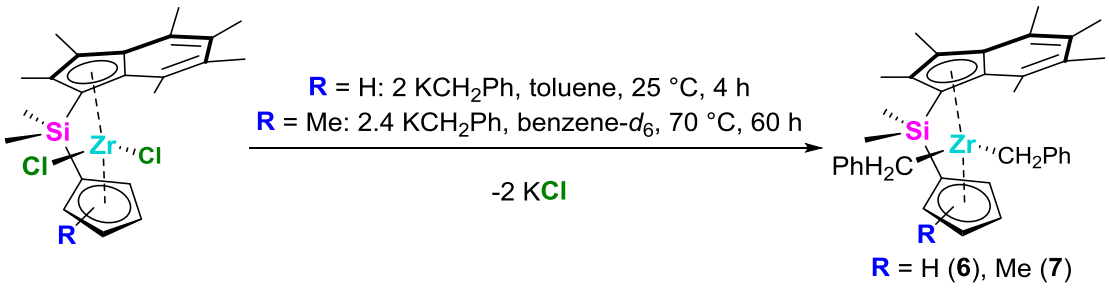


Figure 2.9 Solid-state molecular structures of (a) *E*-^{Me_2}SB(Cp^{nBu},I*)ZrCl$_2$ (***E*-5**) and (b) Z-^{Me_2}SB(Cp^{nBu},I*)ZrCl$_2$ (***Z*-5**) showing the angle between the planes of the cyclopentadienyl ring and *n*-butyl chain. Viewed along the plane of the cyclopentadienyl ring. H atoms omitted for clarity.

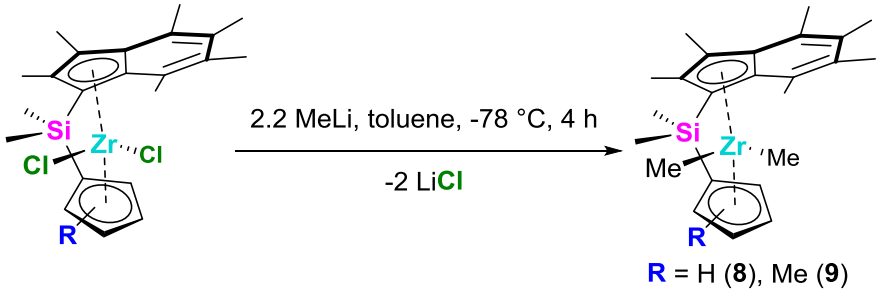
2.3 Synthesis of ^{Me_2}SB(Cp^{R},I*)ZrX$_2$ (R = H, Me; X = Me, CH$_2$Ph)

The reaction of stoichiometric quantities of ^{Me_2}SB(Cp,I*)ZrCl$_2$ (**1**) and KCH$_2$Ph at 25 °C for 4 hours afforded ^{Me_2}SB(Cp,I*)Zr(CH$_2$Ph)$_2$ (**6**) as a yellow solid in 44% yield, while the reaction of ^{Me_2}SB(Cp^{Me},I*)ZrCl$_2$ (**3**) with 2.4 equivalents of KCH$_2$Ph at 70 °C for 60 hours yielded ^{Me_2}SB(Cp^{Me},I*)Zr(CH$_2$Ph)$_2$ (**7**) as an orange oil in 78% yield (Equation 2.1). It is proposed that the much longer reaction time and necessity of heat required for the production of **7** are due to the increased steric bulk of the system, in addition to the lack of efficient mixing owing to the reaction being conducted in an NMR tube.



Equation 2.1 Synthesis of ^{Me_2}SB(Cp^{R},I*)Zr(CH$_2$Ph)$_2$ (R = H and Me).

The salt metathesis reaction of **1** and **3** with an excess of MeLi in toluene lead to the formation of ^{Me_2}SB(Cp,I*)ZrMe$_2$ (**8**) and ^{Me_2}SB(Cp^{Me},I*)ZrMe$_2$ (**9**) after 4 hours in 18 and 72% yield respectively (Equation 2.2).



Equation 2.2 Synthesis of ^{Me_2}SB(Cp^{R},I*)ZrMe$_2$ (R = H and Me).

2.3.1 NMR spectroscopy

The ^{1}H NMR spectra of **6** and **7** (Figures 2.10 and A2.6) show the diagnostic resonances for the silyl bridge methyl, I* methyl and cyclopentadienyl protons at 0.53 and 0.56 ppm, 1.81, 2.10, 2.23, 2.30 and 2.52 ppm, and 5.04, 5.12, 6.10 and 6.28 ppm respectively for **6**. The spectra also show resonances at corresponding to the diastereotopic CH_2 protons and the phenyl protons of the benzyl group at 0.05, 0.33, 1.62 and 1.83 ppm, and 6.54, 6.91, 7.13 and 7.24 ppm respectively for **6**.

The ^{1}H NMR spectrum of **7** confirms that the 60:40 isomeric mixture present in the parent complex is retained in the product, and shows additional resonances when compared to **6** corresponding to the methyl group on the cyclopentadienyl ring of the *E*- and *Z*-isomers (δ = 1.82 and 1.57 ppm respectively). When compared to the parent complexes, the ^{1}H NMR spectra of **6** and **7** show shifts to lower frequencies for the resonances corresponding to the protons on the cyclopentadienyl ring (a shift of ~0.4 ppm for **6**). It is proposed that this is due to additional shielding provided by the phenyl rings.

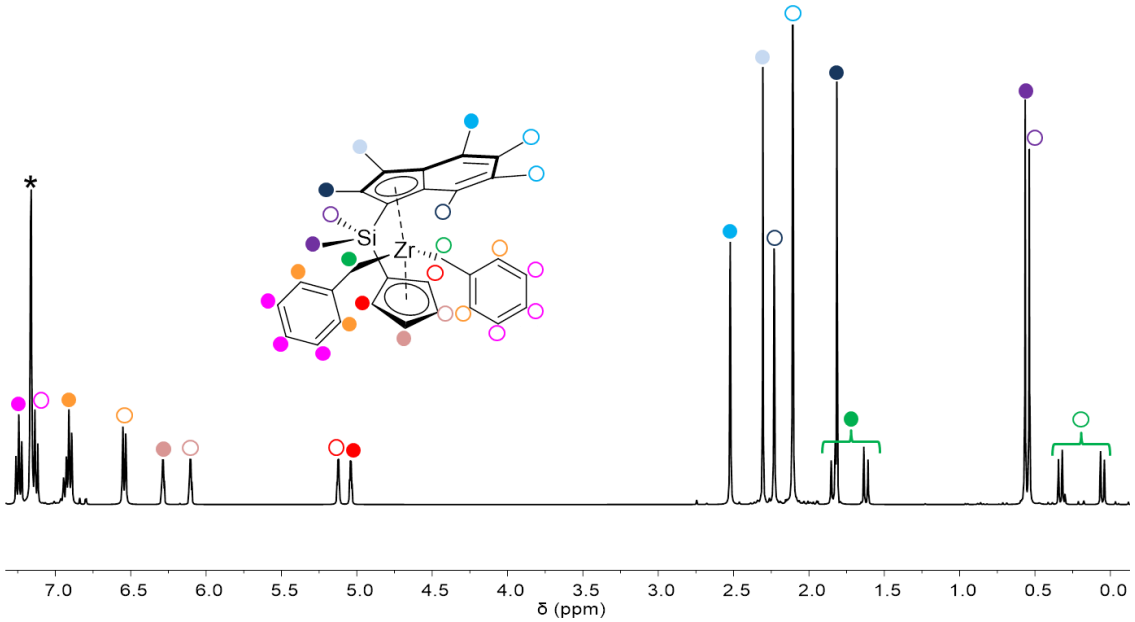


Figure 2.10 ^{1}H NMR spectrum (benzene-d_6, 400 MHz, 298 K) of ^{Me_2}SB(Cp,I*)Zr(CH_2Ph)$_2$ (**6**).

Utilising rotating-frame nuclear Overhauser effect spectroscopy (^{1}H,^{1}H ROESY), the ^{1}H NMR spectrum of **6** can be fully assigned. Analysis of the I* methyl region shows that the resonance at 1.81 ppm couples to the silyl bridge methyl resonance at 0.57 ppm and the Cp resonance at 5.04 ppm (distances of 2.207 and 2.343 Å respectively, Figure 2.11), and is therefore assigned as the first methyl group on the five-membered ring of the I* ligand (Figure 2.12a, navy). Due to the close proximity of each methyl group to its neighbour the other I* methyl resonances can be assigned. The cyclopentadienyl resonance at 5.04 ppm is shown to couple to the I* methyl resonance at 1.81 ppm and the Cp resonance at 6.28 ppm (distances of 2.343 and 2.520 Å respectively), and is therefore assigned to the part of the Cp ring closest to the five-membered ring of I* (Figure 2.12b, red). The benzylic resonance at 1.62 ppm couples to the first methyl group on the five-membered ring of the I* ligand and is therefore in close proximity to it (distance of 3.176 Å) (Figure 2.12a, green). The phenyl region shows that the resonance at 6.91 ppm couples to the CH_2 resonances at 1.62 and 1.83 ppm and the Ph resonance at 7.24 ppm (average distances of 2.439 and 2.348 Å respectively), these resonances are therefore assigned to the Ph ring positioned closest to the five-membered ring of the I* ligand (Figure 2.12b, orange).

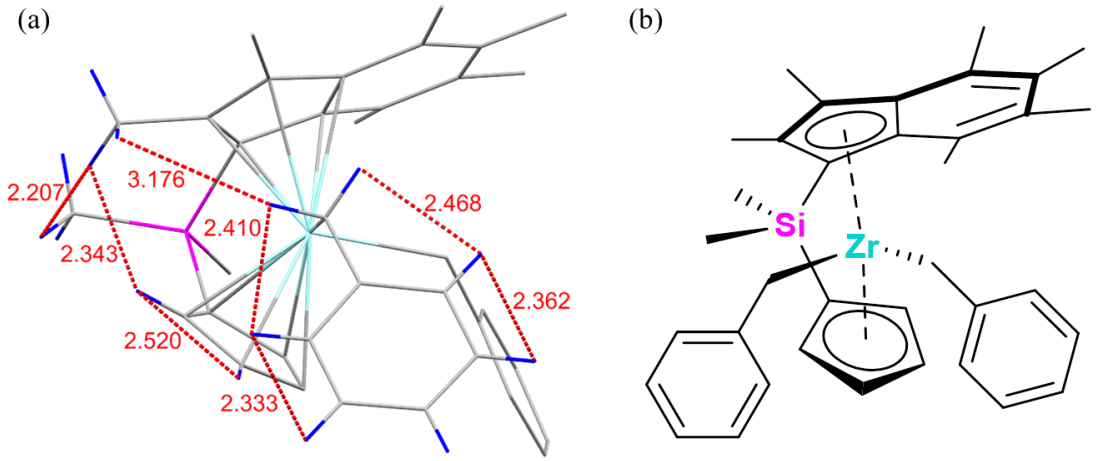


Figure 2.11 (a) Solid-state molecular structure of ^{Me_2}SB(Cp,I*)Zr(CH_2Ph)$_2$ (**6**) with selected distances (Å). Selected H atoms omitted for clarity. (b) ChemDraw structure of **6**.

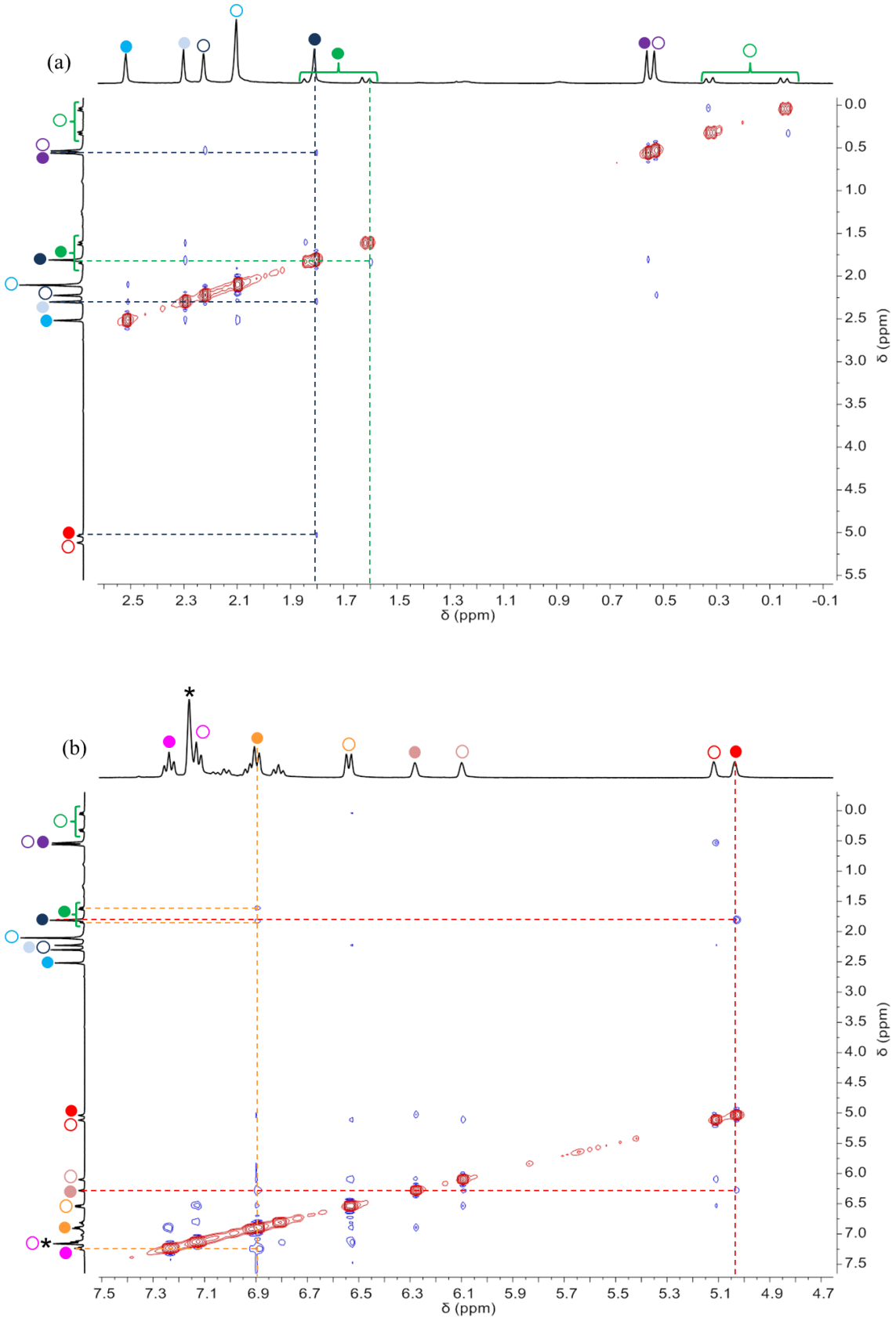


Figure 2.12 ^{1}H,^{1}H ROESY NMR spectra (benzene-d_6, 400 MHz, 298 K) of ^{Me_2}SB(Cp,I*)Zr(CH$_2$Ph)$_2$ (**6**) showing (a) −0.11–2.61 ppm and (b) 4.69–7.50 ppm.

The variable temperature ^{1}H NMR spectra of **6** between 298 and 363 K at 10 K intervals shows a change in chemical shift of the benzylic protons positioned closest to the five-membered ring of the permethylindenyl ligand, with the resonances overlapping at 353 K (Figure 2.13, full spectrum Figure A2.10). A change in chemical shift of only one set of benzylic protons is due to the sterics of the system; the benzyl group positioned away from the permethylindenyl ligand is more freely able to rotate than the benzyl group positioned below the bulky permethylindenyl ligand. The spectrum recorded at 363 K also shows coalescence of the silyl bridge methyl groups and separation of the two overlapping permethylindenyl methyl resonances. Separation of the permethylindenyl methyl resonances may be due to slight changes in the conformation of the permethylindenyl ligand at elevated temperatures, which forces the methyl groups into chemically inequivalent environments.

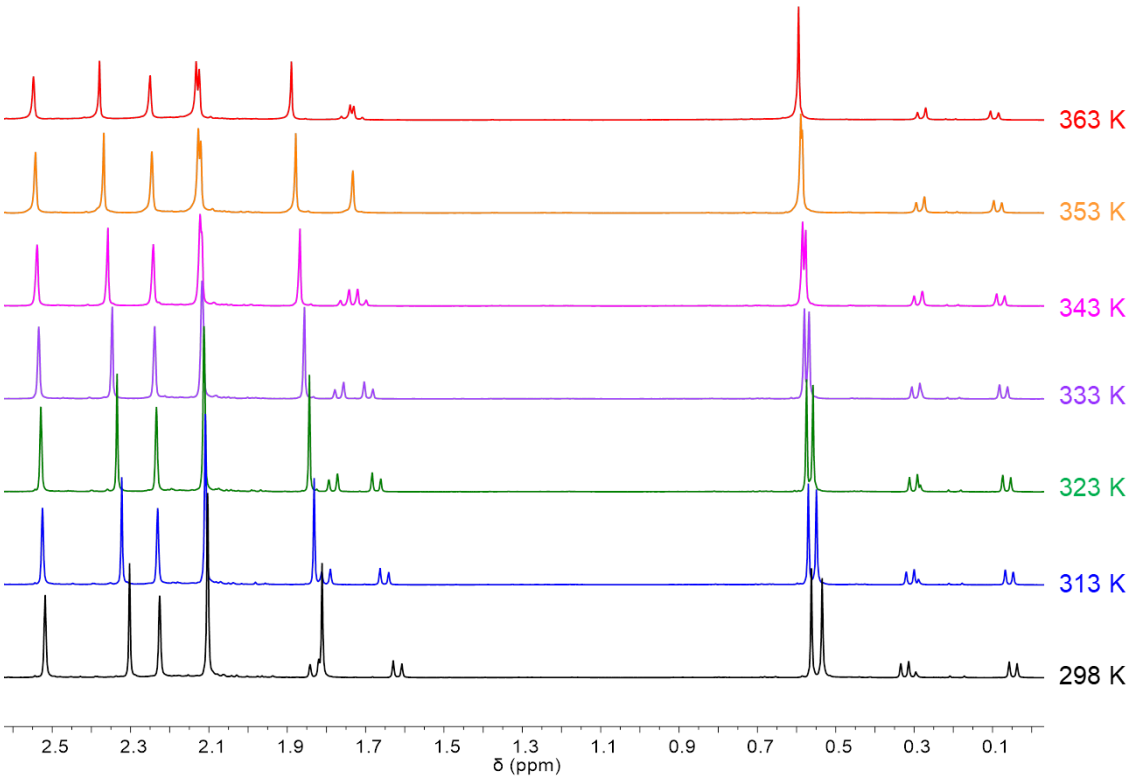


Figure 2.13 Variable temperature ^{1}H NMR spectrum (benzene-d_6, 500 MHz) of ^{Me_2}SB(Cp,I*)Zr(CH$_2$Ph)$_2$ (**6**) between 298 and 363 K showing −0.03–2.63 ppm.

When compared to the parent compounds **1** and **3**, the ^{1}H NMR spectra of the dimethyl complexes **8** and **9** show two additional singlet resonances between −1.18 and −0.11 ppm corresponding to the methyl groups directly bound to the zirconium (Figures 2.14 and A2.7). Similar to the benzyl substituted complex **7**, the ^{1}H NMR spectrum of **9** shows that the 60:40 isomeric mixture of the parent complex is retained in the product.

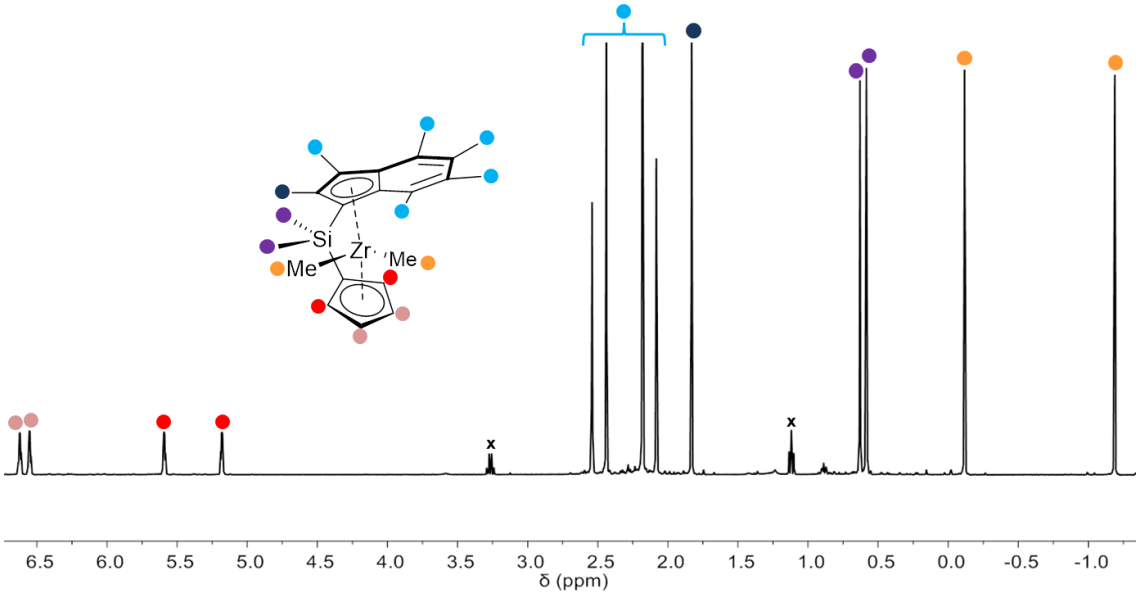


Figure 2.14 ^{1}H NMR spectrum (benzene-d_6, 400 MHz, 298 K) of ^{Me_2}SB(Cp,I*)ZrMe$_2$ (**8**). x is residual diethyl ether.

The variable temperature ^{1}H NMR spectrum of **8** shows splitting of the permethylindenyl methyl resonance at 2.18 ppm into two singlets at 2.21 and 2.18 ppm (Figure 2.15, full spectrum Figure A2.11). As for **6**, this splitting is most likely due to a slight change in conformation of the permethylindenyl ligand. However, the splitting in **8** is more pronounced than in **6**, suggesting a more significant conformational change.

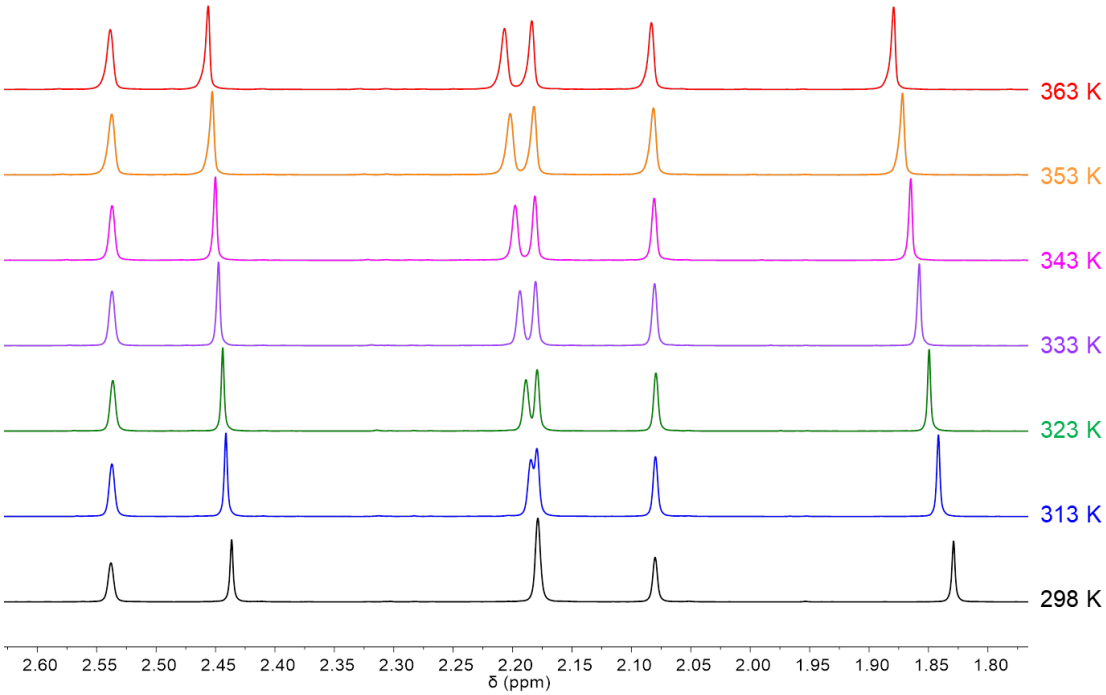


Figure 2.15 Variable temperature ^{1}H NMR spectrum (benzene-d_6, 500 MHz) of ^{Me_2}SB(Cp,I*)ZrMe$_2$ (**8**) between 298 and 363 K showing 1.77–2.62 ppm.

2.3.2 X-ray crystallography

Yellow crystals of **6** and **8** suitable for single-crystal X-ray diffraction studies were obtained from saturated pentane solutions at −34 °C in the monoclinic space group $P2_1/c$ and orthorhombic space group $Fdd2$. The solid-state molecular structures are depicted in Figure 2.16, with selected bond lengths and angles presented in Table 2.2.

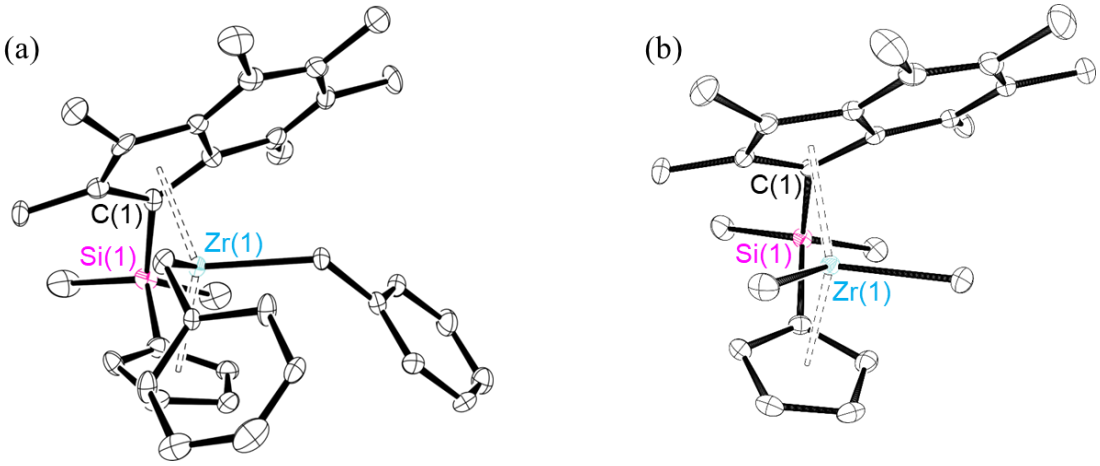


Figure 2.16 Solid-state molecular structures of (a) ^{Me_2}SB(Cp,I*)Zr(CH$_2$Ph)$_2$ (**6**) and (b) ^{Me_2}SB(Cp,I*)ZrMe$_2$ (**8**). H atoms omitted for clarity; ellipsoids given at 30% probability.

Table 2.2 Selected bond lengths (Å) and angles (°) for ^{Me_2}SB(Cp,I*)ZrCl$_2$ (**1**), ^{Me_2}SB(Cp,I*)Zr(CH$_2$Ph)$_2$ (**6**), ^{Me_2}SB(Cp,I*)ZrMe$_2$ (**8**) and other related zirconocenes.

Complex	Zr-Ind$_{cent}$	Zr-Cp$^R_{cent}$	α	δ
^{Me_2}SB(Cp,I*)ZrCl$_2$	2.2244(1)	2.2076(1)	60.19	126.37(1)
^{Me_2}SB(Cp,I*)Zr(CH$_2$Ph)$_2$	2.2615(1)	2.1943(1)	59.80	126.88(1)
^{Me_2}SB(Cp,I*)ZrMe$_2$	2.2442(1)	2.2201(1)	59.16	126.96(1)
meso-EBI*Zr(CH$_2$Ph)$_2$ [4]	2.299 [a]	-	61.85	127.32
Ind$_2$ZrMe$_2$ [21]	2.252 [a]	-	53.01	133.02

(a) Average Zr-Ind$_{cent}$ distance.

The Zr-Cp$^R_{cent}$ distance of **6** is comparable to **1** (Zr-Cp$^R_{cent}$ = 2.1943 and 2.2076 Å respectively). However, **6** possesses a longer Zr-Ind$_{cent}$ distance than **1** due to the increased steric bulk of benzyl compared to chloride (Zr-Ind$_{cent}$ = 2.2615 and 2.2244 Å respectively); the same trend was also observed for *meso*-EBI*ZrX$_2$ when moving from chloride to benzyl ligands (average Zr-Ind$_{cent}$ = 2.246 and 2.299 Å respectively).[4] **6** displays smaller Zr-Ind$_{cent}$ and Zr-Cp$^R_{cent}$ distances than *meso*-EBI*Zr(CH$_2$Ph)$_2$ due to the decreased steric bulk of the cyclopentadienyl basal ligand compared to permethylindenyl. **6** also experiences a slightly smaller ring tilt angle (α) than **1** and *meso*-EBI*Zr(CH$_2$Ph)$_2$, indicating that the system is more strained with a less open metal centre (α = 59.80°, 60.19° and 61.85° respectively).[4]

8 possesses longer Zr-Ind$_{cent}$ and Zr-Cp$^R_{cent}$ distances than **1** (Zr-Ind$_{cent}$ = 2.2442 and 2.2244 Å respectively; Zr-Cp$^R_{cent}$ = 2.2201 and 2.2076 Å respectively), consistent with the Zr-Centroid values recorded for the Cp$_2$ZrX$_2$ and Ind$_2$ZrX$_2$ series; for Cp$_2$ZrX$_2$ Zr-Cp$^R_{cent}$ = 2.196 and 2.230 Å when X = Cl and Me respectively, and for Ind$_2$ZrX$_2$ Zr-Ind$_{cent}$ = 2.231 and 2.252 Å when X = Cl and Me respectively.[18, 24, 25] **8** experiences a shorter Zr-Ind$_{cent}$ and longer Zr-Cp$^R_{cent}$ distance than **6**, showing that the zirconium atom

in **8** is positioned closer to the I* ring than in **6**. **8** displays a smaller α and larger δ than **1** (α = 59.16° and 60.19° respectively; δ = 126.96° and 126.37° respectively), consistent with the trends seen for Cp_2ZrX_2 (α = 52.3° and 53.0° when X = Cl and Me respectively; δ = 129.2° and 132.5° when X = Cl and Me respectively)[18, 24] and Ind_2ZrX_2 (α = 59.3° and 53.01° when X = Cl and Me respectively; δ = 128.3° and 133.0° for X = Cl and Me respectively).[18, 25]

2.3.3 Synthesis of [^{Me_2}SB(Cp,I*)ZrMe]$^+$ [X-MAO]$^-$



Equation 2.3 Synthesis of [^{Me_2}SB(Cp,I*)ZrMe]$^+$ [X-MAO]$^-$ (X = Cl, CH_2Ph and Me).

The reaction of ^{Me_2}SB(Cp,I*)ZrX$_2$ (X = Cl, Me and CH_2Ph) with a large excess of methylaluminoxane (MAO) resulted in an instantaneous colour change from orange/yellow to purple (Equation 2.3). Formation of [^{Me_2}SB(Cp,I*)ZrMe]$^+$ [X-MAO]$^-$ was confirmed in quantitative yield by ^{1}H NMR spectroscopy (Figure 2.17). The ^{1}H NMR spectrum clearly shows the permethylindenyl and cyclopentadienyl ligand environments of [^{Me_2}SB(Cp,I*)ZrMe]$^+$, in addition to a sharp singlet at −1.66 ppm corresponding to Zr-Me. The broad resonance at −1.0–0.5 ppm corresponds to the multiple methyl environments within MAO and also contains the resonances corresponding to the silyl bridge methyl groups. The production of polyethylene was observed instantaneously (as a white precipitate) on the addition of ethylene gas.

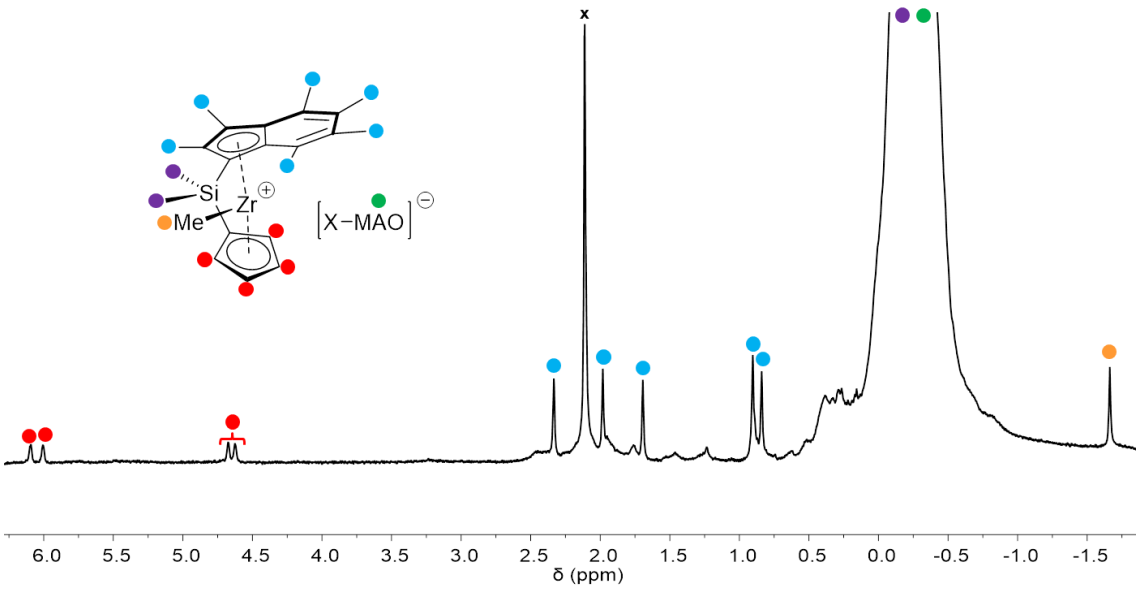
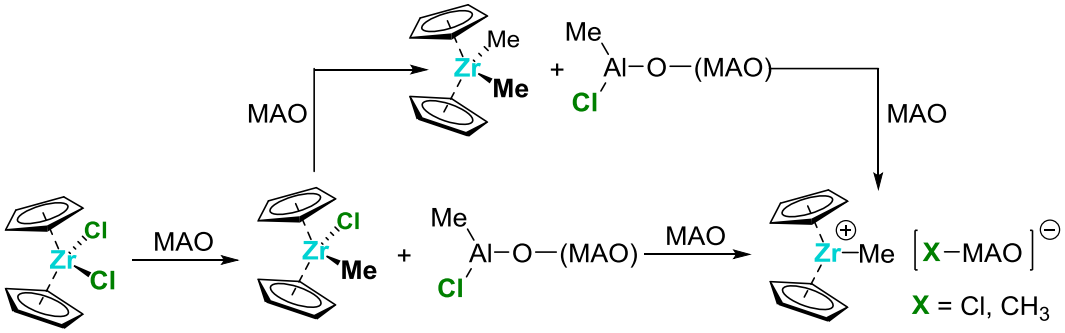


Figure 2.17 ^{1}H NMR spectrum (benzene-d_6, 400 MHz, 298 K) of [^{Me_2}SB(Cp,I*)ZrMe]$^{+}$ [X-MAO]$^{-}$ (where X = Cl, CH_2Ph and Me). x is residual toluene

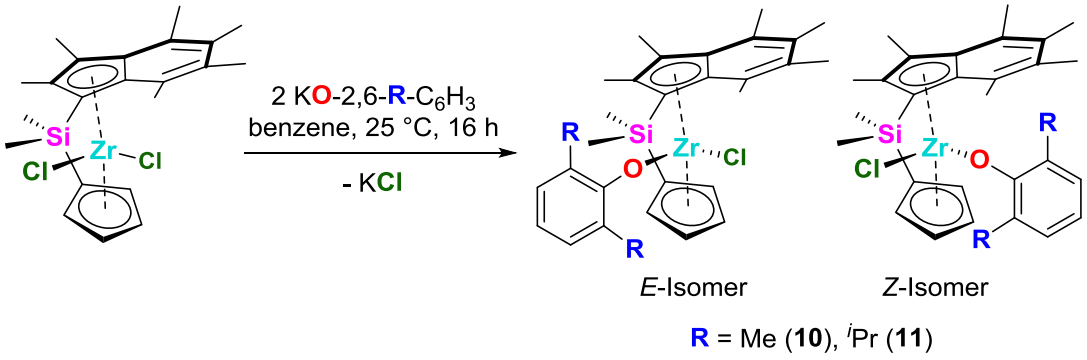
It is generally accepted that within dihalide systems, such as Cp_2ZrCl_2, MAO undergoes a rapid ligand exchange with one of the chloride ligands to generate the monomethyl complex $Cp_2Zr(Me)Cl$ (Scheme 2.2). An excess of MAO then leads to ligand exchange or abstraction to generate Cp_2ZrMe_2 and the catalytically active electron-deficient ion-paired species [Cp_2ZrMe]$^{+}$ [X-MAO]$^{-}$ (X = Cl and Me), which can coordinate and polymerise α-olefin monomers.[11, 26-28] For ^{Me_2}SB(Cp,I*)ZrX$_2$ (X = Cl, Me and CH_2Ph), the three different initiation groups lead to the same product; it is therefore proposed that a similar reaction mechanism occurs with generation of catalytically active [^{Me_2}SB(Cp,I*)ZrMe]$^{+}$ [X-MAO]$^{-}$.



Scheme 2.2 Generation of [Cp_2ZrMe]$^{+}$ [X-MAO]$^{-}$. Adapted from Santos.[27]

2.4 Synthesis of ^{Me_2}SB(Cp,I*)ZrCl(O-2,6-R-C$_6$H$_3$) (R = Me, ^{i}Pr)

^{Me_2}SB(Cp,I*)ZrCl(O-2,6-R-C$_6$H$_3$) (R = Me and ^{i}Pr) were synthesised by the reaction of two equivalents of KO-2,6-R-C$_6$H$_3$ (R = Me and ^{i}Pr) and one equivalent of ^{Me_2}SB(Cp,I*)ZrCl$_2$ (**1**) (Equation 2.4). The crude ^{1}H NMR spectra of both complexes showed a mixture of the two mono-substituted isomers in a 15:85 and 70:30 ratio of *E*- and *Z*-isomers respectively (*E*- refers to when the aryloxide group is positioned away from the I* ligand and *Z*- refers to when the aryloxide group is positioned below the I* ligand). *Z*-^{Me_2}SB(Cp,I*)ZrCl(O-2,6-Me-C$_6$H$_3$) (***Z*-10**) and *E*-^{Me_2}SB(Cp,I*)ZrCl(O-2,6-^{i}Pr-C$_6$H$_3$) (***E*-11**) were obtained as single isomers from pentane solutions at −34 °C in 13 and 14% yield respectively. Two equivalents of potassium salt were required in order to drive the reactions to completion. However, only monosubstitution occurred as the bulky permethylindeyl ligand and aryloxide substituents hindered substitution of the second chloride ligand.



Equation 2.4 Synthesis of ^{Me_2}SB(Cp,I*)ZrCl(O-2,6-R-C$_6$H$_3$) (R = Me and ^{i}Pr).

2.4.1 NMR spectroscopy

The ^{1}H NMR spectra of ***Z*-10** and ***E*-11** (Figures 2.18 and 2.19) show the diagnostic cyclopentadienyl, permethylindenyl methyl and silyl bridge methyl resonances at 5.71–6.51, 1.48–2.62 and 0.61–0.80 ppm respectively. The spectra also display

resonances confirming mono-substitution of one chloride ligand for one aryloxide substituent (phenyl resonances at 6.70–7.14 ppm).

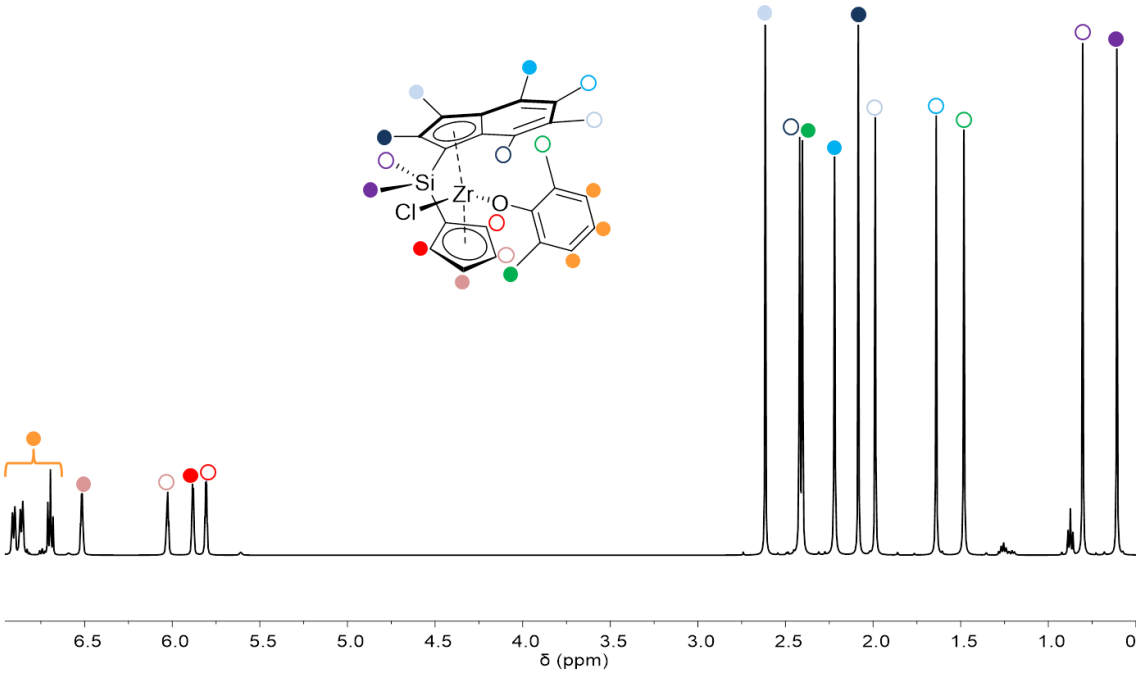


Figure 2.18 ^{1}H NMR spectrum (benzene-d_6, 400 MHz, 298 K) of *Z*-^{Me_2}SB(Cp,I*)ZrCl(O-2,6-Me-C_6H_3) (***Z*-10**).

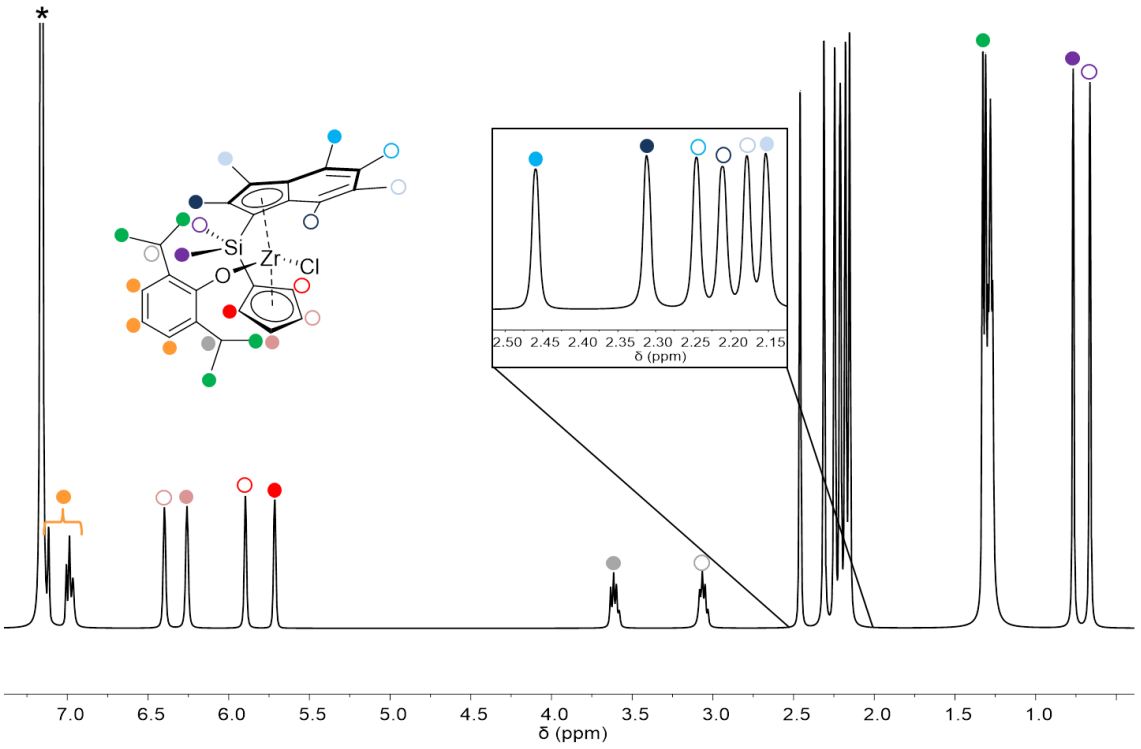


Figure 2.19 ^{1}H NMR spectrum (benzene-d_6 (*), 400 MHz, 298 K) of *E*-^{Me_2}SB(Cp,I*)ZrCl(O-2,6-^{i}Pr-C_6H_3) (***E*-11**).

Utilising ROESY NMR spectroscopy, the ^{1}H NMR spectra of ***Z*-10** and ***E*-11** can be fully assigned, and the location of the aryloxide group determined (Figures 2.21 and 2.22). The cyclopentadienyl and I* methyl resonances were assigned following a similar procedure to **6** (Section 2.3.1). For ***Z*-10**, analysis of the cyclopentadienyl region of the spectrum reveals the location of the aryloxide group; the cyclopentadienyl resonances at 6.03 and 5.80 ppm couple to the aryloxide methyl resonance at 1.48 ppm (distances of 2.412 and 2.604 Å respectively, Figure 2.20a) (Figure 2.21, pink and red). In addition, the aryloxide methyl resonance at 1.48 ppm couples to the I* methyl resonances at 1.99 and 1.64 ppm (distances of 2.745 and 4.040 Å respectively); confirming placement of the aryloxide group below the I* ligand (*Z*-isomer).

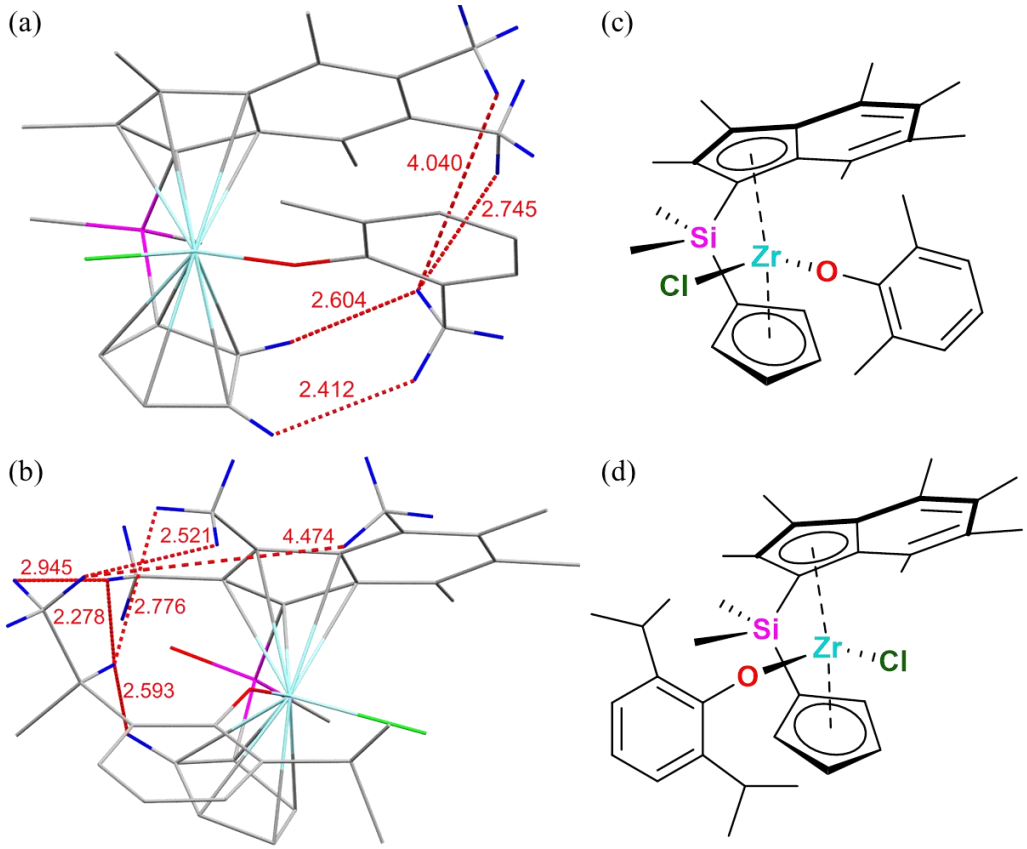


Figure 2.20 Solid-state molecular structures of (a) *Z*-^{Me_2}SB(Cp,I*)ZrCl(O-2,6-Me-C$_6$H$_3$) (***Z*-10**) and (b) *E*-^{Me_2}SB(Cp,I*)ZrCl(O-2,6-^{i}Pr-C$_6$H$_3$) (***E*-11**) with selected distances (Å). Selected H atoms omitted for clarity. ChemDraw structures of (c) *Z*-^{Me_2}SB(Cp,I*)ZrCl(O-2,6-Me-C$_6$H$_3$) (***Z*-10**) and (d) *E*-^{Me_2}SB(Cp,I*)ZrCl(O-2,6-^{i}Pr-C$_6$H$_3$) (***E*-11**).

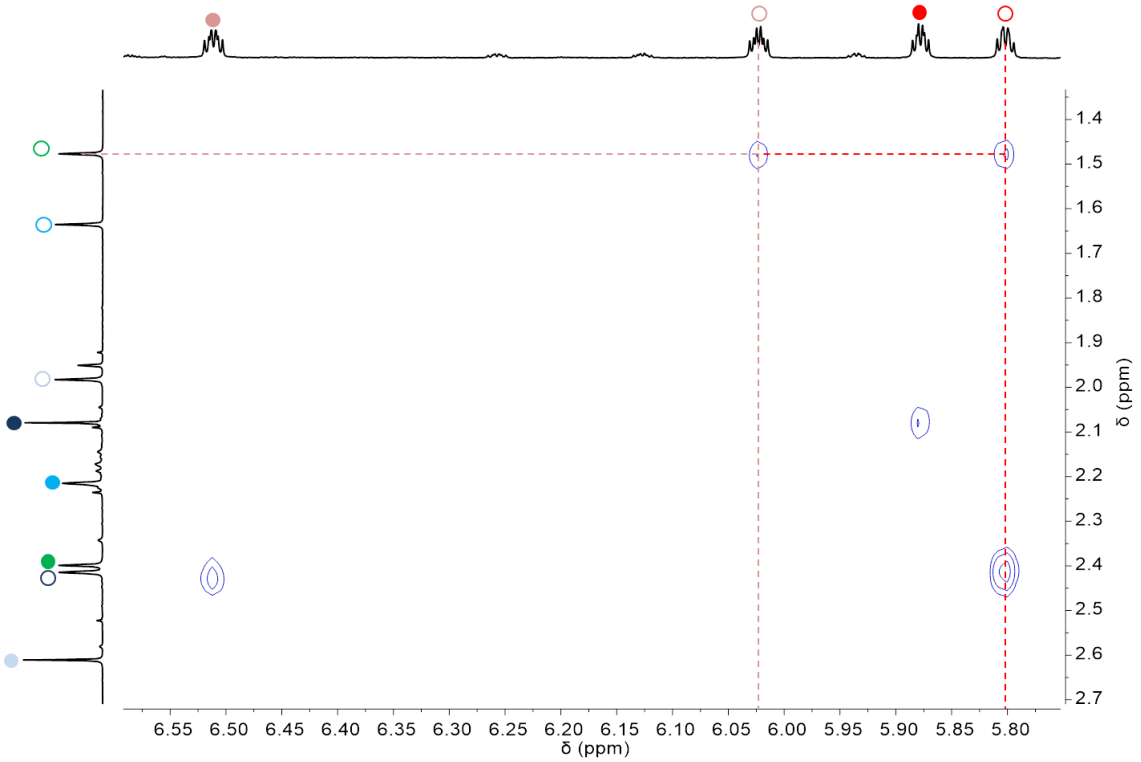


Figure 2.21 ^{1}H,^{1}H ROESY NMR spectrum (benzene-d_6, 500 MHz, 298 K) of *Z*-^{Me_2}SB(Cp,I*)ZrCl(O-2,6-Me-C$_6$H$_3$) (***Z*-10**) showing 5.73–6.61 ppm.

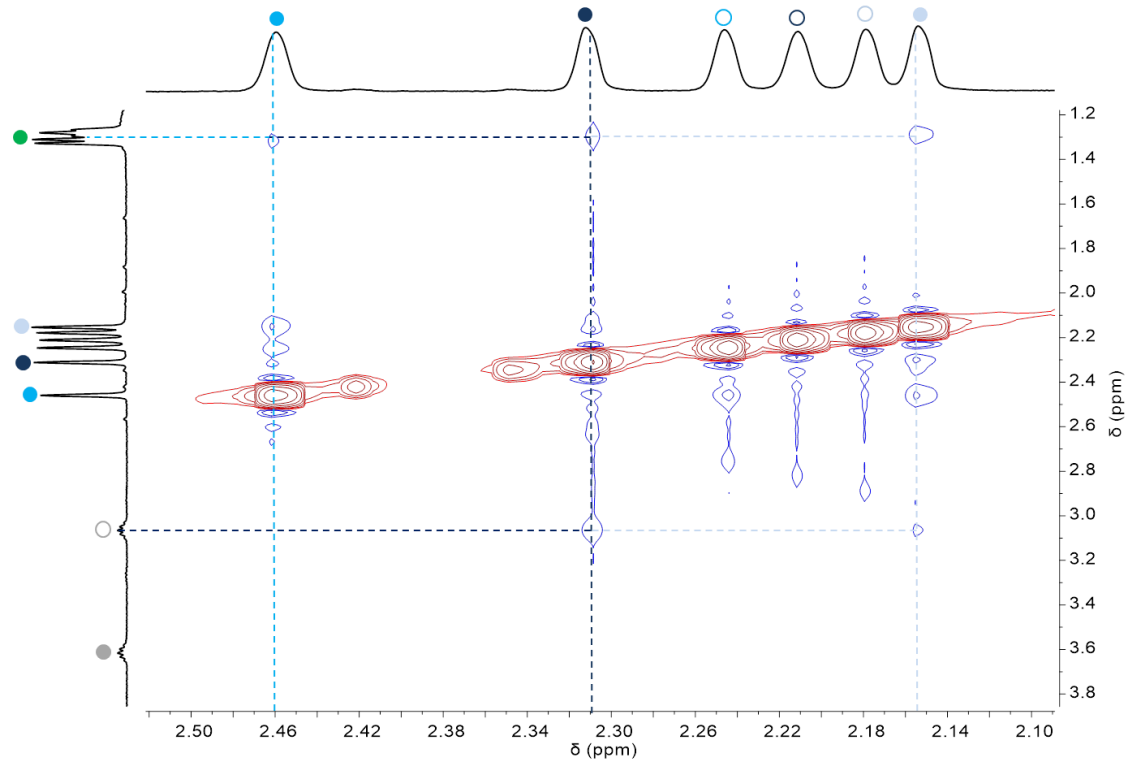


Figure 2.22 ^{1}H,^{1}H ROESY NMR spectrum (benzene-d_6, 500 MHz, 298 K) of *E*-^{Me_2}SB(Cp,I*)ZrCl(O-2,6-^{i}Pr-C$_6$H$_3$) (***E*-11**) showing 2.09–2.52 ppm.

Analysis of the I* methyl region of the spectrum for ***E*-11** reveals the location of the aryloxide group. The I* methyl resonances at 2.46, 2.31 and 2.15 ppm couple to the isopropyl methyl resonances at 1.30 ppm (distances of 4.474, 2.945 and 2.521 Å respectively, Figure 2.20b) (Figure 2.22, blue, navy and pale blue). The resonances at 2.31 and 2.15 ppm also couple to the isopropyl hydrogen resonance at 3.07 ppm (distances of 2.278 and 2.776 Å respectively) (Figure 2.22, blue and navy). In addition, the cyclopentadienyl resonance at 5.71 ppm couples to the isopropyl hydrogen resonance at 3.07 ppm (distance of 2.593 Å); confirming that the aryloxide group is positioned away from the I* ligand (*E*-isomer).

Variable temperature ^{1}H NMR of ***Z*-10** between 298 and 363 K shows movement and broadening of the aryloxide methyl resonances as temperature increases, while ***E*-11** shows broadening and coalescence of the isopropyl protons (Figures 2.23 and A2.13, full spectra Figures A2.12 and A2.14).

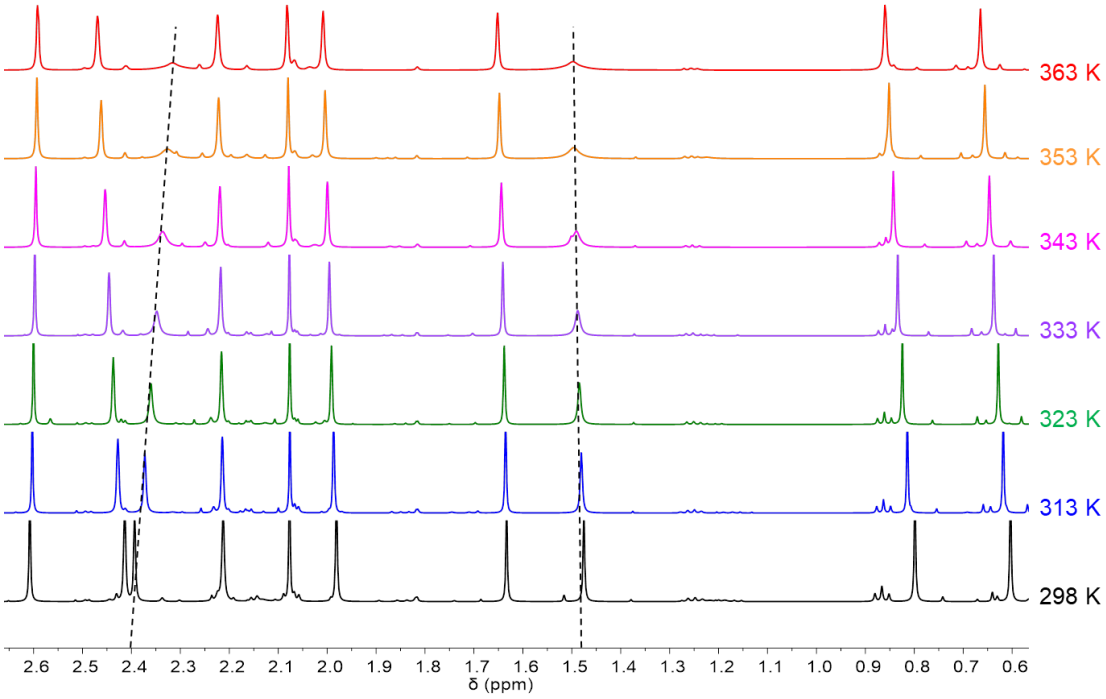


Figure 2.23 Variable temperature ^{1}H NMR spectrum (benzene-d_6, 500 MHz) of *Z*-^{Me_2}SB(Cp,I*)ZrCl(O-2,6-Me-C$_6$H$_3$) (***Z*-10**) between 298 and 363 K, showing 0.58–2.66 ppm.

Both complexes also show coalescence of the aryl protons as temperature increases. The broadening and coalescence of these groups is attributed to rapid rotation of the aryloxide groups; at elevated temperatures greater energy of the system allows the energy barrier of rotation to be overcome and as a result, the resonances corresponding to the aryloxide groups become chemically equivalent.[29]

2.4.2 X-ray crystallography

Yellow crystals of ***Z*-10** and ***E*-11** suitable for single-crystal X-ray diffraction studies were obtained from saturated pentane solutions at −34 °C in the monoclinic space group $P2_1/n$. The solid-state molecular structures are depicted in Figure 2.24, with selected bond lengths and angles presented in Table 2.3. The geometric parameters of other zirconocene aryloxide complexes are provided for comparison.

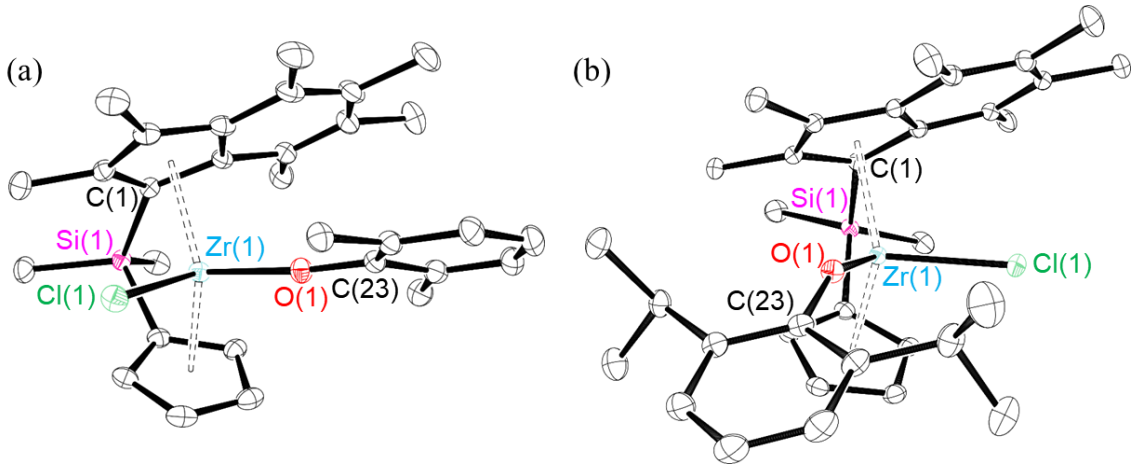


Figure 2.24 Solid-state molecular structures of (a) *Z*-^{Me_2}SB(Cp,I*)ZrCl(O-2,6-Me-C_6H_3) (***Z*-10**) and (b) *E*-^{Me_2}SB(Cp,I*)ZrCl(O-2,6-^{i}Pr-C_6H_3) (***E*-11**). H atoms omitted for clarity; ellipsoids given at 30% probability.

The solid-state structure of ***Z*-10** demonstrates aryloxide group placement below the I* ligand, while the solid-state structure of ***E*-11** confirms isolation of *E*-^{Me_2}SB(Cp,I*)ZrCl(O-2,6-^{i}Pr-C_6H_3) with the aryloxide group positioned away from the I* ligand. The change in preference for the *E*-isomer over the *Z*-isomer when moving from the methyl substituted aryloxide moiety to the isopropyl substituted

aryloxide moiety can be rationalised due to the sterics of the systems; the bulkier isopropyl group is less likely to be positioned in the more sterically inaccessible *Z*-position below the permethylindenyl ring.

Table 2.3 Selected bond lengths (Å) and angles (°) for ^{Me_2}SB(Cp,I*)ZrCl$_2$ (**1**), *Z*-^{Me_2}SB(Cp,I*)ZrCl(O-2,6-Me-C$_6$H$_3$) (***Z*-10**), *E*-^{Me_2}SB(Cp,I*)ZrCl(O-2,6-^{i}Pr-C$_6$H$_3$) (***E*-11**) and other related zirconocene aryloxide complexes. Displayed in order of increasing Zr-O distance.

Complex	Zr-Ind$_{cent}$	Zr-Cp$^R_{cent}$	Zr-O	Zr-O-C
^{Me_2}SB(Cp,I*)ZrCl$_2$	2.2244(1)	2.2076(1)	-	-
rac-EBIZrCl(O-2,6-Me-C$_6$H$_3$) [30]	2.255 [a]	-	1.942	171.4
Cp$_2$ZrCl(O-2,6-Me-C$_6$H$_3$) [30]	-	2.219 [b]	1.955	171.6
Z-^{Me_2}SB(Cp,I*)ZrCl(O-2,6-Me-C$_6$H$_3$)	2.2504(1)	2.2201(1)	1.9628(1)	173.09(1)
Cp$_2$ZrCl(O-2,6-^{i}Pr-C$_6$H$_3$) [31]	-	2.233 [b]	1.97	172.1
Cp$_2$ZrCl(OC$_6$H$_5$) [31]	-	2.224 [b]	1.98	150.2
E-^{Me_2}SB(Cp,I*)ZrCl(O-2,6-^{i}Pr-C$_6$H$_3$)	2.2462(1)	2.2070(1)	1.9873(1)	148.31(1)
Cp$_2$Zr(O-2,6-Me-C$_6$H$_3$)$_2$ [32]	-	2.235 [b]	1.997 [c]	146.0 [d]
Cp$_2$ZrCl(O-2,6-^{t}Bu-C$_6$H$_3$) [33]	-	2.227 [b]	2.008	144.1

(a) Average Zr-Ind$_{cent}$ distance; (b) average Zr-Cp$_{cent}$ distance; (c) average Zr-O distance; (d) average Zr-O-C angle.

***Z*-10** and ***E*-11** show Zr-O distances comparable to the values reported for aryloxide zirconocene complexes Cp$_2$ZrCl(O-2,6-Me-C$_6$H$_3$), Cp$_2$Zr(O-2,6-Me-C$_6$H$_3$)$_2$, *rac*-EBIZrCl(O-2,6-Me-C$_6$H$_3$) and Cp$_2$ZrCl(2,6-^{i}Pr-C$_6$H$_3$); Zr-O = 1.9628, 1.9873, 1.955, 1.997, 1.942, 1.97 Å respectively.[30-33] The Zr-O bond lengths reported for ***Z*-10** and ***E*-11** are significantly shorter than the sum of the covalent radii of zirconium and oxygen (1.75 and 0.66 Å respectively), indicating that there is a partial ionic character to the Zr-O bond (i.e. Zr$^{\delta+}$-O$^{\delta-}$).[34]

***Z*-10** and ***E*-11** display Zr-O-C angles of 173.09° and 148.31° respectively. The near-linear nature of the Zr-O-C angle in ***Z*-10** suggests some π-orbital interaction between Zr and O, and is in good agreement with the values reported for $Cp_2ZrCl(O\text{-}2,6\text{-}Me\text{-}C_6H_3)$, *rac*-EBIZrCl(O-2,6-Me-C_6H_3) and $Cp_2ZrCl(2,6\text{-}^{i}Pr\text{-}C_6H_3)$ (Zr-O-C angle of 171.6° and 171.4° and 172.1° respectively).[30, 31] The much sharper Zr-O-C angle for ***E*-11** is most likely due to a decrease in π-orbital overlap between Zr and O, stemming from the slightly longer Zr-O bond of ***E*-11** compared to ***Z*-10**. The increase in the steric bulk of the aryloxide ligand for ***E*-11** compared to ***Z*-10** may also contribute to the distortion away from linearity. From a literature comparison, a large decrease in Zr-O-C angle from near-linear to less than 150° occurs when Zr-O is greater than 1.98 Å; $Cp_2ZrCl(OC_6H_5)$, $Cp_2Zr(O\text{-}2,6\text{-}Me\text{-}C_6H_3)_2$ and $Cp_2ZrCl(2,6\text{-}^{t}Bu\text{-}C_6H_3)$ show Zr-O bond lengths of 1.98, 1.997 and 2.008 Å respectively with corresponding Zr-O-C angles of 150.2°, 146.0° and 144.1°.[31-33]

The Zr-Cp$^R_{cent}$ distances of ***Z*-10** and ***E*-11** are comparable to those found in the literature.[30, 32, 33] ***Z*-10** shows longer Zr-Cp$^R_{cent}$ and Zr-Ind$_{cent}$ distances than ***E*-11** and the parent dichloride complex **1** (Zr-Cp$^R_{cent}$ = 2.2201, 2.2070 and 2.2076 Å respectively; Ind$_{cent}$ = 2.2504, 2.2462 and 2.2244 Å respectively). It is proposed that this is due to the sterics of the systems; the positioning of the aryloxide group under the permethylindenyl ligand in ***Z*-10** causes additional strain on the system, which forces the zirconium atom further away from the cyclopentadienyl and permethylindenyl ligands. α and δ are unaffected by ligand substitution from chloride to aryloxide (α = 60.19°, 60.88° and 59.62°, and δ = 126.37°, 126.90° and 125.29° for **1**, ***Z*-10** and ***E*-11** respectively).

2.5 Conclusions

Twelve new unsymmetrical permethylindenyl zirconocene systems based on the $^{Me_2}SB(Cp^R,I^*)ZrX(Y)$ motif (R = H, Me and ^{n}Bu; X = Cl, Br, CH_2Ph and Me; Y = Cl, Br, Me, CH_2Ph, O-2,6-Me-C_6H_3 and O-2,6-^{i}Pr-C_6H_3) have been synthesised and fully characterised by NMR spectroscopy. Analysis of the cyclopentadienyl region of the spectra revealed splitting patterns indicative of non-conventional coupling. Variable temperature ^{1}H NMR spectroscopy studies highlighted the thermal stability of these complexes up to 363 K and showed the fluxionality of aryloxide initiation groups at elevated temperatures.

Nine new solid-state structures have been reported and their key features discussed. In all cases Zr-Cp^R_{cent} was found to be shorter than Zr-Ind_{cent} due to the bulkier sterics of the permethylindenyl ligand compared to the cyclopentadienyl ligand. It was observed that the *E*- and *Z*-isomers of $^{Me_2}SB(Cp^{Me},I^*)ZrCl_2$ experienced substantial differences in the ring tilt angle and angle about the metal centre, while for *E*- and *Z*-$^{Me_2}SB(Cp^{n\text{Bu}},I^*)ZrCl_2$ the plane of the *n*-butyl chain relative to the cyclopentadienyl ring dramatically changed from near-perpendicular to near-linear respectively.

Finally, initial studies into the reactivity of these complexes with MAO found that the same cationic species was formed regardless of the identity of the initiation group for $^{Me_2}SB(Cp,I^*)ZrX_2$ (X = Cl, Me and CH_2Ph) complexes.

2.6 References

1. P. Ransom, A. E. Ashley, N. D. Brown, A. L. Thompson and D. O'Hare, *Organometallics*, 2011, **30**, 800-814.
2. G. W. Coates, *Chem. Rev.*, 2000, **100**, 1223-1252.
3. L. Resconi, L. Cavallo, A. Fait and F. Piemontesi, *Chem. Rev.*, 2000, **100**, 1253-1346.
4. T. A. Q. Arnold, Z. R. Turner, J.-C. Buffet and D. O'Hare, *J. Organomet. Chem.*, 2016, **822**, 85-90.
5. K. P. Bryliakov, N. V. Semikolenova, D. V. Yudaev, V. A. Zakharov, H. H. Brintzinger, M. Ystenes, E. Rytter and E. P. Talsi, *J. Organomet. Chem.*, 2003, **683**, 92-102.
6. J.-C. Buffet, T. A. Q. Arnold, Z. R. Turner, P. Angpanitcharoen and D. O'Hare, *RSC Adv.*, 2015, **5**, 87456-87464.
7. P. J. Shapiro, *Coord. Chem. Rev.*, 2002, **231**, 67-81.
8. J. Tudor, S. Barlow, B. R. Payne, D. O'Hare, P. Nguyen, C. E. B. Evans and I. Manners, *Organometallics*, 1999, **18**, 2281-2284.
9. W. J. Gauthier, J. F. Corrigan, N. J. Taylor and S. Collins, *Macromolecules*, 1995, **28**, 3771-3778.
10. M. L. H. Green and N. Ishihara, *J. Chem. Soc., Dalton Trans.*, 1994, 657-665.
11. A. Razavi and J. Ferrara, *J. Organomet. Chem.*, 1992, **435**, 299-310.
12. Y. X. Chen, M. D. Rausch and J. C. W. Chien, *J. Organomet. Chem.*, 1995, **497**, 1-9.
13. A. Razavi and J. L. Atwood, *J. Organomet. Chem.*, 1993, **459**, 117-123.
14. R. C. Bruch, M. D. Bruch, J. H. Noggle and H. B. White, *Biochem. Biophys. Res. Commun.*, 1984, **123**, 555-561.
15. F. Piemontesi, I. Camurati, L. Resconi, D. Balboni, A. Sironi, M. Moret, R. Zeigler and N. Piccolrovazzi, *Organometallics*, 1995, **14**, 1256-1266.
16. J.-C. Buffet, Z. R. Turner and D. O'Hare, *Chem. Commun.*, 2018, **54**, 10970-10973.
17. D. O'Hare, V. Murphy, G. M. Diamond, P. Arnold and P. Mountford, *Organometallics*, 1994, **13**, 4689-4694.
18. T. Repo, M. Klinga, I. Mutikainen, Y. C. Su, M. Leskela and M. Polamo, *Acta Chem. Scand.*, 1996, **50**, 1116-1120.
19. J. Abell, Part II Thesis, University of Oxford, 2017.
20. S. K. Ritter, *Chem. Eng. News*, 2007, **85**, 42-43.
21. R. D. Shannon, *Acta Crystallogr. Sect. A*, 1976, **32**, 751-767.
22. M. A. Bush and G. A. Sim, *J. Chem. Soc. A*, 1971, 2225-2229.
23. M. Buhl, G. Hopp, W. vonPhilipsborn, S. Beck, M. H. Prosenc, U. Rief and H. H. Brintzinger, *Organometallics*, 1996, **15**, 778-785.
24. W. E. Hunter, D. C. Hrncir, R. V. Bynum, R. A. Penttila and J. L. Atwood, *Organometallics*, 1983, **2**, 750-755.
25. J. L. Atwood, W. E. Hunter, D. C. Hrncir, E. Samuel, H. Alt and M. D. Rausch, *Inorg. Chem.*, 1975, **14**, 1757-1762.

26. A. Shamiri, M. H. Chakrabarti, S. Jahan, M. A. Hussain, W. Kaminsky, P. V. Aravind and W. A. Yehye, *Materials*, 2014, **7**, 5069-5108.

27. L. S. Santos, *J. Braz. Chem. Soc.*, 2011, **22**, 1827-1840.

28. W. Kaminsky and R. Steiger, *Polyhedron*, 1988, **7**, 2375-2381.

29. J. J. Bergman and W. D. Chandler, *Can. J. Chem.*, 1972, **50**, 353-363.

30. J.-C. Buffet, G. R. Harris, J. J. Coward, T. A. Q. Arnold, Z. R. Turner and D. O'Hare, *J. Organomet. Chem.*, 2016, **801**, 87-95.

31. A. V. Firth, J. C. Stewart, A. J. Hoskin and D. W. Douglas, *J. Organomet. Chem.*, 1999, **591**, 185-193.

32. F. Benetollo, G. Cavinato, L. Crosara, F. Milani, G. Rossetto, C. Scelza and P. Zanella, *J. Organomet. Chem.*, 1998, **555**, 177-185.

33. T. Repo, G. Jany, M. Salo, M. Polamo and M. Leskela, *J. Organomet. Chem.*, 1997, **541**, 363-366.

34. W. A. Howard, T. M. Trnka and G. Parkin, *Inorg. Chem.*, 1995, **34**, 5900-5909.

Chapter 3

Olefin Polymerisation

3.1 Introduction

3.1.1 Overview

Altering the ligand environment of α-olefin polymerisation pre-catalysts can significantly affect polymerisation activity and polymer properties.[1-3] In slurry-phase α-olefin polymerisation, the identity of the support material has also been found to have significant influence over polymerisation performance and polymer microstructure.[4, 5] Additionally, the conditions of polymerisation, such as temperature, scale, scavenger and concentration can influence catalyst activity and polymer structure.[5, 6]

This chapter discusses how the complexes synthesised in Chapter 2 perform as α-olefin polymerisation catalysts, with the aim of understanding how the composition of the metallocene affects activity. The homogeneous solution-phase polymerisation of propylene and ethylene in the presence of methylaluminoxane (MAO) activator is briefly covered. However, the majority of this chapter focuses on the slurry-phase polymerisation of ethylene. A range of inorganic solid supports and polymerisation conditions have been studied, with the aim of evaluating and understanding their effects on polymerisation activity and polymer properties. A variety of techniques have been employed to analyse both the solid catalysts and polymers.

3.1.2 Gel permeation chromatography (GPC)

There are many techniques available for the characterisation of polyolefins, including nuclear magnetic resonance (NMR) spectroscopy, differential scanning calorimetry (DSC), scanning electron microscopy (SEM) and infrared (IR) spectroscopy. However, gel permeation chromatography (GPC) is one of the most useful characterisation techniques. GPC is a type of high performance liquid chromatography that separates molecules based on their size. It can be used to identify polymer molecular weights and determine dispersity, as well as to separate mixtures into discrete fractions (polymer, oligomer and monomer). GPC employs a stagnant liquid in the pores of beads as the stationary phase, and a flowing liquid as the mobile phase. Higher molecular weight polymers are eluted first as they cannot enter the pores of the stationary phase.[7, 8]

Polymer molecular weights occur as a distribution, and several molecular weight values can therefore be reported. The number average molecular weight (M_n) is the value at which there are equal numbers of molecules on each side of the distribution, where N_i is the number of molecules with weight 'i' (Equation 3.1).[9] The weight average molecular weight (M_w) is the value at which there are equal masses of molecules on each side of the distribution (Equation 3.2).[9] The ratio of M_w to M_n gives the molecular weight distribution (MWD), also known as dispersity (Equation 3.3).

$$M_n = \frac{\sum_i N_i M_i}{\sum_i N_i} \qquad \textbf{Equation 3.1}$$

$$M_w = \frac{\sum_i N_i M_i^2}{\sum_i N_i M_i} \qquad \textbf{Equation 3.2}$$

$$\text{MWD} = \frac{M_w}{M_n} \qquad \textbf{Equation 3.3}$$

3.2 Homogeneous Polymerisation

3.2.1 Propylene polymerisation

To determine the effects of catalyst stereochemistry and ligand environment on polymer tacticity (discussed in Section 1.2.2) the solution-phase polymerisation of propylene using C_1-symmetric ^{Me_2}SB(Cp,I*)ZrCl$_2$ (**1**) and ^{Me_2}SB(Cp^{Me},I*)ZrCl$_2$ (**3**) was studied (Chart 3.1a and b). Polymerisations were conducted in 150 mL Rotaflo ampoules with 50 mL hexane, 0.5 mg pre-catalyst, 60 mg MAO activator with an initial aluminium to metal ratio ($[Al_{MAO}]_0/[M]_0$) of 1000 and 2 bar propylene for 30 minutes. As demonstrated in Section 2.3.3, MAO reacts with the complexes to form the active cationic species. Known propylene polymerisation catalysts C_2-symmetric ^{Me_2}SB($^{2\text{-Me,4-Ph}}$Ind)ZrCl$_2$ (**A**) and ^{Me_2}SB($^{2\text{-Me,benzene}}$Ind)ZrCl$_2$ (**B**) were also studied (Chart 3.1c and d).

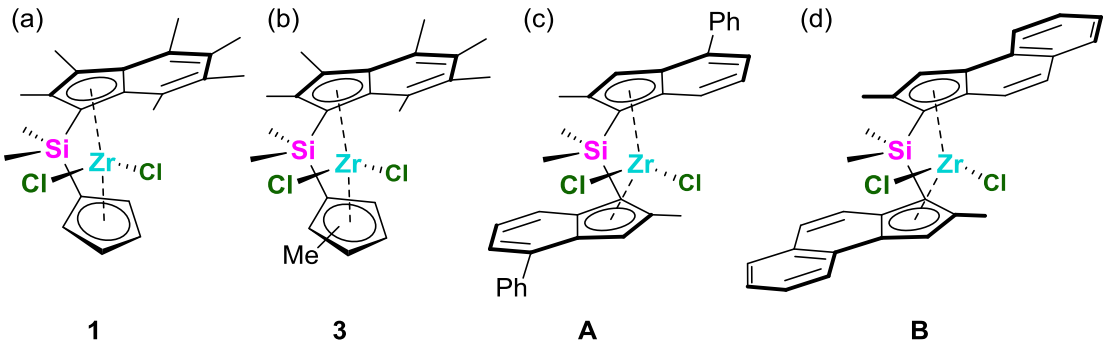


Chart 3.1 Zirconocenes used in this study.

Table 3.1 displays the solution-phase propylene polymerisation activity of **1**, **3**, **A** and **B** and the molecular weights (M_w) of the polymers produced. **1** and **3** were found to be relatively inactive for the polymerisation of propylene with activities of 62 and 61 $kg_{PP}\ mol_M^{-1}\ h^{-1}\ bar^{-1}$ respectively at 80 °C. Increasing the temperature to 90 °C led to similar activities for **1** and a slight decrease in activity for **3** (66 and 46 $kg_{PP}\ mol_M^{-1}\ h^{-1}\ bar^{-1}$ respectively). The polymer was initially isolated as an oil.

However, repeated cycles of pentane washing and drying lead to the isolation of a solid product. **1** and **3** showed significantly lower propylene polymerisation activities than **A** and **B** at 80 °C after 5 minutes (activities of 25064 and 5537 $kg_{PP}\ mol_M^{-1}\ h^{-1}\ bar^{-1}$ respectively). **1** and **3** also showed lower propylene polymerisation activities than analogous $^{Me_2}SB(Cp,I)ZrCl_2$; activity of 727 $kg_{PP}\ mol_M^{-1}\ h^{-1}\ bar^{-1}$ at 25 °C with MAO co-catalyst (1.1 bar propylene and $[Al_{MAO}]_0/[M]_0 = 2000$).[10]

Table 3.1 Solution-phase propylene polymerisation activity and polymer molecular weights (M_w) using selected zirconocene catalysts.[a]

Catalyst	Temperature [b]	Activity [c]	M_w [d]	M_w/M_n
$^{Me_2}SB(Cp,I^*)ZrCl_2$ (**1**)	80	62	1	1.2
$^{Me_2}SB(Cp,I^*)ZrCl_2$ (**1**)	90	66	-	-
$^{Me_2}SB(Cp^{Me},I^*)ZrCl_2$ (**3**)	80	61	1	1.2
$^{Me_2}SB(Cp,I^*)ZrCl_2$ (**1**)	90	46	-	-
$^{Me_2}SB(^{2\text{-Me,4-Ph}}Ind)ZrCl_2$ (**A**)	80	25064 [e]	43	2.9
$^{Me_2}SB(^{2\text{-Me,benzene}}Ind)ZrCl_2$ (**B**)	80	5537 [e]	68	3.0

(a) Polymerisation conditions: pre-catalyst (0.5 mg), MAO co-catalyst ($[Al_{MAO}]_0/[M]_0 = 1000$), propylene (2 bar), hexane (50 mL) and 30 minutes; (b) °C; (c) $kg_{PP}\ mol_M^{-1}\ h^{-1}\ bar^{-1}$, (d) $kg\ mol^{-1}$; (e) polymerisation time of 5 minutes.

1 and **3** produced polypropylene with very low molecular weights (M_w = 1 $kg\ mol^{-1}$) and dispersity (M_w/M_n = 1.2), consistent with the formation of an oil and indicating that these species behave as single-site catalysts. The polymer molecular weights produced using **1** and **3** were lower than those produced using **A** and **B** (M_w = 43 and 68 $kg\ mol^{-1}$ respectively), and lower than the polypropylene produced using analogous $^{Me_2}SB(Cp,I)ZrCl_2$ (M_w = 9 $kg\ mol^{-1}$).[10] ^1H NMR spectroscopy indicated the formation of atactic polypropylene, with a major broad resonance at

0.95 ppm corresponding to CH_3, multiple broad resonances between 1.05 and 1.40 ppm corresponding to several CH_2 environments and a broad resonance at 1.73 ppm corresponding to CH protons (Figure A3.1).[6]

3.2.2 Ethylene polymerisation

Due to the poor polymerisation activity observed with propylene, the solution-phase polymerisation of ethylene using **1** was studied. Polymerisations were conducted between 50 and 90 °C in 150 mL Rotaflo ampoules with 50 mL hexane, 0.5 mg pre-catalyst, 15 mg MAO activator ($[Al_{MAO}]_0/[M]_0 = 200$) and 2 bar ethylene. Polymerisation runs were run for 5 minutes or until stirring ceased.

1 was much more active towards ethylene than propylene with an activity of 6284 $kg_{PE}\ mol_M^{-1}\ h^{-1}\ bar^{-1}$ at 80 °C (Figure 3.1a). It is noted that the poor morphology of the polymer produced led to reactor fouling, which hindered efficient stirring and limits the large-scale applications of these species. SEM images showed the formation of very inhomogeneous and aggregated polymer particles with poorly defined structures (Figure 3.1b). **1** displayed a polymerisation activity significantly higher than previously reported ($(^{2,4\text{-Me}}Ind)_2ZrCl_2$ and $(^{2,4,6\text{-Me}}Ind)_2ZrCl_2$ (Chart 3.2); activities of 3590 and 3890 $kg_{PE}\ mol_M^{-1}\ h^{-1}\ bar^{-1}$ respectively at 50 °C with MAO co-catalyst (1 bar ethylene and $[Al_{MAO}]_0/[M]_0 = 3000$).[11]

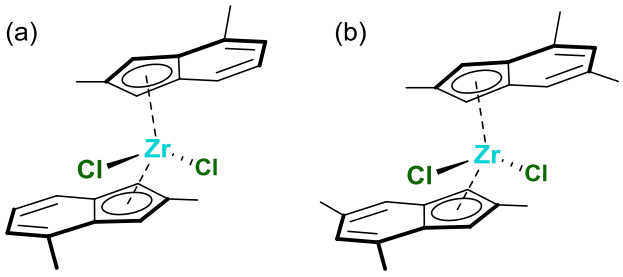


Chart 3.2 Structures of (a) $(^{2,4\text{-Me}}Ind)_2ZrCl_2$ and (b) $(^{2,4,6\text{-Me}}Ind)_2ZrCl_2$.[11]

The molecular weights (M_w) of the polymers produced by **1** were between 452 and 127 kg mol^{-1} (Figure 3.1a). M_w was observed to decrease with increasing polymerisation temperature due to the changing ratio of chain propagation relative to termination.[12, 13] The molecular weight distributions of the polyethylenes were much larger than those observed for the polypropylenes (M_w/M_n = 3.9–6.9), which is in agreement with the poor polymer morphology. The wider MWD indicates that **1** does not behave as a single-site catalyst for the solution-phase polymerisation of ethylene. This may be due to the aggregated polymer morphology, which can lead to burying of the catalytically active centres.

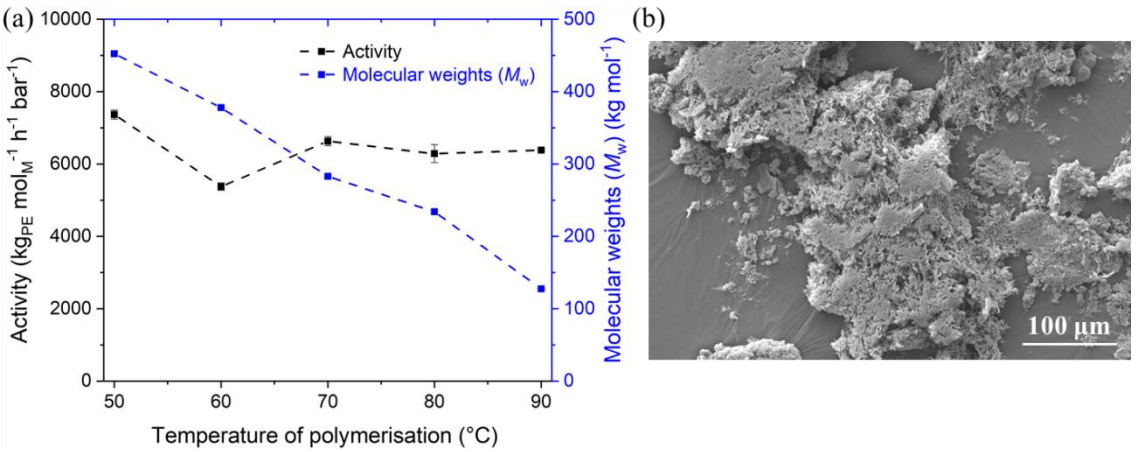


Figure 3.1 (a) Solution-phase ethylene polymerisation activity (black) and polymer molecular weights (M_w) (blue) as a function of temperature of polymerisation using ^{Me_2}SB(Cp,I*)ZrCl$_2$ (**1**); (b) SEM image at ×250 magnification of the polymer produced from the solution-phase polymerisation of ethylene using ^{Me_2}SB(Cp,I*)ZrCl$_2$ (**1**). Polymerisation conditions: pre-catalyst (0.5 mg), MAO co-catalyst ([Al$_{MAO}$]$_0$/[M]$_0$ = 200), ethylene (2 bar), hexane (50 mL), 80 °C and 5 minutes.

3.3 Slurry-Phase Ethylene Polymerisation

As ^{Me_2}SB(Cp,I*)ZrCl$_2$ (**1**) was significantly more active for the homogeneous polymerisation of ethylene compared to propylene, the slurry-phase polymerisation of ethylene was studied using a range of permethylindenyl zirconocenes and inorganic solid supports. The goal of immobilising the complexes was to preserve the high activity of homogeneous polymerisation while improving polymer morphology *via* the templating effect of the solid support.[14] In order to study the effects of the solid support on slurry-phase ethylene polymerisation activity and polymer morphology, ^{Me_2}SB(Cp,I*)ZrCl$_2$ (**1**), ^{Me_2}SB(Cp^{Me},I*)ZrCl$_2$ (**3**), ^{Me_2}SB(Cp,I*)Zr(CH$_2$Ph)$_2$ (**6**) and ^{Me_2}SB(Cp,I*)ZrMe$_2$ (**8**) (Chart 3.3) were immobilised onto three types of activating inorganic solid supports utilising the principles of surface organometallic chemistry (SOMC).[4, 15]

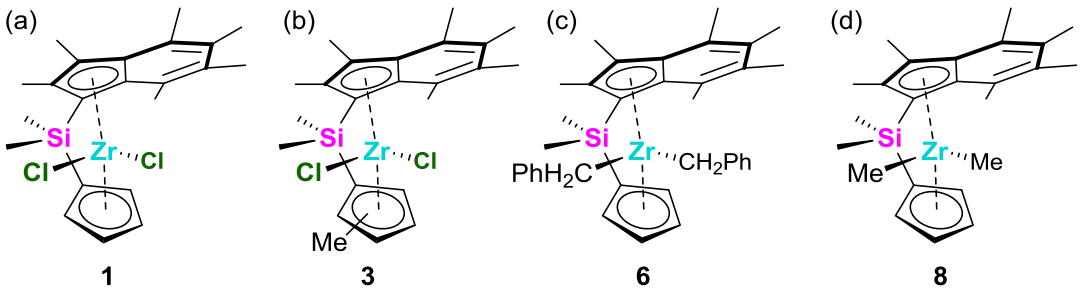


Chart 3.3 Permethylindenyl complexes used in this study.

The supports studied were first-generation solid polymethylaluminoxane (sMAO(1G)), MAO modified aqueous miscible organic layered double hydroxide/Mg$_3$Al-CO$_3$ (LDHMAO) and MAO modified silica (SSMAO) (Figure 3.2). Both LDH and silica were calcined under vacuum for 6 hours at 150 °C prior to modification with MAO.

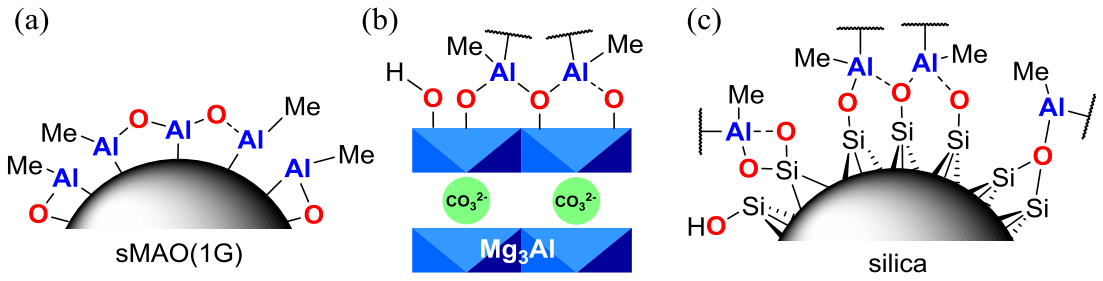


Figure 3.2 Proposed structures of (a) sMAO(1G), (b) LDHMAO and (c) SSMAO.

3.3.1 Support morphology

The SEM images of sMAO(1G), LDHMAO and SSMAO showed that sMAO(1G) had a uniform 'popcorn' morphology with particle sizes between 5 and 8 µm, LDHMAO had a poorly defined, aggregated 'cauliflower' morphology with particle sizes between 5 and 10 µm, and SSMAO was composed of uniform, monodisperse, granular particles about 30 µm in size (Figure 3.3).

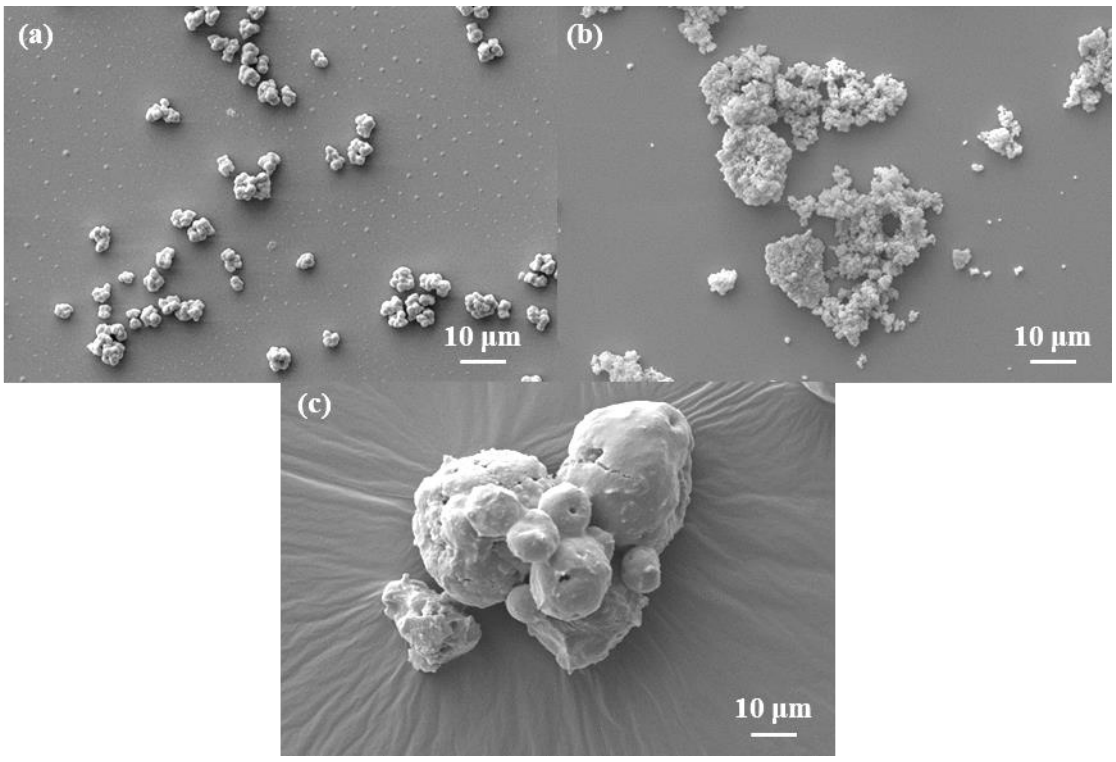


Figure 3.3 SEM images at ×1000 magnification of inorganic solid supports (a) sMAO(1G), (b) LDHMAO and (c) SSMAO.

Based on the support morphology, sMAO(1G) should produce the most industrially desirable and uniform polymer product due to the templating effect of the solid support, whereby the morphology of the starting support is replicated in the final polymer product.[5]

3.3.2 Complex immobilisation

Complex immobilisation was achieved by heating the solid support and complex in toluene at 60 °C while swirling. The coloured pre-catalyst was then allowed to settle, the colourless supernatant decanted and the solid pre-catalyst dried under vacuum (Figure 3.4).[16] In some cases, the solvent was removed from the decanted toluene solution and the residue checked by ^{1}H NMR spectroscopy to ensure that all the complex had been immobilised.

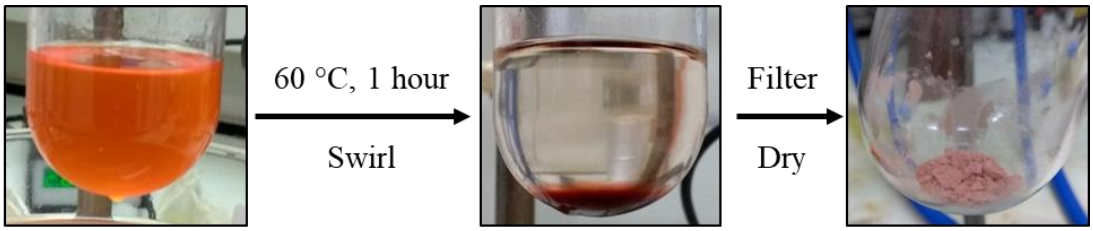


Figure 3.4 Immobilisation of ^{Me_2}SB(Cp,I*)ZrMe$_2$ (**8**) on sMAO(1G).

3.3.3 Catalyst characterisation

Characterisation of **1** supported on sMAO(1G) (**1**$_{\mathbf{sMAO(1G)}}$) and SSMAO (**1**$_{\mathbf{SSMAO}}$) was achieved using solid-state NMR (SSNMR) spectroscopy. The ^{29}Si cross-polarisation magic-angle spinning (CP/MAS) SSNMR spectra of **1**$_{\mathbf{sMAO(1G)}}$ and **1**$_{\mathbf{SSMAO}}$ show distinct resonances at −12 and −16 ppm respectively corresponding to the bridged silicon atom (Figure 3.5). These resonances are in good agreement with the solution ^{29}Si NMR spectrum of **1** in benzene-d_6, where the silicon resonance appears at −15 ppm. The ^{29}Si CP/MAS SSNMR spectrum of **1**$_{\mathbf{SSMAO}}$ also shows an intense broad

resonance at −102 ppm corresponding to SiO_2,[16] and resonances between −15 and 25 ppm corresponding to other species within silica such as $(SiO)_3SiR$, $(SiO)_2SiROH$ and $(SiO)SiR(OH)_2$ (where R is bound MAO).[17]

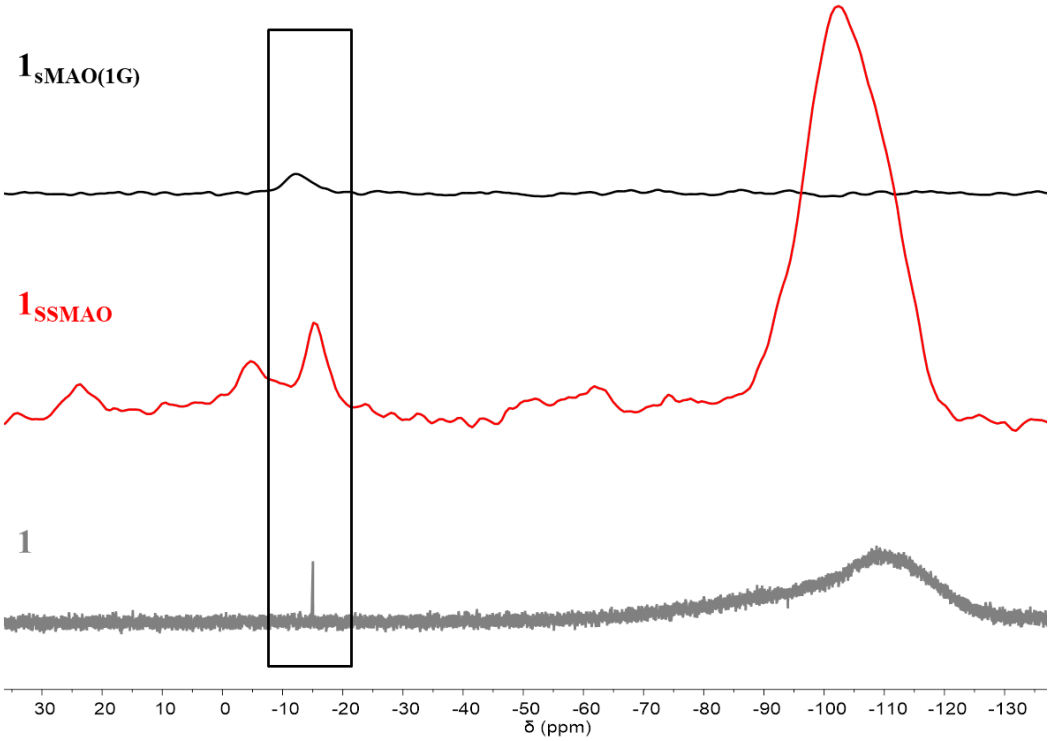


Figure 3.5 ^{29}Si CP/MAS SSNMR spectra (10 kHz, 298 K) of ^{Me_2}SB(Cp,I*)$ZrCl_2$ (**1**) supported on sMAO(1G) (**1**$_{\mathbf{sMAO(1G)}}$) (black) and SSMAO (**1**$_{\mathbf{SSMAO}}$) (red), and ^{29}Si NMR spectrum (benzene-d_6, 100 MHz, 298 K) of **1** (grey).

The ^{13}C CP/MAS SSNMR spectra of both **1**$_{\mathbf{sMAO(1G)}}$ and **1**$_{\mathbf{SSMAO}}$ show a major, broad resonance at approximately −8 ppm corresponding to the methyl environments of solid MAO and immobilised MAO respectively (Figure A3.2). By comparison with the solution-phase ^{13}C{^{1}H} NMR spectrum of **1**, the methyl groups on the permethylindenyl ring can be identified at 16–25 ppm, while the aromatic carbons of the permethylindenyl ring are observed at 128–138 ppm. The ^{13}C CP/MAS SSNMR spectrum of **1**$_{\mathbf{SSMAO}}$ showed an additional resonance at 51 ppm corresponding to bound ZrMe. The ^{27}Al direct polarisation magic angle spinning (DP/MAS) SSNMR spectra of **1**$_{\mathbf{sMAO(1G)}}$ and **1**$_{\mathbf{SSMAO}}$ showed a series of broad resonances between −245 and 350 ppm

due to the quadropolar aluminium nucleus (I = 5/2) (Figure A3.3).[18, 19] Kilpatrick *et al.* reported the same effect for an sMAO species and postulated that at least two major ^{27}Al components were present.[18]

3.3.4 Slurry-phase ethylene polymerisation

Slurry-phase ethylene polymerisation reactions were conducted at 50–90 °C in 150 mL Rotaflo ampoules with 50 mL hexane, 10 mg pre-catalyst, 150 mg triisobutylaluminium (TiBA) scavenger ($[TiBA]_0/[M]_0 = 1000$), 2 bar ethylene and an initial aluminium to metal ($[Al_{support}]_0/[M]_0$) loading of 200 (Figure 3.6).

To test for the possibility of complex leaching from the solid support during polymerisation, $\mathbf{1}_{\mathbf{sMAO(1G)}}$ and $\mathbf{8}_{\mathbf{sMAO(1G)}}$ were heated to 100 °C in toluene-d_8 at 10 °C increments and monitored by ^{1}H NMR spectroscopy. Even at 100 °C, 10 °C higher than the maximum polymerisation temperature used in this work, no complex leaching was observed. Furthermore, during polymerisation no reactor fouling was observed, indicating that no homogeneous ethylene polymerisation from complex leaching occurred.[20]

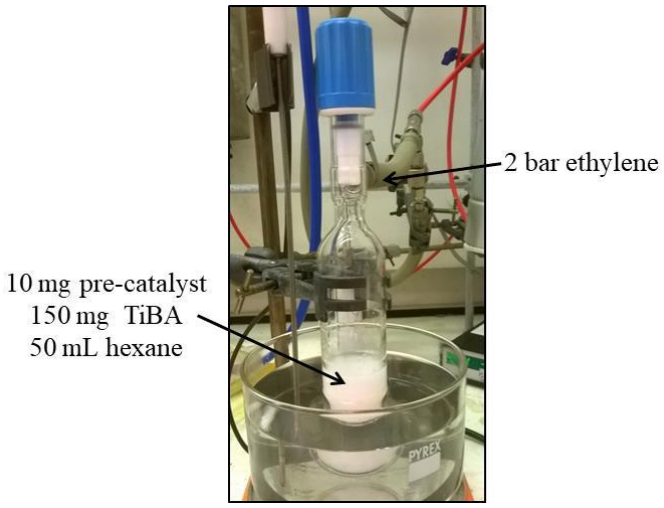


Figure 3.6 Slurry-phase ethylene polymerisation set-up.

1$_{sMAO(1G)}$, **3**$_{sMAO(1G)}$, **6**$_{sMAO(1G)}$ and **8**$_{sMAO(1G)}$ gave catalytic activities much higher than the analogous LDHMAO and SSMAO supported complexes (Figures 3.7, A3.4a and A3.5a); activities of 5067, 1192 and 87 $kg_{PE}\ mol_M^{-1}\ h^{-1}\ bar^{-1}$ for **1**$_{sMAO(1G)}$, **1**$_{SSMAO}$ and **1**$_{LDHMAO}$ respectively at 80 °C. **1**$_{sMAO(1G)}$ also gave much higher polymerisation activities in slurry-phase than **1**/MAO in solution-phase; activities of 9864 and 6284 $kg_{PE}\ mol_M^{-1}\ h^{-1}\ bar^{-1}$ respectively at 80 °C after 5 minutes. **1**$_{SSMAO}$, **3**$_{SSMAO}$ and **8**$_{SSMAO}$ consistently outperformed **1**$_{LDHMAO}$, **3**$_{LDHMAO}$ and **8**$_{LDHMAO}$, with a maximum activity of 1227 $kg_{PE}\ mol_M^{-1}\ h^{-1}\ bar^{-1}$ recorded for **8**$_{SSMAO}$ at 80 °C. It is hypothesised that the lower activity of the LDHMAO supported complexes is due to catalyst decomposition.

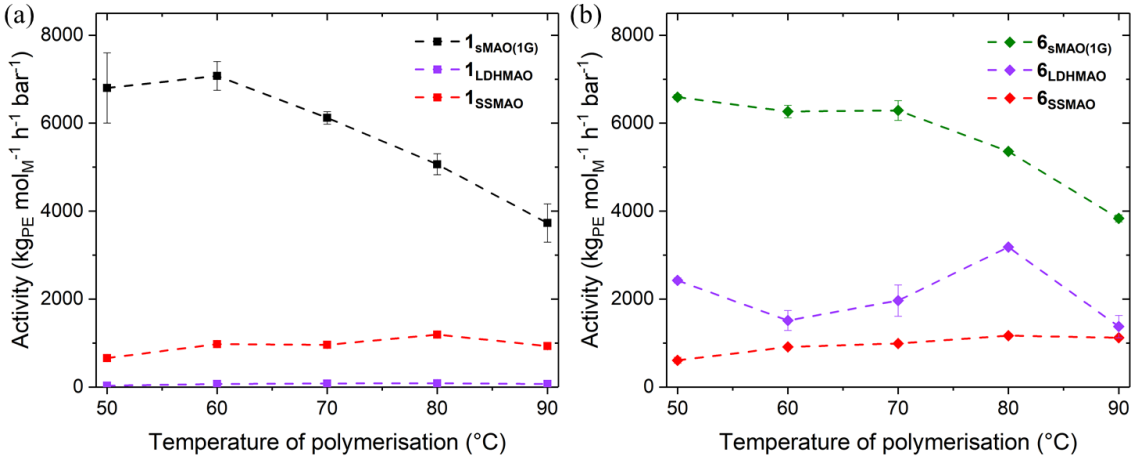


Figure 3.7 Slurry-phase ethylene polymerisation activity as a function of temperature of polymerisation using (a) ^{Me_2}SB(Cp,I*)ZrCl$_2$ (**1**) (square) and (b) ^{Me_2}SB(Cp,I*)Zr(CH$_2$Ph)$_2$ (**6**) (diamond) supported on sMAO(1G) (black and green respectively), LDHMAO (lilac) and SSMAO (red). Polymerisation conditions: $[Al_{support}]_0/[M]_0$ = 200, TiBA (150 mg), ethylene (2 bar), pre-catalyst (10 mg), hexane (50 mL) and 30 minutes.

The slurry-phase ethylene polymerisation activity and polymer molecular weights (M_w) of **1**$_{SSMAO}$, **3**$_{SSMAO}$, **6**$_{SSMAO}$ and **8**$_{SSMAO}$ are displayed in Table 3.2, in addition to other SSMAO supported permethylindenyl zirconocenes run under the same conditions. When compared to SSMAO supported *rac*-^{Me_2}SBI*ZrCl$_2$ (activity of

611 kg_{PE} mol_M^{-1} h^{-1} bar^{-1} at 70 °C),[16] $\mathbf{1_{SSMAO}}$, $\mathbf{6_{SSMAO}}$ and $\mathbf{8_{SSMAO}}$ were found to be 57, 62 and 84% more active respectively, and $\mathbf{3_{SSMAO}}$ 20% less active; activities of 959, 992, 1125 and 490 kg_{PE} mol_M^{-1} h^{-1} bar^{-1} respectively. It is postulated that the decrease in the activity of $\mathbf{3_{SSMAO}}$ is due to the increase in steric bulk of the cyclopentadienyl substituent compared to $\mathbf{1_{SSMAO}}$, $\mathbf{6_{SSMAO}}$ and $\mathbf{8_{SSMAO}}$. In the presence of MAO, it was found that **1**, **6** and **8** formed the same $[^{Me_2}SB(Cp,I^*)ZrMe]^+$ $[MAO]^-$ species (Section 2.2.3). Therefore, it is postulated that **3** would likely form $[^{Me_2}SB(Cp^{Me},I^*)ZrMe]^+$ $[MAO]^-$ in the presence of MAO, with the bulkier R group possibly inhibiting ethylene monomer coordination during polymerisation. The effects of steric bulk on polymerisation activity have been studied by Janiak *et al.* for the solution-phase polymerisation of ethylene in the presence of MAO.[21] It was observed that activity was inversely proportional to the steric demand of the cyclopentadienyl ligand with activity following the order Cp_2ZrCl_2 > $(Cp^*)CpZrCl_2$ > $(Cp^*)_2ZrCl_2$.

Table 3.2 Slurry-phase ethylene polymerisation activity and polymer molecular weights (M_w) using selected zirconocene catalysts supported on MAO modified silica (SSMAO).[a]

SSMAO supported complex	Activity [b]	M_w [c]
$^{Me_2}SB(Cp,I^*)ZrCl_2$ (**1**)	959	367
$^{Me_2}SB(Cp^{Me},I^*)ZrCl_2$ (**3**)	490	343
$^{Me_2}SB(Cp,I^*)Zr(CH_2Ph)_2$ (**6**)	992	429
$^{Me_2}SB(Cp,I^*)ZrMe_2$ (**8**)	1125	399
rac-$^{Me_2}SBI^*ZrCl_2$ [16]	611	262
rac-EBI^*ZrCl_2 [16]	2647	196

(a) Polymerisation conditions: $[Al_{support}]_0/[M]_0$ = 200, TiBA (150 mg), ethylene (2 bar), pre-catalyst (10 mg), hexane (50 mL), 70 °C and 30 minutes; (b) kg_{PE} mol_M^{-1} h^{-1} bar^{-1}; (c) kg mol^{-1}.

When compared to SSMAO supported *rac*-EBI*$ZrCl_2$,[16] **1$_{SSMAO}$**, **3$_{SSMAO}$**, **6$_{SSMAO}$** and **8$_{SSMAO}$** showed activities 64, 81, 63 and 57% lower respectively at 70 °C; activities of 2647, 959, 490, 992 and 1125 $kg_{PE}\ mol_M^{-1}\ h^{-1}\ bar^{-1}$. This series of catalysts also showed activities much lower than *rac*-EBI$ZrCl_2$ supported on MAO modified silica (activity of 3111 $kg_{PE}\ mol_M^{-1}\ h^{-1}\ bar^{-1}$ with $[Al_{support}]_0/[M]_0$ = 1700 at 40 °C with 1.3 bar ethylene; silica calcined at 300 °C prior to activation with MAO).[22] However, **1$_{SSMAO}$**, **3$_{SSMAO}$**, **6$_{SSMAO}$** and **8$_{SSMAO}$** showed higher ethylene polymerisation activities than an industrial standard, $(Cp^{nBu})_2ZrCl_2$, supported on SSMAO with $[Al_{support}]_0/[M]_0$ of 148 (activity of 226 $kg_{PE}\ mol_M^{-1}\ h^{-1}\ bar^{-1}$ at 80 °C with 8 bar ethylene; silica calcined at 600 °C prior to activation with MAO).[19]

The slurry-phase ethylene polymerisation activity and polymer molecular weights (M_w) of **1$_{LDHMAO}$**, **3$_{LDHMAO}$**, **6$_{LDHMAO}$** and **8$_{LDHMAO}$** are displayed in Table 3.3, in addition to other literature LDHMAO supported zirconocenes run under the same conditions. Surprisingly, **6$_{LDHMAO}$** gave a consistently higher activity than **6$_{SSMAO}$** over the temperature range with peak activity of 3182 $kg_{PE}\ mol_M^{-1}\ h^{-1}\ bar^{-1}$ at 80 °C (Figure 3.7b). At 80 °C, **6$_{LDHMAO}$** is a very active LDHMAO pre-catalyst, with activity 49% higher than $(Cp^{nBu})_2ZrCl_2$ supported on LDHMAO (activity of 2141 $kg_{PE}\ mol_M^{-1}\ h^{-1}\ bar^{-1}$ at 60 °C).[23] When compared to LDHMAO supported *rac*-EBI*$ZrCl_2$ (activity of 4325 $kg_{PE}\ mol_M^{-1}\ h^{-1}\ bar^{-1}$ at 70 °C),[16] **1$_{LDHMAO}$**, **3$_{LDHMAO}$**, **6$_{LDHMAO}$** and **8$_{LDHMAO}$** showed activities 98, 94, 66 and 78% lower respectively.

It is suggested that the differences in the activities observed when using the three supports were due to the nature of the active species formed.[24, 25] LDHMAO and SSMAO produced catalysts with lower activities than sMAO(1G) as even after calcination some –OH groups may remain on the surface of the LDH and SiO_2. These

–OH groups can hydrolyse MAO, reducing its performance as an activator and decreasing the overall performance of the support.[26] The presence of free trimethylaluminium (TMA) within sMAO(1G) can also have enhancing or detrimental effects on polymerisation activity.[18, 27]

Table 3.3 Slurry-phase ethylene polymerisation activity and polymer molecular weights (M_w) using selected zirconocene catalysts supported on MAO modified LDH (LDHMAO).[a]

LDHMAO supported complex	Activity [b]	M_w [c]
^{Me_2}SB(Cp,I*)ZrCl$_2$ (**1**)	80	-
^{Me_2}SB(Cp^{Me},I*)ZrCl$_2$ (**3**)	254	311
^{Me_2}SB(Cp,I*)Zr(CH$_2$Ph)$_2$ (**6**)	1571	423
^{Me_2}SB(Cp,I*)ZrMe$_2$ (**8**)	967	391
rac-EBI*ZrCl$_2$ [16]	4325	252
(Cp$^{n\text{Bu}}$)$_2$ZrCl$_2$ [23]	2141 [d]	-

(a) Polymerisation conditions: $[Al_{support}]_0/[M]_0$ = 200, TiBA (150 mg), ethylene (2 bar), pre-catalyst (10 mg), hexane (50 mL), 70 °C and 30 minutes; (b) $kg_{PE}\ mol_M^{-1}\ h^{-1}\ bar^{-1}$; (c) kg mol^{-1}; (d) 60 °C.

3.3.5 Polymer characterisation

The polymers produced from **3**, **6** and **8** supported on sMAO(1G), LDHMAO and SSMAO were analysed by GPC (Figures 3.8, A3.4b and A3.5b). sMAO(1G) supported complexes produced polymers with significantly lower molecular weights (M_w) than SSMAO and LDHMAO supported complexes; M_w of 84, 252 and 316 kg mol^{-1} at 80 °C for $\mathbf{6_{sMAO(1G)}}$, $\mathbf{6_{SSMAO}}$ and $\mathbf{6_{LDHMAO}}$ respectively. This is expected due to the presence of free TMA within MAO, which can act as a chain transfer agent and therefore lower the molecular weights.[28] The polymers produced from the SSMAO and LDHMAO supported complexes showed similar molecular weights;

M_w = 251–699 kg mol^{-1} and 228–603 kg mol^{-1} for **6**$_{\mathbf{SSMAO}}$ and **6**$_{\mathbf{LDHMAO}}$ respectively across the temperature range.

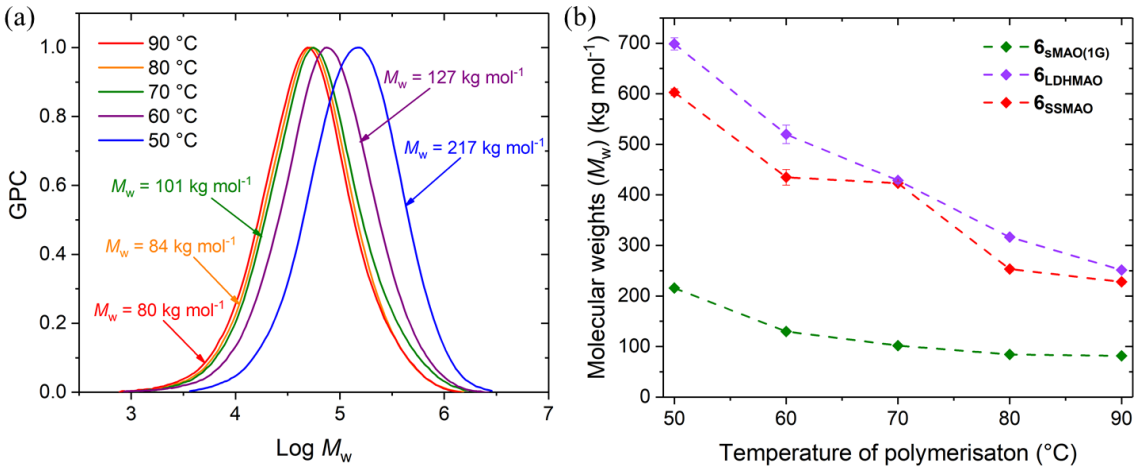


Figure 3.8 (a) Molecular weights distribution for ^{Me_2}SB(Cp,I*)Zr(CH$_2$Ph)$_2$ (**6**) supported on sMAO(1G) (**6**$_{\mathbf{sMAO(1G)}}$) at 50 °C (blue), 60 °C (purple), 70 °C (green), 80°C (orange) and 90 °C (red), normalised for clarity; (b) molecular weights (M_w) as a function of temperature of polymerisation using **6**$_{\mathbf{sMAO(1G)}}$ (green), **6**$_{\mathbf{LDHMAO}}$ (lilac) and **6**$_{\mathbf{SSMAO}}$ (red). Polymerisation conditions: [Al$_{support}$]$_0$/[M]$_0$ = 200, TiBA (150 mg), ethylene (2 bar), pre-catalyst (10 mg), hexane (50 mL) and 30 minutes.

6$_{\mathbf{SSMAO}}$ and **6**$_{\mathbf{LDHMAO}}$ produced polymers with much higher molecular weights than *rac*-^{Me_2}SBI*ZrCl$_2$ supported on SSMAO and LDHMAO; M_w = 429 and 262 kg mol^{-1} for **6**$_{\mathbf{SSMAO}}$ and SSMAO supported *rac*-^{Me_2}SBI*ZrCl$_2$ respectively at 70 °C, and M_w = 423 and 277 kg mol^{-1} for **6**$_{\mathbf{LDHMAO}}$ and LDHMAO supported *rac*-^{Me_2}SBI*ZrCl$_2$ respectively at 70 °C.[16] This is opposite to the trend seen when **6** was supported on sMAO(1G); **6**$_{\mathbf{sMAO(1G)}}$ produced polyethylenes with molecular weights 29% lower than sMAO(1G) supported *rac*-^{Me_2}SBI*ZrCl$_2$ (M_w = 130 and 183 kg mol^{-1} respectively). The molecular weight distributions of all the polymers were found to be relatively narrow over the temperature range (M_w/M_n = 2.7–3.1) indicating that the species largely behaved as single-site catalysts.[14, 29]

The morphologies of the polyethylenes produced using $\mathbf{1}_{\mathbf{SSMAO}}$, $\mathbf{1}_{\mathbf{LDHMAO}}$ and $\mathbf{1}_{\mathbf{sMAO(1G)}}$ at 80 °C were analysed by SEM (Figure 3.9). $\mathbf{1}_{\mathbf{sMAO(1G)}}$ was shown to form polyethylene as industrially desirable monodisperse, 'popcorn' shaped particles of uniform size (approximately 20 μm) and morphology. $\mathbf{1}_{\mathbf{LDHMAO}}$ and $\mathbf{1}_{\mathbf{SSMAO}}$ produced much more aggregated polymer particles with sizes between 30–100 μm, which are likely to lead to reactor fouling and difficulty processing on a larger scale. The SEM images of the polymer clearly show that the characteristics of the support (Figure 3.3) are replicated in the resultant polymer morphology.

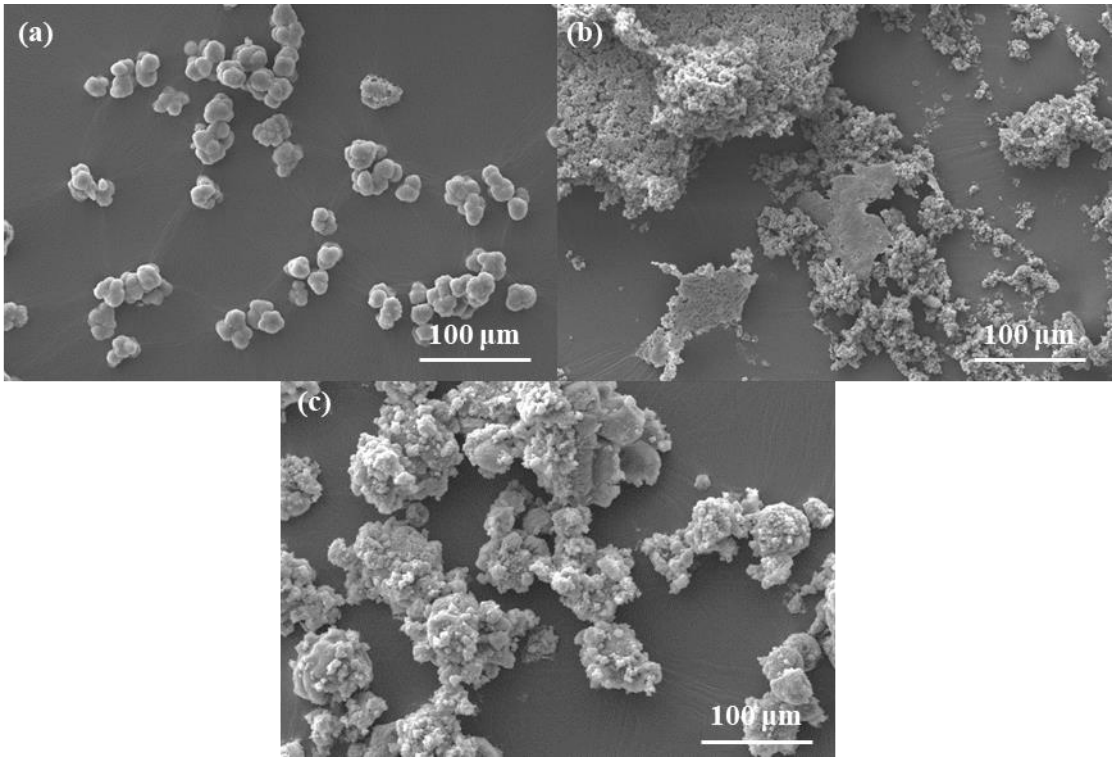


Figure 3.9 SEM images at ×250 magnification of the polymers produced from the slurry-phase polymerisation of ethylene using ^{Me_2}SB(Cp,I*)ZrCl$_2$ (**1**) supported on (a) sMAO ($\mathbf{1}_{\mathbf{sMAO(1G)}}$), (b) LDHMAO ($\mathbf{1}_{\mathbf{LDHMAO}}$) and (c) SSMAO ($\mathbf{1}_{\mathbf{SSMAO}}$). Polymerisation conditions: $[Al_{support}]_0/[M]_0$ = 200, TiBA (150 mg), ethylene (2 bar), pre-catalyst (10 mg), hexane (50 mL), 80 °C and 30 minutes.

DSC is a thermal analysis technique that measures the heat flux provided to a sample as the temperature of the sample is varied (i.e. it monitors how a material's heat

capacity changes with temperature).[30, 31] DSC analysis of the polyethylenes produced by **1**$_{\mathbf{SSMAO}}$, **1**$_{\mathbf{LDHMAO}}$ and **1**$_{\mathbf{sMAO(1G)}}$ at 80 °C revealed crystallisation temperatures (T_c) of 118–122 °C during the first cooling cycle and melting temperatures (T_m) of 133–136 °C during the second heating cycle (Figure 3.10); a melting temperature of ~134 °C is indicative of high-density polyethylene (HDPE) with minimal defects and branching.[32, 33] The lack of branching in HDPE produces polymers with stronger intermolecular forces and higher tensile strength than low-density polyethylene (LDPE), allowing applications in the production of materials such as plastic bottles and pipes.[34, 35]

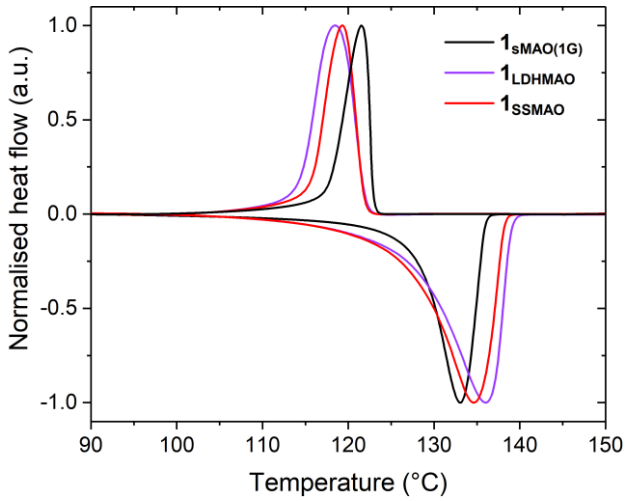


Figure 3.10 DSC plot showing the first cooling cycle and second heating cycle for the polyethylenes produced from ^{Me_2}SB(Cp,I*)ZrCl$_2$ supported on sMAO(1G) (**1**$_{\mathbf{sMAO(1G)}}$) (black), LDHMAO (**1**$_{\mathbf{LDHMAO}}$) (lilac) and SSMAO (**1**$_{\mathbf{SSMAO}}$) (red). Normalised for clarity. Polymerisation conditions: $[Al_{support}]_0/[M]_0$ = 200, TiBA (150 mg), ethylene (2 bar), pre-catalyst (10 mg), hexane (50 mL), 80 °C and 30 minutes.

By integrating the areas under the peaks for T_m and T_c and dividing by the heating rate, the enthalpy of melting (ΔH_m) and crystallisation (ΔH_c) were calculated in the range 152–220 J g^{-1} (typically 204 J g^{-1} for unbranched HDPE)[31] and 142–208 J g^{-1} respectively. Based on the theoretical maximum enthalpy of melting for 100% crystalline polyethylene (293 J g^{-1}),[36] polymer crystallinity was calculated as 75% for

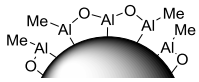
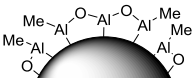
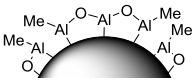
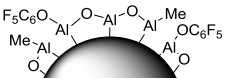
1$_{\mathbf{sMAO(1G)}}$, 52% for **1**$_{\mathbf{LDHMAO}}$ and 58% for **1**$_{\mathbf{SSMAO}}$. Crystallinity is usually reasonably high for HDPE as the lack of branching allows the chains to pack closely together, which leads to a higher degree of long-range order in the material.[37] The lower crystallinity of the polymers produced from **1**$_{\mathbf{LDHMAO}}$ and **1**$_{\mathbf{SSMAO}}$ compared to **1**$_{\mathbf{sMAO(1G)}}$ might be expected based on the inhomogeneous polymer morphology observed by SEM. Crystallinity can also be affected by polymer molecular weights; lower molecular weight polymers typically have a lesser degree of chain entanglement, which can lead to a higher crystallinity when relaxing from the melt.[38, 39]

Overall, the complexes supported on sMAO(1G) gave higher activities, lower polymer molecular weights, higher polymer crystallinity and more uniform polymer morphologIES than those supported on LDHMAO and SSMAO.

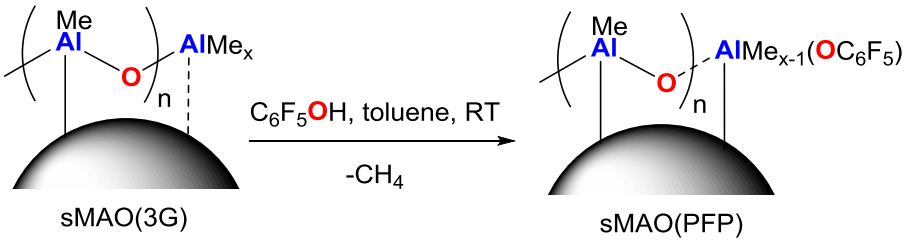
3.4 Solid MAO Support Variation

sMAO was chosen as the desired support due to its enhanced catalytic performance and the more industrially desirable polymer produced by sMAO(1G) supported complexes compared to LDHMAO and SSMAO supported complexes. In order to further investigate the uses of sMAO as a solid support for ethylene polymerisation, the type of sMAO support was varied. Tosoh Finechem Corp. supplied the different types of solid polymethylaluminoxane used in this study as slurries in toluene, which were dried under vacuum before use. Their characteristics are displayed in Table 3.4.

Table 3.4 Properties of sMAO(1G), sMAO(3G), sMAO(GAS) and sMAO(PFP).

	sMAO(1G)	**sMAO(3G)**	**sMAO(GAS)**	**sMAO(PFP)**
Composition				
Al content (%)	41.1	40.2	40.2	20.3
Particle Size (μm)	~5	~5	~23	~5

Third-generation solid MAO (sMAO(3G)) and gas-phase solid MAO (sMAO(GAS)) are variants of sMAO(1G) where the synthetic procedure has been altered in order to affect the rates of nucleation and crystallisation. sMAO(PFP) corresponds to sMAO(3G) modified with pentafluorophenol (C_6F_5OH, PFP) at 40 wt%. On a laboratory scale, this can be achieved by the post-synthetic modification of solid polymethylaluminoxane with C_6F_5OH (Scheme 3.1).[40] It is proposed by Kilpatrick *et al.* that the free $AlMe_x$ groups of sMAO(3G) react preferentially with the C_6F_5OH modifier, leading to a material with reduced aluminium content and lower specific surface area.



Scheme 3.1 Post-synthetic modification of sMAO(3G) with C_6F_5OH according to Kilpatrick *et al.*.[40]

3.4.1 Support morphology

Unlike the uniform 'popcorn' morphology of sMAO(1G) (Figure 3.11a), sMAO(3G) was shown by SEM to have a much less uniform morphology with a poorly defined structure (Figure 3.11b), likely caused by the drying process. sMAO(PFP) and sMAO(GAS) showed similar morphologies to sMAO(1G) (Figures 3.11c and d). However, the individual particles of sMAO(GAS) were observed to be much larger; approximately 20 and 5 μm for sMAO(GAS) and sMAO(1G) respectively.

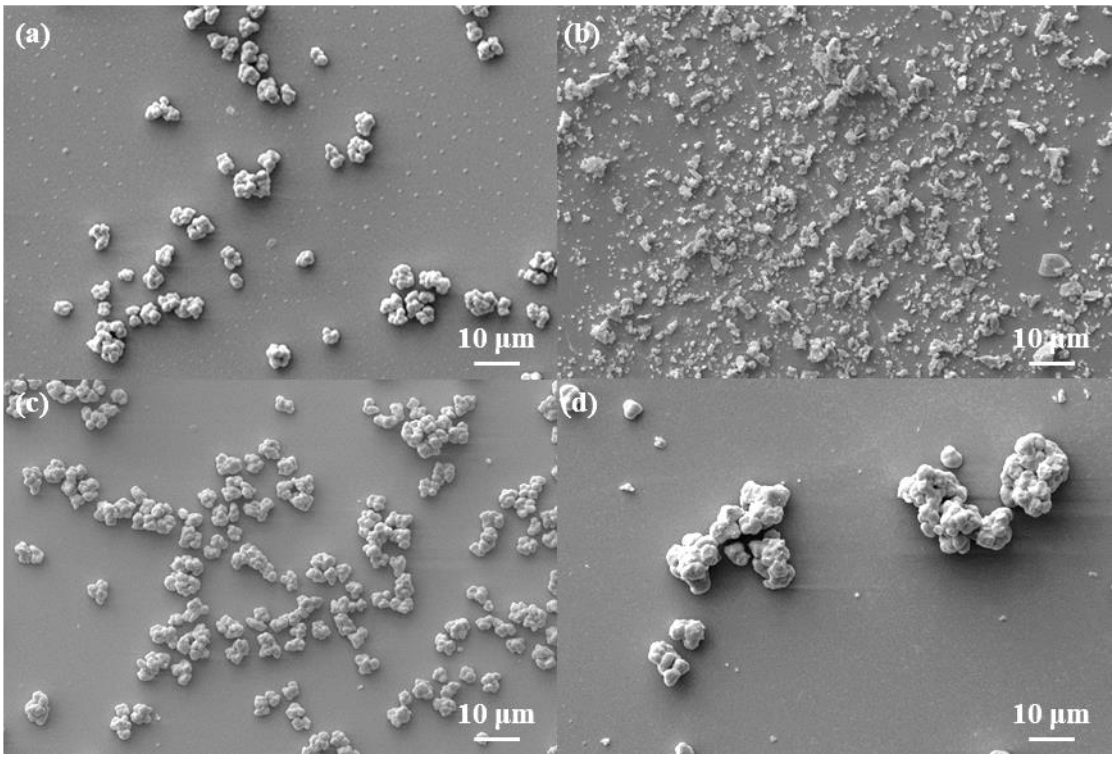


Figure 3.11 SEM images at ×1000 magnification of (a) sMAO(1G), (b) sMAO(3G), (c) sMAO(PFP) and (d) sMAO(GAS).

3.4.2 Complex immobilisation

Three permethylindenyl complexes with different initiating groups were used in this study: ^{Me_2}SB(Cp,I*)ZrCl$_2$ (**1**), ^{Me_2}SB(Cp,I*)Zr(CH$_2$Ph)$_2$ (**6**) and ^{Me_2}SB(Cp,I*)ZrMe$_2$ (**8**) (Chart 3.4). Industrial standard (Cp$^{n\text{Bu}}$)$_2$ZrCl$_2$ (**C**) was also tested for comparison.

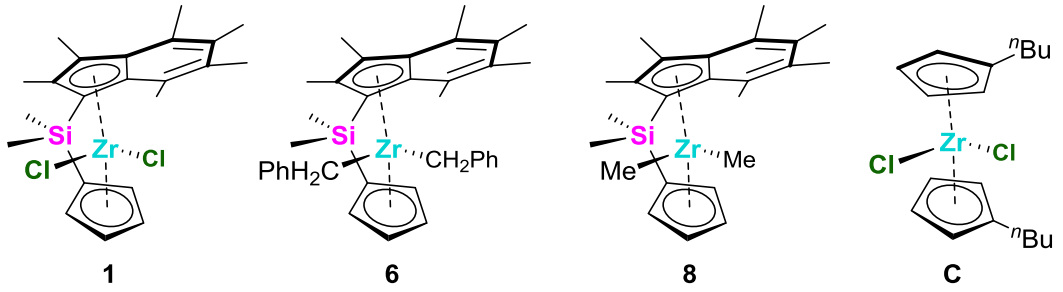


Chart 3.4 Zirconocene complexes used in this study.

Complex immobilisation was achieved as described in Section 3.3.2, and the pre-catalysts isolated as pink/purple powders in near quantitative yield. It is worth noting that some issues were encountered when immobilising complexes onto sMAO(PFP). Unlike the other three sMAO supports, sMAO(PFP) appeared to react with the complex if the immobilisation procedure was not conducted within approximately 30 minutes of the support and complex being put into contact in the Schlenk. This resulted in the formation of brown pre-catalysts with ethylene polymerisation activities much lower than expected. It was also observed that when supported correctly, the sMAO(PFP) pre-catalysts decomposed much faster than pre-catalysts made from the other sMAO supports. It is proposed that these observations are due to the presence of the oxygen atom within the pentafluorophenol group; the interaction of the complex with the support exchanges between the oxygen atoms of the –AlO(Me) group and –OC$_6$F$_5$ moiety, which leads to a scrambling effect.

3.4.3 Catalyst characterisation

The SSNMR spectra of **1** supported on sMAO(3G), sMAO(GAS) and sMAO(PFP) were recorded. Similarly to $\mathbf{1}_{\mathbf{sMAO(1G)}}$, the ^{29}Si CP/MAS SSNMR spectra of $\mathbf{1}_{\mathbf{sMAO(3G)}}$, $\mathbf{1}_{\mathbf{sMAO(GAS)}}$ and $\mathbf{1}_{\mathbf{sMAO(PFP)}}$ each show a single resonance at approximately −12 ppm in good agreement with the solution ^{29}Si NMR spectrum (Figure A3.6). The ^{13}C CP/MAS SSNMR spectra show the expected resonances at 10–25 ppm corresponding to the methyl groups on the permethylindenyl ring, resonances between 110–140 ppm corresponding to the aromatic carbons of the permethylindenyl and cyclopentadienyl rings, and one resonance at approximately 50 ppm corresponding to bound ZrMe (Figures 3.12 and A3.7). The ^{13}C CP/MAS SSNMR spectrum of $\mathbf{1}_{\mathbf{sMAO(PFP)}}$ also shows two additional resonances at 139.3 and 132.8 ppm corresponding to the carbons of the $–OC_6F_5$ moiety. The ^{19}F distortionless enhancement by polarisation transfer (DEPT) SSNMR spectrum of $\mathbf{1}_{\mathbf{sMAO(PFP)}}$ shows a series of resonances centred at −165 ppm corresponding to the fluorine atoms of the $–OC_6F_5$ moiety, which are postulated to be two overlapping resonances with spinning sidebands (Figure A3.8). This is complementary to the ^{19}F DEPT SSNMR patterns observed by Kilpatrick *et al.* for sMAO(PFP),[35] and by other authors for a variety of ^{19}F systems.[40-42] The spinning sidebands occur due to the anisotropic electronic environment around the nucleus, which results in anisotropic chemical shifts that change as the orientation of the molecule in the magnetic field changes. In solution NMR spectroscopy, the anisotropy of the chemical shift is averaged due to fast molecular tumbling.[43] However, in SSNMR spectroscopy molecules are oriented in all possible directions with respect to the external magnetic field, resulting in a superposition of all possible chemical shifts.[44]

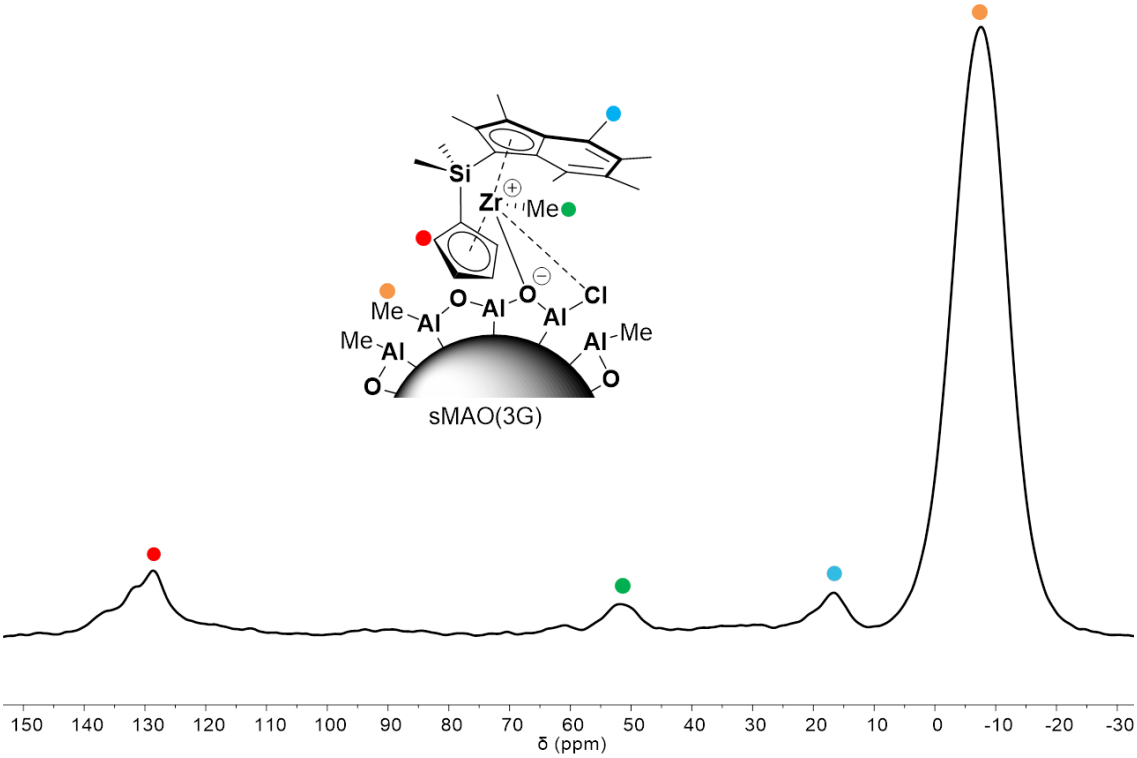


Figure 3.12 ^{13}C CP/MAS NMR spectrum (10 kHz, 298 K) of ^{Me_2}SB(Cp,I*)ZrCl$_2$ (**1**) supported on sMAO(3G) (**1**$_{\mathbf{sMAO(3G)}}$).

3.4.4 Slurry-phase ethylene polymerisation

The same polymerisation set up, polymerisation conditions and catalyst loading ([Al$_{sMAO}$]$_0$/[M]$_0$ = 200) were employed as in Section 3.3.4. [Al$_{sMAO}$]$_0$/[M]$_0$ = 100 was also employed for sMAO(PFP) due to the lower Al content of the support (approximately 20 and 40% for sMAO(PFP) and the other sMAO supports respectively); for sMAO(PFP) supported complexes, when [Al$_{sMAO}$]$_0$/[M]$_0$ = 200 the moles of complex used in the supporting procedure is approximately half of that of the other pre-catalysts.

1$_{\mathbf{sMAO(PFP)}}$ displayed an activity 25% higher than **1**$_{\mathbf{sMAO(1G)}}$ with [Al$_{sMAO}$]$_0$/[M]$_0$ = 200 at 80 °C; 6454 and 5144 kg$_{PE}$ mol$_M^{-1}$ h^{-1} bar^{-1} respectively (Figure 3.13a and Table 3.5). The same trend was also observed for slurry-phase ethylene polymerisation using *rac*-EBIZrCl$_2$ supported on sMAO(PFP).[40] The increase

in activity may be due to the bulky $–OC_6F_5$ moiety weakening the interaction between the cationic catalyst and anionic counterion, which may allow more space for ethylene monomers to coordinate and decrease the energy barrier to ethylene insertion.[45, 46]

However, when the moles of zirconium were made approximately equal for **1$_{sMAO(1G)}$** and **1$_{sMAO(PFP)}$** (i.e. $[Al_{sMAO}]_0/[M]_0$ = 200 and 100 for **1$_{sMAO(1G)}$** and **1$_{sMAO(PFP)}$** respectively), **1$_{sMAO(PFP)}$** showed an activity 25% lower than **1$_{sMAO(1G)}$**; 3851 and 5144 $kg_{PE}\ mol_M^{-1}\ h^{-1}\ bar^{-1}$. At 80 °C, **1$_{sMAO(3G)}$** and **1$_{sMAO(GAS)}$** displayed activities 10 and 27% lower than **1$_{sMAO(1G)}$** respectively; 4622, 3768 and 5144 $kg_{PE}\ mol_M^{-1}\ h^{-1}\ bar^{-1}$.

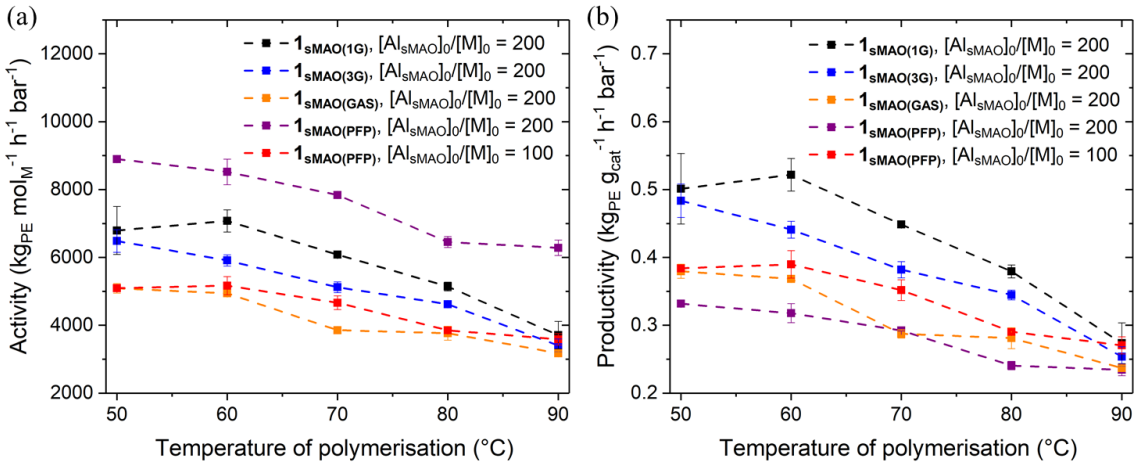


Figure 3.13 Slurry-phase ethylene polymerisation (a) activity and (b) productivity as a function of temperature of polymerisation using $^{Me_2}SB(Cp,I^*)ZrCl_2$ (**1**) (square) supported on sMAO(1G) (**1$_{sMAO(1G)}$**) with $[Al_{sMAO}]_0/[M]_0$ = 200 (black), sMAO(3G) (**1$_{sMAO(3G)}$**) with $[Al_{sMAO}]_0/[M]_0$ = 200 (blue), sMAO(GAS) (**1$_{sMAO(GAS)}$**) with $[Al_{sMAO}]_0/[M]_0$ = 200 (orange), sMAO(PFP) (**1$_{sMAO(PFP)}$**) with $[Al_{sMAO}]_0/[M]_0$ = 200 (purple) and $[Al_{sMAO}]_0/[M]_0$ = 100 (red). Polymerisation conditions: TiBA (150 mg), ethylene (2 bar), pre-catalyst (10 mg), hexane (50 mL) and 30 minutes.

When immobilised on all four supports, **1** outperformed industrial standard $(Cp^{nBu})_2ZrCl_2$ (**C**) across the temperature range under the same polymerisation conditions; at 80 °C, **1$_{sMAO(1G)}$**, **1$_{sMAO(3G)}$**, **1$_{sMAO(GAS)}$** and **1$_{sMAO(PFP)}$** showed polymerisation activities 49, 59, 114 and 6% higher than **C$_{sMAO(1G)}$**, **C$_{sMAO(3G)}$**, **C$_{sMAO(GAS)}$** and **C$_{sMAO(PFP)}$** respectively (activities of 5144, 4622, 3768 and

3851 $kg_{PE}\ mol_M^{-1}\ h^{-1}\ bar^{-1}$ for $\mathbf{1_{sMAO(1G)}}$, $\mathbf{1_{sMAO(3G)}}$, $\mathbf{1_{sMAO(GAS)}}$ and $\mathbf{1_{sMAO(PFP)}}$ respectively, and activities of 3459, 2912, 1762 and 3649 $kg_{PE}\ mol_M^{-1}\ h^{-1}\ bar^{-1}$ for $\mathbf{C_{sMAO(1G)}}$, $\mathbf{C_{sMAO(3G)}}$, $\mathbf{C_{sMAO(GAS)}}$ and $\mathbf{C_{sMAO(PFP)}}$ respectively).

Table 3.5 Slurry-phase ethylene polymerisation activity, productivity and polymer molecular weights (M_w) using selected zirconocene catalysts supported on various types of sMAO.[a]

Complex	sMAO	Activity [b]	Productivity [c]	M_w [d]
^{Me_2}SB(Cp,I*)$ZrCl_2$ (**1**)	1G	5144	0.38	76
^{Me_2}SB(Cp,I*)$ZrCl_2$ (**1**)	3G	4622	0.34	93
^{Me_2}SB(Cp,I*)$ZrCl_2$ (**1**)	GAS	3768	0.28	102
^{Me_2}SB(Cp,I*)$ZrCl_2$ (**1**)	PFP	6454	0.24	149
^{Me_2}SB(Cp,I*)$ZrCl_2$ (**1**) [e]	PFP	3851	0.28	-
$(Cp^{n\mathrm{Bu}})_2ZrCl_2$ (**C**)	1G	3459	0.26	130
$(Cp^{n\mathrm{Bu}})_2ZrCl_2$ (**C**)	3G	2912	0.22	146
$(Cp^{n\mathrm{Bu}})_2ZrCl_2$ (**C**)	GAS	1762	0.13	160
$(Cp^{n\mathrm{Bu}})_2ZrCl_2$ (**C**)	PFP	3649	0.14	193

(a) Polymerisation conditions: $[Al_{sMAO}]_0/[M]_0$ = 200, TiBA (150 mg), ethylene (2 bar), pre-catalyst (10 mg), hexane (50 mL), 80 °C and 30 minutes; (b) $kg_{PE}\ mol_M^{-1}\ h^{-1}\ bar^{-1}$, (c) $kg_{PE}\ g_{cat}^{-1}\ h^{-1}\ bar^{-1}$, (d) kg mol^{-1}; (e) $[Al_{sMAO}]_0/[M]_0$ = 100.

The trends in productivity can also be compared (Figure 3.13b and Table 3.5); productivity considers the grams of catalyst used in the polymerisation procedure, rather than the moles of complex. Due to the much lower Al content of sMAO(PFP) compared to sMAO(1G), when $[Al_{sMAO}]_0/[M]_0 = 200$, $\mathbf{1_{sMAO(PFP)}}$ displayed a productivity 37% lower than $\mathbf{1_{sMAO(1G)}}$; 0.24 and 0.38 $kg_{PE}\ g_{cat}^{-1}\ h^{-1}\ bar^{-1}$. Due to the similar Al content of the supports, productivity followed the same trend as activity for

sMAO(1G), sMAO(3G) and sMAO(GAS) with $[Al_{sMAO}]_0/[M]_0 = 200$ and sMAO(PFP) with $[Al_{sMAO}]_0/[M]_0 = 100$.

3.4.5 Polymer characterisation

GPC analysis of the polyethylenes produced by $\mathbf{1}_{\mathbf{sMAO(1G)}}$, $\mathbf{1}_{\mathbf{sMAO(3G)}}$, $\mathbf{1}_{\mathbf{sMAO(PFP)}}$ and $\mathbf{1}_{\mathbf{sMAO(GAS)}}$ with $[Al_{sMAO}]_0/[M]_0 = 200$ showed that all four catalysts produced low molecular weight (M_w) polyethylenes (M_w <150 kg mol^{-1} at 80 °C), with $\mathbf{1}_{\mathbf{sMAO(1G)}}$ consistently producing polyethylenes with the lowest molecular weights (Figure 3.14). The molecular weights of the polymers produced using $\mathbf{1}_{\mathbf{sMAO(PFP)}}$ were consistently higher than those produced from the other supports. This may be due to the lower free $AlMe_x$ content of sMAO(PFP) compared to the other sMAO supports, which may reduce the amount of termination by chain transfer. The molecular weight distributions of the polymers were all relatively low, indicating the presence of only one type of active site (M_w/M_n = 2.7–3.9 for $\mathbf{1}_{\mathbf{sMAO(1G)}}$, 2.9–3.6 for $\mathbf{1}_{\mathbf{sMAO(3G)}}$, 3.4–4.2 for $\mathbf{1}_{\mathbf{sMAO(GAS)}}$ and 2.6–3.6 for $\mathbf{1}_{\mathbf{sMAO(PFP)}}$).

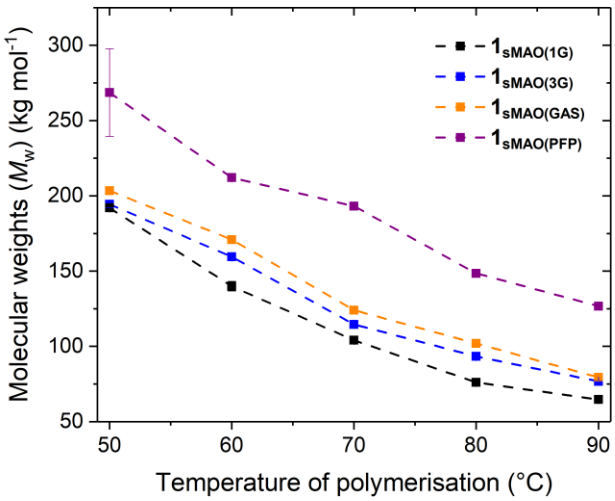


Figure 3.14 Molecular weights (M_w) as a function of temperature of polymerisation using ^{Me_2}SB(Cp,I*)$ZrCl_2$ (**1**) supported on sMAO(1G) ($\mathbf{1}_{\mathbf{sMAO(1G)}}$) (black), sMAO(3G) ($\mathbf{1}_{\mathbf{sMAO(3G)}}$) (blue), sMAO(GAS) ($\mathbf{1}_{\mathbf{sMAO(GAS)}}$) (orange) and sMAO(PFP) ($\mathbf{1}_{\mathbf{sMAO(PFP)}}$) (purple). Polymerisation conditions: $[Al_{sMAO}]_0/[M]_0 = 200$, TiBA (150 mg), ethylene (2 bar), pre-catalyst (10 mg), hexane (50 mL) and 30 minutes.

When compared to industrial standard $(Cp^{nBu})_2ZrCl_2$ (**C**) immobilised on the same supports with $[Al_{sMAO}]_0/[M]_0 = 200$, $\mathbf{1_{sMAO(1G)}}$, $\mathbf{1_{sMAO(3G)}}$, $\mathbf{1_{sMAO(GAS)}}$ and $\mathbf{1_{sMAO(PFP)}}$ produced polymers with lower molecular weights; M_w = 76, 93, 102 and 149 kg mol^{-1} at 80 °C for $\mathbf{1_{sMAO(1G)}}$, $\mathbf{1_{sMAO(3G)}}$, $\mathbf{1_{sMAO(GAS)}}$ and $\mathbf{1_{sMAO(PFP)}}$ respectively, and M_w = 130, 146, 160 and 193 kg mol^{-1} at 80 °C for $\mathbf{C_{sMAO(1G)}}$, $\mathbf{C_{sMAO(3G)}}$, $\mathbf{C_{sMAO(GAS)}}$ and $\mathbf{C_{sMAO(PFP)}}$ respectively.

The same trends in activity, productivity and molecular weights as seen for **1** were also observed for **6** and **8** when supported on sMAO(1G), sMAO(3G), sMAO(GAS) and sMAO(PFP) with $[Al_{sMAO}]_0/[M]_0 = 200$ (Figures 3.15 and A3.9–A3.11). However, for **6** and **8** the sMAO(3G) and sMAO(GAS) supported complexes were much closer in activity than for **1**. The activity of $\mathbf{8_{sMAO(PFP)}}$ also drastically decreased as temperature increased (activities of 10814 and 4061 kg_{PE} mol_M^{-1} h^{-1} bar^{-1} at 50 and 90 °C respectively), most likely due to the decomposition of the catalyst.

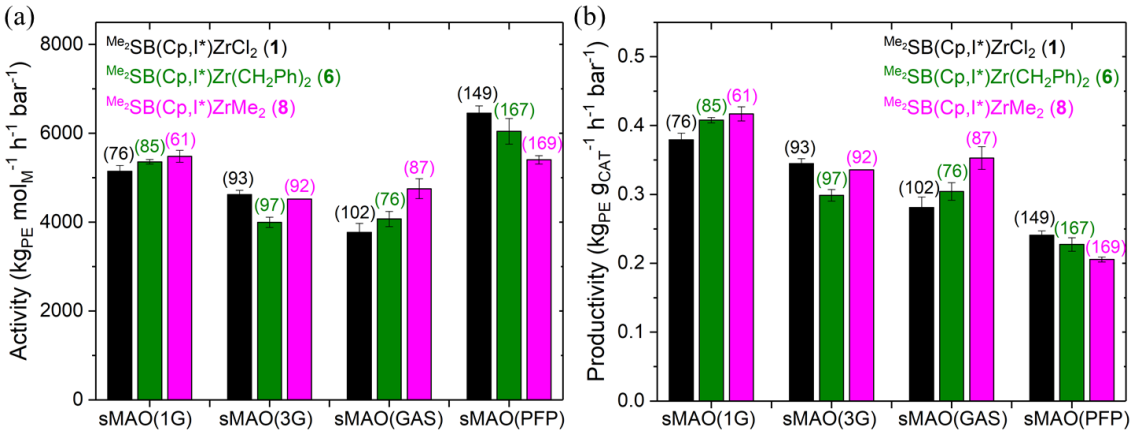


Figure 3.15 Slurry-phase ethylene polymerisation (a) activity and (b) productivity for ^{Me_2}SB(Cp,I*)ZrCl$_2$ (**1**), ^{Me_2}SB(Cp,I*)Zr(CH$_2$Ph)$_2$ (**6**) and ^{Me_2}SB(Cp,I*)ZrMe$_2$ (**8**) supported on sMAO(1G), sMAO(3G), sMAO(GAS) and sMAO(PFP) with molecular weights (M_w) in parenthesis (kg mol^{-1}). Polymerisation conditions: $[Al_{sMAO}]_0/[M]_0$ = 200, TiBA (150 mg), ethylene (2 bar), pre-catalyst (10 mg), hexane (50 mL), 80 °C and 30 minutes.

DSC analysis of the polyethylenes produced by $\mathbf{1}_{\mathbf{sMAO(1G)}}$, $\mathbf{1}_{\mathbf{sMAO(3G)}}$, $\mathbf{1}_{\mathbf{sMAO(PFP)}}$ and $\mathbf{1}_{\mathbf{sMAO(GAS)}}$ at 80 °C revealed T_c of 119–122 °C during the first cooling cycle and T_m of 133 °C during the second heating cycle; indicative of HDPE with minimal defects and branching (Figure 3.16).[32, 33] ΔH_m and ΔH_c were calculated as 200–220 J g^{-1} and 197–208 J g^{-1} respectively, with polymer crystallinity of 68–75%.

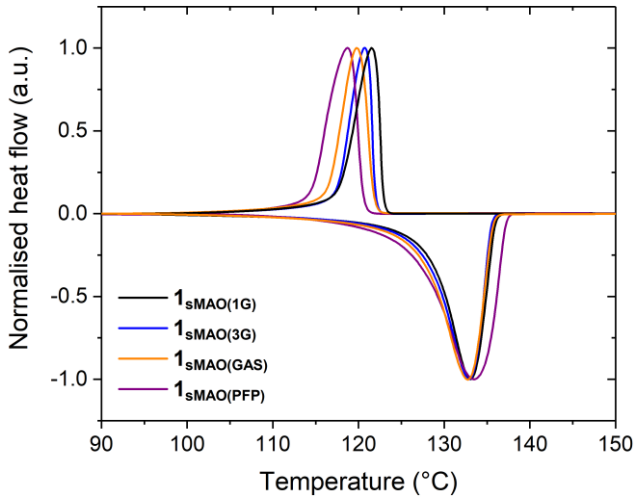


Figure 3.16 DSC plot showing the first cooling cycle and second heating cycle for the polyethylenes produced using ^{Me_2}SB(Cp,I*)$ZrCl_2$ (**1**) supported on sMAO(1G) ($\mathbf{1}_{\mathbf{sMAO(1G)}}$) (black), sMAO(3G) ($\mathbf{1}_{\mathbf{sMAO(3G)}}$) (blue), sMAO(GAS) ($\mathbf{1}_{\mathbf{sMAO(GAS)}}$) (orange) and sMAO(PFP) ($\mathbf{1}_{\mathbf{sMAO(PFP)}}$) (purple). Normalised for clarity. Polymerisation conditions: $[Al_{sMAO}]_0/[M]_0$ = 200, TiBA (150 mg), ethylene (2 bar), pre-catalyst (10 mg), hexane (50 mL), 80 °C and 30 minutes.

SEM analysis of the polyethylenes produced using $\mathbf{1}_{\mathbf{sMAO(1G)}}$, $\mathbf{1}_{\mathbf{sMAO(3G)}}$, $\mathbf{1}_{\mathbf{sMAO(PFP)}}$ and $\mathbf{1}_{\mathbf{sMAO(GAS)}}$ showed that $\mathbf{1}_{\mathbf{sMAO(1G)}}$ gave the most uniform and untextured polymer morphology, while $\mathbf{1}_{\mathbf{sMAO(3G)}}$ gave polyethylenes of uniform size but with a much more textured surface. $\mathbf{1}_{\mathbf{sMAO(PFP)}}$ and $\mathbf{1}_{\mathbf{sMAO(GAS)}}$ were shown to form polyethylenes with a less uniform and more aggregated morphology, with $\mathbf{1}_{\mathbf{sMAO(GAS)}}$ producing polyethylene particles about two times larger than from the other supports (approximately 60 and 30 μm respectively). It is postulated that the more textured surface of the polymer produced from $\mathbf{1}_{\mathbf{sMAO(PFP)}}$ was due to the methane gas released during the support modification process; the reaction of C_6F_5OH with free TMA is

thought to have a 'volcano-like' effect in the pores of the sMAO, which leads to a more uneven support morphology.[40] The large increase in particle size for polymers produced using $\mathbf{1}_{\mathbf{sMAO(GAS)}}$ was expected due to the larger particle and templating effects of the solid support.[18] Overall, sMAO(1G) was found to be the best solid support in terms of catalyst activity, productivity and polymer morphology.

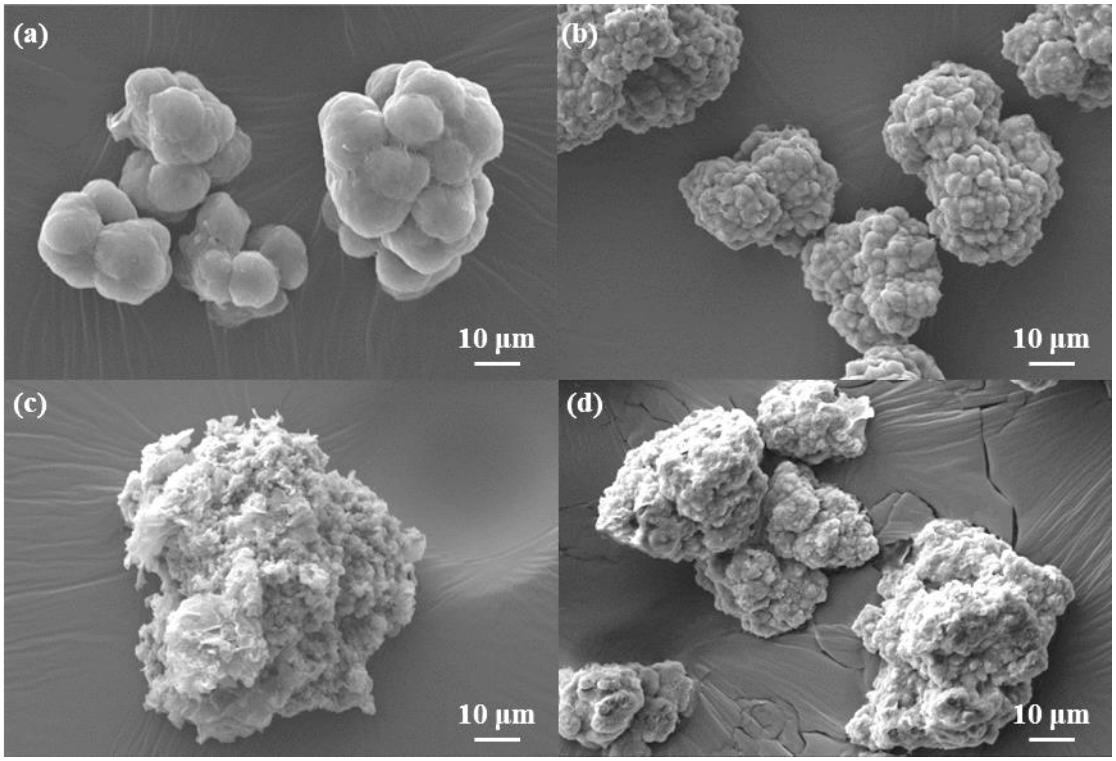


Figure 3.17 SEM images at ×1000 magnification of the polymers produced from the slurry-phase polymerisation of ethylene at 80 °C using ^{Me_2}SB(Cp,I*)ZrCl$_2$ (**1**) supported on (a) sMAO(1G) ($\mathbf{1}_{\mathbf{sMAO(1G)}}$), (b) sMAO(3G) ($\mathbf{1}_{\mathbf{sMAO(3G)}}$), (c) sMAO(GAS) ($\mathbf{1}_{\mathbf{sMAO(GAS)}}$) and (d) sMAO(PFP) ($\mathbf{1}_{\mathbf{sMAO(PFP)}}$).

3.4.6 Scale increase

The effect of scale on polymerisation activity was studied for **1** supported on sMAO(1G), sMAO(3G), sMAO(GAS) and sMAO(PFP) with $[Al_{sMAO}]_0/[M]_0 = 200$. The reactor size was increased from 150 to 500 mL, the solvent volume increased from 50 to 250 mL and the mass of TiBA scavenger increased from 150 to 750 mg

(Figure 3.18). The mass of pre-catalyst (10 mg) and ethylene pressure (2 bar) were kept constant and the polymerisations conducted at 80 °C for 30 minutes.

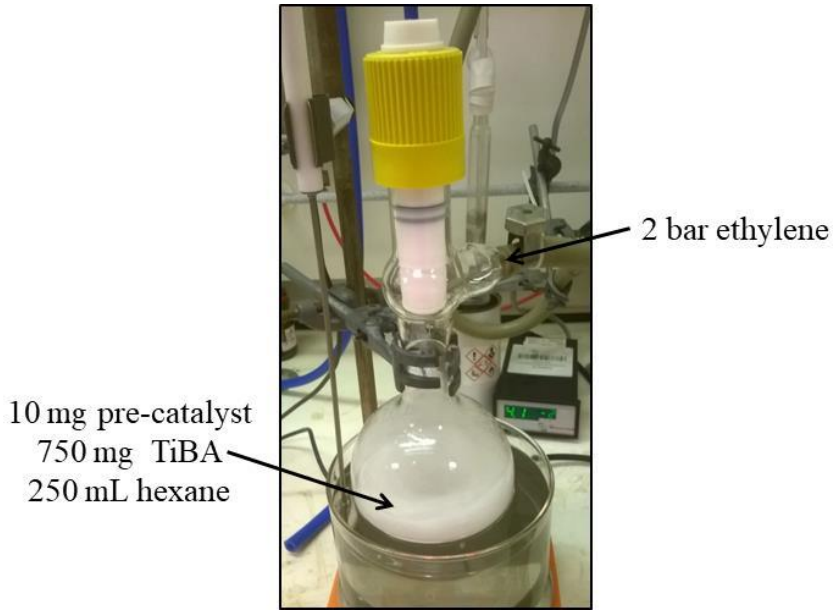


Figure 3.18 Larger scale ethylene polymerisation set-up.

On the small scale, $\mathbf{1}_{\mathbf{sMAO(PFP)}}$ was found to be the most active catalyst, followed by $\mathbf{1}_{\mathbf{sMAO(1G)}}$, $\mathbf{1}_{\mathbf{sMAO(3G)}}$ and $\mathbf{1}_{\mathbf{sMAO(GAS)}}$. On a larger scale $\mathbf{1}_{\mathbf{sMAO(PFP)}}$ was still the most active, followed by $\mathbf{1}_{\mathbf{sMAO(GAS)}}$, $\mathbf{1}_{\mathbf{sMAO(3G)}}$ and $\mathbf{1}_{\mathbf{sMAO(1G)}}$ (Figure 3.19a and Table 3.6). This effect has been observed in large scale studies at SCG Chemicals Co., Ltd. where sMAO(3G) supported complexes were found to perform better than sMAO(1G) supported complexes in 2 L batch reactors.

On increasing the solvent volume five-fold, activity approximately doubled for all four catalysts; an increase from 5144 to 9161 $kg_{PE}\ mol_M^{-1}\ h^{-1}\ bar^{-1}$ for $\mathbf{1}_{\mathbf{sMAO(1G)}}$, 4622 to 10257 $kg_{PE}\ mol_M^{-1}\ h^{-1}\ bar^{-1}$ for $\mathbf{1}_{\mathbf{sMAO(3G)}}$, 3768 to 10653 $kg_{PE}\ mol_M^{-1}\ h^{-1}\ bar^{-1}$ for $\mathbf{1}_{\mathbf{sMAO(GAS)}}$ and 6454 to 15848 $kg_{PE}\ mol_M^{-1}\ h^{-1}\ bar^{-1}$ for $\mathbf{1}_{\mathbf{sMAO(PFP)}}$ at 80 °C Productivity was also observed to significantly increase; for example, from 0.75 to 1.39 $kg_{PE}\ g_{cat}^{-1}\ h^{-1}$ for $\mathbf{1}_{\mathbf{sMAO(1G)}}$ (Figure 3.19b and Table 3.6).

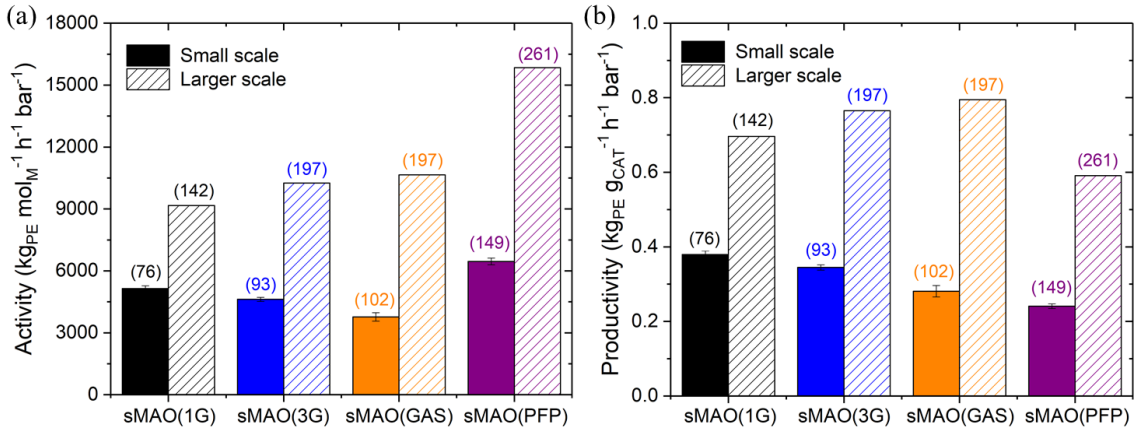


Figure 3.19 Ethylene polymerisation (a) activity and (b) productivity as a function of temperature of polymerisation with molecular weights (M_w) in parenthesis (kg mol^{-1}) for ^{Me_2}SB(Cp,I*)$ZrCl_2$ (**1**) supported on sMAO(1G) (black), sMAO(3G) (blue), sMAO(GAS) (orange) and sMAO(PFP) (purple) on the small scale (block colour) and larger scale (dashed colour). Small scale polymerisation conditions: $[Al_{sMAO}]_0/[M]_0$ = 200, TiBA (150 mg), ethylene (2 bar), pre-catalyst (10 mg), hexane (50 mL) and 30 minutes. Larger scale polymerisation conditions: $[Al_{sMAO}]_0/[M]_0$ = 200, TiBA (750 mg), ethylene (2 bar), pre-catalyst (10 mg), hexane (250 mL), 80 °C and 30 minutes.

The substantial increase in activity and productivity is likely due to a decrease in gas-liquid mass transfer limitations on a larger scale.[47] In the polymerisation set up, ethylene is introduced as a gas, which encounters four levels of diffusional resistance before reaching an active site on the surface of a catalyst fragment: the gas-liquid interface, the liquid film surrounding the polymer macroparticle, the small pores of the polymer macroparticle and the polymeric shell encapsulating the catalyst fragment.[48] If the rate of polymerisation is sufficiently fast then the gas-liquid mass transfer of the monomer at the gas-liquid interface (i.e. dissolution of the gaseous monomer) can become the rate-limiting step.[49, 50] Gas-to-liquid mass transfer limitations can also affect polymer properties, with higher molecular weight distributions shown to arise in the presence of gas-liquid mass transfer limitations for some systems.[48] For systems where the rate of polymerisation is very fast, increasing solvent volume and reactor size can increase the rate of gas-to-liquid mass transfer, and subsequently increase activity.

Table 3.6 Slurry-phase ethylene polymerisation activity, productivity and polymer molecular weights (M_w) using ^{Me_2}SB(Cp,I*)$ZrCl_2$ (**1**) supported on various types of sMAO on the small and larger scale.[a, b]

Scale	sMAO	Activity [c]	Productivity [d]	M_w [e]	M_w/ M_n
Small	1G	5144	0.75	76	3.3
Small	3G	4622	0.68	93	3.3
Small	GAS	3768	0.56	102	4.2
Small	PFP	6454	0.48	149	3.4
Larger	1G	9161	1.39	142	4.1
Larger	3G	10257	1.53	197	3.2
Larger	GAS	10653	1.59	197	3.6
Larger	PFP	15848	1.18	261	3.1

(a) Small scale polymerisation conditions: $[Al_{sMAO}]_0/[M]_0$ = 200, TiBA (150 mg), ethylene (2 bar), pre-catalyst (10 mg), hexane (50 mL) and 30 minutes; (b) larger scale polymerisation conditions: $[Al_{sMAO}]_0/[M]_0$ = 200, TiBA (750 mg), ethylene (2 bar), pre-catalyst (10 mg), hexane (250 mL), 80 °C and 30 minutes; (c) $kg_{PE}\ mol_M^{-1}\ h^{-1}\ bar^{-1}$; (d) $kg_{PE}\ g_{cat}^{-1}\ h^{-1}\ bar^{-1}$; (e) $kg\ mol^{-1}$.

GPC analysis of the polymers produced on from the larger-scale system showed that molecular weights (M_w) increased by 87, 118, 93 and 75% for $\mathbf{1}_{\mathbf{sMAO(1G)}}$, $\mathbf{1}_{\mathbf{sMAO(3G)}}$, $\mathbf{1}_{\mathbf{sMAO(GAS)}}$ and $\mathbf{1}_{\mathbf{sMAO(PFP)}}$ respectively when compared to the smaller scale; an increase from 76 to 142 $kg\ mol^{-1}$ for $\mathbf{1}_{\mathbf{sMAO(1G)}}$ (Figure 3.19 and Table 3.6). This shows that although the rate of polymerisation and catalytic activity is higher on a larger scale, fewer termination steps occured relative to propagation. The molecular weight distributions were unaffected by the scale of the polymerisation (M_w/M_n of 3.3 and 4.1 for $\mathbf{1}_{\mathbf{sMAO(1G)}}$ on the small and larger scale respectively).

3.5 sMAO(1G) Polymerisation

Due to the enhanced activity and improved polymer morphology of sMAO(1G) supported complexes compared to sMAO(3G), sMAO(PFP) and sMAO(GAS) supported complexes, twelve permethylindenyl species were immobilised onto sMAO(1G) and their slurry-phase ethylene polymerisation activity studied. sMAO(1G) supported ^{Me_2}SB(Cp,I*)ZrCl$_2$ (**1**), ^{Me_2}SB(Cp,I*)ZrBr$_2$ (**2**), ^{Me_2}SB(Cp^{Me},I*)ZrCl$_2$ (**3**), ^{Me_2}SB(Cp^{Me},I*)ZrBr$_2$ (**4**), *E*-^{Me_2}SB(Cp$^{n\text{Bu}}$,I*)ZrCl$_2$ (***E*-5**), *Z*-^{Me_2}SB(Cp$^{n\text{Bu}}$,I*)ZrCl$_2$ (***Z*-5**), ^{Me_2}SB(Cp,I*)Zr(CH$_2$Ph)$_2$ (**6**), ^{Me_2}SB(Cp^{Me},I*)Zr(CH$_2$Ph)$_2$ (**7**), ^{Me_2}SB(Cp,I*)ZrMe$_2$ (**8**), ^{Me_2}SB(Cp^{Me},I*)ZrMe$_2$ (**9**), *Z*-^{Me_2}SB(Cp,I*)ZrCl(O-2,6-Me-C$_6$H$_3$) (***Z*-10**) and *E*-^{Me_2}SB(Cp,I*)ZrCl(O-2,6-^{i}Pr-C$_6$H$_3$) (***E*-11**) were studied (Chart 3.5).

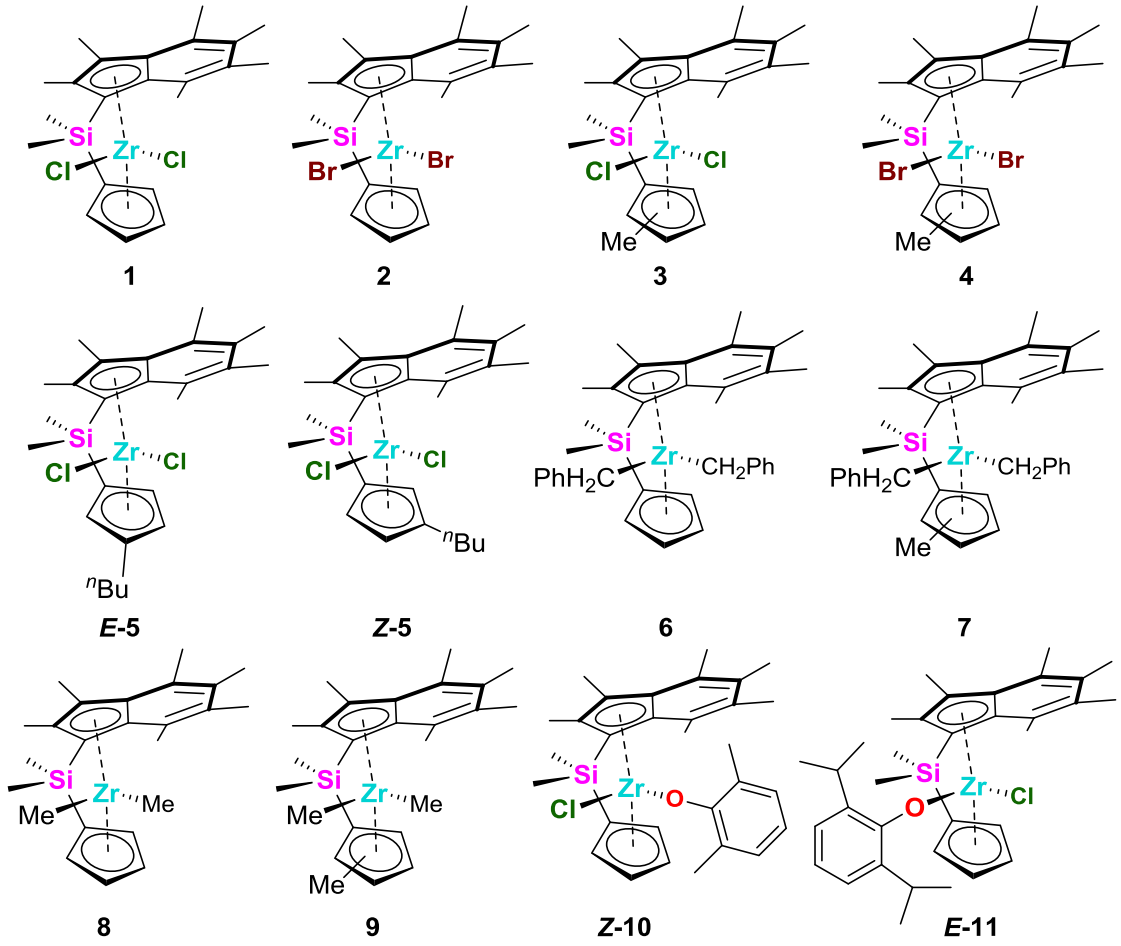


Chart 3.5 Permethylindenyl zirconocenes used in this study.

3.5.1 Slurry-phase ethylene polymerisation

Complex immobilisation was achieved as described in Section 3.3.2 and the resultant pre-catalysts were obtained as pale purple-pink powders in quantitative yield. **3** was used as a 60:40 mixture of its *E*- and *Z*-isomers. The slurry-phase ethylene polymerisation reactions were carried out as described in Section 3.3.4.

Three different types of initiation groups were used in this work; halides, alkyls and aryloxides. For ^{Me_2}SB(Cp^{R},I*)ZrX$_2$ (R = H and Me) at 80 °C, polymerisation activity followed the series: X = Me > CH_2Ph > Cl > Br (**8**$_{sMAO(1G)}$ > **6**$_{sMAO(1G)}$ > **1**$_{sMAO(1G)}$ > **2**$_{sMAO(1G)}$ and **9**$_{sMAO(1G)}$ > **7**$_{sMAO(1G)}$ > **3**$_{sMAO(1G)}$ > **4**$_{sMAO(1G)}$) (Figures 3.20a and 3.21a).

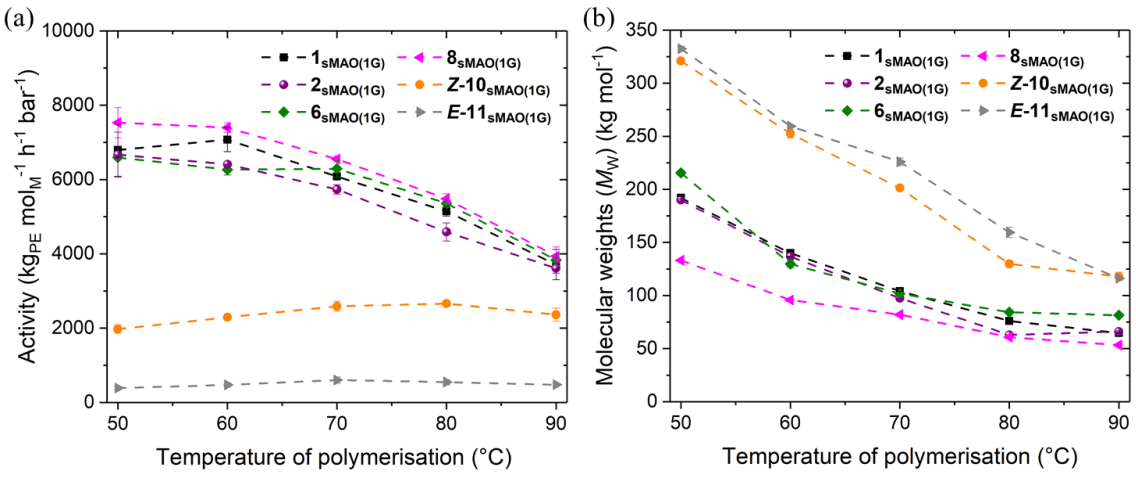


Figure 3.20 Slurry-phase ethylene polymerisation (a) activity and (b) molecular weights (M_w) as a function of temperature of polymerisation using sMAO(1G) supported ^{Me_2}SB(Cp,I*)ZrCl$_2$ (**1**$_{sMAO(1G)}$) (black square), ^{Me_2}SB(Cp,I*)ZrBr$_2$ (**2**$_{sMAO(1G)}$) (purple sphere), ^{Me_2}SB(Cp,I*)Zr(CH_2Ph)$_2$ (**6**$_{sMAO(1G)}$) (green diamond), ^{Me_2}SB(Cp,I*)ZrMe$_2$ (**8**$_{sMAO(1G)}$) (pink left triangle), *Z*-^{Me_2}SB(Cp,I*)ZrCl(O-2,6-Me-C_6H_3) (***Z*-10**$_{sMAO(1G)}$) (orange circle) and *E*-^{Me_2}SB(Cp,I*)ZrCl(O-2,6-^{i}Pr-C_6H_3) (***E*-11**$_{sMAO(1G)}$) (grey right triangle). Polymerisation conditions: [Al$_{sMAO(1G)}$]$_0$/[M]$_0$ = 200, TiBA (150 mg), ethylene (2 bar), pre-catalyst (10 mg), hexane (50 mL) and 30 minutes.

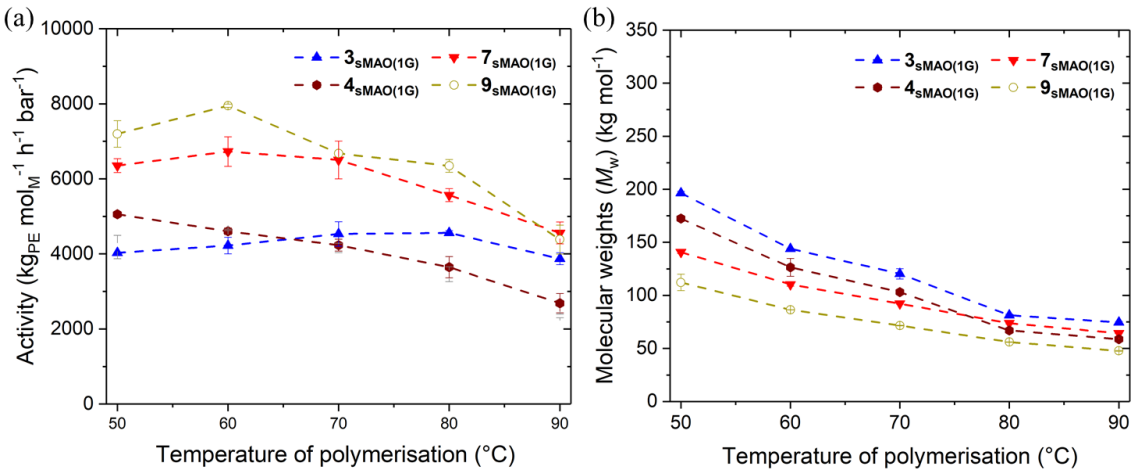


Figure 3.21 Slurry-phase ethylene polymerisation (a) activity and (b) molecular weights (M_w) as a function of temperature of polymerisation using sMAO(1G) supported ^{Me_2}SB(Cp^{Me},I*)ZrCl$_2$ (**3$_{sMAO(1G)}$**) (blue triangle), ^{Me_2}SB(Cp^{Me},I*)ZrBr$_2$ (**4$_{sMAO(1G)}$**) (brown hexagon), ^{Me_2}SB(Cp^{Me},I*)Zr(CH$_2$Ph)$_2$ (**7$_{sMAO(1G)}$**) (red down triangle) and ^{Me_2}SB(Cp^{Me},I*)ZrMe$_2$ (**9$_{sMAO(1G)}$**) (yellow ring). Polymerisation conditions: [Al$_{sMAO(1G)}$]$_0$/[M]$_0$ = 200, TiBA (150 mg), ethylene (2 bar), pre-catalyst (10 mg), hexane (50 mL) and 30 minutes.

As discussed in Section 2.3.3, the same cationic [^{Me_2}SB(Cp^{R},I*)ZrMe]$^+$ species is formed in the presence of an excess of MAO regardless of the identity of the initiation group. The same result has also been demonstrated with Cp$_2$ZrX$_2$ systems (X = Cl or Me), where upon the addition of MAO to both species cationic [Cp$_2$ZrMe]$^+$ was generated.[6, 51, 52] The decrease in activity on moving from alkyl to halide initiation groups therefore suggests that polymerisation activity is at least partially dependent on the efficiency of initiation group abstraction by the co-catalyst.[53] The decrease in activity on moving from alkyl to halide initiation groups can also potentially be rationalised due to the changes in electron density at the metal centre, stemming from the electron-withdrawing and donating abilities of the 'non-innocent' initiating groups, which are postulated to become bound to the solid support during immobilisation (Figure 3.22).[54]

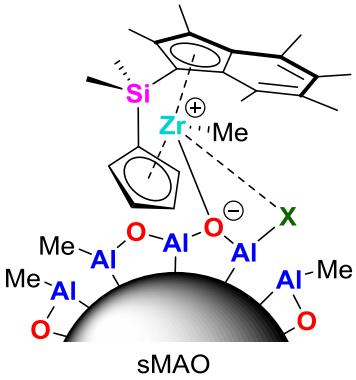


Figure 3.22 Proposed structure of the supported complex.

Larger and more flexible ligands, such as benzyl, may also weaken the interaction between the cationic catalyst and anionic counterion, allowing more space for ethylene monomers to coordinate and leading to an increase in catalytic activity.[55] An increase in ethylene polymerisation activity on moving from halide to alkyl initiation groups has also been observed for *meso*-EBI*ZrR_2, where R = CH_2Ph displayed an activity approximately two times higher than R = H (activities of 5179 and 2246 kg_{PE} mol^{-1} h^{-1} bar^{-1} respectively at 50 °C with 2 bar ethylene).[1] Interestingly, bulky ^{Me_2}SB(Cp,I*)Zr(CH_2SiMe_3)$_2$ supported on sMAO(1G) showed a slurry-phase ethylene polymerisation activity lower than **1**$_{sMAO(1G)}$, **2**$_{sMAO(1G)}$, **6**$_{sMAO(1G)}$ and **8**$_{sMAO(1G)}$ (4240 kg_{PE} mol_M^{-1} h^{-1} bar^{-1} at 80 °C),[56] suggesting that the larger steric bulk of the system may inhibit monomer coordination.

The addition of an aryloxide group significantly reduced polymerisation activity compared to the parent dichloride compound (activities of 5144, 2262 and 549 kg_{PE} mol_M^{-1} h^{-1} bar^{-1} for **1**$_{sMAO(1G)}$, ***Z*-10**$_{sMAO(1G)}$ and ***E*-11**$_{sMAO(1G)}$ respectively at 80 °C). The lower polymerisation activity of ***E*-11**$_{sMAO(1G)}$ compared to ***Z*-10**$_{sMAO(1G)}$ can be rationalised due to the increased steric bulk of the diisopropyl aryloxide group compared to the dimethyl aryloxide group, which it is postulated becomes bound to the solid support during immobilisation and may therefore prevent monomer

coordination.[54] The decrease in polymerisation activity when moving from chloride to aryloxide initiation groups is opposite to the effect seen by Firth *et al.*, where the solution-phase polymerisation of ethylene using $Cp_2ZrCl(O\text{-}2,6\text{-}^{i}Pr\text{-}C_6H_3)$ showed an 11% increase in activity compared to the parent dichloride complex Cp_2ZrCl_2 (1 bar ethylene at room temperature).[57] Conversely, Repo *et al*. reported that the solution-phase polymerisation of ethylene with $Cp_2ZrCl(O\text{-}2,6\text{-}^{i}Pr\text{-}C_6H_3)$ with 2 bar ethylene at 30 °C gave a slightly lower polymerisation activity than Cp_2ZrCl_2 (995 and 1100 $kg_{PE}\,mol_M^{-1}\,h^{-1}\,bar^{-1}$ respectively), while the bulky aryloxide complex $Cp_2ZrCl(O\text{-}2,6\text{-}^{t}Bu\text{-}C_6H_3)$ showed a polymerisation activity approximately five times lower than parent Cp_2ZrCl_2 (200 $kg_{PE}\,mol^{-1}\,h^{-1}\,bar^{-1}$).[58] Also in agreement is the solution-phase polymerisation data recorded by Benetollo *et al.*, in which the authors report a decrease in activity from 10667 to 3667 $kg_{PE}\,mol_M^{-1}\,h^{-1}\,bar^{-1}$ for Cp_2ZrMe_2 and $Cp_2ZrMe(O\text{-}2,6\text{-}Me\text{-}C_6H_3)$ respectively (14.8 bar ethylene and 0.2 bar hydrogen at 90 °C).[59] In order to further understand the mechanism of polymerisation Firth *et al*. demonstrated that the reaction of $Cp_2ZrCl(O\text{-}2,6\text{-}^{i}Pr\text{-}C_6H_3)$ with two equivalents of TMA resulted in the formation of Cp_2ZrMe_2 (*via* $Cp_2ZrMe(O\text{-}2,6\text{-}^{i}Pr\text{-}C_6H_3)$) and aluminium by-product $[AlMe_2(O\text{-}2,6\text{-}^{i}Pr\text{-}C_6H_3)]_n$.[57] This study further confirms that activity is affected by the efficiency of leaving group abstraction.

In addition to the effects of initiation groups on polymerisation activity, the sterics and electronics of the cyclopentadienyl ligand may also enhance, or hinder, polymerisation activity. Figure 3.23a shows that polymerisation activity for this series decreased with increased steric hindrance around the metal centre when the initiation group was kept constant, according to the series $\boldsymbol{E}\text{-}\mathbf{5}_{\mathbf{sMAO(1G)}} > \mathbf{1}_{\mathbf{sMAO(1G)}} > \mathbf{3}_{\mathbf{sMAO(1G)}} \approx \boldsymbol{Z}\text{-}\mathbf{5}_{\mathbf{sMAO(1G)}}$ (activities of 5554, 5144, 4561 and 4330 $kg_{PE}\,mol_M^{-1}\,h^{-1}\,bar^{-1}$ respectively at 80 °C).

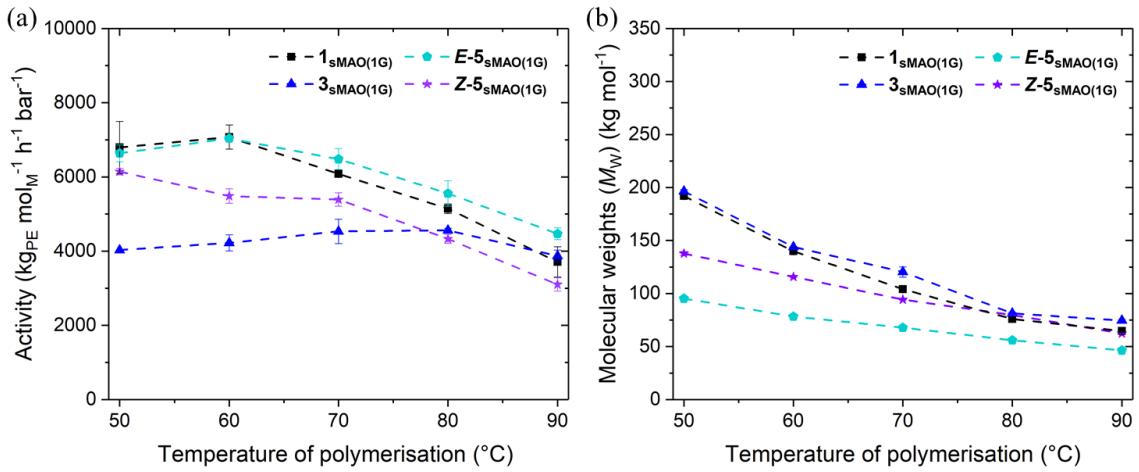


Figure 3.23 Slurry-phase ethylene polymerisation (a) activity and (b) molecular weights (M_w) as a function of temperature of polymerisation using sMAO(1G) supported ^{Me_2}SB(Cp,I*)ZrCl$_2$ (**1$_{sMAO(1G)}$**) (black square), ^{Me_2}SB(Cp^{Me},I*)ZrCl$_2$ (**3$_{sMAO(1G)}$**) (blue triangle), *E*-^{Me_2}SB(Cp^{nBu},I*)ZrCl$_2$ (***E*-5$_{sMAO(1G)}$**) (teal pentagon) and *Z*-^{Me_2}SB(Cp^{nBu},I*)ZrCl$_2$ (***Z*-5$_{sMAO(1G)}$**) (lilac star). Polymerisation conditions: [Al$_{sMAO(1G)}$]$_0$/[M]$_0$ = 200, TiBA (150 mg), ethylene (2 bar), pre-catalyst (10 mg), hexane (50 mL) and 30 minutes.

The decrease in activity was most likely due to the increase in the relative size of the R substituent, with bulkier R groups inhibiting initial coordination of ethylene monomers to the metal centre. At 80 °C, ***E*-5$_{sMAO(1G)}$** was found to be 28% more active than ***Z*-5$_{sMAO(1G)}$** under the same polymerisation conditions (activities of 5554 and 4330 kg$_{PE}$ mol$_M^{-1}$ h^{-1} bar^{-1} respectively). This can be rationalised due to the additional steric hindrance provided by *n*-butyl chain when positioned below the permethylindenyl ligand, which may obstruct the metal centre and prevent coordination of ethylene monomers. This effect has also been observed both in solution- and slurry-phase ethylene polymerisation using EBI*ZrCl$_2$, where *rac*-EBI*ZrCl$_2$ was found to have a higher activity than more sterically crowded *meso*-EBI*ZrCl$_2$ at 60 °C (Chart 3.6); activities of 677 and 416 kg$_{PE}$ mol$_M^{-1}$ h^{-1} bar^{-1} respectively in solution-phase polymerisation,[60] and activities of 5006 and 1331 kg$_{PE}$ mol$_M^{-1}$ h^{-1} bar^{-1} when supported on sMAO with [Al$_{sMAO}$]$_0$/[M]$_0$ of 200 and 300 respectively (Table 3.7).[1]

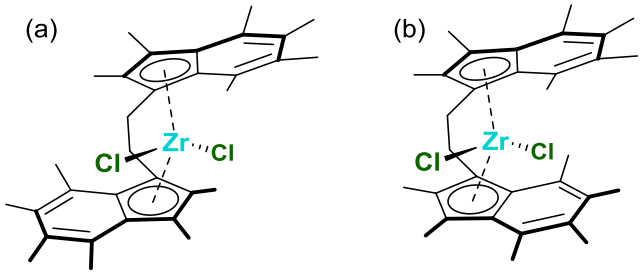


Chart 3.6 Structures of (a) *rac*-EBI*$ZrCl_2$ and (b) *meso*-EBI*$ZrCl_2$.[1]

The improved polymerisation activity of ***E*-5$_{sMAO(1G)}$** relative to **1$_{sMAO(1G)}$** and **3$_{sMAO(1G)}$** may be explained by the enhanced donor ability of *n*-butyl over methyl or hydrogen, which can potentially provide additional stabilisation to the charged intermediates present in the polymerisation mechanism.[61] The effects of ring substitution on ethylene polymerisation activity has been studied for the homogeneous $Cp^R{}_2ZrCl_2$/MAO system where R = ^{n}Bu was found to have a higher polymerisation activity than both R = H and Me; activities of 23400, 17100 and 14300 $kg_{PE}\ mol_M^{-1}\ h^{-1}\ bar^{-1}$ respectively at 70 °C with 2 bar ethylene.[3] Lee *et al.* also found that increasing the electron-donating ability of $(^{5,6\text{-}X}Ind)_2ZrCl_2$/MAO (where X = H and Me) increased the solution-phase ethylene polymerisation activity.[61]

Across the twelve pre-catalysts, the optimum activity was recorded for sMAO(1G) supported $^{Me_2}SB(Cp^{Me},I^*)ZrMe_2$ (**9$_{sMAO(1G)}$**) after 5 minutes of polymerisation at 80 °C (activity of 9509 $kg_{PE}\ mol_M^{-1}\ h^{-1}\ bar^{-1}$); the temperature at which these polymerisations are commonly conducted in industry. At a polymerisation time of 30 minutes, **9$_{sMAO(1G)}$** was found to be 83% more active than an industrial standard, $(Cp^{n\text{Bu}})_2ZrCl_2$ (**C**), supported on sMAO(1G) under the same polymerisation conditions (activities of 6346 and 3459 $kg_{PE}\ mol_M^{-1}\ h^{-1}\ bar^{-1}$ respectively at 80 °C). At 60 °C, after 30 minutes of polymerisation **9$_{sMAO(1G)}$** had an activity 59% higher than the previously reported *rac*-EBI*$ZrCl_2$ supported on sMAO; activities of 7948 and 5006 $kg_{PE}\ mol_M^{-1}\ h^{-1}\ bar^{-1}$ respectively.[1] Above 60 °C, the activity of **9$_{sMAO(1G)}$**

decreased to afford an activity of 4382 $kg_{PE}\ mol_M^{-1}\ h^{-1}\ bar^{-1}$ at 90 °C (Figure 3.21a). A decrease in activity was observed for all twelve sMAO(1G) supported complexes at 90 °C, suggesting either deactivation or decomposition at elevated temperature, or that polymerisation activity is significantly affected by the decrease in the solubility of ethylene in hexane at higher temperatures.[62]

Table 3.7 Slurry-phase ethylene polymerisation activity and molecular weights (M_w) using selected sMAO(1G) supported complexes.[a]

sMAO(1G) supported complex	$[Al_{sMAO}]_0/[M]_0$	Activity [b]	M_w [c]
^{Me_2}SB(Cp,I*)$ZrCl_2$ (**1**)	200	7075	140
^{Me_2}SB(Cp,I*)$Zr(CH_2Ph)_2$ (**6**)	200	6264	130
^{Me_2}SB(Cp^{Me},I*)$ZrMe_2$ (**9**)	200	7948	86
rac-EBI*$ZrCl_2$ [1]	200	5006	-
meso-EBI*$ZrCl_2$ [1]	300	1331	-
meso-EBI*$Zr(CH_2Ph)_2$ [1]	300	5179	177
rac-^{Me_2}SBI*$ZrCl_2$ [63]	300	5971	183
^{Me_2}SB(^{tBu_2}Flu,I*)$ZrCl_2$ [64]	200	6755	648
^{Me_2}SB(^{tBu}N,I*)$TiCl_2$ [65]	200	3602	490
^{Me_4}DSB(Cp,I*)$ZrCl_2$ [66]	200	843	491
$(Cp^{nBu})_2ZrCl_2$ (**C**)	200	4641	201

(a) Polymerisation conditions: TiBA (150 mg), ethylene (2 bar), pre-catalyst (10 mg), hexane (50 mL), 60 °C and 30 minutes; (b) $kg_{PE}\ mol_M^{-1}\ h^{-1}\ bar^{-1}$; (c) $kg\ mol^{-1}$.

Table 3.7 displays the slurry-phase ethylene polymerisation activity and molecular weights (M_w) of the polymers produced using a range of sMAO(1G) supported permethylindenyl complexes and $(Cp^{nBu})_2ZrCl_2$ (**C**). At 60 °C, $\mathbf{1_{sMAO(1G)}}$ displayed an activity almost double that of $\mathbf{C_{sMAO(1G)}}$ (7075 and

4641 $kg_{PE}\ mol_M^{-1}\ h^{-1}\ bar^{-1}$ respectively), highlighting the very high ethylene polymerisation activities of these catalysts. At 60 °C, $\mathbf{1_{sMAO(1G)}}$ also displayed a polymerisation activity 18, 41 and 532% greater than analogous sMAO(1G) supported symmetrical bis(permethylindenyl) zirconocenes *rac*-^{Me_2}SBI*$ZrCl_2$, *rac*-EBI*$ZrCl_2$ and *meso*-EBI*$ZrCl_2$ (activities of 7075, 5971, 5006 and 1331 $kg_{PE}\ mol_M^{-1}\ h^{-1}\ bar^{-1}$ respectively).[1, 63] In addition to the high activity of $\mathbf{1_{sMAO(1G)}}$ compared to the symmetrical bis(permethylindenyl) systems, **1** also does not require the separation of different isomers.

The very high slurry-phase ethylene activity of these unsymmetrical *ansa*-bridged permethylindenyl complexes can be further confirmed by the comparison of $\mathbf{6_{sMAO(1G)}}$ with analogous sMAO(1G) supported *meso*-EBI*$Zr(CH_2Ph)_2$. At 60 °C, $\mathbf{6_{sMAO(1G)}}$ was 21% more active than sMAO(1G) supported *meso*-EBI*$Zr(CH_2Ph)_2$ under the same polymerisation conditions with $[Al_{sMAO(1G)}]_0/[M]_0 = 200$ and 300 respectively (activities of 6264 and 5179 $kg_{PE}\ mol_M^{-1}\ h^{-1}\ bar^{-1}$ respectively).[1] A plausible explanation for the large increase in polymerisation activity lies in the sterics of the system; the decrease in the steric bulk of Cp^R compared to Ind* opens up the metal centre and allows for easier coordination of ethylene monomers.

$\mathbf{1_{sMAO(1G)}}$ also showed higher slurry-phase ethylene polymerisation activities than analogous mono(permethylindenyl) systems; $\mathbf{1_{sMAO(1G)}}$ displayed a polymerisation activity 5 and 96% higher than sMAO(1G) supported ^{Me_2}SB(^{tBu_2}Flu,I*)$ZrCl_2$ and ^{Me_2}SB($^{t\text{Bu}}$N,I*)$TiCl_2$ respectively at 60 °C under the same conditions (activities of 7075, 6755 and 3602 $kg_{PE}\ mol_M^{-1}\ h^{-1}\ bar^{-1}$ respectively) (Chart 3.7a and b).[64, 65] The higher polymerisation activity of $\mathbf{1_{sMAO(1G)}}$ compared to ^{Me_2}SB(^{tBu_2}Flu,I*)$ZrCl_2$ can be rationalised due to the much larger steric bulk of the ^{tBu_2}Flu group when compared to

Cp. When the length of the bridge was increased by one atom to give a tetramethyldisilane bridge (^{Me_4}DSB) polymerisation activity drastically decreased, likely due to the increased flexibility and bulky steric effect of the bridge;[67] sMAO(1G) supported ^{Me_4}DSB(Cp,I*)$ZrCl_2$ displayed a maximum activity of 954 kg_{PE} mol_M^{-1} h^{-1} bar^{-1} at 50 °C (Chart 3.7c).[66]

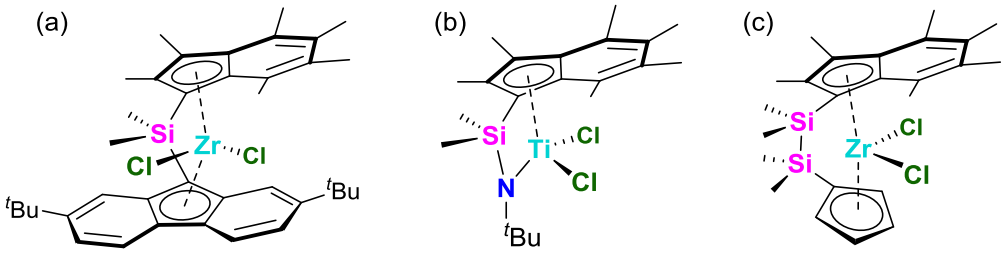


Chart 3.7 Structures of (a) ^{Me_2}SB(^{tBu_2}Flu,I*)$ZrCl_2$,[64] (b) ^{Me_2}SB(^{tBu}N,I*)$TiCl_2$,[65] and (c) ^{Me_4}DSB(Cp,I*)$ZrCl_2$.[66]

Interestingly, sMAO(1G) supported ^{Me_2}SB(Cp,I*)$HfCl_2$ displayed an activity ten times lower than sMAO(1G) supported ^{Me_2}SB(Cp,I*)$ZrCl_2$ (**$1_{sMAO(1G)}$**); activities of 508 and 5144 kg_{PE} mol_M^{-1} h^{-1} bar^{-1} respectively at 80 °C under the same polymerisation conditions.[68] The decrease in polymerisation activity going down the group 4 metals is in good agreement with trends previously reported in the literature.[23, 63, 69] However, the cause is currently unknown as the so-called lanthanide contraction makes the size, properties and metal-chloride binding energy of hafnium very similar to zirconium.[70]

3.5.2 Polymer characterisation

The molecular weights (M_w) of the polyethylenes were characterised by GPC (Figures 3.20b, 3.21b and 3.23b). Molecular weights were seen to decrease with increasing temperature of polymerisation, attributed to stronger chain transfer reactions at higher temperatures[71] and an increase in the rate of termination relative to propagation; at elevated temperatures the system has more energy to overcome the

higher activation barrier of termination.[12] The lowest molecular weights were recorded for ***E*-5$_{\mathbf{sMAO(1G)}}$** and **9$_{\mathbf{sMAO(1G)}}$** (M_w = 46 and 48 kg mol^{-1} respectively at 80 °C).

The presence of an aryloxide group was found to increase the molecular weights of the polyethylenes produced by about 75% compared to the parent dichloride complex (M_w = 253, 240 and 140 kg mol^{-1} for ***Z*-10$_{\mathbf{sMAO(1G)}}$** and ***E*-11$_{\mathbf{sMAO(1G)}}$** and **1$_{\mathbf{sMAO(1G)}}$** respectively at 60 °C). It is usually expected that catalysts with bulkier ligands produce polyethylenes with higher molecular weights as bulkier coordination environments slow down the rate of β-hydride elimination and chain transfer termination reactions.[55] The increase in molecular weights for ***Z*-10$_{\mathbf{sMAO(1G)}}$** and ***E*-11$_{\mathbf{sMAO(1G)}}$** compared to **1$_{\mathbf{sMAO(1G)}}$** is opposite to the effect seen by Firth *et al.* where the molecular weights of the polymers produced from the solution-phase polymerisation of ethylene by $Cp_2ZrCl(O\text{-}2,6\text{-}^{i}Pr\text{-}C_6H_3)$/MAO were observed to be much lower than for the polyethylenes produced from the parent dichloride complex Cp_2ZrCl_2/MAO (M_w = 23 and 116 kg mol^{-1} respectively with 1 bar ethylene at room temperature).[57] However, $Cp_2ZrCl(O\text{-}2,6\text{-}^{i}Pr\text{-}C_6H_3)$/MAO was shown to have a higher activity than Cp_2ZrCl_2/MAO, which is opposite to the trend for **1$_{\mathbf{sMAO(1G)}}$** and ***E*-11$_{\mathbf{sMAO(1G)}}$** (as discussed previously) and may lead to a decrease in molecular weights due to changes in chain termination and propagation rates.

When compared to previously reported *rac*-^{Me_2}SBI*$ZrCl_2$ and *meso*-EBI*$Zr(CH_2Ph)_2$ supported on sMAO(1G), **1$_{\mathbf{sMAO(1G)}}$** and **6$_{\mathbf{sMAO(1G)}}$** produced polyethylenes with molecular weights 23 and 27% lower respectively at 60 °C (M_w = 183, 177, 140 and 130 kg mol^{-1} respectively).[1, 63] This series of unsymmetrical permethylindenyl catalysts were shown to consistently produce polyethylenes with low molecular weights across the entire temperature range, with M_w approximately half of

that produced from $\mathbf{C_{sMAO(1G)}}$ (M_w = 201 kg mol^{-1} at 60 °C). The polymers produced from $\mathbf{1_{sMAO(1G)}}$ also showed molecular weights significantly lower than those produced from unsymmetrical mono(permethylindenyl) systems ^{Me_2}SB(^{tBu_2}Flu,I*)ZrCl$_2$ and ^{Me_2}SB(^{tBu}N,I*)TiCl$_2$ supported on sMAO(1G); M_w = 140, 648 and 490 kg mol^{-1} respectively at 60 °C.[64, 65] This is expected for the constrained geometry complex (CGC) ^{Me_2}SB(^{tBu}N,I*)TiCl$_2$, as CGCs are well known for producing polyethylene with moderate to high molecular weights.[72-74]

The molecular weight distributions of the polymers produced from these systems were low (M_w/M_n = 2.7–4.2), with the narrowest MWD recorded for $\mathbf{3_{sMAO(1G)}}$ (average M_w/M_n = 2.8 across the temperature range). The low dispersity indicates that the species behave mostly as single-site catalysts and that the resultant polymer is therefore relatively homogeneous.

The homogeneity of the polymer can be further confirmed by SEM, which showed that these catalysts produced polyethylene as discrete, 'popcorn' shaped particles of uniform size (~30 μm) and morphology (Figure 3.24), as expected based on the morphology of the solid support.[41] The addition of an aryloxide group caused the polymer to become slightly more aggregated and less uniform, although still of an industrially desirable morphology (Figure 3.24c and d).

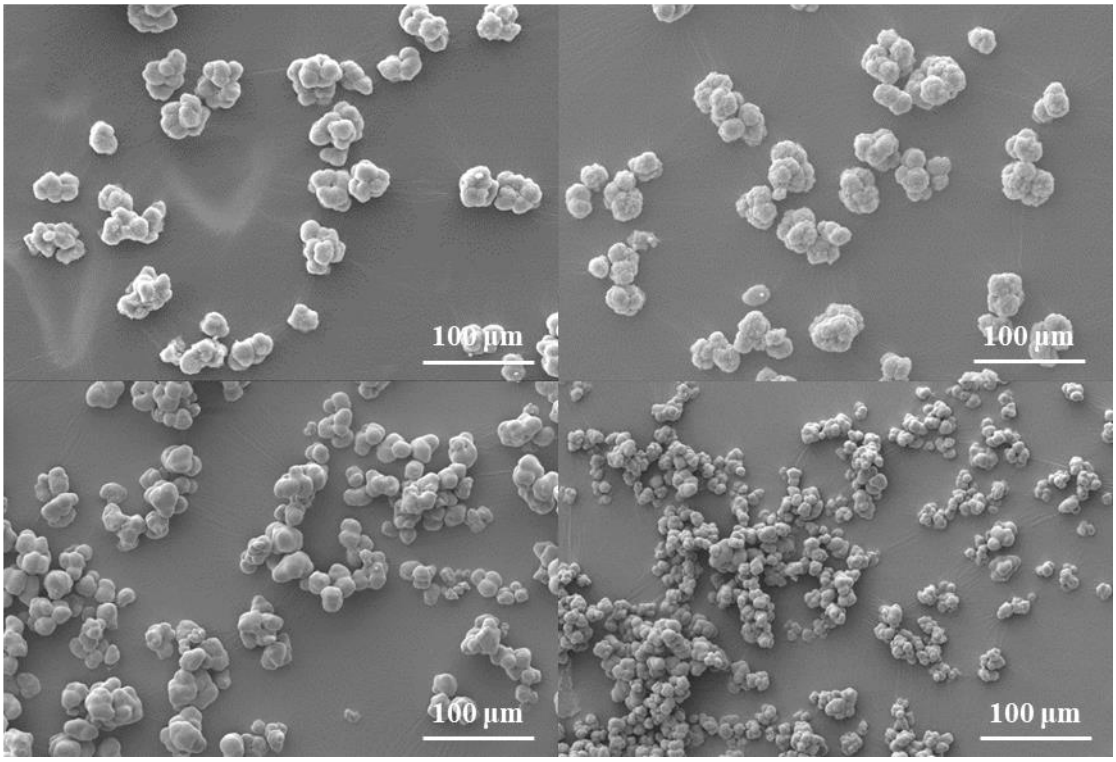


Figure 3.24 SEM images at ×250 magnification of the polymers produced from the slurry-phase polymerisation of ethylene with sMAO(1G) supported (a) ^{Me_2}SB(Cp,I*)Zr(CH_2Ph)$_2$ (**6$_{sMAO(1G)}$**), (b) ^{Me_2}SB(Cp,I*)ZrMe_2 (**8$_{sMAO(1G)}$**), (c) *Z*-^{Me_2}SB(Cp,I*)ZrCl(O-2,6-Me-C_6H_3) (***Z*-10$_{sMAO(1G)}$**) and (d) *E*-^{Me_2}SB(Cp,I*)ZrCl(O-2,6-^{i}Pr-C_6H_3) (***E*-11$_{sMAO(1G)}$**) at 80 °C.

DSC analysis of the polyethylenes produced at 80 °C revealed melting temperatures of 131–135 °C and crystallisation temperatures of 117–123 °C (Figures 3.25 and A3.12), indicative of HDPE with no defects or branching.[32, 33] ΔH_m and ΔH_c were calculated in the range 167–220 J g^{-1} and 166–212 J g^{-1} respectively with 57–75% polymer crystallinity. ***E*-11$_{sMAO(1G)}$** displayed the lowest T_c and highest T_m; 117 and 135 °C respectively compared to 122 and 133 °C for **1$_{sMAO(1G)}$**. A higher T_m usually indicates a higher density polymer with fewer branches,[75] however it can also be caused by the increased chain entanglements of higher molecular weight polymers. The crystallinity of the polymer produced from ***E*-11$_{sMAO(1G)}$** was significantly less than for the polymer produced from **1$_{sMAO(1G)}$** (57 and 75% respectively). This is to be expected based on the higher molecular weights of the polymers produced from ***E*-11$_{sMAO(1G)}$**

compared to **1**$_{\mathbf{sMAO(1G)}}$ leading to more chain entanglement, which hinders crystal formation and growth.[38, 39]

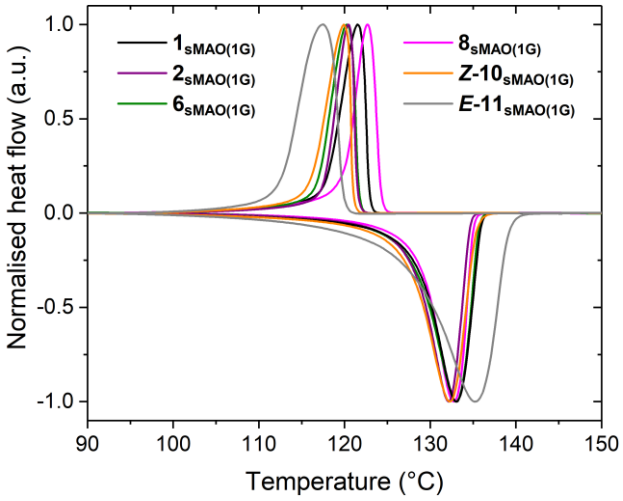


Figure 3.25 DSC plot showing the first cooling cycle and second heating cycle for the polyethylenes produced using sMAO(1G) supported ^{Me_2}SB(Cp,I*)ZrCl$_2$ (**1**$_{\mathbf{sMAO(1G)}}$) (black), ^{Me_2}SB(Cp,I*)ZrBr$_2$ (**2**$_{\mathbf{sMAO(1G)}}$) (purple), ^{Me_2}SB(Cp,I*)Zr(CH$_2$Ph)$_2$ (**6**$_{\mathbf{sMAO(1G)}}$) (green), ^{Me_2}SB(Cp,I*)ZrMe$_2$ (**8**$_{\mathbf{sMAO(1G)}}$) (pink), Z-^{Me_2}SB(Cp,I*)ZrCl(O-2,6-Me-C$_6$H$_3$) (***Z*-10**$_{\mathbf{sMAO(1G)}}$) (orange) and *E*-^{Me_2}SB(Cp,I*)ZrCl(O-2,6-^{i}Pr-C$_6$H$_3$) (***E*-11**$_{\mathbf{sMAO(1G)}}$) (grey). Normalised for clarity. Polymerisation conditions: [Al$_{sMAO(1G)}$]$_0$/[M]$_0$ = 200, TiBA (150 mg), ethylene (2 bar), pre-catalyst (10 mg), hexane (50 mL), 80 °C, 30 minutes.

The polyethylene formed from **1**$_{\mathbf{sMAO(1G)}}$ at 80 °C was also characterised by ^{13}C{^{1}H} NMR spectroscopy with chromium(III) acetylacetonate (Cr(acac)$_3$) as a relaxation agent (Figure 3.26). Peak assignments were made based on literature data.[76-78] The methylene carbons along the backbone are identified by the distance to branches in either direction (α = 1 carbon away, β = 2 carbons away, γ = 3 carbons away, δ = 4 carbons and δ$^+$ = more than four carbons away). Carbons on the branches (B) are identified by nB$_m$ where n refers to the position of the carbon in the branch starting with the methyl carbon at position 1, and m indicates the length of the branch.[79, 80]

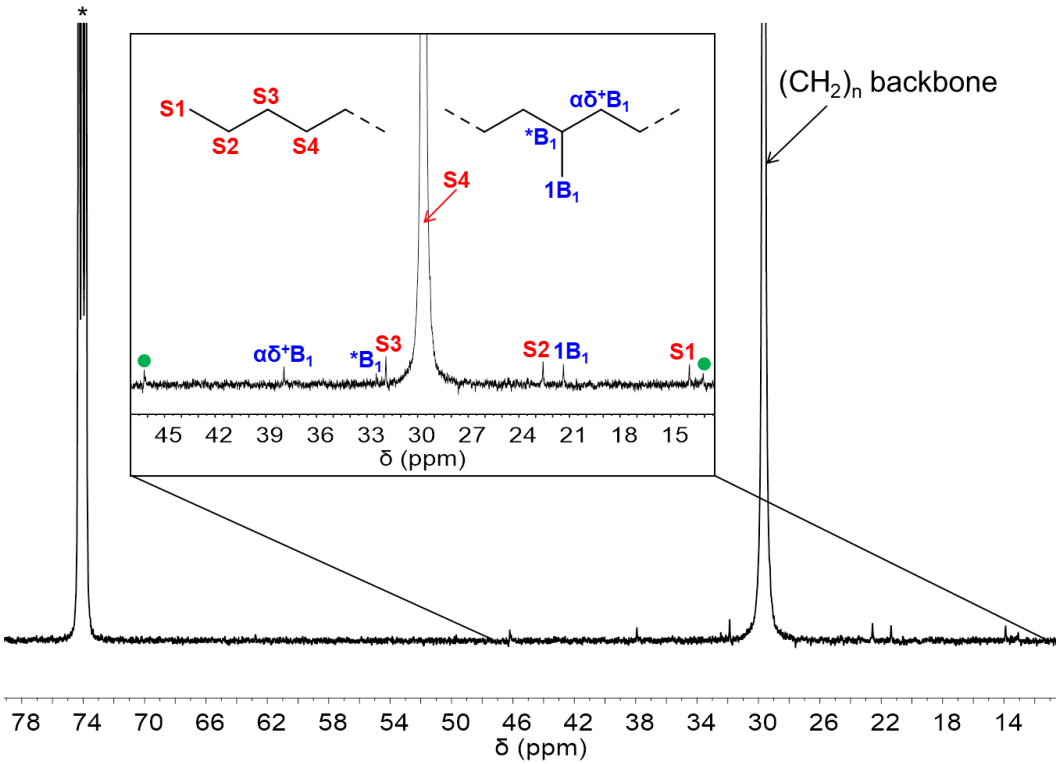


Figure 3.26 $^{13}C\{^{1}H\}$ NMR spectrum of the polyethylene produced using sMAO(1G) supported $^{Me_2}SB(Cp,I^*)ZrCl_2$ (**1**$_{sMAO(1G)}$) at 80 °C (1,2-dichloroethane-d_4 (*), 125 MHz, 418 K with 0.5 wt% chromium(III) acetylacetonate as a relaxation agent).

The $^{13}C\{^{1}H\}$ NMR spectrum of the polyethylene formed using **1**$_{sMAO(1G)}$ indicates a largely unbranched polyethylene chain with an unbranched saturated end group, consistent with the DSC data for unbranched HDPE. The NMR spectrum also suggests the presence of a potential one carbon branch, although it is perhaps more likely that these resonances correspond to a $-CH(CH_3)_2$ end group due to chain termination by transfer to TiBA.[76, 81] Despite a thorough literature search,[76-80, 82-84] two resonances remain unassigned in the spectrum at approximately 13 and 46 ppm. Due to the paramagnetic nature and low concentration of the $Cr(acac)_3$ relaxation agent, these unknown resonances are likely due to features in the polyethylene chain.[85]

3.5.3 Conditions variation

All the sMAO(1G) supported complexes studied show a similar trend in activity over time, with a decrease in activity observed at longer polymerisation time; from 10289 to 4967 $kg_{PE}\ mol_M^{-1}\ h^{-1}\ bar^{-1}$ for $\mathbf{1_{sMAO(1G)}}$ after 5 and 60 minutes respectively (Figure 3.27). This is most likely due to decomposition of the catalyst or due to a decrease in the rate of diffusion of the monomer at longer polymerisation times, which leads to a decrease in the concentration of monomer present at the catalytically active sites. The result is consistent with literature reports for other heterogeneous polymerisation systems.[16, 24, 71, 86, 87]

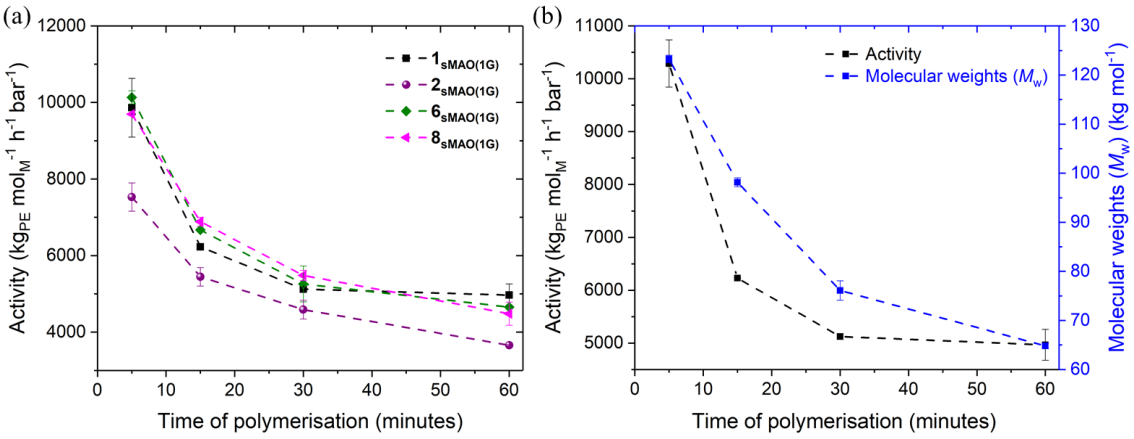


Figure 3.27 (a) Slurry-phase ethylene polymerisation activity as a function of time of polymerisation using sMAO(1G) supported ^{Me_2}SB(Cp,I*)$ZrCl_2$ ($\mathbf{1_{sMAO(1G)}}$) (black square), ^{Me_2}SB(Cp,I*)$ZrBr_2$ ($\mathbf{2_{sMAO(1G)}}$) (purple sphere), ^{Me_2}SB(Cp,I*)$Zr(CH_2Ph)_2$ ($\mathbf{6_{sMAO(1G)}}$) (green diamond) and ^{Me_2}SB(Cp,I*)$ZrMe_2$ ($\mathbf{8_{sMAO(1G)}}$) (pink left triangle); (b) slurry-phase ethylene polymerisation activity (black) and molecular weights (M_w) (blue) as a function of time of polymerisation using sMAO(1G) supported ^{Me_2}SB(Cp,I*)$ZrCl_2$ ($\mathbf{1_{sMAO(1G)}}$). Polymerisation conditions: $[Al_{sMAO(1G)}]_0/[M]_0$ = 200, TiBA (150 mg), ethylene (2 bar), pre-catalyst (10 mg), hexane (50 mL) and 80 °C.

Polymer molecular weights (M_w) were also shown to decrease with time, likely due to an increase in the number of termination steps relative to propagation at prolonged polymerisation time; M_w = 124 to 65 kg mol^{-1} for $\mathbf{1_{sMAO(1G)}}$ after 5 and

60 minutes respectively (Figure 3.27b). **1**$_{\mathbf{sMAO(1G)}}$ produced polymers with molecular weights approximately half of that of solution-phase polymerisation using **1**/MAO; M_w of 124 and 234 kg mol^{-1} respectively after 5 minutes.

As discussed in Section 1.3.6, the choice of scavenger can affect catalyst activity and polymer properties in α-olefin polymerisation. The type of alkyl aluminium scavenger was varied for **1**$_{\mathbf{sMAO(1G)}}$ and **7**$_{\mathbf{sMAO(1G)}}$. For both catalysts the highest polymerisation activity was recorded with triisobutylaluminium (TiBA), followed by triethylaluminium (TEA) and trimethylaluminium (TMA) (Figure 3.28); activities of 5144, 4649 and 3013 kg$_{PE}$ mol$_M^{-1}$ h^{-1} bar^{-1} respectively for **1**$_{\mathbf{sMAO(1G)}}$. It is noted that utilising MAO as the scavenger resulted in the formation of very aggregated polymer particles, likely caused by leaching of the metallocene into solution, which caused stirring to cease after approximately 15 minutes of polymerisation.

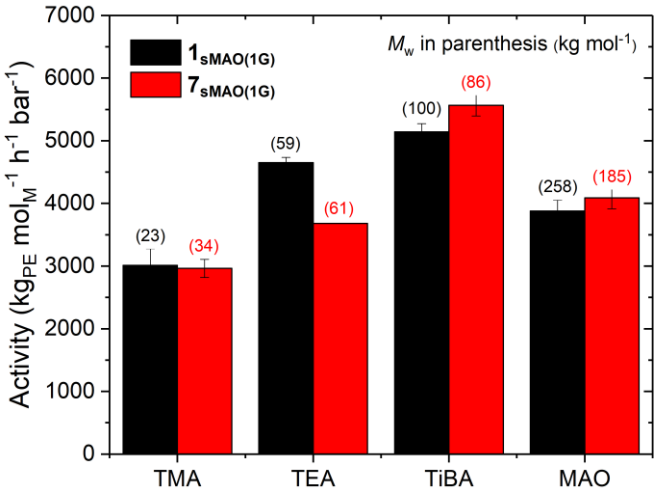
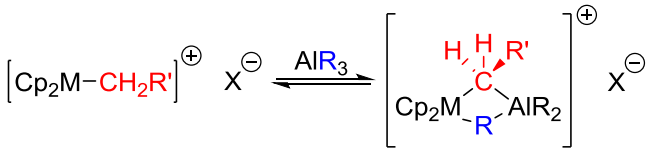


Figure 3.28 Slurry-phase ethylene polymerisation activity using sMAO(1G) supported ^{Me_2}SB(Cp,I*)ZrCl$_2$ (**1**$_{\mathbf{sMAO(1G)}}$) (black) and ^{Me_2}SB(Cp^{Me},I*)Zr(CH$_2$Ph)$_2$ (**7**$_{\mathbf{sMAO(1G)}}$) (red) when scavenger is varied. Polymerisation conditions: [Al$_{sMAO(1G)}$]$_0$/[M]$_0$ = 200, scavenger (0.76 mmol), ethylene (2 bar), pre-catalyst (10 mg), hexane (50 mL), 80 °C and 30 minutes.

Complementary to these results, a decrease in polymerisation activity was observed for ethylene polymerisation using (Cp$^{n\text{Bu}}$)$_2$ZrCl$_2$ supported on MAO modified

silica with TiBA and TEA scavengers; activities of 226 and 166 $kg_{PE}\ mol_M^{-1}\ h^{-1}\ bar^{-1}$ respectively at 80 °C with 8 bar ethylene.[19] Tisse *et al.* also observed the same effect for ethylene/1-hexene copolymerisation using *rac*-EBIZrCl$_2$ supported on an MAO activated silica support; a decrease in polymerisation productivity from 125 to 45 $g_{PE}\ g_{cat}^{-1}\ h^{-1}\ bar^{-1}$ was observed when moving from TiBA to TEA (80 °C, 10 bar ethylene and 0.1 mol L^{-1} 1-hexene).[29] The authors proposed that the decrease in activity was due to the formation of inactive heterobimetallic species such as $[Cp_2M(\mu\text{-}CH_2R')(\mu\text{-}R)AlR_2]^+$ where R is an alkyl group from the aluminium species (Scheme 3.2).[88-90] It is reported that the stability of μ-alkyl complexes decrease with increasing bulk of the alkyl group, and when $Cp_2Zr^iBu_2$ precursors or Al^iBu_3 scavengers are used there is no evidence of inactive heterobimetallic μ-^{i}Bu intermediates.[89, 91] It can therefore be concluded that the lower activity observed using **1**$_{\mathbf{sMOA(1G)}}$ and **7**$_{\mathbf{sMAO(1G)}}$ with TEA and TMA scavengers was due to the higher stability of the heterobimetallic formed compared to when using TiBA scavenger.



Scheme 3.2 Formation of heterobimetallic species $[Cp_2M(\mu\text{-}CH_2R')(\mu\text{-}R)AlR_2]^+$. Adapted from Bochmann *et al.*.[90]

The lower molecular weights of the polymers produced using TMA and TEA compared to TiBA and MAO can be attributed to the bulkier alkyl ligands of TiBA and MAO, which reduce the amount of termination by chain transfer to aluminium; the ability for chain transfer to aluminium follows the order TMA > TEA > TiBA.[29, 92]

Varying the initial scavenger to metal ratio ($[TiBA]_0/[M]_0$) had interesting effects on the slurry-phase polymerisation activity (Figure 3.29a). $[TiBA]_0/[M]_0$ was

varied between 0 and 6000 for $\mathbf{1}_{\mathbf{sMAO(1G)}}$ and $\mathbf{7}_{\mathbf{sMAO(1G)}}$. For $\mathbf{1}_{\mathbf{sMAO(1G)}}$, activity reached a maximum at $[TiBA]_0/[M]_0 = 250$ (0.19 mmol TiBA) and then began to decrease (maximum activity of 5176 $kg_{PE}\, mol_M^{-1}\, h^{-1}\, bar^{-1}$). The same effect was also as observed by Hammawa *et al.* for polymerisation using $(Cp^{nBu})_2ZrCl_2$/MAO.[93] $[TiBA]_0/[M]_0 = 250$ is four times less TiBA scavenger used in the standard slurry-phase ethylene polymerisation; this has an industrial impact as the scavenger is a large industrial expense. The decrease in activity above $[TiBA]_0/[M]_0 = 250$ was likely due to deactivation and poisoning of the active sites, possibly due to increased formation of heterobimetallic species discussed previously.[89] For $\mathbf{7}_{\mathbf{sMAO(1G)}}$, $[TiBA]_0/[M]_0$ had less of an effect on activity, with activities ranging between 4601 and 5269 $kg_{PE}\, mol_M^{-1}\, h^{-1}\, bar^{-1}$ over the range studied. It is of interest to note that when no scavenger was included in the polymerisation set-up, the activity decreased to 85 and 175 $kg_{PE}\, mol_M^{-1}\, h^{-1}\, bar^{-1}$ for $\mathbf{1}_{\mathbf{sMAO(1G)}}$ and $\mathbf{7}_{\mathbf{sMAO(1G)}}$ respectively. The polymer morphology also changed from free-flowing, discrete, spherical particles to aggregated clumps.

For $\mathbf{1}_{\mathbf{sMAO(1G)}}$, polymer molecular weights followed the same trend as activity; M_w decreased as polymerisation activity decreased (Figure 3.29b). This may be due to the ability of alkyl aluminium agents to act as chain transfer agents;[94] at higher TiBA concentrations there is a greater likelihood of termination by chain transfer to aluminium, resulting in a decrease in polymer molecular weights.

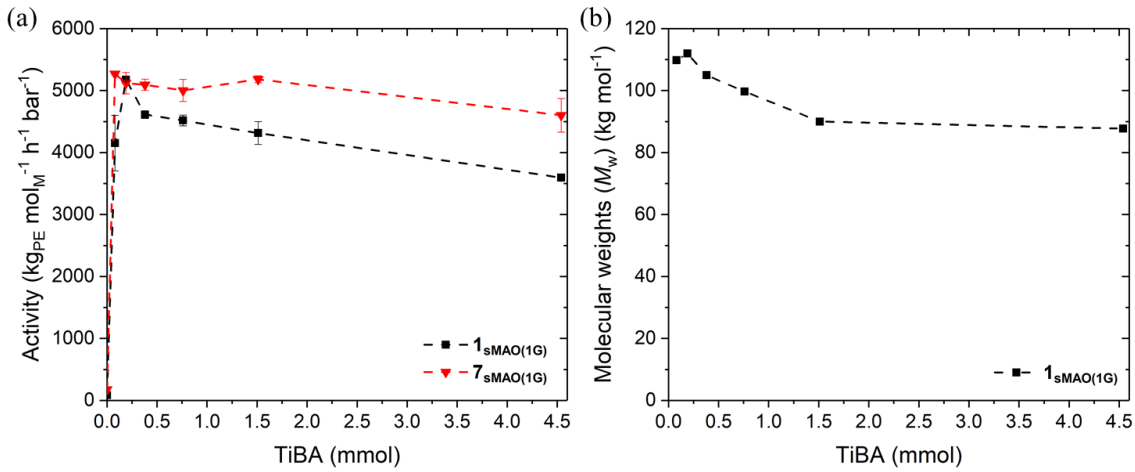


Figure 3.29 Slurry-phase ethylene polymerisation (a) activity as a function of the amount of TiBA using sMAO(1G) supported ^{Me_2}SB(Cp,I*)$ZrCl_2$ (**$1_{sMAO(1G)}$**) (black square) and ^{Me_2}SB(Cp^{Me},I*)$Zr(CH_2Ph)_2$ (**$7_{sMAO(1G)}$**) (red down triangle); (b) molecular weights (M_w) as a function of the amount of TiBA using sMAO(1G) supported ^{Me_2}SB(Cp,I*)$ZrCl_2$ (**$1_{sMAO(1G)}$**) (black square). Polymerisation conditions: $[Al_{sMAO(1G)}]_0/[M]_0$ = 200, ethylene (2 bar), pre-catalyst (10 mg), hexane (50 mL), 80 °C and 30 minutes.

The initial aluminium to metal ratio ($[Al_{sMAO(1G)}]_0/[M]_0$) of **$1_{sMAO(1G)}$**, **$6_{sMAO(1G)}$** and **$8_{sMAO(1G)}$** was varied between 100 and 300 (Figure 3.30a). It was found that activity decreased as $[Al_{sMAO(1G)}]_0/[M]_0$ loading decreased (from 5856 to 2030 kg_{PE} mol_M^{-1} h^{-1} bar^{-1} for **$8_{sMAO(1G)}$**), implying that at higher catalyst loading the effectiveness of the individual catalytic sites decrease.[23] Severn and Chadwick observed the same effect, where a lower catalyst loading accompanied a higher polymerisation activity for Cp_2TiCl_2 and ^{Me_2}Si($^{t\text{Bu}}$N,Cp*)$TiCl_2$ immobilised on $MgCl_2$/alkylaluminium ethoxide supports; activities of 301 and 692 kg_{PE} mol_M^{-1} h^{-1} bar^{-1} with catalyst loadings of 100 and 5 μmol g^{-1} respectively for Cp_2TiCl_2 supported on $MgCl_2(Al_{0.24})Et_{2.30}(OEt)_{0.70}$ (50 °C and 10 bar ethylene).[95] Velthoen *et al.* also found a decrease in ethylene/1-hexene copolymerisation activity with an increase in zirconium concentration using $(Cp^{1\text{-Me},3\text{-Bu}})_2ZrCl_2$ supported on MAO modified silica; a decrease in activity from 11104 to 1802 kg_{PE} mol_M^{-1} h^{-1} bar^{-1} with $[Al_{support}]_0/[M]_0$ of 132 and 51 respectively (65 °C and 8.6 bar ethylene).[96] This trend is perhaps counterintuitive as a

higher catalyst loading equates to more zirconium sites immobilised onto the sMAO support. However, it is hypothesised that overloading of the solid support increases the number of inactive catalytic sites relative to active sites;[22] two electron-deficient zirconium centres in close contact can react to form inactive bimolecular species.[97] GPC analysis of the polymers showed that polymer molecular weights were fairly constant when $[Al_{sMAO(1G)}]_0/[M]_0$ = 150–300, however decreased by about 10 kg mol^{-1} when $[Al_{sMAO(1G)}]_0/[M]_0$ = 100 (Figure 3.30b). This indicates that a higher rate of termination relative to propagation occurs when more zirconium sites are present. The molecular weight distributions were relatively independent of the $[Al_{sMAO(1G)}]_0/[M]_0$ ratio; M_w/M_n = 2.9–3.6 and 3.1–4.5 for **1$_{sMAO(1G)}$** with $[Al_{sMAO(1G)}]_0/[M]_0$ = 100 and 300 respectively.

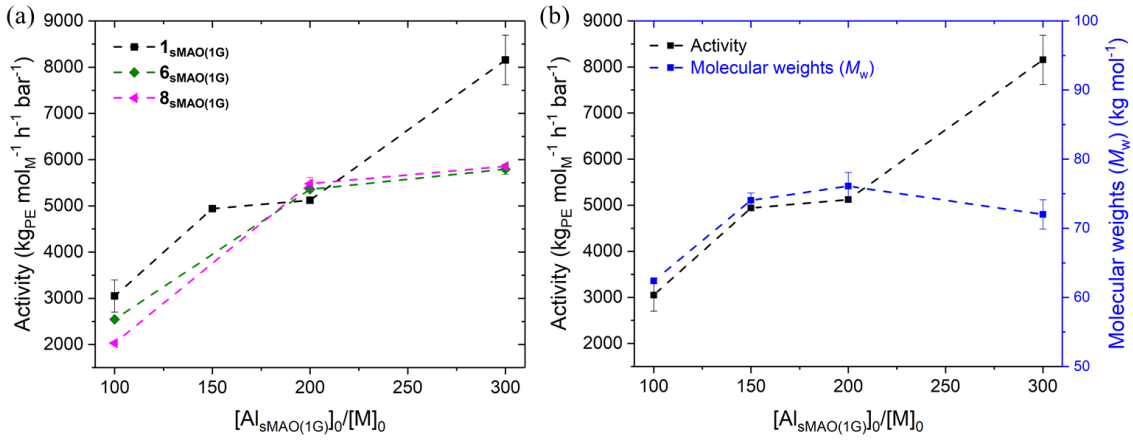


Figure 3.30 Slurry phase ethylene polymerisation (a) activity as a function of $[Al_{sMAO(1G)}]_0/[M]_0$ ratio using sMAO(1G) supported ^{Me_2}SB(Cp,I*)ZrCl$_2$ (**1$_{sMAO(1G)}$**) (black square), ^{Me_2}SB(Cp,I*)Zr(CH$_2$Ph)$_2$ (**6$_{sMAO(1G)}$**) (green diamond) and ^{Me_2}SB(Cp,I*)ZrMe$_2$ (**8$_{sMAO(1G)}$**) (pink left triangle); (b) slurry-phase ethylene polymerisation activity (black) and molecular weights (M_w) (blue) as a function of amount of zirconium using sMAO(1G) supported ^{Me_2}SB(Cp,I*)ZrCl$_2$ (**1$_{sMAO(1G)}$**). Polymerisation conditions: TiBA (150 mg), ethylene (2 bar), pre-catalyst (10 mg), hexane (50 mL), 80 °C and 30 minutes.

The effect of scale on polymerisation activity using **1$_{sMAO(1G)}$**, **6$_{sMAO(1G)}$**, **7$_{sMAO(1G)}$** and **8$_{sMAO(1G)}$** was studied using the set-up described in Section 3.4.6. On a

larger scale, the trend in activity remained the same as on the small scale according to the series **8**$_{\mathbf{sMAO(1G)}}$ > **7**$_{\mathbf{sMAO(1G)}}$ > **6**$_{\mathbf{sMAO(1G)}}$ > **1**$_{\mathbf{sMAO(1G)}}$ (Figure 3.31). However, activity approximately doubled for each supported complex (activity of 5482 and 12036 kg_{PE} mol_M^{-1} h^{-1} bar^{-1} for **8**$_{\mathbf{sMAO(1G)}}$ on the small and larger scale respectively). It is postulated that this is due to a decrease in the gas-liquid mass transfer limitations on a larger scale (as discussed in Section 3.4.6); the increase in solvent volume means that the dissolution of the gaseous ethylene monomers into the polymerisation solvent is no longer the rate-limiting step.[49, 50]

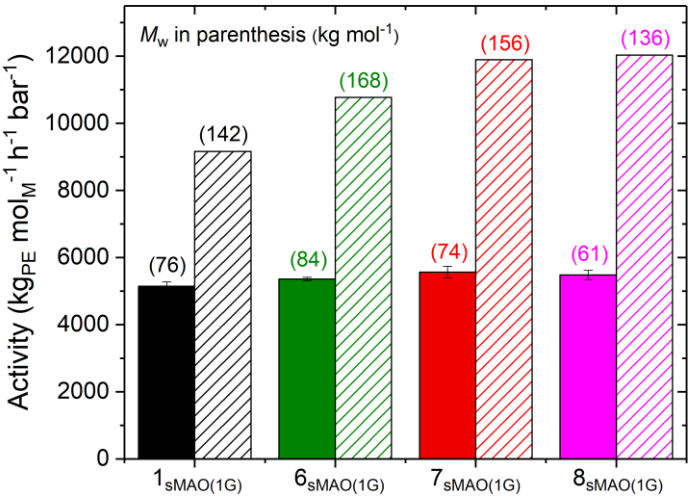


Figure 3.31 Slurry phase polymerisation activity with molecular weights (M_w) in parenthesis (kg mol^{-1}) using sMAO(1G) supported ^{Me_2}SB(Cp,I*)$ZrCl_2$ (**1**$_{\mathbf{sMAO(1G)}}$) (black), ^{Me_2}SB(Cp,I*)$Zr(CH_2Ph)_2$ (**6**$_{\mathbf{sMAO(1G)}}$) (green), ^{Me_2}SB(Cp^{Me},I*)$Zr(CH_2Ph)_2$ (**7**$_{\mathbf{sMAO(1G)}}$) (red) and ^{Me_2}SB(Cp,I*)$ZrMe_2$ (**8**$_{\mathbf{sMAO(1G)}}$) (pink). Small scale polymerisation conditions (block colour): 150 mL ampoule, $[Al_{sMAO(1G)}]_0/[M]_0$ = 200, TiBA (150 mg), ethylene (2 bar), pre-catalyst (10 mg), hexane (50 mL), 80 °C and 30 minutes. Larger scale polymerisation conditions (dashed colour): 500 mL ampoule, $[Al_{sMAO(1G)}]_0/[M]_0$ = 200, TiBA (750 mg), ethylene (2 bar), pre-catalyst (10 mg), hexane (250 mL), 80 °C and 30 minutes.

Analysis of the polymers produced from the larger-scale system showed that molecular weights (M_w) approximately doubled when compared to the small scale (an increase in M_w from 61 to 136 kg mol^{-1} for **8**$_{\mathbf{sMAO(1G)}}$). This effect was also observed for

1$_{sMAO(3G)}$, **1**$_{sMAO(PFP)}$ and **1**$_{sMAO(GAS)}$ discussed previously, and indicates that the rate of propagation changes with the change in the rate-limiting step.

SEM images of the polymers demonstrated that solvent volume had little effect on polymer morphology. However, the relative size of the individual particles increased by about 30% (from approximately 35 to 45 µm for the polymer produced from **1**$_{sMAO(1G)}$ on the small and larger scale respectively) (Figure 3.32b).

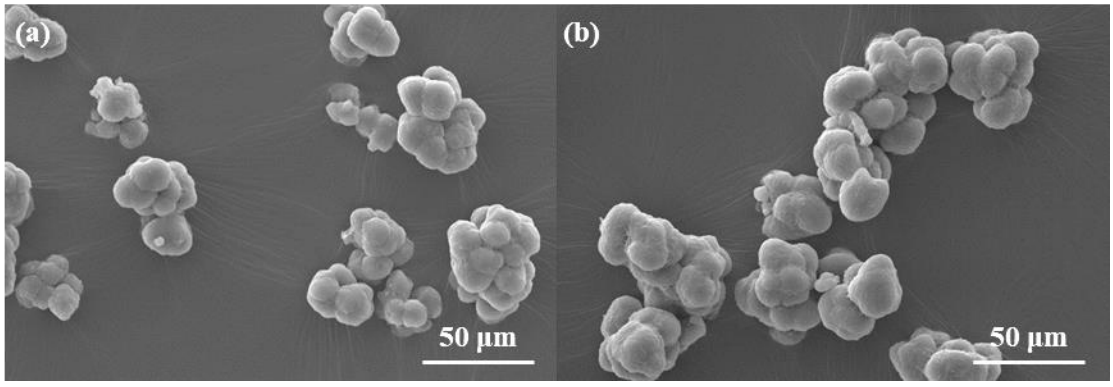


Figure 3.32 SEM images at ×500 magnification of the polymers produced from the slurry-phase polymerisation of ethylene using sMAO(1G) supported ^{Me_2}SB(Cp,I*)ZrCl$_2$ (**1**$_{sMAO(1G)}$) on the (a) small scale (150 mL ampoule, $[Al_{sMAO(1G)}]_0/[M]_0$ = 200, TiBA (150 mg), ethylene (2 bar), pre-catalyst (10 mg), hexane (50 mL), 80 °C and 30 minutes) and (b) larger scale (500 mL ampoule, $[Al_{sMAO(1G)}]_0/[M]_0$ = 200, TiBA (750 mg), ethylene (2 bar), pre-catalyst (10 mg), hexane (250 mL), 80 °C and 30 minutes).

3.6 Conclusions

Twelve unsymmetrical permethylindenyl *ansa*-metallocenes of the type $^{Me_2}SB(Cp^R,I^*)ZrX(Y)$ were found to be active catalysts for the polymerisation of ethylene, both in solution-phase and when immobilised on a range of inorganic solid supports. First-generation solid polymethylaluminoxane was found to be the best support, both in terms of polymerisation activity and polymer morphology, when compared to MAO modified silica (SSMAO), MAO modified LDH (LDHMAO) and three types of solid polymethylaluminoxane (sMAO). DSC analysis showed that the catalysts produced HDPE with minimal defects and branching, while SEM showed polymer particles with industrially desirable 'popcorn' morphology. GPC analysis showed that these catalysts produced polyethylenes with molecular weights (M_w) significantly lower than other sMAO(1G) supported permethylindenyl metallocenes (M_w <100 kg mol^{-1} at 80 °C), with the lowest polymer molecular weights recorded for *E*-$^{Me_2}SB(Cp^{nBu},I^*)ZrCl_2$ (***E*-5$_{sMAO(1G)}$**) and $^{Me_2}SB(Cp^{Me},I^*)ZrMe_2$ (**9$_{sMAO(1G)}$**). The molecular weight distributions of the polymers were narrow, indicating that the catalysts mostly behave as single-site species.

The catalysts were found to be highly active for slurry-phase ethylene polymerisation with activities significantly higher than other 'symmetrical' and 'unsymmetrical' sMAO(1G) supported permethylindenyl metallocenes. **9$_{sMAO(1G)}$** was found to be the most active catalyst across the temperature range with an activity 83% higher than an industrial standard, $(Cp^{nBu})_2ZrCl_2$, supported on sMAO(1G) under the same polymerisation conditions (activity of 6347 $kg_{PE}\,mol_M^{-1}\,h^{-1}\,bar^{-1}$ at 80 °C after 30 minutes). Polymerisation activity was found to decrease on moving from alkyl to halide to aryloxide initiation groups and with increased steric bulk in the

cyclopentadienyl substituent; likely due to the decrease in efficiency of initiation group abstraction by the co-catalyst, and the steric bulk of the ligands leading to obstruction of the metal centre and preventing monomer coordination.

A variation of conditions concluded that TiBA was the best scavenger for polymerisation, most likely due to the very low stability of the inactive heterobimetallic species formed by the reaction of the active species with the aluminium scavenger. It was also found that activity decreased as $[Al_{sMAO(1G)}]_0/[M]_0$ loading decreased, likely due to reaction of zirconium centres in close proximity forming inactive bimolecular species. A five-fold increase in scale was found to double polymerisation activity and polymer molecular weights due to the decrease in gas liquid mass transfer limitations of these highly active catalysts on a larger scale.

The very high slurry-phase ethylene polymerisation activity of these catalysts, in addition to the low molecular weights and uniform morphology of the polymers produced, makes them very promising candidates for industrial scale polymerisation and warrants further investigation into their ethylene/α-olefin polymerisation ability and response to chain transfer agents.

3.7 References

1. T. A. Q. Arnold, Z. R. Turner, J.-C. Buffet and D. O'Hare, *J. Organomet. Chem.*, 2016, **822**, 85-90.
2. L. Resconi, F. Piemontesi, I. Camurati, O. Sudmeijer, I. E. Nifant'ev, P. V. Ivchenko and L. G. Kuz'mina, *J. Am. Chem. Soc.*, 1998, **120**, 2308-2321.
3. K. P. Bryliakov, N. V. Semikolenova, D. V. Yudaev, V. A. Zakharov, H. H. Brintzinger, M. Ystenes, E. Rytter and E. P. Talsi, *J. Organomet. Chem.*, 2003, **683**, 92-102.
4. C. Copéret, F. Allouche, K. W. Chan, M. P. Conley, M. F. Delley, A. Fedorov, I. B. Moroz, V. Mougel, M. Pucino, K. Searles, K. Yamamoto and P. A. Zhizhko, *Angew. Chem., Int. Ed.*, 2018, **57**, 6398-6440.
5. J. R. Severn, J. C. Chadwick, R. Duchateau and N. Friederichs, *Chem. Rev.*, 2005, **105**, 4073-4147.
6. L. Resconi, L. Cavallo, A. Fait and F. Piemontesi, *Chem. Rev.*, 2000, **100**, 1253-1346.
7. Agilent, *An Introduction to Gel Permeation Chromatography and Size-Exclusion Chromatography*, Agilent Technologies Inc., 2015.
8. K. Jenkins, *Beginner's Guide to Size-Exclusion Chromatography*, Waters Corporation, 2014.
9. L. Wild and R. Guliana, *J. Polym. Sci., Part B: Polym. Phys.*, 1967, **5**, 1087-1101.
10. W. J. Gauthier, J. F. Corrigan, N. J. Taylor and S. Collins, *Macromolecules*, 1995, **28**, 3771-3778.
11. W. Wang, Z. Q. Fan and L. X. Feng, *Eur. Polym. J.*, 2005, **41**, 2380-2387.
12. M. Eskelinen and J. V. Seppala, *Eur. Polym. J.*, 1996, **32**, 331-335.
13. L. D 'Agnillo, J. B. P. Soares and A. Penlidis, *Macromol. Chem. Phys.*, 1998, **199**, 955-962.
14. V. F. Tisse, F. Prades, R. Briquel, C. Boisson and T. F. L. McKenna, *Macromol. Chem. Phys.*, 2010, **211**, 91-102.
15. M. K. Samantaray, E. Pump, A. Bendjeriou-Sedjerari, V. D'Elia, J. D. A. Pelletier, M. Guidotti, R. Psaro and J.-M. Basset, *Chem. Soc. Rev.*, 2018, **47**, 8403-8437.
16. J.-C. Buffet, T. A. Q. Arnold, Z. R. Turner, P. Angpanitcharoen and D. O'Hare, *RSC Adv.*, 2015, **5**, 87456-87464.
17. M. Lelli, D. Gajan, A. Lesage, M. A. Caporini, V. Vitzthum, P. Mieville, F. Heroguel, F. Rascon, A. Roussey, C. Thieuleux, M. Boualleg, L. Veyre, G. Bodenhausen, C. Copéret and L. Emsley, *J. Am. Chem. Soc.*, 2011, **133**, 2104-2107.
18. A. F. R. Kilpatrick, J.-C. Buffet, P. Nørby, N. H. Rees, N. P. Funnell, S. Sripothongnak and D. O'Hare, *Chem. Mater.*, 2016, **28**, 7444-7450.
19. M. A. Bashir, T. Vancompernolle, R. M. Gauvin, L. Delevoye, N. Merle, V. Monteil, M. Taoufik, T. F. L. McKenna and C. Boisson, *Catal. Sci. Technol.*, 2016, **6**, 2962-2974.
20. M. A. Bashir, V. Monteil, C. Boisson and T. F. L. McKenna, *React. Chem. Eng.*, 2017, **2**, 521-530.

21. C. Janiak, U. Versteeg, K. C. H. Lange, R. Weimann and E. Hahn, *J. Organomet. Chem.*, 1995, **501**, 219-234.

22. P. G. Belelli, M. L. Ferreira and D. E. Damiani, *Appl. Catal., A*, 2002, **228**, 189-202.

23. J.-C. Buffet, Z. R. Turner, R. T. Cooper and D. O'Hare, *Polym. Chem.*, 2015, **6**, 2493-2503.

24. J.-C. Buffet, N. Wanna, T. A. Q. Arnold, E. K. Gibson, P. P. Wells, Q. Wang, J. Tantirungrotechai and D. O'Hare, *Chem. Mater.*, 2015, **27**, 1495-1501.

25. S. O'Brien, J. Tudor, T. Maschmeyer and D. Ohare, *Chem. Commun.*, 1997, 1905-1906.

26. C. M. R. Wright, K. Ruengkajorn, A. F. R. Kilpatrick, J.-C. Buffet and D. O'Hare, *Inorg. Chem.*, 2017, **56**, 7842-7850.

27. F. Zaccaria, C. Zuccaccia, R. Cipullo, P. H. M. Budzelaar, A. Macchioni, V. Busico and C. Ehm, *ACS Catalysis*, 2019, 2996-3010.

28. A. Tynys, J. L. Eilertsen and E. Rytter, *Macromol. Chem. Phys.*, 2006, **207**, 295-303.

29. V. F. Tisse, C. Boisson and T. F. L. McKenna, *Macromol. Chem. Phys.*, 2014, **215**, 1358-1369.

30. W. M. Groenewoud, in *Characterisation of Polymers by Thermal Analysis*, ed. W. M. Groenewoud, Elsevier Science B.V., Amsterdam, 2001, pp. 10-60.

31. PerkinElmer, *A Beginner's Guide to Differential Scanning Calorimetry*, PerkinElmer Inc., 2013.

32. J. E. O'Hara and K. B. Wagener, *Makromol. Chem., Rapid Commun.*, 1993, **14**, 657-662.

33. G. Rojas, B. Inci, Y. Wei and K. B. Wagener, *J. Am. Chem. Soc.*, 2009, **131**, 17376-17386.

34. G. A. Campbell and E. Vallejo, *J. Pharm. Sci.*, 2015, **104**, 52-62.

35. D. K. Khatri, J. Han, R. L. Parsons, B. Young, J. J. Brennan and R. Corey, *J. Mater. Civ. Eng.*, 2013, **25**, 1964-1969.

36. F. M. Mirabella and A. Bafna, *J. Polym. Sci., Part B: Polym. Phys.*, 2002, **40**, 1637-1643.

37. A. S. Vaughan and D. C. Bassett, in *Comprehensive Polymer Science and Supplements*, eds. G. Allen and J. C. Bevington, Pergamon, Amsterdam, 1989, pp. 415-457.

38. C. F. Luo, M. Kroger and J. U. Sommer, *Polymer*, 2017, **109**, 71-84.

39. C. B. Crawford and B. Quinn, in *Microplastic Pollutants*, eds. C. B. Crawford and B. Quinn, Elsevier, 2017, pp. 57-100.

40. A. F. R. Kilpatrick, N. H. Rees, S. Sripothongnak, J.-C. Buffet and D. O'Hare, *Organometallics*, 2018, **37**, 156-164.

41. D. S. Hall, U. Werner-Zwanziger and J. R. Dahn, *J. Electrochem. Soc.*, 2017, **164**, A2171-A2175.

42. J. Giraudet, M. Dubois, A. Hamwi, W. E. E. Stone, P. Pirotte and F. Masin, *J. Phys. Chem. B*, 2005, **109**, 175-181.

43. M. Odelius and A. Laaksonen, in *Theoretical and Computational Chemistry*, eds. P. B. Balbuena and J. M. Seminario, Elsevier, 1999, vol. 7, pp. 281-324.

44. S. Ando, R. K. Harris and U. Scheler, in *Encyclopedia of Nuclear Magnetic Resonance*, 2007.

45. E. Zurek and T. Ziegler, *Organometallics*, 2002, **21**, 83-92.

46. E. Zurek and T. Ziegler, *Prog. Polym. Sci.*, 2004, **29**, 107-148.

47. D. G. Boucher, I. W. Parsons and R. N. Haward, *Macromol. Chem. Phys.*, 1974, **175**, 3461-3473.

48. M. S. Bhagwat, S. S. Bhagwat and M. M. Sharma, *Ind. Eng. Chem. Res.*, 1994, **33**, 2322-2330.

49. J. Li, Z. Tekie, T. I. Mizan, B. I. Morsi, E. E. Maier and C. P. P. Singh, *Chem. Eng. Sci.*, 1996, **51**, 549-559.

50. S. Floyd, R. A. Hutchinson and W. H. Ray, *J. Appl. Polym. Sci.*, 1986, **32**, 5451-5479.

51. A. Shamiri, M. H. Chakrabarti, S. Jahan, M. A. Hussain, W. Kaminsky, P. V. Aravind and W. A. Yehye, *Materials*, 2014, **7**, 5069-5108.

52. V. Chandrasekhar, *Inorganic and Organometallic Polymers*, Springer, 2005.

53. A. F. R. Kilpatrick, unpublished work.

54. C. M. R. Wright, Z. R. Turner, J.-C. Buffet and D. O'Hare, *Chem. Commun.*, 2016, **52**, 2850-2853.

55. K. F. Liu, Q. L. Wu, X. D. Mu, W. Gao and Y. Mu, *Polyhedron*, 2013, **52**, 222-226.

56. J. E. McLaren, Part II Thesis, University of Oxford, 2018.

57. A. V. Firth, J. C. Stewart, A. J. Hoskin and D. W. Douglas, *J. Organomet. Chem.*, 1999, **591**, 185-193.

58. T. Repo, G. Jany, M. Salo, M. Polamo and M. Leskela, *J. Organomet. Chem.*, 1997, **541**, 363-366.

59. F. Benetollo, G. Cavinato, L. Crosara, F. Milani, G. Rossetto, C. Scelza and P. Zanella, *J. Organomet. Chem.*, 1998, **555**, 177-185.

60. P. Ransom, A. E. Ashley, N. D. Brown, A. L. Thompson and D. O'Hare, *Organometallics*, 2011, **30**, 800-814.

61. I. M. Lee, W. J. Gauthier, J. M. Ball, B. Iyengar and S. Collins, *Organometallics*, 1992, **11**, 2115-2122.

62. G. Sivalingam, V. Natarajan, K. R. Sarma and U. Parasuveera, *Ind. Eng. Chem. Res.*, 2008, **47**, 8940-8946.

63. T. A. Q. Arnold, D. Phil Thesis, University of Oxford, 2015.

64. J.-C. Buffet, Z. R. Turner and D. O'Hare, *Chem. Commun.*, 2018, **54**, 10970-10973.

65. T. J. Williams, J.-C. Buffet, Z. R. Turner and D. O'Hare, *Catal. Sci. Technol.*, 2018, **8**, 5454-5461.

66. J. Abell, Part II Thesis, University of Oxford, 2017.

67. B. Wang, *Coord. Chem. Rev.*, 2006, **250**, 242-258.

68. J. E. Matley, Part II Thesis, University of Oxford, 2015.

69. G. Jany, M. Gustafsson, T. Repo, E. Aitola, J. A. Dobado, M. Klinga and M. Leskelä, *J. Organomet. Chem.*, 1998, **553**, 173-178.

70. I. Silanes, J. M. Mercero and J. M. Ugalde, *Organometallics*, 2006, **25**, 4483-4490.

71. M. A. Parvez, M. Rahaman, M. A. Suleiman, J. B. P. Soares and I. A. Hussein, *Int. J. Polym. Sci.*, 2014, 1-10.

72. J. H. Woo and S. C. Hong, *Polym.-Plast. Technol. Eng.*, 2011, **50**, 1557-1563.

73. Y. T. Zhang, Y. Mu, C. S. Lu, G. H. Li, J. S. Xu, Y. R. Zhang, D. S. Zhu and S. H. Feng, *Organometallics*, 2004, **23**, 540-546.

74. H. Braunschweig and F. M. Breitling, *Coord. Chem. Rev*, 2006, **250**, 2691-2720.

75. M. D. F. V. Marques and R. B. Tiosso, *J. Mater. Sci. Eng. Adv. Tech.*, 2011, **4**, 149-173.

76. P. Kenyon, M. Wörner and S. Mecking, *J. Am. Chem. Soc.*, 2018, **140**, 6685-6689.

77. T. Wiedemann, G. Voit, A. Tchernook, P. Roesle, I. Göttker-Schnetmann and S. Mecking, *J. Am. Chem. Soc.*, 2014, **136**, 2078-2085.

78. J. F. Kleinsasser, E. D. Reinhart, J. Estrada, R. F. Jordan and V. Lavallo, *Organometallics*, 2018, **37**, 4773-4783.

79. W. X. Liu, P. L. Rinaldi, L. H. McIntosh and R. P. Quirk, *Macromolecules*, 2001, **34**, 4757-4767.

80. J. D. Azoulay, G. C. Bazan and G. B. Galland, *Macromolecules*, 2010, **43**, 2794-2800.

81. Q. Chen, W. J. Zhang, G. A. Solan, R. D. Zhang, L. W. Guo, X. Hao and W. H. Sun, *Organometallics*, 2018, **37**, 4002-4014.

82. A. C. Kolbert, J. G. Didier and L. S. Xu, *Macromolecules*, 1996, **29**, 8591-8598.

83. M. Kanazawa, S. Ito and K. Nozaki, *Organometallics*, 2011, **30**, 6049-6052.

84. K. M. Skupov, L. Piche and J. P. Claverie, *Macromolecules*, 2008, **41**, 2309-2310.

85. G. C. Levy and Komorosk.Ra, *J. Am. Chem. Soc.*, 1974, **96**, 679-681.

86. P. Angpanitcharoen, G. Hay, J.-C. Buffet, Z. R. Turner, T. A. Q. Arnold and D. O'Hare, *Polyhedron*, 2016, **116**, 216–222.

87. J.-C. Buffet, C. F. H. Byles, R. Felton, C. P. Chen and D. O'Hare, *Chem. Commun.*, 2016, **52**, 4076-4079.

88. J. T. Hirvi, M. Bochmann, J. R. Severn and M. Linnolahti, *ChemPhysChem*, 2014, **15**, 2732-2742.

89. F. Q. Song, R. D. Cannon and M. Bochmann, *J. Am. Chem. Soc.*, 2003, **125**, 7641-7653.

90. M. Bochmann and S. J. Lancaster, *Angew. Chem., Int. Ed.*, 1994, **33**, 1634-1637.

91. A. G. Carr, D. M. Dawson, M. Thornton-Pett and M. Bochmann, *Organometallics*, 1999, **18**, 2933-2935.

92. W. Michiels and A. Munozescalona, *Macromol. Symp.*, 1995, **97**, 171-183.

93. H. Hammawa, T. M. Mannan, D. T. Lynch and S. E. Wanke, *J. Appl. Polym. Sci.*, 2004, **92**, 3549-3560.

94. R. A. Collins, A. F. Russell and P. Mountford, *Appl. Petrochem. Res.*, 2015, **5**, 153-171.

95. J. R. Severn and J. C. Chadwick, *Macromol. Chem. Phys.*, 2004, **205**, 1987-1994.

96. M. E. Z. Velthoen, A. Munoz-Murillo, A. Bouhmadi, M. Cecius, S. Diefenbach and B. M. Weckhuysen, *Macromolecules*, 2018, **51**, 343-355.

97. J. H. Z. dos Santos, P. P. Greco, F. C. Stedile and J. Dupont, *J. Mol. Catal. A: Chem.*, 2000, **154**, 103-113.

Chapter 4

Ethylene/1-Hexene Copolymerisation and Hydrogen Response

4.1 Introduction

4.1.1 Overview

Due to their hydrophobicity and chemical and heat stability,[1, 2] ultra-low molecular weight polyethylenes (ULMWPE) are used in plastic processing applications to improve product physical appearance and thermal properties.[3] ULMWPE with molecular weights (M_w) less than 10 kg mol^{-1} are referred to as polyethylene (PE) waxes.[2] PE waxes are commonly used to impart mark and scratch resistance in printing inks and paints and to act as lubricating agents for plastics.[2, 4] PE wax emulsions are also used as softening agents in the textile industry and have applications in packaging.[5]

This chapter first discusses how the complexes synthesised in Chapter 2 perform as slurry-phase ethylene/1-hexene copolymerisation catalysts when immobilised on first-generation solid polymethylaluminoxane (sMAO(1G)). This was studied as the incorporation of longer chain α-olefin monomers into PE chains increases the degree of branching, which lowers polymer density and changes the potential applications of the polymers.[6] The effects of hydrogen on ethylene polymerisation and ethylene/1-hexene copolymerisation are then evaluated with the ultimate aim of producing ULMWPE. A

variety of polymerisation conditions were studied, including large scale batch reactors and miniaturised high-throughput screening.

4.1.2 High-throughput screening

High-throughput screening is a process by which large numbers of compounds and conditions can be simultaneously synthesised and tested *via* robotic systems that automate sample preparation, handling and data analysis.[7, 8] It allows for reduced time in the design of new materials and faster optimisation of reaction conditions.[9] High-throughput screening was initially implemented in the pharmaceutical industry for the identification of novel drugs and has since revolutionised small molecule synthesis, materials science and organometallic catalysis.[10, 11]

High-throughput screening is usually empirical (i.e. the chance of obtaining the desired result is proportional to the number of attempts) with an aim to increase the number of simultaneous experiments. Miniaturised, automated, parallel reaction set-ups have been implemented for the rapid assessment of novel catalyst applications, while also being used for the generation of reliable kinetic data for mechanistic studies.[11] High-throughput screening approaches are highly demanding in terms of infrastructure and equipment, are usually not very efficient and experience the mass transfer limitations of working on a small scale.[11] However, high-throughput screening offers multiple technical, economic and environmental advantages over conventional processes; the small size of the reactors leads to decreased costs, chemical consumption and waste, in addition to the increased probability of discovering materials or conditions with the desired properties or results in a shorter time.[10, 11]

4.2 Ethylene/1-Hexene Copolymerisation

4.2.1 Slurry-phase ethylene/1-hexene copolymerisation

Slurry-phase ethylene/1-hexene copolymerisation reactions were conducted at 80 °C for 5 minutes in 150 mL ampoules with a sidearm by which the desired amount of 1-hexene in 5 mL hexane was added at the start of the polymerisation (0–80 mg, 0–0.02 M). Polymerisations were run in a total hexane volume of 50 mL with 10 mg pre-catalyst, 150 mg triisobutylaluminium (TiBA) scavenger, 2 bar ethylene and an initial aluminium to metal loading ($[Al_{sMAO(1G)}]_0/[M]_0$) of 200 (Figure 4.1). 80 °C was chosen to more closely mimic SCG Chemicals Co., Ltd.'s industrial conditions. sMAO(1G) supported $^{Me_2}SB(Cp,I^*)ZrCl_2$ (**$1_{sMAO(1G)}$**), $^{Me_2}SB(Cp^{Me},I^*)ZrCl_2$ (**$3_{sMAO(1G)}$**), $^{Me_2}SB(Cp,I^*)Zr(CH_2Ph)_2$ (**$6_{sMAO(1G)}$**), $^{Me_2}SB(Cp^{Me},I^*)Zr(CH_2Ph)_2$ (**$7_{sMAO(1G)}$**) and $^{Me_2}SB(Cp,I^*)ZrMe_2$ (**$8_{sMAO(1G)}$**) were studied.

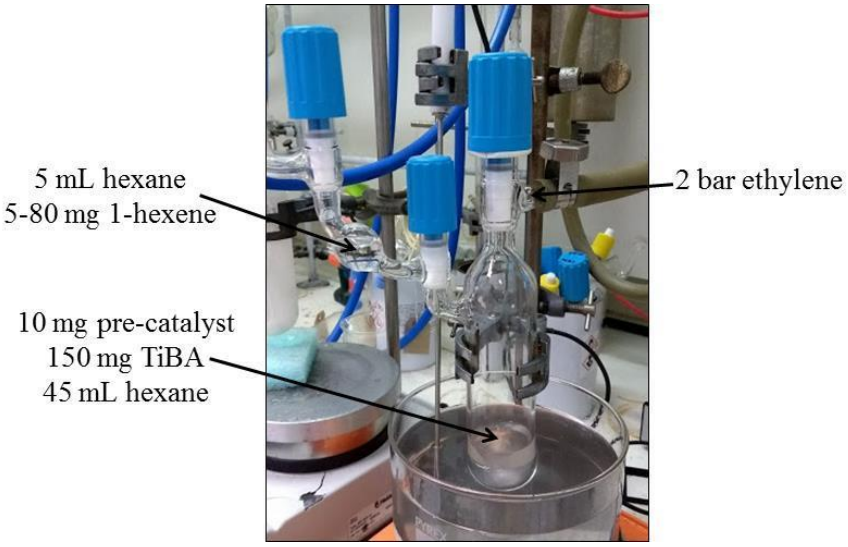


Figure 4.1 Slurry-phase ethylene/1-hexene copolymerisation set-up.

Except for **$3_{sMAO(1G)}$**, polymerisation activity decreased on the introduction of 1-hexene for all catalysts; most likely due to competition coordination between ethylene and 1-hexene monomers at the active metal centre. Upon coordination, if the rate of 1-hexene insertion is slower than ethylene insertion, the rate of ethylene uptake

decreases and leads to a decrease in polymerisation activity (Figure 4.2a and Table A4.1).[12] A decrease in activity in the presence of 1-hexene has been observed in other zirconocene systems,[13] such as for the solution-phase copolymerisation of ethylene and 1-hexene using ($^{2\text{-Ph}}$Ind)$_2$ZrCl$_2$ with methylaluminoxane (MAO) co-catalyst where activity decreased from 2200 to 960 $kg_{PE}\ mol_M^{-1}\ h^{-1}\ bar^{-1}$ in the presence of 0 and 0.16 M 1-hexene respectively at 50 °C with 1 bar ethylene.[14] The deactivating effects of 1-hexene have also been observed in heterogeneous systems; the copolymerisation of ethylene and 1-hexene using ($^{2,4\text{-Me}}$Ind)$_2$ZrCl$_2$ supported on silica with MAO co-catalyst showed a decrease in activity from 4460 to 200 $kg_{PE}\ mol_M^{-1}\ h^{-1}\ bar^{-1}$ in the presence of 0 and 0.8 M 1-hexene respectively at 50 °C with 1 bar ethylene.[15] The authors proposed that the decrease in activity was in part due to the slower diffusion rate of bulkier 1-hexene compared to ethylene, which then obstructed the diffusion of ethylene monomers towards the active metal centre.

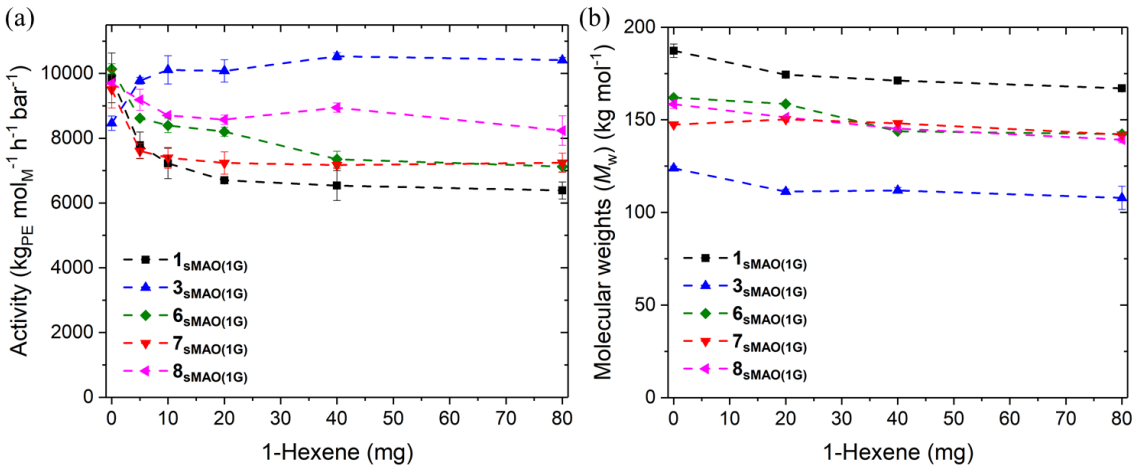


Figure 4.2 Slurry-phase ethylene/1-hexene copolymerisation (a) activity and (b) molecular weights (M_w) as a function of amount of 1-hexene using sMAO(1G) supported ^{Me_2}SB(Cp,I*)ZrCl$_2$ (**1$_{sMAO(1G)}$**) (black square), ^{Me_2}SB(Cp^{Me},I*)ZrCl$_2$ (**3$_{sMAO(1G)}$**) (blue triangle), ^{Me_2}SB(Cp,I*)Zr(CH$_2$Ph)$_2$ (**6$_{sMAO(1G)}$**) (green diamond), ^{Me_2}SB(Cp^{Me},I*)Zr(CH$_2$Ph)$_2$ (**7$_{sMAO(1G)}$**) (red down triangle) and ^{Me_2}SB(Cp,I*)ZrMe$_2$ (**8$_{sMAO(1G)}$**) (pink left triangle). Polymerisation conditions: [Al$_{sMAO(1G)}$]$_0$/[M]$_0$ = 200, TiBA (150 mg), ethylene (2 bar), pre-catalyst (10 mg), hexane (50 mL), 80 °C and 5 minutes.

The polymers produced from this series were analysed by gel-permeation chromatography (GPC). In general, polymer molecular weights (M_w) decreased as the amount of 1-hexene in the system increased; M_w of 187 and 167 kg mol^{-1} for $\mathbf{1}_{\mathbf{sMAO(1G)}}$ with 0 and 80 mg 1-hexene respectively (Figure 4.2b and Table A4.2). The decrease in M_w was likely due to the higher degree of end group branching caused by termination after 1-hexene monomer insertion.[16] The molecular weight distributions (MWD = M_w/M_n) were found to be slightly larger for ethylene/1-hexene copolymerisation than for ethylene homopolymerisation; M_w/M_n of 2.8–4.6 and 2.6–3.8 respectively for $\mathbf{1}_{\mathbf{sMAO(1G)}}$.

Differential scanning calorimetry (DSC) analysis of the polymers produced using $\mathbf{1}_{\mathbf{sMAO(1G)}}$ showed that the crystallisation and melting temperatures (T_c and T_m) decreased as the amount of 1-hexene in the system increased (Figure 4.3a and Table A4.3). The decrease in T_m was likely due to the increased degree of chain branching, which reduces the intermolecular forces between the polymer chains; unbranched high-density polyethylene (HDPE) has a melting temperature of ~134 °C while poly(1-hexene) has a melting temperature of less than 20 °C.[17, 18] The small decrease in T_c and T_m (from 120 to 116 °C and 133 to 128 °C respectively with 0 and 80 mg 1-hexene) suggests a small amount of 1-hexene incorporation; the incorporation of 1-hexene produces short-chain branches, which leads to the formation of different crystal sizes and crystalline lattice imperfections that reduce T_m.[19] A decrease in T_m for ethylene/1-hexene copolymerisation compared to ethylene homopolymerisation has also been observed using ^{Me_2}SB($^{t\text{Bu}}$N,$^{3\text{-Et}}$Ind)ZrMe$_2$ supported on sulfonated alumina, where T_m decreased from 137 to 133 °C in the presence of 0.8 M 1-hexene at 60 °C with 5.2 bar ethylene.[20]

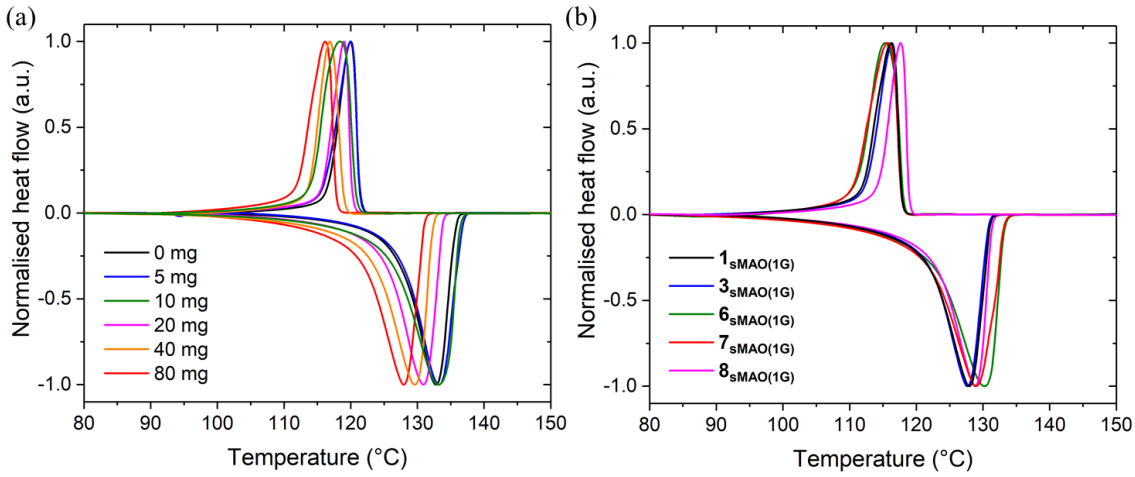


Figure 4.3 DSC plot showing the first cooling cycle and second heating cycle for the polyethylenes produced using sMAO(1G) supported (a) ^{Me_2}SB(Cp,I*)ZrCl$_2$ (**1$_{sMAO(1G)}$**) with 0 mg 1-hexene (black), 5 mg 1-hexene (blue), 10 mg 1-hexene (green), 20 mg 1-hexene (pink), 40 mg 1-hexene (orange) and 80 mg 1-hexene (red) and (b) ^{Me_2}SB(Cp,I*)ZrCl$_2$ (**1$_{sMAO(1G)}$**) (black), ^{Me_2}SB(Cp^{Me},I*)ZrCl$_2$ (**3$_{sMAO(1G)}$**) (blue), ^{Me_2}SB(Cp,I*)Zr(CH$_2$Ph)$_2$ (**6$_{sMAO(1G)}$**) (green), ^{Me_2}SB(Cp^{Me},I*)Zr(CH$_2$Ph)$_2$ (**7$_{sMAO(1G)}$**) (red) and ^{Me_2}SB(Cp,I*)ZrMe$_2$ (**8$_{sMAO(1G)}$**) (pink) with 80 mg 1-hexene. Normalised for clarity. Polymerisation conditions: [Al$_{sMAO(1G)}$]$_0$/[M]$_0$ = 200, TiBA (150 mg), ethylene (2 bar), pre-catalyst (10 mg), hexane (50 mL), 80 °C and 5 minutes.

Polymer crystallinity decreased slightly when the amount of 1-hexene in the system was increased; the short-chain branches produced from 1-hexene incorporation influence chain folding and can lead to defective crystal formation (crystallinity of 59 and 55% for **1$_{sMAO(1G)}$** in the presence of 0 and 80 mg 1-hexene respectively).[19] The polymers produced in the presence of 80 mg 1-hexene showed T_c of 115–118 °C and T_m of 128–130 °C for all five catalysts, indicating similar amounts of 1-hexene incorporation (Figure 4.3b).

The morphology of the polymers produced from the copolymerisation of ethylene and 1-hexene with 80 mg 1-hexene using **6$_{sMAO(1G)}$** was analysed by scanning electron microscopy (SEM) (Figure 4.4). SEM showed that even minimal 1-hexene incorporation changed polymer morphology; the polymer particles maintained uniform 'popcorn' morphology, however became slightly smaller and more aggregated.

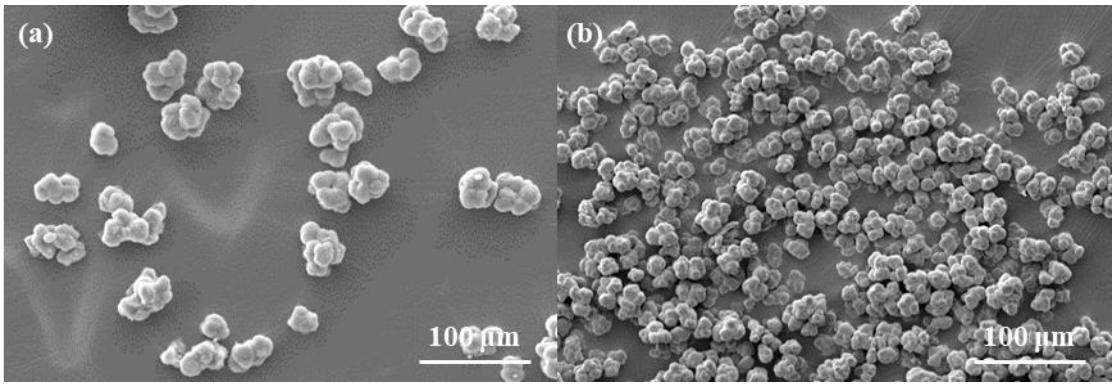


Figure 4.4 SEM images at ×250 magnification of the polymers produced from the slurry-phase polymerisation of ethylene using sMAO(1G) supported ^{Me_2}SB(Cp,I*)Zr(CH_2Ph)$_2$ (**6$_{sMAO(1G)}$**) with (a) 0 mg 1-hexene and (b) 80 mg 1-hexene. Polymerisation conditions: $[Al_{sMAO(1G)}]_0/[M]_0 = 200$, TiBA (150 mg), ethylene (2 bar), pre-catalyst (10 mg), hexane (50 mL), 80 °C and 5 minutes.

4.2.2 High-throughput ethylene/1-hexene copolymerisation

High-throughput studies were conducted at HTExplore (University of Naples, Italy) in collaboration with Prof. Vincenzo Busico. Polymerisation runs were conducted by Dr Alessio Mingione in 23 mL cells at 80 °C with overhead stirring using 5 mL heptane, 10 µmol TiBA, 0.05–0.15 mg pre-catalyst, $[Al_{sMAO(1G)}]/[M]_0 = 200$, 8.3 bar ethylene and the desired quantity of 1-hexene (0, 125 or 250 µL). The reactions were run for 1 hour or until a certain ethylene uptake was reached (8.3 bar for ethylene homopolymerisation and 5.5 bar for ethylene/1-hexene copolymerisation). Ethylene uptake rate was measured *in situ*, which allowed for a quantitative assessment of polymerisation trends and catalyst stability. sMAO(1G) supported ^{Me_2}SB(Cp,I*)$ZrCl_2$ (**1$_{sMAO(1G)}$**), ^{Me_2}SB(Cp,I*)$ZrBr_2$ (**2$_{sMAO(1G)}$**), ^{Me_2}SB(Cp^{Me},I*)$ZrCl_2$ (**3$_{sMAO(1G)}$**), ^{Me_2}SB(Cp^{Me},I*)$ZrCl_2$ (**4$_{sMAO(1G)}$**), *Z*-^{Me_2}SB(Cp$^{n\text{Bu}}$,I*)$ZrCl_2$ (***Z*-5$_{sMAO(1G)}$**), ^{Me_2}SB(Cp,I*)Zr(CH_2Ph)$_2$ (**6$_{sMAO(1G)}$**), ^{Me_2}SB(Cp^{Me},I*)Zr(CH_2Ph)$_2$ (**7$_{sMAO(1G)}$**), ^{Me_2}SB(Cp,I*)$ZrMe_2$ (**8$_{sMAO(1G)}$**) and ^{Me_2}SB(Cp^{Me},I*)$ZrMe_2$ (**9$_{sMAO(1G)}$**) were tested for their ethylene/1-hexene copolymerisation ability in the high-throughput system.

During ethylene homopolymerisation, the uptake rate profiles generally showed a steady increase in ethylene uptake over time, which stabilised after approximately 10 minutes (Figures 4.5 and A4.1–A4.3). The presence of 1-hexene initially caused a significant increase in ethylene uptake rate; this phenomenon is known as the comonomer effect and has been observed for a number of metallocene catalysts.[21-24] The origin of this effect is unknown, however it is postulated that α-olefin incorporation increases polymer solubility in the reaction medium, which causes the catalytic sites to become more accessible and allows for easier monomer diffusion.[19, 25, 26] Molecular simulations show that the ethylene solubility is enhanced by up to 10% on the addition of 5 mol% 1-hexene at 70–100 °C, which could lead to an increase in activity.[27]

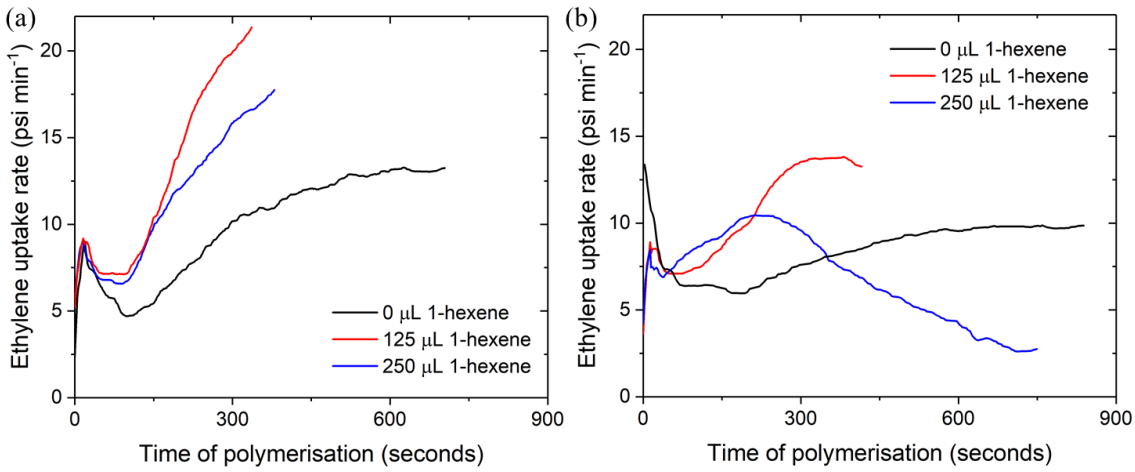


Figure 4.5 Slurry-phase polymerisation ethylene uptake rate as a function of time of polymerisation using sMAO(1G) supported (a) ^{Me_2}SB(Cp,I*)Zr(CH_2Ph)$_2$ (**6$_{sMAO(1G)}$**) and (b) ^{Me_2}SB(Cp^{Me},I*)Zr(CH_2Ph)$_2$ (**7$_{sMAO(1G)}$**) with 0 μL 1-hexene (black), 125 μL 1-hexene (red) and 250 μL 1-hexene (blue). Polymerisation conditions: $[Al_{sMAO(1G)}]_0/[M]_0$ = 200, TiBA (10 μmol), ethylene (8.3 bar), pre-catalyst (0.05–0.15 mg), heptane (5 mL) and 80 °C. Reactions quenched at 5.5 or 8.3 bar ethylene uptake for co- and homopolymerisation respectively.

The overall effect of the comonomer on polymerisation activity is largely dependent on nature of the catalytic species and on the polymerisation system.[12] For Ziegler-Natta catalysts, the comonomer usually modifies the active sites of catalyst,

which generates new active species and activates dormant sites.[14, 24] However, for metallocene systems comonomer concentration, competitive coordination between monomers and polymerisation conditions have a greater influence over activity.[12, 25]

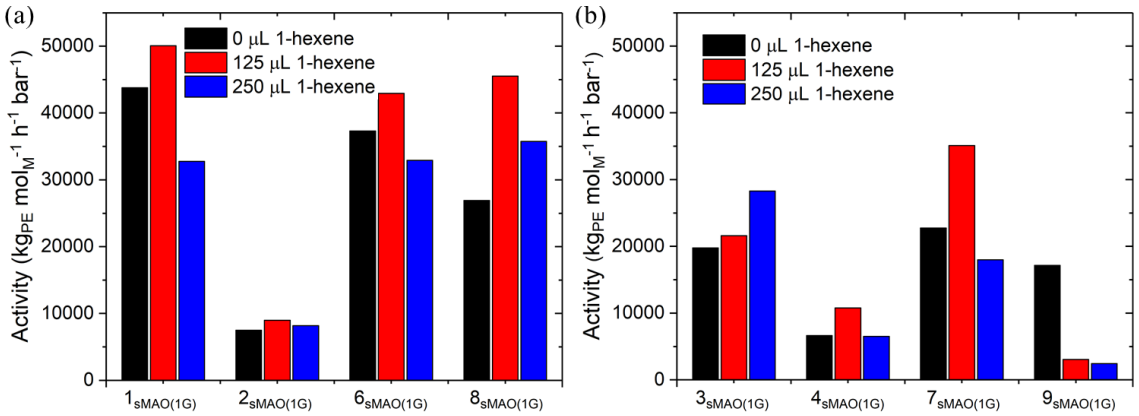


Figure 4.6 Slurry-phase ethylene polymerisation activity using sMAO(1G) supported (a) ^{Me_2}SB(Cp,I*)ZrCl$_2$ (**1$_{sMAO(1G)}$**), ^{Me_2}SB(Cp,I*)ZrBr$_2$ (**2$_{sMAO(1G)}$**), ^{Me_2}SB(Cp,I*)Zr(CH$_2$Ph)$_2$ (**6$_{sMAO(1G)}$**) and ^{Me_2}SB(Cp,I*)ZrMe$_2$ (**8$_{sMAO(1G)}$**) and (b) ^{Me_2}SB(Cp^{Me},I*)ZrCl$_2$ (**3$_{sMAO(1G)}$**), ^{Me_2}SB(Cp^{Me},I*)ZrBr$_2$ (**4$_{sMAO(1G)}$**), ^{Me_2}SB(Cp^{Me},I*)Zr(CH$_2$Ph)$_2$ (**7$_{sMAO(1G)}$**) and ^{Me_2}SB(Cp^{Me},I*)ZrMe$_2$ (**9$_{sMAO(1G)}$**) with 0 µL 1-hexene (black), 125 µL 1-hexene (red) and 250 µL 1-hexene (blue). Polymerisation conditions: [Al$_{sMAO(1G)}$]$_0$/[M]$_0$ = 200, TiBA (10 µmol), ethylene (8.3 bar), pre-catalyst (0.05–0.15 mg), heptane (5 mL) and 80 °C. Reactions quenched at 5.5 or 8.3 bar ethylene uptake for co- and homopolymerisation respectively or after 1 hour.

All catalysts except **9$_{sMAO(1G)}$** experienced an increase in polymerisation activity with 125 µL 1-hexene (2.5% of the reaction volume) compared to ethylene homopolymerisation, likely due to the increased solublity of ethylene in the presence of 1-hexene (Figures 4.6 and A4.4 and Table A4.4).[27] This observation is in contrast to the ampoule system where **1$_{sMAO(1G)}$**, **6$_{sMAO(1G)}$**, **7$_{sMAO(1G)}$** and **8$_{sMAO(1G)}$** experienced a decrease in activity when 1-hexene was added to the system, and is likely due to the different reaction conditions. In the high-throughput system, all catalysts except **3$_{sMAO(1G)}$** experienced a decrease in polymerisation activity with 250 µL 1-hexene (5% of the reaction volume) compared to 125 µL 1-hexene, likely due to competitive monomer coordination; activities of 37309, 42942 and 32934 kg$_{PE}$ mol$_M^{-1}$ h^{-1} bar^{-1}

using **6**$_{\mathbf{sMAO(1G)}}$ with 0, 125 and 250 μL 1-hexene respectively. The increase in activity for ethylene/1-hexene copolymerisation using **3**$_{\mathbf{sMAO(1G)}}$ in the high-throughput system with up to 250 μL 1-hexene was also observed in the ampoule system with up to 80 mg 1-hexene (0.24% of the reaction volume). The increase in activity suggests that **3**$_{\mathbf{sMAO(1G)}}$ may have a higher 1-hexene homopolymerisation activity than the other catalysts, which could reduce the adverse effects of competitive monomer coordination on activity. Although this is perhaps unlikely as **3**$_{\mathbf{sMAO(1G)}}$ experiences a similar amount of 1-hexene incorporation to the other catalysts (Table 4.1).

Table 4.1 Slurry-phase ethylene/1-hexene copolymerisation polymer molecular weights (M_w) and percentage comonomer incorporation for sMAO(1G) supported complexes.[a]

sMAO(1G) supported complex	**0 μL 1-Hexene**	**125 μL 1-Hexene**		**250 μL 1-Hexene**	
	M_w [b]	M_w [b]	x_H [c]	M_w [b]	x_H [c]
^{Me_2}SB(Cp,I*)ZrCl$_2$ (**1**)	354	326	0.5	-	1.0
^{Me_2}SB(Cp,I*)ZrBr$_2$ (**2**)	296	340	0.5	350	0.8
^{Me_2}SB(Cp^{Me},I*)ZrCl$_2$ (**3**)	349	294	0.5	289	0.9
^{Me_2}SB(Cp^{Me},I*)ZrBr$_2$ (**4**)	348	278	0.6	307	1.0
Z-^{Me_2}SB(Cp$^{n\text{Bu}}$,I*)ZrCl$_2$ (***Z*-5**)	154	176	0.8	198	1.3
^{Me_2}SB(Cp,I*)Zr(CH$_2$Ph)$_2$ (**6**)	311	262	0.5	278	0.9
^{Me_2}SB(Cp^{Me},I*)Zr(CH$_2$Ph)$_2$ (**7**)	342	244	0.5	257	0.9
^{Me_2}SB(Cp,I*)ZrMe$_2$ (**8**)	358	255	0.5	259	0.9
^{Me_2}SB(Cp^{Me},I*)ZrMe$_2$ (**9**)	337	255	0.5	276	0.9

(a) Polymerisation conditions: $[Al_{sMAO(1G)}]_0/[M]_0$ = 200, TiBA (10 μmol), ethylene (8.3 bar), pre-catalyst (0.05–0.15 mg), heptane (5 mL) and 80 °C; reactions quenched at 5.5 or 8.3 bar ethylene uptake for co- and homopolymerisation respectively or after 1 hour; (b) molecular weights (kg mol^{-1}); (c) percentage 1-hexene incorporation (mol%).

The percentage incorporation of 1-hexene into the polymer chain (x_H) was determined by $^{13}C\{^1H\}$ NMR spectroscopy (Table 4.1). As expected, when the amount of 1-hexene introduced into the system was increased, the amount of comonomer incorporated into the polymer chain increased (maximum incorporation of 1.3 mol% for ***Z*-5$_{sMAO(1G)}$**). The polymer was also analysed by crystallisation elution fractionation (CEF); a separation process based on fractional crystallisation.[28] CEF showed that the temperature at maximum elution ($T_{el,max.}$) decreased as the proportion of 1-hexene in the polymer increased; $T_{el,max.}$ = 113.3, 108.1 and 105.7 °C for **6$_{sMAO(1G)}$** with 0, 125 and 250 µL 1-hexene respectively (Table A4.5). $T_{el,max.}$ decreased as melting temperature and crystallinity decreased due to the increase in chain branching caused by 1-hexene incorporation weakening the intramolecular interactions between polymer chains.[17, 19]

All catalysts except **2$_{sMAO(1G)}$** and ***Z*-5$_{sMAO(1G)}$** experienced a decrease in M_w when 1-hexene was added to the system due to the increase in chain end-group branching and the potential for termination by chain transfer to 1-hexene monomers.[16] The polymers produced by ***Z*-5$_{sMAO(1G)}$** showed molecular weights approximately half of those produced from the other catalysts, possibly due to the very high ethylene uptake rate and increased 1-hexene incorporation when using ***Z*-5$_{sMAO(1G)}$**. The molecular weight distributions were found to be unaffected by 1-hexene incorporation (M_w/M_n = 2.3–2.6 for ***Z*-5$_{sMAO(1G)}$**).

4.2.3 Large scale copolymerisation studies

Large scale ethylene/1-hexene copolymerisation studies were conducted at SCG Chemicals Co., Ltd., (Rayong, Thailand) by Mr Thawesak Parawan, Mr Somjet Songnoey and Mr Pongsiri Kaeoyok. Polymerisation runs were conducted in 2 L steel reactors at 80 °C with 1 L hexane, 0.5 mmol triethylaluminium (TEA) scavenger,

0.025–0.050 g pre-catalyst, $[Al_{sMAO(1G)}]_0/[M]_0 = 200$, 8 bar ethylene and 10 mL 1-hexene for 1 hour. sMAO(1G) supported $^{Me_2}SB(Cp,I^*)ZrCl_2$ (**$1_{sMAO(1G)}$**), $^{Me_2}SB(Cp^{Me},I^*)ZrCl_2$ (**$3_{sMAO(1G)}$**) and $^{Me_2}SB(Cp,I^*)Zr(CH_2Ph)_2$ (**$6_{sMAO(1G)}$**) were studied.

For ethylene homopolymerisation using **$3_{sMAO(1G)}$** and **$6_{sMAO(1G)}$** a steady decrease in ethylene uptake rate was observed after approximately 800 seconds; from 11 to 6 L mg_{CAT}^{-1} min^{-1} for **$3_{sMAO(1G)}$** and from 15 to 13 L mg_{CAT}^{-1} min^{-1} for **$6_{sMAO(1G)}$** after 800 and 3600 seconds respectively (Figure 4.7). However, during ethylene/1-hexene copolymerisation, **$3_{sMAO(1G)}$** showed a constant ethylene uptake rate after approximately 800 seconds (11 L mg_{CAT}^{-1} min^{-1}), while **$6_{sMAO(1G)}$** experienced a steady increase in uptake rate over the time studied (from 10 to 13 L mg_{CAT}^{-1} min^{-1} after 800 and 3600 seconds respectively). This suggests that the rate enhancing abilities of the comonomer effect were sustained for a much longer period of time on the large scale batch than in the miniaturised high-throughput system; possibly due to the lower 1-hexene content (approximately 1% of the total reaction volume) minimising competitive monomer insertion while still increasing ethylene solubility.[12, 27]

Overall, **$1_{sMAO(1G)}$** and **$6_{sMAO(1G)}$** experienced a 40 and 21% decrease in polymerisation activity on the addition of 1-hexene, while **$3_{sMAO(1G)}$** experienced a 35% increase in polymerisation activity; from 30229 to 18191 $kg_{PE}\,mol_M^{-1}\,h^{-1}\,bar^{-1}$ for **$1_{sMAO(1G)}$** and from 11812 to 15997 $kg_{PE}\,mol_M^{-1}\,h^{-1}\,bar^{-1}$ for **$3_{sMAO(1G)}$** (Figure A4.5 and Table A4.6). The increased activity for **$3_{sMAO(1G)}$** compared to **$1_{sMAO(1G)}$** may be due to the slight increase in electron density of Cp^{Me} compared to Cp; Klosin *et al.* observed an increase in solution-phase ethylene/1-octene copolymerisation activity using $^{Me_2}SB(^{tBu}N,^{2\text{-}R}I)ZrMe_2$ with $B(C_6F_5)_3$ activator when the electron density of the indenyl substituent was increased (polymerisation activity was 3.5 times larger when R = OEt than when R = H).[29]

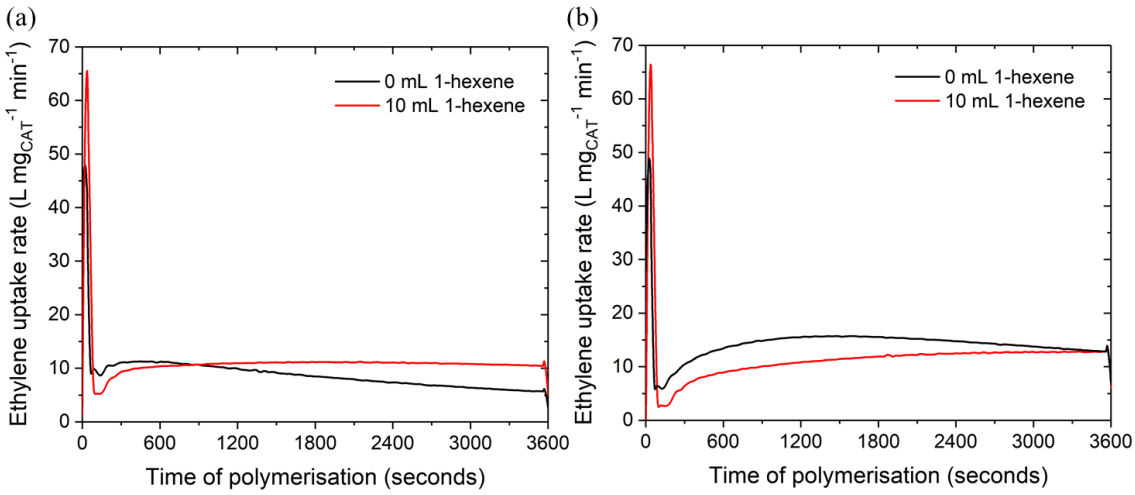


Figure 4.7 Slurry-phase polymerisation ethylene uptake rate as a function of time of polymerisation using sMAO(1G) supported (a) ^{Me_2}SB(Cp^{Me},I*)ZrCl$_2$ (**3$_{sMAO(1G)}$**) and (b) ^{Me_2}SB(Cp,I*)Zr(CH$_2$Ph)$_2$ (**6$_{sMAO(1G)}$**) with 0 mL 1-hexene (black) and 10 mL 1-hexene (red). Polymerisation conditions: [Al$_{sMAO(1G)}$]$_0$/[M]$_0$ = 200, TEA (0.5 mmol), ethylene (8 bar), pre-catalyst (0.025–0.050 g), hexane (1 L), 80 °C and 1 hour.

For **3$_{sMAO(1G)}$** and **6$_{sMAO(1G)}$** polymer molecular weights (M_w) increased on the addition of 1-hexene (from 247 to 307 kg mol^{-1} for **3$_{sMAO(1G)}$** and from 268 to 317 kg mol^{-1} for **6$_{sMAO(1G)}$** with 0 and 10 mL 1-hexene respectively).[19] The molecular weight distributions were found to be unaffected by 1-hexene incorporation with M_w/M_n between 3.6 and 3.9 for both catalysts. The percentage incorporation of 1-hexene using **3$_{sMAO(1G)}$** was determined by ^{13}C{^{1}H} NMR spectroscopy to be 0.2 mol%, which is lower than that recorded in the high-throughput system and is likely due to the reduced percentage of 1-hexene in the reactor.

4.3 Ethylene/Hydrogen Homopolymerisation

4.3.1 Slurry-phase ethylene/hydrogen homopolymerisation

Slurry-phase ethylene polymerisation reactions were conducted in the presence of hydrogen and the ethylene uptake rate monitored *in situ*. The polymerisations were run in 150 mL ampoules with a mixed ethylene/hydrogen feed (2 bar, 2% hydrogen), 50 mL hexane, 10 mg pre-catalyst, 150 mg TiBA and $[Al_{sMAO(1G)}]_0/[M]_0$ of 200 for 30 minutes using sMAO(1G) supported ^{Me_2}SB(Cp,I*)$ZrCl_2$ (**1**$_{\mathbf{sMAO(1G)}}$) and ^{Me_2}SB(Cp,I*)$ZrMe_2$ (**8**$_{\mathbf{sMAO(1G)}}$).

For polymerisations conducted at 50–70 °C ethylene uptake rate was relatively constant over the time period (Figures 4.8a and A4.6a). However, at 80 and 90 °C, ethylene uptake rate steadily decreased with time, possibly due to the decrease in ethylene solubility in hexane at higher temperatures or due to catalyst decomposition.[30] The polymerisation activity was found to be fairly constant over the temperature range; activities of 2157–3315 and 2230–2791 $kg_{PE}\ mol_M^{-1}\ h^{-1}\ bar^{-1}$ for **1**$_{\mathbf{sMAO(1G)}}$ and **8**$_{\mathbf{sMAO(1G)}}$ respectively with a maximum polymerisation activity recorded at 70 °C for both catalysts (Figures 4.8b and A4.6b). At 80 °C, the activities of **1**$_{\mathbf{sMAO(1G)}}$ and **8**$_{\mathbf{sMAO(1G)}}$ with 2% hydrogen were found to be 45 and 55% lower than for the polymerisation of ethylene without hydrogen; activities of 2850 and 5144 $kg_{PE}\ mol_M^{-1}\ h^{-1}\ bar^{-1}$, and 2447 and 5482 $kg_{PE}\ mol_M^{-1}\ h^{-1}\ bar^{-1}$ for **1**$_{\mathbf{sMAO(1G)}}$ and **8**$_{\mathbf{sMAO(1G)}}$ with and without hydrogen respectively (Table A4.7). The deactivating effect of hydrogen has been demonstrated in other metallocene systems, such as for homogeneous ethylene polymerisation using Cp_2ZrCl_2/MAO where activity decreased from 45000 to 21400 $kg_{PE}\ mol_M^{-1}\ h^{-1}\ bar^{-1}$ in the presence of 0.5 mol% hydrogen (8 bar ethylene and 70 °C).[31] Cp_2ZrCl_2 has also been shown to experience a decrease in

ethylene polymerisation activity in the presence of hydrogen when supported on MAO activated silica; a decrease from approximately 430 to 400 kg_{PE} mol_M^{-1} h^{-1} bar^{-1} with 0 and 4.1 bar hydrogen respectively (5.5 bar ethylene and 60 °C).[32] Deactivation in the presence of hydrogen is likely due to increased formation of the metal hydride termination species formed from polymer termination by chain transfer to hydrogen, or due to formation of a bimetallic dormant resting state (such as $[(L_2MMe)_2(\mu\text{-H})]^+$) formed from the reaction of the catalyst with hydrogen (discussed in Section 1.2.4).[33-36] Both of these species require reactivation for propagation, either by insertion of a monomer for the $[L_2MH]^+$ termination product, or by loss of Cp_2MMeH for the dormant resting state $[(L_2MMe)_2(\mu\text{-H})]^+$. In addition, the presence of hydrogen is also likely to cause a reduction in ethylene concentration around the active catalytic sites.

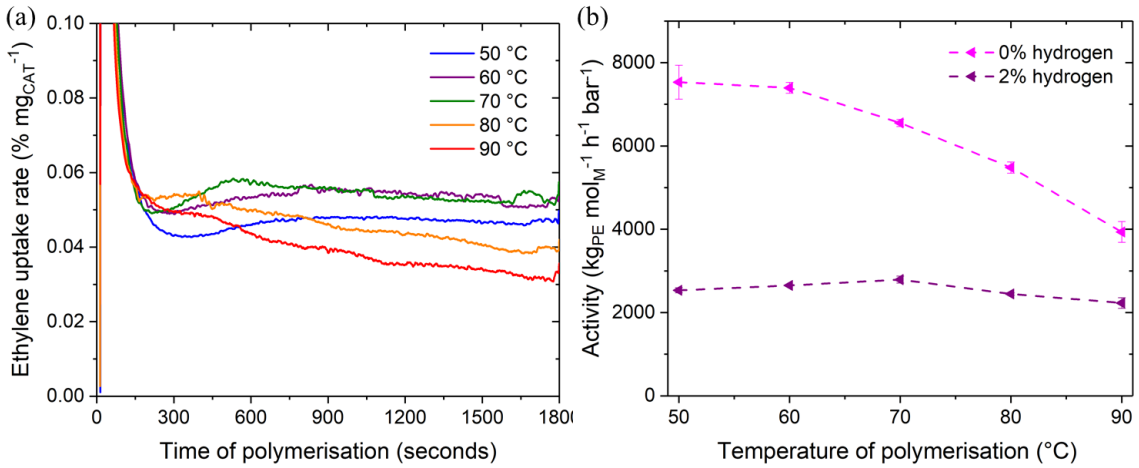


Figure 4.8 (a) Slurry-phase polymerisation ethylene uptake rate as a function of time of polymerisation using sMAO(1G) supported ^{Me_2}SB(Cp,I*)$ZrMe_2$ (**8**$_{sMAO(1G)}$) with 2% hydrogen at 50 °C (blue), 60 °C (purple), 70 °C (green), 80 °C (orange) and 90 °C (red). The Y-axis provides a quantitative measure of uptake; (b) slurry-phase ethylene polymerisation activity as a function of temperature of polymerisation using sMAO(1G) supported ^{Me_2}SB(Cp,I*)$ZrMe_2$ (**8**$_{sMAO(1G)}$) with 0% (pink) and 2% hydrogen (purple). Polymerisation conditions: $[Al_{sMAO(1G)}]_0/[M]_0$ = 200, TiBA (150 mg), ethylene/hydrogen (2 bar, 2%), pre-catalyst (10 mg), hexane (50 mL) and 30 minutes.

DSC analysis of the polyethylenes produced at 80 °C revealed a melting temperature of 133 °C and crystallisation temperature of 119 °C for both catalysts (Figure A4.7), consistent with the values recorded when no hydrogen was in the system (T_m = 133 and T_c = 122 °C for both catalysts) and indicative of HDPE with minimal defects and branching.[18, 37] The enthalpy of melting and crystallisation (ΔH_m and ΔH_c) were calculated as 195 and 194 J g^{-1} for $\mathbf{1}_{\mathbf{sMAO(1G)}}$, and 186 and 185 J g^{-1} for $\mathbf{8}_{\mathbf{sMAO(1G)}}$ with a crystallinity of 67 and 64% respectively; only slightly lower than when no hydrogen was present (70 and 67% for $\mathbf{1}_{\mathbf{sMAO(1G)}}$ and $\mathbf{8}_{\mathbf{sMAO(1G)}}$ respectively).

4.3.2 High-throughput ethylene/hydrogen polymerisation

High-throughput studies were conducted in 23 mL cells with 5 mL heptane, 10 µmol TiBA, 0.05–0.15 mg pre-catalyst, $[Al_{sMAO(1G)}]/[M]_0$ = 200, 8.3 bar ethylene and 0.8% (0.07 bar) or 1.6% (0.13 bar) hydrogen supplied by a mixed hydrogen/nitrogen feed. Reactions were run at 80 °C for 1 hour or until 8.3 bar ethylene uptake was reached. sMAO(1G) supported ^{Me_2}SB(Cp,I*)$ZrCl_2$ ($\mathbf{1}_{\mathbf{sMAO(1G)}}$), ^{Me_2}SB(Cp,I*)$ZrBr_2$ ($\mathbf{2}_{\mathbf{sMAO(1G)}}$), ^{Me_2}SB($Cp^{Me}$,I*)$ZrCl_2$ ($\mathbf{3}_{\mathbf{sMAO(1G)}}$), ^{Me_2}SB($Cp^{Me}$,I*)$ZrCl_2$ ($\mathbf{4}_{\mathbf{sMAO(1G)}}$), *Z*-^{Me_2}SB($Cp^{n\mathrm{Bu}}$,I*)$ZrCl_2$ (***Z*-5**$_{\mathbf{sMAO(1G)}}$), ^{Me_2}SB(Cp,I*)$Zr(CH_2Ph)_2$ ($\mathbf{6}_{\mathbf{sMAO(1G)}}$), ^{Me_2}SB($Cp^{Me}$,I*)$Zr(CH_2Ph)_2$ ($\mathbf{7}_{\mathbf{sMAO(1G)}}$), ^{Me_2}SB(Cp,I*)$ZrMe_2$ ($\mathbf{8}_{\mathbf{sMAO(1G)}}$) and ^{Me_2}SB($Cp^{Me}$,I*)$ZrMe_2$ ($\mathbf{9}_{\mathbf{sMAO(1G)}}$) were studied.

The *in situ* ethylene uptake rate profiles demonstrated the relative stability of these catalysts in the presence of hydrogen (Figures 4.9 and A4.8–A4.10). When hydrogen was present, the ethylene uptake rate was lower than polymerisation without hydrogen; uptake rates of 13.36, 6.64 and 4.14 psi min^{-1}, and 11.77, 4.82 and 3.58 psi min^{-1} for $\mathbf{6}_{\mathbf{sMAO(1G)}}$ and $\mathbf{8}_{\mathbf{sMAO(1G)}}$ with 0, 0.8 and 1.6% hydrogen respectively after 600 seconds. The uptake rate was also observed to slowly decrease over time

(from 4.69 psi min^{-1} after 200 seconds to 2.98 psi min^{-1} after 1800 seconds for **$6_{sMAO(1G)}$**); however, all catalysts maintained some activity on completion of the polymerisation run. **$8_{sMAO(1G)}$** showed the highest stability and resilience to hydrogen with a constant ethylene uptake rate of approximately 3.50 psi min^{-1} over the monitored time period with 1.6% hydrogen. These unsymmetrical *ansa*-bridged complexes are much more resilient to hydrogen than the constrained geometry analogues; **$6_{sMAO(1G)}$** maintained an uptake rate of 2.72 psi min^{-1} after 33 minutes with 1.6% hydrogen, whereas sMAO(1G) supported ^{Me_2}SB(^{tBu}N,I*)Ti($CH_2Ph)_2$ registered 0.78 psi min^{-1} ethylene uptake after the same amount of time.[38]

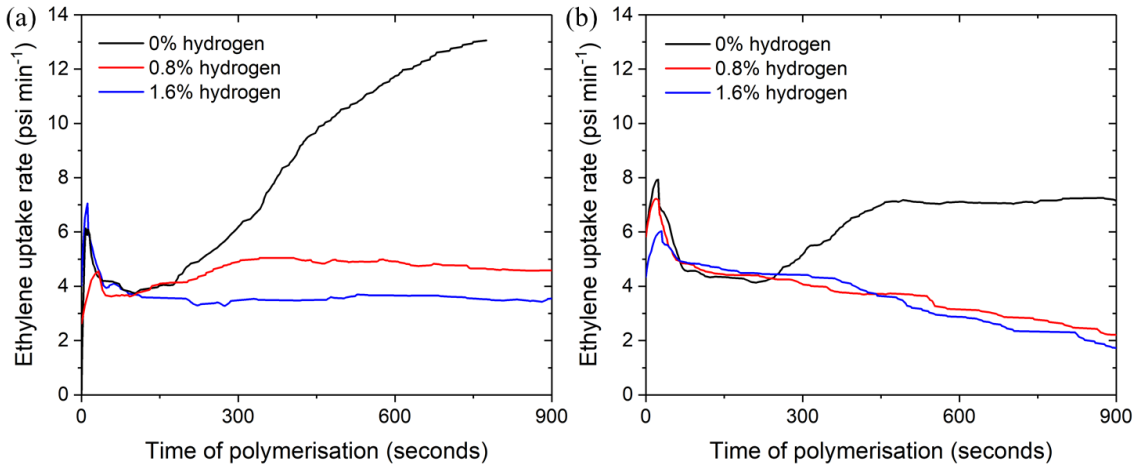


Figure 4.9 Slurry-phase polymerisation ethylene uptake rate as a function of time of polymerisation using sMAO(1G) supported (a) ^{Me_2}SB(Cp,I*)$ZrMe_2$ (**$8_{sMAO(1G)}$**) and (b) ^{Me_2}SB(Cp^{Me},I*)$ZrMe_2$ (**$9_{sMAO(1G)}$**) with 0% hydrogen (black), 0.8% hydrogen (red) and 1.6% hydrogen (blue). Polymerisation conditions: $[Al_{sMAO(1G)}]_0/[M]_0$ = 200, TiBA (10 μmol), ethylene (8.3 bar), pre-catalyst (0.05–0.15 mg), heptane (5 mL) and 80 °C. Reactions quenched at 8.3 bar ethylene uptake or after 1 hour.

All the catalysts showed a significant decrease in ethylene polymerisation activity when hydrogen was introduced to the system; in addition to forming the metal hydride termination product, hydrogen molecules can also coordinate to the active metal centre in competition with ethylene monomers and subsequently decrease the rate of propagation (Figures 4.10a, A4.11a and A4.12a and Table A4.8).[39] Despite the

decrease in ethylene polymerisation activity in the presence of hydrogen, these catalysts remain very active; **8$_{sMAO(1G)}$** showed activities of 13849 and 7386 $kg_{PE}\ mol_M^{-1}\ h^{-1}\ bar^{-1}$ with 0.8 and 1.6% hydrogen respectively.

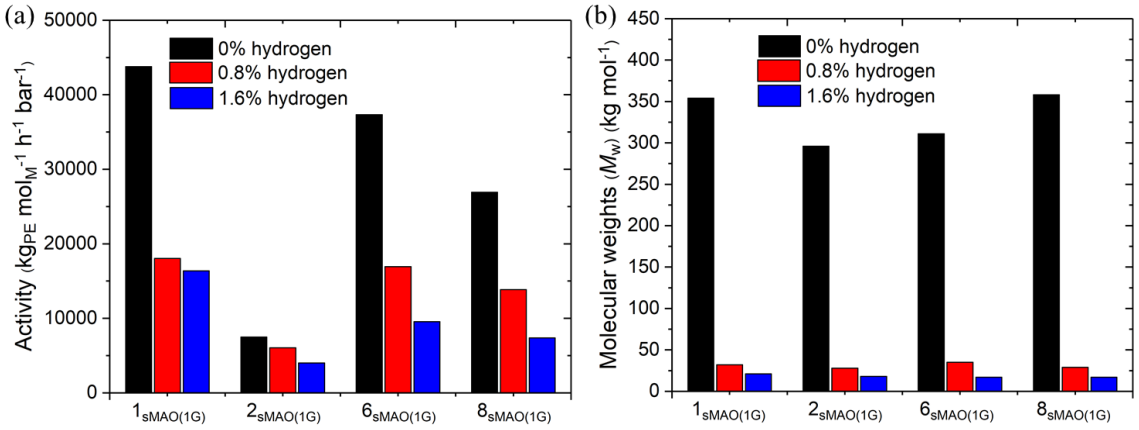


Figure 4.10 (a) Slurry-phase ethylene polymerisation activity and (b) polymer molecular weights (M_w) using sMAO(1G) supported ^{Me_2}SB(Cp,I*)$ZrCl_2$ (**1$_{sMAO(1G)}$**), ^{Me_2}SB(Cp,I*)$ZrBr_2$ (**2$_{sMAO(1G)}$**), ^{Me_2}SB(Cp,I*)$Zr(CH_2Ph)_2$ (**6$_{sMAO(1G)}$**) and ^{Me_2}SB(Cp,I*)$ZrMe_2$ (**8$_{sMAO(1G)}$**) with 0% hydrogen (black), 0.8% hydrogen (red) and 1.6% hydrogen (blue). Polymerisation conditions: $[Al_{sMAO(1G)}]_0/[M]_0$ = 200, TiBA (10 µmol), ethylene (8.3 bar), pre-catalyst (0.05–0.15 mg), heptane (5 mL) and 80 °C. Reactions quenched at 8.3 bar ethylene uptake or after 1 hour.

The polymers produced in the presence of hydrogen demonstrated much lower molecular weights (M_w) than in the systems without hydrogen. M_w was also observed to decrease with increasing hydrogen content; M_w = 358, 29 and 17 kg mol^{-1} for **8$_{sMAO(1G)}$** with 0, 0.8 and 1.6% hydrogen respectively (Figures 4.10b, A4.11b and A4.12b and Table A4.9). The polymers produced in the presence of hydrogen are classed as low molecular weight polyethylenes, with M_w approaching that of PE wax (<10 kg mol^{-1}). The decrease in molecular weights in the presence of hydrogen is most likely due to the increased amount of chain termination that occurs when hydrogen acts as a chain transfer agent (discussed in Section 1.2.4). A decrease in polymer molecular weights in the presence of hydrogen has also been observed when using $EBIZrCl_2$ supported on MAO-treated silica; M_w decreased from approximately 100 to 3 kg mol^{-1} in the

presence of 2 bar hydrogen (60 °C and 5.5 bar ethylene).[32] Kaminsky and Lüker also found the same effect in the homogeneous Cp_2ZrCl_2/MAO system where M_w decreased from 135 to 40 kg mol^{-1} in the presence of 0.08 bar hydrogen (70 °C and 8 bar ethylene).[31] The activation barrier for hydrogen insertion has been calculated to be lower than that for ethylene insertion, indicating why only a small amount of hydrogen is required to reduce polymer molecular weights drastically.[40] The molecular weight distributions and $T_{el,max.}$ were found to be reasonably constant in the presence of hydrogen, ranging between 2.4–3.0 and 109.3–110.9 °C respectively for **8$_{sMAO(1G)}$**.

The key challenge when using metallocene polymerisation catalysts for the production of low molecular weight polyethylenes is to balance the desired decrease in polymer molecular weights observed in the presence of hydrogen with the undesired reduction in polymerisation activity that also commonly occurs.

4.3.3 Large scale ethylene/hydrogen homopolymerisation

Large scale ethylene/hydrogen polymerisation studies were conducted in 2 L steel reactors with 1 L hexane, 0.5 mmol TEA scavenger, 0.025–0.050 g pre-catalyst, $[Al_{sMAO(1G)}]_0/[M]_0 = 200$, 8 bar ethylene gas and either 0, 0.38 (0.03 bar) or 0.86% (0.07 bar) hydrogen. Polymerisations were run at 80 °C for 1 hour using sMAO(1G) supported ^{Me_2}SB(Cp,I*)ZrCl$_2$ (**1$_{sMAO(1G)}$**), ^{Me_2}SB(Cp^{Me},I*)ZrCl$_2$ (**3$_{sMAO(1G)}$**), ^{Me_2}SB(Cp,I*)Zr(CH$_2$Ph)$_2$ (**6$_{sMAO(1G)}$**), ^{Me_2}SB(Cp^{Me},I*)Zr(CH$_2$Ph)$_2$ (**7$_{sMAO(1G)}$**) and ^{Me_2}SB(Cp,I*)ZrMe$_2$ (**8$_{sMAO(1G)}$**).

Similarly to the high-throughput system, the presence of hydrogen decreased the ethylene uptake rate; uptake rates of 12.77 and 3.08 L mg$_{CAT}^{-1}$ min^{-1} for **6$_{sMAO(1G)}$**, and 17.81 and 5.28 L mg$_{CAT}^{-1}$ min^{-1} for **8$_{sMAO(1G)}$** after 60 minutes with 0 and 0.86% hydrogen respectively (Figures 4.11 and A4.13). Uptake rate was also shown to

decrease gradually over time with **8**$_{\mathbf{sMAO(1G)}}$ maintaining the highest stability; uptake rates of 5.70 and 3.08 L mg_{CAT}^{-1} min^{-1} for **6**$_{\mathbf{sMAO(1G)}}$, and 6.77 and 5.28 L mg_{CAT}^{-1} min^{-1} for **8**$_{\mathbf{sMAO(1G)}}$ after 200 and 3600 seconds respectively with 0.86% hydrogen.

As seen in the high-throughput and ampoule systems, catalyst activity decreased when hydrogen was introduced to the system; activity decreased by approximately one third from 27186 to 8926 kg_{PE} mol_{M}^{-1} h^{-1} bar^{-1} for **8**$_{\mathbf{sMAO(1G)}}$ with 0 and 0.86% hydrogen respectively (Figure 4.12a and Table A4.10). In addition to formation of the metal hydride species, the reduction in activity may be due to the decreased solubility of ethylene monomers in hexane in the presence of hydrogen,[30] or due to the β-agostic interactions formed in the product of the first monomer insertion into the metal hydride species, which can stabilise the metal centre in addition to blocking the free coordination site and preventing monomer coordination (discussed in Section 1.2.4).[41, 42]

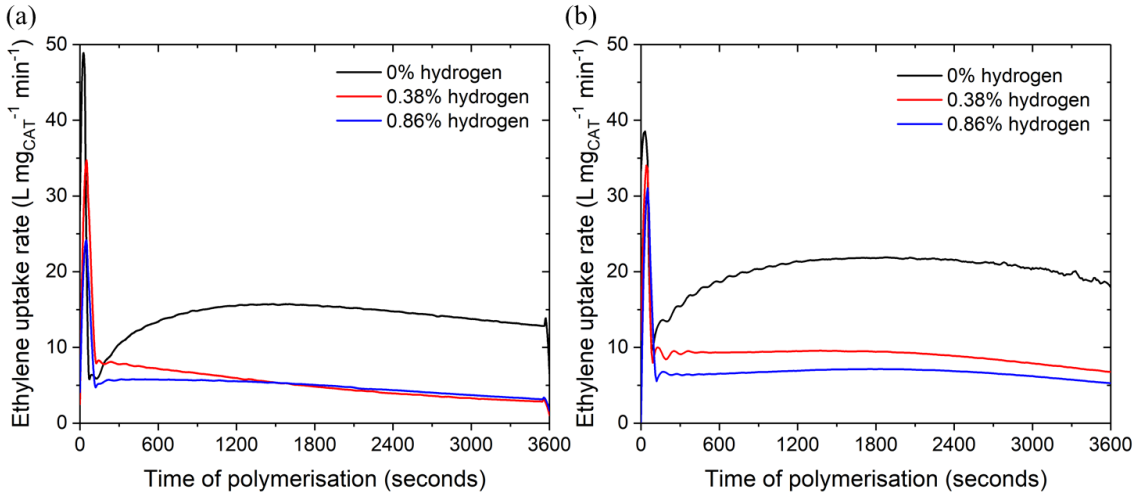


Figure 4.11 Slurry-phase polymerisation ethylene uptake rate as a function of time of polymerisation using sMAO(1G) supported (a) ^{Me_2}SB(Cp,I*)Zr(CH_2Ph)$_2$ (**6**$_{\mathbf{sMAO(1G)}}$) and (b) ^{Me_2}SB(Cp,I*)ZrMe_2 (**8**$_{\mathbf{sMAO(1G)}}$) with 0% hydrogen (black), 0.38% hydrogen (red) and 0.86% hydrogen (blue). Polymerisation conditions: $[Al_{sMAO(1G)}]_0/[M]_0$ = 200, TEA (0.5 mmol), ethylene (8 bar), pre-catalyst (0.025–0.050 g), hexane (1 L), 80 °C and 1 hour.

Polymer molecular weights (M_w) significantly decreased with increasing hydrogen concentration (from 225 to 15 kg mol^{-1} for **8**$_{\mathbf{sMAO(1G)}}$ with 0 and 0.86% hydrogen respectively), demonstrating that hydrogen is a strong chain transfer agent and showing the potential applications of these catalysts for the production of ULMWPE (Figure 4.12b and Table A4.11).[32] The molecular weight distributions of the polymers were unaffected by the presence of hydrogen (M_w/M_n between 3.0 and 3.8 for **8**$_{\mathbf{sMAO(1G)}}$).

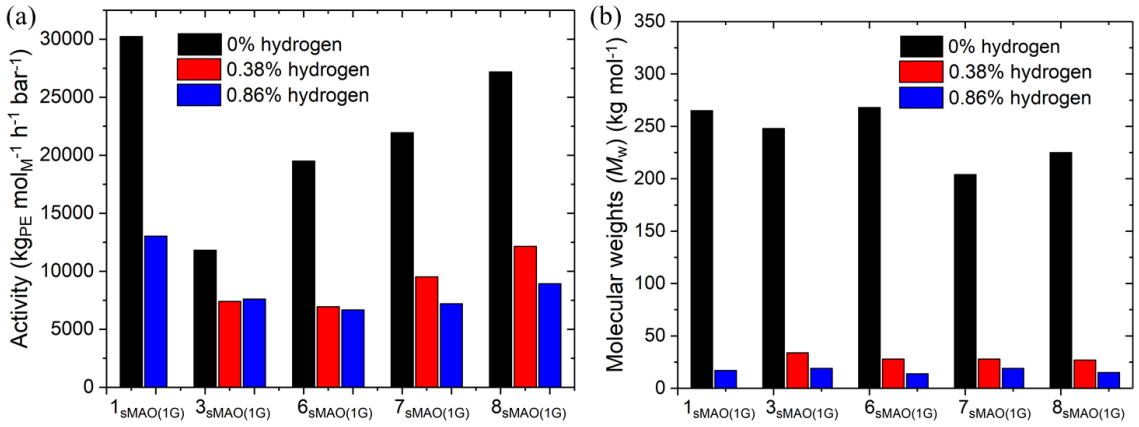


Figure 4.12 Slurry-phase ethylene polymerisation (a) activity and (b) polymer molecular weights (M_w) using sMAO(1G) supported ^{Me_2}SB(Cp,I*)ZrCl$_2$ (**1**$_{\mathbf{sMAO(1G)}}$), ^{Me_2}SB(Cp^{Me},I*)ZrCl$_2$ (**3**$_{\mathbf{sMAO(1G)}}$), ^{Me_2}SB(Cp,I*)Zr(CH$_2$Ph)$_2$ (**6**$_{\mathbf{sMAO(1G)}}$), ^{Me_2}SB(Cp^{Me},I*)Zr(CH$_2$Ph)$_2$ (**7**$_{\mathbf{sMAO(1G)}}$) and ^{Me_2}SB(Cp,I*)ZrMe$_2$ (**8**$_{\mathbf{sMAO(1G)}}$) with 0% hydrogen (black), 0.38% hydrogen (red) and 0.86% hydrogen (blue). Polymerisation conditions: [Al$_{sMAO(1G)}$]$_0$/[M]$_0$ = 200, TEA (0.5 mmol), ethylene (8 bar), pre-catalyst (0.025–0.050 mg), hexane (1 L), 80 °C and 1 hour.

The polymers produced from **7**$_{\mathbf{sMAO(1G)}}$ and **8**$_{\mathbf{sMAO(1G)}}$ were found to have a high crystallinity (83 and 86% respectively in the presence of 0.86% hydrogen) and a melting temperature indicative of HDPE (130 °C in the presence of 0.86% hydrogen). Density measurements confirmed the production of HDPE, with a density of 0.98 g cm^{-3} recorded for all polymers.

4.3.4 Solution-phase ethylene/hydrogen homopolymerisation

The hydrogen response for the solution-phase polymerisation of ethylene using ^{Me_2}SB(Cp,I*)Zr(CH_2Ph)$_2$ (**6**), ^{Me_2}SB(Cp^{Me},I*)Zr(CH_2Ph)$_2$ (**7**) and ^{Me_2}SB(Cp,I*)ZrMe_2 (**8**) in the presence of MAO activator was tested on a large scale at SCG Chemicals Co., Ltd. (Thailand). Polymerisations were conducted in 2 L steel reactors with 1 L hexane, 0.5 mmol MAO and 3 mg pre-catalyst at 80 °C with 8 bar ethylene gas and 0.38% hydrogen for 1 hour. Dialkyl complexes were tested in preference to their parent dihalide complexes due to their increased solubility in hexane;[43] ^{Me_2}SB(Cp^{R},I*)ZrCl_2 (R = H and Me) complexes are largely insoluble in hexane and therefore require the use of small amount of toluene in the polymerisation. The addition of toluene to the polymerisation is industrially undesirable as its higher boiling temperature requires heat treatment to remove residual solvent from the polymer product.[44]

The *in situ* uptake rate plots showed a sharp decrease in ethylene uptake rate after approximately 1800 and 900 seconds using **6** and **8** respectively in the presence of hydrogen, while **7** displayed a continual decline in uptake rate over the time period (Figure 4.13a). For **8**, the sharp reduction in uptake rate was observed due to the limiting size of the reactor; after 15 minutes the quantity of polymer produced (315 g) inhibited more ethylene dissolving into the solution and therefore ceased polymerisation. For **6** and **7** this was not observed and the decrease in uptake rate was most likely due to catalyst deactivation. The much larger initial ethylene uptake rate found for **8** when compared to **6** and **7** may be due to the identity of the initiation groups (methyl *vs* benzyl). It is generally accepted that during α-olefin polymerisation with MAO activator, MAO first methylates the complex and then abstracts a methyl group from the pre-catalyst to generate the catalytically active species [Cp$^{R}_2$ZrMe]$^+$ [X-MAO]$^-$.[45-48] During polymerisation using the dimethyl species,

methylation of the complex by MAO does not need to occur, possibly leading to faster generation of the active cationic species and a subsequent increase in initial ethylene uptake.

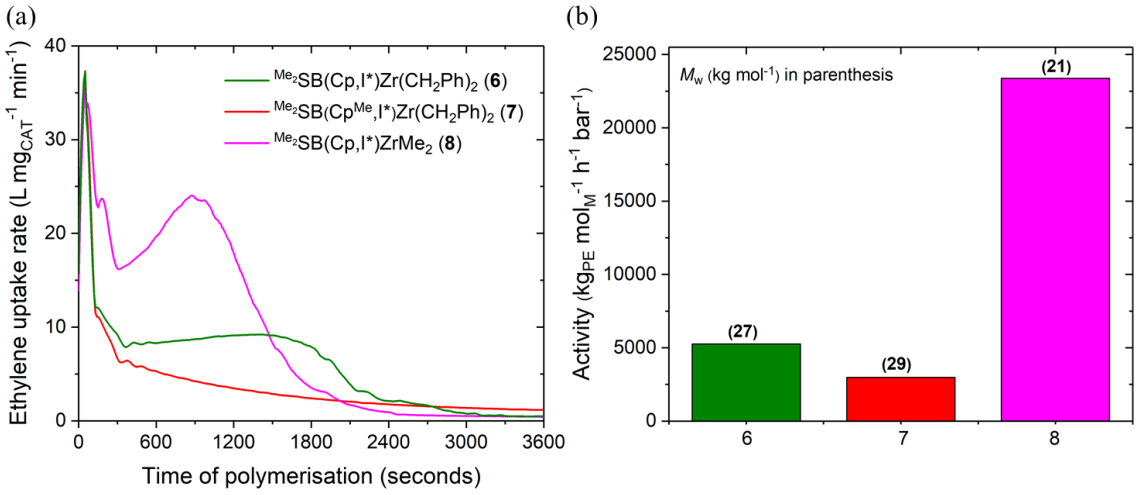


Figure 4.13 Solution-phase ethylene polymerisation (a) ethylene uptake rate as a function of time of polymerisation and (b) activity using ^{Me_2}SB(Cp,I*)Zr(CH$_2$Ph)$_2$ (**6**) (green), ^{Me_2}SB(Cp^{Me},I*)Zr(CH$_2$Ph)$_2$ (**7**) (red) and ^{Me_2}SB(Cp,I*)ZrMe$_2$ (**8**) (pink) with molecular weights (M_w) in parenthesis. Polymerisation conditions: 0.38% hydrogen, MAO (0.5 mmol), ethylene (8 bar), complex (3 mg), hexane (1 L), 80 °C and 1 hour (the activity of **8** was calculated after 15 minutes of polymerisation).

Complementary to the slurry-phase polymerisation study, **8** shows a much higher polymerisation activity than **6** and **7** in the presence of hydrogen; activities of 23370, 5255 and 2977 kg$_{PE}$ mol$_M^{-1}$ h^{-1} bar^{-1} respectively (calculated after 15 minutes of polymerisation for **8**) (Figure 4.13b and Table A4.12). The lower polymerisation activity seen in the solution-phase compared to the slurry-phase can be attributed to reactor fouling in the solution-phase, which reduces stirring efficiency and subsequently decreases the rate of polymerisation; activities of 23370 and 27186 kg$_{PE}$ mol$_M^{-1}$ h^{-1} bar^{-1} for **8** and **8$_{sMAO(1G)}$**. The lower activity in solution could also be due to the presence of free trimethylaluminium (TMA) within MAO, which can act as a reducing agent to form inactive methyl-bridged dinuclear species.[49] In addition, the higher amount of complex in the reaction vessel during solution-phase

polymerisation compared to slurry-phase polymerisation may also contribute to the changes in activity. The molecular weights of the polymer produced were similar to those produced from slurry-phase polymerisation with 0.38% hydrogen; M_w = 21 and 27 kg mol^{-1} for **8** and **8**$_{\mathbf{sMAO(1G)}}$.

Further solution-phase ethylene polymerisation studies were carried out at Norner AS (Norway) using **6** with MAO activator. Polymerisations were conducted in 3.5 L reactors at 80 °C for 30 minutes with $[Al_{MAO}]_0/[M]_0$ = 1000, 7.8 bar ethylene, 5 mg complex and 1.5 L hexane. Without hydrogen, the solution-phase polymerisation of ethylene using **6** gave an activity of 14333 kg_{PE} mol_M^{-1} h^{-1} bar^{-1}; approximately 30% lower than that of industrial standard $(Cp^{nBu})_2ZrCl_2$ (20500 kg_{PE} mol_M^{-1} h^{-1} bar^{-1}). Unusually, in the presence of 0.3% hydrogen **6** saw an increase in polymerisation activity to 15205 kg_{PE} mol_M^{-1} h^{-1} bar^{-1}. The increase in polymerisation activity in the presence of hydrogen was attributed to reactor fouling during polymerisation without hydrogen, which led to poor heat transfer and reduced stirring efficiency.[50] The increase in activity when compared SCG Chemicals Co., Ltd. is likely due to the increased amount of complex and lower percentage of hydrogen in the system.

4.4 Ethylene/1-Hexene/Hydrogen Copolymerisation

4.4.1 Slurry-phase ethylene/1-hexene/hydrogen copolymerisation

Slurry-phase ethylene/1-hexene copolymerisation reactions in the presence of hydrogen were conducted at 80 °C for 30 minutes in 150 mL ampoules with a sidearm by which the desired quantity of 1-hexene in hexane was added at the start of the polymerisation (Figure 4.1). The polymerisations were run with 50 mL hexane, 10 mg pre-catalyst, 150 mg TiBA, 80 mg 1-hexene with a mixed ethylene/hydrogen feed (2 bar, 2% hydrogen) and $[Al_{sMAO(1G)}]_0/[M]_0$ of 200 using sMAO(1G) supported ^{Me_2}SB(Cp,I*)ZrCl$_2$ (**1$_{sMAO(1G)}$**) and ^{Me_2}SB(Cp,I*)ZrMe$_2$ (**8$_{sMAO(1G)}$**).

1$_{sMAO(1G)}$ experienced a slight increase in polymerisation activity when 1-hexene was added to the ethylene/hydrogen system (from 2850 to 3060 $kg_{PE}\ mol_M^{-1}\ h^{-1}\ bar^{-1}$), likely caused by the increased solubility of the polymer chain due to 1-hexene incorporation (Figure 4.14 and Table A4.13).[25] However, **8$_{sMAO(1G)}$** maintained the same polymerisation activity when 1-hexene was introduced to the ethylene/hydrogen system (~2400 $kg_{PE}\ mol_M^{-1}\ h^{-1}\ bar^{-1}$).

DSC analysis showed that T_c, T_m, ΔH_c and ΔH_m for the polymers produced in the presence of hydrogen remained the same when 1-hexene was added; 133 °C, 119 °C, 195 J g^{-1} and 194 J g^{-1} respectively for **1$_{sMAO(1G)}$** in the presence of hydrogen and 133 °C, 119 °C, 203 J g^{-1} and 202 J g^{-1} respectively in the presence of hydrogen and 1-hexene. The constant values of T_c and T_m suggest that there was minimal 1-hexene incorporation in the presence of hydrogen.

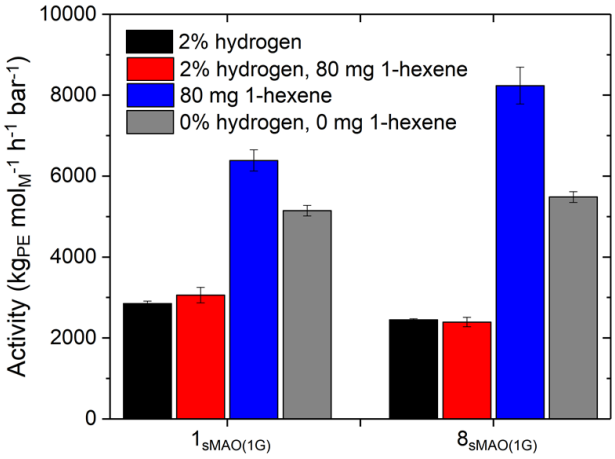


Figure 4.14 Slurry-phase ethylene polymerisation activity using sMAO(1G) supported ^{Me_2}SB(Cp,I*)ZrCl$_2$ (**1$_{sMAO(1G)}$**) and ^{Me_2}SB(Cp,I*)ZrMe$_2$ (**8$_{sMAO(1G)}$**) with 2% hydrogen (black), 2% hydrogen and 80 mg 1-hexene (red), 80 mg 1-hexene (blue) and 0% hydrogen and 0 mg 1-hexene (grey). Polymerisation conditions: $[Al_{sMAO(1G)}]_0/[M]_0$ = 200, TiBA (150 mg), ethylene (2 bar) or ethylene/hydrogen (2 bar, 2%), pre-catalyst (10 mg), hexane (50 mL), 80 °C, 30 minutes for ethylene, ethylene/hydrogen and ethylene/hydrogen/1-hexene run and 5 minutes for ethylene/1-hexene RUNS.

4.4.2 High-throughput ethylene/1-hexene/hydrogen copolymerisation

High-throughput studies were conducted at 80 °C for 1 hour or until 8.3 bar ethylene uptake was reached with 5 mL heptane, 10 µmol TiBA scavenger, 0.05–0.10 mg pre-catalyst, the desired quantity of 1-hexene, $[Al_{sMAO(1G)}]_0/[M]_0$ = 200, 8.3 bar ethylene and 0.8% (0.07 bar) hydrogen supplied by a mixed hydrogen/nitrogen feed. sMAO(1G) supported ^{Me_2}SB(Cp^{Me},I*)ZrCl$_2$ (**4$_{sMAO(1G)}$**), *Z*-^{Me_2}SB(Cp^{nBu},I*)ZrCl$_2$ (***Z*-5$_{sMAO(1G)}$**), ^{Me_2}SB(Cp^{Me},I*)Zr(CH$_2$Ph)$_2$ (**7$_{sMAO(1G)}$**) and ^{Me_2}SB(Cp^{Me},I*)ZrMe$_2$ (**9$_{sMAO(1G)}$**) were studied. It was postulated that combining the increase in ethylene uptake rate observed for ethylene/1-hexene copolymerisation with the significant decrease in polymer molecular weights experienced when hydrogen was introduced to the ethylene polymerisation system should reduce some of the deactivating effects of hydrogen. The incorporation of longer chain α-olefin monomers into the polyethylene chains may also

increase the degree of polymer branching and therefore lower the density of the copolymer.[6]

The ethylene uptake rate profiles showed an initial increase in ethylene uptake rate for ethylene/1-hexene copolymerisation in the presence of hydrogen, which began to decrease after approximately 200 seconds (Figures A4.14 and A4.15). All catalysts experienced an increase in polymerisation activity with 125 µL 1-hexene and 0.8% hydrogen when compared to ethylene/hydrogen homopolymerisation (Figure 4.15a and Table A4.14). However, with 250 µL 1-hexene all catalysts except **7$_{sMAO(1G)}$** experienced a decrease in polymerisation activity compared to the ethylene/hydrogen system with 125 µL 1-hexene.

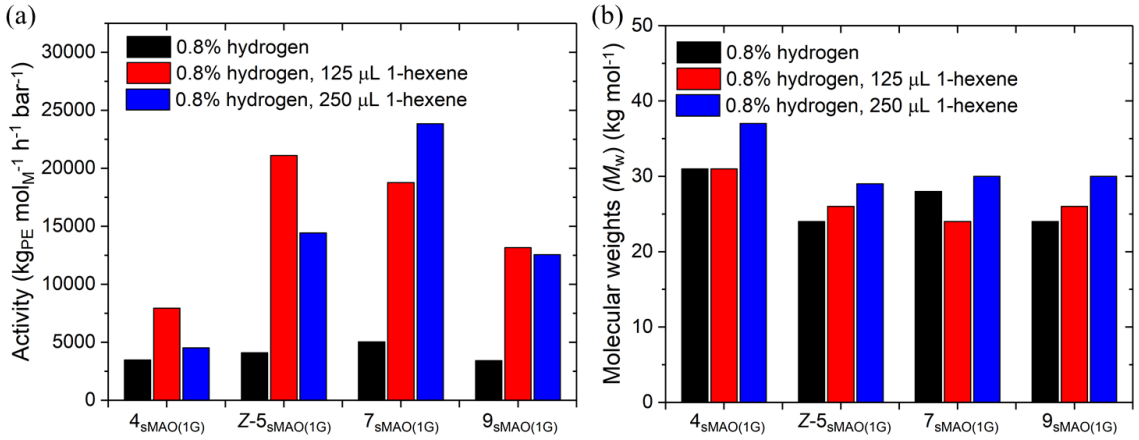


Figure 4.15 Slurry-phase ethylene polymerisation (a) activity and (b) polymer molecular weights (M_w) for sMAO(1G) supported ^{Me_2}SB(Cp^{Me},I*)ZrCl$_2$ (**4$_{sMAO(1G)}$**), *Z*-^{Me_2}SB(Cp^{nBu},I*)ZrCl$_2$ (***Z*-5$_{sMAO(1G)}$**), ^{Me_2}SB(Cp^{Me},I*)Zr(CH$_2$Ph)$_2$ (**7$_{sMAO(1G)}$**) and ^{Me_2}SB(Cp^{Me},I*)ZrMe$_2$ (**9$_{sMAO(1G)}$**) with 0.8% hydrogen (black), 0.8% hydrogen and 125 µL 1-hexene (red) and 0.8% hydrogen and 250 µL 1-hexene (blue). Polymerisation conditions: [Al$_{sMAO(1G)}$]$_0$/[M]$_0$ = 200, TiBA (10 µmol), ethylene (8.3 bar), pre-catalyst (0.05–0.10 mg), heptane (5 mL) and 80 °C. Reactions quenched at 5.5 or 8.3 bar ethylene uptake for co- and homopolymerisation respectively or after 1 hour.

Polymer molecular weights (M_w) were observed to increase slightly when 1-hexene was added to the system, suggesting that competitive monomer coordination between ethylene, hydrogen and 1-hexene hindered termination processes (Figure 4.15b

and Table A4.15). The percentage incorporation of 1-hexene in the polymer chain was determined by $^{13}C\{^{1}H\}$ NMR spectroscopy to be 0.6 and 1.1 mol% with 125 and 250 μL 1-hexene respectively in the presence of 0.8% hydrogen for all catalysts. This is consistent with the values reported for ethylene/1-hexene copolymerisation without hydrogen (approximately 0.5 and 0.9 mol% with 125 and 250 μL 1-hexene respectively). The increase in 1-hexene incorporation was accompanied by the expected decrease in $T_{el,max.}$; 110.5, 105.7 and 103.2 for ***Z*-5$_{sMAO(1G)}$** with 0.8% hydrogen and 0, 125 and 250 μL 1-hexene respectively.

4.4.3 Large scale ethylene/1-hexene/hydrogen copolymerisation

Large scale ethylene/hydrogen/1-hexene polymerisation studies were conducted in 2 L steel reactors with 1 L hexane, 0.5 mmol TEA, 0.025–0.050 g pre-catalyst, $[Al_{sMAO(1G)}]/[M]_0 = 200$ and 8 bar ethylene. Polymerisations were run at 80 °C for 1 hour with either 0 or 0.86% (0.07 bar) hydrogen and 10 mL 1-hexene when required using sMAO supported ^{Me_2}SB(Cp^{Me},I*)ZrCl$_2$ (**3$_{sMAO(1G)}$**), ^{Me_2}SB(Cp,I*)Zr(CH$_2$Ph)$_2$ (**6$_{sMAO(1G)}$**), ^{Me_2}SB(Cp^{Me},I*)Zr(CH$_2$Ph)$_2$ (**7$_{sMAO(1G)}$**) and ^{Me_2}SB(Cp,I*)ZrMe$_2$ (**8$_{sMAO(1G)}$**).

On the addition of 1-hexene to the ethylene/hydrogen system all catalysts except **7$_{sMAO(1G)}$** experienced an initial increase in ethylene uptake rate and an increase in polymerisation activity due to the comonomer effect (Figures 4.16, A4.16 and A4.17 and Table A4.16). The addition of 1-hexene to the ethylene/hydrogen system did not affect polymer molecular weights as competitive monomer coordination reduced termination processes (M_w of approximately 16 kg mol^{-1}). **7$_{sMAO(1G)}$** and **8$_{sMAO(1G)}$** produced polymers with 0.3 and 0.2 mol% 1-hexene incorporation respectively. The polymers produced using **7$_{sMAO(1G)}$** and **8$_{sMAO(1G)}$** showed a 7% decrease in polymer crystallinity (76 and 80% respectively) and a 1 °C decrease in T_m (129 °C for both

catalysts) compared to ethylene/hydrogen homopolymerisation, likely due to the increased amount of chain branching. The addition of 1-hexene to the ethylene/hydrogen system had little effect on the density of the polymers produced using **8**$_{\mathbf{sMAO(1G)}}$ (density above 0.98 g cm^{-3}). However, the density of the polymers produced using **7**$_{\mathbf{sMAO(1G)}}$ decreased by 3% (density of 0.95 g cm^{-3}).

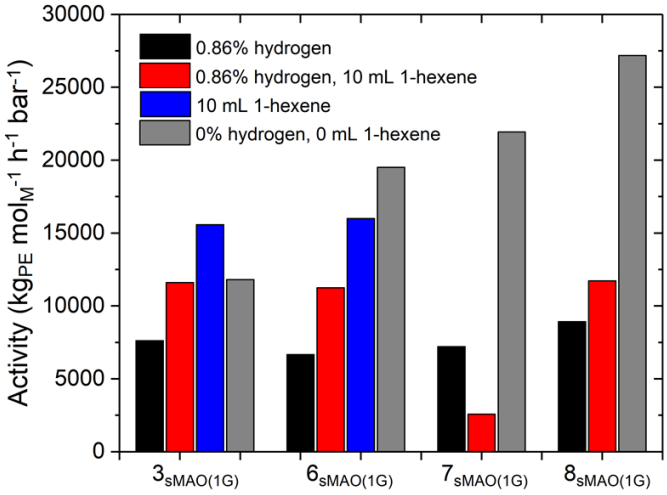


Figure 4.16 Slurry-phase ethylene polymerisation activity and for sMAO(1G) supported ^{Me_2}SB(Cp^{Me},I*)ZrCl$_2$ (**3**$_{\mathbf{sMAO(1G)}}$), ^{Me_2}SB(Cp,I*)Zr(CH$_2$Ph)$_2$ (**6**$_{\mathbf{sMAO(1G)}}$), ^{Me_2}SB(Cp^{Me},I*)Zr(CH$_2$Ph)$_2$ (**7**$_{\mathbf{sMAO(1G)}}$) and ^{Me_2}SB(Cp,I*)ZrMe$_2$ (**8**$_{\mathbf{sMAO(1G)}}$) with 0.86% hydrogen (black), 0.86% hydrogen and 10 mL 1-hexene (red), 10 mL 1-hexene (blue) and 0% hydrogen and 0 mL 1-hexene (grey). Polymerisation conditions: [Al$_{sMAO(1G)}$]$_0$/[M]$_0$ = 200, TEA (0.5 mmol), ethylene (8 bar), pre-catalyst (0.025–0.050 g), hexane (1 L), 80 °C and 1 hour.

4.5 Conclusions

Nine sMAO(1G) supported permethylindenyl *ansa*-bridged zirconocenes were tested for their ethylene/1-hexene copolymerisation ability and hydrogen response in three polymerisation set-ups; laboratory scale 150 mL ampoules, miniaturised high pressure high-throughput screening and high pressure 2 L batch reactors.

It was found that in the presence of 1-hexene the catalysts experienced an initial increase in ethylene uptake rate due to the comonomer effect; *Z*-^{Me_2}SB(Cp$^{n\text{Bu}}$,I*)ZrCl$_2$ (***Z*-5$_{\text{sMAO(1G)}}$**) experienced a peak uptake rate of 20.25 psi mg^{-1} in the high-throughput system after 184 seconds. However, the overall effect of 1-hexene on polymerisation activity was found to vary depending on the catalyst and amount of 1-hexene in the system. The catalysts were found to incorporate a small amount of 1-hexene (maximum of 1.3% for ***Z*-5$_{\text{sMAO(1G)}}$** in the high-throughput system) with an accompanying decrease in polymer melting temperature as the amount of incorporated 1-hexene increased (from 120 to 116 °C for sMAO(1G) supported ^{Me_2}SB(Cp,I*)ZrCl$_2$ (**1$_{\text{sMAO(1G)}}$**) with 0 and 80 mg 1-hexene respectively in the 150 mL ampoule).

In the presence of hydrogen the catalysts experienced a reduction in ethylene uptake rate and polymerisation activity (from 27186 to 8926 $kg_{PE}\,mol_M^{-1}\,h^{-1}\,bar^{-1}$ for sMAO(1G) supported ^{Me_2}SB(Cp,I*)ZrMe$_2$ (**8$_{\text{sMAO(1G)}}$**) with 0 and 0.86% hydrogen respectively in the 2 L batch reactor). However, the catalysts showed resistance to hydrogen deactivation with some ethylene uptake maintained throughout the polymerisations (up to one hour). The catalysts experienced a substantial decrease in polymer molecular weights (M_w) in the presence of hydrogen due to the additional termination process of chain transfer to hydrogen; polymer molecular weights were fifteen times smaller for **8$_{\text{sMAO(1G)}}$** in the presence of 0.86% hydrogen than without

hydrogen (M_w of 15 and 225 kg mol^{-1} respectively). Although the catalysts experienced a large decrease in polymerisation activity when hydrogen was introduced to the system, the low molecular weights of the polymers produced, coupled with the fact that the catalysts were not completely deactivated by hydrogen over the time period studied, makes them potential candidates for the production of ultra-low molecular weight polyethylenes.

The results discussed in this chapter highlight the importance of polymerisation conditions on catalyst activity and polymer molecular weights and indicate how polymer properties can be fine-tuned by changing reaction conditions. The catalysts experienced an increase in polymerisation activity and polymer molecular weights when ethylene pressure was increased from 2 to 8 bar, most likely due to the increased solubility of ethylene at higher pressures and the ready availability of the monomer.[30] Increasing the reactor size and solvent volume was found to lead to a significant increase in catalyst activity and polymer molecular weights, likely due to the decrease in gas-liquid mass transfer limitations on moving to a larger solvent volume (as discussed in Section 3.4.6). Polymerisation activities and polymer molecular weights were also observed to increase when more efficient overhead stirring was introduced in the 2 L batch reactor and high-throughput system due to the increased accessibility of the active catalyst sites. For example, $\mathbf{1}_{\mathbf{sMAO(1G)}}$ showed activities of 4967, 43766 and 30229 $kg_{PE}\,mol_M^{-1}\,h^{-1}\,bar^{-1}$ for ethylene homopolymerisation conducted in the ampoule, high-throughput system and 2 L batch reactor respectively at 80 °C for 1 hour with corresponding molecular weights of 65, 354 and 265 kg mol^{-1}.

4.6 References

1. H. H. El-Nahas, Y. H. Gad, M. A. El-Hady and A. B. Ramadan, *Radiat. Eff. Defects Solids*, 2012, **167**, 367-376.
2. W. Ciesińska, B. Liszyńska and J. Zieliński, *J. Therm. Anal. Calorim.*, 2016, **125**, 1439-1443.
3. SCG Chemicals Company Limited, www.scgchemicals.com/en/.
4. P. S. Umare, A. J. Tiwari, R. Antony, G. L. Tembe and B. Trivedi, *Appl. Organomet. Chem.*, 2007, **21**, 652-660.
5. X. Xu, A. N. Zheng, X. D. Zhou, Y. Guan, Y. F. Pan and H. N. Xiao, *J. Appl. Polym. Sci.*, 2015, **132**, 42214.
6. B. Paredes, R. van Grieken, A. Carrero, I. Suarez and J. B. P. Soares, *Macromol. Chem. Phys.*, 2011, **212**, 1590-1599.
7. J. R. Broach and J. Thorner, *Nature*, 1996, **384**, 14-16.
8. T. R. Boussie, G. M. Diamond, C. Goh, K. A. Hall, A. M. LaPointe, M. Leclerc, C. Lund, V. Murphy, J. A. W. Shoemaker, U. Tracht, H. Turner, J. Zhang, T. Uno, R. K. Rosen and J. C. Stevens, *J. Am. Chem. Soc.*, 2003, **125**, 4306-4317.
9. M. A. R. Meier, R. Hoogenboom and U. S. Schubert, *Macromol. Rapid Commun.*, 2004, **25**, 21-33.
10. M. Goldberg, K. Mahon and D. Anderson, *Adv. Drug Deliv. Rev.*, 2008, **60**, 971-978.
11. V. Busico, R. Pellecchia, F. Cutillo and R. Cipullo, *Macromol. Rapid Commun.*, 2009, **30**, 1697-1708.
12. J. C. W. Chien and T. Nozaki, *J. Polym. Sci. Polym. Chem.*, 1993, **31**, 227-237.
13. K. F. Liu, Q. L. Wu, X. D. Mu, W. Gao and Y. Mu, *Polyhedron*, 2013, **52**, 222-226.
14. Y. Jian-ding, F. Zhi-qiang and W. Wei, *J. Zhejiang Univ., Sci., B*, 2005, **6**, 1009-1014.
15. W. Wang, Z. Q. Fan and L. X. Feng, *Eur. Polym. J.*, 2005, **41**, 2380-2387.
16. J. Klosin, P. P. Fontaine and R. Figueroa, *Acc. Chem. Res.*, 2015, **48**, 2004-2016.
17. J. E. Mark, *Polymer Data Handbook*, Oxford University Press, 2009.
18. G. Rojas, B. Inci, Y. Wei and K. B. Wagener, *J. Am. Chem. Soc.*, 2009, **131**, 17376-17386.
19. M. D. F. V. Marques and R. B. Tiosso, *J. Mater. Sci. Eng. Adv. Tech.*, 2011, **4**, 149-173.
20. L. A. Williams and T. J. Marks, *Organometallics*, 2009, **28**, 2053-2061.
21. W. Kaminsky, *Catal. Today*, 1994, **20**, 257-271.
22. W. Kaminsky and C. Piel, *J. Mol. Catal. A: Chem.*, 2004, **213**, 15-19.
23. C. Piel, P. Starck, J. V. Seppälä and W. Kaminsky, *J. Polym. Sci., Part A: Polym. Chem.*, 2006, **44**, 1600-1612.
24. T. M. Ushakova, E. E. Starchak, V. G. Krasheninnikov, A. A. Samoilenko, P. V. Ivchenko, I. E. Nifant'ev and L. A. Novokshonova, *Kinet. Catal.*, 2012, **53**, 75-83.
25. J. A. M. Awudza and P. J. T. Tait, *J. Polym. Sci. Polym. Chem.*, 2008, **46**, 267-277.

26. A. Novak, M. Bobak, J. Kosek, B. J. Banaszak, D. Lo, T. Widya, W. H. Ray and J. J. de Pablo, *J. Appl. Polym. Sci.*, 2006, **100**, 1124-1136.
27. B. J. Banasazak, D. Lo, T. Widya, W. H. Ray, J. J. de Pablo, A. Novak and J. Kosek, *Macromolecules*, 2004, **37**, 9139-9150.
28. B. Monrabal, J. Sancho-Tello, N. Mayo and L. Romero, *Macromol. Symp.*, 2007, **257**, 71-79.
29. J. Klosin, W. J. Kruper, P. N. Nickias, G. R. Roof, P. De Waele and K. A. Abboud, *Organometallics*, 2001, **20**, 2663-2665.
30. G. Sivalingam, V. Natarajan, K. R. Sarma and U. Parasuveera, *Ind. Eng. Chem. Res.*, 2008, **47**, 8940-8946.
31. W. Kaminsky and H. Lüker, *Makromol. Chem. Rapid. Comm.*, 1984, **5**, 225-228.
32. K. J. Chu, J. B. P. Soares and A. Penlidis, *Macromol. Chem. Phys.*, 2000, **201**, 552-557.
33. A. T. Rappe, W. M. Skiff and C. J. Casewit, *Chem. Rev.*, 2000, **100**, 1435-1456.
34. W. Posch, in *Applied Plastics Engineering Handbook*, ed. M. Kutz, William Andrew Publishing, Oxford, 2011, pp. 23-48.
35. F. Q. Song, R. D. Cannon and M. Bochmann, *J. Am. Chem. Soc.*, 2003, **125**, 7641-7653.
36. M. Bochmann, *Organometallics*, 2010, **29**, 4711-4740.
37. J. E. O'Hara and K. B. Wagener, *Makromol. Chem., Rapid Commun.*, 1993, **14**, 657-662.
38. T. J. Williams, J. V. Lamb, J.-C. Buffet, Z. R. Turner, A. Mingione, V. Busico and D. O'Hare, *Manuscript in preparation*.
39. T. K. Han, H. K. Choi, D. W. Jeung, Y. S. Ko and S. I. Woo, *Macromol. Chem. Phys.*, 1995, **196**, 2637-2647.
40. J. Ramos, V. Cruz, A. Munoz-Escalona and J. Martinez-Salazar, *Polymer*, 2000, **41**, 6161-6169.
41. T. Garoff, S. Johansson, K. Pesonen, P. Waldvogel and D. Lindgren, *Eur. Polym. J.*, 2002, **38**, 121-132.
42. Y. V. Kissin, R. I. Mink, T. E. Nowlin and A. J. Brandolini, *Top. Catal.*, 1999, **7**, 69-88.
43. M. E. Wright, US20130253236, 2012.
44. B. Rieger and C. Janiak, *Angew. Chem.*, 1994, **215**, 35-46.
45. A. Shamiri, M. H. Chakrabarti, S. Jahan, M. A. Hussain, W. Kaminsky, P. V. Aravind and W. A. Yehye, *Materials*, 2014, **7**, 5069-5108.
46. A. Razavi and J. Ferrara, *J. Organomet. Chem.*, 1992, **435**, 299-310.
47. L. S. Santos, *J. Braz. Chem. Soc.*, 2011, **22**, 1827-1840.
48. W. Kaminsky and R. Steiger, *Polyhedron*, 1988, **7**, 2375-2381.
49. V. Busico, R. Cipullo, F. Cutillo, N. Friederichs, S. Ronca and B. Wang, *J. Am. Chem. Soc.*, 2003, **125**, 12402-12403.
50. A. Entezami and P. N. Moghadam, *Polym. Int.*, 2005, **54**, 1326-1329.

Chapter 5

Ring-Opening Polymerisation of *L*-, *D*- and *rac*-Lactide

5.1 Introduction

5.1.1 Overview

Polylactic acids (PLAs) are biodegradable polymers produced from the ring-opening polymerisation (ROP) of lactide.[1-3] The key advantages of PLAs over traditional polyolefin materials are primarily that they are derived from renewable resources and can be broken down into smaller molecules naturally by microorganisms.[1-4] Due to the many different polymer tacticities that can be produced from lactide monomers, single-site catalysts with the ability to control polymer properties are highly sought after.

Given the relative lack of literature available on group 4 metallocenes as initiators for lactide polymerisation, this chapter aims to explore how some of the complexes synthesised in Chapter 2 behave as single-site catalysts for the ROP of lactide monomers. A range of conditions and analytical techniques have been employed to study the kinetics of polymerisation and polymer properties, allowing for the determination of the overall rate equations and polymer structure.

5.2 ROP of Lactide

^{Me_2}SB(Cp,I*)ZrCl$_2$ (**1**), ^{Me_2}SB(Cp^{Me},I*)ZrCl$_2$ (**3**), *Z*-^{Me_2}SB(Cp,I*)ZrCl(O-2,6-Me-C$_6$H$_3$) (***Z*-10**) and *E*-^{Me_2}SB(Cp,I*)ZrCl(O-2,6-^{i}Pr-C$_6$H$_3$) (***E*-11**) were investigated as initiators for the ROP of *L*-, *D*- and *rac*-lactide monomers (Chart 5.1). The effects of monomer stereochemistry, scale, co-initiator concentration, catalyst concentration, temperature and solvent were studied.

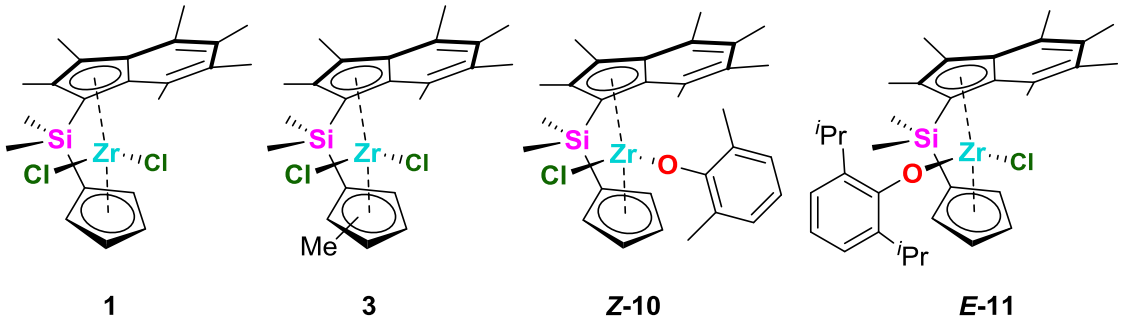


Chart 5.1 Permethylindenyl zirconocene complexes used in this study.

Zirconocene alkoxides tend to show faster rates for the ROP of lactide than zirconocene aryloxidies,[5] however synthesising such species was unsuccessful for this series of complexes. **1** and **3** were selected for this study due to the possibility of reaction with an alcohol co-initiator, such as benzyl alcohol (BnOH), in order to form active aryloxide initiators *in situ*. The relatively high yields of **1** and **3** when compared to ***E*-** and ***Z*-5** enabled a full study of polymerisation kinetics to be conducted. ***Z*-10** and ***E*-11** were selectively synthesised with the aim of testing their efficiency as initiators for the ROP of lactide, both with and without a co-initiator.

5.2.1 Monomer variation

Polymerisations were conducted in Young's tap NMR tubes in chloroform-d_1 with two equivalents of BnOH co-initiator, an initial lactide to catalyst ratio ([LA]$_0$/[M]$_0$) of 50 and an initial lactide monomer concentration ([LA]$_0$) of 0.5 M. Compound **3** was used

as a 60:40 mixture of its *E*- and *Z*-isomers. Polymerisations were run at 80 °C and halted at certain time intervals by submerging the NMR tubes in an ice bath. On completion, the reaction mixture was decanted into −5 °C pentane. The conversion was monitored by ^{1}H NMR spectroscopy. The compounds required no initiation period with some conversion to PLA recorded after 30 minutes for all runs.

Several assumptions have been made throughout the work, which may provide sources of error and limit the overall conclusions. Firstly, it is assumed that by submerging the NMR tubes in an ice bath polymerisation is completely halted at the desired time; evidence for this was obtained by attempting to polymerise at room temperature, which led to 0% conversion to PLA after several hours. Secondly, it is assumed that the addition of benzyl alcohol to the reaction mixture leads to the formation of aryloxide initiators *in situ*, with complete conversion of the permethylindenyl complexes to the active bisbenzyl alcohol species being achieved before polymerisation begins (i.e. initial initiaor concentration is equal to $[cat]_0$). Finally, it is assumed that the data recorded after 30 minutes of polymerisation gives a true representation of the kinetics during the early stages of polymerisation.

5.2.1.1 ROP of *L*-lactide

Plots of $1/[LA]_t$ *vs* Time for the ROP of *L*-lactide using **1** and **3** revealed linear relationships with the expected y-intercept of approximately $2\ M^{-1}$, indicating second-order dependence with respect to monomer concentration (Figure 5.1a and Table 5.1). Plots of $\ln([LA]_0/[LA]_t)$ *vs* Time were also considered. However, these plots showed a non-linear relationship, which is inconsistent with a first-order dependence on monomer concentration. The gradients of the $1/[LA]_t$ *vs* Time plots afforded the observed second-order rate constants (k_{obs}). **1** and **3** showed very similar rates for the

ROP of *L*-lactide; k_{obs} of 1.30 and 1.49 M^{-1} h^{-1} respectively with 77 and 79% conversion to PLA after 5 hours (Figure 5.1b). This suggests that the increase in the steric bulk of the cyclopentadienyl substituent on moving from **1** to **3** did not hinder *L*-lactide monomer insertion. When compared to analogous ^{Me_2}SB(Cp,I*)$HfCl_2$, **1** displayed very similar polymerisation kinetics indicating that there was no preference of *L*-lactide for zirconium or hafnium with this ligand system (77% conversion after 5 hours and k_{obs} of 1.21 ± 0.10 M^{-1} h^{-1} for ^{Me_2}SB(Cp,I*)$HfCl_2$).[6]

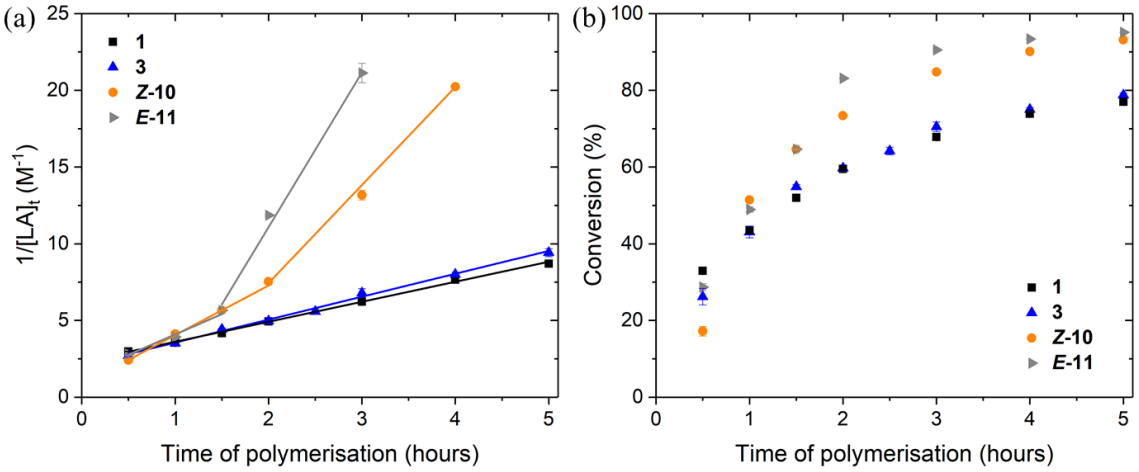


Figure 5.1 (a) $1/[LA]_t$ and (b) percentage conversion to PLA as a function of time of polymerisation for the ROP of *L*-lactide using ^{Me_2}SB(Cp,I*)$ZrCl_2$ (**1**) (black square, k_{obs} = 1.30 ± 0.03 M^{-1} h^{-1}), ^{Me_2}SB(Cp^{Me},I*)$ZrCl_2$ (**3**) (blue triangle, k_{obs} = 1.49 ± 0.02 M^{-1} h^{-1}), *Z*-^{Me_2}SB(Cp,I*)ZrCl(O-2,6-Me-C_6H_3) (***Z*-10**) (orange circle, k_{obs} = 3.23 ± 0.06 M^{-1} h^{-1} (0.5–2 h) and 6.39 ± 0.19 M^{-1} h^{-1} (2–4 h)) and *E*-^{Me_2}SB(Cp,I*)ZrCl(O-2,6-^{i}Pr-C_6H_3) (***E*-11**) (grey right triangle, k_{obs} = 2.65 ± 0.35 M^{-1} h^{-1} (0.5–1.5 h) and 10.08 ± 0.50 M^{-1} h^{-1} (1.5–3 h)). Polymerisation conditions: two equivalents benzyl alcohol co-initiator, chloroform-d_1, 80 °C, $[LA]_0/[M]_0$ = 50 and $[LA]_0$ = 0.5 M.

It has been proposed that a second-order dependence on monomer concentration is consistent with a mechanism requiring two molecules of lactide per active site; in second-order lanthanide systems, Binda *et al.* found that doubling the concentration of monomer caused a four-fold increase in the rate of monomer consumption.[7] This suggests that in order for the two potential active sites of **1**, **3**, ***Z*-10** and ***E*-11** to

polymerise lactide at the same time, four monomer molecules are required to bind to the metal centre. Once the two lactide monomers are bound, the close contact of the monomers associated with each active site could lead to an increased likelihood of a propagation reaction occurring. However, as two monomer molecules are required to bind to the metal centre per active site, steric interactions may limit the rate at which coordination can occur. In coordination-insertion mechanisms insertion of the monomer unit into the growing polymer chain is usually the rate-limiting step. However, for the ROP of *L*-lactide using these initiators it is hypothesised that coordination of the monomer to the metal centre may be the rate-limiting step.

Table 5.1 *L*-Lactide polymerisation using ^{Me_2}SB(Cp,I*)ZrCl$_2$ (**1**), ^{Me_2}SB(Cp^{Me},I*)ZrCl$_2$ (**3**), *Z*-^{Me_2}SB(Cp,I*)ZrCl(O-2,6-Me-C$_6$H$_3$) (***Z*-10**) and *E*-^{Me_2}SB(Cp,I*)ZrCl(O-2,6-^{i}Pr-C$_6$H$_3$) (***E*-11**).[a]

Initiator	k_{obs} (M^{-1} h^{-1})	Conversion [b] (%)	M_n [c] (g mol^{-1})
^{Me_2}SB(Cp,I*)ZrCl$_2$	1.30 ± 0.03	91	2782
^{Me_2}SB(Cp^{Me},I*)ZrCl$_2$	1.49 ± 0.02	93	3183
Z-^{Me_2}SB(Cp,I*)ZrCl(O-2,6-Me-C$_6$H$_3$) [d]	3.23 ± 0.06 6.39 ± 0.19	93	1667
E-^{Me_2}SB(Cp,I*)ZrCl(O-2,6-^{i}Pr-C$_6$H$_3$) [d]	2.65 ± 0.35 10.08 ± 0.50	95	2377

(a) Polymerisation conditions: two equivalents benzyl alcohol co-initiator, chloroform-d_1, 80 °C, $[LA]_0/[M]_0 = 50$ and $[LA]_0 = 0.5$ M; (b) average over two repeats; (c) determined by GPC analysis calibrated with polystyrene standards in THF (correction factor of 0.58);[8] (d) two linear fit regions in the $1/[LA]_t$ *vs* time plot.

***Z*-10** and ***E*-11** demonstrated more complex kinetics than **1** and **3** for the olymerisation of *L*-lactide. These species showed two linear regions in the $1/[LA]_t$ *vs* Time plots with an increase in initial polymerisation rate observed after 1.5 and 2 hours respectively (k_{obs} = 3.23 to 6.39 M^{-1} h^{-1} and k_{obs} = 2.65 to 10.08 M^{-1} h^{-1} for ***Z*-10** and

***E*-11** respectively). ***E*-11** showed the expected y-intercept at approximately 2 M^{-1}, whereas ***Z*-10** showed a y-intercept of approximately 1 M^{-1}. ***Z*-10** and ***E*-11** polymerised *L*-lactide much faster than **1** and **3**, giving 85 and 91% conversion to PLA after 3 hours (Figure 5.1b). It is proposed that the increase in initial rate may be due to the presence of the two different potential leaving groups (halide and aryloxide), which may lead to a mixture of active species where either one or two equivalents of benzyl alcohol co-initiator are substituted.

The kinetics observed for the ROP of *L*-lactide using **1**, **3**, ***Z*-10** and ***E*-11** with BnOH co-initiator were different from those observed for related zirconocenes $Ind_2ZrCl(O\text{-}2,6\text{-}Me\text{-}C_6H_3)$ and *rac*-EBIZrCl(O-2,6-Me-C_6H_3) (Chart 5.2a and b), which displayed first-order dependence on monomer concentration.[5] $Ind_2ZrCl(O\text{-}2,6\text{-}Me\text{-}C_6H_3)$ and *rac*-EBIZrCl(O-2,6-Me-C_6H_3) required longer initiation periods than ***Z*-10** and ***E*-11** and showed lower conversions to PLA after 25 hours under the similar conditions (k_{obs} = 0.004 and 0.002 h^{-1} respectively). **1**, **3**, ***Z*-10** and ***E*-11** showed faster polymerisation rates than neutral bis(ester enolate)s $Cp_2Zr[OC(O^iPr)CMe_2]_2$ and *rac*-EBIZr$[OC(C^iPr)CMe_2]_2$ (Chart 5.2c and d), which showed first-order kinetic data and only reached 7% conversion after 26 and 18 hours respectively at 80 °C with $[LA]_0/[M]_0$ = 200.[9] However, **1**, **3**, ***Z*-10** and ***E*-11** displayed slower rates of polymerisation than $^{Ph_2}CB(Cp,Flu)Zr(OC(O^iPr)CMe_2)_2$ (Chart 5.2e), which showed first-order kinetics and 92% conversion to PLA after 105 minutes at 80 °C with $[LA]_0/[M]_0$ = 50.[9]

1, **3**, ***Z*-10** and ***E*-11** displayed the same second-order dependence on monomer concentration observed for the ROP of *L*-lactide using $[(SalenMe)Mg(\mu\text{-}OCH_2Ph)]_2$ (Chart A5.1a), however experienced lower rates of polymerisation (k_{obs} = 6.6 M^{-1} h^{-1} at 25 °C with $[LA]_0/[M]_0$ = 42).[10] **1**, **3**, ***Z*-10** and ***E*-11** also displayed second-order rate

constants much lower than for the ROP of *L*-lactide using β-diketiminato (BDI) zinc alkoxide [(BDI-OMe)Zn(μ-OCH$_2$Ph)]$_2$Zn(μ-OCH$_2$Ph)$_2$ (k_{obs} = 118.8 M^{-1} h^{-1} at 25 °C with [LA]$_0$/[M]$_0$ = 200; Chart A5.1b),[11] and slower rates of conversion than using lanthanide phenolate [N(SiMe$_3$)$_2$]$_2$La[O-2,4-^{t}Bu-6-CH$_2$NCH$_2$CH$_2$NMe$_2$-C$_6$H$_2$]$_2$ (99% conversion to PLA after 1 minute at room temperature with [LA]$_0$/[M]$_0$ = 100; Chart A5.1c).[7]

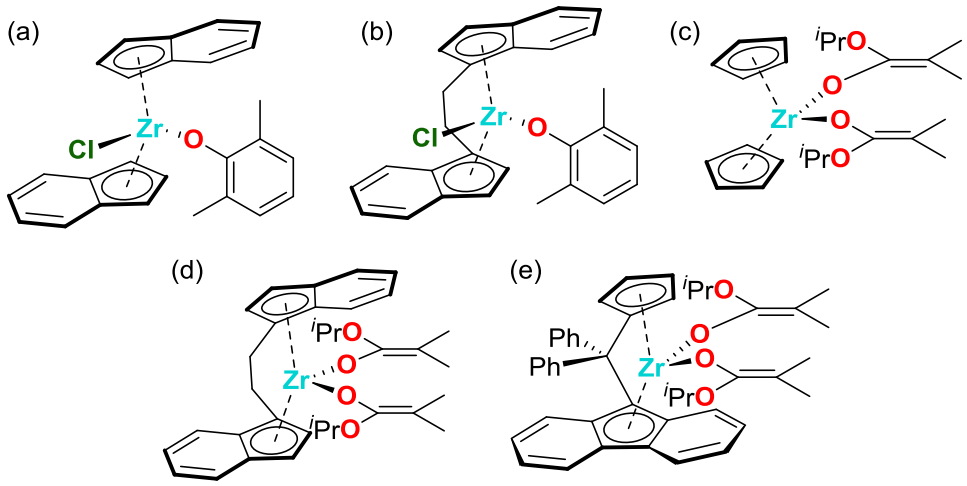


Chart 5.2 Structures of (a) Ind$_2$ZrCl(O-2,6-Me-C$_6$H$_3$),[5] (b) *rac*-EBIZrCl(O-2,6-Me-C$_6$H$_3$),[5] (c) Cp$_2$Zr[OC(O^{i}Pr)CMe$_2$]$_2$,[9] (d) *rac*-EBIZr[OC(C^{i}Pr)CMe$_2$]$_2$[9] and (e) ^{Ph_2}CB(Cp,Flu)Zr(OC(O^{i}Pr)CMe$_2$)$_2$.[9]

The experimental molecular weights (M_n) of the poly-*L*-lactide (PLLA) produced using **1**, **3**, ***Z*-10** and ***E*-11** were within the range of those reported in the literature (2000–20000 g mol^{-1}) (Figure 5.2a and Table 5.1).[5, 9, 12-14] The molecular weights of the PLLA produced using **1** and **3** were approximately half of the theoretical molecular weights ($M_{n,theo.}$) (M_n = 2782 and 3183 g mol^{-1}; $M_{n,theo.}$ = 6660 and 6804 g mol^{-1}), and half of the M_n recorded for Cp$_2$ZrMe(O-2,6-Me-C$_6$H$_3$) (M_n = 7278 g mol^{-1} at 80 °C).[5] $M_{n,theo.}$ was calculated assuming one growing polymer chain per initiator and full conversion to the active species on the addition of benzyl alcohol. As M_n was approximately half of $M_{n,theo.}$ this suggests that polymerisation proceeds *via* two growing polymer chains stemming from the two potential active sites.

The molecular weights of the PLLA produced using ***Z*-10** and ***E*-11** were about a quarter and a third of $M_{n,theo.}$ (M_n = 1667 and 2377 g mol^{-1} respectively; $M_{n,theo.}$ = 6840 and 6948 g mol^{-1} respectively), potentially due to a mixture of active species. The molecular weight distributions (MWD = M_w/M_n) of all the polymers were relatively narrow (M_w/M_n = 1.11–1.14) indicating controlled polymerisation.

The homonuclear decoupled ^{1}H{^{1}H} NMR spectra of the PLLA produced using **1**, **3**, ***Z*-10** and ***E*-11** demonstrated that no epimerisation had occurred. Only the resonance corresponding to the '*mmm*' tetrad was observed in the spectra, confirming the production of isotactic PLA (Figures 5.2b and A5.1).

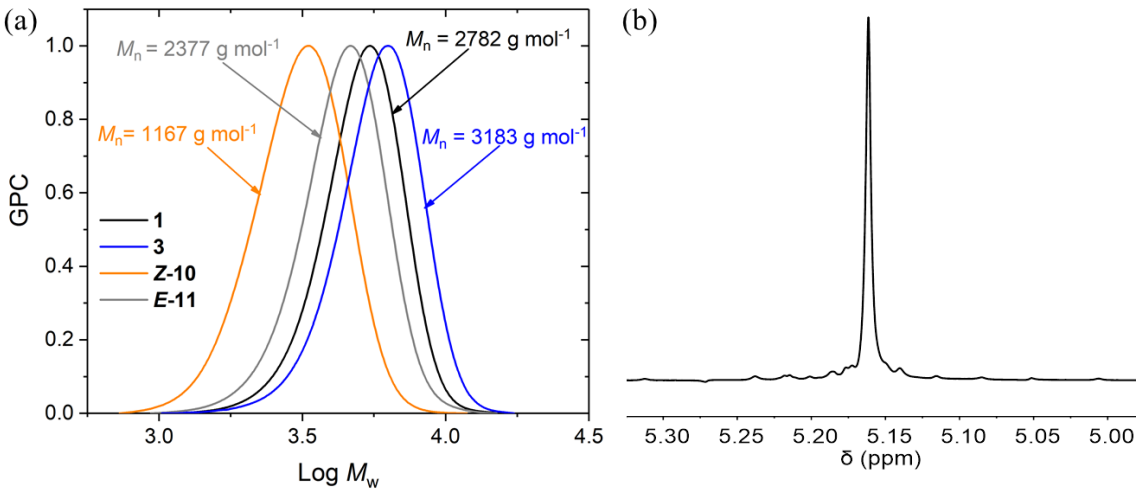


Figure 5.2 (a) GPC plot of the PLLA produced using ^{Me_2}SB(Cp,I*)ZrCl$_2$ (**1**) (black), ^{Me_2}SB(Cp^{Me},I*)ZrCl$_2$ (**3**) (blue), *Z*-^{Me_2}SB(Cp,I*)ZrCl(O-2,6-Me-C$_6$H$_3$) (***Z*-10**) (orange) and *E*-^{Me_2}SB(Cp,I*)ZrCl(O-2,6-^{i}Pr-C$_6$H$_3$) (***E*-11**) (grey); (b) ^{1}H{^{1}H} NMR spectrum (chloroform-d_1, 500 MHz, 298 K) of the PLLA produced using ^{Me_2}SB(Cp,I*)ZrCl$_2$ (**1**). Polymerisation conditions: two equivalents benzyl alcohol co-initiator, chloroform-d_1, 80 °C, [LA]$_0$/[M]$_0$ = 50 and [LA]$_0$ = 0.5 M.

Matrix-assisted laser desorption/ionisation time of flight (MALDI-TOF) mass spectrometry was used to determine the end groups of the polymer. The MALDI-TOF spectra for the PLLA produced using **1**, **3**, ***Z*-10** and ***E*-11** showed a series of peaks *m*/*z* 72 apart, indicative of transesterification, and revealed polymer chains consisting of

PLA repeat units with one –OCH_2Ph and one –OH end group per chain (exemplar spectrum in Figure A5.2). The presence of the benzyl alcohol end group can also be seen in the ^{1}H and $^{13}C\{^{1}H\}$ NMR spectra (exemplar spectra in Figures A5.3 and 5.3).

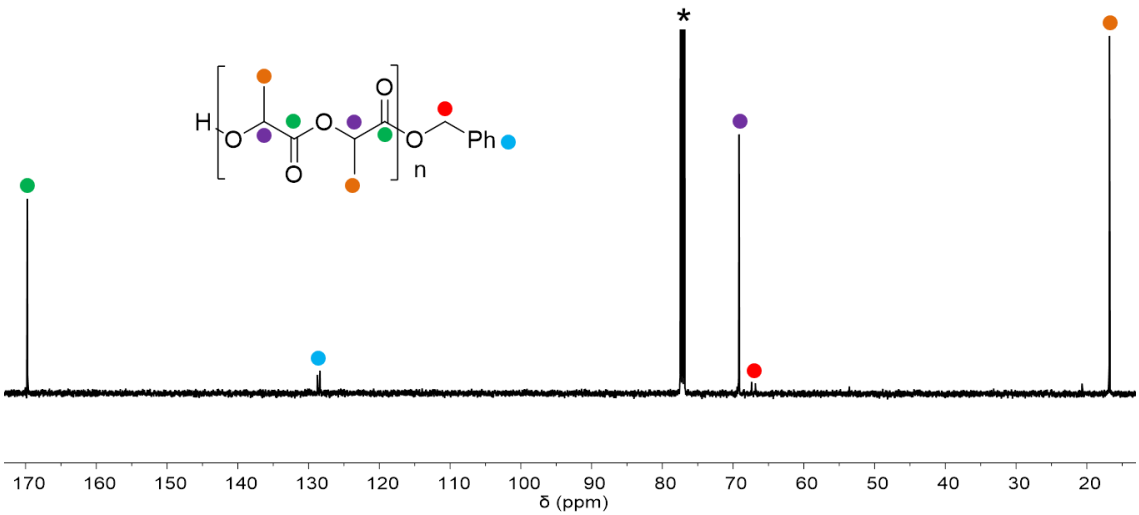


Figure 5.3 $^{13}C\{^{1}H\}$ NMR spectrum (chloroform-d_1, 125 MHz, 298 K) of the PLLA produced using $^{Me_2}SB(Cp,I^*)ZrCl_2$ (**1**). Polymerisation conditions: two equivalents benzyl alcohol co-initiator, chloroform-d_1, 80 °C, $[LA]_0/[M]_0 = 50$ and $[LA]_0 = 0.5$ M.

Differential scanning calorimetry (DSC) analysis of the PLLA produced using **1** and ***E*-11** showed features typical of a semi-crystalline thermoplastic (Figures 5.4 and A5.4).[15, 16] For the PLLA produced using **1**, the glass transition temperature (T_g) was observed as a slight exotherm at 68 °C during the first heating cycle; slightly higher than the T_g typically reported for PLLA (T_g = 50–65 °C).[17-19] T_g is defined as the temperature at which the polymer changes from a hard, rigid or 'glassy' state to a more pliable, compliant or 'rubbery' state.[20] Many factors affect T_g and can explain derivations from the typically reported range. These include sample history, molecular weights, molecular weight distribution, tacticity, the degree of crystallinity and the presence of residual solvent.[18] During the first heating cycle the melting temperature (T_m) of the PLLA produced using **1** was observed at 152 °C, which is lower than the typical literature values of 170–180 °C.[19, 21] This can be justified due to the relatively

low molecular weights of the PLLA; it has been reported that shorter polymer chains decrease the value of T_m as their higher mobility allows for reorientation in the crystalline regions.[22] The flat heat flow during the cooling cycle indicates that the PLLA did not crystallise at the DSC ramp rate (5 °C min^{-1}).[15] However, the sample was shown to crystallise at 90 °C during the second heating cycle, which is consistent with literature reports (T_c = 90–130 °C).[23-25] Crystallisation during the heating cycle is not unusual and is a result of incomplete recrystallisation during the cooling cycle.[15]

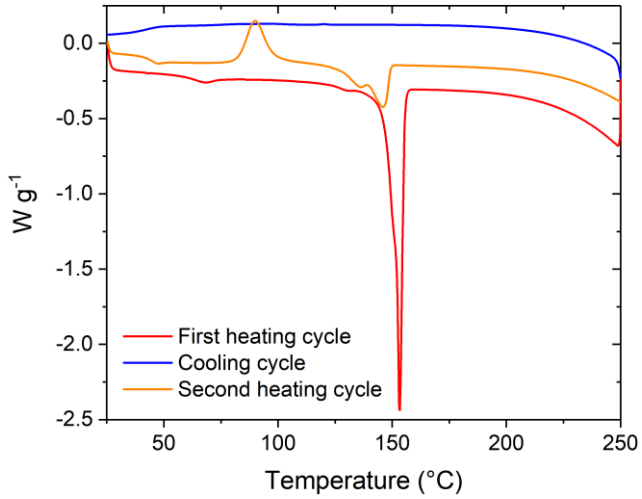


Figure 5.4 DSC plot of the PLLA produced using ^{Me_2}SB(Cp,I*)$ZrCl_2$ (**1**) showing the first heating cycle (red, T_m = 152 °C), cooling cycle (blue) and second heating cycle (orange, T_c = 90 °C, T_m = 136 and 146 °C). Polymerisation conditions: two equivalents benzyl alcohol co-initiator, chloroform-d_1, 80 °C, $[LA]_0/[M]_0$ = 50 and $[LA]_0$ = 0.5 M.

The second heating cycle showed two melting temperatures (T_m = 136 and 146 °C), as has been observed in the literature for different types of polymers.[15, 16, 26] It is proposed that the occurrence of two melting endotherms is due to the existence of two kinds of crystal lamellae with different thicknesses, resulting from two different stages of crystallisation.[15, 27, 28] The presence of two melting temperatures can also be attributed to changes in the polymer during melting and recrystallisation. It has been hypothesised that during the melting/recrystallisation process small and imperfect crystals recrystallise successively to more stable ones.[23] It is therefore suggested that

the lower temperature endotherm occurs from the lamellae initially present, while the higher temperature endotherm occurs from the more crystalline lamellae formed when the partially melted amorphous polymer particles recrystallise.[15, 26, 29]

5.2.1.2 ROP of *D*-lactide

Plots of $1/[LA]_t$ *vs* Time for the ROP of *D*-lactide using **1**, **3**, ***Z*-10** and ***E*-11** revealed second-order dependence on monomer concentration with k_{obs} of 0.72, 2.46, 6.38 and 2.07 $M^{-1} h^{-1}$ and 60, 83, 92 and 79% conversion to PLA after 4 hours respectively (Figure 5.5 and Table 5.2). **1** and **3** showed the expected y-intercept of approximately 2 M^{-1}, while ***Z*-10** and ***E*-11** crossed the y-axis below zero. This indicates that ***Z*-10** and ***E*-11** may have more complex kinetics within the first 30 minutes of polymerisation and leads to doubt in the assumption that the first data point recorded after 30 minutes gives a true representation of the kinetics during the early stages of polymerisation.

1 and ***E*-11** showed rates of polymerisation two and five times slower than *L*-lactide (k_{obs} of 1.30 and 10.08 $M^{-1} h^{-1}$ respectively), giving k_L/k_D of 1.80 and 4.87 respectively and suggesting that the ligand environment favours the insertion of *L*-lactide monomers. The ROP of *D*-lactide using **3** revealed rates of polymerisation faster than those recorded for the polymerisation of *L*-lactide (k_{obs} of 1.49 $M^{-1} h^{-1}$), giving k_L/k_D of 0.61 and demonstrating a preference of the ligand environment for *D*-lactide. ***Z*-10** showed similar rates for the ROP of *L*- and *D*-lactide (k_{obs} of 6.39 and 6.38 $M^{-1} h^{-1}$ respectively with $k_L/k_D = 1.00$), implying no preference for the insertion of either monomer. The k_L/k_D ratios for these initiators were found to be much smaller than those reported by Zhong *et al.* for the polymerisation of *L*- and *D*-lactide with the aluminium alkoxide (cyclohexylsalen)AlO^iPr (Chart A5.1d); k_L/k_D = ~14 with pseudo-first-order rate constants of 0.038 and 0.003 h^{-1} for *L*- and *D*-lactide

polymerisation respectively at 70 °C with $[LA]_0/[M]_0 = 62$.[30] The k_L/k_D ratio for ***Z*-10** was similar to those obtained by Darensbourg *et al.* for the ROP of *L*- and *D*-lactide by a range of amino-acid-based zinc initiators ($k_L/k_D \approx 1$ with pseudo-first-order rate constants between 2.30 and 3.13 h^{-1} at room temperature with $[LA]_0/[M]_0 = 49$).[31]

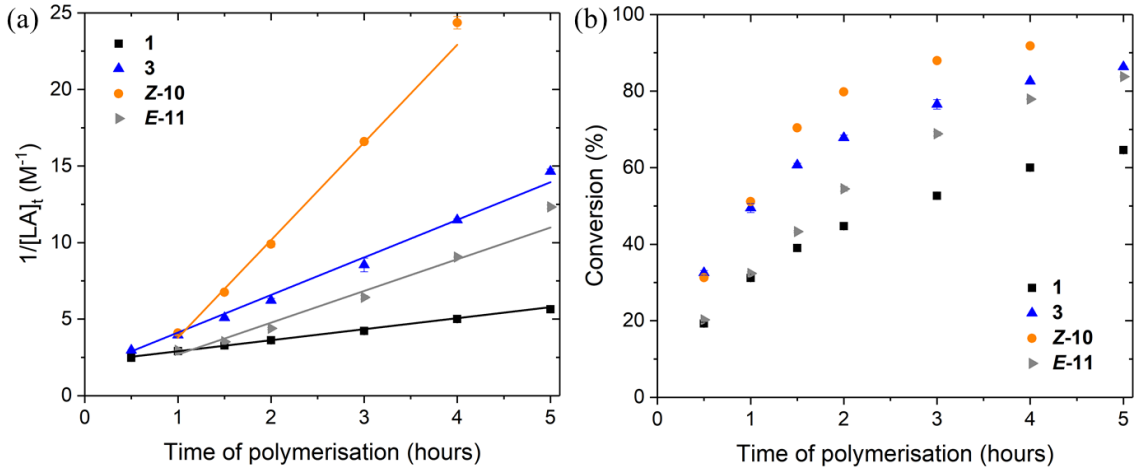


Figure 5.5 (a) $1/[LA]_t$ and (b) percentage conversion to PLA as a function of time of polymerisation for the ROP of *D*-lactide using ^{Me_2}SB(Cp,I*)ZrCl$_2$ (**1**) (black square, k_{obs} = 0.72 ± 0.03 M^{-1} h^{-1}), ^{Me_2}SB(Cp^{Me},I*)ZrCl$_2$ (**3**) (blue triangle, k_{obs} = 2.46 ± 0.07 M^{-1} h^{-1}), *Z*-^{Me_2}SB(Cp,I*)ZrCl(O-2,6-Me-C$_6$H$_3$) (***Z*-10**) (orange circle, k_{obs} = 6.38 ± 0.14 M^{-1} h^{-1}) and *E*-^{Me_2}SB(Cp,I*)ZrCl(O-2,6-^{i}Pr-C$_6$H$_3$) (***E*-11**) (grey right triangle, k_{obs} = 2.07 ± 0.17 M^{-1} h^{-1}). Polymerisation conditions: two equivalents benzyl alcohol co-initiator, chloroform-d_1, 80 °C, $[LA]_0/[M]_0 = 50$ and $[LA]_0 = 0.5$ M.

M_n for the poly-*D*-lactide (PDLA) produced using **1**, **3**, ***Z*-10** and ***E*-11** were approximately a third of $M_{n,theo.}$ (M_n = 2086, 2325, 1828 and 2549 g mol^{-1} respectively; $M_{n,theo.}$ = 6588, 6660, 6732 and 6156 g mol^{-1} respectively) (Figure 5.6a and Table 5.2). This suggests that in addition to polymerisation proceeding *via* two growing polymer chains (giving $M_{n,theo.}$ of 3294, 3330, 3366 and 3078 g mol^{-1} for **1**, **3**, ***Z*-10** and ***E*-11** respectively) there may be free benzyl alcohol present in the reaction mixture acting as a chain transfer agent and leading to a reduction in experimental molecular weight. The presence of free benzyl alcohol in the reaction mixture suggests possible incomplete activation of the permethylindenyl complexes to the active bisbenzyl alcohol substituted

initiators. This leads to doubt in the assumption that the addition of benzyl alcohol leads to full conversion to the bisbenzyl alcohol initiators *in situ* before polymerisation begins and brings a source of error to the overall conclusions. **1** and **3** produced PDLA with molecular weights approximately 30% lower than PLLA (M_n = 2782 and 3183 g mol^{-1} respectively for PLLA), while ***Z*-10** and ***E*-11** produced PDLA with molecular weights similar to PLLA (M_n = 1667 and 2377 g mol^{-1} respectively for PLLA). The molecular weight distributions of the PDLA produced using **1**, **3**, ***Z*-10** and ***E*-11** were narrow, indicating controlled polymerisation (M_w/M_n = 1.09–1.13).

Table 5.2 *D*-Lactide polymerisation using ^{Me_2}SB(Cp,I*)ZrCl$_2$ (**1**), ^{Me_2}SB(Cp^{Me},I*)ZrCl$_2$ (**3**), *Z*-^{Me_2}SB(Cp,I*)ZrCl(O-2,6-Me-C$_6$H$_3$) (***Z*-10**) and *E*-^{Me_2}SB(Cp,I*)ZrCl(O-2,6-^{i}Pr-C$_6$H$_3$) (***E*-11**).[a]

Initiator	k_{obs} (M^{-1} h^{-1})	Conversion [b] (%)	M_n [c] (g mol^{-1})
^{Me_2}SB(Cp,I*)ZrCl$_2$	0.72 ± 0.03	90	2086
^{Me_2}SB(Cp^{Me},I*)ZrCl$_2$	2.46 ± 0.07	91	2325
Z-^{Me_2}SB(Cp,I*)ZrCl(O-2,6-Me-C$_6$H$_3$)	6.38 ± 0.14	92	1828
E-^{Me_2}SB(Cp,I*)ZrCl(O-2,6-^{i}Pr-C$_6$H$_3$)	2.07 ± 0.17	84	2549

(a) Polymerisation conditions: two equivalents benzyl alcohol co-initiator, chloroform-d_1, 80 °C, $[LA]_0/[M]_0$ = 50 and $[LA]_0$ = 0.5 M; (b) average over two repeats; (c) determined by GPC analysis calibrated with polystyrene standards in THF (correction factor of 0.58).[8]

Similarly to the ROP of *L*-lactide, the homonuclear decoupled ^{1}H{^{1}H} NMR spectra of the PDLA produced using **1**, **3**, ***Z*-10** and ***E*-11** showed the production of isotactic PDLA (Figures 5.6b and A5.5). The MALDI-TOF mass spectra showed a series of peaks *m/z* = 72 apart, indicative of transesterification, while the presence of a benzyl alcohol end group was observed in the ^{1}H and ^{13}C{^{1}H} NMR spectra.

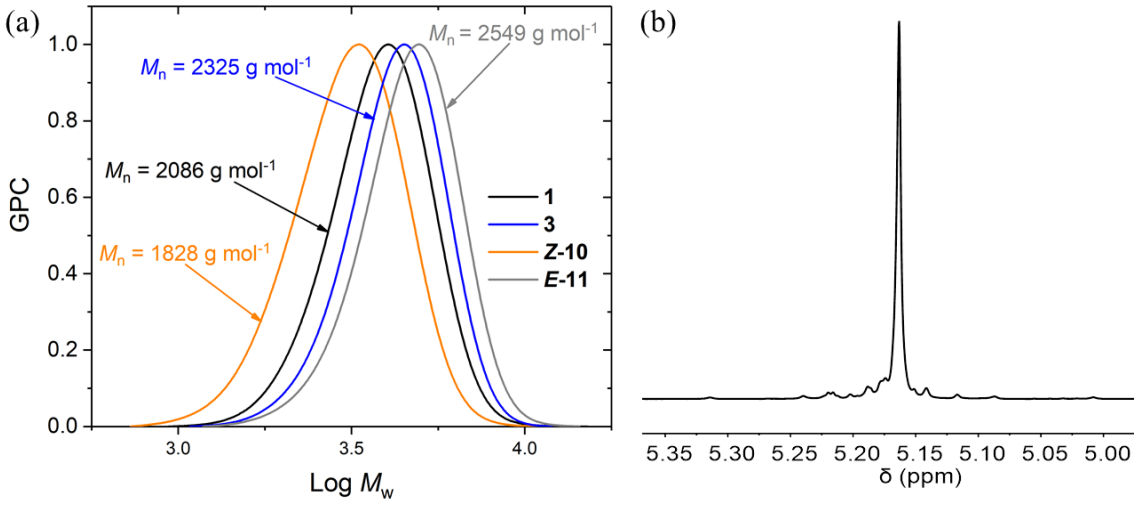


Figure 5.6 (a) GPC plot of the PDLA produced using ^{Me_2}SB(Cp,I*)ZrCl$_2$ (**1**) (black), ^{Me_2}SB(Cp^{Me},I*)ZrCl$_2$ (**3**) (blue), *Z*-^{Me_2}SB(Cp,I*)ZrCl(O-2,6-Me-C$_6$H$_3$) (***Z*-10**) (orange) and *E*-^{Me_2}SB(Cp,I*)ZrCl(O-2,6-^{i}Pr-C$_6$H$_3$) (***E*-11**) (grey); (b) ^{1}H{^{1}H} NMR spectrum (chloroform-d_1, 500 MHz, 298 K) of the PDLA produced using ^{Me_2}SB(Cp,I*)ZrCl$_2$ (**1**). Polymerisation conditions: two equivalents benzyl alcohol co-initiator, chloroform-d_1, 80 °C, $[LA]_0/[M]_0 = 50$ and $[LA]_0 = 0.5$ M.

Complementary to the PLLA produced using **1** and ***E*-11**, DSC analysis of the PDLA produced using **1**, **3** and ***E*-11** showed features typical of a semi-crystalline thermoplastic (Figures 5.7 and A5.6). For the PDLA produced using **1**, T_m was observed at 143 °C during the first heating cycle; approximately 10 °C lower than for PLLA. This can be attributed to the lower molecular weights of the PDLA when compared to PLLA, which lowers the melting point.[22, 32] The second heating cycle showed T_c at 104 °C and two melting temperatures at 126 and 138 °C; approximately 10 °C higher and lower respectively than the values recorded for PLLA. The higher value of T_c indicates a slower rate of crystallisation for PDLA when compared to PLLA, while the lower values of T_m indicate a less ordered crystalline morphology.

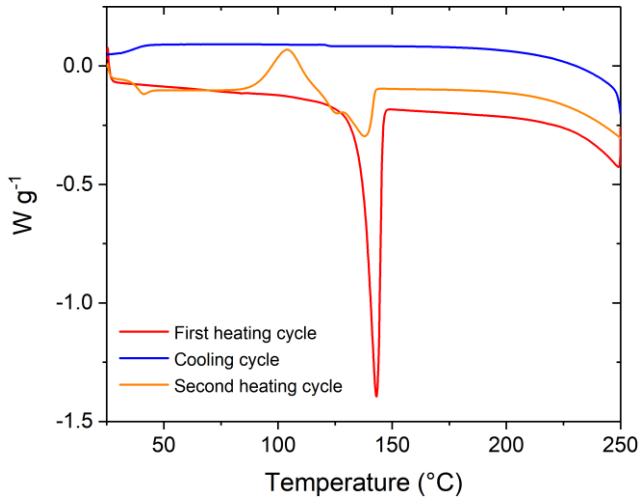


Figure 5.7 DSC plot of the PDLA produced using ^{Me_2}SB(Cp,I*)ZrCl$_2$ (**1**) showing the first heating cycle (red, T_m = 143 °C), cooling cycle (blue) and second heating cycle (orange, T_c = 104 °C, T_m = 126 and 138 °C). Polymerisation conditions: two equivalents benzyl alcohol co-initiator, chloroform-d_1, 80 °C, $[LA]_0/[M]_0$ = 50 and $[LA]_0$ = 0.5 M.

5.2.1.3 ROP of *rac*-lactide

Plots of $1/[LA]_t$ *vs* Time for the ROP of *rac*-lactide using **1**, **3**, ***Z*-10** and ***E*-11** revealed second-order dependence on monomer concentration (Figure 5.8 and Table 5.3). ***Z*-10** polymerised *rac*-lactide the fastest, showing 91% conversion to PLA after 4 hours and k_{obs} of 5.89 M^{-1} h^{-1}. Similar to the ROP of *D*-lactide, **1** and **3** showed the expected y-intercept of approximately 2 M^{-1}, while ***Z*-10** and ***E*-11** crossed the y-axis below zero. **1**, **3** and ***E*-11** demonstrated a large decrease in rate for the ROP of *rac*-lactide compared to *L*-lactide; 48, 64 and 86% conversion to PLA after 5 hours and k_{obs} of 0.29, 0.60 and 3.16 M^{-1} h^{-1} respectively. Jones *et al.* demonstrated similar results for zirconium and hafnium alkoxide complexes of a bipyrrolidine derived salan ligand (Chart A5.2a); the complexes were 37 and 55% more active for the polymerisation of *L*-lactide than *rac*-lactide respectively (at 20 and 70 °C respectively with $[LA]_0/[M]_0$ = 100).[33, 34] **1** and **3** also showed a decrease in rate when polymerising *rac*-lactide compared to *D*-lactide with 49 and 64% conversion to PLA recorded after 5 hours and k_{obs} of 0.29 and 0.60 M^{-1} h^{-1} respectively. Conversely, ***E*-11** showed a 53%

increase in rate when polymerising *rac*-lactide compared to *D*-lactide (k_{obs} = 3.16 and 2.07 M^{-1} h^{-1} respectively). ***Z*-10** only showed a slightly lower rate for the ROP of *rac*-lactide compared to *L*- and *D*-lactide (k_{obs} = 5.89, 6.39 and 6.38 M^{-1} h^{-1}).

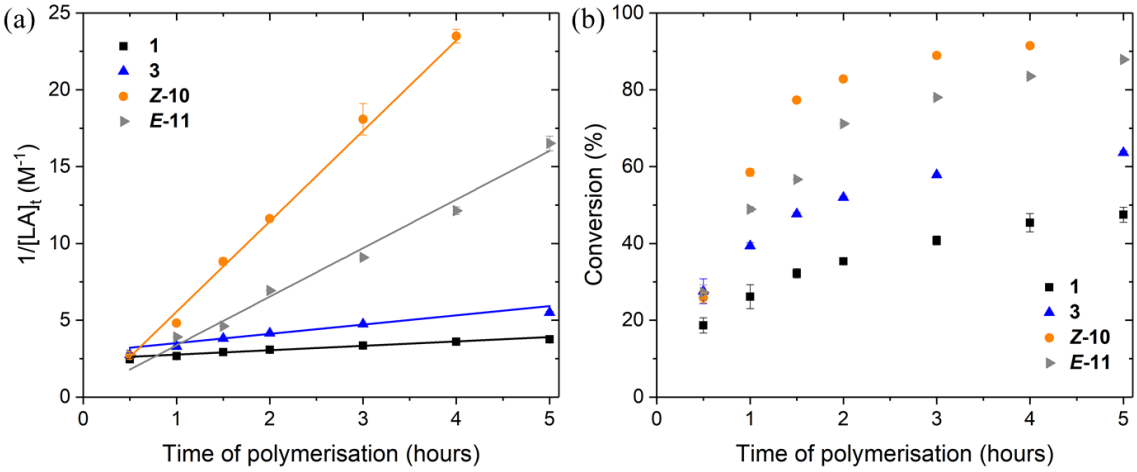


Figure 5.8 (a) $1/[LA]_t$ and (b) percentage conversion to PLA as a function of time of polymerisation for the ROP of *rac*-lactide using ^{Me_2}SB(Cp,I*)ZrCl$_2$ (**1**) (black square, k_{obs} = 0.29 ± 0.03 M^{-1} h^{-1}), ^{Me_2}SB(Cp^{Me},I*)ZrCl$_2$ (**3**) (blue triangle, k_{obs} = 0.60 ± 0.06 M^{-1} h^{-1}), *Z*-^{Me_2}SB(Cp,I*)ZrCl(O-2,6-Me-C$_6$H$_3$) (***Z*-10**) (orange circle, k_{obs} = 5.89 ± 0.25 M^{-1} h^{-1}) and *E*-^{Me_2}SB(Cp,I*)ZrCl(O-2,6-^{i}Pr-C$_6$H$_3$) (***E*-11**) (grey right triangle, k_{obs} = 3.16 ± 0.43 M^{-1} h^{-1}). Polymerisation conditions: two equivalents benzyl alcohol co-initiator, chloroform-d_1, 80 °C, $[LA]_0/[M]_0$ = 50 and $[LA]_0$ = 0.5 M.

Table 5.3 *rac*-Lactide polymerisation using ^{Me_2}SB(Cp,I*)ZrCl$_2$ (**1**), ^{Me_2}SB(Cp^{Me},I*)ZrCl$_2$ (**3**), *Z*-^{Me_2}SB(Cp,I*)ZrCl(O-2,6-Me-C$_6$H$_3$) (***Z*-10**) and *E*-^{Me_2}SB(Cp,I*)ZrCl(O-2,6-^{i}Pr-C$_6$H$_3$) (***E*-11**).[a]

Initiator	k_{obs} (M^{-1} h^{-1})	Conversion [b] (%)	M_n [c] (g mol^{-1})
^{Me_2}SB(Cp,I*)ZrCl$_2$	0.29 ± 0.03	89	1060
^{Me_2}SB(Cp^{Me},I*)ZrCl$_2$	0.60 ± 0.06	94	1983
Z-^{Me_2}SB(Cp,I*)ZrCl(O-2,6-Me-C$_6$H$_3$)	5.89 ± 0.25	92	1153
E-^{Me_2}SB(Cp,I*)ZrCl(O-2,6-^{i}Pr-C$_6$H$_3$)	3.16 ± 0.43	95	2260

(a) Polymerisation conditions: two equivalents benzyl alcohol co-initiator, chloroform-d_1, 80 °C, $[LA]_0/[M]_0$ = 50 and $[LA]_0$ = 0.5 M; (b) average over two repeats; (c) determined by GPC analysis calibrated with polystyrene standards in THF (correction factor of 0.58).[8]

Surprisingly, ^{Me_2}SB(Cp,I*)HfCl$_2$ was found to polymerise *rac*-lactide much slower than the zirconium analogue **1** (k_{obs} = 0.06 M^{-1} h^{-1} with 22% conversion after 5 hours),[6] despite the similarity in their geometric parameters and their similar rates when polymerising *L*-lactide. This is in contrast to the effects seen for the polymerisation of *rac*-lactide using M($O_2CN^iPr_2$)$_4$ (M = Zr and Hf) where similar rates of conversion to PLA were observed after 13 hours; 95 and 92% conversion for Zr and Hf respectively with isopropanol (^{i}PrOH) co-initiator at 100 °C with $[LA]_0/[M]_0$ = 90.[35] The lower rate of *rac*-lactide polymerisation observed for ^{Me_2}SB(Cp,I*)HfCl$_2$ compared to **1** is opposite to the trend reported by Jones *et al*. when using zirconium and hafnium alkoxide species of bipyrrolidine derived salan ligands (Chart A5.2a); the zirconium complex required 8 hours to reach 94% conversion, while the hafnium complex showed 91% conversion after only 4 hours (70 °C with $[LA]_0/[M]_0$ = 100).[33, 34]

The kinetics observed for the polymerisation of *rac*-lactide using **1**, **3**, ***Z*-10** and ***E*-11** are different from those observed using $Cp_2ZrMe(O\text{-}2,6\text{-}Me\text{-}C_6H_3)$, Pn*(H)Zr(*S*-OCH($CH_3$)$C_6H_5$)$_3$ and Pn*(H)Zr(*rac*-OCH(CH_3)C_6H_5)$_3$ (where Pn* = permethylpentalene, Chart A5.2b), which displayed first-order dependence on monomer concentration. **1**, **3**, ***Z*-10** and ***E*-11** displayed faster rates of polymerisation than $Cp_2ZrMe(O\text{-}2,6\text{-}Me\text{-}C_6H_3)$ (k_{obs} = 0.009 h^{-1} at 80 °C),[5] however were much slower for the ROP of *rac*-lactide than Pn*(H)Zr(*S*-OCH(CH_3)C_6H_5)$_3$ (k_{obs} = 1.34 h^{-1} at 80 °C) and Pn*(H)Zr(*rac*-OCH(CH_3)C_6H_5)$_3$ (k_{obs} = 1.67 h^{-1} at 80 °C) under similar conditions.[13]

Second-order dependence on *rac*-lactide is unusual but not unprecedented, and has been demonstrated with various metal initiators including calcium, strontium, yttrium and indium.[36-39] **1**, **3**, ***Z*-10** and ***E*-11** displayed second-order rate constants lower than $Ca_2(DBP)_4(DME)_4$(μ-DME), $Sr_2(DBP)$(μ-$DBP)_3(DME)_3$ (where H-DBP is

di-tert-butylphenol and DME is dimethoxyethane, Chart A5.2c and d) and zwitterionic $Y(O_2NN')(HO_2NN')$ (where O_2NN' is $^{Me_2}NCH_2CH_2N(CH_2\text{-}2\text{-}O\text{-}3,5\text{-}^{t}Bu\text{-}C_6H_2)_2$, Chart A5.2e) in the presence of benzylamine ($BnNH_2$) co-initiator; k_{obs} = 31.8 M^{-1} h^{-1} ($[LA]_0/[M]_0$ = 400),[36] 16.8 M^{-1} h^{-1} ($[LA]_0/[M]_0$ = 400)[36] and 48.6 M^{-1} h^{-1} ($[LA]_0/[M]_0$ = 100)[37] respectively in THF at room temperature. However, **1**, **3**, ***Z*-10** and ***E*-11** showed faster second-order rate constants for the polymerisation of *rac*-lactide than $In(^{Ts}NCH_2CH_2NCH_2C_5H_5N)(O^{i}Pr)Cl\{Li(THF)\}$ (where Ts is $CH_3C_6H_4SO_2$, Chart A5.2f), which experienced 83% conversion to PLA after 98 hours and k_{obs} of 0.049 M^{-1} h^{-1} at 70 °C with $[LA]_0/[M]_0$ = 100.[38]

The molecular weights (M_n) of the polymers produced from the ROP of *rac*-lactide using **1**, **3**, ***Z*-10** and ***E*-11** were lower than from the ROP of *L*- and *D*-lactide (Figure 5.9a and Table 5.3). The recorded M_n were also between three and six times smaller than $M_{n,theo.}$ (M_n = 1060, 1983, 1153 and 2260 g mol^{-1} respectively; $M_{n,theo.}$ = 6516, 6876, 6732 and 6948 g mol^{-1} respectively). Similar to the ROP of *D*-lactide, this suggests that polymerisation proceeds *via* two growing polymer chains and the likely presence of unreacted benzyl alcohol co-initiator acting as a chain transfer agent. It is also possible that the differences between the theoretical and experimental molecular weights are due to catalyst decomposition, which may be significant at longer polymerisation times. The molecular weight distributions were narrow for all polymers, indicating well-controlled polymerisation (M_w/M_n = 1.09–1.16).

The homonuclear decoupled $^1H\{^1H\}$ NMR spectra of the polymers produced from the ROP of *rac*-lactide using **1**, **3**, ***Z*-10** and ***E*-11** confirmed the production of heterotactic enriched PLA; P_r = 0.81, 0.84, 0.77 and 0.83 respectively, where P_r is the probability of forming racemic linkages (Figures 5.9b and A5.7). P_r was determined

using the probabilities calculated by Coudane *et al.*;[40] each tetrad signal was analysed and the average value calculated. As the formation of heterotactic PLA requires the alternative incorporation of *L*- and *D*-lactide monomers, it is likely that polymerisation proceeds *via* a chain-end control mechanism.[13] The MALDI-TOF mass spectra of the polymers showed peaks consistent with transesterification processes and revealed polymer chains with one –OCH_2Ph and one –OH end group.

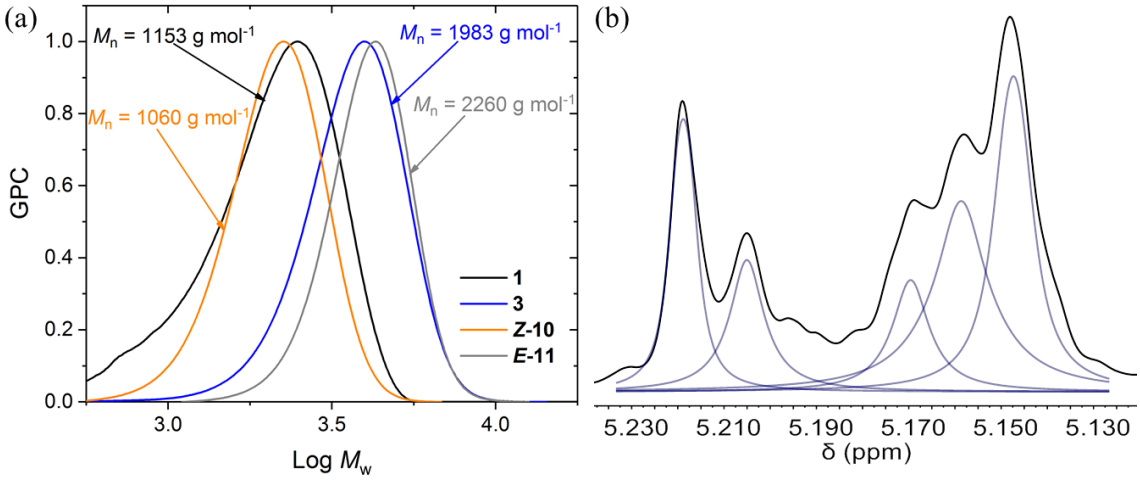


Figure 5.9 (a) GPC plot of the poly-*rac*-lactide produced using ^{Me_2}SB(Cp,I*)$ZrCl_2$ (**1**) (black), ^{Me_2}SB(Cp^{Me},I*)$ZrCl_2$ (**3**) (blue), *Z*-^{Me_2}SB(Cp,I*)ZrCl(O-2,6-Me-C_6H_3) (***Z*-10**) (orange) and *E*-^{Me_2}SB(Cp,I*)ZrCl(O-2,6-^{i}Pr-C_6H_3) (***E*-11**) (grey); (b) $^1H\{^1H\}$ NMR spectrum (chloroform-d_1, 500 MHz, 298 K) of the poly-*rac*-lactide produced using *Z*-^{Me_2}SB(Cp,I*)ZrCl(O-2,6-Me-C_6H_3) (***Z*-10**) (P_r = 0.77). Polymerisation conditions: two equivalents benzyl alcohol co-initiator, chloroform-d_1, 80 °C, $[LA]_0/[M]_0$ = 50 and $[LA]_0$ = 0.5 M.

Considering that the poly-*rac*-lactides produced using **1** and **3** are heterotactic, it is difficult to explain why the polymerisation of *L*- and *D*-lactide was significantly faster than the polymerisation of *rac*-lactide for these initiators. It is postulated that the two stereochemical control mechanisms (enantiomorphic site-control and chain-end control) were in competition during the ROP *rac*-lactide using **1** and **3**. During enantiomorphic site-control the configuration of the next inserted monomer is determined by the configuration of the surrounding ligand and catalyst stereochemistry, whereas in chain-end-control the stereochemistry of the previous monomer determines

the configuration of the next inserted monomer.[2] For **1**, k_{obs} follows the order *L*- > *D*- > *rac*-lactide, whereas for **3** k_{obs} follows the order *D*- > *L*- > *rac*-lactide. The ligand environment of **1** therefore has a preference for *L*-lactide monomer insertion, while the ligand environment of **3** has a preference for *D*-lactide monomer insertion (k_L/k_D = 1.80 and 0.61 respectively). The change in preference for *L*- and *D*-lactide on moving from **1** to **3** is possibly due to the sterics of the systems. For the ROP of *rac*-lactide using **1** and **3**, a chain-end-control mechanism must dominate with *racemic* enchainment favoured in order to permit the alternating insertion of *L*- and *D*- lactide monomer units that make up heterotactic PLA. It is postulated that the ROP of *rac*-lactide using **1** and **3** is slower than the ROP of pure *L*- and *D*-lactide as the ligand environment inhibits coordination of the unfavoured monomer.

For ***Z*-10**, k_{obs} follows the order *L*- ≈ *D*- > *rac*-lactide ($k_L/k_D \approx 1$). The ligand environment therefore shows no preference for *L*- or *D*-lactide and does not inhibit coordination of either monomer. This is reflected in the k_{obs} value for the ROP of *rac*-lactide, which is only 8% lower than the k_{obs} recorded for the ROP of pure *L*- and *D*-lactide and is the largest k_{obs} recorded for the ROP of *rac*-lactide with this series of initiators. For ***E*-11**, k_{obs} follows the order *L*- ≈ *rac*- > *D*-lactide ($k_L/k_D \approx 3.18$); the ligand environment shows a strong preference for the insertion of *L*-lactide monomers. Similarly to **1** and **3**, it is proposed that during the polymerisation of *rac*-lactide enantiomorphic site-control and chain-end control mechanisms compete, with the ligand environment inhibiting the insertion of *D*-lactide monomers.

5.2.2 Scale dependency

The scale of *L*- and *rac*-lactide polymerisation using **1** and **3** was increased five-fold and stirring was introduced (Figures 5.10 and A5.8 and Table 5.4). Polymerisations

were conducted in 5 mL ampoules at 80 °C in toluene with two equivalents of benzyl alcohol co-initiator, $[LA]_0/[M]_0 = 50$ and $[LA]_0 = 0.5$ M. Polymerisation was halted at the desired time by decanting the solution into −5 °C pentane. Second-order dependence on monomer concentration was observed in all cases. On the smaller scale, **1** showed the expected y-intercept of approximately 2 M^{-1} for the ROP of *L*- and *rac*-lactide. However, on the larger scale, the ROP of *L*- and *rac*-lactide using **1** crossed the y-axis at –0.5 and 0.5 M^{-1} respectively. This suggests that more complex kinetics may occur once the solution is agitated.

The rate of polymerisation was observed to be significantly faster on the larger scale; for the ROP of *L*- and *rac*-lactide using **1** $k_{obs} = 1.69$ and 1.05 M^{-1} h^{-1} on the small scale and $k_{obs} = 4.91$ and 4.31 M^{-1} h^{-1} on the larger scale. It is proposed that the substantial increase in rate on moving to larger scale was due to the introduction of stirring, in addition to overcoming the potential mass and heat transfer limitations of the small scale. As polymerisation proceeds the viscosity of the reaction medium increases, leading to a slower rate of diffusion, poor mixing and a reduction in polymerisation rate.[41] The formation of a viscous reaction medium also reduces heat transfer rate at the reactor walls, potentially leading to hot spots, which may cause catalyst degradation. A small scale system with no stirring amplifies these effects.[41]

The heterotacticity of the polymer produced from the ROP *rac*-lactide using **1** and **3** was maintained on the larger scale; $P_r = 0.81$ and 0.84 on the small scale and $P_r = 0.80$ and 0.85 on the larger scale. The MALDI-TOF mass spectrum of the PLLA produced using **1** on the larger scale displayed peaks *m/z* 72 apart, indicating that increased scale and the introduction of stirring did not eliminate transesterification processes.

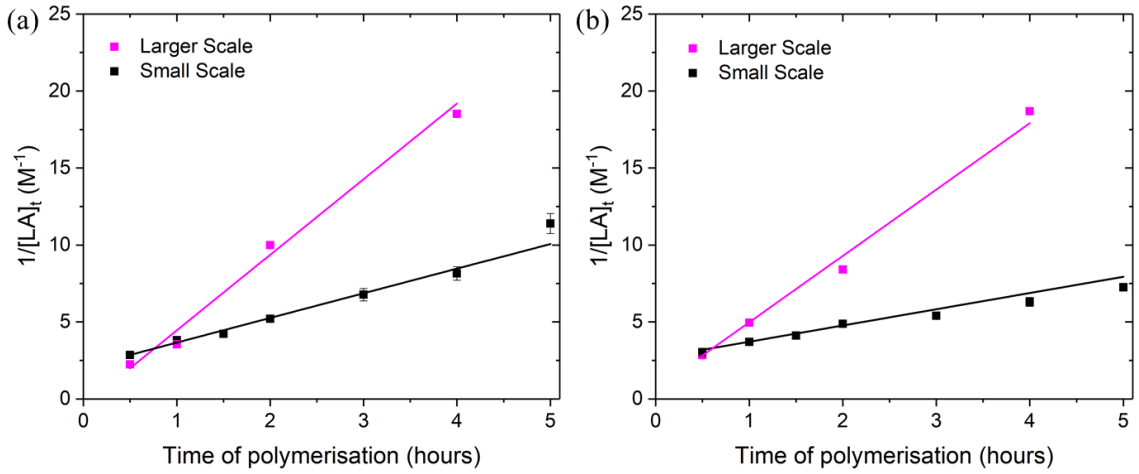


Figure 5.10 $1/[LA]_t$ as a function of time of polymerisation using ^{Me_2}SB(Cp,I*)ZrCl$_2$ (**1**) as an initiator for the ROP of (a) *L*-lactide on a small scale (black, k_{obs} = 1.69 ± 0.03 M^{-1} h^{-1}) and larger scale (pink, k_{obs} = 4.91 ± 0.65 M^{-1} h^{-1}); (b) *rac*-lactide on a small scale (black, k_{obs} = 1.05 ± 0.10 M^{-1} h^{-1}) and larger scale (pink, k_{obs} = 4.31 ± 0.16 M^{-1} h^{-1}). Small scale polymerisation conditions: lactide (40 mg), two equivalents benzyl alcohol co-initiator, toluene-d_8 (0.56 mL), 80 °C, $[LA]_0/[M]_0$ = 50 and $[LA]_0$ = 0.5 M. Larger scale polymerisation conditions: lactide (200 mg), two equivalents of benzyl alcohol co-initiator, toluene (2.80 mL), 80 °C, $[LA]_0/[M]_0$ = 50 and $[LA]_0$ = 0.5 M.

Table 5.4 *L*- and *rac*-lactide polymerisation using ^{Me_2}SB(Cp,I*)ZrCl$_2$ (**1**) and ^{Me_2}SB(Cp^{Me},I*)ZrCl$_2$ (**3**) on a small and larger scale.[a, b]

Initiator	Lactide	k_{obs} Small Scale[c]	k_{obs} Larger Scale[c]
^{Me_2}SB(Cp,I*)ZrCl$_2$	*L*	1.69 ± 0.03	4.91 ± 0.65
^{Me_2}SB(Cp,I*)ZrCl$_2$	*rac*	1.05 ± 0.10	4.31 ± 0.16
^{Me_2}SB(Cp^{Me},I*)ZrCl$_2$	*L*	5.10 ± 0.32	6.29 ± 0.10
^{Me_2}SB(Cp^{Me},I*)ZrCl$_2$	*rac*	1.42 ± 0.05	5.82 ± 0.44

(a) Small scale polymerisation conditions: lactide (40 mg), two equivalents benzyl alcohol co-initiator, toluene-d_8 (0.56 mL), 80 °C, $[LA]_0/[M]_0$ = 50 and $[LA]_0$ = 0.5 M; (b) larger scale polymerisation conditions: lactide (200 mg), two equivalents benzyl alcohol co-initiator, toluene (2.80 mL), 80 °C, $[LA]_0/[M]_0$ = 50 and $[LA]_0$ = 0.5 M; (c) M^{-1} h^{-1}.

The molecular weights of the PLLA produced using **3** on the larger scale were recorded as polymerisation proceeded (Figure A5.9). M_n were observed to increase

linearly as the percentage conversion to PLA increased, while the molecular weight distribution remained constant (M_w/M_n = 1.11), indicating controlled polymerisation. It was found that the experimental polymer molecular weights were consistently about 20% lower than the theoretical molecular weights, attributed to unreacted benzyl alcohol acting as a chain transfer agent. The final molecular weights of the PLLA produced using **3** on the larger scale were similar to the small scale; M_n = 2801 and 2438 g mol^{-1} respectively.

5.2.3 Co-initiator concentration dependency

The benzyl alcohol co-initiator concentration was varied in order to determine the likelihood of lactide polymerisation using **1** and **3** proceeding *via* a coordination-insertion or activated monomer mechanism. During an activated monomer mechanism the nucleophilic co-initiator is an external molecule, which initiates polymerisation *via* attack of the carbonyl group of the lactide monomer. An activated monomer mechanism follows the rate law defined in Equations 5.1 and 5.2.[42] However, in a coordination-insertion mechanism the nucleophile is an inherent part of the active catalyst and follows the rate law defined in Equations 5.3 and 5.4.

$$-\frac{d[\mathrm{LA}]}{d\mathrm{T}} = k_p [\mathrm{LA}]^a [\mathrm{cat}]_0^b [\mathrm{ROH}]_0^c \qquad \textbf{Equation 5.1}$$

$$k_{obs} = k_p [\mathrm{cat}]_0^b [\mathrm{ROH}]_0^c \qquad \textbf{Equation 5.2}$$

$$-\frac{d[\mathrm{LA}]}{d\mathrm{T}} = k_p [\mathrm{LA}]^a [\mathrm{cat}]_0^b \qquad \textbf{Equation 5.3}$$

$$k_{obs} = k_p [\mathrm{cat}]_0^b \qquad \textbf{Equation 5.4}$$

Note: $-d$[LA]/dt is the rate of monomer consumption, k_p is the propagation rate constant, [LA] is the lactide concentration, $[\mathrm{cat}]_0$ is the initial catalyst concentration, $[\mathrm{ROH}]_0$ is the initial co-initiator concentration and k_{obs} is the observed rate constant.

The ROP of *L*- and *rac*-lactide using **1** and **3** was conducted at 80 °C in chloroform-d_1 with varying concentrations of benzyl alcohol co-initiator, $[LA]_0/[M]_0 = 50$ and $[LA]_0 = 0.5$ M. Rate of polymerisation was observed to decrease with increasing BnOH concentration (k_{obs} decreased from 4.59 to 0.67 M^{-1} h^{-1} for the ROP of *L*-lactide using **3** with one and four equivalents BnOH) (Figures 5.11 and A5.10). Decomposition of the active species occurred with eight equivalents of BnOH.

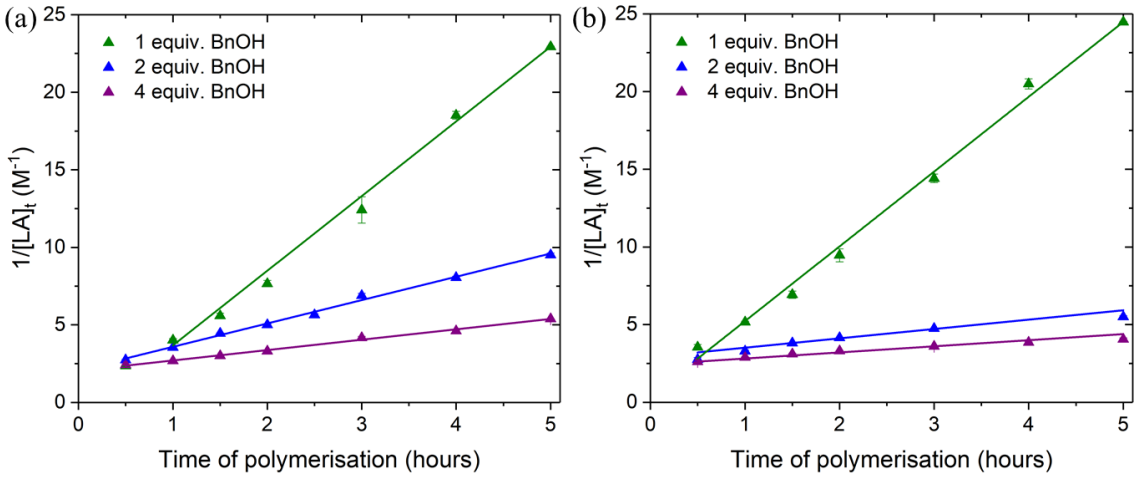


Figure 5.11 $1/[LA]_t$ as a function of time of polymerisation using $^{Me_2}SB(Cp^{Me},I^*)ZrCl_2$ (**3**) as an initiator for the ROP of (a) *L*-lactide with one equivalent BnOH (green, k_{obs} = 4.59 ± 0.06 M^{-1} h^{-1}), two equivalents BnOH (blue, k_{obs} = 1.49 ± 0.02 M^{-1} h^{-1}) and four equivalents BnOH (purple, k_{obs} = 0.67 ± 0.01 M^{-1} h^{-1}); (b) *rac*-lactide with one equivalent BnOH (green, k_{obs} = 4.81 ± 0.05 M^{-1} h^{-1}), two equivalents BnOH (blue, k_{obs} = 0.60 ± 0.06 M^{-1} h^{-1}) and four equivalents BnOH (purple, k_{obs} = 0.39 ± 0.01 M^{-1} h^{-1}). Polymerisation conditions: chloroform-d_1, 80 °C, $[LA]_0/[M]_0 = 50$ and $[LA]_0 = 0.5$ M.

Plots of $-\ln(k_{obs})$ *vs* $-\ln([BnOH]_0)$ gave linear relationships with negative orders in respect to benzyl alcohol concentration; as expected based on the observed decrease in rate with increasing $[BnOH]_0$ (Figure A5.11). In an activated monomer mechanism, the rate of polymerisation increases with increasing concentration of nucleophile (according to the rate expression in Equation 5.1). As the reverse trend is seen here, it is more likely that polymerisation proceeds *via* a coordination-insertion mechanism, with a rate expression of the type in Equation 5.3.

The molecular weights of the PLLA produced using **1** and **3** with one equivalent of benzyl alcohol showed similar experimental and theoretical values (M_n = 5341 and 5019 g mol^{-1} respectively; $M_{n,theo}$ = 6804 and 6660 g mol^{-1} respectively). The molecular weights were also approximately double those obtained when using two equivalents of co-initiator, suggesting that polymerisation proceeded *via* one growing polymer chain due to activation of only one of the potential active sites. M_n of the polymers produced from the ROP of *rac*-lactide using **1** and **3** with one equivalent of benzyl alcohol were approximately 30 and 50% lower than $M_{n,theo.}$ (M_n = 4492 and 3383 g mol^{-1} respectively; $M_{n,theo.}$ = 6588 and 6876 g mol^{-1} respectively). The molecular weights were approximately four and two times higher than those recorded with two equivalents of benzyl alcohol, indicating activation of only one of the potential active sites. The heterotacticity of the polymer was maintained regardless of co-initiator concentration with P_r varying between 0.81 and 0.86.

It is noted that the NMR spectroscopy scale reactions of **1** and **3** with one and two equivalents of benzyl alcohol in chloroform-d_1 at 80 °C lead to a colour change from orange to pale yellow. A complex mixture of products was observed, presumed to include the mono- and bis-substituted products $^{Me_2}SB(Cp^R,I^*)ZrCl(OCH_2Ph)$ and $^{Me_2}SB(Cp^R,I^*)Zr(OCH_2Ph)_2$ in addition to decomposition products. This leads to further doubt in the assumption that the reaction of benzyl alcohol with **1** and **3** leads to full conversion to the bisbenzyl alcohol initiators.

The ROP of *L*- and *rac*-lactide using **1** and **3** without benzyl alcohol co-initiator required an initiation period of 10 hours, after which the rate of polymerisation was slow. After four days, the ROP of *L*-lactide by **1** and **3** only showed 46 and 43% conversion to PLA respectively, while the ROP of *rac*-lactide by **1** and **3** showed 67 and 71% conversion respectively (Figure A5.12). The aryloxide ligands of ***Z*-10** and

***E*-11** were found to act as initiators for the ROP of *L*- and *rac*-lactide without a co-initiator (although polymerisation did not fit first- or second-order dependence with respect to monomer concentration). Without a co-initiator, the polymerisation of *L*- and *rac*-lactide by ***Z*-10** and ***E*-11** experienced a 1.5 hour initiation period, with approximately 90% conversion to PLA recorded after 25 hours (Figure A5.12). The molecular weights of the polymer produced by the ROP of *L*- and *rac*-lactide using ***Z*-10** and ***E*-11** without a co-initiator were higher than when a co-initiator was used and displayed broader molecular weight distributions (M_n = 10923–19853 g mol^{-1} and M_w/M_n = 1.21–1.58). The higher values of M_n suggest that not all the potential active sites were able to initiate polymerisation. The wider MWD suggests that polymerisation was a lot less controlled in the absence of a co-initiator. The homonuclear decoupled ^{1}H{^{1}H} NMR spectra of the polymers produced from the ROP of *L*- and *rac*-lactide using ***Z*-10** and ***E*-11** without a co-initiator confirmed the production of isotactic and heterotactic enriched PLA respectively (P_r = 0.82 and 0.85 for ***Z*-10** and ***E*-11**).

5.2.4 Initiator concentration dependency

Investigations into the effect of initiator concentration on polymerisation rate were conducted. The ROP of *L*- and *rac*-lactide using **1** and **3** was carried out at various catalyst loadings at 80 °C in chloroform-d_1 with two equivalents of benzyl alcohol co-initiator and $[LA]_0$ = 0.5 M (Figures A5.13 and A5.14). k_{obs} was observed to increase with increasing initiator concentration due to the increase in surface area and total number of active sites;[13, 32] k_{obs} = 0.13 and 7.51 M^{-1} h^{-1} for the polymerisation of *L*-lactide by **1** with $[LA]_0/[M]_0$ = 100 and 10 respectively.

Plots of $-\ln(k_{obs})$ *vs* $-\ln([M]_0)$ gave linear relationships with orders of 1.6 ± 0.2 and 1.4 ± 0.1 in respect to initiator concentration for the ROP of *L*-lactide by **1** and **3**

respectively, and orders of 1.3 ± 0.1 and 1.5 ± 0.1 in respect to initiator concentration for the ROP of *rac*-lactide by **1** and **3** respectively (b in Equations 5.3 and 5.4) (Figures 5.12a). These values, and the associated error, suggest that the actual order with respect to initiator concentration may be closer to 1, as was further confirmed by the linear relationships obtained from plots of k_{obs} *vs* $[M]_0$ (Figure 5.12b). The non-integer orders obtained from the $-\ln(k_{obs})$ *vs* $-\ln([M]_0)$ plots may be a further consequence of incomplete conversion to the active aryloxide species *in situ*.

The gradients of the k_{obs} *vs* $[M]_0$ plots gave the propagation rate constants k_p (Equation 5.4); when $[LA]_0 = 0.5$ M, $k_p = 171$ and 260 $M^{-2}\ h^{-1}$ for the polymerisation of *L*-lactide by **1** and **3** respectively, and $k_p = 83$ and 148 $M^{-2}\ h^{-1}$ for the polymerisation of *rac*-lactide by **1** and **3** respectively. The values of k_p for the ROP of *L*-lactide using **1** and **3** were much lower than those reported for other complexes with the same rate equation ($-d[LA]/dt = k_p[cat]_0[LA]^2$), such as magnesium aryloxide $[(SalenMe)Mg(OCH_2Ph)]_2$ (Chart A5.1a), β-diketiminato zinc alkoxide $[(BDI\text{-}OMe)Zn(\mu\text{-}OCH_2Ph)]_2Zn(\mu\text{-}OCH_2Ph)_2$ (Chart A5.1b) and lanthanide phenolate $[N(SiMe_3)_2]_2La[O\text{-}2,4\text{-}^tBu\text{-}6\text{-}CH_2NCH_2CH_2NMe_2\text{-}C_6H_2]_2$ (Chart A5.1c); $k_p = 1711$, 43920 and 29160 $M^{-2}\ h^{-1}$ respectively.[7, 10, 11] The values of k_p for the ROP of *rac*-lactide using **1** and **3** were also much lower than those reported for $Ca_2(DBP)_4(DME)_4(\mu\text{-}DME)$ and $Sr_2(DBP)(\mu\text{-}DBP)_3(DME)_3$ (where H-DBP is di-*tert*-butylphenol and DME is dimethoxyethane, Chart A5.2c and d); $k_p = 276 \times 10^7\ M^{-4.5}\ h^{-1}$ and $156 \times 10^7\ M^{-4.5}\ h^{-1}$ respectively with $BnNH_2$ co-initiator.[36] The lower values of k_p observed for the ROP of *L*- and *rac*-lactide using **1** and **3** are to be expected due to their lower k_{obs} values when compared to the other species discussed (k_{obs} between 6.6 and 118.8 $M^{-1}\ h^{-1}$ for the literature initiators).

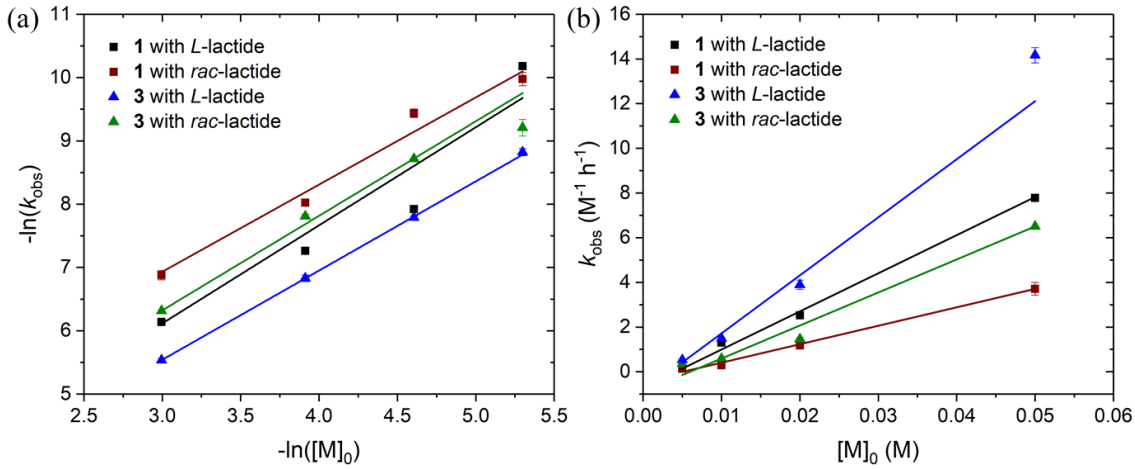


Figure 5.12 (a) $-\ln(k_{obs})$ as a function of $-\ln([M]_0)$ for the ROP *L*-lactide using ^{Me_2}SB(Cp,I*)ZrCl$_2$ (**1**) (black square, slope = 1.6 ± 0.2 with R^2 = 0.958) and ^{Me_2}SB(Cp^{Me},I*)ZrCl$_2$ (**3**) (blue triangle, slope = 1.4 ± 0.1 with R^2 = 0.999), and for the ROP of *rac*-lactide using ^{Me_2}SB(Cp,I*)ZrCl$_2$ (**1**) (brown square, slope = 1.3 ± 0.1 with R^2 = 0.982) and ^{Me_2}SB(Cp^{Me},I*)ZrCl$_2$ (**3**) (green triangle, slope = 1.5 ± 0.1 with R^2 = 0.999); (b) k_{obs} as a function of $[M]_0$ for the ROP of *L*-lactide using ^{Me_2}SB(Cp,I*)ZrCl$_2$ (**1**) (black square, k_p = 171 ± 8 M^{-2} h^{-1} with R^2 = 0.996) and ^{Me_2}SB(Cp^{Me},I*)ZrCl$_2$ (**3**) (blue triangle, k_p = 260 ± 38 M^{-2} h^{-1} with R^2 = 0.959), and for the ROP of *rac*-lactide using ^{Me_2}SB(Cp,I*)ZrCl$_2$ (**1**) (brown square, k_p = 83 ± 2 M^{-2} h^{-1} with R^2 = 0.999) and ^{Me_2}SB(Cp^{Me},I*)ZrCl$_2$ (**3**) (green triangle, k_p = 148 ± 3 M^{-2} h^{-1} with R^2 = 0.999). Polymerisation conditions: two equivalents benzyl alcohol co-initiator, chloroform-d_1, 80 °C and $[LA]_0$ = 0.5 M.

The molecular weights of the PLLA produced using **3** increased with decreasing initiator concentration as the increased amount of monomer relative to initiator increased the likelihood of a propagation processes occurring (M_n of 1204 and 4706 g mol^{-1} with $[LA]_0/[M]_0$ = 25 and 100 respectively) (Figure A5.15). When $[LA]_0/[M]_0$ = 100, a bimodal molecular weight distribution was observed for the PLLA produced using **3**, suggesting the presence of two active species (possibly the mono- and bis-benzyl alcohol substituted complexes). The tacticity of the polymer was unchanged by initiator concentration; the ROP of *L*-lactide produced isotactic PLA, while the ROP of *rac*-lactide produced heterotactic enriched PLA (P_r = 0.81–0.86).

5.2.5 Temperature variation

By varying the temperature of *L*-, *D*- and *rac*-lactide polymerisation using **1** and **3** the enthalpy ($\Delta H^{\ddagger}$) and entropy of activation ($\Delta S^{\ddagger}$) were calculated from Eyring plots of $\ln(k_{obs}/T)$ vs (1/T) (Figure 5.13 and Table 5.5). Polymerisations were run between 60 and 100 °C in chloroform-d_1 with two equivalents of benzyl alcohol co-initiator, $[LA]_0/[M]_0 = 50$ and $[LA]_0 = 0.5$ M.

The values of $\Delta H^{\ddagger}$ were found to be between 54 and 96 kJ mol^{-1}, with $\Delta S^{\ddagger}$ between −163 and −40 J mol^{-1} K^{-1}. $\Delta H^{\ddagger}$ and $\Delta S^{\ddagger}$ for the ROP of *L*-lactide using **1** and **3** were similar to those obtained with $Cp_2ZrMe(O\text{-}2,6\text{-}Me\text{-}C_6H_3)$,[5] $(Ind)_2ZrMe(O^tBu)$[5] and $(p\text{-}MeOC_6H_4)_2Sn(O^iPr)_2$;[43] $\Delta H^{\ddagger}$ = 94, 47 and 51 kJ mol^{-1} and $\Delta S^{\ddagger}$ = −85, −194 and −53 J mol^{-1} K^{-1} respectively.

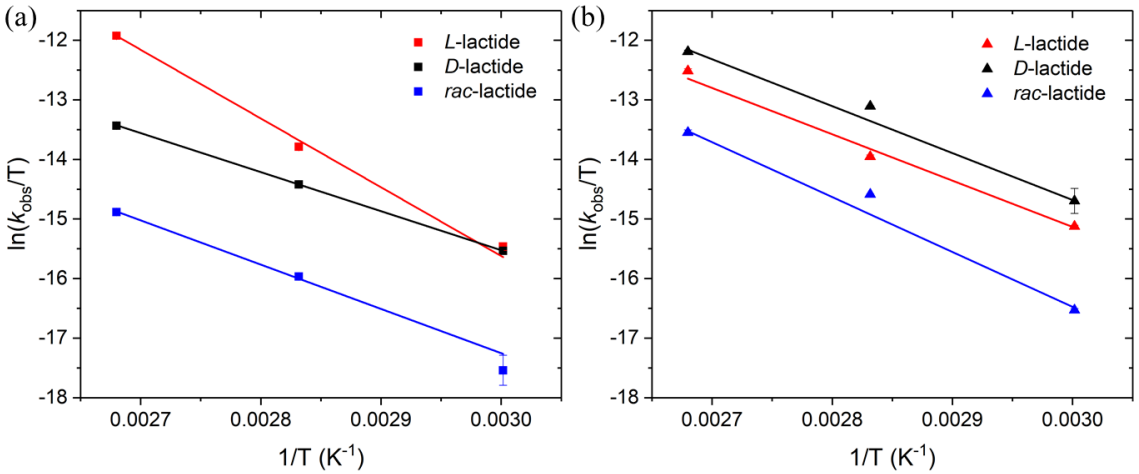


Figure 5.13 Eyring plot of $\ln(k_{obs})/T$ as a function of 1/T using (a) $^{Me_2}SB(Cp,I^*)ZrCl_2$ (**1**) as an initiator for the ROP of *L*-lactide (red, $\Delta H^{\ddagger}$ = 96 ± 5 kJ mol^{-1}, $\Delta S^{\ddagger}$ = −40 ± 15 J mol^{-1} K^{-1}), *D*-lactide (black, $\Delta H^{\ddagger}$ = 54 ± 1 kJ mol^{-1}, $\Delta S^{\ddagger}$ = −163 ± 1 J mol^{-1} K^{-1}) and *rac*-lactide (blue, $\Delta H^{\ddagger}$ = 62b ± 5 kJ mol^{-1}, $\Delta S^{\ddagger}$ = −155 ± 13 J mol^{-1} K^{-1}); (b) $^{Me_2}SB(Cp^{Me},I^*)ZrCl_2$ (**3**) as an initiator for the ROP of *L*-lactide (red, $\Delta H^{\ddagger}$ = 65 ± 6 kJ mol^{-1}, $\Delta S^{\ddagger}$ = −129 ± 17 J mol^{-1} K^{-1}), *D*-lactide (black, $\Delta H^{\ddagger}$ = 66 ± 4 kJ mol^{-1}, $\Delta S^{\ddagger}$ = −123 ± 10 J mol^{-1} K^{-1}) and *rac*-lactide (blue, $\Delta H^{\ddagger}$ = 77 ± 6 kJ mol^{-1}, $\Delta S^{\ddagger}$ = −104 ± 16 J mol^{-1} K^{-1}). Polymerisation conditions: two equivalents benzyl alcohol co-initiator, chloroform-d_1, $[LA]_0/[M]_0 = 50$ and $[LA]_0 = 0.5$ M.

Table 5.5 Enthalpy ($\Delta H^{\ddagger}$) and entropy of activation ($\Delta S^{\ddagger}$) for the polymerisation of *L*-, *D*- and *rac*-lactide using ^{Me_2}SB(Cp,I*)ZrCl$_2$ (**1**) and ^{Me_2}SB(Cp^{Me},I*)ZrCl$_2$ (**3**).[a]

Initiator	Lactide	$\Delta H^{\ddagger}$ (kJ mol^{-1})	$\Delta S^{\ddagger}$ (J mol^{-1} K^{-1})
^{Me_2}SB(Cp,I*)ZrCl$_2$	*L*	96 ± 5	−40 ± 15
^{Me_2}SB(Cp,I*)ZrCl$_2$	*D*	54 ± 1	−163 ± 1
^{Me_2}SB(Cp,I*)ZrCl$_2$	*rac*	62 ± 5	−155 ± 13
^{Me_2}SB(Cp^{Me},I*)ZrCl$_2$	*L*	65 ± 6	−129 ± 17
^{Me_2}SB(Cp^{Me},I*)ZrCl$_2$	*D*	66 ± 4	−123 ± 10
^{Me_2}SB(Cp^{Me},I*)ZrCl$_2$	*rac*	77 ± 6	−104 ± 16

(a) Polymerisation conditions: two equivalents benzyl alcohol co-initiator, chloroform-d_1, $[LA]_0/[M]_0 = 50$ and $[LA]_0 = 0.5$ M.

The rate of polymerisation of *L*-, *D*- and *rac*-lactide using **1** and **3** increased with increasing temperature as the system had more energy to overcome the activation barriers for polymerisation (Figures A5.16–A5.18, Tables A5.1 and A5.2); $k_{obs} = 0.31$ and 5.15 M^{-1} h^{-1} at 60 and 100 °C for the ROP of *L*-lactide by **3**. In general, polymer molecular weights and molecular weight distributions increased with increasing temperature (Figures A5.19 and A5.20). This demonstrates that polymerisation was slightly less controlled at higher temperatures.

For the ROP of *rac*-lactide using **1** and **3**, the heterotacticity of the polymer decreased with increasing temperature; $P_r = 0.83$ and 0.75 at 60 and 100 °C respectively when using **1**. This can potentially be explained due to the differences in the rates of polymerisation of *L*- and *D*-lactide as temperature was increased; at 60 °C the ROP of *L*- and *D*-lactide showed similar rates of polymerisation (0.29 and 0.24 M^{-1} h^{-1} respectively), however at 100 °C the ROP of *L*-lactide was 3.5 times faster than *D*-lactide (7.78 and 2.16 M^{-1} h^{-1} respectively).

5.2.6 Solvent variation

The effects of solvent on polymerisation rate were investigated for the ROP of *L*- and *rac*-lactide using **3** at 80 °C in the presence of two equivalents benzyl alcohol with $[LA]_0[M] = 50$ and $[LA]_0 = 0.5$ M (Figure 5.14).

For the ROP of *L*- and *rac*-lactide, benzene-d_6 showed the fastest rate of polymerisation ($k_{obs} = 7.83$ and 7.67 M^{-1} h^{-1} respectively), followed by toluene-d_8 ($k_{obs} = 5.10$ and 1.42 M^{-1} h^{-1} respectively) and chloroform-d_1 ($k_{obs} = 1.49$ and 0.60 M^{-1} h^{-1} respectively), suggesting that a decrease in solvent polarity increased polymerisation rate. Tetrahydrofuran-d_8, the most polar solvent, ceased polymerisation as coordination of tetrahydrofuran-d_8 molecules to the metal centre inhibited lactide monomer coordination. This is opposite to the effect observed in calcium Schiff base complexes.[44] For the polymerisation of *rac*-lactide the heterotactic nature of the polymer was independent of the solvent ($P_r = 0.84$).

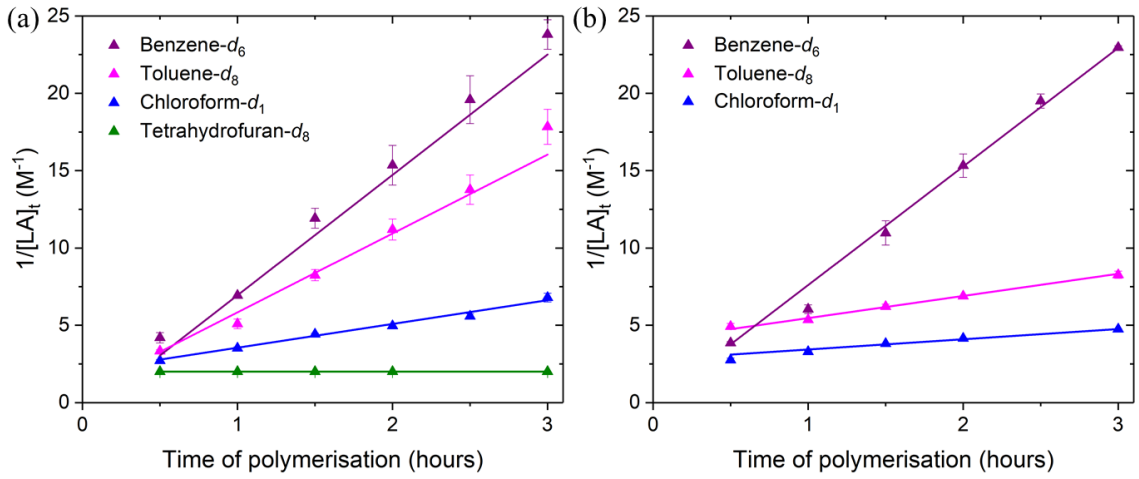


Figure 5.14 $1/[LA]_t$ as a function of time of polymerisation using ^{Me_2}SB(Cp^{Me},I*)$ZrCl_2$ (**3**) as an initiator for the ROP of (a) *L*-lactide in benzene-d_6 (purple, $k_{obs} = 7.83 \pm 0.70$ M^{-1} h^{-1}), toluene-d_8 (pink, $k_{obs} = 5.10 \pm 0.32$ M^{-1} h^{-1}), chloroform-d_1 (blue, $k_{obs} = 1.49 \pm 0.05$ M^{-1} h^{-1}) and tetrahydrofuran-d_8 (green, $k_{obs} = 0$ M^{-1} h^{-1}); (b) *rac*-lactide in benzene-d_6 (purple, $k_{obs} = 7.67 \pm 0.16$ M^{-1} h^{-1}), toluene-d_8 (pink, $k_{obs} = 1.42 \pm 0.05$ M^{-1} h^{-1}) and chloroform-d_1 (blue, $k_{obs} = 0.60 \pm 0.06$ M^{-1} h^{-1}). Polymerisation conditions: two equivalents benzyl alcohol co-initiator, 80 °C, $[LA]_0/[M]_0 = 50$ and $[LA]_0 = 0.5$ M.

5.3 Conclusions

It was found that in the presence of benzyl alcohol co-initiator, ^{Me_2}SB(Cp,I*)ZrCl$_2$ (**1**), ^{Me_2}SB(Cp^{Me},I*)ZrCl$_2$ (**3**), *Z*-^{Me_2}SB(Cp,I*)ZrCl(O-2,6-Me-C$_6$H$_3$) (***Z*-10**) and *E*-^{Me_2}SB(Cp,I*)ZrCl(O-2,6-^{i}Pr-C$_6$H$_3$) (***E*-11**) displayed second-order dependence on monomer concentration for the ROP of *L*-, *D*- and *rac*-lactide. The complexes required no initiation period with some conversion to PLA recorded after 30 minutes. ***Z*-10** was found to have the fastest rate of polymerisation towards *L*-, *D*- and *rac*-lactide (k_{obs} = 6.39, 6.38 and 5.89 M^{-1} h^{-1} respectively). **1**, **3** and ***E*-11** displayed trends in the rates of *L*-, *D*- and *rac*-lactide polymerisation suggesting that enantiomorphic site-control and chain-end control mechanisms were in competition during the polymerisation of *rac*-lactide. ***Z*-10** showed similar polymerisation rates for the ROP of *L*-, *D*- and *rac*-lactide, indicating that the ligand environment did not have a preference for *L*- or *D*-lactide monomer insertion, and therefore demonstrated a true chain-end control mechanism for the polymerisation of *rac*-lactide.

The polymers produced from the ROP of *L*-lactide using **1** and **3** with one and two equivalents of benzyl alcohol showed molecular weights (M_n) consistent with one and two chain polymer growth respectively, indicating that two equivalents of co-initiator were required in order to activate both potential active sites. The MALDI-TOF mass spectra of the polymers indicated the presence of transesterification processes. All polymerisations were shown to have narrow molecular weight distributions (M_n/M_w <1.16) indicating controlled polymerisation. The initiators were found to produce isotactic PLA for the ROP of *L*- and *D*-lactide, and heterotactic-enriched PLA for the ROP of *rac*-lactide (P_r ~0.80) with one –OCH$_2$Ph and one –OH end group per chain.

Further studies into the kinetics of the ROP of *L*- and *rac*-lactide using **1** and **3** indicated that polymerisation proceeded *via* a coordination-insertion mechanism. Investigations also revealed an order of 1 with respect to catalyst concentration, giving the overall rate expression displayed in Equation 5.5. When $[LA]_0 = 0.5$ M, $k_p(\mathbf{3}) = \sim 1.5 \times k_p(\mathbf{1})$ and $k_p(\mathbf{3}) = \sim 1.7 \times k_p(\mathbf{1})$ the for the ROP of *L*- and *rac*-lactide respectively.

$$-\frac{d[\mathrm{LA}]}{d\mathrm{T}} = k_p \left[\mathrm{LA}\right]^2 \left[\mathrm{cat}\right]_0 \qquad \textbf{Equation 5.5}$$

It is important to note that the assumptions stated at the beginning of this chapter may affect the reliability of the devised rate equation. It was assumed that the addition of benzyl alcohol to the reaction mixture led to full conversion to the active bisbenzyl alcohol initiators *in situ*. However, the lower values of the experimentally determined polymer molecular weights when compared to the theoretical values (when polymerisation is considered as proceeding *via* two growing chains) suggests the presence of an additional chain transfer agent, postulated to be unreacted benzyl alcohol co-initiator. In addition, the NMR scale reaction of **1** and **3** with BnOH led to a highly complex mixture of products. Together these results suggest incomplete activation of the permethylindenyl complexes, with the reaction mixture likely containing multiple species including unreacted starting materials, the mono- and bisbenzyl substituted products and decomposition products. It was also assumed that the data recorded after the first 30 minutes of polymerisation gave a true representation of the kinetic profile during the early stages of polymerisation. However, in some cases the value of the y-intercept deviates from the expected value, indicating more complex kinetic processes may be occurring.

5.4 References

1. P. A. Gunatillake and R. Adhikari, *Eur. Cells Mater.*, 2003, **5**, 1-16.
2. P. J. Dijkstra, H. Z. Du and J. Feijen, *Polym. Chem.*, 2011, **2**, 520-527.
3. M. J. Stanford and A. P. Dove, *Chem. Soc. Rev.*, 2010, **39**, 486-494.
4. G. E. Luckachan and C. K. S. Pillai, *J. Polym. Environ.*, 2011, **19**, 637-676.
5. J.-C. Buffet, G. R. Harris, J. J. Coward, T. A. Q. Arnold, Z. R. Turner and D. O'Hare, *J. Organomet. Chem.*, 2016, **801**, 87-95.
6. J. E. Matley, Part II Thesis, University of Oxford, 2015.
7. P. I. Binda and E. E. Delbridge, *Dalton Trans.*, 2007, 4685-4692.
8. M. Save, M. Schappacher and A. Soum, *Macromol. Chem. Phys.*, 2002, **203**, 889-899.
9. Y. Ning, Y. Zhang, A. Rodriguez-Delgado and E. Y. X. Chen, *Organometallics*, 2008, **27**, 5632-5640.
10. J. C. Wu, B. H. Huang, M. L. Hsueh, S. L. Lai and C. C. Lin, *Polymer*, 2005, **46**, 9784-9792.
11. H. Y. Chen, B. H. Huang and C. C. Lin, *Macromolecules*, 2005, **38**, 5400-5405.
12. A. Sauer, A. Kapelski, C. Fliedel, S. Dagorne, M. Kol and J. Okuda, *Dalton Trans.*, 2013, **42**, 9007-9023.
13. Z. R. Turner, J.-C. Buffet and D. O'Hare, *Organometallics*, 2014, **33**, 3891-3903.
14. X. K. Wang, A. Thevenon, J. L. Brosmer, I. S. Yu, S. I. Khan, P. Mehrkhodavandi and P. L. Diaconescu, *J. Am. Chem. Soc.*, 2014, **136**, 11264-11267.
15. C. A. Gracia-Fernandez, S. Gomez-Barreiro, J. Lopez-Beceiro, S. Naya and R. Artiaga, *J. Mater. Res.*, 2012, **27**, 1379-1382.
16. M. A. Cuiffo, J. Snyder, A. M. Elliott, N. Romero, S. Kannan and G. P. Halada, *Appl. Sci.*, 2017, **7**, 14.
17. C. Nakafuku and S. Y. Takehisa, *J. Appl. Polym. Sci.*, 2004, **93**, 2164-2173.
18. G. L. Baker, E. B. Vogel and M. R. Smith, *Polym. Rev.*, 2008, **48**, 64-84.
19. A. Sodergard and M. Stolt, *Prog. Polym. Sci.*, 2002, **27**, 1123-1163.
20. S. Ebnesajjad, in *Chemical Resistance of Commodity Thermoplastics*, eds. E. Baur, K. Ruhrberg and W. Woishnis, William Andrew Publishing, 2016, pp. 13-25.
21. J. C. Middleton and A. J. Tipton, *Biomaterials*, 2000, **21**, 2335-2346.
22. V. Arias, A. Hoglund, K. Odelius and A. C. Albertsson, *Biomacromolecules*, 2014, **15**, 391-402.
23. R. C. Zhang, D. Sun, A. Lu, M. L. Zhong, G. Y. Xiong and Y. Z. Wan, *Polymers*, 2017, **9**, 16.
24. J. Q. Li, P. T. Xiao, H. F. Li, Y. Zhang, F. F. Xue, B. J. Luo, S. Y. Huang, Y. R. Shang, H. Y. Wen, J. D. Christiansen, D. H. Yu and S. C. Jiang, *Polym. Chem.*, 2015, **6**, 3988-4002.
25. T. Kawai, N. Rahman, G. Matsuba, K. Nishida, T. Kanaya, M. Nakano, H. Okamoto, J. Kawada, A. Usuki, N. Honma, K. Nakajima and M. Matsuda, *Macromolecules*, 2007, **40**, 9463-9469.

26. M. Yasuniwa, S. Tsubakihara, K. Ohoshita and S. Tokudome, *J. Polym. Sci., Part B: Polym. Phys.*, 2001, **39**, 2005-2015.
27. D. C. Bassett, R. H. Olley and I. A. M. Alraheil, *Polymer*, 1988, **29**, 1745-1754.
28. P. Cebe and S. D. Hong, *Polymer*, 1986, **27**, 1183-1192.
29. M. Yasuniwa and T. Satou, *J. Polym. Sci., Part B: Polym. Phys.*, 2002, **40**, 2411-2420.
30. Z. Y. Zhong, P. J. Dijkstra and J. Feijen, *J. Am. Chem. Soc.*, 2003, **125**, 11291-11298.
31. D. J. Darensbourg and O. Karroonnirun, *Inorg. Chem.*, 2010, **49**, 2360-2371.
32. R. Dattatray Karande, V. K. Abitha, A. Vasudeo Rane and R. K. Mishra, *J. Mater. Sci. Eng. Adv. Tech.*, 2015, **12**, 1-37.
33. M. D. Jones, S. L. Hancock, P. McKeown, P. M. Schafer, A. Buchard, L. H. Thomas, M. F. Mahon and J. P. Lowe, *Chem. Commun.*, 2014, **50**, 15967-15970.
34. M. D. Jones, L. Brady, P. McKeown, A. Buchard, P. M. Schafer, L. H. Thomas, M. F. Mahon, T. J. Woodman and J. P. Lowe, *Chem. Sci.*, 2015, **6**, 5034-5039.
35. F. Marchetti, G. Pampaloni, C. Pinzino, F. Renili, T. Repo and S. Vuorinen, *Dalton Trans.*, 2013, **42**, 2792-2802.
36. L. Clark, G. B. Deacon, C. M. Forsyth, P. C. Junk, P. Mountford, J. P. Townley and J. Wang, *Dalton Trans.*, 2013, **42**, 9294-9312.
37. L. Clark, M. G. Cushion, H. E. Dyer, A. D. Schwarz, R. Duchateau and P. Mountford, *Chem. Commun.*, 2010, **46**, 273-275.
38. M. P. Blake, A. D. Schwarz and P. Mountford, *Organometallics*, 2011, **30**, 1202-1214.
39. T. P. A. Cao, A. Buchard, X. F. Le Goff, A. Auffrant and C. K. Williams, *Inorg. Chem.*, 2012, **51**, 2157-2169.
40. J. Coudane, C. UstarizPeyret, G. Schwach and M. Vert, *J. Polym. Sci. Polym. Chem.*, 1997, **35**, 1651-1658.
41. B. T. Safrit, G. E. Schlager and Z. Li, presented in part at the 71st Annual Technical Conference of the Society of Plastics Engineers, 2013.
42. N. Ajellal, J.-F. Carpentier, C. Guillaume, S. M. Guillaume, M. Helou, V. Poirier, Y. Sarazin and A. Trifonov, *Dalton Trans.*, 2010, **39**, 8363-8376.
43. M. H. Chisholm, J. C. Gallucci and C. Krempner, *Polyhedron*, 2007, **26**, 4436-4444.
44. D. J. Darensbourg, W. Choi, O. Karroonnirun and N. Bhuvanesh, *Macromolecules*, 2008, **41**, 3493-3502.

Chapter 6

Experimental

6.1 General Details

6.1.1 Air- and moisture-sensitive compounds

Air- and moisture-sensitive compounds and reactions were handled under an inert nitrogen atmosphere using standard Schlenk line techniques and an MBraun Unilab glove box.

6.1.2 Commercially supplied reagents

Bis(*n*-butylcyclopentadienyl)zirconium (Sigma Aldrich), lithiumcyclopentadienyl (Alfer Aesar), lithium cyclopentadienylmethyl (MCAT GmbH), lithium *n*-butylcyclopentadienyl (Sigma Aldrich), *n*-butyllithium (2.5 M in hexanes, Sigma Aldrich), methyl lithium (1.6 M in diethyl ether, Sigma Aldrich), triisobutylaluminium (Sigma Aldrich), *D*-lactide (Purac) and Ind$^{\#}$H (Shanghai Sunway Pharmaceutical Technology Ltd.) were used as supplied. Prior to use, dimethyldichlorosilane (Sigma Aldrich) was degassed and stored over pre-activated 4 Å molecular sieves; zirconium tetrachloride (Sigma Aldrich) and zirconium tetrabromide (Sigma Aldrich) were dried under vacuum; 1-hexene (Sigma Aldrich) was dried over calcium hydride, freeze-thaw degassed and stored over pre-activated 4 Å molecular sieves; *L*- and *rac*-lactide (Alfa Aeser) were recrystallised from toluene and dried under vacuum; silica (SCG Chemicals Co., Ltd.) and Mg_3AlCO_3-LDH (SCG Chemicals Co., Ltd.) were calcined at

150 °C under vacuum for 6 hours; solid polymethylaluminoane (Tosoh Finechem Corporation) and methylaluminoxane (Chemtura) were supplied as slurries in toluene which were dried under vacuum. Ethylene, ethylene/hydrogen (2%) and propylene lecture bottles, CONCOA regulators and flashback arrestors were supplied by CK Gas Products Limited.

6.1.3 Synthesis of literature compounds

2,6-di-methyl potassium phenoxide (K(O-2,6-Me-C_6H_3)) and 2,6-di-isopropyl potassium phenoxide (K(O-2,6-^{i}Pr-C_6H_3)) were prepared following a modified literature procedure.[1] Potassium benzyl (K($CH_2C_6H_5$)) was prepared according to a literature procedure and stored at −20 °C.[2]

6.1.4 Solvent preparation

Pentane, hexane, toluene and benzene were dried using an MBraun SPS-800 solvent purification system, stored over a potassium mirror and degassed under partial vacuum before use. Tetrahydrofuran was distilled from sodium/benzophenone, stored over 4 Å molecular sieves and degassed under partial vacuum before use. Diethyl ether was distilled from potassium metal, stored over a potassium mirror and degassed under partial vacuum before use.

Deuterated solvents were dried over NaK (benzene-d_6 and toluene-d_8) or calcium hydride (pyridine-d_5, chloroform-d_1 and tetrahydrofuran-d_8) at 40–60 °C, distilled under static vacuum, freeze-thaw degassed and stored over pre-activated 4 Å molecular sieves.

6.1.5 Solution nuclear magnetic resonance (NMR) spectroscopy

Non-air-sensitive samples were prepared in 5 mm NMR spectroscopy tubes. Air- and moisture-sensitive samples were prepared in a glove box and sealed in 5 mm Young's tap NMR spectroscopy tubes. Spectra were recorded on either a Bruker Avance III HD nanobay NMR equipped with a 9.4 T magnet (400 MHz), a Bruker Avance III NMR equipped with an 11.75 T magnet (500 MHz) or a Bruker Avance NMR equipped with an 11.75 T magnet and a ^{13}C detect cryoprobe (500 MHz). Spectra were recorded at 298 K unless otherwise stated and referenced internally to the residual *protio* solvent resonance. Spectra are reported relative to tetramethylsilane ($\delta = 0$ ppm). Two dimensional ^{1}H-^{1}H and ^{13}C-^{1}H correlation experiments were used to confirm ^{1}H and ^{13}C assignments.

For polyethylene samples, NMR spectra were recorded in 1,2-dichloroethane-d_4 at 120 °C with chromium(III) acetylacetonate as a relaxation agent (0.5 wt%).

6.1.6 Solid-state nuclear magnetic resonance (NMR) spectroscopy

Air- and moisture-sensitive samples were prepared in a glove box under a nitrogen atmosphere and sealed in 4 mm ZrO_2 rotors. Spectra were recorded by Dr Nicholas Rees (University of Oxford) on a Bruker AVIII HD NanoBay solid-state NMR (400 MHz). Samples were spun at the magic angle (54.71°) at spin rates of 10 kHz for ^{13}C CP/MAS and ^{29}Si CP/MAS, and 15 kHz for ^{27}Al DP/MAS and ^{19}F DEPT. ^{13}C NMR CP/MAS spectra were referenced to adamantane, ^{27}Al DP/MAS to aluminum nitrate, ^{29}Si CP/MAS to kaolinite and ^{19}F DEPT to Teflon.

6.1.7 Elemental analysis (EA)

Samples were prepared in a glove box under a nitrogen atmosphere and sealed in glass vials. CHN analyses were carried out in duplicate by Mr Stephen Boyer (London Metropolitan University).

6.1.8 Fourier transform infrared (FTIR) spectroscopy

Samples were prepared in a glove box and ground with anhydrous potassium bromide. Samples were pressed into discs using a specially designed press and airtight holder. IR spectra were recorded on a Nicolet iS5 ThermoScientific spectrometer (resolution = 1 cm^{-1} and range = 4000–400 cm^{-1}) in transmission mode. A background spectrum was run prior to the samples and subtracted from the sample spectra.

6.1.9 Mass spectrometry (MS)

Samples were prepared in a glove box under a nitrogen atmosphere and sealed in glass tubes. Samples were run as electron impact (EI) mass spectra on an Agilent GC-TOF-MS by Dr James Wickens (University of Oxford) or Dr Victor Mikhailov (University of Oxford).

6.1.10 Single-crystal X-ray diffraction (XRD)

Single-crystal X-ray diffraction data collection and structure determinations were performed by Dr Zoë Turner (University of Oxford). Crystals were mounted on MiTeGen MicroMounts using perfluoropolyether oil and rapidly transferred to a goniometer head on a diffractometer fitted with an Oxford Cryosystems Cryostream open-flow nitrogen cooling device.[3] Data collections were carried out at 150 K using an Oxford Diffraction Supernova diffractometer with mirror-monochromated Cu Kα radiation (λ = 1.54178 Å) and the data processed using CrysalisPro.[4] The structures were solved using direct methods (SIR-92)[5] or a charge flipping algorithm

(SUPERFLIP)[6] and refined by full-matrix least-squares procedures using the Win-GX software suite.[7, 8] Molecular structures were depicted utilising Ortep,[8] with ellipsoids shown at 30% probability. Molecular bond lengths and angles were calculated using Platon.[9, 10]

6.1.11 Scanning electron microscopy (SEM)

Scanning electron microscopy (SEM) analysis was performed on a JOEL JSM 6610LV scanning electron microscope with an accelerating voltage of 3.0 kV. Polymer samples were spread on carbon tape adhered to an SEM stage. Air- and moisture-sensitive samples were prepared in a glove box whereby a suspension of the sample in pentane was prepared and placed onto a silicon wafer adhered to carbon tape on an SEM stage. Before imaging, the samples were coated with a thin platinum layer (20 nm) to prevent charging and improve image quality.

6.1.12 Differential scanning calorimetry (DSC)

Differential scanning calorimetry experiments were performed on a Mettler Toledo TGA/DSC 1 System at 25–250 °C with a heating rate of 5 °C min^{-1}.

6.2 Experimental Details for Chapter 2

6.2.1 Synthesis of Ind*SiMe$_2$Cl

1.0 equivalent Ind$^{\#}$H (10.0 g, 50.0 mmol) was dissolved in pentane (100 mL) in a Schlenk tube. The solution was cooled to 0 °C and 1.1 equivalents ^{n}BuLi (22.0 mL, 2.5 M in hexanes, 55.0 mmol) were added dropwise. The reaction was allowed to warm to room temperature, stirred for 18 h and the solvent removed *in vacuo*. The resulting lithium salt was dissolved in THF (100 mL) and added dropwise to a solution of 3.0 equivalents Me_2SiCl_2 (28.9 mL, 150 mmol). The reaction was stirred for 2 h at room temperature, the solvent removed and the product extracted with pentane (3 × 50 mL). Storage at −34 °C yielded Ind*SiMe$_2$Cl as a pale yellow solid in 88% yield (12.8 g, 43.7 mmol). ^{1}H NMR (benzene-d_6, 400 MHz, 298 K) δ (ppm): 3.49 (Ind**H**, 1H, s). 2.43 (C=C**Me**, 3H, s), 2.16 (Ar**Me**, 3H, s), 2.15 (Ar**Me**, 3H, s), 2.13 (Ar**Me**, 3H, s), 2.12 (Ar**Me**, 3H, s), 2.09 (C=C**Me**, 3H, s), 0.20 (Si**Me**, 3H, s), 0.08 (Si**Me**, 3H, s). ^{13}C{^{1}H} NMR (benzene-d_6, 125 MHz, 298 K) δ (ppm): 142.1 (**Ar**), 139.8 (**Ar**), 138.0 (**Ar**), 134.5 (**Ar**), 133.1 (**Ar**), 130.5 (**Ar**), 127.6 (**Ar**), 126.6 (**Ar**), 49.8 (**Ar**H), 19.3 (Ar**Me**), 16.4 (Ar**Me**), 16.4 (Ar**Me**), 16.3 (Ar**Me**), 15.4 (Ar**Me**), 15.2 (Ar**Me**), 3.3 (Si**Me**), −0.4 (Si**Me**). CHN analysis (%): expected C 69.71, H 8.60; observed C 69.64, H 8.75.

6.2.2 Synthesis of ^{Me_2}SB(Cp,I*)Li$_2$

1.0 equivalent LiCp (0.61 g, 8.53 mmol) and 1.0 equivalent Ind*SiMe$_2$Cl (2.50 g, 8.53 mmol) were dissolved in THF (50 mL) in a Schlenk tube and stirred for 2 h at room temperature. 2.2 equivalents ^{n}BuLi (7.50 mL, 2.5 M in hexanes, 18.8 mmol) were added dropwise at 0 °C, resulting in a colour change from orange to dark red, and the reaction mixture stirred for 1 h at 0 °C. The solvent was removed *in vacuo* and the

resulting dark orange solid washed with pentane (3 × 50 mL) and diethyl ether (3 × 50 mL). The solid was dried to afford a pale orange powder (2.48 g) which was confirmed by ^{1}H NMR spectroscopy to be a 10:90 mixture of starting materials and ^{Me_2}SB(Cp,I*)Li$_2$. ^{Me_2}SB(Cp,I*)Li$_2$ was therefore obtained in 78% yield (2.23 g, 6.68 mmol). ^{1}H NMR (pyridine-d_5, 400 MHz, 298 K) δ (ppm): 6.92 (Cp**H**, 2H, m), 6.69 (Cp**H**, 2H, m), 3.09 (Ar**Me**, 3H, s), 3.03 (Ar**Me**, 3H, s), 2.98 (Ar**Me**, 3H, s), 2.71 (Ar**Me**, 3H, s), 2.48 (Ar**Me**, 3H, s), 2.31 (Ar**Me**, 3H, s), 1.00 (Si**Me**, 6H, s). ^{13}C{^{1}H} NMR (pyridine-d_5, 125 MHz, 298 K) δ (ppm): 136.5 (**Ar**), 135.3 (**Ar**), 131.3 (**Ar**), 124.7 (**Ar**), 124.5 (**Ar**), 122.5 (**Ar**), 119.9 (**Ar**), 118.8 (**Cp**Si), 113.6 (**Cp**), 106.9 (**Cp**), 104.7 (**Ar**), 93.8 (**Ar**Si), 24.1 (Ar**Me**), 18.7 (Ar**Me**), 18.3 (Ar**Me**), 17.8 (Ar**Me**), 17.3 (Ar**Me**), 16.4 (Ar**Me**), 16.0 (Si**Me**), 9.3 (Si**Me**).

6.2.3 Synthesis of ^{Me_2}SB(Cp,I*)ZrCl$_2$ (1)

1.0 equivalent ^{Me_2}SB(Cp,I*)Li$_2$ (1.20 g, 3.59 mmol) and 1.0 equivalent ZrCl$_4$ (0.84 g, 3.59 mmol) were dissolved in benzene (50 mL) in a Schlenk tube and stirred for 18 h at room temperature. The resulting dark orange solution was filtered, the solvent removed *in vacuo* and the product extracted with pentane (3 × 50 mL). The insoluble orange powder was shown by ^{1}H NMR spectroscopy to be the desired product in 7% yield (0.12 g, 2.50 mmol). Storage of the pentane solution at −34 °C overnight yielded ^{Me_2}SB(Cp,I*)ZrCl$_2$ as orange crystals in 21% yield (0.36 g, 7.50 mmol). Crystals suitable for a single-crystal X-ray diffraction study were obtained from a hexane solution at −34 °C by Mr Joshua Matley. ^{1}H NMR (benzene-d_6, 400 MHz, 298 K) δ (ppm): 6.63 (Cp**H**, 1H, m), 6.59 (Cp**H**, 1H, m), 5.62 (Cp**H**, 1H, m), 5.49 (Cp**H**, 1H, m), 2.52 (Ar**Me**, 3H, s), 2.48 (Ar**Me**, 3H, s), 2.26 (Ar**Me**, 3H, s), 2.15 (Ar**Me**, 3H, s), 2.05 (Ar**Me**, 3H, s), 1.97 (Ar**Me**, 3H, s), 0.72 (Si**Me**, 3H, s), 0.64 (Si**Me**, 3H, s). ^{13}C{^{1}H} NMR (benzene-d_6, 125 MHz, 298 K) δ (ppm): 135.2 (**Ar**), 134.8 (**Ar**), 134.6

(**Ar**), 132.8 (**Ar**), 131.3 (**Ar**), 130.8 (**Ar**), 128.8 (**Ar**), 128.3 (**Ar**), 126.0 (**Cp**), 125.6 (**Cp**), 115.5 (**Cp**), 115.2 (**Cp**), 106.0 (**Cp**Si), 84.0 (**Ar**Si), 21.4 (Ar**Me**), 17.7 (Ar**Me**), 17.4 (Ar**Me**), 16.9 (Ar**Me**), 16.7 (Ar**Me**), 15.8 (Ar**Me**), 5.3 (Si**Me**), 3.0 (Si**Me**). ^{29}Si NMR (benzene-d_6, 100 MHz, 298 K) δ (ppm): −15.04 (**Si**Me). CHN analysis (%): expected C 54.74, H 5.85; observed C 54.85, H 5.94. MS (EI): expected *m*/*z* 482.04; observed *m*/*z* 482.04. IR (KBr) (cm^{-1}): 2962, 2922, 1542, 1261, 1093 (b), 1029 (b), 809 (b), 667.

6.2.4 Synthesis of ^{Me_2}SB(Cp,I*)ZrBr$_2$ (2)

1.0 equivalent ^{Me_2}SB(Cp,I*)Li$_2$ (1.00 g, 3.00 mmol) and 1.0 equivalent ZrBr$_4$ (1.23 g, 3.00 mmol) were dissolved in benzene (50 mL) in a Schlenk tube and stirred for 18 h at room temperature. The resulting dark orange solution was filtered, the solvent removed *in vacuo* and the product extracted with pentane (3 × 50 mL). The insoluble red/brown powder was shown by ^{1}H NMR spectroscopy to be the desired product in 9% yield (154 mg, 0.27 mmol). Storage of the pentane solution at −34 °C overnight yielded ^{Me_2}SB(Cp,I*)ZrBr$_2$ as red crystals in 6% yield (97 mg, 0.17 mmol). Crystals suitable for a single-crystal X-ray diffraction study were obtained from a benzene solution at 5 °C. ^{1}H NMR (benzene-d_6, 400 MHz, 298 K) δ (ppm): 6.81 (Cp**H**, 1H, m), 6.77 (Cp**H**, 1H, m), 5.63 (Cp**H**, 1H, m), 5.35 (Cp**H**, 1H, m), 2.62 (Ar**Me**, 6H, s), 2.20 (Ar**Me**, 3H, s), 2.14 (Ar**Me**, 3H, s), 2.03 (Ar**Me**, 3H, s), 1.86 (Ar**Me**, 3H, s), 0.59 (Si**Me**, 3H, s), 0.53 (Si**Me**, 3H, s). ^{13}C{^{1}H} NMR (benzene-d_6, 125 MHz, 298 K) δ (ppm): 135.4 (**Ar**), 135.1 (**Ar**), 134.4 (**Ar**), 133.8 (**Ar**), 131.9 (**Ar**), 130.6 (**Ar**), 130.2 (**Ar**), 129.1 (**Ar**), 127.3 (**Cp**H), 124.2 (**Cp**H), 116.2 (**Cp**H), 114.5 (**Cp**H), 104.8 (**Cp**Si), 82.5 (**Ar**Si), 34.5 (Ar**Me**), 21.2 (Ar**Me**), 17.9 (Ar**Me**), 17.4 (Ar**Me**), 17.3 (Ar**Me**), 16.8 (Ar**Me**), 5.1 (Si**Me**), 3.0 (Si**Me**). CHN analysis (%): expected C 46.23, H 4.94; observed C 46.27, H 5.12. MS (EI): expected: *m*/*z* 567.94; observed *m*/*z* 567.94.

6.2.5 Synthesis of ^{Me_2}SB(Cp^{Me},I*)Li$_2$

1.0 equivalent LiCp^{Me} (0.87 g, 10.2 mmol) and 1.0 equivalent Ind*SiMe$_2$Cl (3.00 g, 10.2 mmol) were dissolved in THF (50 mL) in a Schlenk tube and stirred for 2 h at room temperature. 2.2 equivalents ^{n}BuLi (9.00 mL, 2.5 M in hexanes, 22.5 mmol) were added dropwise at 0 °C, resulting in a colour change from orange to dark red, and the reaction mixture stirred for 1 h at 0 °C. The solvent was removed *in vacuo* and the resulting red oil washed with pentane (3 × 50 mL) and diethyl ether (6 × 50 mL). The resultant solid was dried to afford a pale orange powder (2.66 g) which was confirmed by ^{1}H NMR spectroscopy to be a 15:85 mixture of starting materials and ^{Me_2}SB(Cp^{Me},I*)Li$_2$. ^{Me_2}SB(Cp^{Me},I*)Li$_2$ was therefore obtained in 64% yield (2.26 g, 6.49 mmol). ^{1}H NMR (pyridine-d_5, 400 MHz, 298 K) δ(ppm): 6.75 (Cp**H**, 1H, m), 6.58 (Cp**H**, 1H, m), 6.43 (Cp**H**, 1H, m), 3.08 (Ar**Me**, 3H, s), 3.02 (Cp**Me**, 3H, s), 2.97 (Ar**Me**, 3H, s), 2.69 (Ar**Me**, 3H, s), 2.48 (Ar**Me**, 3H, s), 2.46 (Ar**Me**, 3H, s), 2.31 (Ar**Me**, 3H, s), 0.97 (Si**Me**, 6H, s). ^{13}C{^{1}H} NMR (pyridine-d_5, 125 MHz, 298 K) δ (ppm): 124.5 (**Ar**), 124.4 (**Ar**), 124.1 (**Ar**), 123.9 (**Ar**), 123.4 (**Ar**), 122.5 (**Ar**), 119.0 (**Ar**), 119.6 (**Ar**), 117.7 (**Cp**Si), 117.0 (**Cp**Me), 113.8 (**Cp**), 112.9 (**Cp**), 107.4 (**Cp**), 104.7 (**Cp**), 94.0 (**Ar**Si), 24.1 (Cp**Me**), 18.7 (Ar**Me**), 18.2 (Ar**Me**), 17.8 (Ar**Me**), 17.3 (Ar**Me**), 16.6 (Ar**Me**), 16.4 (Ar**Me**), 16.0 (Si**Me**), 9.3 (Si**Me**).

6.2.6 Synthesis of ^{Me_2}SB(Cp^{Me},I*)ZrCl$_2$ (3)

1.0 equivalent ^{Me_2}SB(Cp^{Me},I*)Li$_2$ (1.40 g, 4.02 mmol) and 1.0 equivalent ZrCl$_4$ (0.94 g, 4.02 mmol) were dissolved in benzene (50 mL) in a Schlenk tube and stirred for 18 h at room temperature. The resulting dark orange solution was filtered, the solvent removed *in vacuo* and the product extracted with pentane (3 × 50 mL). Storage at −34 °C overnight yielded a 60:40 isomeric mixture of *E*-^{Me_2}SB(Cp^{Me},I*)ZrCl$_2$ and

Z-^{Me_2}SB(Cp^{Me},I*)ZrCl$_2$ as orange crystals suitable for a single-crystal X-ray diffraction study in 20% yield (0.40 g, 0.81 mmol). CHN analysis (%): expected C 55.62, H 6.09; observed C 55.72, H 6.20. MS (EI): expected *m*/*z* 494.05; observed *m*/*z* 494.05. IR (KBr) (cm^{-1}): 2955, 2923 (b), 1452 (b), 1258, 1098, 841, 810, 704, 677, 489.

E-^{Me_2}SB(Cp^{Me},I*)ZrCl$_2$: ^{1}H NMR (benzene-d_6, 400 MHz, 298 K) δ (ppm): 6.29 (Cp**H**, 1H, m), 5.65 (Cp**H**, 1H, m), 5.13 (Cp**H**, 1H, m), 2.55 (Ar**Me**, 6H, s), 2.27 (Ar**Me**, 3H, s), 2.19 (Cp**Me**, 3H, s), 2.18 (Ar**Me**, 3H, s), 2.07 (Ar**Me**, 3H, s), 1.91 (Ar**Me**, 3H, s), 0.68 (Si**Me**, 3H, s), 0.59 (Si**Me**, 3H, s). ^{13}C{^{1}H} NMR (benzene-d_6, 125 MHz, 298 K) δ(ppm): 136.7 (**Ar**), 135.5 (**Ar**), 134.8 (**Ar**), 134.4 (**Ar**), 133.0 (**Ar**), 131.2 (**Ar**), 130.6 (**Ar**), 127.9 (**Ar**), 126.3 (**Cp**), 125.7 (**Cp**), 116.5 (**Cp**), 116.3 (**Cp**Me), 105.1 (**Cp**Si), 82.5 (**Ar**Si), 21.5 (Ar**Me**), 17.7 (Ar**Me**), 17.4 (Ar**Me**), 16.9 (Ar**Me**), 16.7 (Ar**Me**), 15.8 (Cp**Me**), 15.4 (Ar**Me**), 5.2 (Si**Me**), 3.1 (Si**Me**).

Z-^{Me_2}SB(Cp^{Me},I*)ZrCl$_2$: ^{1}H NMR (benzene-d_6, 400 MHz, 298 K) δ (ppm): 6.34 (Cp**H**, 1H, m), 5.53 (Cp**H**, 1H, m), 5.32 (Cp**H**, 1H, m), 2.61 (Ar**Me**, 6H, s), 2.22 (Ar**Me**, 3H, s), 2.16 (Ar**Me**, 3H, s), 2.06 (Cp**Me**, 3H, s), 2.03 (Ar**Me**, 3H, s), 1.98 (Ar**Me**, 3H, s), 0.67 (Si**Me**, 3H, s), 0.60 (Si**Me**, 3H, s). ^{13}C{^{1}H} NMR (benzene-d_6, 125 MHz, 298 K) δ (ppm): 136.7 (**Ar**), 134.9 (**Ar**), 134.5 (**Ar**), 134.2 (**Ar**), 132.6 (**Ar**), 131.2 (**Ar**), 130.8 (**Ar**), 128.2 (**Ar**), 126.3 (**Cp**), 126.3 (**Cp**), 116.6 (**Cp**), 116.4 (**Cp**Me), 105.2 (**Cp**Si), 82.9 (**Ar**Si), 21.5 (Ar**Me**), 17.8 (Ar**Me**), 17.4 (Cp**Me**), 17.0 (Ar**Me**), 16.7 (Ar**Me**), 15.4 (Ar**Me**), 14.3 (Ar**Me**), 5.3 (Si**Me**), 3.0 (Si**Me**).

6.2.7 Synthesis of ^{Me_2}SB(Cp^{Me},I*)ZrBr$_2$ (4)

1.0 equivalent ^{Me_2}SB(Cp^{Me},I*)Li$_2$ (1.00 g, 2.87 mmol) and 1.0 equivalent ZrBr$_4$ (1.18 g, 2.88 mmol) were dissolved in benzene (50 mL) in a Schlenk tube and stirred for 18 h at room temperature. The resulting dark orange solution was filtered, the solvent removed

in vacuo and the product extracted with pentane (3 × 50 mL). Storage at −80 °C yielded a 60:40 isomeric mixture, assumed to be *E*-^{Me_2}SB(Cp^{Me},I*)ZrBr$_2$ and *Z*-^{Me_2}SB(Cp^{Me},I*)ZrBr$_2$ respectively based on analogous ^{Me_2}SB(Cp^{Me},I*)ZrCl$_2$ assignment, as an orange solid in 5% yield (84 mg, 1.38 mmol). CHN analysis (%): expected C 47.17, H 5.16; observed C 47.26, H 5.31.

E-^{Me_2}SB(Cp^{Me},I*)ZrBr$_2$: ^{1}H NMR (benzene-d_6, 400 MHz, 298 K) δ (ppm): 6.54 (Cp**H**, 1H, m), 5.45 (Cp**H**, 1H, m), 5.39 (Cp**H**, 1H, m), 2.65 (Ar**Me**, 3H, s), 2.63 (Ar**Me**, 3H, s), 2.24 (Ar**Me**, 3H, s), 2.17 (Ar**Me**, 3H, s), 2.13 (Cp**Me**, 3H, s), 2.03 (Ar**Me**, 3H, s), 1.93 (Ar**Me**, 3H, s), 0.61 (Si**Me**, 3H, s), 0.58 (Si**Me**, 3H, s). ^{13}C{^{1}H} NMR (benzene-d_6, 125 MHz, 298 K) δ (ppm): 135.5 (**Ar**), 134.9 (**Ar**), 134.6 (**Ar**), 134.4 (**Ar**), 134.2 (**Ar**), 131.9 (**Ar**), 130.0 (**Ar**), 129.9 (**Ar**), 129.2 (**Cp**Me), 128.8 (**Cp**H), 119.0 (**Cp**H), 115.2 (**Cp**H), 104.4 (**Cp**Si), 82.2 (**Ar**Si), 21.2 (Cp**Me**), 17.9 (Ar**Me**), 17.5 (Ar**Me**), 17.4 (Ar**Me**), 16.7 (2 × Ar**Me**), 16.3 (Ar**Me**), 4.7 (Si**Me**), 3.2 (Si**Me**), 1 quaternary carbon missing.

Z-^{Me_2}SB(Cp^{Me},I*)ZrBr$_2$: ^{1}H NMR (benzene-d_6, 400 MHz, 298 K) δ (ppm): 6.46 (Cp**H**, 1H, m), 5.69 (Cp**H**, 1H, m), 5.08 (Cp**H**, 1H, m), 2.61 (Ar**Me**, 6H, s), 2.28 (Ar**Me**, 3H, s), 2.21 (Ar**Me**, 3H, s), 2.19 (Cp**Me**, 3H, s), 2.03 (Ar**Me**, 3H, s), 1.87 (Ar**Me**, 3H, s), 0.64 (Si**Me**, 3H, s), 0.55 (Si**Me**, 3H, s). ^{13}C{^{1}H} NMR (benzene-d_6, 125 MHz, 298 K) δ (ppm): 136.6 (**Ar**), 135.2 (**Ar**), 135.1 (**Ar**), 134.8 (**Ar**), 133.5 (**Ar**), 131.8 (**Ar**), 130.6 (**Ar**), 129.1 (**Ar**), 129.1 (**Cp**Me), 126.0 (**Cp**H), 116.9 (**Cp**H), 116.5 (**Cp**H), 103.9 (**Cp**Si), 81.8 (**Ar**Si), 21.4 (Cp**Me**), 18.0 (Ar**Me**), 17.4 (2 × Ar**Me**), 16.8 (2 × Ar**Me**), 16.5 (Ar**Me**), 5.1 (Si**Me**), 3.0 (Si**Me**).

6.2.8 Synthesis of ^{Me_2}SB(Cp^{nBu},I*)Li$_2$

1.0 equivalent LiCp^{nBu} (1.52 g, 11.9 mmol) and 1.0 equivalent Ind*SiMe$_2$Cl (3.50 g, 11.9 mmol) were dissolved in THF (50 mL) in a Schlenk tube and stirred for 2 h at room temperature. 2.2 equivalents ^{n}BuLi (10.4 mL, 2.5 M in hexanes, 22.5 mmol) were added dropwise at 0 °C, resulting in a colour change from dark orange to red, and the reaction mixture stirred for 1 h at 0 °C. The solvent was removed *in vacuo* and the resulting dark orange solid washed with pentane (3 × 50 mL) and diethyl ether (3 × 50 mL). The solid was dried to afford a red powder (2.81 g) which was confirmed by ^{1}H NMR spectroscopy to be a 50:50 mixture of starting materials and ^{Me_2}SB(Cp^{nBu},I*)Li$_2$. ^{Me_2}SB(Cp^{nBu},I*)Li$_2$ was therefore obtained in a 30% yield (1.41 g, 3.63 mmol). ^{1}H NMR (pyridine-d_5, 400 MHz, 298 K) δ (ppm): 6.73 (Cp**H**, 1H, m), 6.62 (Cp**H**, 1H, m), 6.44 (Cp**H**, 1H, m), 3.08 (C**H$_2$**, 2H, m), 3.06 (Ar**Me**, 3H, s), 2.99 (Ar**Me**, 3H, s), 2.95 (Ar**Me**, 3H, s), 2.65 (Ar**Me**, 3H, s), 2.46 (Ar**Me**, 3H, s), 2.30 (Ar**Me**, 3H, s), 1.64 (C**H$_2$**, 2H, m), 1.26 (C**H$_2$**, 2H, m), 0.97 (Si**Me**, 6H, s), 0.78 (CH$_2$**Me**, 3H, m).

6.2.9 Synthesis of ^{Me_2}SB(Cp^{nBu},I*)ZrCl$_2$ (5)

1.0 equivalent of the 50:50 ^{Me_2}SB(Cp^{nBu},I*)Li$_2$:LiCp^{nBu} mixture (1.93 g, 4.96 mmol) and 1.0 equivalent ZrCl$_4$ (1.16 g, 4.96 mmol) were dissolved in benzene (50 mL) in a Schlenk tube and stirred for 16 h at room temperature. The resulting dark red solution was filtered, the solvent removed *in vacuo* and the product extracted with pentane (3 × 50 mL). Storage at −80 °C yielded an orange crystalline solid confirmed by ^{1}H NMR to be a mixture of (Cp^{nBu})$_2$ZrCl$_2$ and two ^{Me_2}SB(Cp^{nBu},I*)ZrCl$_2$ isomers. Through a series of pentane washes *E*-^{Me_2}SB(Cp^{nBu},I*)ZrCl$_2$ and *Z*-^{Me_2}SB(Cp^{nBu},I*)ZrCl$_2$ were isolated in 1% (13 mg, 0.02 mmol) and 2% (25 mg,

0.05 mmol) yield respectively. Crystals of *E*-^{Me_2}SB(Cp$^{n\text{Bu}}$,I*)ZrCl$_2$ and *Z*-^{Me_2}SB(Cp$^{n\text{Bu}}$,I*)ZrCl$_2$, suitable for single-crystal X-ray diffraction studies, were grown from pentane solutions stored at −34 °C for 1 and 6 months respectively.

E-^{Me_2}SB(Cp$^{n\text{Bu}}$,I*)ZrCl$_2$: ^{1}H NMR (benzene-d_6, 500 MHz, 298 K) δ (ppm): 6.40 (Cp**H**, 1H, m), 5.71 (Cp**H**, 1H, m), 5.32 (Cp**H**, 1H, m), 2.72 (C**H$_2$**, 2H, m), 2.62 (Ar**Me**, 3H, s), 2.57 (Ar**Me**, 3H, s), 2.30 (Ar**Me**, 3H, s), 2.18 (Ar**Me**, 3H, s), 2.06 (Ar**Me**, 3H, s), 1.96 (Ar**Me**, 3H, s), 1.48 (C**H$_2$**, 2H, m), 1.25 (C**H$_2$**, 2H, m), 0.81 (CH$_2$**Me**), 3H, t, $^3J_{\text{H-H}}$ = 8 Hz), 0.71 (Si**Me**, 3H, s), 0.60 (Si**Me**, 3H, s). ^{13}C{^{1}H} NMR (benzene-d_6, 125 MHz, 298 K) δ (ppm): 141.3 (**Cp**^{n}Bu), 135.3 (**Ar**), 134.6 (**Ar**), 134.4 (**Ar**), 132.6 (**Ar**), 131.3 (**Ar**), 130.7 (**Ar**), 128.6 (**Ar**), 128.0 (**Ar**) 125.2 (**Cp**H), 115.9 (**Cp**H), 115.8 (**Cp**H), 104.8 (**Cp**Si), 82.3 (**Ar**Si), 32.7 (**C**H$_2$), 30.1 (**C**H$_2$), 22.9 (**C**H$_2$), 21.5 (Ar**Me**), 17.8 (Ar**Me**), 17.5 (Ar**Me**), 16.9 (Ar**Me**), 16.7 (Ar**Me**), 15.8 (Ar**Me**), 14.1 (CH$_2$**Me**), 5.3 (Si**Me**), 3.0 (Si**Me**).

Z-^{Me_2}SB(Cp$^{n\text{Bu}}$,I*)ZrCl$_2$: ^{1}H NMR (benzene-d_6, 500 MHz, 298 K) δ (ppm): 6.44 (Cp**H**, 1H, m), 5.62 (Cp**H**, 1H, m), 5.49 (Cp**H**, 1H, m), 2.61 (Ar**Me**, 3H, s), 2.58 (C**H$_2$**, 2H, m), 2.56 (Ar**Me**, 3H, s), 2.26 (Ar**Me**, 3H, s), 2.16 (Ar**Me**, 3H, s), 2.05 (Ar**Me**, 3H, s), 2.01 (Ar**Me**, 3H, s), 1.41 (C**H$_2$**, 2H, m), 1.18 (C**H$_2$**, 2H, m), 0.78 (CH$_2$**Me**, 3H, t, $^3J_{\text{H-H}}$ = 8 Hz), 0.69 (Si**Me**, 3H, s), 0.61 (Si**Me**, 3H, s). ^{13}C{^{1}H} NMR (benzene-d_6, 125 MHz, 298 K) δ (ppm): 141.9 (**Cp**^{n}Bu), 136.0 (**Ar**), 134.5 (**Ar**), 134.1 (**Ar**), 132.9 (**Ar**), 131.2 (**Ar**), 130.8 (**Ar**), 128.4 (**Ar**), 128.0 (**Ar**), 124.8 (**Cp**H), 117.1 (**Cp**H), 115.6 (**Cp**H), 105.0 (**Cp**Si), 83.2 (**Ar**Si), 32.1 (**C**H$_2$), 29.9 (**C**H$_2$), 22.9 (**C**H$_2$), 21.6 (CH$_2$**Me**), 17.8 (Ar**Me**), 17.4 (Ar**Me**), 17.1 (Ar**Me**), 16.7 (Ar**Me**), 15.7 (Ar**Me**), 14.1 (Ar**Me**), 5.2 (Si**Me**), 3.0 (Si**Me**).

6.2.10 Synthesis of ^{Me_2}SB(Cp,I*)Zr(CH$_2$Ph)$_2$ (6)

1.0 equivalent ^{Me_2}SB(Cp,I*)ZrCl$_2$ (0.19 g, 0.38 mmol) and 2.0 equivalents K(CH$_2$Ph) (0.10 g, 0.77 mmol) were added to a Schlenk tube, dissolved in benzene (10 mL) and stirred for 4 h at room temperature. Filtration and removal of the solvent *in vacuo* yielded ^{Me_2}SB(Cp,I*)Zr(CH$_2$Ph)$_2$ as a yellow solid in 44% yield (0.10 g, 0.17 mmol). Yellow crystals, suitable for a single-crystal X-ray diffraction study, were obtained from a saturated pentane solution stored −34 °C for 1 week. ^{1}H NMR (benzene-d_6, 400 MHz, 298 K) δ (ppm): 7.24 (*o*-**Ph**, 2H, m, $^3J_{H-H}$ = 8 Hz), 7.13 (*m*-**Ph**, *p*-**Ph**, 3H, m), 6.91 (*m*-**Ph**, *p*-**Ph**, 3H, m), 6.54 (*o*-**Ph**, 2H, d, $^3J_{H-H}$ = 8 Hz), 6.28 (Cp**H**, 1H, m), 6.10 (Cp**H**, 1H, m), 5.12 (Cp**H**, 1H, m), 5.04 (Cp**H**, 1H, m), 2.52 (Ar**Me**, 3H, s), 2.30 (Ar**Me**, 3H, s), 2.23 (Ar**Me**, 3H, s), 2.10 (Ar**Me**, 6H, s), 1.81 (Ar**Me**, 3H, s), 1.83 (PhC**H**, 1H, d, $^2J_{H-H}$ = 12 Hz), 1.62 (PhC**H**, 1H, d, $^2J_{H-H}$ = 12 Hz), 0.56 (Si**Me**, 3H, s), 0.53 (Si**Me**, 3H, s), 0.33 (PhC**H**, 1H, d, $^2J_{H-H}$ = 12 Hz), 0.05 (PhC**H**, 1H, d, $^2J_{H-H}$ = 12 Hz). ^{13}C{^{1}H} NMR (benzene-d_6, 125 MHz, 298 K) δ (ppm): 153.9 (**Ph**CH$_2$), 153.5 (**Ph**CH$_2$), 133.5 (**Ar**), 133.4 (**Ar**), 133.2 (**Ar**), 130.8 (**Ar**), 130.0 (**Ar**), 129.1 (**Ph**), 128.3 (**Ar**), 128.2 (**Ph**), 128.0 (**Ph**), 127.7 (**Ph**), 126.4 (**Cp**), 126.2 (**Ph**), 125.5 (**Ar**), 124.6 (**Ph**), 121.9 (**Ar**), 121.0 (**Ph**), 120.8 (**Ph**), 119.3 (**Cp**), 118.7 (**Cp**), 113.0 (**Cp**), 100.6 (**Cp**Si), 77.1 (**Ar**Si), 67.9 (Ph**C**H$_2$), 61.3 (Ph**C**H$_2$), 21.4 (Ar**Me**), 21.2 (Ar**Me**), 17.1 (Ar**Me**), 16.4 (Ar**Me**), 16.2 (Ar**Me**), 14.4 (Ar**Me**), 4.2 (Si**Me**), 3.0 (Si**Me**). ^{29}Si NMR (benzene-d_6, 100 MHz, 298 K) δ (ppm): −15.45 (**Si**Me). CHN analysis (%): expected C 72.79, H 7.13; observed C 72.34, H 6.89. MS (EI): molecular ion not found, major ^{Me_2}SB(Cp,I*)Zr(CH$_2$Ph)$^+$ fragment observed at *m*/*z* 501.15. IR (KBr) (cm^{-1}): 3061, 3007, 2905 (b), 1572, 1481, 1374 (b), 1254, 1208, 983, 821 (b), 746, 697, 673.

6.2.11 Synthesis of ^{Me_2}SB(Cp^{Me},I*)Zr(CH$_2$Ph)$_2$ (7)

1.0 equivalent ^{Me_2}SB(Cp^{Me},I*)ZrCl$_2$ (50 mg, 0.10 mmol) and 2.4 equivalents K(CH$_2$Ph) (31.5 mg, 0.24 mmol) were added to a Young's tap NMR tube, dissolved in benzene-d_6 (0.5 mL) and heated at 70 °C for 60 h. Filtration on a frit and removal of the solvent *in vacuo* yielded a 60:40 isomeric mixture, assumed to be *E*-^{Me_2}SB(Cp^{Me},I*)Zr(CH$_2$Ph)$_2$ and *Z*-^{Me_2}SB(Cp^{Me},I*)Zr(CH$_2$Ph)$_2$ respectively based on the composition of the parent complex, as an orange oil which was freeze-dried in benzene to give a yellow solid in 78% yield (48 mg, 0.08 mmol). CHN analysis (%): expected C 73.09, H 7.29; observed C 72.92, H 7.20. IR (KBr) (cm^{-1}): 2945 (b), 1596, 1480, 1450, 1378 (b), 1096 (b), 1030 (b), 845, 805, 742, 700.

E-^{Me_2}SB(Cp^{Me},I*)Zr(CH$_2$Ph)$_2$: ^{1}H NMR (benzene-d_6, 400 MHz, 298 K) δ (ppm): 7.24-6.60 (**Ph**, 10H, m), 5.84 (Cp**H**, 1H, m), 5.26 (Cp**H**, 1H, m), 5.12 (Cp**H**, 1H, m), 2.57 (Ar**Me**, 3H, s), 2.47 (Ar**Me**, 3H, s), 2.27 (Ar**Me**, 3H, s), 2.11 (Ar**Me**, 3H, s), 2.07 (Ar**Me**, 3H, s), 1.99 (PhC**H**, 1H, d, $^2J_{H\text{-}H}$ = 12 Hz), 1.82 (Cp**Me**, 3H, s), 1.79 (Ar**Me**, 3H, s), 1.79 (PhC**H**, 1H, d, $^2J_{H\text{-}H}$ = 12 Hz), 1.68 (PhC**H**, 1H, d, $^2J_{H\text{-}H}$ = 8 Hz), 0.72 (PhC**H**, 1H, d, $^2J_{H\text{-}H}$ = 12 Hz), 0.63 (Si**Me**, 3H, s), 0.53 (Si**Me**, 3H, s), −0.01 (PhC**H**, 1H, d, $^2J_{H\text{-}H}$ = 8 Hz). ^{13}C{^{1}H} NMR (benzene-d_6, 125 MHz, 298 K) δ (ppm): 154.0 (**Ph**CH$_2$), 151.5 (**Ph**CH$_2$), 133.3 (**Cp**Me), 123.0 (**Cp**), 116.7 (**Cp**), 115.5 (**Cp**), 100.7 (**Cp**Si), 79.3 (**Ar**Si), 67.7 (Ph**C**H$_2$), 63.7 (Ph**C**H$_2$), 21.8 (Ar**Me**), 21.8 (Cp**Me**), 17.3 (Ar**Me**), 17.6 (Ar**Me**), 16.5 (Ar**Me**), 16.4 (Ar**Me**), 14.7 (Ar**Me**), 5.2 (Si**Me**), 3.4 (Si**Me**). Resonances between 128.6-121.0 (**Ph**) and 120.7-136.4 (**Ar**) cannot be further assigned.

Z-^{Me_2}SB(Cp^{Me},I*)Zr(CH$_2$Ph)$_2$: ^{1}H NMR (benzene-d_6, 400 MHz, 298 K) δ (ppm): 7.24-6.60 (**Ph**, 10H, m), 6.17 (Cp**H**, 1H, m), 5.37 (Cp**H**, 1H, m), 5.06 (Cp**H**, 1H, m),

2.29 (Ar**Me**, 3H, s), 2.28 (Ar**Me**, 3H, s), 2.25 (Ar**Me**, 3H, s), 2.19 (PhC**H**, 1H, d, $^{2}J_{H\text{-}H}$ = 8 Hz), 2.09 (Ar**Me**, 3H, s), 2.03 (Ar**Me**, 3H, s), 1.88 (Ar**Me**, 3H, s), 1.57 (Cp**Me**, 3H, s), 1.43 (PhC**H**, 1H, d, $^{2}J_{H\text{-}H}$ = 12 Hz), 0.68 (PhC**H**, 1H, d, $^{2}J_{H\text{-}H}$ = 12 Hz), 0.63 (Si**Me**, 3H, s), 0.53 (Si**Me**, 3H, s), 0.08 (PhC**H**, 1H, d, $^{2}J_{H\text{-}H}$ = 8 Hz). $^{13}C\{^{1}H\}$ NMR (benzene-d_6, 125 MHz, 298 K) δ (ppm): 154.0 (**Ph**CH_2), 151.0 (**Ph**CH_2), 130.0 (**Cp**Me), 126.7 (**Cp**), 120.7 (**Cp**), 113.4 (**Cp**), 100.5 (**Cp**Si), 78.3 (**Ar**Si), 65.7 (Ph**C**H_2), 60.2 (Ph**C**H_2), 21.7 (Ar**Me**), 17.7 (Ar**Me**), 17.2 (Ar**Me**), 13.4 (Cp**Me**), 15.0 (Ar**Me**), 14.7 (Ar**Me**), 14.4 (Ar**Me**), 3.6 (Si**Me**), 3.2 (Si**Me**). Resonances between 128.6-121.0 (**Ph**) and 120.7-136.4 (**Ar**) cannot be further assigned.

6.2.12 Synthesis of ^{Me_2}SB(Cp,I*)$ZrMe_2$ (8)

1.0 equivalent ^{Me_2}SB(Cp,I*)$ZrCl_2$ (0.20 g, 0.41 mmol) was dissolved in toluene in a Schlenk tube and cooled to −78 °C. 2.2 equivalents MeLi (0.57 mL, 0.92 mmol, 1.6 M in diethyl ether) were added dropwise and the solution stirred for 4 h at room temperature, resulting in a colour change from orange to yellow. Filtration and removal of the solvent *in vacuo* yielded ^{Me_2}SB(Cp,I*)$ZrMe_2$ as a yellow solid in 18% yield (33 mg, 0.17 mmol). Yellow crystals, suitable for a single-crystal X-ray diffraction study, were obtained from a saturated pentane solution stored at −34 °C for 6 months. ^{1}H NMR (benzene-d_6, 400 MHz, 298 K) δ (ppm): 6.62 (Cp**H**, 1H, m), 6.55 (Cp**H**, 1H, m), 5.59 (Cp**H**, 1H, m), 5.18 (Cp**H**, 1H, m), 2.54 (Ar**Me**, 3H, s), 2.44 (Ar**Me**, 3H, s), 2.18 (Ar**Me**, 6H, s), 2.08 (Ar**Me**, 3H, s), 1.83 (Ar**Me**, 3H, s), 0.63 (Si**Me**, 3H, s), 0.58 (Si**Me**, 3H, s), −0.11 (Zr**Me**, 3H, s), −1.18 (Zr**Me**, 3H, s). $^{13}C\{^{1}H\}$ NMR (benzene-d_6, 125 MHz, 298 K) δ (ppm): 132.0 (**Ar**), 131.7 (**Ar**), 131.4 (**Ar**), 131.2 (**Ar**), 129.4 (**Ar**), 129.1 (**Ar**), 126.9 (**Ar**), 121.0 (**Cp**H), 119.9 (**Ar**), 117.8 (**Cp**H), 114.4 (**Cp**H), 111.6 (**Cp**H), 99.4 (**Cp**Si), 78.1 (**Ar**Si), 33.5 (Zr**Me**), 31.7 (Zr**Me**), 21.0 (Ar**Me**), 17.2 (Ar**Me**), 17.0 (Ar**Me**), 16.3 (Ar**Me**), 16.1 (Ar**Me**), 14.6 (Ar**Me**), 5.1 (Si**Me**), 3.3

(Si**Me**). ^{29}Si NMR (benzene-d_6, 100 MHz, 298 K) δ (ppm): −16.28 (**Si**Me). MS (EI): molecular ion not found, major ^{Me_2}SB(Cp,I*)ZrMe$^+$ fragment observed at *m*/*z* 425.12. IR (KBr) (cm^{-1}): 2982, 2911, 2854, 1453 (b), 1381 (b), 1287, 1252, 1168, 1051, 839, 808, 677.

6.2.13 Synthesis of ^{Me_2}SB(Cp^{Me},I*)ZrMe$_2$ (9)

1.0 equivalent ^{Me_2}SB(Cp^{Me},I*)ZrCl$_2$ (150 mg, 0.30 mmol) was dissolved in toluene in a Schlenk tube and cooled to −78 °C. 2.2 equivalents MeLi (0.42 mL, 0.60 mmol, 1.6 M in diethyl ether) were added dropwise and the solution stirred for 4 h at room temperature, resulting in a colour change from orange to yellow. Filtration and removal of the solvent *in vacuo* yielded a 60:40 isomeric mixture, assumed to be *E*-^{Me_2}SB(Cp^{Me},I*)ZrMe$_2$ and *Z*-^{Me_2}SB(Cp^{Me},I*)ZrMe$_2$ respectively based on the composition of the parent complex, as a dark orange oil which was freeze-dried in benzene to give a yellow solid in 72% yield (99 mg, 0.22 mmol).

E-^{Me_2}SB(Cp^{Me},I*)ZrMe$_2$: ^{1}H NMR (benzene-d_6, 400 MHz, 298 K) δ (ppm): 6.24 (Cp**H**, 1H, m), 5.57 (Cp**H**, 1H, m), 4.87 (Cp**H**, 1H, m), 2.46 (Ar**Me**, 6H, s), 2.21 (Cp**Me**, 3H, s), 2.13 (Ar**Me**, 3H, s), 2.10 (Ar**Me**, 6H, s), 1.81 (Ar**Me**, 3H, s), 0.65 (Si**Me**, 3H, s), 0.60 (Si**Me**, 3H, s), −0.24 (Zr**Me**, 3H, s), −1.19 (Zr**Me**, 3H, s). ^{13}C{^{1}H} NMR (benzene-d_6, 125 MHz, 298 K) δ (ppm): 132.2 (**Ar**), 131.9 (**Ar**), 131.7 (**Ar**), 131.2 (**Ar**), 129.6 (**Ar**), 129.5 (**Ar**), 127.5 (**Ar**), 127.0 (**Ar**), 130.5 (**Cp**Me), 118.8 (**Cp**H), 115.3 (**Cp**H), 112.5 (**Cp**H), 99.2 (**Cp**Si), 77.7 (**Ar**Si), 36.6 (Zr**Me**), 33.0 (Zr**Me**), 21.3 (Cp**Me**), 17.5 (Ar**Me**), 17.2 (Ar**Me**), 16.5 (Ar**Me**), 16.4 (Ar**Me**), 14.9 (2 × Ar**Me**), 5.1 (Si**Me**), 3.5 (Si**Me**).

Z-^{Me_2}SB(Cp^{Me},I*)ZrMe$_2$: ^{1}H NMR (benzene-d_6, 400 MHz, 298 K) δ (ppm): 6.33 (Cp**H**, 1H, m), 5.40 (Cp**H**, 1H, m), 5.14 (Cp**H**, 1H, m), 2.58 (Ar**Me**, 6H, s), 2.19

(Ar**Me**, 3H, s), 2.17 (Cp**Me**, 3H, s), 2.11 (Ar**Me**, 6H, s), 1.88 (Ar**Me**, 3H, s), 0.62 (Si**Me**, 3H, s), 0.61 (Si**Me**, 3H, s), −0.14 (Zr**Me**, 3H, s), −1.28 (Zr**Me**, 3H, s). $^{13}C\{^{1}H\}$ NMR (benzene-d_6, 125 MHz, 298 K) δ (ppm): 132.3 (**Ar**), 132.2 (**Ar**), 131.8 (**Ar**), 131.2 (**Ar**), 127.5 (**Cp**Me), 129.6 (**Ar**), 129.5 (**Ar**), 128.6 (**Ar**), 126.9 (**Ar**), 122.0 (**Cp**H), 116.2 (**Cp**H), 112.3 (**Cp**H), 99.0 (**Cp**Si), 78.3 (**Ar**Si), 35.6 (Zr**Me**), 30.2 (Zr**Me**), 21.3 (Cp**Me**), 17.5 (Ar**Me**), 17.2 (Ar**Me**), 16.5 (2 × Ar**Me**), 15.0 (2 × Ar**Me**), 5.0 (Si**Me**), 3.6 (Si**Me**).

6.2.14 Synthesis of $[^{Me_2}SB(Cp,I^*)ZrMe]^+$ $[X\text{-}MAO]^-$

1.0 equivalent $^{Me_2}SB(Cp,I^*)ZrX_2$ (2 mg, 3.4–4.5 × 10^{-3} mmol, X = Cl, Me and CH_2Ph) and 50 equivalents MAO (9.8–13.1 mg, 0.17–0.23 mmol) were added to a Young's tap NMR tube. Benzene-d_6 (0.5 mL) was added, resulting in an immediate colour change to bright purple. The formation of $[^{Me_2}SB(Cp,I^*)ZrMe]^+$ $[X\text{-}MAO]^-$ was confirmed by ^1H NMR spectroscopy in quantitative yield. ^1H NMR (benzene-d_6, 400 MHz, 298 K) δ (ppm): 6.09 (Cp**H**, 1H, m), 6.00 (Cp**H**, 1H, m), 4.68 (Cp**H**, 1H, m), 4.62 (Cp**H**, 1H, m), 2.33 (Ar**Me**, 3H, s), 1.98 (Ar**Me**, 3H, s), 1.69 (Ar**Me**, 3H, s), 0.90 (Ar**Me**, 6H, s), 0.84 (Ar**Me**, 3H, s), −1.66 (Zr**Me**, 3H, s).

6.2.15 Synthesis of *Z*-$^{Me_2}SB(Cp,I^*)ZrCl(O\text{-}2,6\text{-}Me\text{-}C_6H_3)$ (*Z*-10)

$^{Me_2}SB(Cp,I^*)ZrCl_2$ (300 mg, 0.62 mmol) and 2.2 equivalents $K(O\text{-}2,6\text{-}Me\text{-}C_6H_3)$ (219 mg, 1.37 mmol) were added to a Schlenk tube, dissolved in benzene (20 mL) and stirred at room temperature for 16 h. The solvent was removed *in vacuo* to give a crude mixture of *E*- and *Z*-$^{Me_2}SB(Cp,I^*)ZrCl(O\text{-}2,6\text{-}Me\text{-}C_6H_3)$. Extraction in pentane (2 × 20 mL) and storage at −34 °C overnight yielded *Z*-$^{Me_2}SB(Cp,I^*)ZrCl(O\text{-}2,6\text{-}Me\text{-}C_6H_3)$ as yellow crystals suitable for a single-crystal X-ray diffraction study in 13% yield (46 mg, 0.08 mmol).

Z-^{Me_2}SB(Cp,I*)ZrCl(O-2,6-Me-C_6H_3): ^{1}H NMR (benzene-d_6, 500 MHz, 298 K) δ (ppm): 6.91 (OAr**H**, 1H, d, $^3J_{H\text{-}H}$ = 10 Hz), 6.87 (OAr**H**, 1H, d, $^3J_{H\text{-}H}$ = 10 Hz), 6.70 (OAr**H**, 1H, t, $^3J_{H\text{-}H}$ = 10 Hz), 6.51 (Cp**H**, 1H, m), 6.03 (Cp**H**, 1H, m), 5.88 (Cp**H**, 1H, m), 5.81 (Cp**H**, 1H, m), 2.62 (Ar**Me**, 3H, s), 2.42 (Ar**Me**, 3H, s), 2.40 (OAr**Me**, 3H, s), 2.22 (Ar**Me**, 3H, s), 2.08 (Ar**Me**, 3H, s), 1.99 (Ar**Me**, 3H, s), 1.64 (Ar**Me**, 3H, s), 1.48 (OAr**Me**, 3H, s), 0.80 (Si**Me**, 3H, s), 0.61 (Si**Me**, 3H, s). ^{13}C{^{1}H} NMR (benzene-d_6, 125 MHz, 298 K) δ (ppm): 160.0 (O**Ar**), 137.4 (**Ar**), 133.5 (**Ar**), 132.7 (**Ar**), 131.5 (**Ar**), 129.3 (**Ar**), 129.0 (O**Ar**H), 128.6 (**Ar**), 128.4 (O**Ar**H), 128.2 (O**Ar**Me), 127.5 (**Ar**), 126.0 (**Cp**), 124.0 (O**Ar**Me), 123.3 (**Ar**), 122.2 (**Cp**), 119.4 (O**Ar**H), 118.2 (**Cp**), 110.4 (**Cp**Si), 110.2 (**Cp**), 88.1 (**Ar**Si), 22.0 (Ar**Me**), 18.9 (OAr**Me**), 17.4 (Ar**Me**), 17.3 (Ar**Me**), 16.9 (Ar**Me**), 16.5 (OAr**Me**), 16.1 (Ar**Me**), 15.8 (Ar**Me**), 6.1 (Si**Me**), 2.9 (Si**Me**).

E-^{Me_2}SB(Cp,I*)ZrCl(O-2,6-Me-C_6H_3): ^{1}H NMR (benzene-d_6, 400 MHz, 298 K) δ (ppm): 7.09 (OAr**H**, 1H, d, $^3J_{H\text{-}H}$ = 8 Hz), 7.01 (OAr**H**, 1H, d, $^3J_{H\text{-}H}$ = 8 Hz), 6.83 (OAr**H**, 1H, t, $^3J_{H\text{-}H}$ = 8 Hz), 6.26 (Cp**H**, 1H, m), 6.13 (Cp**H**, 1H, m), 5.94 (Cp**H**, 1H, m), 5.61 (Cp**H**, 1H, m), 2.42 (Ar**Me**, 3H, s), 2.34 (Ar**Me**, 3H, s), 2.24 (Ar**Me**, 3H, s), 2.22 (Ar**Me**, 3H, s), 2.19 (Ar**Me**, 3H, s), 2.18 (Ar**Me**, 3H, s), 2.15 (Ar**Me**, 3H, s), 2.09 (Ar**Me**, 3H, s), 0.75 (Si**Me**, 3H, s), 0.64 (Si**Me**, 3H, s).

6.2.16 Synthesis of *E*-^{Me_2}SB(Cp,I*)ZrCl(O-2,6-^{i}Pr-C_6H_3) (*E*-11)

^{Me_2}SB(Cp,I*)$ZrCl_2$ (300 mg, 0.62 mmol) and 2.2 equivalents K(O-2,6-^{i}Pr-C_6H_3) (296 mg, 1.37 mmol) were added to a Schlenk tube, dissolved in benzene (20 mL) and stirred at room temperature for 16 h. Filtration and removal of the solvent *in vacuo* yielded a crude mixture of *E*- and *Z*-^{Me_2}SB(Cp,I*)ZrCl(O-2,6-^{i}Pr-C_6H_3). Extraction in pentane (2 × 20 mL) and storage at −34 °C overnight yielded

E-^{Me_2}SB(Cp,I*)ZrCl(O-2,6-^{i}Pr-C_6H_3) as yellow crystals suitable for a single-crystal X-ray diffraction study in 14% yield (56 mg, 0.09 mmol).

E-^{Me_2}SB(Cp,I*)ZrCl(O-2,6-^{i}Pr-C_6H_3): ^{1}H NMR (benzene-d_6, 400 MHz, 298 K) δ (ppm): 7.14 (OAr**H**, 2H, d, $^{3}J_{H-H}$ = 8 Hz), 7.12 (OAr**H**, 2H, d, $^{3}J_{H-H}$ = 8 Hz), 6.99 (OAr**H**, 1H, t, $^{3}J_{H-H}$ = 8 Hz), 6.40 (Cp**H**, 1H, m), 6.26 (Cp**H**, 1H, m), 5.89 (Cp**H**, 1H, m), 5.71 (Cp**H**, 1H, m), 3.61 (OArC**H**Me$_2$, 1H, sep, $^{3}J_{H-H}$ = 8 Hz), 3.07 (OArC**H**Me$_2$, 1H, sep, $^{3}J_{H-H}$ = 8 Hz), 2.46 (Ar**Me**, 3H, s), 2.31 (Ar**Me**, 3H, s), 2.25 (Ar**Me**, 3H, s), 2.21 (Ar**Me**, 3H, s), 2.18 (Ar**Me**, 3H, s), 2.15 (Ar**Me**, 3H, s), 1.30 (OArCH**Me**, 12H, m), 0.77 (Si**Me**, 3H, s), 0.66 (Si**Me**, 3H, s). ^{13}C{^{1}H} NMR (benzene-d_6, 125 MHz, 298 K) δ (ppm): 158.9 (O**Ar**), 138.5 (O**Ar**^{i}Pr), 136.9 (**Ar**), 135.5 (**Ar**), 134.8 (O**Ar**^{i}Pr), 133.9 (**Ar**), 133.9 (**Ar**), 129.7 (**Ar**), 129.5 (**Ar**), 128.2 (**Ar**), 126.9 (**Ar**), 125.1 (**Cp**), 123.9 (O**Ar**H), 123.8 (O**Ar**H), 120.6 (O**Ar**H), 120.1 (**Cp**), 120.0 (**Cp**) 113.1 (**Cp**Si), 109.1 (**Cp**), 85.8 (**Ar**Si), 27.4 (OArCH**Me**), 25.7 (OAr**C**H), 25.3 (OArCH**Me**), 25.0 (OAr**C**H), 23.7 (OArCH**Me**), 23.0 (OArCH**Me**), 21.2 (Ar**Me**), 17.5 (Ar**Me**), 17.4 (Ar**Me**), 16.7 (Ar**Me**), 16.6 (Ar**Me**), 15.1 (Ar**Me**), 4.4 (Si**Me**), 3.2 (Si**Me**).

Z-^{Me_2}SB(Cp,I*)ZrCl(O-2,6-^{i}Pr-C_6H_3): ^{1}H NMR (benzene-d_6, 400 MHz, 298 K) δ (ppm): 7.05 (OAr**H**, 2H, m), 6.83 (OAr**H**, 1H, t, $^{3}J_{H-H}$ = 8 Hz), 6.79 (Cp**H**, 1H, m), 6.19 (Cp**H**, 1H, m), 6.12 (Cp**H**, 1H, m), 5.61 (Cp**H**, 1H, m), 3.56 (OArC**H**Me$_2$, 1H, sep, $^{3}J_{H-H}$ = 10 Hz), 2.93 (OArC**H**Me$_2$, 1H, sep, $^{3}J_{H-H}$ = 10 Hz), 2.57 (Ar**Me**, 3H, s) 2.42 (Ar**Me**, 3H, s), 2.35 (Ar**Me**, 3H, s), 1.99 (Ar**Me**, 3H, s), 1.88 (Ar**Me**, 3H, s), 1.66 (Ar**Me**, 3H, s), 1.15 (OArCH**Me**, 12H, m), 0.85 (Si**Me**, 3H, s), 0.69 (Si**Me**, 3H, s).

6.3 Experimental Details for Chapter 3

6.3.1 Solution-phase propylene polymerisation

1000 equivalents MAO (60 mg) was added to a 150 mL Rotaflo ampoule and washed in with hexane (10 mL). A stock solution of complex in toluene was prepared (3 mg in 6 mL), 1 mL was added to the ampoule and washed in with hexane (39 mL). The ampoule headspace was degassed while heating to temperature. The ampoule was opened to propylene gas (2 bar) and the solution stirred at 1000 rpm for the duration of the run. On completion, the reaction mixture was degassed and decanted into methanol. The oily polymer was isolated, washed with pentane and dried under vacuum. All runs were carried out, at least, in duplicate.

6.3.2 Solution-phase ethylene polymerisation

200 equivalents MAO (15 mg) were added to a 150 mL Rotaflo ampoule and washed in with hexane (10 mL). A stock solution of the complex in toluene was prepared (5 mg in 10 mL), 1 mL added to the ampoule and washed in with hexane (39 mL). The ampoule headspace was degassed while heating to temperature. The ampoule was opened to ethylene (2 bar) and the solution stirred at 1000 rpm for the duration of the run. On completion, the reaction mixture was degassed, the polymer filtered, washed with pentane (50 mL) and dried under vacuum. All runs were carried out, at least, in duplicate.

6.3.3 Synthesis of activated supports (SSMAO and LDHMAO)

Toluene (40 mL) was added to 1.0 equivalent SiO_2 or LDH (Mg_3Al-CO_3) and 0.5 equivalents MAO in a Schlenk tube and the slurry heated at 80 °C for 2 h with swirling. The colourless solid was allowed to settle, the supernatant decanted and the product dried under vacuum to give the activated supports in quantitative yield.

6.3.4 Synthesis of supported catalysts

The activated support and complex were weighed into a Schlenk tube. Toluene (40 mL) was added and the slurry heated at 60 °C for 1 h with swirling. The coloured solid was allowed to settle and the clear, colourless supernatant decanted. The solid was dried *in vacuo* for at least 4 h to give the pre-catalyst product as a faintly coloured powder in quantitative yield.

sMAO(1G)-^{Me_2}SB(Cp,I*)$ZrCl_2$: ^{29}Si CP/MAS SSNMR (10 kHz, 298 K) δ (ppm): −12.2 (**Si**Me). ^{13}C CP/MAS SSNMR (10 kHz, 298 K) δ (ppm): 137.5 (**Ar**), 135.2 (**Ar**), 131.6 (**Ar**), 128.5 (**Ar**), 25.1 (Ar**Me**), 20.4 (Ar**Me**), 18.9 (Ar**Me**), 17.1 (Ar**Me**), 16.1 (Ar**Me**), 7.8 (Si**Me**), −7.9 (AlO**Me**). ^{27}Al DP/MAS SSNMR (15 kHz, 298 K) δ (ppm): 347.1, 208.8, 82.6, −83.1, −240.8. IR (KBr) (cm^{-1}): 2948 (b), 1593, 1536, 1272, 732 (b).

sMAO(3G)-^{Me_2}SB(Cp,I*)$ZrCl_2$: ^{29}Si CP/MAS SSNMR (10 kHz, 298 K) δ (ppm): −13.3 (**Si**Me). ^{13}C CP/MAS SSNMR (10 kHz, 298 K) δ (ppm): 130.0 (**Ar**), 131.4 (**Ar**), 128.7 (**Ar**), 51.8 (Zr**Me**), 16.7 (Ar**Me**), −7.6 (AlOMe). ^{27}Al DP/MAS SSNMR (15 kHz, 298 K) δ (ppm): 348.7, 210.9, 79.2, −84.0, −241.3. IR (KBr) (cm^{-1}): 2953 (b), 1598, 1536, 1485, 1222, 738 (b).

sMAO(GAS)-^{Me_2}SB(Cp,I*)$ZrCl_2$: ^{29}Si CP/MAS SSNMR (10 kHz, 298 K) δ (ppm): −13.7 (**Si**Me). ^{13}C CP/MAS SSNMR (10 kHz, 298 K) δ (ppm): 135.6 (**Ar**), 132.0 (**Ar**), 128.5 (**Ar**), 51.8 (Zr**Me**), 16.7 (Ar**Me**), −8.0 (AlO**Me**). ^{27}Al DP/MAS SSNMR (15 kHz, 298 K) δ (ppm): 345.6, 207.5, 77.2, −82.7, −242.0. IR (KBr) (cm^{-1}): 2926 (b), 1603, 1530, 1440, 1225, 732 (b).

sMAO(PFP)-^{Me_2}SB(Cp,I*)$ZrCl_2$: ^{29}Si CP/MAS SSNMR (10 kHz, 298 K) δ (ppm): −12.0 (**Si**Me). ^{13}C CP/MAS SSNMR (10 kHz, 298 K) δ (ppm): 139.3 (O**C**$_6$F$_5$),

132.8 (O**C**$_6$F$_5$), 128.4 (**Ar**), 41.6 (Zr**Me**), 19.3 (Ar**Me**), 15.9 (Ar**Me**), −9.8 (AlO**Me**). ^{27}Al DP/MAS SSNMR (15 kHz, 298 K) δ (ppm): 342.9, 203.2, −87.8, −246.7. ^{19}F DEPT SSNMR (15 kHz, 298 K) δ (ppm): −165.0. IR (KBr) (cm^{-1}): 2953 (b), 1530 (b), 1437, 1364, 1315, 1222, 1040, 1004, 813 (b), 683 (b).

SSMAO-^{Me_2}SB(Cp,I*)ZrCl$_2$: ^{29}Si CP/MAS SSNMR (10 kHz, 298 K) δ (ppm): −102.2 (**Si**O$_2$), −15.5–25 ((**Si**O)$_3$SiR, (**Si**O)$_2$**Si**ROH and (**Si**O)**Si**R(OH)$_2$ where R is bound MAO). ^{13}C CP/MAS SSNMR (10 kHz, 298 K) δ (ppm): 139.1 (**Ph**), 129.3 (**Ph**), 120.0 (**Ar**), 111.1 (**Ar**), 51.0 (Zr**Me**), 29.9 (Ar**Me**), 22.9 (Ar**Me**), 23.1 (Ar**Me**), 13.8 (Ar**Me**), −9.0 (AlO**Me**). ^{27}Al DP/MAS SSNMR (15 kHz, 298 K) δ (ppm): 344.2, 207.0, −82.0, −236.8. IR (KBr) (cm^{-1}): 2947 (b), 1152 (b), 820 (b), 722 (b), 478 (b).

sMAO(1G)-^{Me_2}SB(Cp,I*)Zr(CH$_2$Ph)$_2$: ^{29}Si CP/MAS SSNMR (10 kHz, 298 K) δ (ppm): −12.1 (**Si**Me). ^{13}C CP/MAS SSNMR (10 kHz, 298 K) δ (ppm): 137.1 (**Ph**), 131.2 (**Ph**), 128.2 (**Ar**), 125.4 (**Ar**), 32.6 (Ar**Me**), 26.8 (Ar**Me**), 23.1 (Ar**Me**), 19.4 (Ar**Me**), 15.3 (Ar**Me**), −7.6 (AlO**Me**). ^{27}Al DP/MAS SSNMR (15 kHz, 298 K) δ (ppm): 343.5, 204.5, 82.5, −83.1, −238.8. IR (KBr) (cm^{-1}): 2953 (b), 1598, 1534, 1449, 1382, 753 (b).

sMAO(1G)-^{Me_2}SB(Cp,I*)ZrMe$_2$: ^{29}Si CP/MAS SSNMR (10 kHz, 298 K) δ (ppm): −13.9 (**Si**Me). ^{13}C CP/MAS SSNMR (10 kHz, 298 K) δ (ppm): 136.0 (**Ph**), 131.1 (**Ph**), 128.7 (**Ar**), 125.4 (**Ar**), 51.7 (Zr**Me**), 20.3 (Ar**Me**), 16.4 (Ar**Me**), −7.7 (AlO**Me**). ^{27}Al DP/MAS SSNMR (15 kHz, 298 K) δ (ppm): 346.5, 208.2, 76.6, −82.9, −241.6. IR (KBr) (cm^{-1}): 2951 (b), 108, 1446, 1217, 742 (b).

sMAO(1G)-^{Me_2}SB(Cp^{Me},I*)ZrCl$_2$: IR (KBr) (cm^{-1}): 3025, 2951 (b), 1598, 1540, 1445, 1367, 1219, 756 (b).

6.3.5 Slurry-phase ethylene polymerisation

TiBA (150 mg) in hexane (10 mL) was added to a 150 mL Rotaflo ampoule. The pre-catalyst (10 mg) was added and washed in with hexane (40 mL). The ampoule headspace was degassed while heating to temperature. The ampoule was opened to ethylene gas (2 bar) and the solution stirred at 1000 rpm for the duration of the run. On completion, the reaction mixture was degassed, the polymer filtered, washed with pentane (50 mL) and dried under reduced pressure on a frit. All runs were carried out, at least, in duplicate.

PE produced using sMAO(1G)-^{Me_2}SB(Cp,I*)$ZrCl_2$ ($[Al]_0/[Zr]_0$ = 200, 80 °C, 30 minutes): $^{13}C\{^1H\}$ NMR (1,2-dichloroethane-d_4, 125 MHz, 393 K) δ (ppm): 37.9 ($(CH_2)_n(\mathbf{C}H_2)CH(CH_3)(CH_2)_n$), 32.5 ($(CH_2)_n\mathbf{C}H(CH_3)(CH_2)_n$), 31.9 ($(CH_2)_n\mathbf{C}H_2CH_2CH_3$), 29.3 ($(CH_2)_n\mathbf{C}H_2CH_2CH_2CH_3$), 22.6 ($(CH_2)_n\mathbf{C}H_2CH_3$), 21.4 ($(CH_2)_nCH(\mathbf{C}H_3)(CH_2)_n$), 13.9 ($(CH_2)_n\mathbf{C}H_3$).

6.3.6 Larger scale slurry-phase ethylene polymerisation

TiBA (750 mg) in hexane (10 mL) was added to a 500 mL Rotaflo ampoule. The pre-catalyst (10 mg) was added and washed in with hexane (240 mL). The ampoule headspace was degassed while heating to temperature. The ampoule was opened to ethylene gas (2 bar) and the solution stirred at 1000 rpm for the duration of the run. On completion, the reaction mixture was degassed, the polymer filtered, washed with pentane (50 mL) and dried under reduced pressure on a frit.

6.3.7 Gel-permeation chromatography (GPC)

GPC samples were collected by Ms Liv Thobrzu at Norner AS (Norway) on a high-temperature gel permeation chromatograph with an IR5 infrared detector (GPC-IR5). Samples were dissolved in 1,2,4-trichlorobenzene (TCB) containing 300 ppm of 3,5-di-tert-buty-4-hydroxytoluene (BHT) at 160 °C for 90 minutes and then filtered with a 10 µm SS filter before being passed through the GPC column. The samples were run under a flow rate of 0.5 mL min^{-1} using TCB containing 300 ppm of BHT as the mobile phase with 1 mg mL^{-1} BHT added as a flow rate marker. The GPC column and detector temperature were set at 145 and 160 °C respectively.

6.4 Experimental Details for Chapter 4

6.4.1 Ethylene/1-hexene and ethylene/1-hexene/hydrogen copolymerisation

TiBA (150 mg) in hexane (10 mL) was added to a 150 mL Rotaflo ampoule with a sidearm. The pre-catalyst (10 mg) was added and washed in with hexane (35 mL). A 1-hexene stock solution was prepared (400 mg in 4 mL hexane), varying amounts added to the sidearm and made up to a total volume of 5 mL with hexane. The ampoule headspace was degassed while heating to temperature. The ampoule was opened to ethylene gas (2 bar) or an ethylene/hydrogen mixture (2 bar, 2%), the sidearm opened and the solution stirred at 1000 rpm for the duration of the run. On completion, the reaction mixture was degassed, the polymer filtered, washed with pentane (50 mL) and dried under reduced pressure on a frit. All runs were carried out, at least, in duplicate.

6.4.2 Ethylene/hydrogen polymerisation

TiBA (150 mg) in hexane (10 mL) was added to a 150 mL Rotaflo ampoule. The pre-catalyst (10 mg) was added and washed in with hexane (40 mL). The ampoule headspace was degassed while heating to temperature. The ampoule was opened to an ethylene/hydrogen mixture (2 bar, 2%) and the solution stirred at 1000 rpm for the duration of the run. The ethylene/hydrogen consumption was monitored using a Bronkhorst EL-FLOW Prestige mass flow meter. On completion, the reaction mixture was degassed, the polymer filtered, washed with pentane (50 mL) and dried under reduced pressure on a frit. All runs were carried out, at least, in duplicate.

6.4.3 High throughput screening (HTExplore, University of Naples)

Polymerisation experiments were conducted by Dr Alessio Mingione in a Freeslate Parallel Pressure Reactor (PPR) platform consisting of 48 reaction cells contained within a triple MBraun LabMaster Glovebox. The cells (geometric volume ~23 mL,

working volume 5 mL) were individually controlled with monitoring of temperature and pressure. Slurry-phase polymerisations were run in semi-continuous mode. Two Vortex stir plates fitted with 6 × 8 racks held the catalyst system components (pre-catalyst and scavenger). The injection system consisted of a dual-arm robot with specialised needles and injectors. Liquid solvents, diluents and monomers were fed through syringe pumps, with gaseous monomers and diluents fed through direct lines with solenoid valves to individual cells.[11]

Heptane solvent (5 mL) and TiBA scavenger (10 μmmol) were added to the PPRs *via* robotic syringes which were then heated to 80 °C and pressurised to 8.3 bar with ethylene. When required, hydrogen was added to the reaction vessel *via* a 0.8 or 1.6% mixed hydrogen/nitrogen feed. Pre-catalyst (0.05–0.15 mg in heptane slurry) and 1-hexene (when required) were injected with robotic syringes and chased by a certain amount of heptane solvent. The reactions were run for 1 hour or until a specific ethylene uptake was reached (8.3 bar for ethylene homopolymerisation and 5.5 bar for ethylene/1-hexene copolymerisation), following which the reaction was quenched with an excess of dry air. The polymer samples were transferred to a Genevac EZ-Plus centrifugal evaporator to remove volatiles and then dried under vacuum overnight.

The polymers were characterised by $^{13}C\{^{1}H\}$ NMR spectroscopy, high-temperature gel permeation chromatography (GPC) and analytical crystallisation elution fractionation (CEF). $^{13}C\{^{1}H\}$ NMR spectra were run at 393 K in 1,1,2,2-tetrachloroethane-d_2 on a 100 MHz Bruker Avance III 400 spectrometer equipped with a 5 mm high-temperature cryoprobe and a robotic sample changer. GPC curves were recorded with a FreeSlate Rapid GPC setup, equipped with a set of two mixed-bed Agilent PLgel 10 μm columns and a Polymer Char IR4 detector. CEF curves

were collected with a Polymer Char CEF setup, equipped with a 42-well auto-sampler, an IR5 detector and a dual-capillary viscometer detector.

6.4.4 Large scale polymerisation (SCG Chemicals Co., Ltd. (Thailand))

Polymerisations were performed by Mr Thawesak Parawan, Mr Somjet Songnoey or Mr Pongsiri Kaeoyok. A 2.5 L steel reactor was charged with hexane (850 mL) and TEA scavenger (0.5 mmol L^{-1}) and saturated with ethylene gas (2 bar). 1-hexene (when required) was added at an overpressure. The reactor was heated to temperature and a mixture of pre-catalyst (0.025–0.050 g) in hexane (20 mL) was added and washed in with a further 130 mL hexane. The ethylene pressure was set to 8 bar and the polymerisations run for 1 hour. On completion, the polymer was decanted and dried in an oven overnight.

6.5 Experimental Details for Chapter 5

6.5.1 Lactide polymerisation

L-, *D*- or *rac*-lactide (40 mg, 0.278 mmol) was weighed into a Young's tap NMR spectroscopy tube. Stock solutions of the complex and benzyl alcohol (when required) in an amount of deuterated solvent corresponding to an initial lactide concentration ($[LA]_0$) of 0.5 M were prepared and the desired quantity added to the NMR tube. Polymerisations were run at 60–100 °C and halted at certain time intervals by submerging the NMR tubes in an ice bath. The conversion was monitored by ^{1}H NMR spectroscopy. On completion, the reaction mixture was decanted into −5 °C pentane (10 mL), the solution allowed to settle and the solvent removed. The polymer was then washed with diethyl ether (2 × 10 mL) and dried under vacuum at 30 °C for 18 hours. All polymerisations were carried out, at least, in duplicate.

6.5.2 Larger scale lactide polymerisation

L- or *rac*-lactide (200 mg, 1.387 mmol) and complex ($[LA]_0/[M]_0 = 50$) were weighed into 10 mL ampoules. A stock solution of benzyl alcohol ($[BnOH]_0/[M]_0 = 2$) in an amount of toluene corresponding to an initial lactide concentration ($[LA]_0$) of 0.5 M was prepared and the desired quantity added to the ampoule. Polymerisations were run at 80 °C with stirring at 1000 rpm for the desired time. On completion, the reaction mixture was decanted into −5 °C pentane (10 mL), the solution allowed to settle and the solvent removed. The polymer was then washed with diethyl ether (2 × 20 mL) and dried under vacuum at 30 °C for 18 hours. Percentage conversion was calculated as (mass $PLA_{experimental}$/mass $PLA_{theoretical}$) × 100.

6.5.3 Gel-permeation chromatography (GPC)

GPC analysis was performed by Dr Christopher Durr (University of Oxford) or Dr Duncan Fraser (University of Oxford) on a Shimadzu LC-20AD instrument at 40 °C. Polymer samples were dissolved in SEC grade THF and filtered prior to analysis. Two Mixed Bed PSS SDV linear S columns were used in series, with THF as the eluent and a flow rate of 1 mL min^{-1}. The instrument was calibrated using narrow molecular weight polystyrene standards (correction factor of 0.58).[12]

6.5.4 MALDI-TOF mass spectrometry

Matrix-assisted laser desorption/ionisation time of flight spectra were collected Dr Victor Mikhailov (University of Oxford) using a Bruker MALDI Autoflex TOF MS. Samples were run using either a DHB or DCTB matrix. The DHB matrix was prepared by mixing the sample with DHB (10 mg mL^{-1} in 70:30 H_2O:CH_3CN) in a 1:1 volume ratio. The DCTB matrix was prepared by mixing 10 µL of the sample with 10 µL DCTB (40 mg mL^{-1} in THF) and 2.5 µL KTFA (5 mg mL^{-1} in THF). 1.5 µL of the mixed solutions were spotted on the MALDI plate and dried prior to the run.

6.6 References

1. M. J. Monreal, R. K. Thomson, T. Cantat, N. E. Travia, B. L. Scott and J. L. Kiplinger, *Organometallics*, 2011, **30**, 2031-2038.
2. P. J. Bailey, R. A. Coxall, C. M. Dick, S. Fabre, L. C. Henderson, C. Herber, S. T. Liddle, D. Loroño-González, A. Parkin and S. Parsons, *Chem. - Eur. J.*, 2003, **9**, 4820-4828.
3. J. Cosier and A. M. Glazer, *J. Appl. Crystallogr.*, 1986, **19**, 105-107.
4. CrysAlisPRO, Oxford Diffraction /Agilent Technologies UK Ltd, Yarnton, England.
5. A. Altomare, G. Cascarano, C. Giacovazzo and A. Guagliardi, *J. Appl. Crystallogr.*, 1993, **26**, 343-350.
6. L. Palatinus and G. Chapuis, *J. Appl. Crystallogr.*, 2007, **40**, 786-790.
7. L. Farrugia, *J. Appl. Crystallogr.*, 1999, **32**, 837-838.
8. L. J. Farrugia, *J. Appl. Crystallogr.*, 2012, **45**, 849-854.
9. A. L. Spek, *J. Appl. Crystallogr.*, 2003, **36**, 7-13.
10. A. L. Spek, *PLATON, a Multipurp. Crystallogr. tool, Utrecht, Netherlands*, 1998.
11. V. Busico, R. Cipullo, A. Mingione and L. Rongot, *Ind. Eng. Chem. Res.*, 2016, **55**, 2686-2695.
12. M. Save, M. Schappacher and A. Soum, *Macromol. Chem. Phys.*, 2002, **203**, 889-899.

Concluding Remarks

The results discussed within the thesis covered three main topics: (i) the synthesis and characterisation of new group 4 metallocenes based on the permethylindenyl ligand, (ii) the synthesis and study of ethylene polymerisation catalyst systems with applications for the production of ultra-low molecular weight polyethylenes, and (iii) investigations into new single-site initiators for the ring-opening polymerisation (ROP) of lactide monomers. The key highlights and conclusions of the thesis are detailed below.

(i) New permethylindenyl zirconocenes

The syntheses of twelve new unsymmetrical permethylindenyl *ansa*-bridged zirconocene systems based on $^{Me_2}SB(Cp^{R},I^*)ZrX(Y)$ (R = H, Me and ^{n}Bu; X = Cl, Br, CH_2Ph and Me; Y = Cl, Br, Me, CH_2Ph, O-2,6-Me-C_6H_3 and O-2,6-^{i}Pr-C_6H_3) were reported and fully characterised. Nine new solid-state structures were detailed, of note was the large differences in the ring tilt angle and angle about the metal centre for the *E*- and *Z*-isomers of $^{Me_2}SB(Cp^{Me},I^*)ZrCl_2$, and the change in the orientation of the *n*-butyl chain for the *E*- and *Z*-isomers of $^{Me_2}SB(Cp^{nBu},I^*)ZrCl_2$. Reaction of $^{Me_2}SB(Cp,I^*)ZrX_2$ (X = Cl, Me and CH_2Ph) with MAO demonstrated that cationic $[^{Me_2}SB(Cp,I^*)ZrMe]^+$ was formed regardless of the identity of the initiation group.

(ii) Highly active ethylene polymerisation catalysts

The unsymmetrical permethylindenyl *ansa*-bridged zirconocenes were found to be highly active catalysts for the solution- and slurry-phase polymerisation of ethylene. Six solid supports were studied for complex immobilisation; MAO modified silica

(SSMAO), MAO modified layered doubled hydroxide (LDHMAO) and four types of solid polymethylaluminoxane (sMAO).

The sMAO supported catalytic systems were found to exhibit some of the highest slurry-phase polymerisation activities reported in the literature. sMAO(1G) supported $^{Me_2}SB(Cp^{Me},I^*)ZrMe_2$ was found to be the most active catalyst (9509 $kg_{PE}\ mol_M^{-1}\ h^{-1}\ bar^{-1}$), with activity 83% higher than industrial standard $(Cp^{nBu})_2ZrCl_2$ supported on sMAO(1G). DSC analysis revealed that the systems produced HDPE with minimal branching and defects, while SEM showed the production of polymer particles with industrially desirable uniform 'popcorn' morphology. GPC analysis confirmed the production of low molecular weight polyethylenes with narrow molecular weight distributions (M_w <100 kg mol^{-1} and M_w/M_n <4 at 80 °C).

The sMAO(1G) supported complexes showed remarkable stability when hydrogen was introduced to the slurry-phase ethylene polymerisation reactions. Only a small amount of hydrogen was required in order to decrease polymer molecular weights significantly; for sMAO(1G) supported $^{Me_2}SB(Cp,I^*)ZrMe_2$ M_w decreased from 225 to 15 kg mol^{-1} in the presence of hydrogen. These catalysts were highlighted as commercial candidates for the production of polyethylene waxes with pilot plant scale testing using sMAO(1G) supported $^{Me_2}SB(Cp,I^*)ZrCl_2$ currently ongoing.

(iii) Active initiators for the ROP of *L*-, *D*- and *rac*-lactide

In the presence of benzyl alcohol co-initiator, $^{Me_2}SB(Cp,I^*)ZrCl_2$, $^{Me_2}SB(Cp^{Me},I^*)ZrCl_2$, *Z*-$^{Me_2}SB(Cp,I^*)ZrCl(O\text{-}2,6\text{-}Me\text{-}C_6H_3)$ and *E*-$^{Me_2}SB(Cp,I^*)ZrCl(O\text{-}2,6\text{-}^{i}Pr\text{-}C_6H_3)$ were found to be active initiators for the ROP of *L*-, *D*- and *rac*-lactide. The complexes required no initiation period and displayed second-order dependence on monomer

concentration; k_{obs} = 6.39, 6.38 and 5.89 M^{-1} h^{-1} for the ROP of *L*-, *D*- and *rac*-lactide using *Z*-^{Me_2}SB(Cp,I*)ZrCl(O-2,6-Me-C_6H_3). Additional investigations indicated that polymerisation proceeded *via* a coordination-insertion mechanism with an order of one in respect to catalyst concentration:

$$-\frac{d[\mathrm{LA}]}{d\mathrm{T}} = k_{\mathrm{p}}\left[\mathrm{LA}\right]^{2}\left[\mathrm{cat}\right]_{0}$$

Analysis of the polymers revealed that the initiators produced isotactic PLA for the ROP of *L*- and *D*-lactide, and heterotactic-enriched PLA for the ROP of *rac*-lactide (P_r ~0.80). GPC showed that the polymers had relatively low molecular weights (M_n <3000 g mol^{-1}) with narrow molecular weight distributions (M_n/M_w <1.16), and MALDI-TOF mass spectrometry confirmed the presence of one –OCH_2Ph and one –OH end group per chain.

Appendix

Supplementary Data for Chapters 2-5

Chapter 2

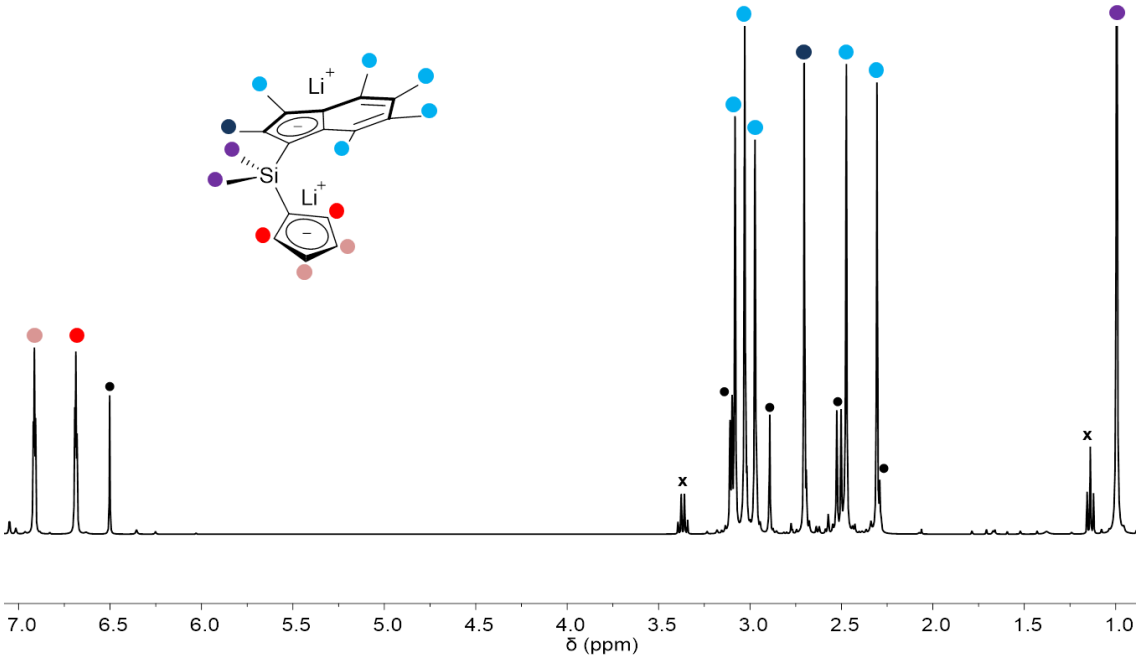


Figure A2.1 ^{1}H NMR spectrum (pyridine-d_5, 400 MHz, 298 K) of ^{Me_2}SB(Cp,I*)Li$_2$. x is residual diethyl ether, • is unreacted LiCp and Ind*SiMe$_2$Cl starting materials.

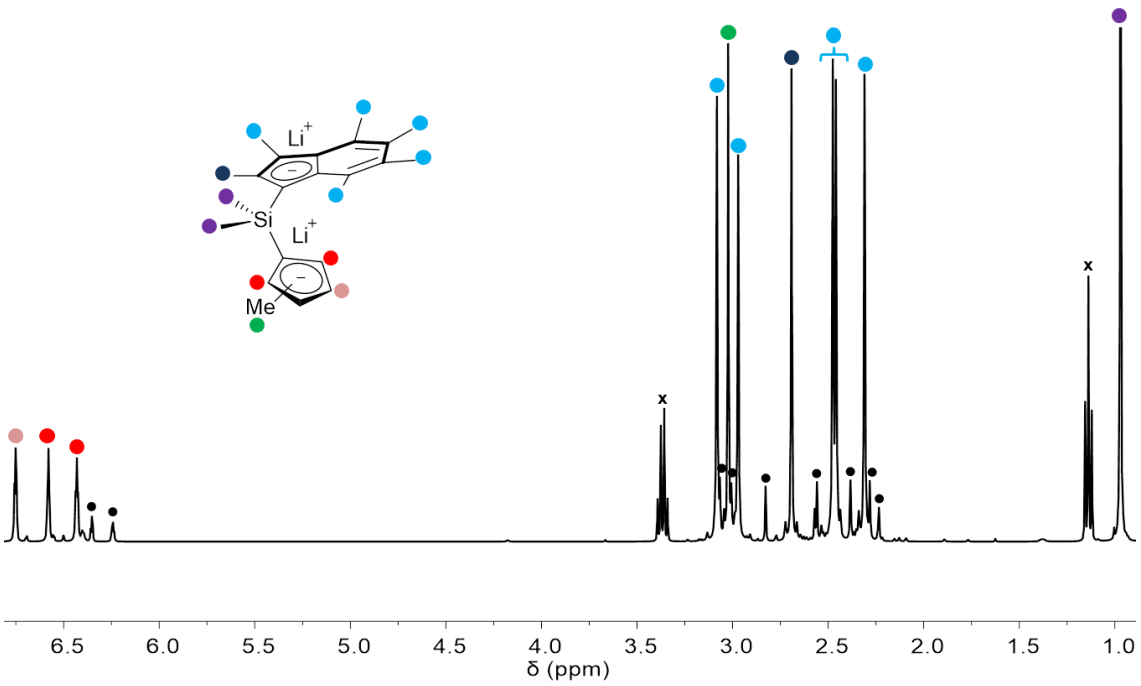


Figure A2.2 ^{1}H NMR spectrum (pyridine-d_5, 400 MHz, 298 K) of ^{Me_2}SB(Cp^{Me},I*)Li$_2$. x is residual diethyl ether, • is unreacted LiCp^{Me} and Ind*SiMe$_2$Cl starting materials.

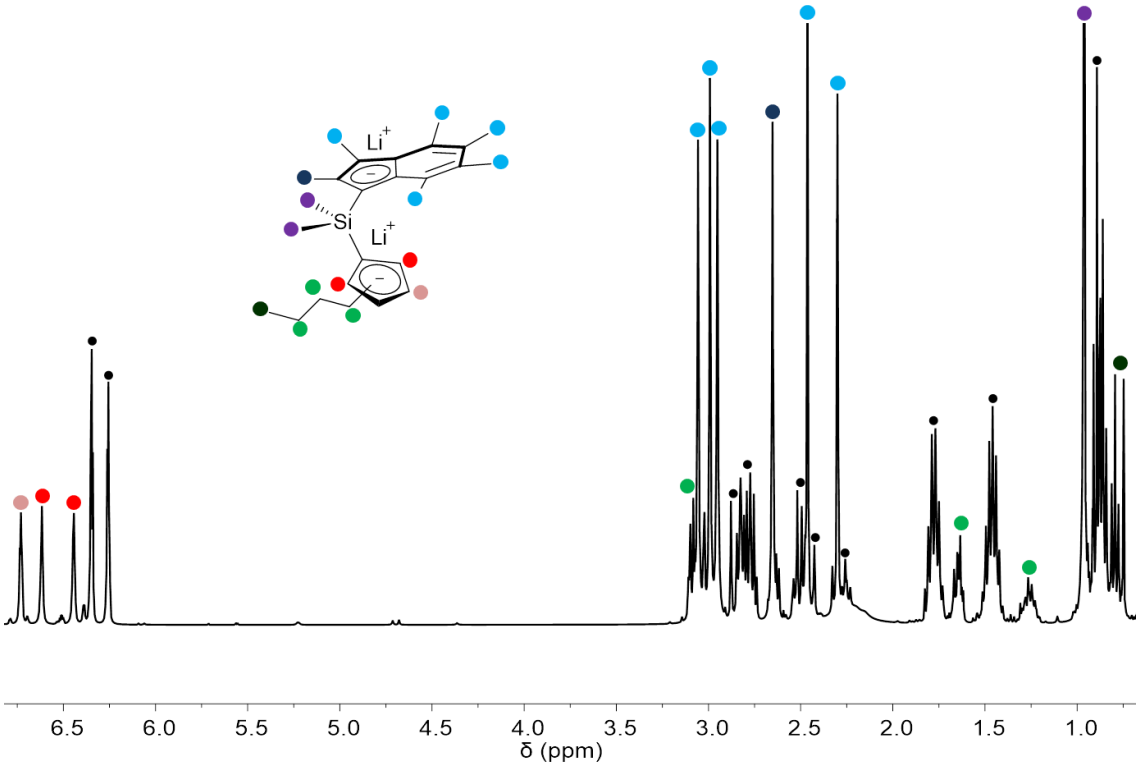


Figure A2.3 ^{1}H NMR spectrum (pyridine-d_5, 400 MHz, 298 K) of ^{Me_2}SB(Cp^{nBu},I*)Li$_2$. • is unreacted LiCp^{nBu} and Ind*SiMe$_2$Cl starting materials.

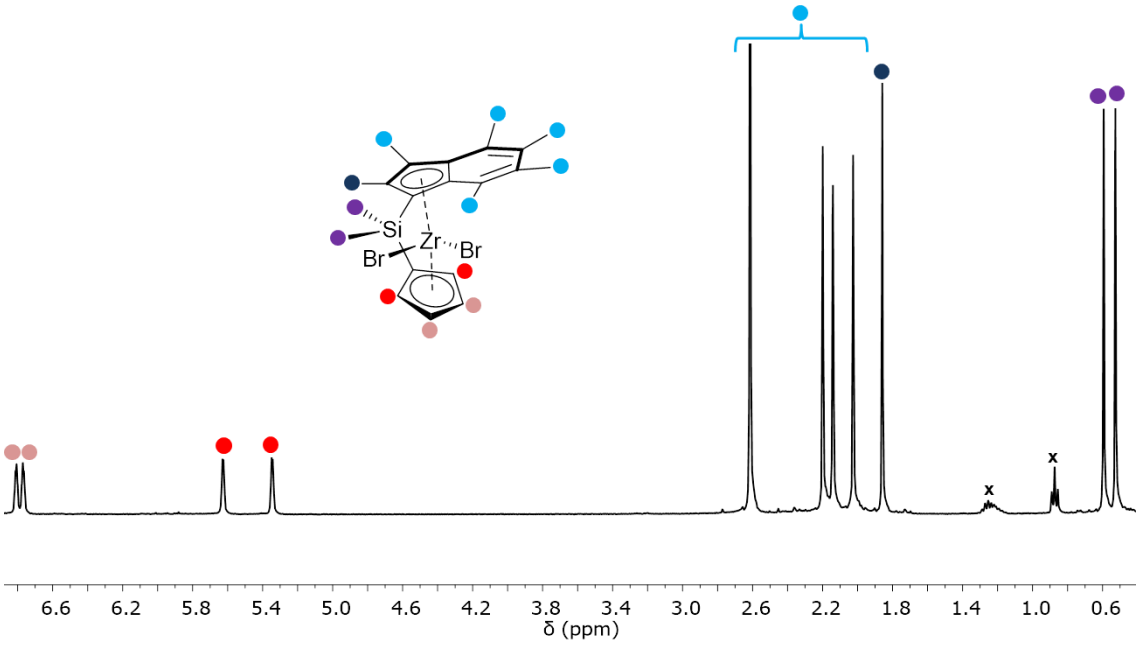


Figure A2.4 ^{1}H NMR spectrum (benzene-d_6, 400 MHz, 298 K) of ^{Me_2}SB(Cp,I*)ZrBr$_2$ (**2**). x is residual pentane.

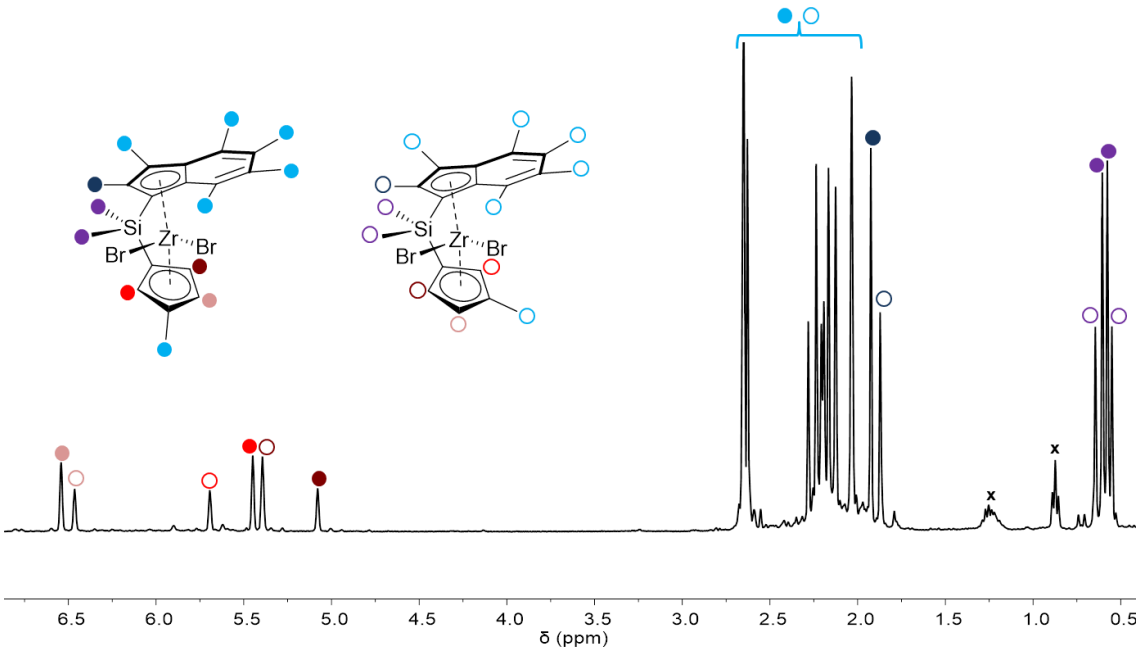


Figure A2.5 ^{1}H NMR spectrum (benzene-d_6, 400 MHz, 298 K) of *E*-^{Me_2}SB(Cp^{Me},I*)ZrBr$_2$ (***E*-4**, ●) and *Z*-^{Me_2}SB(Cp^{Me},I*)ZrBr$_2$ (***Z*-4**, ○). x is residual pentane.

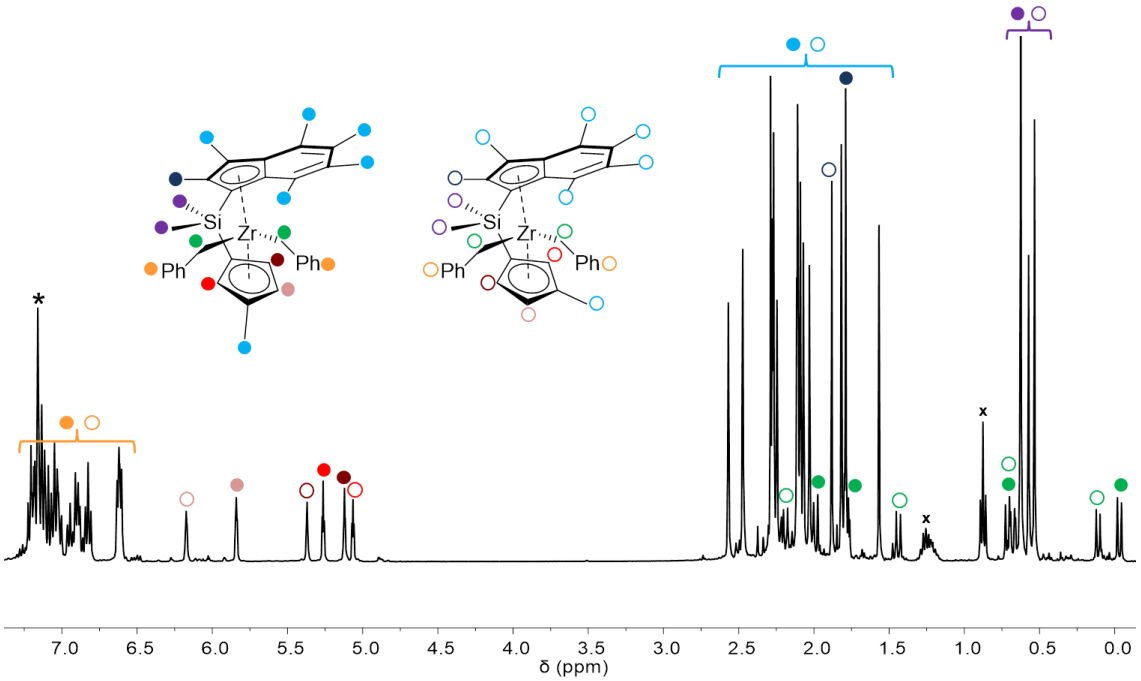


Figure A2.6 ^{1}H NMR spectrum (benzene-d_6 (*), 400 MHz, 298 K) of *E*-^{Me_2}SB(Cp^{Me},I*)Zr(CH$_2$Ph)$_2$ (***E*-7**, ●) and *Z*-^{Me_2}SB(Cp^{Me},I*)Zr(CH$_2$Ph)$_2$ (***Z*-7**, ○). x is residual pentane.

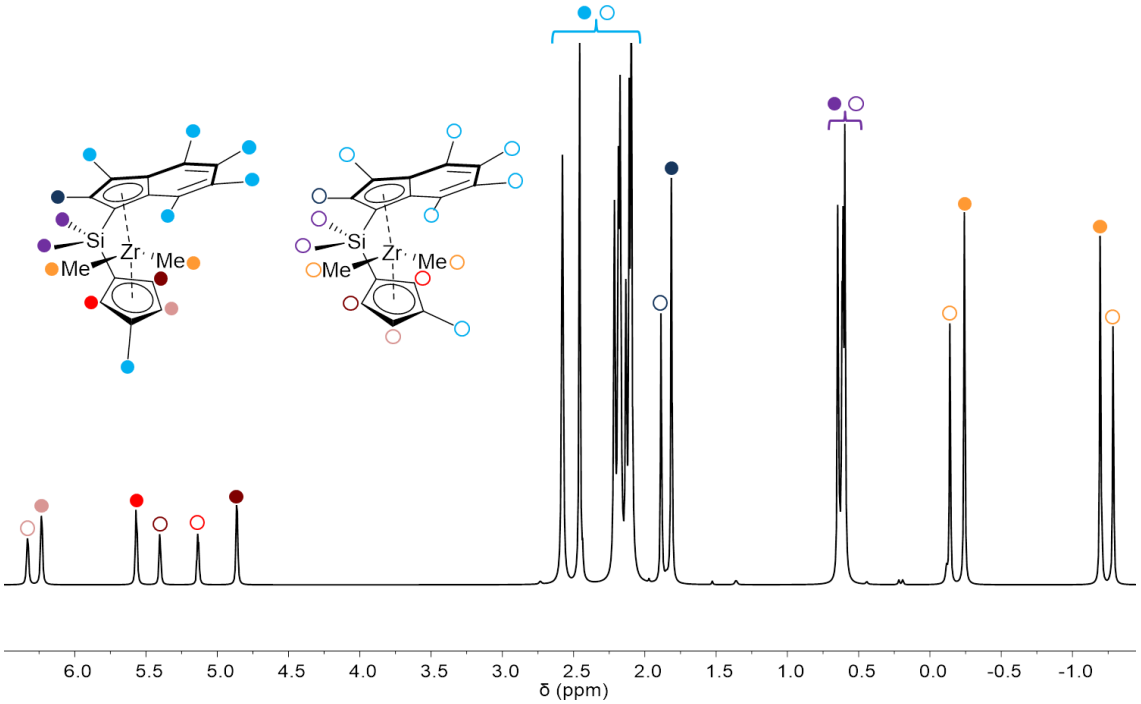


Figure A2.7 ^{1}H NMR spectrum (benzene-d_6, 400 MHz, 298 K) of *E*-^{Me_2}SB(Cp^{Me},I*)ZrMe$_2$ (***E*-9**, ●) and *Z*-^{Me_2}SB(Cp^{Me},I*)ZrMe$_2$ (***Z*-9**, ○).

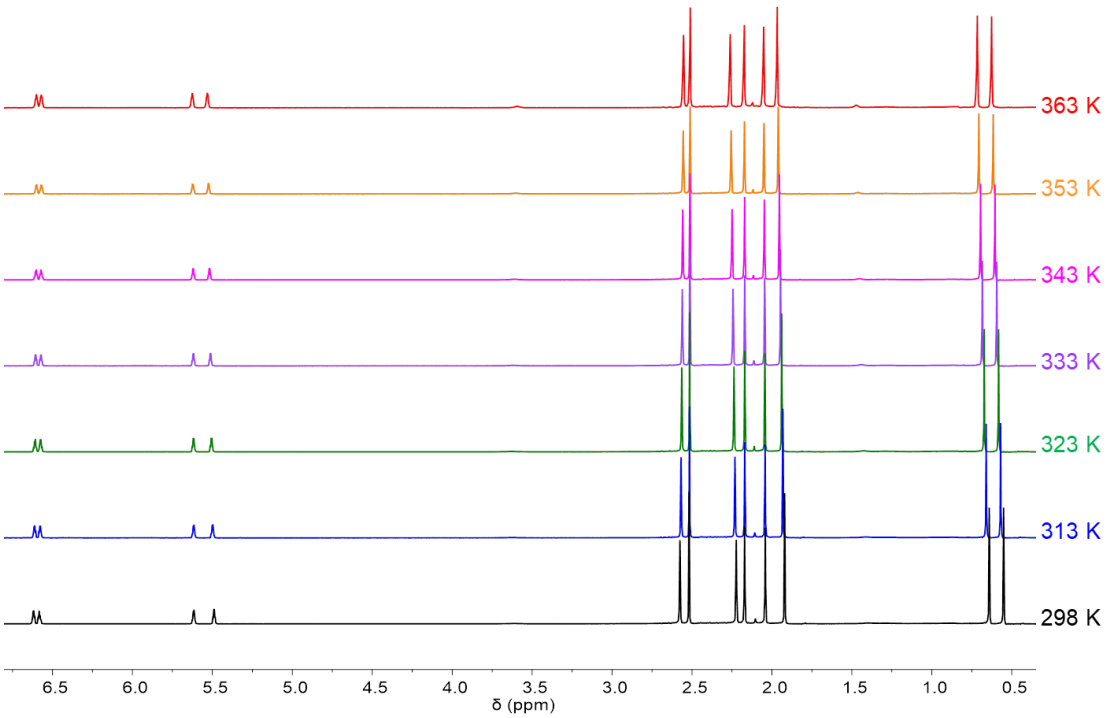


Figure A2.8 Variable temperature ^{1}H NMR spectrum (benzene-d_6, 500 MHz) of ^{Me_2}SB(Cp,I*)ZrCl$_2$ (**1**) between 298 and 363 K.

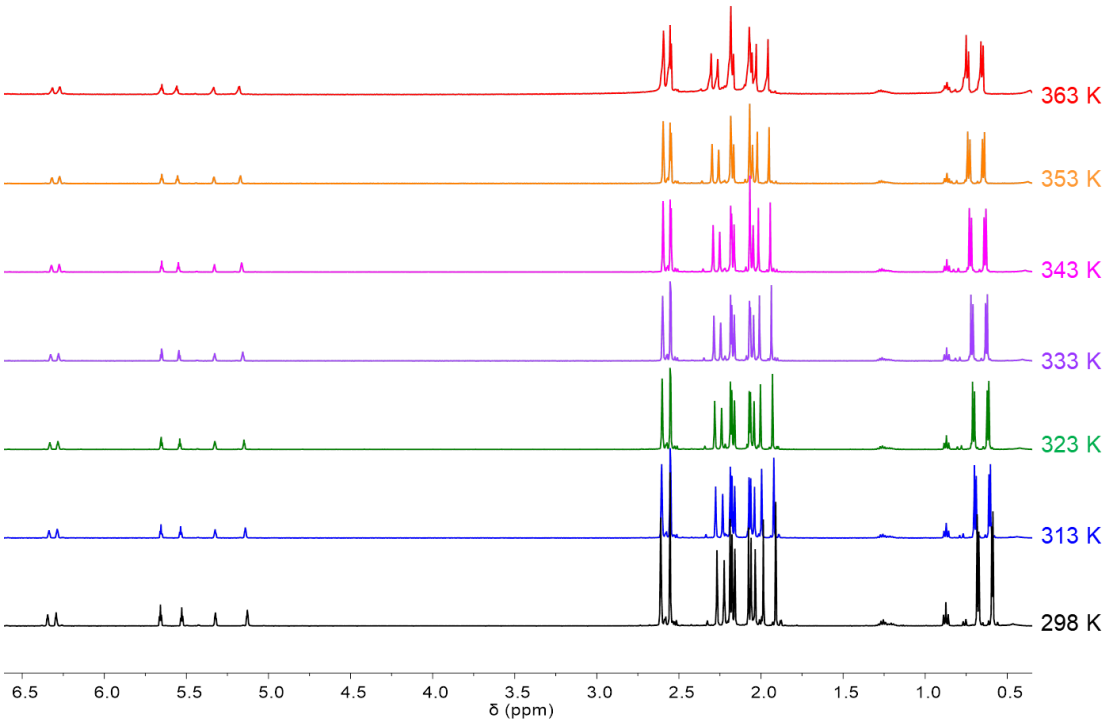


Figure A2.9 Variable temperature ^{1}H NMR spectrum (benzene-d_6, 500 MHz) of ^{Me_2}SB(Cp^{Me},I*)ZrCl$_2$ (**3**) between 298 and 363 K.

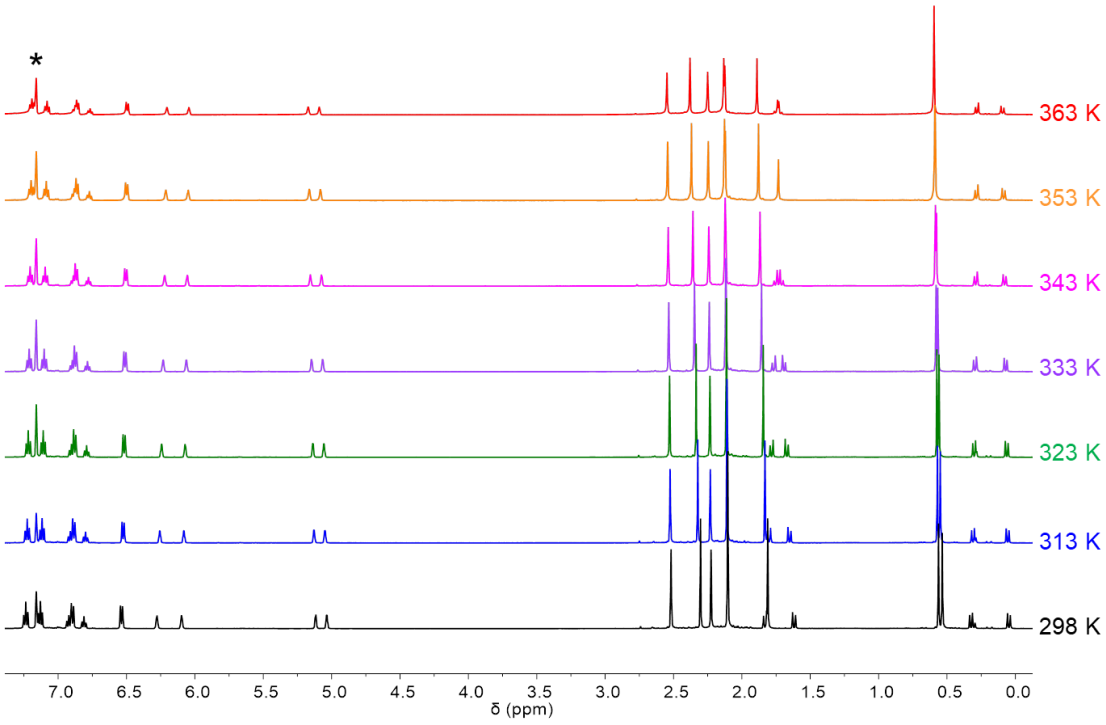


Figure A2.10 Variable temperature ^{1}H NMR spectrum (benzene-d_6 (*), 500 MHz) of ^{Me_2}SB(Cp,I*)Zr(CH$_2$Ph)$_2$ (**6**) between 298 and 363 K.

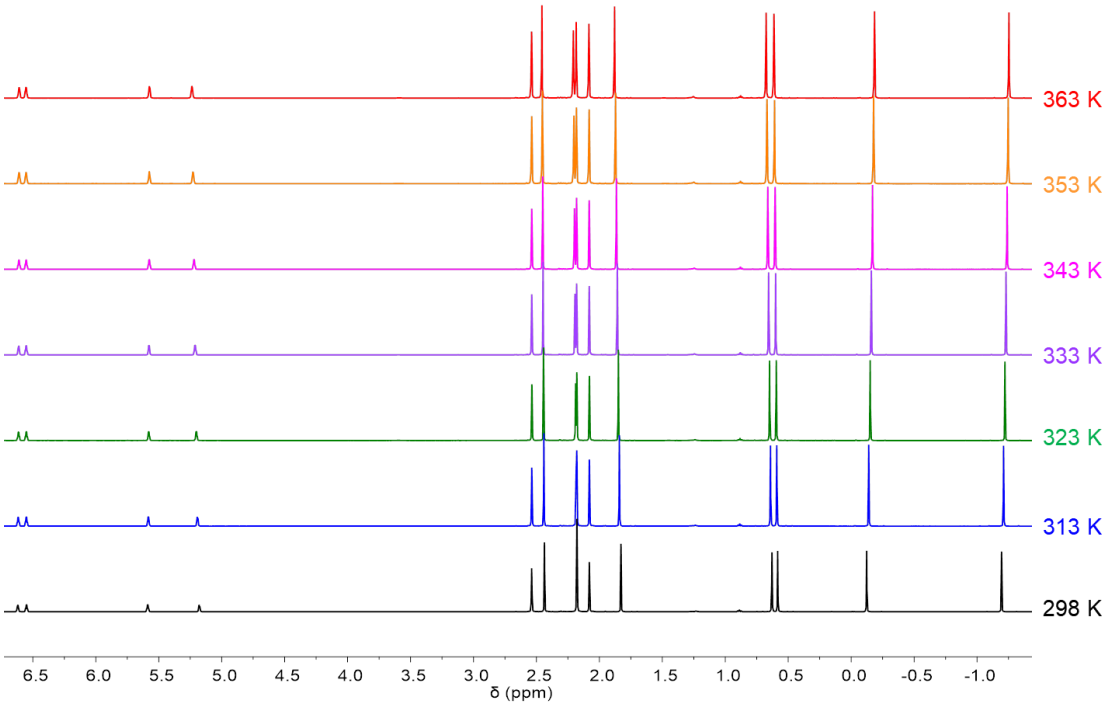


Figure A2.11 Variable temperature ^{1}H NMR spectrum (benzene-d_6, 500 MHz) of ^{Me_2}SB(Cp,I*)ZrMe$_2$ (**8**) between 298 and 363 K.

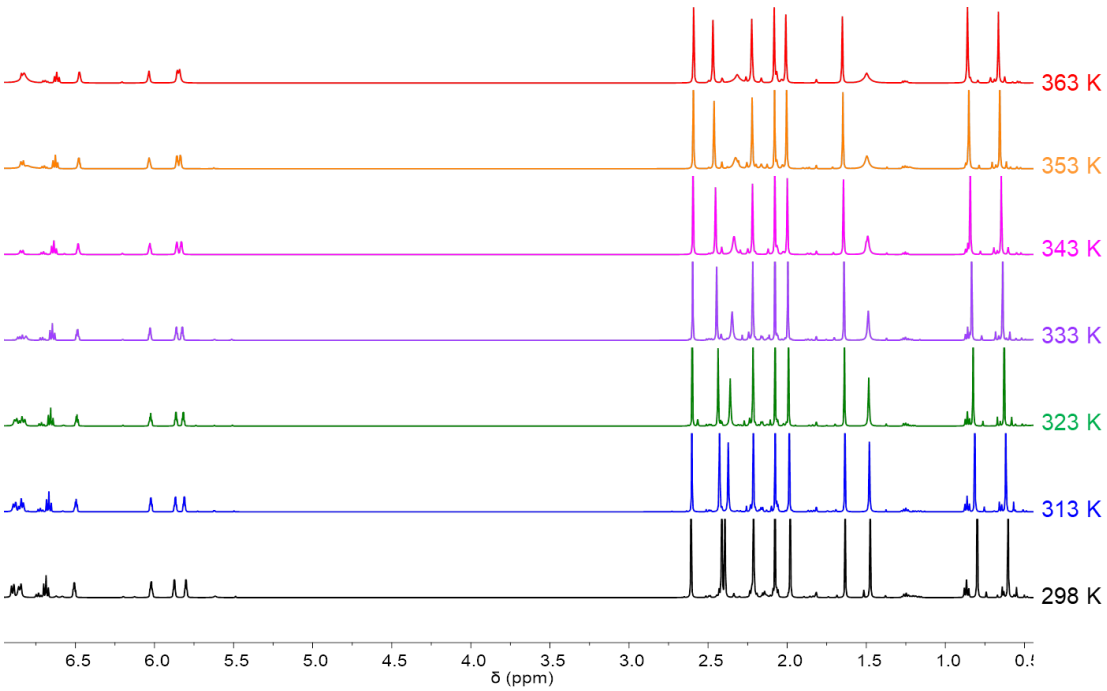


Figure A2.12 Variable temperature ^{1}H NMR spectrum (benzene-d_6, 500 MHz) of *Z*-^{Me_2}SB(Cp,I*)ZrCl(2,6-Me-C$_6$H$_3$) (***Z*-10**) between 298 and 363 K.

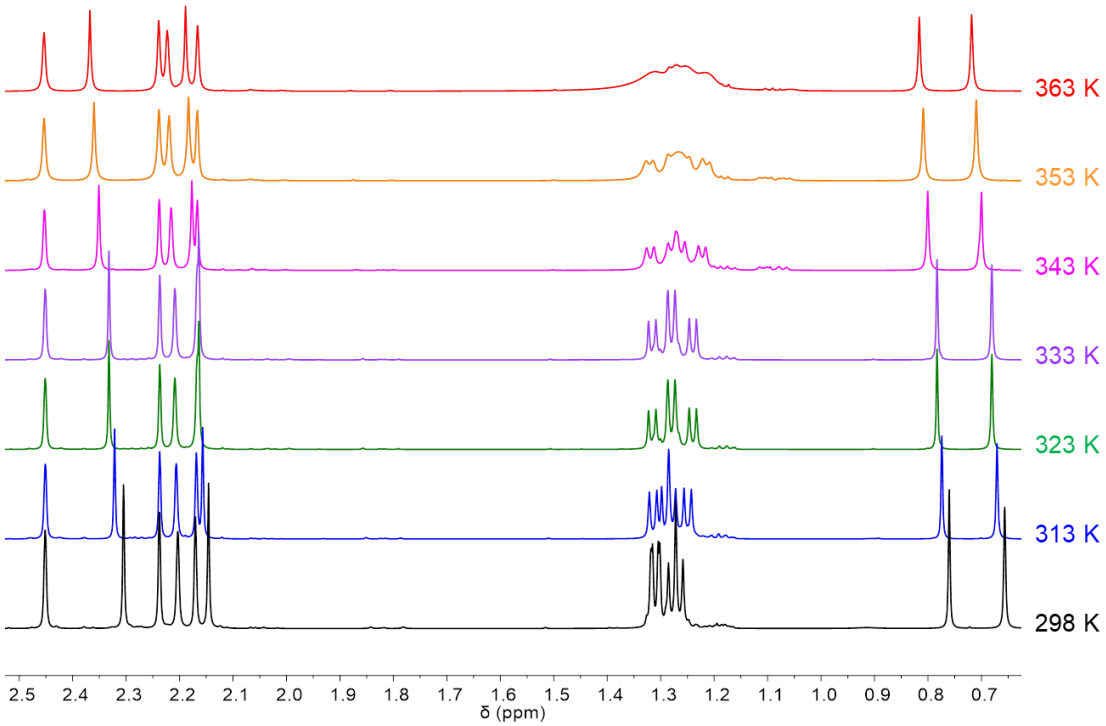


Figure A2.13 Variable temperature ^{1}H NMR spectrum (benzene-d_6, 500 MHz) of *E*-^{Me_2}SB(Cp,I*)ZrCl(O-2,6-^{i}Pr-C_6H_3) (***E*-11**) between 298 and 363 K showing 0.63–2.51 ppm.

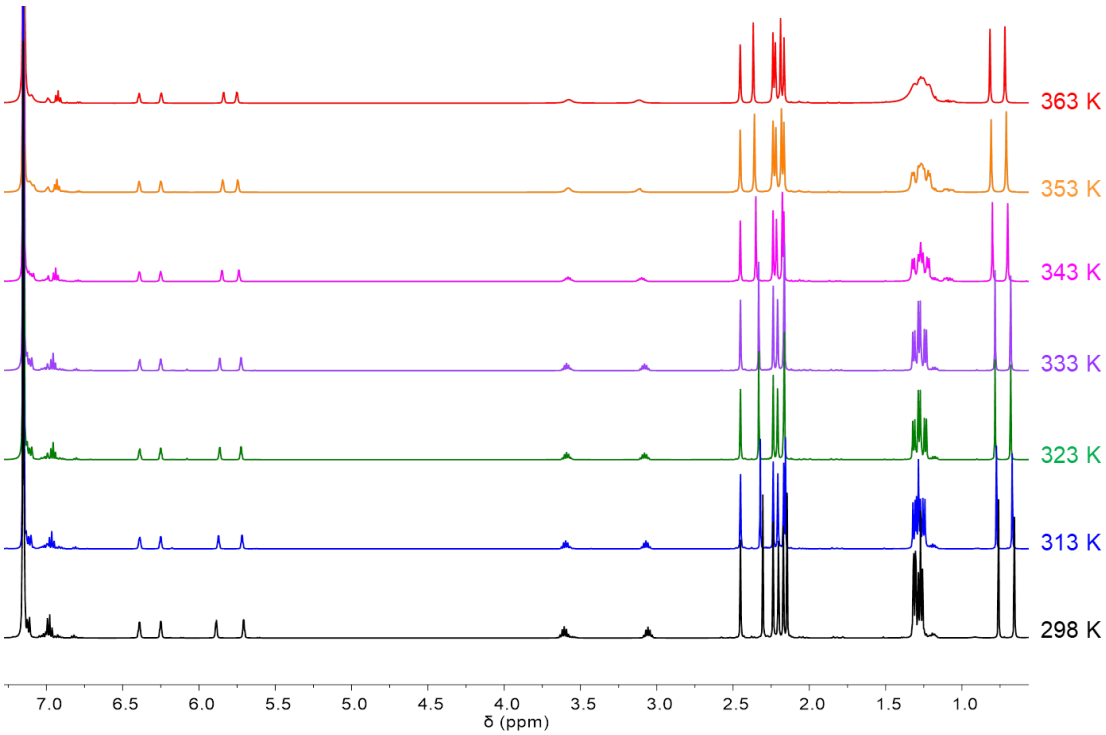


Figure A2.14 Variable temperature ^{1}H NMR spectrum (benzene-d_6, 500 MHz) of *E*-^{Me_2}SB(Cp,I*)ZrCl(O-2,6-^{i}Pr-C_6H_3) (***E*-11**) between 298 and 363 K.

Chapter 3

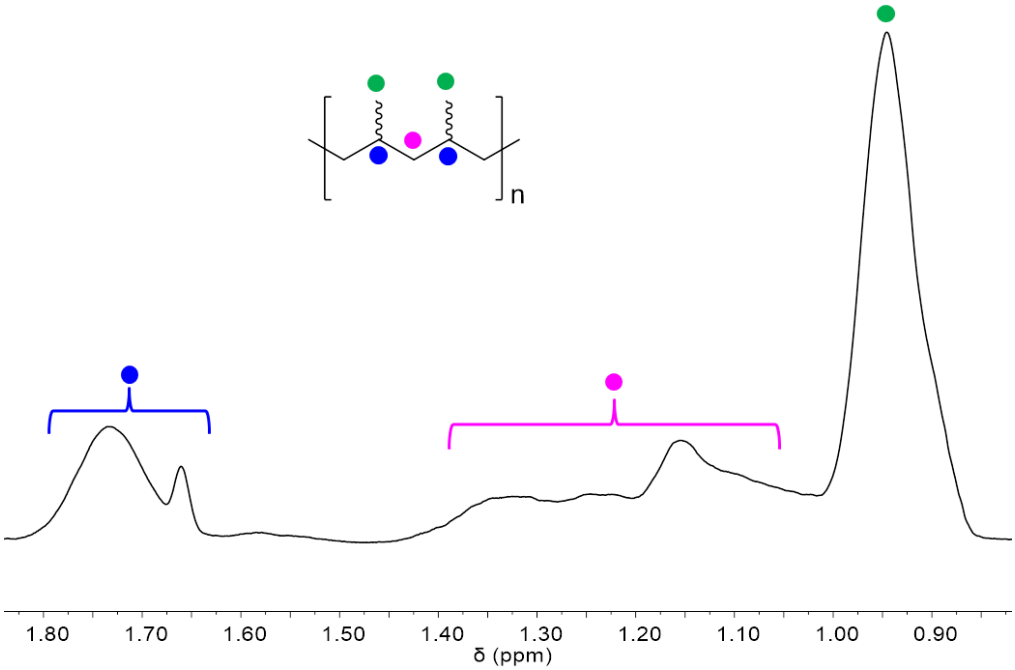


Figure A3.1 ^{1}H NMR spectrum (toluene-d_8, 500 MHz, 298 K) of the polypropylene produced using ^{Me_2}SB(Cp,I*)ZrCl$_2$ (**1**). Polymerisation conditions: pre-catalyst (0.5 mg), MAO co-catalyst ($[Al_{MAO}]_0/[M]_0 = 1000$), propylene (2 bar), hexane (50 mL) and 30 minutes.

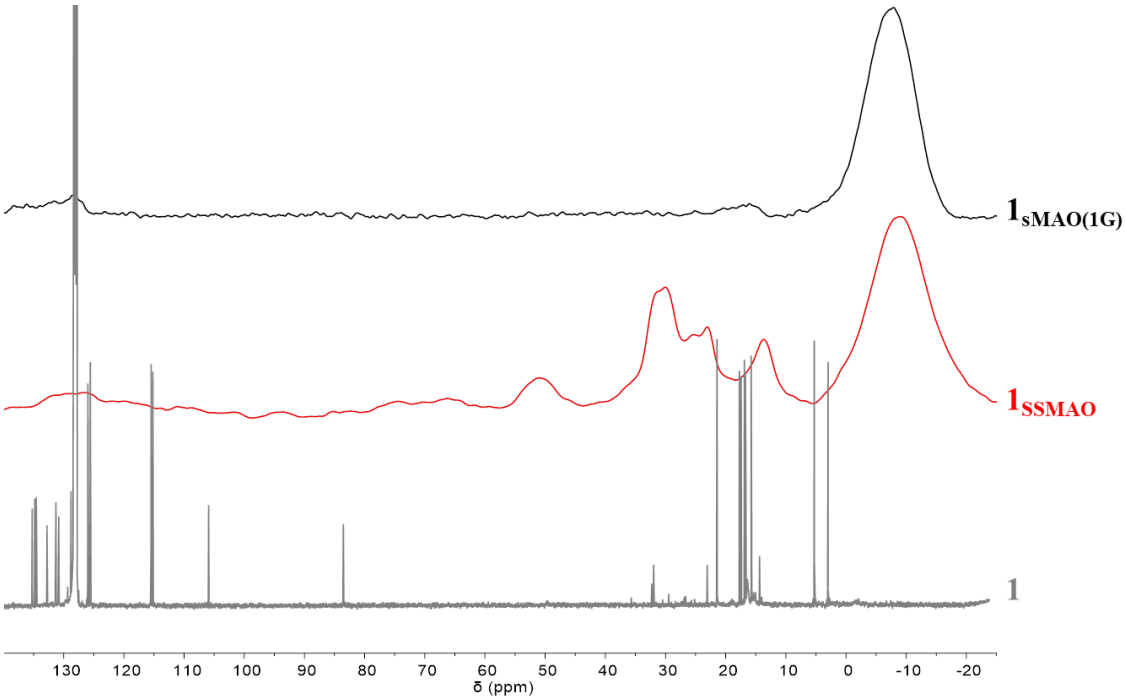


Figure A3.2 ^{13}C CP/MAS SSNMR spectra (10 kHz, 298 K) of ^{Me_2}SB(Cp,I*)ZrCl$_2$ (**1**) supported on sMAO(1G) (**1**$_{\mathbf{sMAO(1G)}}$) (black) and SSMAO (**1**$_{\mathbf{SSMAO}}$) (red), and ^{13}C{^{1}H} NMR spectrum (benzene-d_6, 100 MHz, 298 K) of ^{Me_2}SB(Cp,I*)ZrCl$_2$ (**1**) (grey).

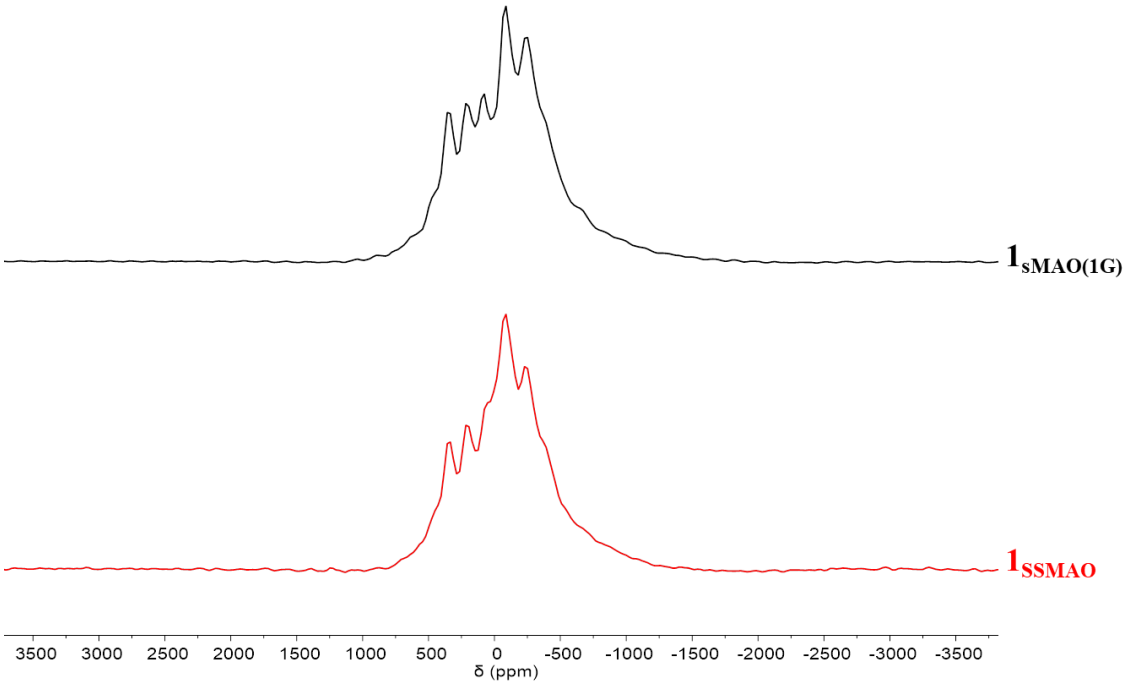


Figure A3.3 ^{27}Al DP/MAS SSNMR spectra (15 kHz, 298 K) of ^{Me_2}SB(Cp,I*)ZrCl$_2$ (**1**) supported on sMAO(1G) (**1**$_{\mathbf{sMAO(1G)}}$) (black) and SSMAO (**1**$_{\mathbf{SSMAO}}$) (red).

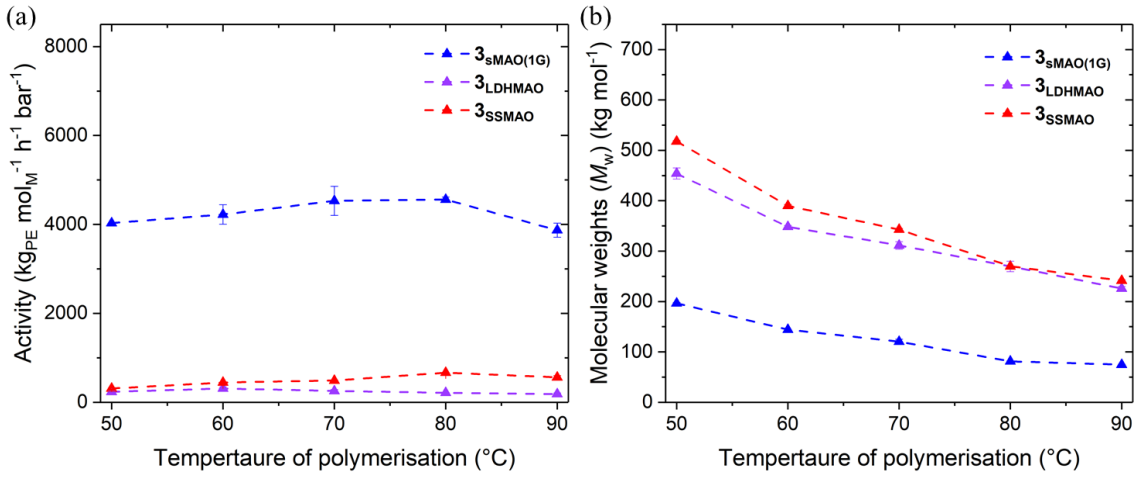


Figure A3.4 Slurry-phase ethylene polymerisation (a) activity and (b) molecular weights (M_w) as a function of temperature of polymerisation using ^{Me_2}SB(Cp^{Me},I*)ZrCl$_2$ (**3**) supported on sMAO(1G) (**3$_{sMAO(1G)}$**) (blue), LDHMAO (**3$_{LDHMAO}$**) (lilac) and SSMAO (**3$_{SSMAO}$**) (red). Polymerisation conditions: [Al$_{support}$]$_0$/[M]$_0$ = 200, TiBA (150 mg), ethylene (2 bar), pre-catalyst (10 mg), hexane (50 mL) and 30 minutes.

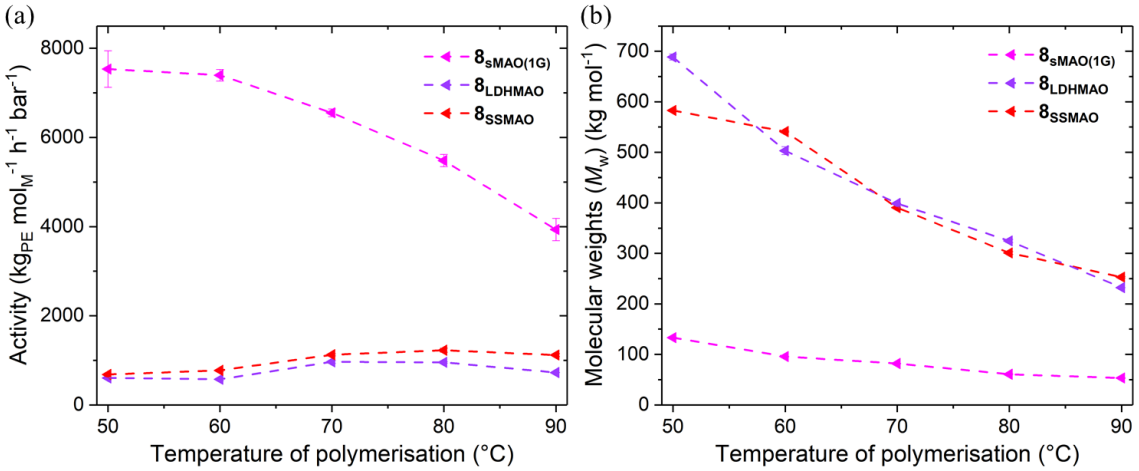


Figure A3.5 Slurry-phase ethylene polymerisation (a) activity and (b) molecular weights (M_w) as a function of temperature of polymerisation using ^{Me_2}SB(Cp,I*)ZrMe$_2$ (**8**) supported on sMAO(1G) (**8$_{sMAO(1G)}$**) (pink), LDHMAO (**8$_{LDHMAO}$**) (lilac) and SSMAO (**8$_{SSMAO}$**) (red). Polymerisation conditions: [Al$_{support}$]$_0$/[M]$_0$ = 200, TiBA (150 mg), ethylene (2 bar), pre-catalyst (10 mg), hexane (50 mL) and 30 minutes.

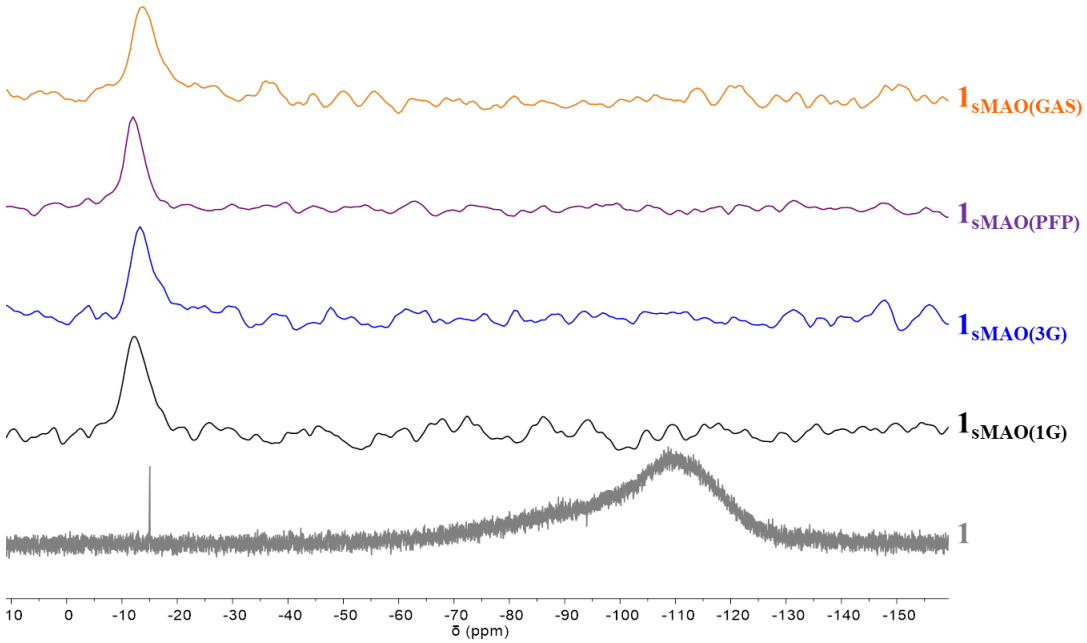


Figure A3.6 ^{29}Si CP/MAS SSNMR spectra (10 kHz, 298 K) of ^{Me_2}SB(Cp,I*)ZrCl$_2$ (**1**) supported on sMAO(GAS) (**1**$_{\mathbf{sMAO(GAS)}}$) (orange), sMAO(PFP) (**1**$_{\mathbf{sMAO(PFP)}}$) (purple), sMAO(3G) (**1**$_{\mathbf{sMAO(3G)}}$) (blue) and sMAO(1G) (**1**$_{\mathbf{sMAO(1G)}}$) (black), and ^{29}Si NMR spectrum (benzene-d_6, 100 MHz, 298 K) of ^{Me_2}SB(Cp,I*)ZrCl$_2$ (**1**) (grey).

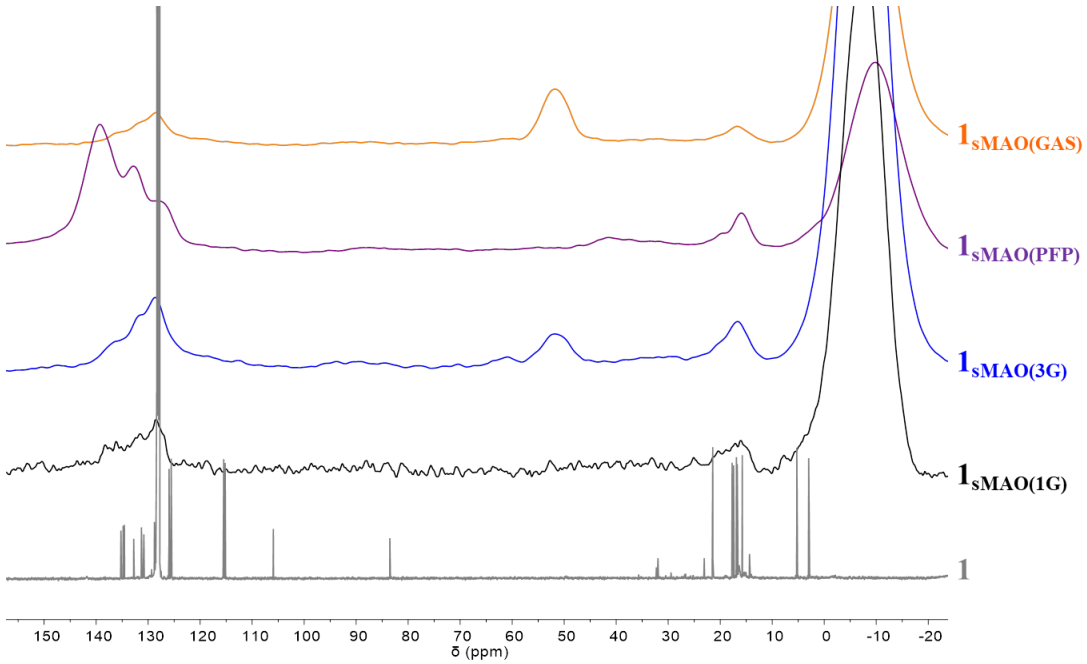


Figure A3.7 ^{13}C CP/MAS SSNMR spectra (10 kHz, 298 K) of ^{Me_2}SB(Cp,I*)ZrCl$_2$ (**1**) supported on sMAO(GAS) (**1**$_{\mathbf{sMAO(GAS)}}$) (orange), sMAO(PFP) (**1**$_{\mathbf{sMAO(PFP)}}$) (purple), sMAO(3G) (**1**$_{\mathbf{sMAO(3G)}}$) (blue) and sMAO(1G) (**1**$_{\mathbf{sMAO(1G)}}$) (black), and ^{13}C NMR spectrum (benzene-d_6, 100 MHz, 298 K) of ^{Me_2}SB(Cp,I*)ZrCl$_2$ (**1**) (grey).

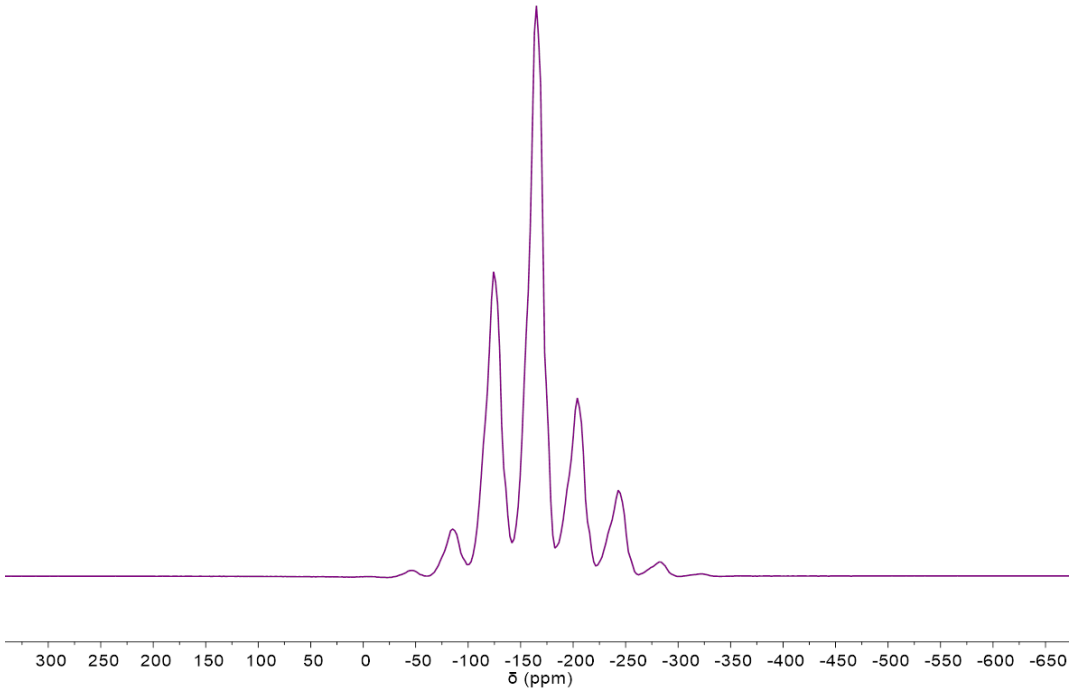


Figure A3.8 ^{19}F DEPT SSNMR spectrum (10 kHz, 298 K) of ^{Me_2}SB(Cp,I*)ZrCl$_2$ (**1**) supported on sMAO(PFP) (**1**$_{\mathbf{sMAO(PFP)}}$) (purple).

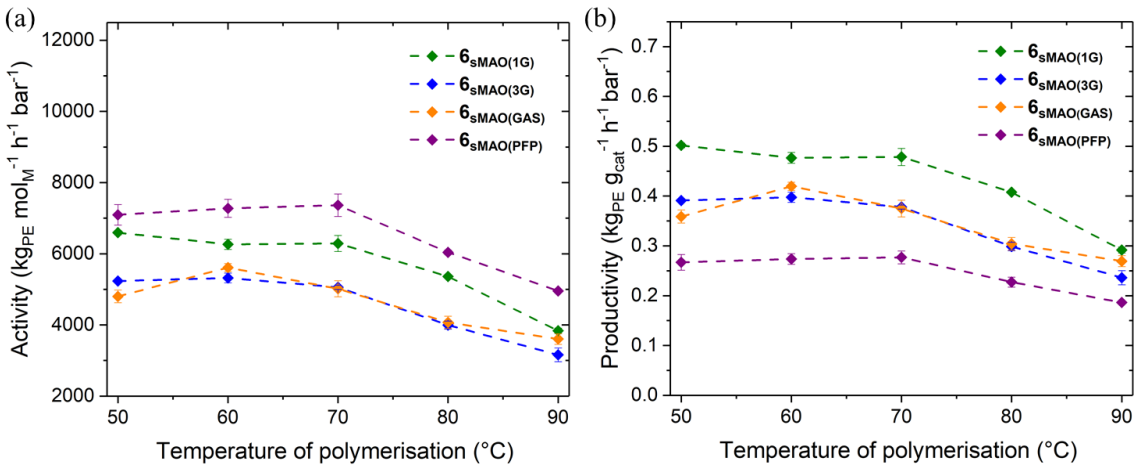


Figure A3.9 Slurry-phase ethylene polymerisation (a) activity and (b) productivity as a function of temperature of polymerisation using ^{Me_2}SB(Cp,I*)Zr(CH$_2$Ph)$_2$ (**6**) supported on sMAO(1G) (**6**$_{\mathbf{sMAO(1G)}}$) (green), sMAO(3G) (**6**$_{\mathbf{sMAO(3G)}}$) (blue), sMAO(GAS) (**6**$_{\mathbf{sMAO(GAS)}}$) (orange) and sMAO(PFP) (**6**$_{\mathbf{sMAO(PFP)}}$) (purple). Polymerisation conditions: $[Al_{sMAO}]_0/[M]_0 = 200$, TiBA (150 mg), ethylene (2 bar), pre-catalyst (10 mg), hexane (50 mL) and 30 minutes.

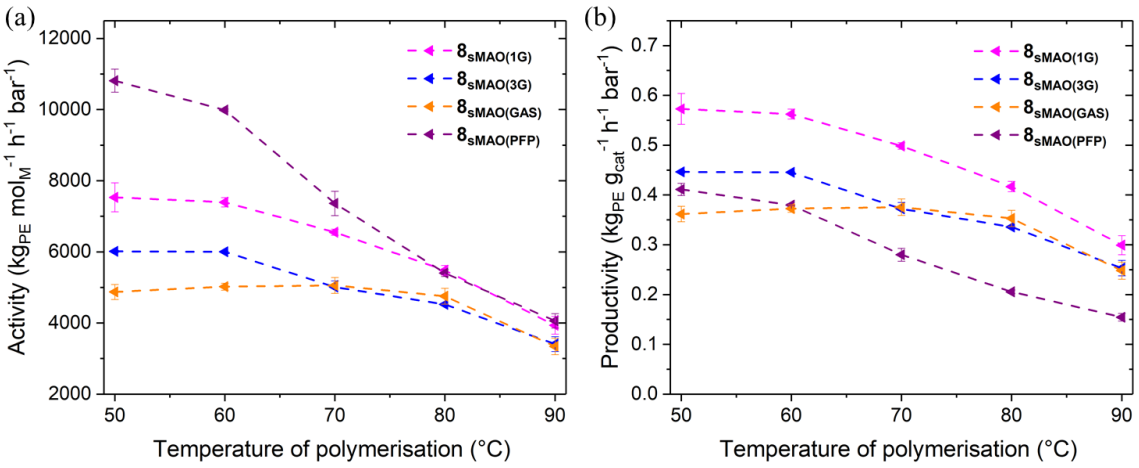


Figure A3.10 Slurry-phase ethylene polymerisation (a) activity and (b) productivity as a function of temperature of polymerisation using ^{Me_2}SB(Cp,I*)ZrMe$_2$ (**8**) supported on sMAO(1G) (**$8_{sMAO(1G)}$**) (pink), sMAO(3G) (**$8_{sMAO(3G)}$**) (blue), sMAO(GAS) (**$8_{sMAO(GAS)}$**) (orange) and sMAO(PFP) (**$8_{sMAO(PFP)}$**) (purple). Polymerisation conditions: $[Al_{sMAO}]_0/[M]_0$ = 200, TiBA (150 mg), ethylene (2 bar), pre-catalyst (10 mg), hexane (50 mL) and 30 minutes.

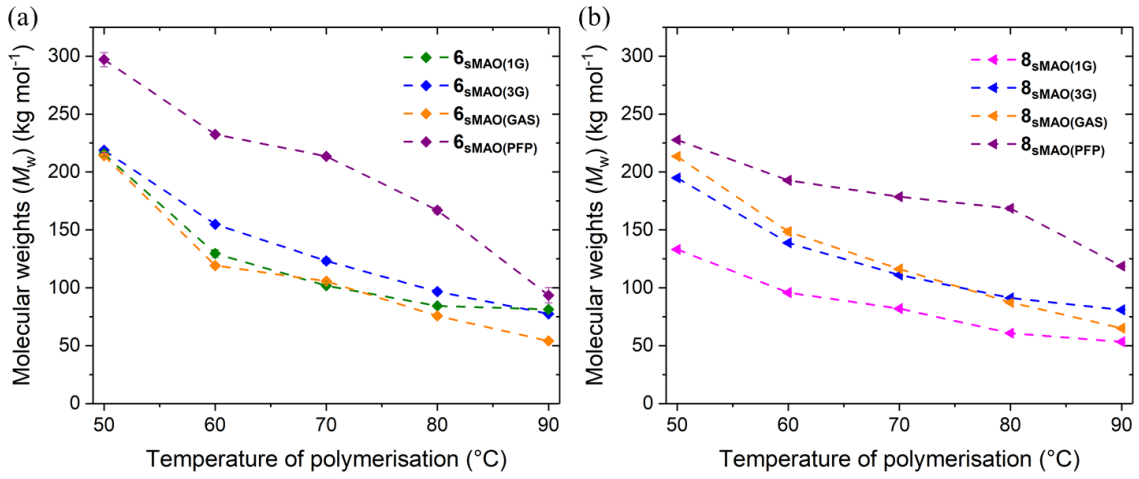


Figure A3.11 Molecular weights (M_w) as a function of temperature of polymerisation using (a) ^{Me_2}SB(Cp,I*)Zr(CH$_2$Ph)$_2$ (**6**) and (b) ^{Me_2}SB(Cp,I*)ZrMe$_2$ (**8**) supported on sMAO(1G) (green and pink respectively), sMAO(3G) (blue), sMAO(GAS) (orange) and sMAO(PFP) (purple). Polymerisation conditions: $[Al_{sMAO}]_0/[M]_0$ = 200, TiBA (150 mg), ethylene (2 bar), pre-catalyst (10 mg), hexane (50 mL) and 30 minutes.

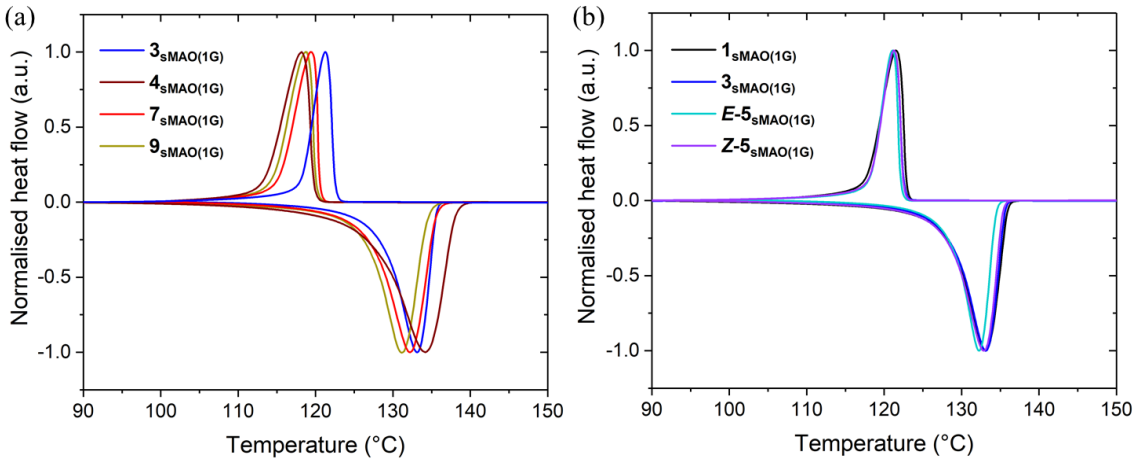


Figure A3.12 DSC plot showing the first cooling cycle and second heating cycle for the polyethylenes produced using sMAO(1G) supported (a) ^{Me_2}SB(Cp^{Me},I*)ZrCl$_2$ (**3$_{sMAO(1G)}$**) (blue), ^{Me_2}SB(Cp^{Me},I*)ZrBr$_2$ (**4$_{sMAO(1G)}$**) (brown), ^{Me_2}SB(Cp^{Me},I*)Zr(CH$_2$Ph)$_2$ (**7$_{sMAO(1G)}$**) (red) and ^{Me_2}SB(Cp^{Me},I*)ZrMe$_2$ (**9$_{sMAO(1G)}$**) (yellow); (b) ^{Me_2}SB(Cp,I*)ZrCl$_2$ (**1$_{sMAO(1G)}$**) (black), ^{Me_2}SB(Cp^{Me},I*)ZrCl$_2$ (**3$_{sMAO(1G)}$**) (blue), *E*-^{Me_2}SB(Cp^{nBu},I*)ZrCl$_2$ (***E*-5$_{sMAO(1G)}$**) (teal) and *Z*-^{Me_2}SB(Cp^{nBu},I*)ZrCl$_2$ (***Z*-5$_{sMAO(1G)}$**) (lilac). Normalised for clarity. Polymerisation conditions: [Al$_{sMAO(1G)}$]$_0$/[M]$_0$ = 200, TiBA (150 mg), ethylene (2 bar), pre-catalyst (10 mg), hexane (50 mL) and 30 minutes.

Chapter 4

Table A4.1 Slurry-phase ethylene/1-hexene copolymerisation activity using selected sMAO(1G) supported complexes.[a]

sMAO(1G) supported complex	0 mg 1-Hexene [b]	80 mg 1-Hexene [b]
^{Me_2}SB(Cp,I*)ZrCl$_2$ (**1**)	9864	6386
^{Me_2}SB(Cp^{Me},I*)ZrCl$_2$ (**3**)	8466	10414
^{Me_2}SB(Cp,I*)Zr(CH$_2$Ph)$_2$ (**6**)	10133	7126
^{Me_2}SB(Cp^{Me},I*)Zr(CH$_2$Ph)$_2$ (**7**)	9509	7245
^{Me_2}SB(Cp,I*)ZrMe$_2$ (**8**)	9716	8558

(a) Polymerisation conditions: $[Al_{sMAO(1G)}]_0/[M]_0 = 200$, TiBA (150 mg), ethylene (2 bar), pre-catalyst (10 mg), hexane (50 mL), 80 °C and 5 minutes; (b) activity ($kg_{PE}\, mol_M^{-1}\, h^{-1}\, bar^{-1}$).

Table A4.2 Slurry-phase ethylene/1-hexene copolymer molecular weights (M_w) produced using selected sMAO(1G) supported complexes.[a]

sMAO(1G) supported complex	0 mg 1-Hexene [b]	80 mg 1-Hexene [b]
^{Me_2}SB(Cp,I*)ZrCl$_2$ (**1**)	187	167
^{Me_2}SB(Cp^{Me},I*)ZrCl$_2$ (**3**)	123	104
^{Me_2}SB(Cp,I*)Zr(CH$_2$Ph)$_2$ (**6**)	162	142
^{Me_2}SB(Cp^{Me},I*)Zr(CH$_2$Ph)$_2$ (**7**)	147	142
^{Me_2}SB(Cp,I*)ZrMe$_2$ (**8**)	158	139

(a) Polymerisation conditions: $[Al_{sMAO(1G)}]_0/[M]_0 = 200$, TiBA (150 mg), ethylene (2 bar), pre-catalyst (10 mg), hexane (50 mL), 80 °C and 5 minutes; (b) molecular weights ($kg\, mol^{-1}$).

Table A4.3 Slurry-phase ethylene/1-hexene copolymer temperature of melting (T_m) and crystallisation (T_c) produced using ^{Me_2}SB(Cp,I*)ZrCl$_2$ (**1**) supported on sMAO(1G) (**1$_{sMAO(1G)}$**).[a]

1-Hexene (mg)	T_m [b] (°C)	T_c [c] (°C)
0	133	120
5	133	120
10	133	119
20	131	118
40	130	117
80	128	116

(a) Polymerisation conditions: $[Al_{sMAO(1G)}]_0/[M]_0$ = 200, TiBA (150 mg), ethylene (2 bar), pre-catalyst (10 mg), hexane (50 mL), 80 °C and 5 minutes; (b) obtained from the second heating cycle; (c) obtained from the first cooling cycle.

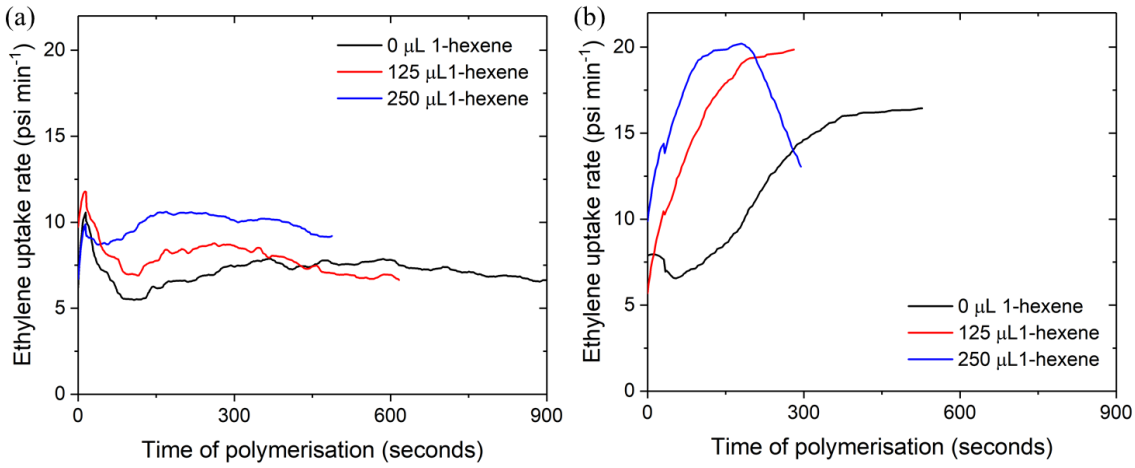


Figure A4.1 Slurry-phase polymerisation ethylene uptake rate as a function of time of polymerisation using sMAO(1G) supported (a) ^{Me_2}SB(Cp^{Me},I*)ZrCl$_2$ (**3$_{sMAO(1G)}$**) and (b) *Z*-^{Me_2}SB(Cp^{nBu},I*)ZrCl$_2$ (**Z-5$_{sMAO(1G)}$**) with 0 µL 1-hexene (black), 125 µL 1-hexene (red) and 250 µL 1-hexene (blue). Polymerisation conditions: $[Al_{sMAO(1G)}]_0/[M]_0$ = 200, TiBA (10 µmol), ethylene (8.3 bar), pre-catalyst (0.05–0.15 mg), heptane (5 mL) and 80 °C. Reactions quenched at 5.5 or 8.3 bar ethylene uptake for co- and homopolymerisation respectively or after 1 hour.

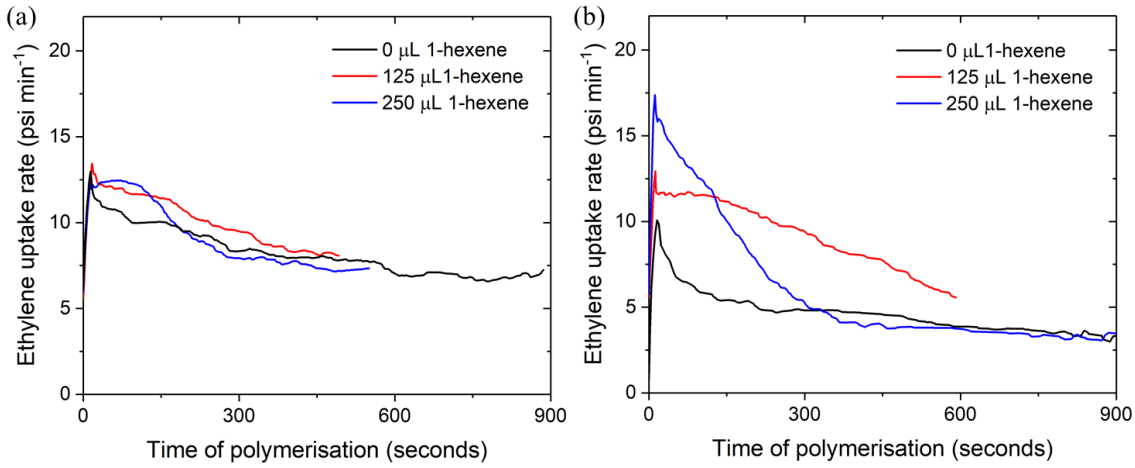


Figure A4.2 Slurry-phase polymerisation ethylene uptake rate as a function of time of polymerisation using sMAO(1G) supported (a) ^{Me_2}SB(Cp,I*)ZrBr$_2$ (**2$_{sMAO(1G)}$**) and (b) ^{Me_2}SB(Cp^{Me},I*)ZrBr$_2$ (**4$_{sMAO(1G)}$**) with 0 µL 1-hexene (black), 125 µL 1-hexene (red) and 250 µL 1-hexene (blue). Polymerisation conditions: [Al$_{sMAO(1G)}$]$_0$/[M]$_0$ = 200, TiBA (10 µmol), ethylene (8.3 bar), pre-catalyst (0.05–0.15 mg), heptane (5 mL) and 80 °C. Reactions quenched at 5.5 or 8.3 bar ethylene uptake for co- and homopolymerisation respectively or after 1 hour.

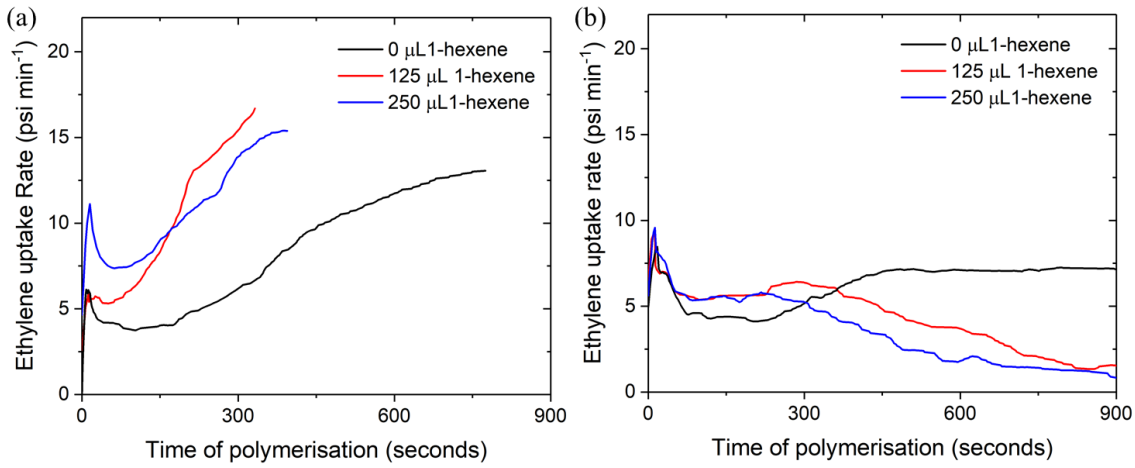


Figure A4.3 Slurry-phase polymerisation ethylene uptake rate as a function of time of polymerisation using sMAO(1G) supported (a) ^{Me_2}SB(Cp,I*)ZrMe$_2$ (**8$_{sMAO(1G)}$**) and (b) ^{Me_2}SB(Cp^{Me},I*)ZrMe$_2$ (**9$_{sMAO(1G)}$**) with 0 µL 1-hexene (black), 125 µL 1-hexene (red) and 250 µL 1-hexene (blue). Polymerisation conditions: [Al$_{sMAO(1G)}$]$_0$/[M]$_0$ = 200, TiBA (10 µmol), ethylene (8.3 bar), pre-catalyst (0.05–0.15 mg), heptane (5 mL) and 80 °C. Reactions quenched at 5.5 or 8.3 bar ethylene uptake for co- and homopolymerisation respectively or after 1 hour.

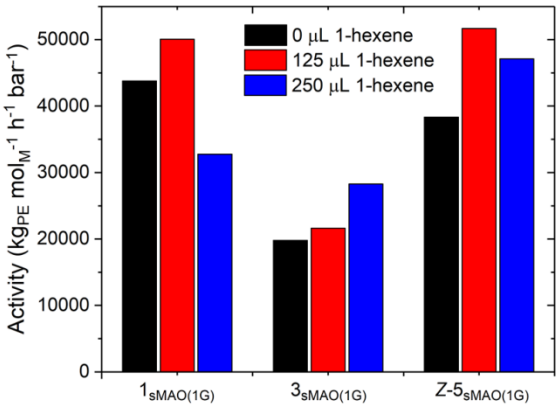


Figure A4.4 Slurry-phase ethylene polymerisation activity using sMAO(1G) supported ^{Me_2}SB(Cp,I*)ZrCl$_2$ (**1$_{sMAO(1G)}$**), ^{Me_2}SB(Cp^{Me},I*)ZrCl$_2$ (**3$_{sMAO(1G)}$**) and *Z*-^{Me_2}SB(Cp^{nBu},I*)ZrCl$_2$ (***Z*-5$_{sMAO(1G)}$**) with 0 µL 1-hexene (black), 125 µL 1-hexene (red) and 250 µL 1-hexene (blue). Polymerisation conditions: [Al$_{sMAO(1G)}$]$_0$/[M]$_0$ = 200, TiBA (10 µmol), ethylene (8.3 bar), pre-catalyst (0.05–0.15 mg), heptane (5 mL) and 80 °C. Reactions quenched at 5.5 or 8.3 bar ethylene uptake for co- and homopolymerisation respectively or after 1 hour.

Table A4.4 Slurry-phase ethylene/1-hexene copolymerisation activity using sMAO(1G) supported complexes.[a]

sMAO(1G) supported complex	0 µL 1-Hexene [b]	125 µL 1-Hexene [b]	250 µL 1-Hexene [b]
^{Me_2}SB(Cp,I*)ZrCl$_2$ (**1**)	43765	50055	32773
^{Me_2}SB(Cp,I*)ZrBr$_2$ (**2**)	7481	8982	8178
^{Me_2}SB(Cp^{Me},I*)ZrCl$_2$ (**3**)	19762	21600	28298
^{Me_2}SB(Cp^{Me},I*)ZrBr$_2$ (**4**)	6639	10783	6498
Z-^{Me_2}SB(Cp^{nBu},I*)ZrCl$_2$ (***Z*-5**)	38331	51694	47092
^{Me_2}SB(Cp,I*)Zr(CH$_2$Ph)$_2$ (**6**)	37309	42942	32934
^{Me_2}SB(Cp^{Me},I*)Zr(CH$_2$Ph)$_2$ (**7**)	22737	35105	17974
^{Me_2}SB(Cp,I*)ZrMe$_2$ (**8**)	26921	45520	35741
^{Me_2}SB(Cp^{Me},I*)ZrMe$_2$ (**9**)	17138	3071	2438

(a) Polymerisation conditions: [Al$_{sMAO(1G)}$]$_0$/[M]$_0$ = 200, TiBA (10 µmol), ethylene (8.3 bar), pre-catalyst (0.05–0.15 mg), heptane (5 mL) and 80 °C; reactions quenched at 5.5 or 8.3 bar ethylene uptake for co- and homopolymerisation respectively or after 1 hour; (b) activity (kg$_{PE}$ mol$_M^{-1}$ h^{-1} bar^{-1}).

Table A4.5 $T_{el,max.}$ [a] for the polymer produced using sMAO(1G) supported complexes.[b]

sMAO(1G) supported complex	0 µL 1-Hexene [c]	125 µL 1-Hexene [c]	250 µL 1-Hexene [c]
^{Me_2}SB(Cp,I*)ZrCl$_2$ (**1**)	111.1	107.2	104.1
^{Me_2}SB(Cp,I*)ZrBr$_2$ (**2**)	112.9	109.0	106.5
^{Me_2}SB(Cp^{Me},I*)ZrCl$_2$ (**3**)	113.1	108.1	105.1
^{Me_2}SB(Cp^{Me},I*)ZrBr$_2$ (**4**)	111.4	107.1	104.2
Z-^{Me_2}SB(Cp$^{n\text{Bu}}$,I*)ZrCl$_2$ (***Z*-5**)	111.0	105.6	103.0
^{Me_2}SB(Cp,I*)Zr(CH$_2$Ph)$_2$ (**6**)	113.2	108.1	105.7
^{Me_2}SB(Cp^{Me},I*)Zr(CH$_2$Ph)$_2$ (**7**)	111.8	106.8	104.2
^{Me_2}SB(Cp,I*)ZrMe$_2$ (**8**)	110.9	107.0	104.5
^{Me_2}SB(Cp^{Me},I*)ZrMe$_2$ (**9**)	111.7	107.3	104.5

(a) Obtained from crystallisation elution fractionation; (b) polymerisation conditions: $[Al_{sMAO(1G)}]_0/[M]_0$ = 200, TiBA (10 µmol), ethylene (8.3 bar), pre-catalyst (0.05–0.15 mg), heptane (5 mL) and 80 °C; reactions quenched at 5.5 or 8.3 bar ethylene uptake for co- and homopolymerisation respectively or after 1 hour; (c) $T_{el,max.}$ (°C).

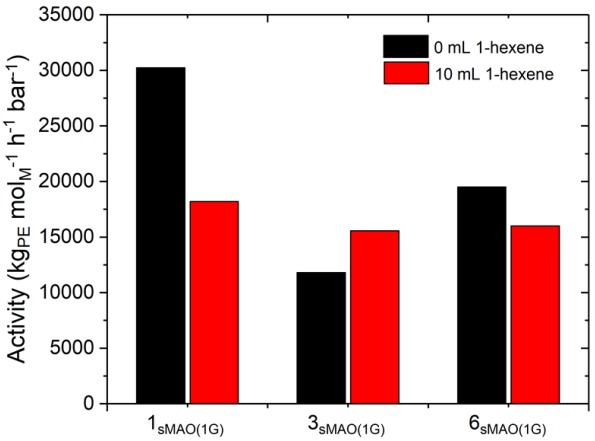


Figure A4.5 Slurry-phase ethylene polymerisation activity using sMAO(1G) supported ^{Me_2}SB(Cp,I*)ZrCl$_2$ (**1$_{sMAO(1G)}$**), ^{Me_2}SB(Cp^{Me},I*)ZrCl$_2$ (**3$_{sMAO(1G)}$**) and ^{Me_2}SB(Cp,I*)Zr(CH$_2$Ph)$_2$ (**6$_{sMAO(1G)}$**) with 0 mL 1-hexene (black) and 10 mL 1-hexene (red). Polymerisation conditions: $[Al_{sMAO(1G)}]_0/[M]_0$ = 200, TEA (0.5 mmol), ethylene (8 bar), pre-catalyst (0.025–0.050 g), hexane (1 L), 80 °C and 1 hour.

Table A4.6 Slurry-phase ethylene/1-hexene copolymerisation activity using sMAO(1G) supported complexes.[a]

sMAO(1G) supported complex	0 mL 1-Hexene [b]	10 mL 1-Hexene [b]
^{Me_2}SB(Cp,I*)ZrCl$_2$ (**1**)	30229	18191
^{Me_2}SB(Cp^{Me},I*)ZrCl$_2$ (**3**)	11812	15570
^{Me_2}SB(Cp,I*)Zr(CH$_2$Ph)$_2$ (**6**)	19505	15997

(a) Polymerisation conditions: $[Al_{sMAO}]_0/[M]_0$ = 200, TEA (0.5 mmol), ethylene (8 bar), pre-catalyst (0.025–0.050 mg), hexane (1 L), 80 °C and 1 hour; (b) activity ($kg_{PE}\ mol_M^{-1}\ h^{-1}\ bar^{-1}$).

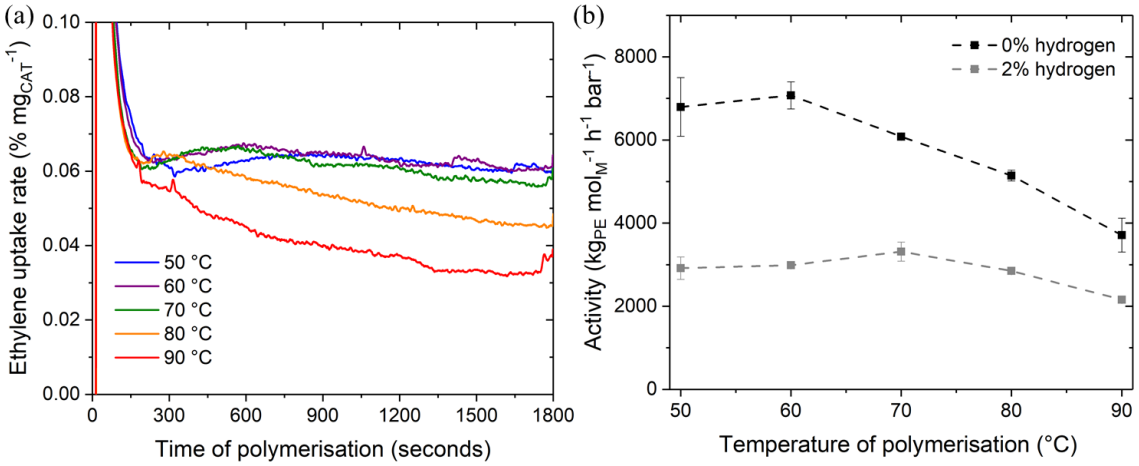


Figure A4.6 (a) Slurry-phase polymerisation ethylene uptake rate as a function of time of polymerisation using sMAO(1G) supported ^{Me_2}SB(Cp,I*)ZrCl$_2$ (**1**$_{\mathbf{sMAO(1G)}}$) with 2% hydrogen at 50 °C (blue), 60 °C (purple), 70 °C (green), 80 °C (orange) and 90 °C (red). The Y-axis provides a quantitative measure of uptake; (b) slurry-phase ethylene polymerisation activity as a function of temperature of polymerisation using sMAO(1G) supported ^{Me_2}SB(Cp,I*)ZrCl$_2$ (**1**$_{\mathbf{sMAO(1G)}}$) with 0% hydrogen (black) and 2% hydrogen (grey). Polymerisation conditions: $[Al_{sMAO(1G)}]_0/[M]_0$ = 200, TiBA (150 mg), ethylene/hydrogen (2 bar, 2%), pre-catalyst (10 mg), hexane (50 mL) and 30 minutes.

Table A4.7 Slurry-phase ethylene/hydrogen polymerisation activity using sMAO(1G) supported complexes.[a]

sMAO(1G) supported complex	0% Hydrogen [b]	2% Hydrogen [b]
^{Me_2}SB(Cp,I*)ZrCl$_2$ (**1**)	5144	2850
^{Me_2}SB(Cp,I*)ZrMe$_2$ (**8**)	5482	2447

(a) Polymerisation conditions: $[Al_{sMAO(1G)}]_0/[M]_0$ = 200, TiBA (150 mg), ethylene (2 bar) or ethylene/hydrogen (2 bar, 2%), pre-catalyst (10 mg), hexane (50 mL), 80 °C and 30 minutes; (b) activity ($kg_{PE}\ mol_M^{-1}\ h^{-1}\ bar^{-1}$).

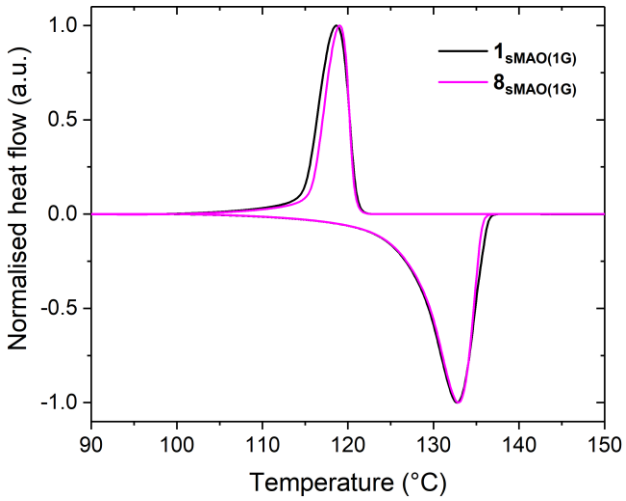


Figure A4.7 DSC plot showing the first cooling cycle and second heating cycle for the polyethylenes produced using sMAO(1G) supported ^{Me_2}SB(Cp,I*)ZrCl$_2$ (**1$_{sMAO(1G)}$**) (black) and ^{Me_2}SB(Cp,I*)ZrMe$_2$ (**8$_{sMAO(1G)}$**) (pink). Normalised for clarity. Polymerisation conditions: $[Al_{sMAO(1G)}]_0/[M]_0$ = 200, TiBA (150 mg), ethylene/hydrogen (2 bar, 2%), pre-catalyst (10 mg), hexane (50 mL), 80 °C and 30 minutes.

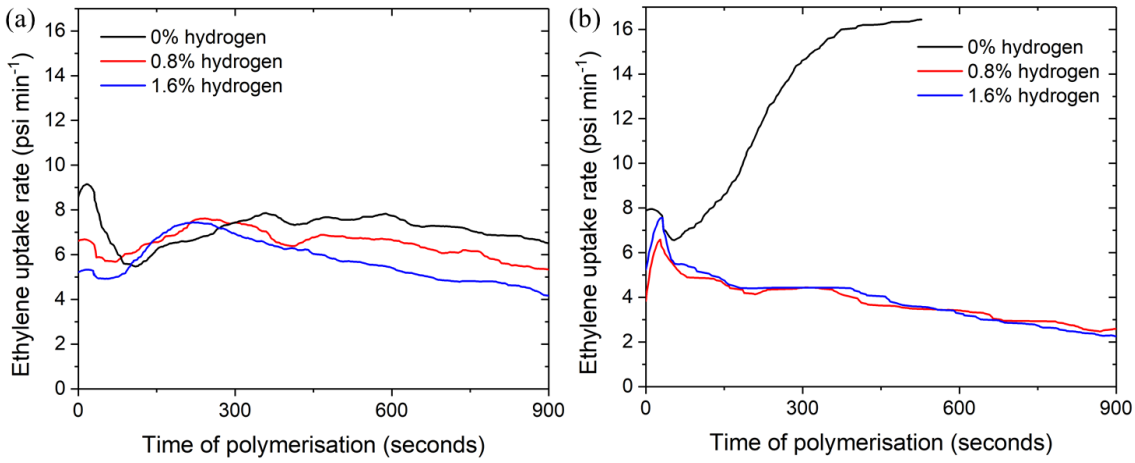


Figure A4.8 Slurry-phase polymerisation ethylene uptake rate as a function of time of polymerisation using sMAO(1G) supported (a) ^{Me_2}SB(Cp^{Me},I*)ZrCl$_2$ (**3$_{sMAO(1G)}$**) and (b) *Z*-^{Me_2}SB(Cp^{nBu},I*)ZrCl$_2$ (**Z-5$_{sMAO(1G)}$**) with 0% hydrogen (black), 0.8% hydrogen (red) and 1.6% hydrogen (blue). Polymerisation conditions: $[Al_{sMAO(1G)}]_0/[M]_0$ = 200, TiBA (10 μmol), ethylene (8.3 bar), pre-catalyst (0.05–0.15 mg), heptane (5 mL) and 80 °C. Reactions quenched at 8.3 bar ethylene uptake or after 1 hour.

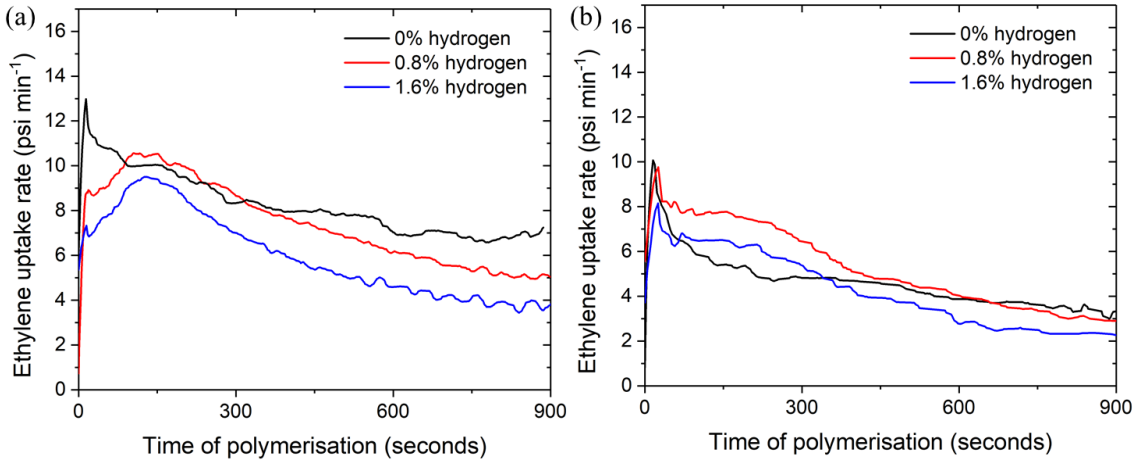


Figure A4.9 Slurry-phase polymerisation ethylene uptake rate as a function of time of polymerisation using sMAO(1G) supported (a) ^{Me_2}SB(Cp,I*)ZrBr$_2$ (**2$_{sMAO(1G)}$**) and (b) ^{Me_2}SB(Cp^{Me},I*)ZrBr$_2$ (**4$_{sMAO(1G)}$**) with 0% hydrogen (black), 0.8% hydrogen (red) and 1.6% hydrogen (blue). Polymerisation conditions: $[Al_{sMAO(1G)}]_0/[M]_0$ = 200, TiBA (10 μmol), ethylene (8.3 bar), pre-catalyst (0.05–0.15 mg), heptane (5 mL) and 80 °C. Reactions quenched at 8.3 bar ethylene uptake or after 1 hour.

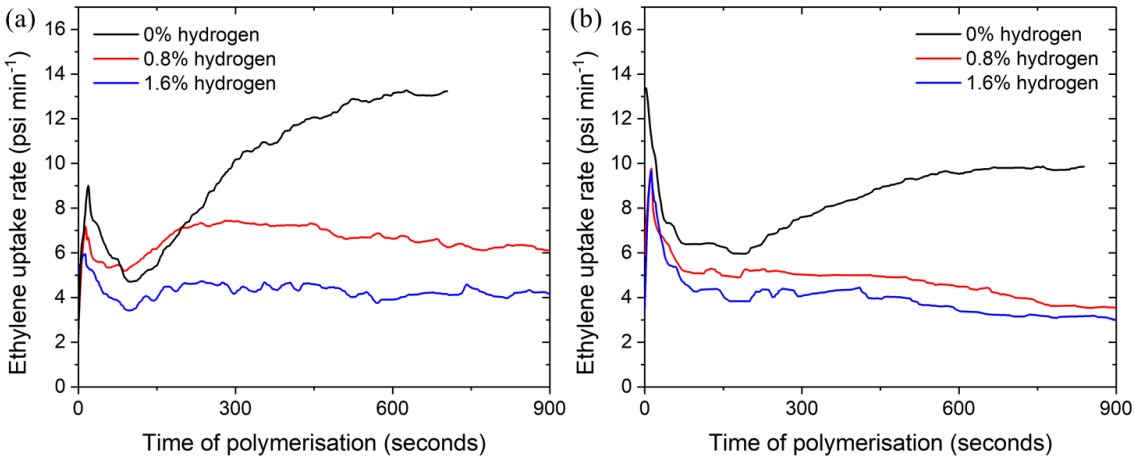


Figure A4.10 Slurry-phase polymerisation ethylene uptake rate as a function of time of polymerisation using sMAO(1G) supported (a) ^{Me_2}SB(Cp,I*)Zr(CH_2Ph)$_2$ (**6$_{sMAO(1G)}$**) and (b) ^{Me_2}SB(Cp^{Me},I*)Zr(CH_2Ph)$_2$ (**7$_{sMAO(1G)}$**) with 0% hydrogen (black), 0.8% hydrogen (red) and 1.6% hydrogen (blue). Polymerisation conditions: [Al$_{sMAO(1G)}$]$_0$/[M]$_0$ = 200, TiBA (10 µmol), ethylene (8.3 bar), pre-catalyst (0.05–0.15 mg), heptane (5 mL) and 80 °C. Reactions quenched at 8.3 bar ethylene uptake or after 1 hour.

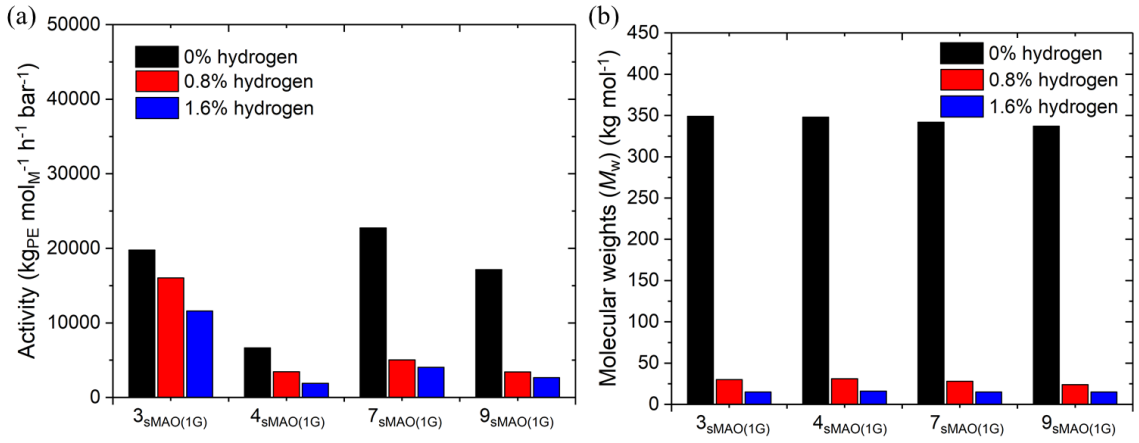


Figure A4.11 (a) Slurry-phase ethylene polymerisation activity and (b) molecular weights (M_w) using sMAO(1G) supported ^{Me_2}SB(Cp^{Me},I*)ZrCl_2 (**3$_{sMAO(1G)}$**), ^{Me_2}SB(Cp^{Me},I*)ZrBr_2 (**4$_{sMAO(1G)}$**), ^{Me_2}SB(Cp^{Me},I*)Zr(CH_2Ph)$_2$ (**7$_{sMAO(1G)}$**) and ^{Me_2}SB(Cp^{Me},I*)ZrMe_2 (**9$_{sMAO(1G)}$**) with 0% hydrogen (black), 0.8% hydrogen (red) and 1.6% hydrogen (blue). Polymerisation conditions: [Al$_{sMAO(1G)}$]$_0$/[M]$_0$ = 200, TiBA (10 µmol), ethylene (8.3 bar), pre-catalyst (0.05–0.15 mg), heptane (5 mL) and 80 °C. Reactions quenched at 8.3 bar ethylene uptake or after 1 hour.

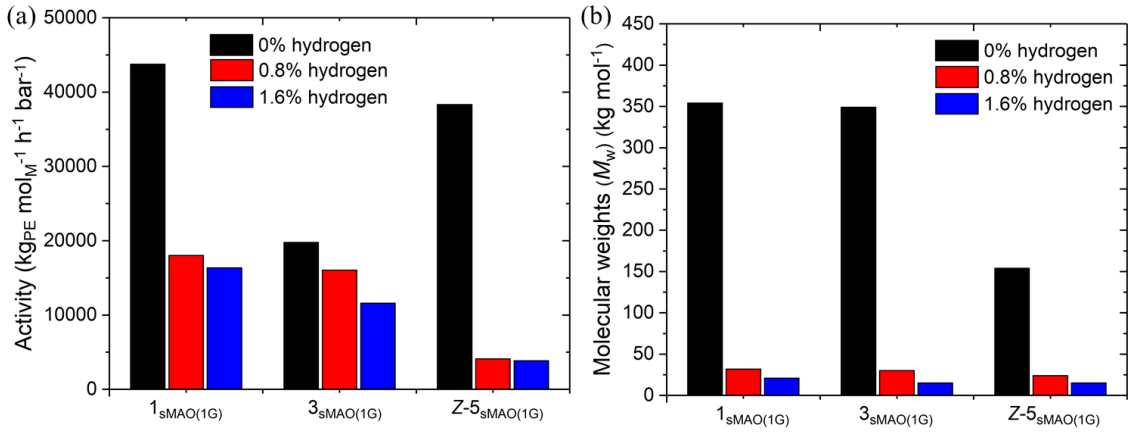


Figure A4.12 (a) Slurry-phase ethylene polymerisation activity and (b) polymer molecular weights (M_w) using sMAO(1G) supported ^{Me_2}SB(Cp,I*)ZrCl$_2$ (**1$_{sMAO(1G)}$**), ^{Me_2}SB(Cp^{Me},I*)ZrCl$_2$ (**3$_{sMAO(1G)}$**) and *Z*-^{Me_2}SB(Cp^{nBu},I*)ZrCl$_2$ (***Z*-5$_{sMAO(1G)}$**) with 0% hydrogen (black), 0.8% hydrogen (red) and 1.6% hydrogen (blue). Polymerisation conditions: [Al$_{sMAO(1G)}$]$_0$/[M]$_0$ = 200, TiBA (10 µmol), ethylene (8.3 bar), pre-catalyst (0.05–0.15 mg), heptane (5 mL) and 80 °C. Reactions quenched at 8.3 bar ethylene uptake or after 1 hour.

Table A4.8 Slurry-phase ethylene/hydrogen polymerisation activity using sMAO(1G) supported complexes.[a]

sMAO(1G) supported complex	0% Hydrogen [b]	0.8% Hydrogen [b]	1.6% Hydrogen [b]
^{Me_2}SB(Cp,I*)ZrCl$_2$ (**1**)	43766	18034	16353
^{Me_2}SB(Cp,I*)ZrBr$_2$ (**2**)	7481	6033	4009
^{Me_2}SB(Cp^{Me},I*)ZrCl$_2$ (**3**)	19762	16054	11588
^{Me_2}SB(Cp^{Me},I*)ZrBr$_2$ (**4**)	6639	3465	1896
Z-^{Me_2}SB(Cp^{nBu},I*)ZrCl$_2$ (***Z*-5**)	38331	4096	3844
^{Me_2}SB(Cp,I*)Zr(CH$_2$Ph)$_2$ (**6**)	37309	16946	9541
^{Me_2}SB(Cp^{Me},I*)Zr(CH$_2$Ph)$_2$ (**7**)	22737	5037	4052
^{Me_2}SB(Cp,I*)ZrMe$_2$ (**8**)	26921	13849	7386
^{Me_2}SB(Cp^{Me},I*)ZrMe$_2$ (**9**)	17138	3420	2660

(a) Polymerisation conditions: [Al$_{sMAO(1G)}$]$_0$/[M]$_0$ = 200, TiBA (10 µmol), ethylene (8.3 bar), pre-catalyst (0.05–0.15 mg), heptane (5 mL) and 80 °C; reactions quenched at 8.5 bar ethylene uptake or after 1 hour; (b) activity (kg_{PE} mol_M^{-1} h^{-1} bar^{-1}).

Table A4.9 Slurry-phase ethylene/hydrogen polymer molecular weights (M_w) using sMAO(1G) supported complexes.[a]

sMAO(1G) supported complex	0% Hydrogen [b]	0.8% Hydrogen [b]	1.6% Hydrogen [b]
^{Me_2}SB(Cp,I*)ZrCl$_2$ (**1**)	354	32	21
^{Me_2}SB(Cp,I*)ZrBr$_2$ (**2**)	296	28	18
^{Me_2}SB(Cp^{Me},I*)ZrCl$_2$ (**3**)	349	30	15
^{Me_2}SB(Cp^{Me},I*)ZrBr$_2$ (**4**)	348	31	16
Z-^{Me_2}SB(Cp$^{n\text{Bu}}$,I*)ZrCl$_2$ (***Z*-5**)	154	24	15
^{Me_2}SB(Cp,I*)Zr(CH$_2$Ph)$_2$ (**6**)	311	35	17
^{Me_2}SB(Cp^{Me},I*)Zr(CH$_2$Ph)$_2$ (**7**)	342	28	15
^{Me_2}SB(Cp,I*)ZrMe$_2$ (**8**)	358	29	17
^{Me_2}SB(Cp^{Me},I*)ZrMe$_2$ (**9**)	337	24	15

(a) Polymerisation conditions: $[Al_{sMAO(1G)}]_0/[M]_0$ = 200, TiBA (10 μmol), ethylene (8.3 bar), pre-catalyst (0.05–0.15 mg), heptane (5 mL) and 80 °C; reactions quenched at 8.5 bar ethylene uptake or after 1 hour; (b) molecular weights (kg mol^{-1}).

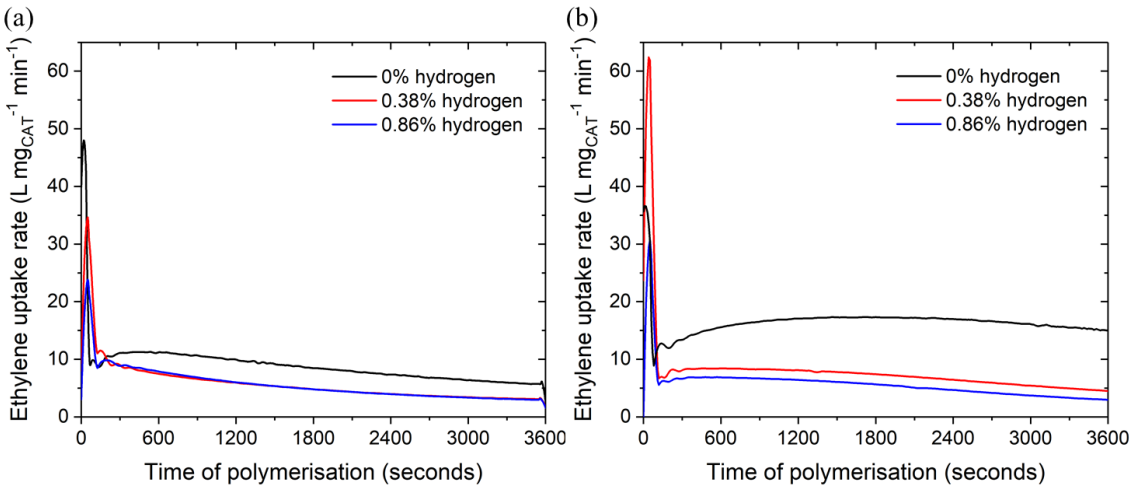


Figure A4.13 Slurry-phase polymerisation ethylene uptake rate as a function of time of polymerisation using sMAO(1G) supported (a) ^{Me_2}SB(Cp^{Me},I*)ZrCl$_2$ (**3$_{sMAO(1G)}$**) and (b) ^{Me_2}SB(Cp^{Me},I*)Zr(CH$_2$Ph)$_2$ (**7$_{sMAO(1G)}$**) with 0% hydrogen (black), 0.38% hydrogen (red) and 0.86% hydrogen (blue). Polymerisation conditions: $[Al_{sMAO(1G)}]_0/[M]_0$ = 200, TEA (0.5 mmol), ethylene (8 bar), pre-catalyst (0.025–0.050 mg), hexane (1 L), 80 °C and 1 hour.

Table A4.10 Slurry-phase ethylene/hydrogen polymerisation activity using sMAO(1G) supported complexes.[a]

sMAO(1G) supported complex	0% Hydrogen [b]	0.38% Hydrogen [b]	0.86% Hydrogen [b]
^{Me_2}SB(Cp,I*)ZrCl$_2$ (**1**)	30229	-	13026
^{Me_2}SB(Cp^{Me},I*)ZrCl$_2$ (**3**)	11812	7409	7611
^{Me_2}SB(Cp,I*)Zr(CH$_2$Ph)$_2$ (**6**)	19505	6943	6663
^{Me_2}SB(Cp^{Me},I*)Zr(CH$_2$Ph)$_2$ (**7**)	21940	9519	7208
^{Me_2}SB(Cp,I*)ZrMe$_2$ (**8**)	27186	12149	8926

(a) Polymerisation conditions: $[Al_{sMAO(1G)}]_0/[M]_0$ = 200, TEA (0.5 mmol), ethylene (8 bar), pre-catalyst (0.025–0.050 mg), hexane (1 L), 80 °C and 1 hour; (b) activity ($kg_{PE}\ mol_M^{-1}\ h^{-1}\ bar^{-1}$).

Table A4.11 Slurry-phase ethylene/hydrogen polymer molecular weights (M_w) using sMAO(1G) supported complexes.[a]

sMAO(1G) supported complex	0% Hydrogen [b]	0.38% Hydrogen [b]	0.86% Hydrogen [b]
^{Me_2}SB(Cp,I*)ZrCl$_2$ (**1**)	265	-	17
^{Me_2}SB(Cp^{Me},I*)ZrCl$_2$ (**3**)	248	34	19
^{Me_2}SB(Cp,I*)Zr(CH$_2$Ph)$_2$ (**6**)	268	28	14
^{Me_2}SB(Cp^{Me},I*)Zr(CH$_2$Ph)$_2$ (**7**)	204	28	19
^{Me_2}SB(Cp,I*)ZrMe$_2$ (**8**)	225	27	15

(a) Polymerisation conditions: $[Al_{sMAO(1G)}]_0/[M]_0$ = 200, TEA (0.5 mmol), ethylene (8 bar), pre-catalyst (0.025–0.050 mg), hexane (1 L), 80 °C and 1 hour; (b) molecular weights ($kg\ mol^{-1}$).

Table A4.12 Solution-phase ethylene/hydrogen polymerisation activity using sMAO(1G) supported complexes.[a]

sMAO(1G) supported complex	0.38% Hydrogen [b]
^{Me_2}SB(Cp,I*)Zr(CH_2Ph)$_2$ (**6**)	5256
^{Me_2}SB(Cp^{Me},I*)Zr(CH_2Ph)$_2$ (**7**)	2977
^{Me_2}SB(Cp,I*)ZrMe_2 (**8**)	23370 [c]

(a) Polymerisation conditions: 0.38% hydrogen, TEA (5 mL), ethylene (8 bar), complex (3 mg), hexane (1 L), 80 °C and 1 hour; (b) activity ($kg_{PE}\,mol_M^{-1}\,h^{-1}\,bar^{-1}$); (c) activity calculated after 15 minutes of polymerisation.

Table A4.13 Slurry-phase ethylene/hydrogen/1-hexene polymerisation activity using sMAO(1G) supported complexes.[a]

sMAO(1G) supported complex	0 mg 1-Hexene [b]	80 mg 1-Hexene [b]
^{Me_2}SB(Cp,I*)ZrCl_2 (**1**)	2850	3060
^{Me_2}SB(Cp,I*)ZrMe_2 (**8**)	2447	2393

(a) Polymerisation conditions: $[Al_{sMAO(1G)}]_0/[M]_0 = 200$, TiBA (150 mg), ethylene/hydrogen (2 bar, 2%), pre-catalyst (10 mg), hexane (50 mL), 80 °C and 30 minutes; (b) activity ($kg_{PE}\,mol_M^{-1}\,h^{-1}\,bar^{-1}$).

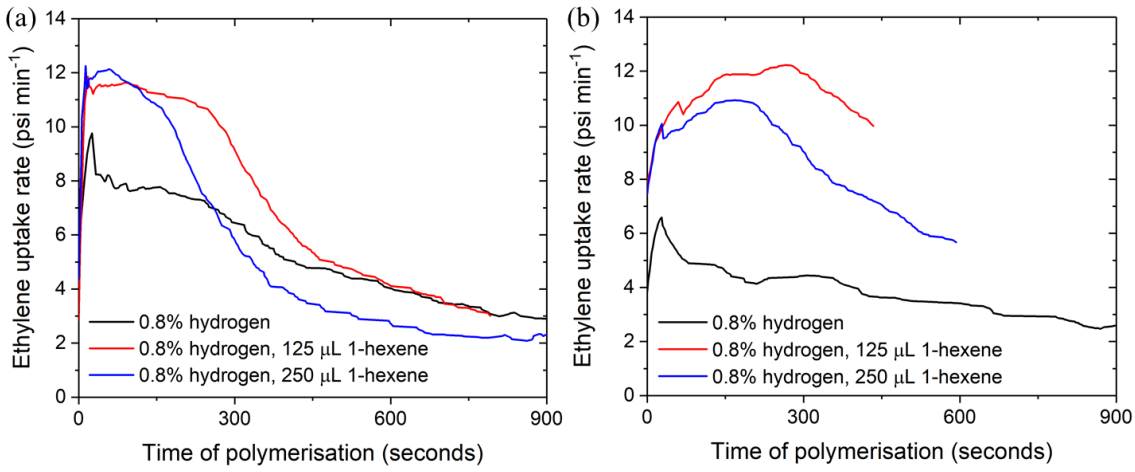


Figure A4.14 Slurry-phase polymerisation ethylene uptake rate as a function of time of polymerisation using sMAO(1G) supported (a) ^{Me_2}SB(Cp^{Me},I*)ZrBr$_2$ (**4$_{sMAO(1G)}$**) and (b) *Z*-^{Me_2}SB(Cp^{nBu},I*)ZrCl$_2$ (**Z-5$_{sMAO(1G)}$**) with 0.8% hydrogen (black), 125 µL 1-hexene (red) and 250 µL 1-hexene (blue). Polymerisation conditions: [Al$_{sMAO(1G)}$]$_0$/[M]$_0$ = 200, TiBA (10 µmol), ethylene (8.3 bar), pre-catalyst (0.05–0.10 mg), heptane (5 mL) and 80 °C. Reactions quenched at 5.5 or 8.3 bar ethylene uptake for co- and homopolymerisation respectively or after 1 hour.

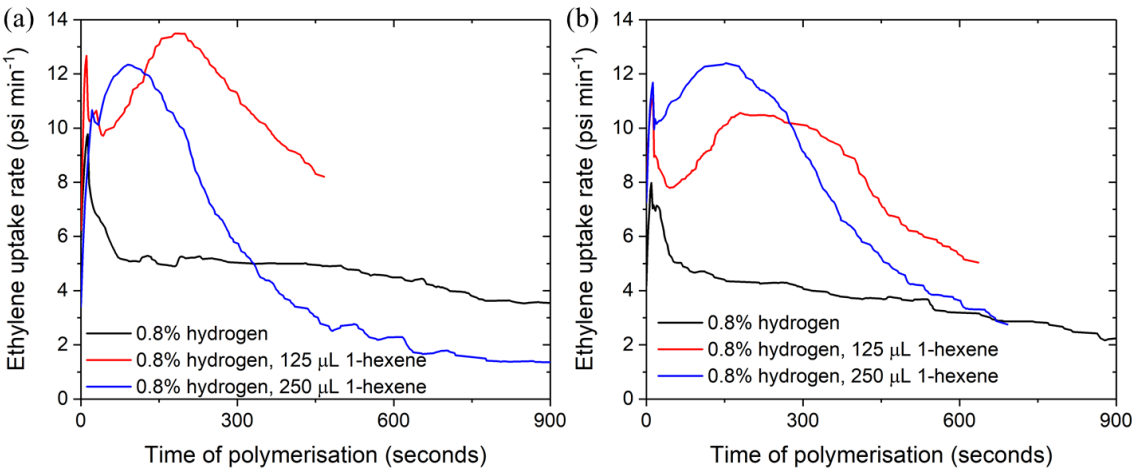


Figure A4.15 Slurry-phase polymerisation ethylene uptake rate as a function of time of polymerisation using sMAO(1G) supported (a) ^{Me_2}SB(Cp^{Me},I*)Zr(CH$_2$Ph)$_2$ (**7$_{sMAO(1G)}$**) and (b) ^{Me_2}SB(Cp^{Me},I*)ZrMe$_2$ (**9$_{sMAO(1G)}$**) with 0.8% hydrogen (black), 125 µL 1-hexene (red) and 250 µL 1-hexene (blue). Polymerisation conditions: [Al$_{sMAO(1G)}$]$_0$/[M]$_0$ = 200, TiBA (10 µmol), ethylene (8.3 bar), pre-catalyst (0.05–0.10 mg), heptane (5 mL) and 80 °C. Reactions quenched at 5.5 or 8.3 bar ethylene uptake for co- and homopolymerisation respectively or after 1 hour.

Table A4.14 Slurry-phase ethylene/hydrogen/1-hexene copolymerisation activity using sMAO(1G) supported complexes.[a]

sMAO(1G) supported complex	0 µL 1-Hexene [b]	125 µL 1-Hexene [b]	250 µL 1-Hexene [b]
^{Me_2}SB(Cp^{Me},I*)ZrBr$_2$ (**4**)	3465	7933	4521
Z-^{Me_2}SB(Cp$^{n\text{Bu}}$,I*)ZrCl$_2$ (***Z*-5**)	4097	21093	14417
^{Me_2}SB(Cp^{Me},I*)Zr(CH$_2$Ph)$_2$ (**7**)	5038	18771	23831
^{Me_2}SB(Cp^{Me},I*)ZrMe$_2$ (**9**)	3420	13150	12544

(a) Polymerisation conditions: 0.8% hydrogen, $[Al_{sMAO(1G)}]_0/[M]_0$ = 200, TiBA (10 µmol), ethylene (8.3 bar), pre-catalyst (0.05–0.10 mg), heptane (5 mL) and 80 °C; reactions quenched at 5.5 or 8.3 bar ethylene uptake for co- and homopolymerisation respectively or after 1 hour; (b) activity ($kg_{PE}\,mol_M^{-1}\,h^{-1}\,bar^{-1}$).

Table A4.15 Slurry-phase ethylene/hydrogen/1-hexene polymer molecular weights (M_w) using sMAO(1G) supported complexes.[a]

sMAO(1G) supported complex	0 µL 1-Hexene [b]	125 µL 1-Hexene [b]	250 µL 1-Hexene [b]
^{Me_2}SB(Cp^{Me},I*)ZrBr$_2$ (**4**)	31	31	37
Z-^{Me_2}SB(Cp$^{n\text{Bu}}$,I*)ZrCl$_2$ (***Z*-5**)	24	26	29
^{Me_2}SB(Cp^{Me},I*)Zr(CH$_2$Ph)$_2$ (**7**)	28	24	30
^{Me_2}SB(Cp^{Me},I*)ZrMe$_2$ (**9**)	24	26	30

(a) Polymerisation conditions: 0.8% hydrogen $[Al_{sMAO(1G)}]_0/[M]_0$ = 200, TiBA (10 µmol), ethylene (8.3 bar), pre-catalyst (0.05–0.10 mg), heptane (5 mL) and 80 °C; reactions quenched at 5.5 or 8.3 bar ethylene uptake for co- and homopolymerisation respectively or after 1 hour; (b) molecular weights ($kg\,mol^{-1}$).

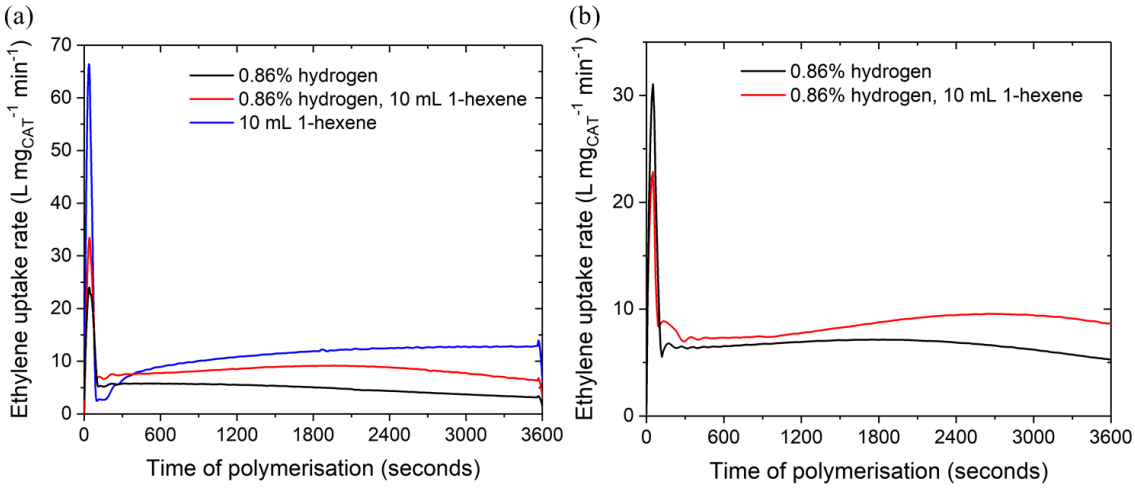


Figure A4.16 Slurry-phase polymerisation ethylene uptake rate as a function of time of polymerisation using sMAO(1G) supported (a) ^{Me_2}SB(Cp,I*)Zr(CH$_2$Ph)$_2$ (**6$_{sMAO(1G)}$**) and (b) ^{Me_2}SB(Cp,I*)ZrMe$_2$ (**8$_{sMAO(1G)}$**) with 0.86% hydrogen (black), 0.86% hydrogen and 10 mL 1-hexene (red) and 10 mL 1-hexene (blue). Polymerisation conditions: [Al$_{sMAO(1G)}$]$_0$/[M]$_0$ = 200, TEA (0.5 mmol), ethylene (8 bar), pre-catalyst (0.025–0.050 mg), hexane (1 L), 80 °C and 1 hour.

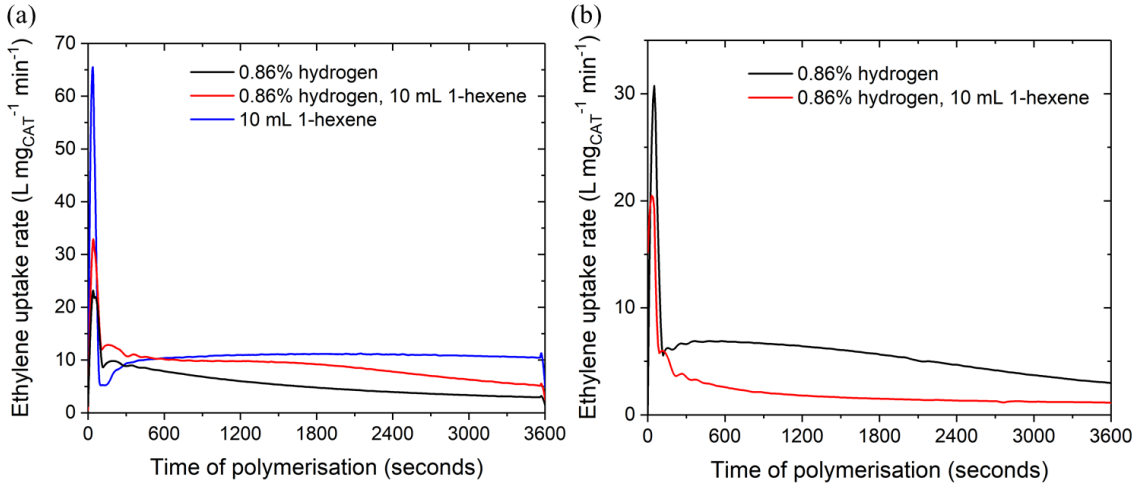


Figure A4.17 Slurry-phase polymerisation ethylene uptake rate as a function of time of polymerisation using sMAO(1G) supported (a) ^{Me_2}SB(Cp^{Me},I*)ZrCl$_2$ (**3$_{sMAO(1G)}$**) and (b) ^{Me_2}SB(Cp^{Me},I*)Zr(CH$_2$Ph)$_2$ (**7$_{sMAO(1G)}$**) with 0.86% hydrogen (black), 0.86% hydrogen and 10 mL 1-hexene (red) and 10 mL 1-hexene (blue). Polymerisation conditions: [Al$_{sMAO(1G)}$]$_0$/[M]$_0$ = 200, TEA (0.5 mmol), ethylene (8 bar), pre-catalyst (0.025–0.050 mg), hexane (1 L), 80 °C and 1 hour.

Table A4.16 Slurry-phase ethylene/hydrogen/1-hexene copolymerisation activity using sMAO(1G) supported complexes.[a]

sMAO(1G) supported complex	0 mL 1-Hexene [b]	10 mL 1-Hexene [b]
$^{Me_2}SB(Cp^{Me},I^*)ZrCl_2$ (**3**)	7611	11599
$^{Me_2}SB(Cp,I^*)Zr(CH_2Ph)_2$ (**6**)	6663	11240
$^{Me_2}SB(Cp^{Me},I^*)Zr(CH_2Ph)_2$ (**7**)	7208	2567
$^{Me_2}SB(Cp^{Me},I^*)ZrMe_2$ (**8**)	8926	11715

(a) Polymerisation conditions: 0.86% hydrogen, $[Al_{sMAO(1G)}]_0/[M]_0$ = 200, TEA (0.5 mmol), ethylene (8 bar), pre-catalyst (0.025–0.050 mg), hexane (1 L), 80 °C and 1 hour; (b) activity ($kg_{PE}\ mol_M^{-1}\ h^{-1}\ bar^{-1}$).

Chapter 5

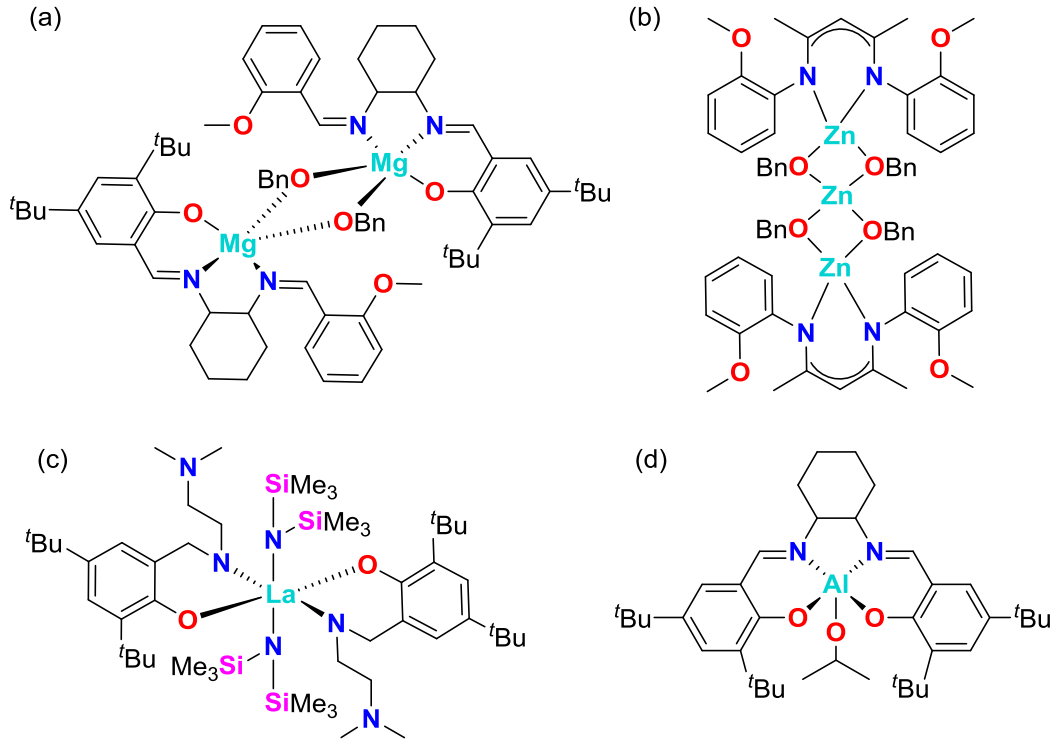


Chart A5.1 Structures of (a) [(SalenMe)Mg(μ-OCH_2Ph)]$_2$,[1] (b) [(BDI-OMe)Zn(μ-OCH_2Ph)]$_2$ Zn(μ-OCH_2Ph)$_2$,[2] (c) [$N(SiMe_3)_2$]$_2$La[O-2,4-^{t}Bu-6-$CH_2NCH_2CH_2NMe_2$-C_6H_2]$_2$,[3] and (d) (cyclohexylsalen)AlO^iPr.[4]

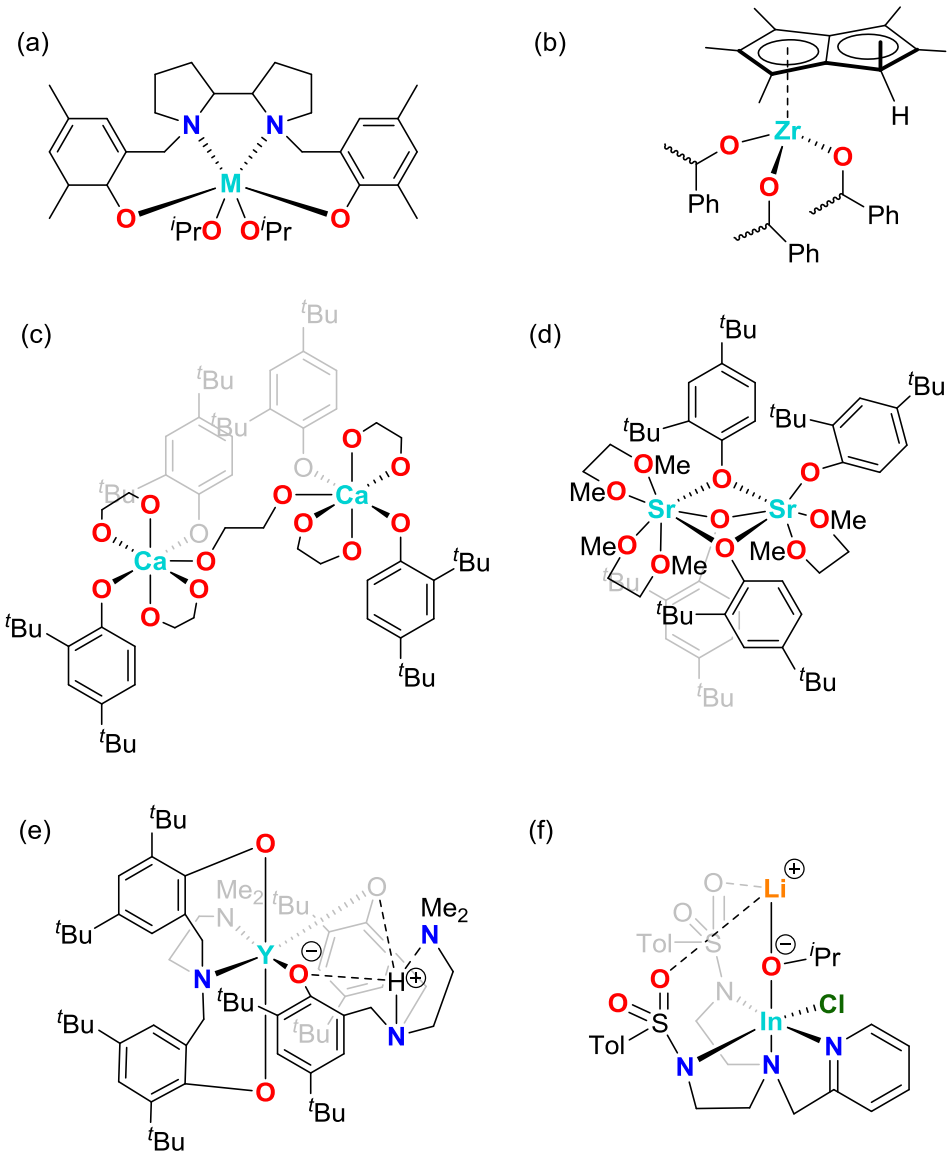


Chart A5.2 Structures of (a) Zr and Hf alkoxides of a bipyrrolidine derived salan ligand,[5, 6] (b) Pn*(H)Zr(OCH(CH$_3$)C$_6$H$_5$)$_3$,[7] (c) Ca$_2$(DBP)$_4$(DME)$_4$(μ-DME),[8] (d) Sr$_2$(DBP)(μ-DBP)$_3$(DME)$_3$,[8] (e) Y(O$_2$NN')(HO$_2$NN') (O$_2$NN' is ^{Me_2}NCH$_2$CH$_2$N(CH$_2$-2-O-3,5-^{t}Bu-C$_6$H$_2$)$_2$),[9] and (g) In(^{Ts}NCH$_2$CH$_2$NCH$_2$C$_5$H$_5$N)(O^{i}Pr)Cl{Li(THF)} where Ts is CH$_3$C$_6$H$_4$SO$_2$.[10]

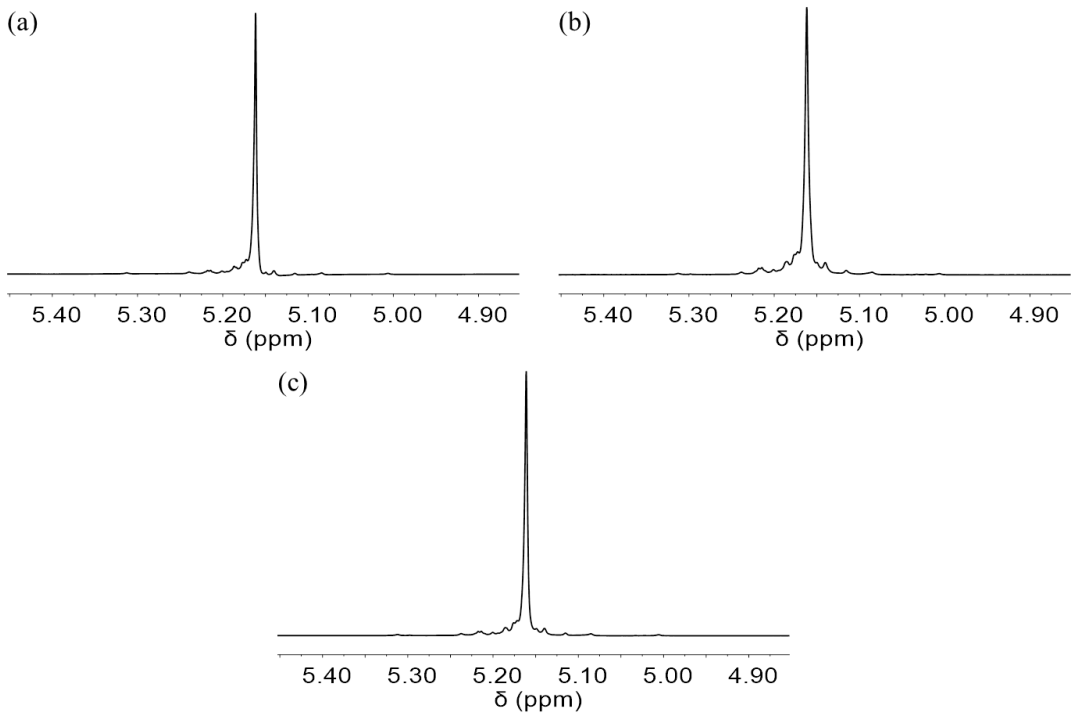
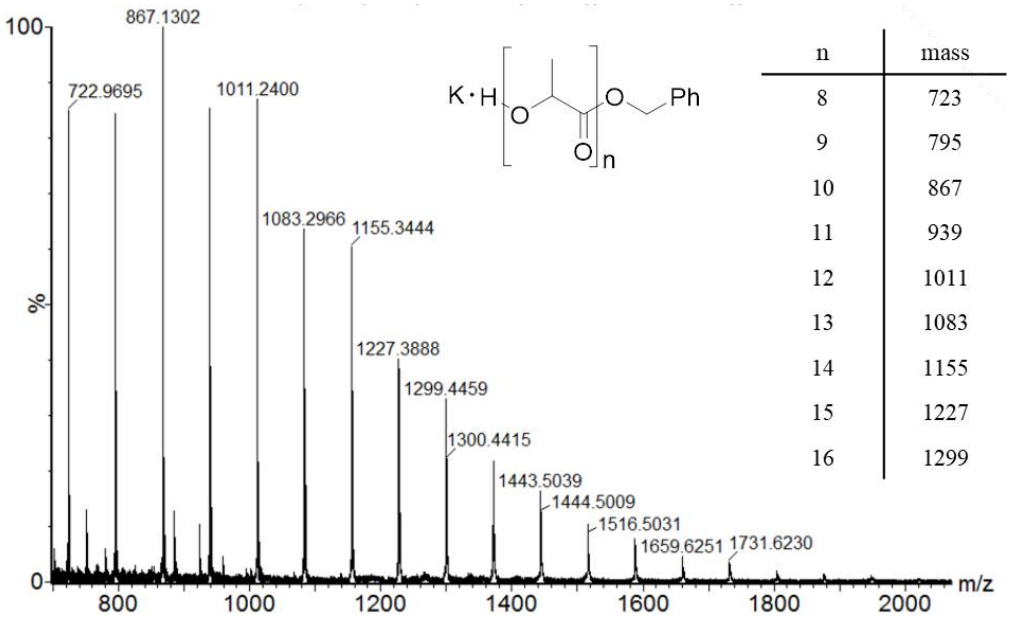


Figure A5.1 $^{1}H\{^{1}H\}$ NMR spectra (chloroform-d_1, 500 MHz, 298 K) of the poly-*L*-lactide produced using (a) ^{Me_2}SB(Cp^{Me},I*)ZrCl$_2$ (**3**), (b) *Z*-^{Me_2}SB(Cp,I*)ZrCl(O-2,6-Me-C$_6$H$_3$) (***Z*-10**) and (c) *E*-^{Me_2}SB(Cp,I*)ZrCl(O-2,6-^{i}Pr-C$_6$H$_3$) (***E*-11**). Polymerisation conditions: two equivalents benzyl alcohol co-initiator, chloroform-d_1, 80 °C, $[LA]_0/[M]_0 = 50$ and $[LA]_0 = 0.5$ M.



n	mass
8	723
9	795
10	867
11	939
12	1011
13	1083
14	1155
15	1227
16	1299

Figure A5.2 MALDI-TOF mass spectrum (recorded in a DCTB + KTFA matrix) of the poly-*L*-lactide produced using ^{Me_2}SB(Cp^{Me},I*)ZrCl$_2$ (**3**). Polymerisation conditions: two equivalents benzyl alcohol co-initiator, chloroform-d_1, 80 °C, $[LA]_0/[M]_0 = 10$ and $[LA]_0 = 0.5$ M.

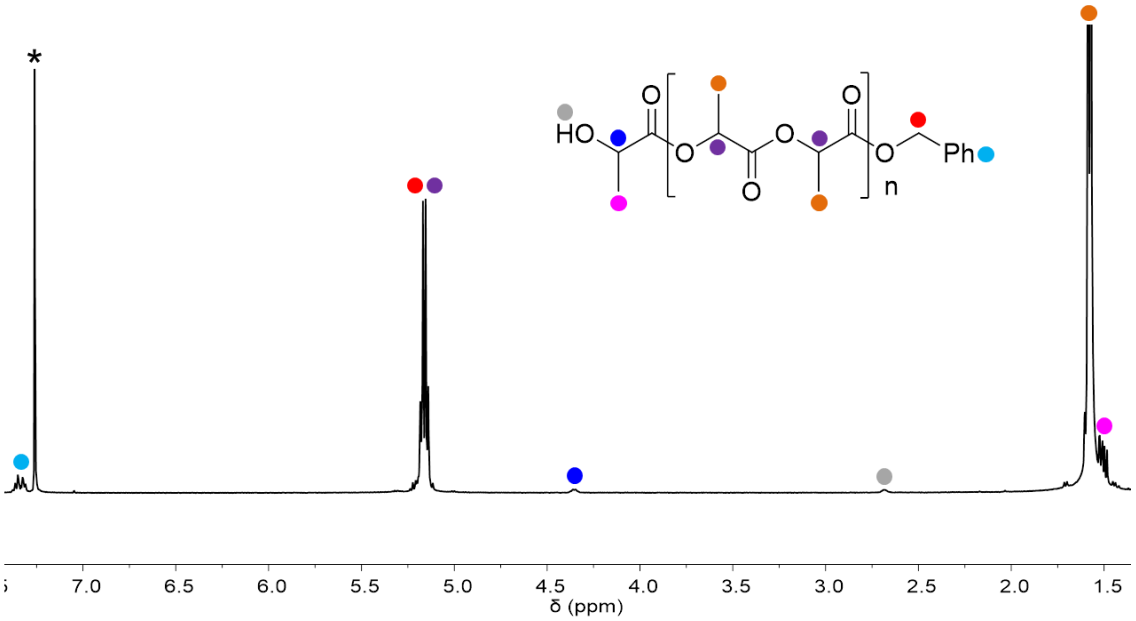


Figure A5.3 ^{1}H NMR spectrum (chloroform-d_1, 125 MHz, 298 K) of the poly-*L*-lactide produced using ^{Me_2}SB(Cp,I*)ZrCl$_2$ (**1**). Polymerisation conditions: two equivalents benzyl alcohol co-initiator, chloroform-d_1, 80 °C, $[LA]_0/[M]_0 = 50$ and $[LA]_0 = 0.5$ M.

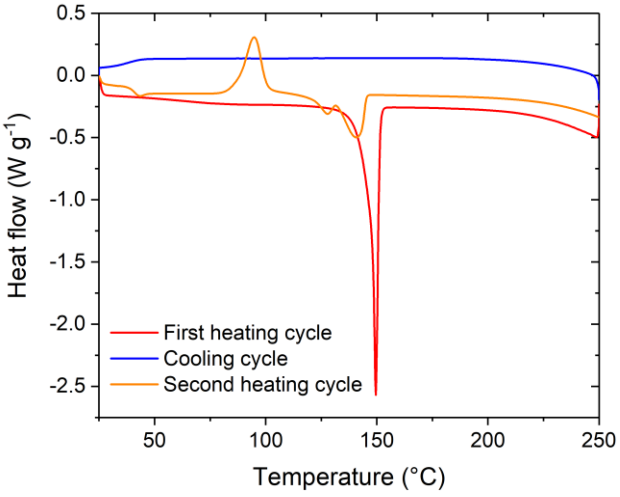


Figure A5.4 DSC plot of the poly-*L*-lactide produced using *E*-^{Me_2}SB(Cp,I*)ZrCl(O-2,6-^{i}Pr-C$_6$H$_3$) (***E*-11**) showing the first heating cycle (red, T_m = 150 °C), cooling cycle (blue) and second heating cycle (orange, T_c = 94.9 °C, T_m = 132 and 149 °C). Polymerisation conditions: two equivalents benzyl alcohol co-initiator, chloroform-d_1, 80 °C, $[LA]_0/[M]_0 = 50$ and $[LA]_0 = 0.5$ M.

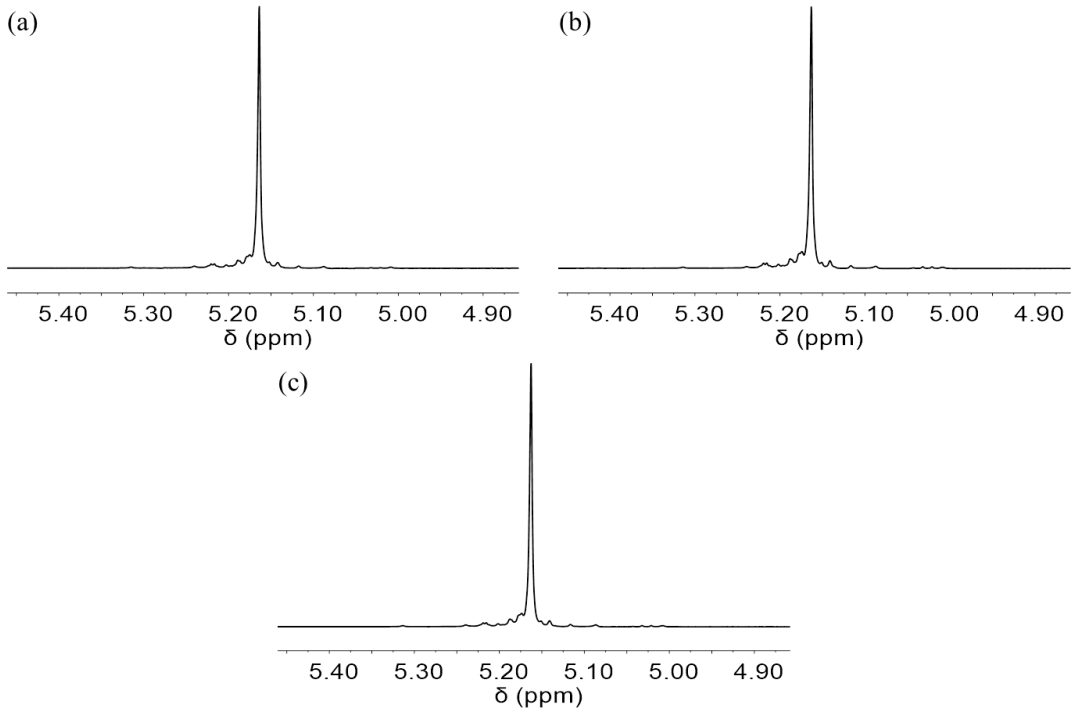


Figure A5.5 $^{1}H\{^{1}H\}$ NMR spectra (chloroform-d_1, 500 MHz, 298 K) of the poly-*D*-lactide produced using (a) $^{Me_2}SB(Cp^{Me},I^*)ZrCl_2$ (**3**), (b) *Z*-$^{Me_2}SB(Cp,I^*)ZrCl(O\text{-}2,6\text{-}Me\text{-}C_6H_3)$ (***Z*-10**) and (c) *E*-$^{Me_2}SB(Cp,I^*)ZrCl(O\text{-}2,6\text{-}^{i}Pr\text{-}C_6H_3)$ (***E*-11**). Polymerisation conditions: two equivalents benzyl alcohol co-initiator, chloroform-d_1, 80 °C, $[LA]_0/[M]_0 = 50$ and $[LA]_0 = 0.5$ M.

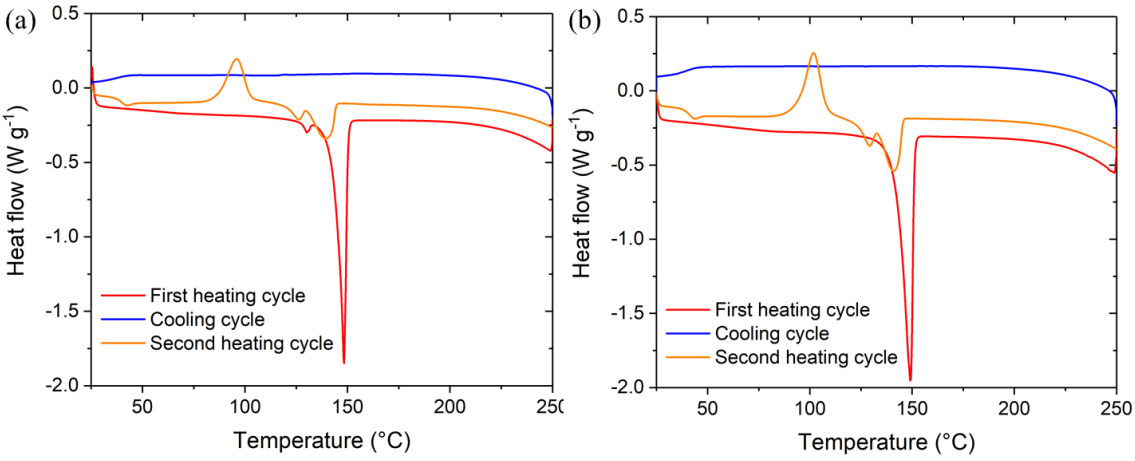


Figure A5.6 DSC plot of the poly-*D*-lactide produced using (a) $^{Me_2}SB(Cp^{Me},I^*)ZrCl_2$ (**3**) showing the first heating cycle (red, $T_m = 148$ °C), cooling cycle (blue) and second heating cycle (orange, $T_c = 96$ °C, $T_m = 126$ and 139 °C) and (b) *E*-$^{Me_2}SB(Cp,I^*)ZrCl(O\text{-}2,6\text{-}^{i}Pr\text{-}C_6H_3)$ (***E*-11**) showing the first heating cycle (red, $T_m = 149$ °C), cooling cycle (blue) and second heating cycle (orange, $T_c = 102$ °C, $T_m = 129$ and 141 °C). Polymerisation conditions: two equivalents benzyl alcohol co-initiator, chloroform-d_1, 80 °C, $[LA]_0/[M]_0 = 50$ and $[LA]_0 = 0.5$ M.

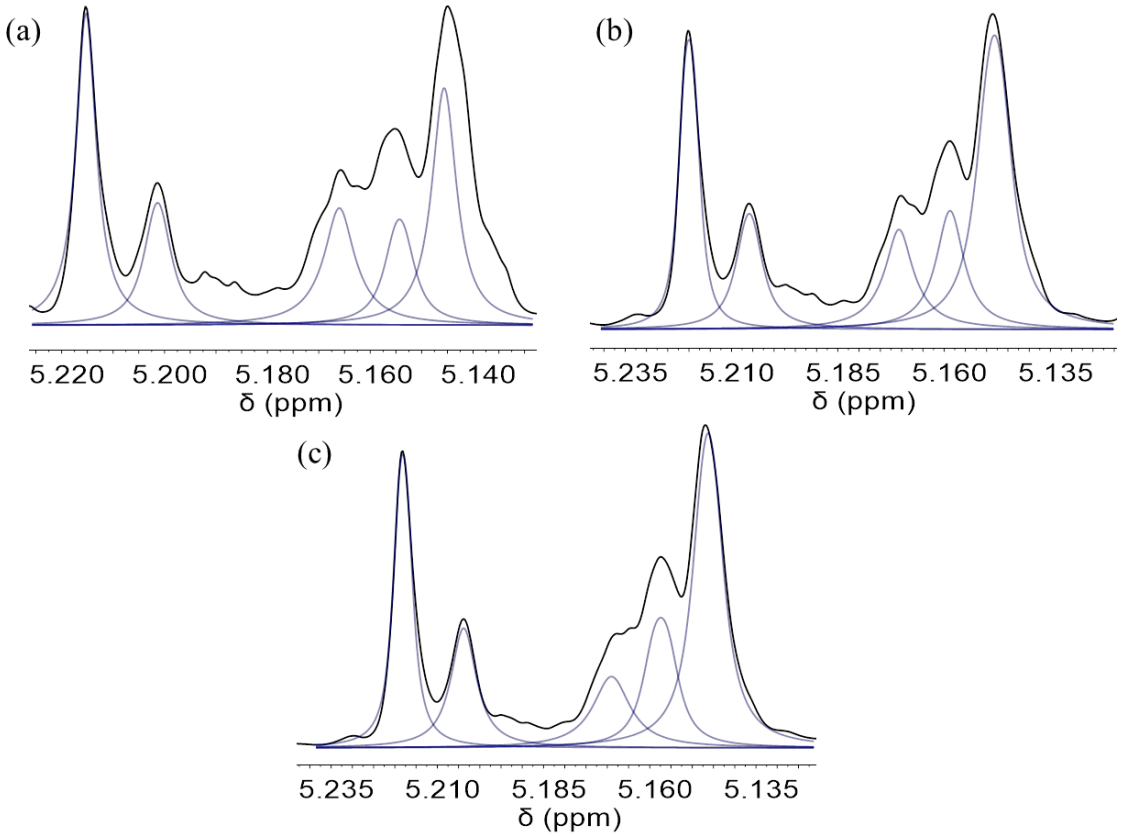


Figure A5.7 $^{1}H\{^{1}H\}$ NMR spectra (chloroform-d_1, 500 MHz, 298 K) of the poly-*rac*-lactide produced using (a) ^{Me_2}SB(Cp,I*)ZrCl$_2$ (**1**) (P_r = 0.81), (b) ^{Me_2}SB(Cp^{Me},I*)ZrCl$_2$ (**3**) (P_r = 0.84) and (c) *E*-^{Me_2}SB(Cp,I*)ZrCl(O-2,6-^{i}Pr-C$_6$H$_3$) (***E*-11**) (P_r = 0.83). Polymerisation conditions: two equivalents benzyl alcohol co-initiator, chloroform-d_1, 80 °C, $[LA]_0/[M]_0$ = 50 and $[LA]_0$ = 0.5 M.

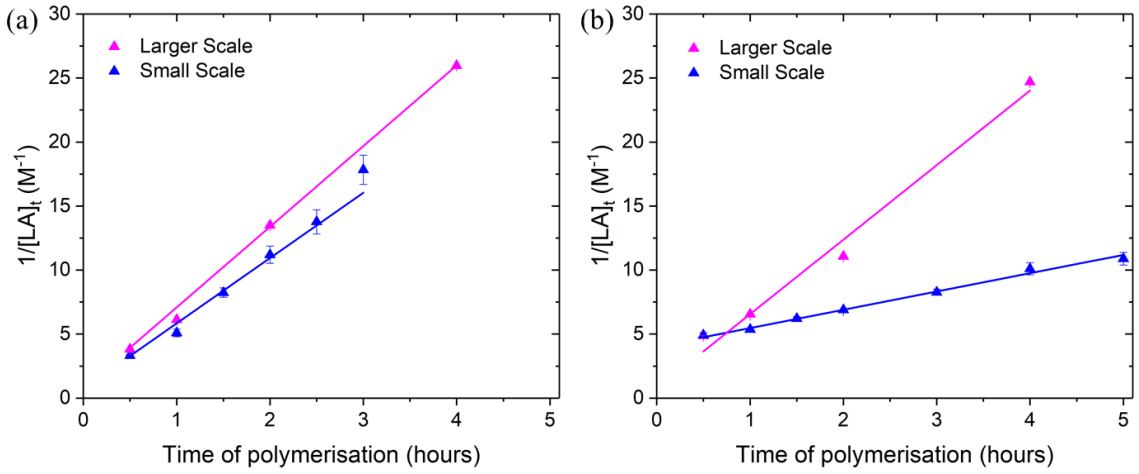


Figure A5.8 $1/[LA]_t$ as a function of time of polymerisation using $^{Me_2}SB(Cp^{Me},I^*)ZrCl_2$ (**3**) as an initiator for the ROP of (a) *L*-lactide on a small scale (blue, k_{obs} = 5.10 ± 0.32 M^{-1} h^{-1}) and larger scale (pink, k_{obs} = 6.29 ± 0.10 M^{-1} h^{-1}); (b) *rac*-lactide on a small scale (blue, k_{obs} = 1.42 ± 0.05 M^{-1} h^{-1}) and larger scale (pink, k_{obs} = 5.82 ± 0.44 M^{-1} h^{-1}). Small scale polymerisation conditions: lactide (40 mg), two equivalents benzyl alcohol co-initiator, toluene-d_8 (0.56 mL), 80 °C, $[LA]_0/[M]_0$ = 50, $[LA]_0$ = 0.5 M. Larger scale polymerisation conditions: lactide (200 mg), two equivalents benzyl alcohol co-initiator, toluene (2.80 mL), 80 °C, $[LA]_0/[M]_0$ = 50, $[LA]_0$ = 0.5 M.

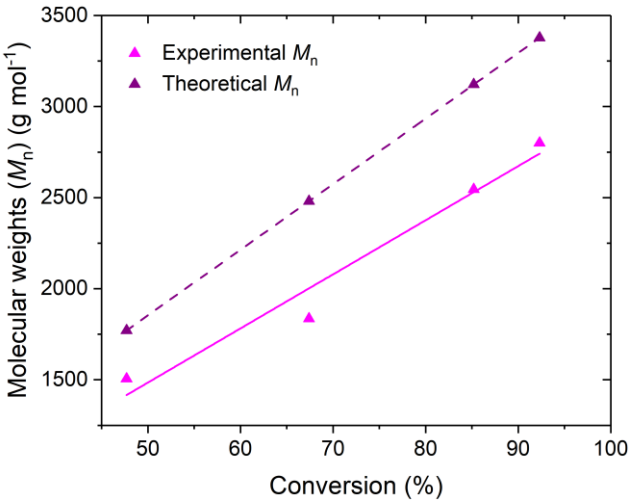


Figure A5.9 Experimental (pink) and theoretical (purple) molecular weight (M_n) as a function of percentage conversion to PLA for the ROP of *L*-lactide using $^{Me_2}SB(Cp^{Me},I^*)ZrCl_2$ (**3**) on a larger scale. Polymerisation conditions: lactide (200 mg), two equivalents benzyl alcohol co-initiator, toluene (2.80 mL), 80 °C, $[LA]_0/[M]_0$ = 50, $[LA]_0$ = 0.5 M.

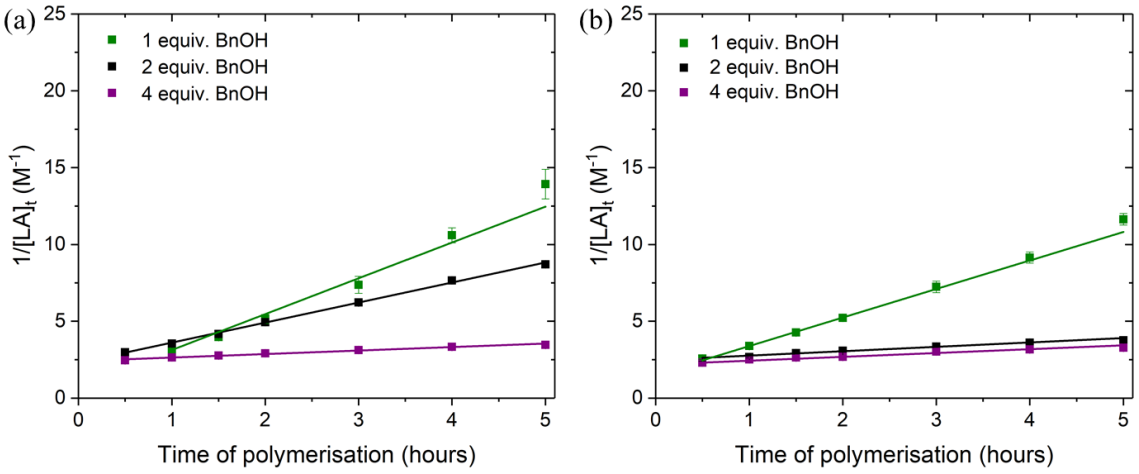


Figure A5.10 $1/[LA]_t$ as a function of time of polymerisation using ^{Me_2}SB(Cp,I*)ZrCl$_2$ (**1**) as an initiator for the ROP of (a) *L*-lactide with one equivalent BnOH (green, k_{obs} = 2.33 ± 0.17 M^{-1} h^{-1}), two equivalents BnOH (black, k_{obs} = 1.30 ± 0.03 M^{-1} h^{-1}) and four equivalents BnOH (purple, k_{obs} = 0.23 ± 0.01 M^{-1} h^{-1}); (b) *rac*-lactide with one equivalent BnOH (green, k_{obs} = 1.86 ± 0.07 M^{-1} h^{-1}), two equivalents BnOH (black, k_{obs} = 0.29 ± 0.03 M^{-1} h^{-1}) and four equivalents BnOH (purple, k_{obs} = 0.25 ± 0.01 M^{-1} h^{-1}). Polymerisation conditions: chloroform-d_1, 80 °C, $[LA]_0/[M]_0$ = 50 and $[LA]_0$ = 0.5 M.

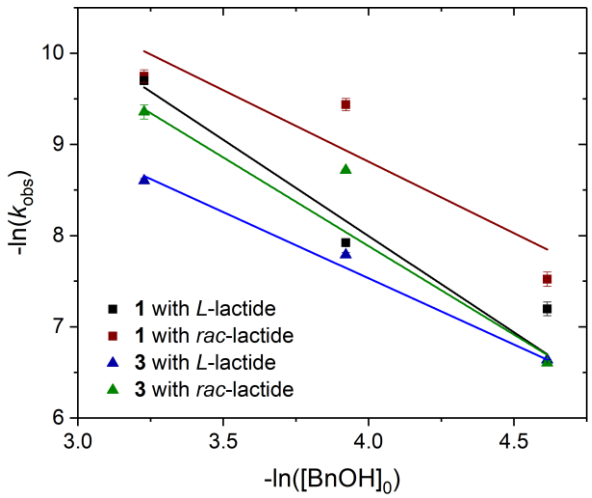


Figure A5.11 –ln(k_{obs}) as a function of –ln($[BnOH]_0$) for the ROP of *L*-lactide using ^{Me_2}SB(Cp,I*)ZrCl$_2$ (**1**) (black square, slope = –2.11 ± 0.47 with R^2 = 0.954) and ^{Me_2}SB(Cp^{Me},I*)ZrCl$_2$ (**3**) (blue triangle, slope = –1.45 ± 0.09 with R^2 = 0.996), and for the ROP of *rac*-lactide using ^{Me_2}SB(Cp,I*)ZrCl$_2$ (**1**) (brown square, slope = –1.57 ± 0.71 with R^2 = 0.9830) and ^{Me_2}SB(Cp^{Me},I*)ZrCl$_2$ (**3**) (green triangle, slope = –1.94 ± 0.30 with R^2 = 0.977). Polymerisation conditions: chloroform-d_1, 80 °C, $[LA]_0/[M]_0$ = 50 and $[LA]_0$ = 0.5 M.

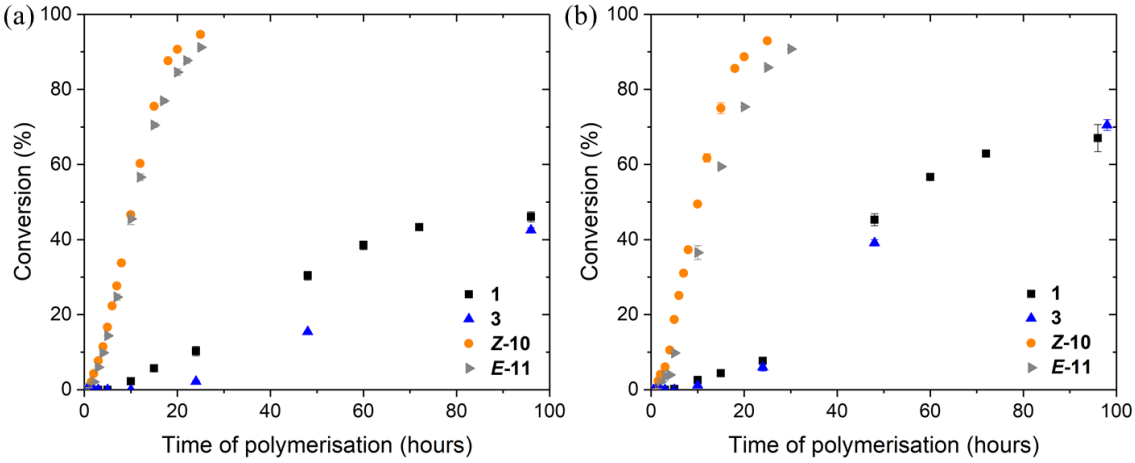


Figure A5.12 Percentage conversion as a function of time of polymerisation for the ROP of (a) *L*-lactide and (b) *rac*-lactide polymerisation using ^{Me_2}SB(Cp,I*)ZrCl$_2$ (**1**) (black square) ^{Me_2}SB(Cp^{Me},I*)ZrCl$_2$ (**3**) (blue triangle), *Z*-^{Me_2}SB(Cp,I*)ZrCl(O-2,6-Me-C$_6$H$_3$) (***Z*-10**) (orange circle) and *E*-^{Me_2}SB(Cp,I*)ZrCl(O-2,6-^{i}Pr-C$_6$H$_3$) (***E*-11**) (grey right triangle). Polymerisation conditions: chloroform-d_1, 80 °C, $[LA]_0/[M]_0 = 50$ and $[LA]_0 = 0.5$ M.

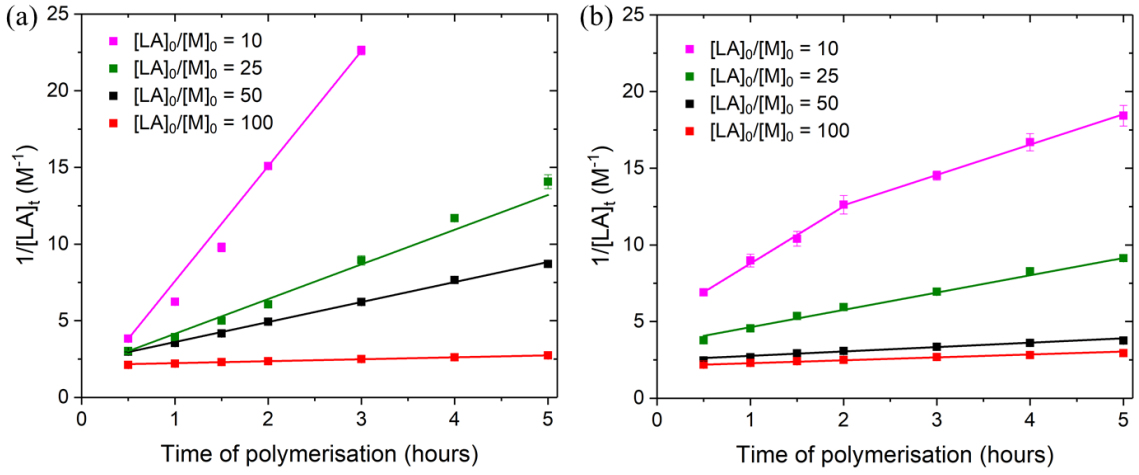


Figure A5.13 $1/[LA]_t$ as a function of time of polymerisation using ^{Me_2}SB(Cp,I*)ZrCl$_2$ (**1**) as an initiator for the ROP of (a) *L*-lactide with $[LA]_0/[M]_0 = 10$ (pink, $k_{obs} = 7.51 \pm 0.09$ M^{-1} h^{-1}), $[LA]_0/[M]_0 = 25$ (green, $k_{obs} = 2.26 \pm 0.12$ M^{-1} h^{-1}), $[LA]_0/[M]_0 = 50$ (black, $k_{obs} = 1.30 \pm 0.03$ M^{-1} h^{-1}) and $[LA]_0/[M]_0 = 100$ (red, $k_{obs} = 0.13 \pm 0.01$ M^{-1} h^{-1}); (b) *rac*-lactide with $[LA]_0/[M]_0 = 10$ (pink, $k_{obs} = 3.73 \pm 0.16$ M^{-1} h^{-1}), $[LA]_0/[M]_0 = 25$ (green, $k_{obs} = 1.13 \pm 0.03$ M^{-1} h^{-1}), $[LA]_0/[M]_0 = 50$ (black, $k_{obs} = 0.29 \pm 0.03$ M^{-1} h^{-1}) and $[LA]_0/[M]_0 = 100$ (red, $k_{obs} = 0.19 \pm 0.01$ M^{-1} h^{-1}). Polymerisation conditions: two equivalents benzyl alcohol co-initiator, chloroform-d_1, 80 °C and $[LA]_0 = 0.5$ M.

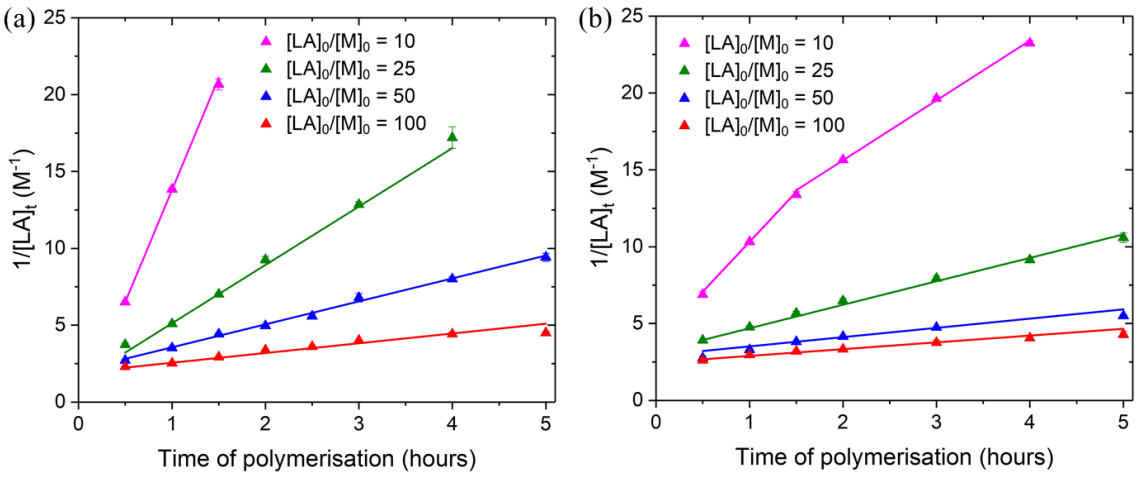


Figure A5.14 $1/[LA]_t$ as a function of time of polymerisation using $^{Me_2}SB(Cp^{Me},I^*)ZrCl_2$ (**3**) as an initiator for the ROP of (a) *L*-lactide with $[LA]_0/[M]_0 = 10$ (pink, $k_{obs} = 14.59 \pm 0.20$ M^{-1} h^{-1}), $[LA]_0/[M]_0 = 25$ (green, $k_{obs} = 3.80 \pm 0.16$ M^{-1} h^{-1}), $[LA]_0/[M]_0 = 50$ (blue, $k_{obs} = 1.49 \pm 0.02$ M^{-1} h^{-1}) and $[LA]_0/[M]_0 = 100$ (red, $k_{obs} = 0.63 \pm 0.05$ M^{-1} h^{-1}); (b) *rac*-lactide with $[LA]_0/[M]_0 = 10$ (pink, $k_{obs} = 6.49 \pm 0.04$ M^{-1} h^{-1}), $[LA]_0/[M]_0 = 25$ (green, $k_{obs} = 1.53 \pm 0.04$ M^{-1} h^{-1}), $[LA]_0/[M]_0 = 50$ (blue, $k_{obs} = 0.60 \pm 0.06$ M^{-1} h^{-1}) and $[LA]_0/[M]_0 = 100$ (red, $k_{obs} = 0.44 \pm 0.04$ M^{-1} h^{-1}). Polymerisation conditions: two equivalents benzyl alcohol co-initiator, chloroform-d_1, 80 °C and $[LA]_0 = 0.5$ M.

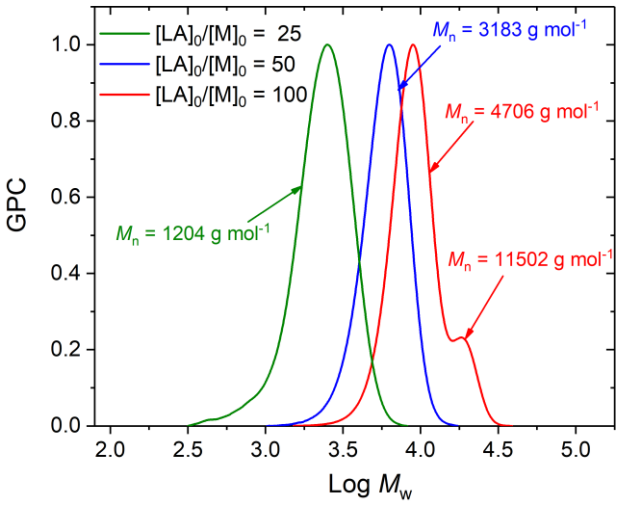


Figure A5.15 GPC plot of the poly-*L*-lactide produced using $^{Me_2}SB(Cp^{Me},I^*)ZrCl_2$ (**3**) with $[LA]_0/[M]_0 = 25$ (green), $[LA]_0/[M]_0 = 50$ (blue) and $[LA]_0/[M]_0 = 100$ (red). Normalised for clarity. Polymerisation conditions: two equivalents benzyl alcohol co-initiator, chloroform-d_1, 80 °C and $[LA]_0 = 0.5$ M.

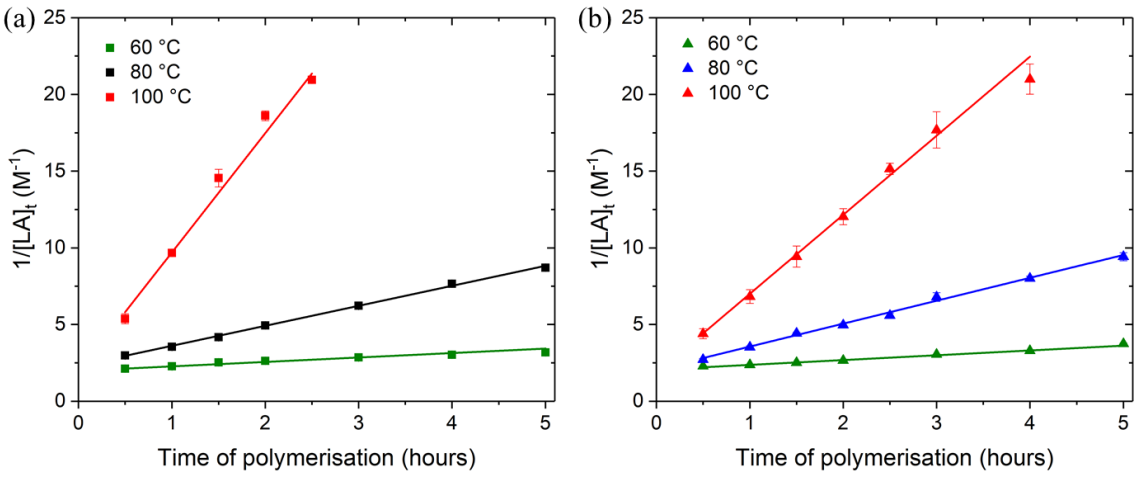


Figure A5.16 $1/[LA]_t$ as a function of time of polymerisation for the ROP of *L*-lactide using (a) ^{Me_2}SB(Cp,I*)ZrCl$_2$ (**1**) (square) at 60 °C (green, k_{obs} = 0.29 ± 0.01 M^{-1} h^{-1}), 80 °C (black, k_{obs} = 1.30 ± 0.03 M^{-1} h^{-1}) and 100 °C (red, k_{obs} = 7.78 ± 0.42 M^{-1} h^{-1}); (b) ^{Me_2}SB(Cp^{Me},I*)ZrCl$_2$ (**3**) (triangle) at 60 °C (green, k_{obs} = 0.31 ± 0.01 M^{-1} h^{-1}), 80 °C (blue, k_{obs} = 1.49 ± 0.02 M^{-1} h^{-1}) and 100 °C (red, k_{obs} = 5.15 ± 0.17 M^{-1} h^{-1}). Polymerisation conditions: two equivalents benzyl alcohol co-initiator, chloroform-d_1, $[LA]_0/[M]_0$ = 50 and $[LA]_0$ = 0.5 M.

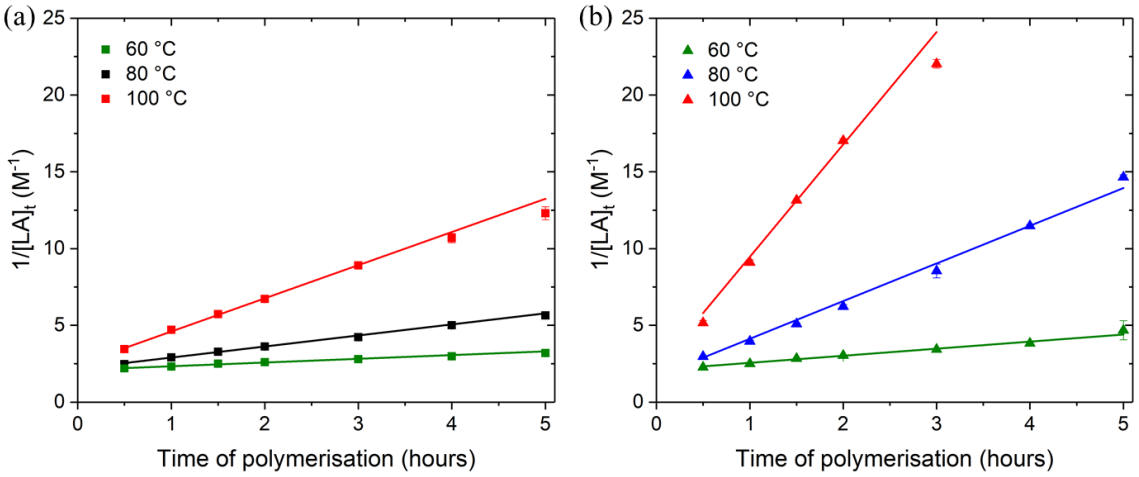


Figure A5.17 $1/[LA]_t$ as a function of time of polymerisation for the ROP of *D*-lactide using (a) ^{Me_2}SB(Cp,I*)ZrCl$_2$ (**1**) (square) at 60 °C (green, k_{obs} = 0.24 ± 0.01 M^{-1} h^{-1}), 80 °C (black, k_{obs} = 0.72 ± 0.03 M^{-1} h^{-1}) and 100 °C (red, k_{obs} = 2.16 ± 0.06 M^{-1} h^{-1}); (b) ^{Me_2}SB(Cp^{Me},I*)ZrCl$_2$ (**3**) (triangle) at 60 °C (green, k_{obs} = 0.46 ± 0.02 M^{-1} h^{-1}), 80 °C (blue, k_{obs} = 2.46 ± 0.06 M^{-1} h^{-1}) and 100 °C (red, k_{obs} = 7.32 ± 0.54 M^{-1} h^{-1}). Polymerisation conditions: two equivalents benzyl alcohol co-initiator, chloroform-d_1, $[LA]_0/[M]_0$ = 50 and $[LA]_0$ = 0.5 M.

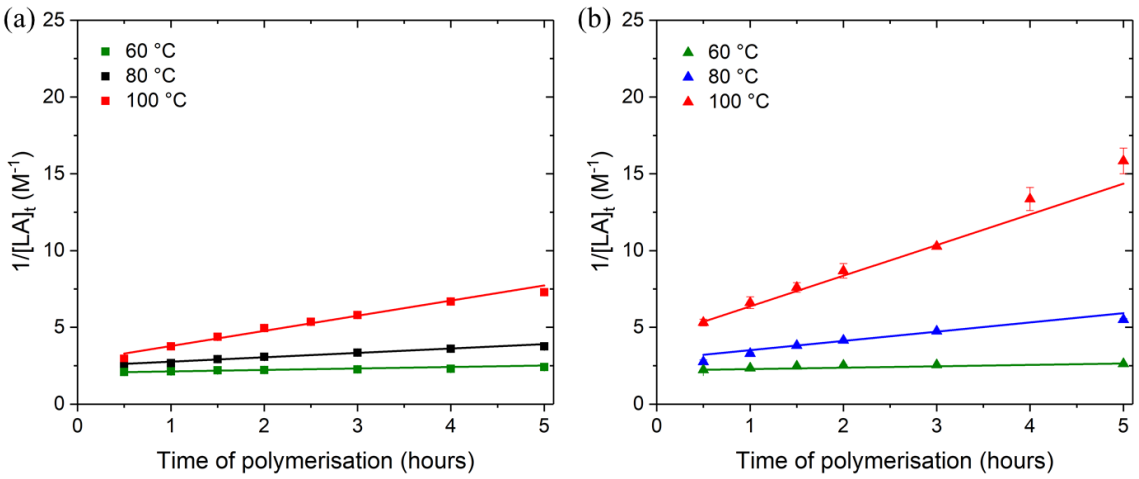


Figure A5.18 $1/[LA]_t$ as a function of time of polymerisation for the ROP of *rac*-lactide using (a) ^{Me_2}SB(Cp,I*)ZrCl$_2$ (**1**) (square) at 60 °C (green, k_{obs} = 0.10 ± 0.01 M^{-1} h^{-1}), 80 °C (black, k_{obs} = 0.29 ± 0.03 M^{-1} h^{-1}) and 100 °C (red, k_{obs} = 0.99 ± 0.05 M^{-1} h^{-1}); (b) ^{Me_2}SB(Cp^{Me},I*)ZrCl$_2$ (**3**) (triangle) at 60 °C (green, k_{obs} = 0.09 ± 0.01 M^{-1} h^{-1}), 80 °C (blue, k_{obs} = 0.60 ± 0.06 M^{-1} h^{-1}) and 100 °C (red, k_{obs} = 2.00 ± 0.10 M^{-1} h^{-1}). Polymerisation conditions: two equivalents benzyl alcohol co-initiator, chloroform-d_1, $[LA]_0/[M]_0$ = 50 and $[LA]_0$ = 0.5 M.

Table A5.2 *L*-, *D*- and *rac*-Lactide polymerisation using ^{Me_2}SB(Cp,I*)$ZrCl_2$ (**1**) at 60, 80 and 100 °C.[a]

Lactide	Temperature (°C)	k_{obs} (M^{-1} h^{-1})	M_n[b] (g mol^{-1})
L	60	0.29 ± 0.01	2156
L	80	1.30 ± 0.03	2782
L	100	7.78 ± 0.42	-
D	60	0.24 ± 0.01	1430
D	80	0.72 ± 0.03	2086
D	100	2.16 ± 0.06	2122
rac	60	0.10 ± 0.01	862
rac	80	0.29 ± 0.03	1060
rac	100	0.99 ± 0.05	1868

(a) Polymerisation conditions: two equivalents benzyl alcohol co-initiator, chloroform-d_1, $[LA]_0/[M]_0 = 50$ and $[LA]_0 = 0.5$ M; (b) determined by GPC analysis calibrated with polystyrene standards in THF (correction factor of 0.58).[11]

Table A5.3 *L*-, *D*- and *rac*-Lactide polymerisation using $^{Me_2}SB(Cp^{Me},I^*)ZrCl_2$ (**3**) at 60, 80 and 100 °C.[a]

Lactide	Temperature (°C)	k_{obs} (M^{-1} h^{-1})	M_n[b] (g mol^{-1})
L	60	0.31 ± 0.01	1884
L	80	1.49 ± 0.02	3183
L	100	5.15 ± 0.17	3380
D	60	0.46 ± 0.02	1784
D	80	2.46 ± 0.06	2325
D	100	7.32 ± 0.54	-
rac	60	0.09 ± 0.01	-
rac	80	0.60 ± 0.06	-
rac	100	2.00 ± 0.10	-

(a) Polymerisation conditions: two equivalents benzyl alcohol co-initiator, chloroform-d_1, $[LA]_0/[M]_0 = 50$ and $[LA]_0 = 0.5$ M; (b) determined by GPC analysis calibrated with polystyrene standards in THF (correction factor of 0.58).[11]

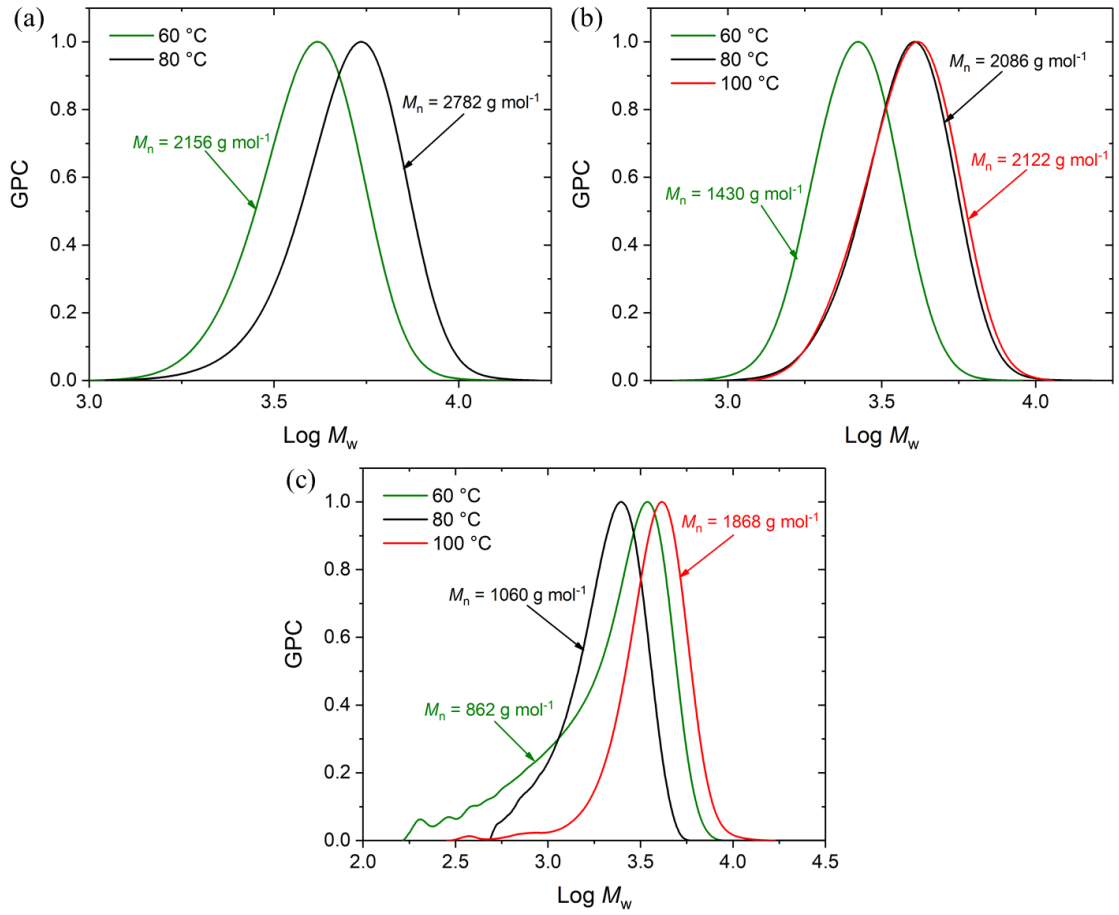


Figure A5.19 GPC plots of the (a) poly-*L*-lactide, (b) poly-*D*-lactide and (c) poly-*rac*-lactide produced using ^{Me_2}SB(Cp,I*)ZrCl$_2$ (**1**) at 60 °C (green), 80 °C (black) and 100 °C (red). Normalised for clarity. Polymerisation conditions: two equivalents benzyl alcohol co-initiator, chloroform-d_1, $[LA]_0/[M]_0$ = 50 and $[LA]_0$ = 0.5 M.

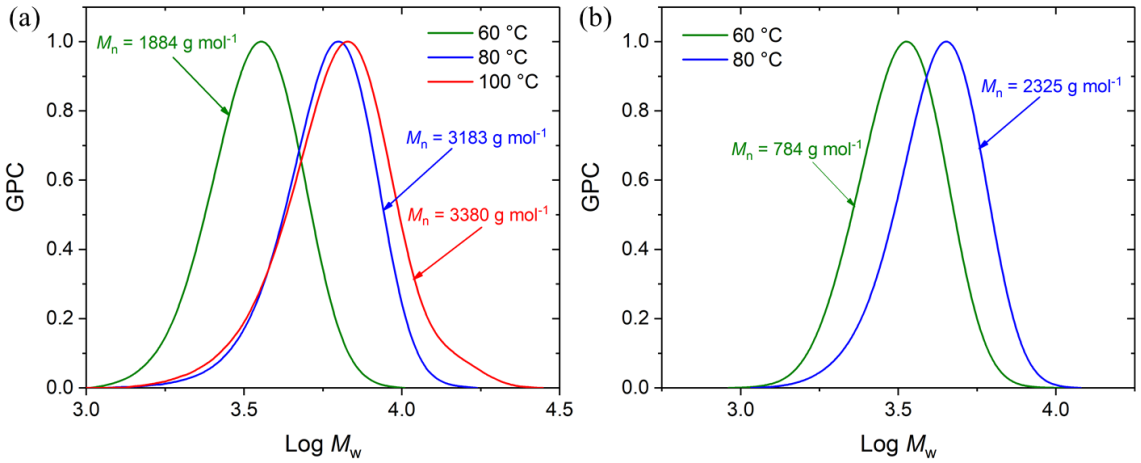


Figure A5.20 GPC plots of the (a) poly-*L*-lactide and (b) poly-*D*-lactide produced using ^{Me_2}SB(Cp^{Me},I*)ZrCl$_2$ (**3**) at 60 °C (green), 80 °C (blue) and 100 °C (red). Normalised for clarity. Polymerisation conditions: two equivalents benzyl alcohol co-initiator, chloroform-d_1, $[LA]_0/[M]_0$ = 50 and $[LA]_0$ = 0.5 M.

References

1. J. C. Wu, B. H. Huang, M. L. Hsueh, S. L. Lai and C. C. Lin, *Polymer*, 2005, **46**, 9784-9792.
2. H. Y. Chen, B. H. Huang and C. C. Lin, *Macromolecules*, 2005, **38**, 5400-5405.
3. P. I. Binda and E. E. Delbridge, *Dalton Trans.*, 2007, 4685-4692.
4. Z. Y. Zhong, P. J. Dijkstra and J. Feijen, *J. Am. Chem. Soc.*, 2003, **125**, 11291-11298.
5. M. D. Jones, S. L. Hancock, P. McKeown, P. M. Schafer, A. Buchard, L. H. Thomas, M. F. Mahon and J. P. Lowe, *Chem. Commun.*, 2014, **50**, 15967-15970.
6. M. D. Jones, L. Brady, P. McKeown, A. Buchard, P. M. Schafer, L. H. Thomas, M. F. Mahon, T. J. Woodman and J. P. Lowe, *Chem. Sci.*, 2015, **6**, 5034-5039.
7. Z. R. Turner, J.-C. Buffet and D. O'Hare, *Organometallics*, 2014, **33**, 3891-3903.
8. L. Clark, G. B. Deacon, C. M. Forsyth, P. C. Junk, P. Mountford, J. P. Townley and J. Wang, *Dalton Trans.*, 2013, **42**, 9294-9312.
9. L. Clark, M. G. Cushion, H. E. Dyer, A. D. Schwarz, R. Duchateau and P. Mountford, *Chem. Commun.*, 2010, **46**, 273-275.
10. M. P. Blake, A. D. Schwarz and P. Mountford, *Organometallics*, 2011, **30**, 1202-1214.
11. M. Save, M. Schappacher and A. Soum, *Macromol. Chem. Phys.*, 2002, **203**, 889-899.